ADVANCES IN CERAMICS - SYNTHESIS AND CHARACTERIZATION, PROCESSING AND SPECIFIC APPLICATIONS

Edited by **Costas Sikalidis**

INTECHWEB.ORG

Advances in Ceramics - Synthesis and Characterization, Processing and Specific Applications
Edited by Costas Sikalidis

Published by InTech
Janeza Trdine 9, 51000 Rijeka, Croatia

Publishing Process Manager Niksa Mandic
Technical Editor Teodora Smiljanic
Cover Designer Jan Hyrat
Image Copyright Alexander Kalina, 2010. Used under license from Shutterstock.com

First published July, 2011
Printed in Croatia

A free online edition of this book is available at www.intechopen.com
Additional hard copies can be obtained from orders@intechweb.org

Advances in Ceramics - Synthesis and Characterization, Processing and Specific Applications, Edited by Costas Sikalidis,
p. cm.
ISBN 978-953-307-505-1

Contents

Preface

Today's advanced ceramics, characterized by improved and specific properties, are studied and/or utilized in a variety of manners in most if not all the scientific and technological research fields, thus ultimately extending an impressive and multilateral contribution via their numerous applications in a broad spectrum of areas.

To obtain such useful materials, conventional methods have been modified and various innovative techniques have been developed many of which over the past recent years.

Some of the most interesting such techniques/methods include: self propagating high temperature synthesis for functional nanostructured materials, combustion and molten salt synthesis for ceramic powders with special characteristics, partial-pressureless sintering and freeze-casting for high strength porous ceramics as well as hot isostatic pressing for tin oxide ceramics with specific optical and other characteristics, precipitation and sol-gel techniques followed by specific thermal treatments for thermoluminescent ceramics, modified sintering techniques for microwave dielectric ceramics, chemical vapor deposition followed by pyrolysis under nitrogen conditions, argon and hydrogen for SiC and other types of ceramic fibers.

Since advanced ceramics demonstrate specific properties, their characterization prefigures the employment of a combination of well known and advanced techniques for material characterization like XRD, TEM-SEM, AFM, TG-DTA etc., with that of specific, advanced and in often times innovative techniques e.g. thermoluminescence.

Furthermore, the demand for advanced ceramics with specific applications enforced the in-depth investigation in addition to the improvement and the optimization of processing techniques as well as the development of new ones. The connection of processes to the obtained properties of the ceramics, as well as with parameters such as efficiency, cost, environmental impact and others, are taken under consideration today much more so than in the past.

Examples of the aforementioned research philosophy in problem-solving approaches include: The healthier and more environmentally friendly production at lower and more competitive costs for the nitride-based ceramics by aqueous processing that

needs to be investigated considering the susceptibility to hydrolysis of the nitride powders, particularly in the case of aluminium nitride. The shape and size optimization problem of ceramic components for space and terrestrial telecommunication systems, which could be tackled by applying sophisticated design methodologies and manufacturing technologies like the 3D stereolithography based rapid prototyping technique. The high sintering temperature problem that precludes ZnNb-oxide ceramics (used in the new era of communication technology) application potential in the multilayer technologies (e.g. low temperature co-fired ceramics), which can be overcome by the usage of nano-sized ZnNb-oxide powders instead of micron-size powders. The case of grinding optimization in which several aspects and parameters of the process need to be carefully considered which include but are not limited to: the properties of grinding media and the work piece, the energy required and its transformation to heat, the temperature generated and its affection of the machined part, the possible generation of undesired stresses. The potential of ceria-based and related materials as solid electrolytes for alternative solid oxide fuel cells, as catalysts etc, needs to be connected to their redox behaviour and the corresponding effects imposed by fuels and fuels conditions. The alloy reinforcement by the addition of ceramic material to the molten metal, needs to overcome matching problems of ceramic materials and molten metals by way of adding the ceramic particles in a complex carbide form preparing a master alloy which in turn will be further used to produce composite castings or parts composed e.g. by a matrix of austenite and discrete carbide particles. The problems arising in certain applications of sintering, which consists the main operation in powder technology, can be identified and described using modern techniques based on the Atomic Force Microscopy, by determining the dihedral surface angle of defined compacts sintered in solid-phase under certain conditions. The surface modification and properties induced by a laser beam in pressings of ceramic powders.

Finally, research on new production technologies and on new raw materials led to the development of many of today's advanced ceramics with unique properties suitable for modern applications, i.e. research on deposition technology of slurries or suspensions constituted of ceramic powders, dispersants, binders, solvents and plasticizers for the preparation of solid oxide fuel cells (environmentally friendly energy conversion systems to produce electrical energy with minimal environmental impact) and of perovskite type ceramics as cathodes, lanthanum strodiun manganites for high temperature cells, zirconia and ceria based ceramics as well as lanthanum gallate as electrolytes in the cells, yttria stabilized zirconia as anodes etc.; research on economical and efficient fabrication techniques and on the properties of many ceramic materials and components for lasers applications; research on fabrication, characterization and modeling of protonic ceramics for applications in intermediate temperature fuel cells and steam electrolyzers, hydrogen separation membranes, and various membrane reactors for chemical synthesis.

The current book contains twenty-two chapters and is divided into three sections.

Section I consists of nine chapters which discuss synthesis through innovative as well as modified conventional techniques of certain advanced ceramics (e.g. target materials, high strength porous ceramics, optical and thermo-luminescent ceramics, ceramic powders and fibers) and their characterization using a combination of well known and advanced techniques.

Section II is also composed of nine chapters, which are dealing with the aqueous processing of nitride ceramics, the shape and size optimization of ceramic components through design methodologies and manufacturing technologies, the sinterability and properties of ZnNb oxide ceramics, the grinding optimization, the redox behaviour of ceria based and related materials, the alloy reinforcement by ceramic particles addition, the sintering study through dihedral surface angle using AFM and the surface modification and properties induced by a laser beam in pressings of ceramic powders.

Section III includes four chapters which are dealing with the deposition of ceramic powders for oxide fuel cells preparation, the perovskite type ceramics for solid fuel cells, the ceramics for laser applications and fabrication and the characterization and modeling of protonic ceramics.

2011

Constantinos A. SIKALIDIS
Department of Chemical Engineering
Aristotle University of Thessaloniki,
Grece

Part 1

Synthesis and Characterization of Advanced Ceramic Materials

1

Advanced Ceramic Target Materials Produced by Self-Propagating High-Temperature Synthesis for Deposition of Functional Nanostructured Coatings - Part 1: Four Elements and Less Systems

Evgeny A. Levashov, Yury S. Pogozhev and Victoria V. Kurbatkina
National University of Science and Technology "MISIS", Russia

1. Introduction

An increase in the exploitation characteristics of various machines and tools is a key engineering–technical problem; solving it is directly associated with the introduction of new functional materials and coatings with improved properties. The industry of nanosystems is a high-priority branch in the development of science and technology that affects almost all scientific directions and spheres of activity.

Surface engineering, as applied to the fabrication of multifunctional nanostructured films (MNFs) whose characteristic crystallite size is from 1 nm to several tens of nanometers, plays an important role in the science of nanomaterials and nanotechnologies. The high volume fraction of interfaces with a strong bond energy, the absence of dislocations inside crystallites, the possibility of obtaining films with a controllable ratio of volume fractions of crystalline and amorphous phases, and the variation in the mutual solubility of the elements in interstitial phases are factors that lead to unique properties of nanostructured films and their multifunctionality which manifests itself in high values of hardness, elastic recovery, strength, thermal stability, heat resistance and corrosion stability. MNFs find application in the field of surfaces protection which are subjected to the simultaneous effect of elevated temperature, aggressive media, and various kinds of wear. These are, first and foremost, cutting and stamping tools; forming rolls; parts in aviation engines, gas turbines, and compressors; slider bearings; nozzles for the extrusion of glass and mineral fiber; etc. MNFs are also irreplaceable in the development of a new generation of biocompatible materials, namely, orthopedic implants, implants for craniofacial and maxillary surgery, fixations for the neck and lumbar spines, etc [1–3].

Currently, in order to obtain MNFs, chemical deposition methods, including plasma-activated methods, and physical deposition methods, such as magnetron sputtering, condensation with ion bombardment, and electron-beam and ion-beam sputtering, are widely used. The advantage of the magnetron sputtering technology is the insignificant heating of the substrate to 50–250°C [4]. This allows one to deposit a coating on almost any

material. In addition, hard and superhard MNFs with a different level of elastic–plastic characteristics can be deposited by this method [5].

The possibilities of magnetron sputtering can be substantially extended due to the use of composite multicomponent cathode targets obtained by self-propagating high-temperature synthesis (SHS) [6–8]. SHS-technology allows one to produce a wide spectrum of targets based on ceramics, metal ceramics, and intermetallic compounds. One fundamental distinction of sputtering processes of composite and metal targets is in fact that, in the former case, the substance is transported by the uniform flow of metal and nonmetal atoms and ions. In this case, all elements necessary for the formation of the coating, including nonmetal coatings (C, O, N, P), can be sputtered from one target [9, 10]. In sputtering installations, both the disc and planar–extended rectangular segment SHS targets can be used [11].

The SHS targets passed successful tests in various types of installations, namely, dc magnetron systems (MS) [1, 9, 12–14, 15–17, 18–24], high-frequency [25] and pulsed MS [11], MS with additional inductively coupled plasma [26], and arc evaporators [27].

Over the last several years, using the magnetron sputtering of SHS targets, hard coatings were obtained in the systems Ti–Si–N [9, 12, 28], Ti–B–N [10, 13, 29, 30], Ti–Si–B–N [4, 13, 29], Ti–Si–C–N [13, 29], Ti–Al–C–N [13, 29], Ti–C–N [31], Ti–Mo–C–N [31], Ti–Al–B–N [32], Ti–Al–Si–B–N [17, 18, 30], Ti–Cr–B–N [10, 12, 14, 17, 30], Cr–B–N [10, 12, 33, 34], Ti–Zr–C–O–N [19], Ti–Ta–Ca–P–C–O–N [23, 24], Ti–Cr–Al–C–N [35, 36], etc.

Taking into account the increase in demand for various compositions of composite targets, we decided that it is important to present the data on the features of the synthesis of the most interesting and necessary classes of SHS targets differing in regards to their combustion mechanisms and structure formation in the form of the review. In this work, we present both recently obtained results and those that we have not yet published.

2. Ceramic materials in system Ti-Cr-Al-C

Let us consider the class of refractory oxygen-free compounds possessing a layered structure and a unique combination of metal and ceramic properties, which are generally described by the formula $M_{n+1}AX_n$, where M is the transition metal, A is the preferentially subgroup IIIA or IVA element of the periodic table, and X is carbon or nitrogen [37]. They are characterized by a low density; high thermal conductivity, electrical conductivity, and strength; reduced (when compared with ceramic materials) elasticity modulus; excellent corrosion resistance in aggressive external media; resistance to high-temperature oxidation; and resistance to thermal shocks. However, due to their layered structure and by analogy with hexagonal boron nitride and graphite, these materials are easily subjected to mechanical treatment [38]. Like ceramics, they have a high melting point, and they are sufficiently stable at elevated temperatures up to 2000°C [39].

The main problem in obtaining the $M_{n+1}AX_n$ phases (MAX phases) is that the final products contain impurity phases (for example, TiC, $TiAl_3$, Cr_2Al, Cr_7C_3, etc), which exert a substantial effect on the exploitation characteristics of the ceramic material. The main cause of the phase nonuniformity in the synthesis of similar compounds is multistage solid-phase interaction, when thermodynamically stable compounds such as titanium carbide are formed during intermediate stages. In addition, local violations in the stoichiometric composition take place. They are associated, for example, with the partial evaporation of aluminum at high temperatures. However, we can confidently predict that using various

methods to obtain them, as well as varying the phase and granulometric compositions of the starting components of the mixture, allows one to extend the range of exploitation properties and the usage region of the $M_{n+1}AX_n$ -based materials.

The works devoted to the use of the SHS method to fabricate $M_{n+1}AX_n$ -based materials in the Ti_3AlC_2 [10, 11], Ti_2AlC [12, 13], and Cr_2AlC ternary systems [2, 14, 40] and in the $Ti_{2-x}Cr_xAlC$ quaternary system [41, 42] are well known. An investigation of the features of the structural and phase formation of the SHS compact synthesis products, depending on the preparation method of the reactionary mixture and the ratio of main reagents (titanium, chromium, aluminum, and carbon), remains topical.

To obtain new composite materials (CM), we used the technology of the forced SHS pressing based on the sequential performance of the SHS and pressing of hot products of the synthesis to the virtually pore-free state. We used PTS titanium powders (TU (Technical Specifications) 14-1-3086-80), PH-1S chromium powders (GOST (State Standard) 5905-79), ASD-1 aluminum powders (TU-48-5-226-87), and P804T ash (TU 38-1154-88) as starting mixture components.

All the compositions of the materials under study in this work are described by the general formula $Ti_{2-x}Cr_xAlC$, where x is the mixture parameter. The experimental compositions of the powder mixtures are presented in Table 1.

Experimental sample	X	Content of initial components, wt %			
		Ti	Cr	Al	C
Ti_2AlC	0	69,7	-	21,6	8,7
$Ti_{1,5}Cr_{0,5}AlC$	0,5	51,5	18,6	21,3	8,6
TiCrAlC	1	33,8	36,7	21,0	8,5
$Ti_{0,5}Cr_{1,5}AlC$	1,5	16,7	54,1	20,8	8,4
Cr_2AlC	2	-	71,3	20,5	8,2

Table 1. Composition of the green mixtures

The procedures for preparing and investigating the experimental samples, as well as a description of the equipment that was used, are presented in detail in [41], where the mechanism of the phase and structure formation of the synthesis products in the ternary (Ti–Al–C) and quaternary (Ti–Cr–Al–C) systems was also investigated. Using a differential thermal analysis, two main stages of formation of complex carbides in the Ti–Al–C system upon heating in a temperature range of 298–1673 K are revealed.

The first stage is associated with the formation of the Ti_yAl_z intermetallic compounds according to the general formula

$$yTi + zAl \rightarrow Ti_yAl_z, \quad (1)$$

and titanium carbide is formed at the second stage with its subsequent interaction with the intermetallic compounds and aluminum melt with the formation of the $Ti_{y+1}AlC_z$ ternary compounds:

$$TiC_y + Ti_yAl_z \rightarrow Ti_{y+1}AlC_z, \quad (2)$$

$$TiC_y + Al \rightarrow Ti_{y+1}AlC_z. \quad (3)$$

The mechanism of formation of the $Ti_{y+1}AlC_z$ compounds during the synthesis in the combustion mode somewhat differs from that described above, which is associated with the higher combustion rate (U_c) and temperature (T_c). Since under the initial conditions $T_0 = T_{room}$, the adiabatic temperature (T_c^{ad} = 1773 K) is lower than the melting point of titanium (1933 K) and its interaction with carbon proceeds through the aluminum melt (liquid phase), which is, in essence, the "diffusion accelerator" in this case. When using the "chemical heater" (the mixture of the Ti, B, and C powders), T_0 increases, which is accompanied by an increase in T_c^{ad} to 2290 K (Table 2). After melting titanium, the reaction surface is formed via spreading of the Ti–Al melt over the ash surface, carbon is saturated by this melt, and titanium carbide grains are isolated from it. In this case, the $Ti_{y+1}AlC_z$ phases are formed from the melt at the stages of both the primary and secondary structure formation.

Experimental sample	X	T_0, K	U_c, cm/s	T_c^{ad}, K	T_c^{ad*}, K
Ti_2AlC	0	1000	2.1	1775	2282
$Ti_{1,5}Cr_{0,5}AlC$	0,5	1050	1.5	1773	2290
TiCrAlC	1	1100	0.9	1776	2289
$Ti_{0,5}Cr_{1,5}AlC$	1,5	1550	1.5	1235	2284
Cr_2AlC	2	2100	1.8	861	2157

Note: T_c^{ad*} is the adiabatic temperature of the combustion allowing for the heat release from the "chemical heater" necessary for the steady-state mode of combustion.

Table 2. Combustion parameters

It is evident from the data of Table 2 that the adiabatic combustion temperature of the mixtures calculated by the THERMO program is almost identical for the formation of Ti_2AlC, $Ti_{1.5}Cr_{0.5}AlC$, and TiCrAlC. As the chromium content in the mixture increases (the compositions $Ti_{0.5}Cr_{1.5}AlC$ and Cr_2AlC), the temperature decreases. It's addition also exerts a similar effect on the combustion rate. The maximal value of U_c (2.1 cm/s) is observed for the synthesis of Ti_2AlC. The introduction of the chromium powder into the green mixture to the molar ratio Ti : Cr = 1 : 1 causes a decrease in U_c to 0.9 cm/s, while an increase in the initial SHS temperature is favorable to an increase in the combustion rate during the synthesis of $Ti_{0.5}Cr_{1.5}$ AlC and Cr_2AlC to 1.5 and 1.8 cm/s, respectively.

The results of an X-ray phase analysis of the products are presented in Table 3 [41]. At x = 0, they include two types of the $M_{n+1}AX_n$ phases, namely, Ti_3AlC_2 (80%) and Ti_2AlC (16%) with the hexagonal crystal lattice. Both phases are formed as a result of the chemical interaction between titanium carbide and the melt of aluminum and titanium. Analogously to [46], the products also contain a small amount (4%) of nonstoichiometric titanium carbide TiC_y with the lattice constant 0.4312 nm and traces of free aluminum (~1%), the presence of which indicates the incomplete transformation by reactions (2) and (3) due to the multistage solid-phase interaction of thermodynamically stable compounds.

Upon the introduction of the chromium powder into the initial mixture to the molar ratio Ti: Cr = 1.5:0.5 (x = 0.5), the $M_{n+1}AX_n$ phase with the stoichiometric composition Ti_3AlC_2 is formed in an amount of 52% with the lattice constant somewhat increased compared with the phase of the same composition at x = 0. The lattice constant of titanium carbide also increases in this case, which is associated with the formation of complex titanium–chromium carbide (Ti,Cr)C in the combustion wave due to the partial substitution of

titanium atoms in the TiC lattice by the Cr atoms. This complex carbide then interacts with the Ti–Al melt with the formation of the $M_{n+1}AX_n$ phase with an increased lattice constant. In addition to the main phases, chromium aluminide Cr_4Al_9 (12%), which is usually present as the intermediate phase, is found in the product [42, 43].

The synthesis products at x = 1 possess the largest distinction with respect to the phase composition compared with other materials under study. It is evident from Table 3 that their main phases are TiC, Cr_4Al_9, and Cr_2Al, while the content of the $(Cr,Ti)_2AlC$ phase is only 8%.

Experimental sample	X	Phase composition	Amount of the phase, wt %	Lattice constant, nm
Ti_2AlC	0	TiC	4	A = 0,4312
		Ti_3AlC_2	80	A = 0,3069 C = 1,8524
		Ti_2AlC	16	A = 0,3062 C = 1,3644
$Ti_{1,5}Cr_{0,5}AlC$	0,5	TiC	36	A = 0,4322
		Ti_3AlC_2	52	A = 0,3071 C = 1,8556
		Cr_4Al_9	12	A = 0,9054
TiCrAlC	1	TiC	66	A = 0,4314
		$(Cr,Ti)_2AlC$	8	A = 0,2866 C = 1,2867
		Cr_4Al_9	20	A = 0,9040
		Cr_2Al	6	A = 0,2997 C = 0,8709
$Ti_{0,5}Cr_{1,5}AlC$	1,5	TiC	19	A = 0,4308
		$(Cr,Ti)_2AlC$	54	A = 0,2864 C = 1,2833
		Cr_2Al	22	A = 0,3005 C = 0,8677
		Cr_7C_3	5	A = 0,4517 B = 0,7015 C = 1,2167
Cr_2AlC	2	Cr_2AlC	98	A = 0,2858 C = 1,2815
		Cr_7C_3	2	A = 0,4517 B = 0,7014 C = 1,2166

Table 3. Results of an X-ray phase analysis of the synthesis products in the Ti–Cr–Al–C system

With a further increase in the chromium concentration in the mixture (x = 1.5), the $M_{n+1}AX_n$ phase of the $(Cr,Ti)_2AlC$ composition (54%) is formed. In this case, the content of titanium carbide decreases to 19% upon an increase in the content of chromium aluminide Cr_2Al to 22%, which also indicates the incompleteness of diffusion in the combustion wave. It should

be noted that the largest amount of chromium carbide Cr_7C_3, which is less stable than the $M_{n+1}AX_n$ phase, is present in this sample. Its presence leads to the embrittlement of the material and the worsening of its strength characteristics; therefore, it is undesirable.

The results of an X-ray phase analysis of the synthesis products at x = 2 showed that they are virtually single-phase and include 98% Cr_2AlC.

Thus, the highest content of the $M_{n+1}AX_n$ phase is achieved for the samples corresponding to the stoichiometric compositions Ti_2AlC and Cr_2AlC, in which only one main element, namely, titanium or chromium, is present.

Figure 1 shows the microstructures of the fractures of the material under study in the Ti–Cr–Al–C system. They are similar for all the alloys (Figs. 1a, 1b, 1d, 1e), except for the sample synthesized at x = 1.

The microstructure of the Ti_2AlC product obtained from the chromium-free mixture at x = 0 preferentially consists of two types of $M_{n+1}AX_n$ phases, namely, Ti_3AlC_2 and Ti_2AlC, which have a characteristic layered (terrace) structure with a small amount of rounded TiC grains (Fig. 1a) with an average particle size of ~3 μm. A more detailed investigation of the alloy microstructure showed [38, 41] that the grains of the $M_{n+1}AX_n$ phases consist of numerous 100–300 nm thick layers (Fig. 2a).

The structure of the products at x = 0.5 differs somewhat from the sample containing no chromium. Here, we clearly observe rounded TiC grains with an average size of 1.5 μm, as well as the inclusions of the Cr_4Al_9 phase (Fig. 1b). The content of the $M_{n+1}AX_n$ phase is lower in this case.

The largest structural distinctions are characteristic of the sample with the molar ratio Ti:Cr = 1:1 (see Fig. 1c). Here, the main phase is titanium carbide with an average grain size of 0.5 μm. In addition, chromium aluminide is observed and, in a small amount, $(Cr,Ti)_2AlC$.

We also found the grains of the $(Cr,Ti)_2AlC$ phase with a characteristic laminate structure in the structure of the alloy at x = 1.5. They are surrounded by grains of titanium carbide, chromium aluminide Cr_2Al, and a small amount of chromium carbide Cr_7C_3 (see Fig. 1d).

Figure 1e shows the microstructure of the synthesis products at x = 2. It is evident that the material under study is highly structurally uniform and almost completely consists of grains of the Cr_2AlC phase with different spatial orientations. However, Cr_7C_3 inclusions are sometimes present on their surface; their amount is ~2%.

Taking into account the positive experience of applying mechanical activation (MA) to the problems of increasing the transformation depth and structural and phase uniformity of the combustion product [44–47], in order to increase the content of the MAX phases, the green mixtures were subjected to MA in a planetary mill. According to the results of our studies, it was established that MA provides an increase in the content of the MAX phases.

In Table 4, the green mixture prepared in a ball mill without MA by procedure [41] is denoted as the NA, while the mixtures after mechanical activation in various modes are denoted as MA1, MA2, and MA3. For example, if the fraction of the MAX phase in the sample with x = 1 was no higher than 8% [41], then it increased to 45% after MA3 (for 60 min). This effect is due to the complex influence of MA on the structure, properties, and reactivity of the mixture.

As shown above, the chromium addition into the Ti–Al–C mixture complicates the synthesis of the materials, which takes place firstly because the Cr_2AlC phase has a very low adiabatic combustion temperature (see Table 2). For this reason, we failed to implement SHS in the mixtures with x = 1 and 2 at the initial temperature close to room temperature. The mechanical activation allowed us to increase the reactivity of green mixture. A special series

of experiments on determining the combustion temperature of the ternary and quaternary MA mixtures was devoted to this problem. It was established that, at T_0 = 295 K, only MA mixtures with a high titanium content (x = 0 and 0.5) burn. We also failed to achieve SHS at room temperature in the MA mixtures with x = 1.0, 1.5, and 2.0.

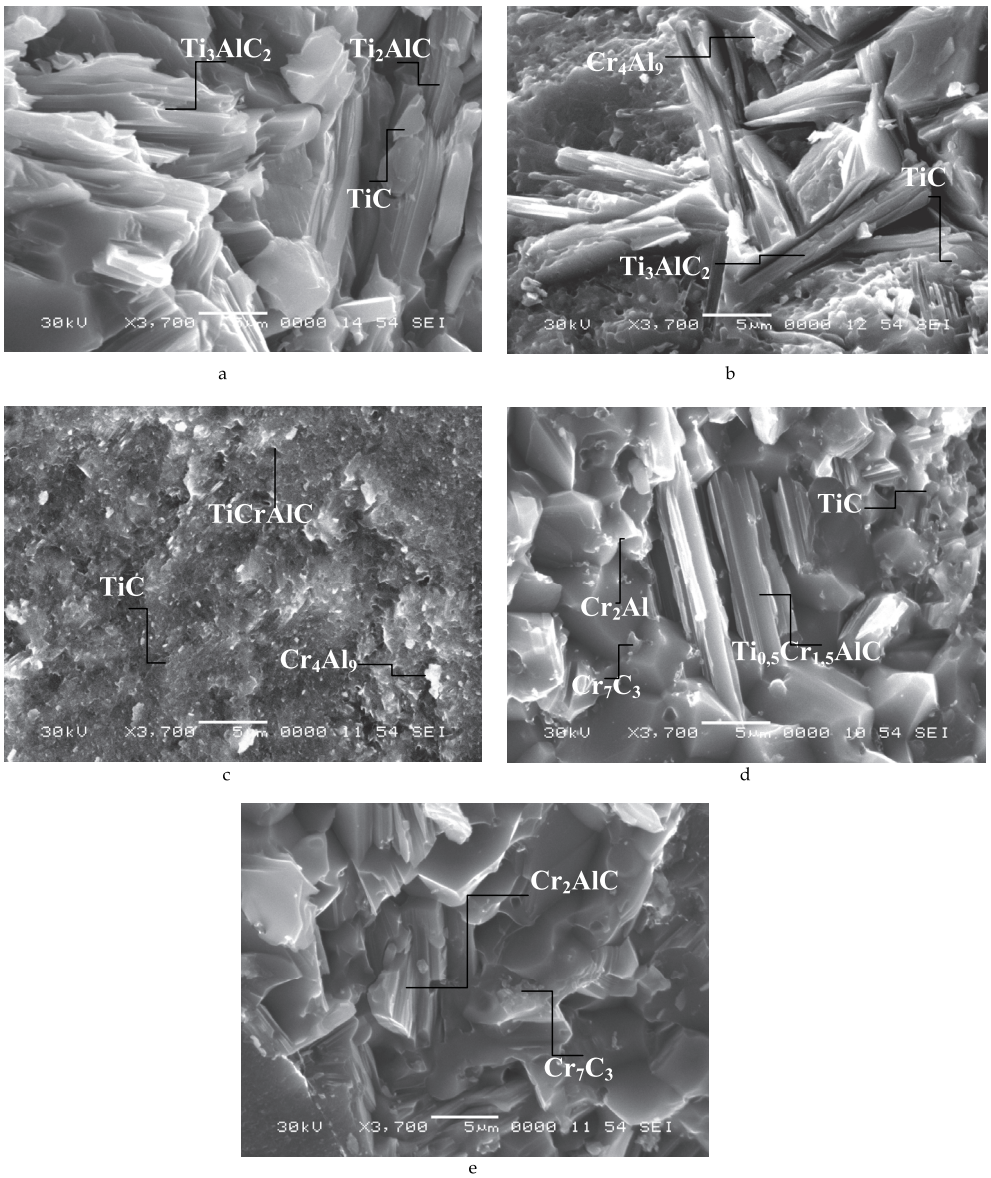

Fig. 1. Microstructure of the synthesis products in the Ti–Cr–Al–C system at various values of the mixture parameter x = (a) 0, (b) 0.5, (c) 1.0, (d) 1.5, and (e) 2.0.

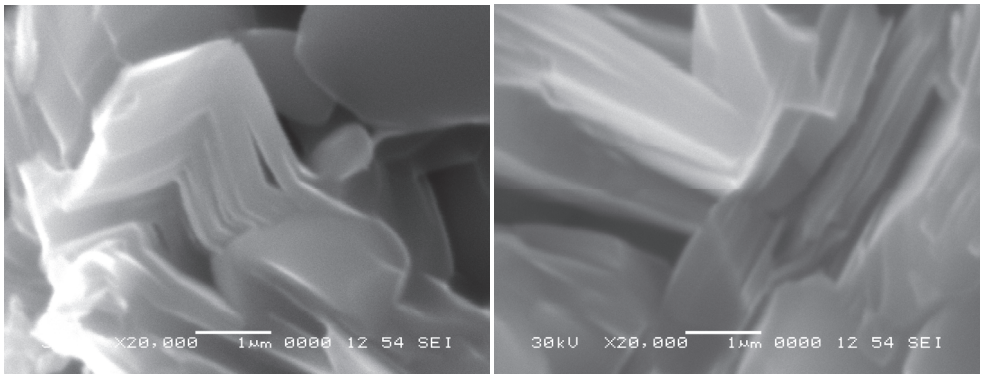

a b

Fig. 2. Microstructure of the Ti_2AlC (a) alloy and Cr_2AlC (b) alloy.

When analyzing the known mechanisms of formation of the MAX phases [38, 39, 41], as well as allowing for the combustion experiments, we can assume that these phases are formed due to the solid-phase diffusion. In this case, the structural factors are of importance, namely, the phase size and the component distribution throughout the mixture volume. We selected the MA modes starting from this point. The contribution of MA to the ternary mixtures with x = 2 (Cr_2AlC) and x = 0 (Ti_2AlC) consisted of intensifying the phase content and increasing the fraction of Ti_2AlC from 16 to 73%. The largest effect was observed for quaternary mixtures with x = 1.5, 1.0, and 0.5. Figure 3 shows the morphology of the starting reagents, and Fig. 4 shows the structure of the mixture with x = 0.5 after MA. The nonactivated mixture consists of the dissimilar Ti, Cr, and Al powders and ash with the scale of the heterogeneity scale close to the characteristic size of metal particles.

After 28 min long MA, the mixture structure undergoes substantial variations. Due to intense plastic deformation, agglomerated particles with a layered structure (Fig. 4a, point 1) appear. They are based on the mixed Ti and Cr layers, while Al and C are distributed over the surface of the layers. However, the number of the layered particles after MA is small. Most of them are the deformed particles of the starting chromium and titanium powders (see Fig. 4a, points 2 and 3). As the MA time increases to 60 min, the fraction of the agglomerated particles reaches 90–95%, while the average agglomerate size decreases to 10 μm (Fig. 4b). The separate layers are not thicker than several micrometers.

The structural variations in the mixture substantially affect the phase composition of the synthesis products. This is evident from Table 4, in which the composition of the samples is obtained by SHS pressing technology from the preliminarily activated mixtures by the modes providing the maximal amount of the MAX phase in the final product.

It is noteworthy that, depending on the MA mode, we can obtain composite materials with different compositions. Figure 5 shows the microstructures of mixtures with x = 1.5 obtained under various MA modes and the corresponding compositions of the SHS products. According to MA1 and MA3 modes, all the components are charged simultaneously and activated in a planetary mill for 18 and 60 min, respectively. Sequential charging is performed in the MA2 mode. Initially, chromium is activated with carbon and then titanium and aluminum are sequentially added. Similarly to MA1, the total duration of the treatment is 18 min. The structure of the mixture in the MA1 mode contains uniaxial agglomerates

Experimental sample	X	Mixture preparation	Content of the phases after SHS pressing, wt %	$\sigma_{bend.}$, MPa	E, GPa	HV, GPa	ρ_t, g/cm^3	$P_{res.}$, %
Ti_2AlC	0	NA	Ti_2AlC - 15 Ti_3AlC_2 -80 TiC -4 Al - 1	312	477	4,4	3.90	11,2
		MA1	Ti_2AlC - 73 Ti_3AlC_2 - 16 TiC - 2 Ti Al_2 - 9	388	386	3.9	4,1	7,2
		MA2	Ti_2AlC - 30 Ti_3AlC_2 65 TiC - 5	401	443	5,5	4,15	5,8
$Ti_{1,5}Cr_{0,5}AlC$	0,5	NA	Ti_3AlC_2 - 52 TiC - 36 Cr_4Al_9 - 12	286	434	5,7	4.30	5,5
		MA2	Ti_3AlC_2- 55 $(TiCr)_2AlC$ - 2 TiC - 29 Cr_4Al_9 - 7 Cr_2Al - 7	254	517	4,7	4,40	6,5
TiCrAlC	1	NA	$(Cr,Ti)_2AlC$ -8 TiC - 66 Cr_4Al_9 - 20 Cr_2Al - 6	129	438	13,5	4,70	4,1
		MA3	$(Cr,Ti)_3AlC_2$ - 45 TiC - 43 Cr_4Al_9 - 12 Cr-Ti - 1	137	334	7.5	4,40	5,4
$Ti_{0,5}Cr_{1,5}AlC$	1,5	NA	Cr_2AlC - 54 TiC - 19 Cr_7C_3 - 5 Cr_2Al - 22	222	507	7,1	5.00	4,9
		MA3	Cr_2AlC - 17 $(Ti,Cr)_3AlC_2$ - 60 $(Cr,Ti)_2AlC$ - 23	383	441	5.1	4,42	4,3
Cr_2AlC	2	NA	Cr_2AlC - 98 Cr_7C_3-2	459	573	4,7	4.90	4,7
		MA1	Cr_2AlC-100	462	516	4,0	5,02	6,8

Note: σ_{bend} is the ultimate bending strength, E is the elasticity modulus, HV is the Vickers hardness, ρ_t is the true density determined using the helium pyknometer, and P_{res} is the residual porosity.

Table 4. Phase composition and physical and mechanical properties of the synthesis products in the Ti–Cr–Al–C system

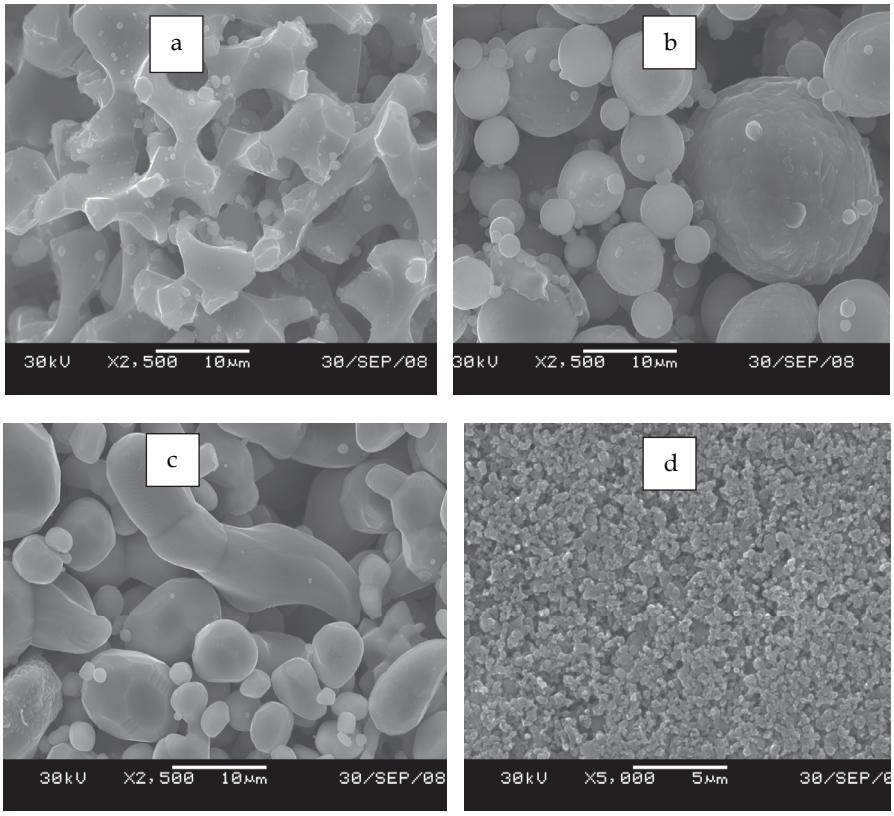

Fig. 3. Structures of the initial powders: (a) the PTS titanium, (b) the ASD_1 aluminum, (c) the PKh-1S chromium, and (d) the P804T ash.

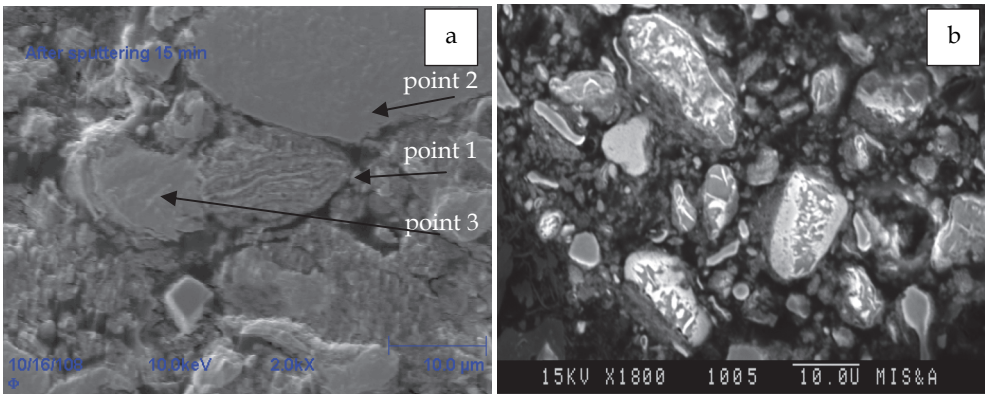

Fig. 4. Structure of the green mixture at x = 0.5 after MA for 28 min (a) and 60 min (b).

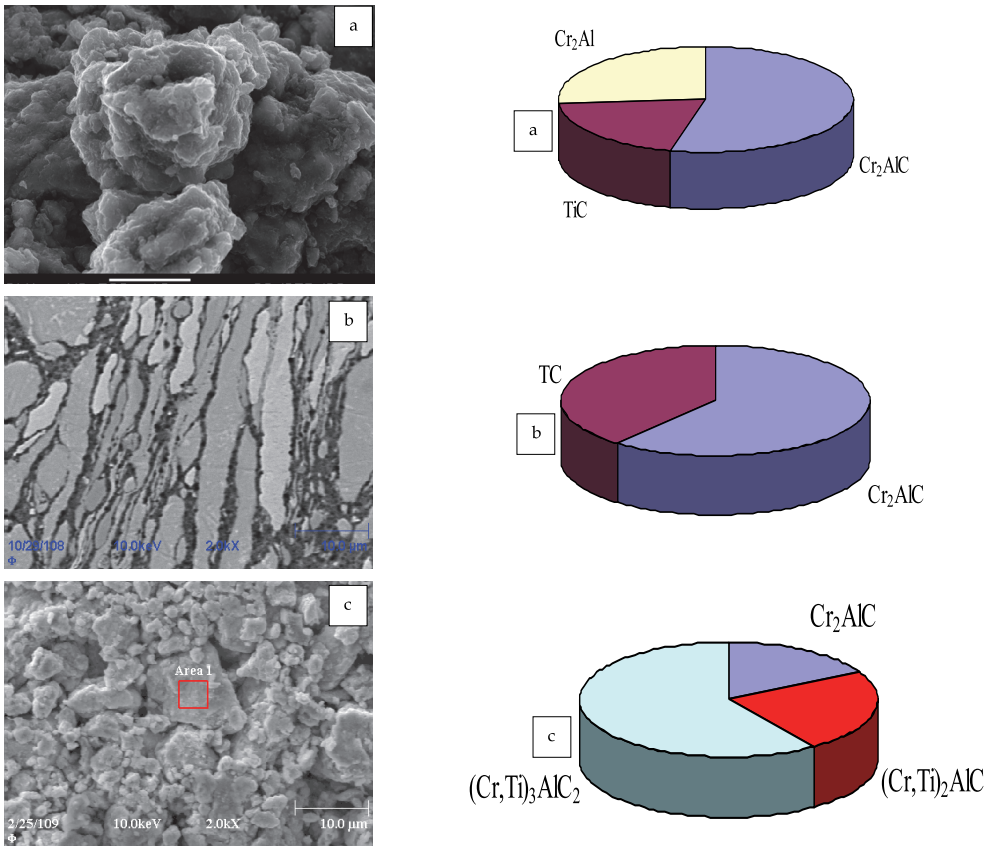

Fig. 5. Structure of the mechanically activated mixture (x = 1.5) and the composition of synthesis products. MA1 (a), MA2 (b), and MA3 (c).

with an average size of >10 μm (see Fig. 5a). The layered structure is observed for the agglomerates in the MA2 mode (see Fig. 5b). The thickness of titanium and chromium layers is from 2 to 10 μm that of aluminum is less than 0.5–1.0 μm, and that of carbon (ash) is less than 100 nm. In the MA3 mode, the mixture has a fine well-mixed structure. The average size of the agglomerates is 10–20 μm, and the size of particles or layers is mostly <1.0 μm. The amount of agglomerated particles is ~90–95% of their total amount. In the first case, the main phase of the synthesized products is Cr_2AlC (54%), although the TiC (21%) and Cr_2Al (23%) are also present. In the second case, chromium aluminide is absent; the Cr_2AlC content increases to 66%, and that of TiC increases to 34%. In the MA3 mode, the sample consists of three MAX phases: $(Cr,Ti)_3AlC_2$, Cr_2AlC, and $(Cr,Ti)_2AlC$. As is evident from the data of Table 4, none of considered MA modes allowed us to obtain samples completely consisting of MAX phases for the mixture with x = 0.5. The maximal amount of the Ti_3AlC_2 phase was 55%. In addition, TiC and chromium aluminides are always present the samples. A similar situation is also observed for the mixture with x = 1. The $(Cr,Ti)_3AlC_2$ content does

not exceed 50%. It is possible that the phase composition is close to the equilibrium composition for these mixture compositions.

As is evident from the data of Table 4, none of the considered MA modes allowed us to obtain samples completely consisting of MAX phases for the mixture with x = 0.5. The maximal amount of the Ti_3AlC_2 phase was 55%. In addition, TiC and chromium aluminides are always present the samples. A similar situation is also observed for the mixture with x = 1. The $(Cr,Ti)_3AlC_2$ content does not exceed 50%. It is possible that the phase composition is close to the equilibrium composition for these mixture compositions.

Analogously with [41], properties of synthesized compact products obtained from mechanically activated and nonactivated mixtures were investigated. The materials with the maximal content of the MAX phase are of greatest interest because the properties of the bulk materials with a characteristic laminate structure have been insufficiently studied. It is evident from Table 4 that studied characteristics depend strongly on the phase composition. If a single-phase material, for example, Cr_2AlC (x = 2), is obtained by the synthesis, then characteristics (density, strength, elasticity modulus, hardness, and heat resistance (Fig. 6)) have close values. On the contrary, if phase compositions of samples differ, the difference in properties can be considerable at the same mixture parameter.

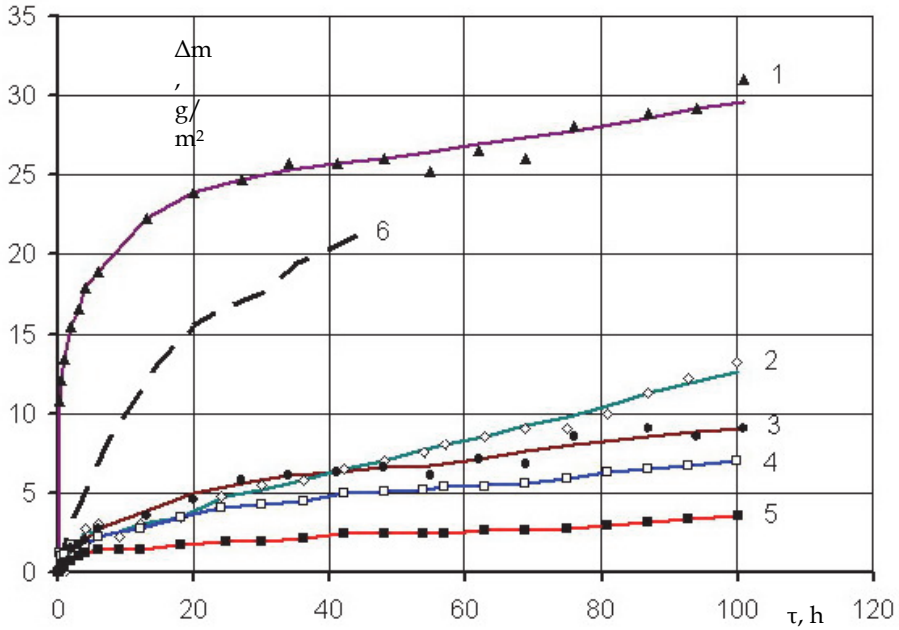

Fig. 6. Time dependence of the variation in the weight of the $Ti_{2-x}Cr_xAlC$ samples at T = 1273 K. (1) x = 0 (NA), (2) 1.0 (NA), (3) 1.5 (NA), (4) 2.0 (NA), (5) 2.0 (MA1), and (6) 83%TiC–17%Cr [48].

Materials with x = 2.0 and 1.5 possess a rather high strength at a large elasticity modulus. Low strength characteristics are mentioned for alloys with a high TiC content. The elasticity modulus was determined from the measurement data of the strength by the three-point

bending method. These results correlate well with the data [38]. The most important service characteristic of this construction ceramic is high-temperature oxidation resistance. Investigations in [41] were carried out at T = 1023 K. Our tests at T = 1273 K developed them. Their results are shown in Fig. 6.

It is seen from curves in Fig. 6 that an increase in the chromium concentration is favorable to a decrease in the weight increment of samples and their oxidation rate and, consequently, to an increase in their heat resistance. The titanium-free Cr_2AlC sample (at x = 2) possesses the highest high-temperature oxidation resistance (Fig. 6, curve 4). When investigating the materials obtained from the activated charge, it was established that their heat resistance is in general somewhat higher than that of materials not subjected to MA and alloys with a high chromium content are better in this respect (Fig. 6, curve 5).

The material synthesized from the MA charge with the mixture parameter x = 1.5 and containing 69 % of Cr_2AlC, 16.6 % TiC, and 14.4 % Cr_4Al_9 has a rather high heat resistance (at T = 1273 K and τ = 100 h, Δm = 7.5 g/m^2 was obtained). Almost the same weight increment (Δm = 9.1 g/m^2) was observed for the sample made from the nonactivated mixture containing 54 % Cr_2AlC, 19 % TiC, 22 % Cr_2Al, and 5 % Cr_7C_3.

For synthesis products with x = 1 obtained from the MA mixture, in which the main phases are TiC (43%) and $(Cr,Ti)_3AlC_2$ (45%), the weight increment for the same temperature and time is 6.6 g/m^2, while for samples with the same mixture parameter made from the nonactivated mixture containing 66 % TiC, 8 % Cr_2AlC, and 26 % of chromium aluminides, the increment is 13.3 g/m^2. The increased level of heat-resistance with the use of the MA mixture is explained by the higher concentration of the Cr_2AlC phase in products.

The heat resistance of samples made from the mixture with x = 0.5 (NA and MA) under the mentioned test conditions is 20–25 g/m^2.

The largest weight increment (32 g/m^2) at T = 1273 K and τ = 100 h was mentioned for the material containing no chromium, which can be also caused by the relatively high residual porosity of synthesis products. At the initial stage of tests, an abrupt jump in the oxidation rate associated with the formation of oxide films was observed. This is also valid for samples synthesized from the activated mixture, the weight increment of which for 100 h holding at 1000°C was 27–37 g/m^2. The worst characteristics were obtained for materials containing the largest amount of the Ti_2AlC phase. This result is caused by the fact that, according to the data of differential scanning calorimetry (DSC), the endotherm associated with the decomposition or reconstruction of the Ti_2AlC phase into the Ti_3AlC_2 phase is observed in heating curves at T = 1524–1557 K. This is confirmed by the results of an X-ray structural analysis of the samples after annealing at T = 1473 and 1573 K. In the first case, the amount of the Ti_2AlC phase abruptly decreases from 73 to 16 % and the TiC and $TiAl_2$ contents simultaneously drop to zero, while the amount of the Ti_3AlC_2 phase increases from 16 to 84 %. After the second annealing (1573 K), TiC appears in the samples again in the amount of 45 %, while the Ti_3AlC_2 content decreases to 55 %; the Ti_2AlC phase is unobservable. The second peak in the heating curves at T = 1720–1750 K is apparently associated with the transformation of the Ti_3AlC_2 phase.

For the obtained experimental data on heat resistance, we selected the regression equations (Table 5), which indicated that, for the alloys of the $Ti_{2-x}Cr_xAlC$ system, the growth rate of the oxide film is limited by the diffusion of oxygen. It is described by the equation $\Delta m/S = K\tau^{1/n}$, where Δm is the difference between the current and initial weights of the sample, K and n are the constant coefficients, and τ is the holding time.

X	Mixture preparation	Regression equation
0	NA	$\Delta m / S = 1{,}40\ \tau^{0{,}161}$
0,5	NA	$\Delta m / S = 0{,}517\ \tau^{0{,}687}$
1	NA	$\Delta m / S = 1{,}14\ \tau^{0{,}453}$
2	NA	$\Delta m / S = 1{,}17\ \tau^{0{,}453}$
2	MA	$\Delta m / S = 0{,}517\ \tau^{0{,}401}$

Table 5. Regression equations of the oxidation kinetics of the alloys at T = 1273 K in air

When evaluating the data on the heat resistance of the Cr–Ti–Al–C alloys, we can see that values of this characteristic for them are higher than for simple carbides TiC and Cr_3C_2 and the TiC–17%Cr alloy. The only exclusion is the materials based on the Ti_2AlC and Ti_3AlC_2 phases. Thus, composite materials in the Ti–Cr–Al–C system, which belong to the class of oxygen-free compounds with a layered structure, possess high heat-resistance and satisfactory mechanical characteristics, which allows us to consider this construction ceramics promising not only as the targets for the magnetron sputtering of heat-resistant, corrosion-resistant, and tribological nanostructured coatings, but also for the fabrication of high-temperature units of constructions operating under extreme exploitation conditions.

3. Borides based ceramic in systems Cr-B and Ti-Cr-B

Borides of transition metals are of special interest in connection with their unique mechanical, thermal, electrical, and magnetic properties. Their use in products of the chemical industry and in the production of abrasives, protective coatings, wear-resistant materials, and construction ceramics is widely known [8, 48–55].

In this section, we consider obtaining ceramic materials based on chromium and titanium borides by SHS pressing [8] from the mixtures, which is preliminarily mechanically activated. The application of MA allows us to perform SHS in low-exothermic systems such as Mo–B and Cr–B [46, 56, 57]. The role of the MA charge manifests itself in a simultaneous increase in the absolute value of heat release and the rate of heat release in the combustion reaction, which exert a positive effect on the thermodynamics and kinetics of the process.

For the studies, we selected a stoichiometric mixture of chromium and boron powders with the weight (in %) component ratio Cr : B = 70.6 : 29.4 calculated for the formation of the CrB_2 compound. The Ti–B–Cr mixtures were formed at a constant ratio Ti/B = 6.14. The composition of the samples under study is presented in Table 6.

Sample	Composition, wt. %		
	Cr	Ti	B
1	70,6	-	29,4
2	30,0	60,2	9,8
3	40,0	51,6	8,4

Table 6. Composition of the green mixtures

Procedures for preparing the samples, carrying out MA, and evaluating the properties of the powder mixtures before and after MA, as well as for determining the SHS parameters and the phase and structure formation in the combustion wave, are presented in [46, 56].
The experimental dependence of the specific heat release (Q) during the chemical reaction on the MA time is presented in Fig. 7. It is evident that the interaction is characterized by a low Q level.

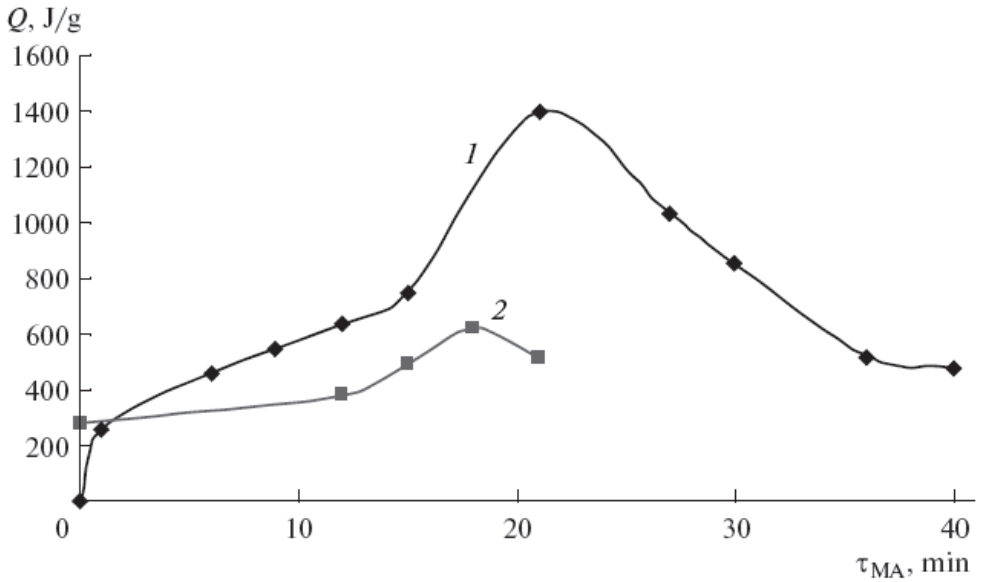

Fig. 7. Effect of mechanical activation duration on the specific heat release. (1) Cr–29.4% B and (2) Ti–40% Cr–8.4% B.

We failed to perform the SHS reaction in calorimeter conditions in the nonactivated Cr–B mixture. Due to the incomplete transformation, the amount of heat released during the combustion was smaller than expected. For example, for weak MA (τ_{MA} = 1 min), the value of Q was 0.3 kJ/g. For comparison, at τ_{MA} = 21 min, Q = 1.4 kJ/g. According to the data of an X-ray phase analysis, intermediate reaction products, lower borides CrB and Cr_3B_4 with lower heats of formation, are present in the combustion products of the Cr–B mixture. A similar pattern was also observed for the Ti–Cr–Br mixtures, where titanium boride TiB and unreacted titanium and chromium are added to lower chromium borides.
Thus, the obtained absolute value of reaction heat turned out to be lower; however, this does not prevent us from following the variation in Q depending on the MA time. As τ_{MA} increases, the amount of released heat increases. This is probably associated with the increase in the transformation depth in the combustion reaction due to the accumulation of macro- and microdefects in starting powders, which leads to an increase in the internal energy of the system, and with the decrease in the heterogeneity scale. The development of the thermal peak in the Cr–29.4% B mixture continues to τ_{MA} = 21 min, while it continues

to τ_{MA} = 18 min in the mixture Ti–40% Cr–8.4% B. Further activation leads to a decrease in the heat release, which is caused by the beginning of mechanochemical reactions of formation of chromium borides during MA. Thus, to obtain the largest Q, the optimal MA time was determined. For the Cr–29.4% B charge, it equals 21 min; for the Ti– 40% Cr–8.4% B mixture, it equals 18 min.

During mechanical treatment, the strain on energy of particles is composed of the energy of subgrain boundaries formed from mosaic blocks, the energy of the new surface formed due to the destruction of the particles, and the elastic deformation energy. In turn, the elastic deformation energy in the crystal depends on the energy of dislocations and vacancies. Each dislocation, possessing a definite energy reserve and being its accumulator in the crystal, is a sublocal limiting distortion of the crystal lattice. The introduction of dislocations into the crystal leads to an increase in its energy, and, as the number of uniformly distributed dislocations increases, the average absorbed energy in the working volume increases [58–62].

The optimal state of the structure of the reagents before SHS corresponds to the definite dislocation structure of the metal and reaction surface of the mixture. To evaluate the effect of MA on the structural state of starting reagents, we analyzed the influence of the treatment time on the structure of the chromium powder. We calculated the size of coherent scattering regions (CSR) according to the broadening X-ray lines. Physical broadening was evaluated by the procedure [63–65]. The results of this investigation are given in Table 7.

τ_{MA}, min	CSR size, nm		Microdeformation, %	
	Cr-29,4%B	Ti-40%Cr-8,4%B	Cr-29,4%B	Ti-40%Cr-8,4%B
1	130,9	-	0.14	-
12	73,1	41,7	0,18	0,150
15	51,6	40,8	0,19	0,211
18	25,6	31,5	0,23	0,267
21	16,0±2	25,9±3	0.27±0,01	0,343±0,05

Table 7. CSR size and microdeformation of the Cr lattice after MA

As the MA time increases, the CSR size decreases, while the microdeformation magnitude increases, which confirms the assumption that the stored energy increases. It should be noted that a decrease in the CSR size in the Cr–29.4%B mixture occurs by an order of magnitude, while the microdeformation increases by a factor of approximately 2. It is evident from the scanning electron microscopy data (Fig. 8) that the mixture initially consists of chromium particles 5–40 μm in size and fine-crystalline boron with the particles of <1 μm. As the MA duration increases, chromium intensely disintegrates and the maximal particle size does not exceed 5 μm, while their spread in regards to size considerably decreases due to the uniform stirring and redistribution of boron over the surface. This leads to an increase in the reaction surface and to a decrease in the kinetic obstacles during the SHS reaction.

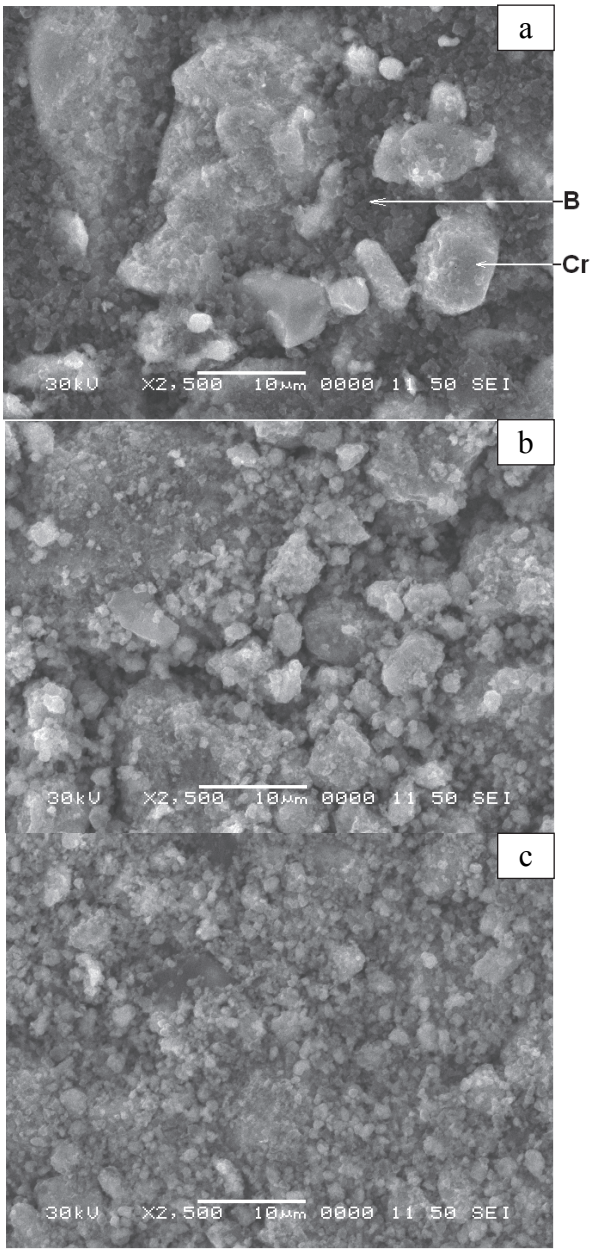

Fig. 8. Morphology of the Cr–29.4% B mixture after MA. τ_{MA}: (a) 1, (b) 21, and (c) 40 min.

During MA, the specific surface of the mixture increases due to the disintegration of powder particles, the formation of cracks, and the accumulation of microstructural and surface

defects. With the MA time longer than a certain critical value (21 min for Cr–B and 18 min for Ti–Cr–B), borides of reagents appear in the mixture; their composition cannot be determined qualitatively by local electron probe microspectral analysis because of the small particle size and difficulties associated with the low atomic number of boron.

The changes that happened in the mixture structure due to MA exert an essential influence on SHS parameters such as the character of propagation of the combustion wave and the combustion temperature and rate. Figure 9 shows the video frames of combustion of the activated Cr–B mixture. The combustion wave is spread along the axis sample downwards. The combustion source (frame 2), like the "spin", moves in the plane perpendicular to the propagation direction of the combustion wave (frame 3). After the source passes through the sample plane (frame 4), the combustion passes to the following layer (frame 5). The pattern is periodic and repeats itself through equal time intervals (0.16 s). This indicates that the character of combustion of the activated sample is time-dependent near the stability limit.

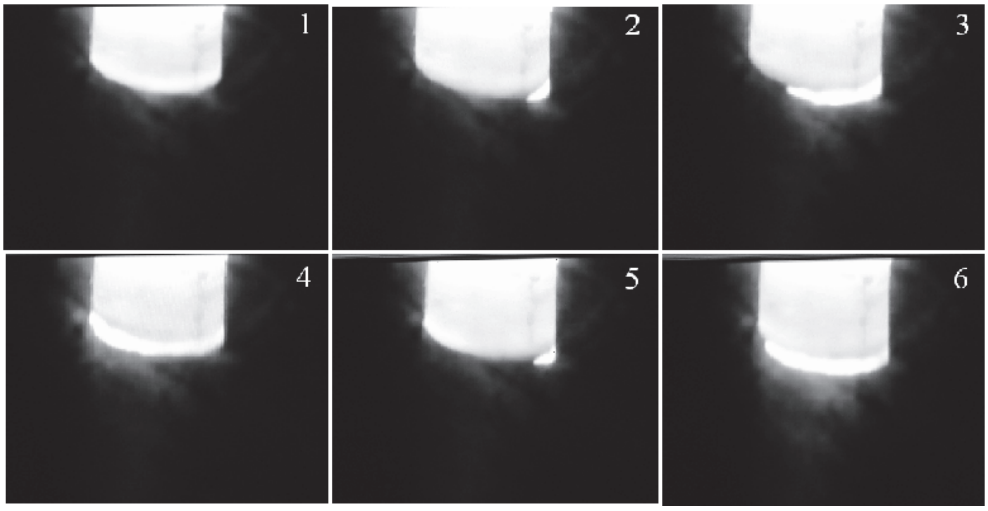

Fig. 9. Frame-by-frame video filming of the combustion of the Cr–B mixture after MA. τ_{MA} = 21 min, T_0 = 293 K, and V_{film} = 25 frame/s.

An investigation of samples macrostructure showed the presence of stratification in products obtained from the Cr–B mixture activated for 21 min. The periodic character of transversal cracks repeats the motion of the combustion front.

On the contrary, the structure of the combusted sample of the slightly activated Cr–B mixture is uniform and contains no visible transversal stratification corresponding to the character of propagation of the combustion front.

The result of a measurement of the combustion rate as a function of the initial temperature is shown in Fig. 10. It is possible to implement SHS in MA mixtures at T_0 = 300 K; in the slightly activated (τ_{MA} = 1 min) Cr–29.4% B mixture, this is possible only at T_0 = 525 K; and in the nonactivated Ti–30% Cr–9.8% B and Ti–40% Cr–8.4% B mixtures, it is possible only at T_0 = 523 and 653 K, respectively. For all compositions, the linear dependence of U_c from T_0 is

observed. In the MA Cr–B mixtures, the formation of chromium boride occurs with a considerably higher rate and depends more strongly on the initial temperature than in the Ti–Cr–B system. For all three MA compositions at T_0 > 530–540 K, the combustion sources are formed throughout the sample volume (combustion is similar to heat burst) and their motion is directed chaotically. The combustion rate cannot be determined under these conditions, because we determined it as the distance passed by the combustion wave along the sample axis for a certain time interval.

It is evident from Fig. 10 that, for activated Cr–B and Ti–Cr–B mixtures, the combustion rate is higher at the same initial temperature than nonactivated or slightly activated mixtures. For example, for the Cr–29.8% B composition at T_0 = 525 K, after activation for 1 min, U_c = 1.8 mm/s, while it is 8.7 mm/s for τ_{MA} = 21 min. Thus, we observe the substantial influence of MA on the combustion process. This effect corresponds to the published data [44–46, 57–60, 62] on the positive influence of MA on combustion kinetics and mechanism for different SHS systems.

One interesting feature of Cr–B and Ti–Cr–B materials under study which is not inherent to other previously studied systems is the fact that the combustion temperature (T_c) depends very weakly on T_0 in a certain range of T_0. This effect manifests itself for the Cr–B mixture both after strong and weak activation (Fig. 10b), while it is observed only after strong activation for the Ti–Cr–B system.

It is established experimentally that, for the slightly activated Cr–B mixture, T_c = 1800–2200 K, which is close to the adiabatic temperature (1900–2200 K) calculated using the THERMO program, while T_c is noticeably lower for the strongly activated mixture (τ_{MA} = 21 min) and equals ~1500 K, despite a considerable increase in the combustion rate.

It should be noted that the T_0-dependences of T_c shown in Fig. 10b for the activated and nonactivated Ti–Cr–B mixtures differ qualitatively. In MA mixtures in the range of T_0 from room temperature to 450 K, an increase in the initial temperature either does not exert the combustion temperature in practice (sample 3) or it affects it insignificantly (sample 2). This character of curves 2 and 3 is usually attributed to the processes with heat absorption. As was mentioned above, the combustion rate of the activated mixtures at T_0 ~ 530–540 K increases abruptly, which leads to the spread of the analyzed material due to the abrupt release of the gases absorbed during MA and the loss of contact between the sample and thermocouple. Therefore, we failed to measure the combustion temperature at T_0 > 530–540 K for the activated Ti–Cr–B samples. In nonactivated Ti–Cr–B mixtures, a linear dependence is observed between the combustion temperature and the heating temperature of the mixture.

To clarify the mechanism of combustion and structure formation, we quenched the sample in a copper wedge. Figure 11 shows the microstructure of the stopped combustion front (SCF). The quenched combustion zone is arranged near the line 1–1; combustion products that formed after the SHS reaction is stopped are above this line, and the heating zone and the starting reaction mixture are below it.

During a detailed analysis of the phase composition in the combustion zone and behind the combustion front in the region of the formed products, we established the following. In the combustion zone, we can distinguish the regions of different coloration, which is caused by different chemical compositions. Light regions (Fig. 12a, point 3a) are enriched with chromium, while gray regions (points 2a, 4a) are enriched with titanium (Table 8). Unreacted oxygen-containing starting components are present in separate dark segments (point 1a).

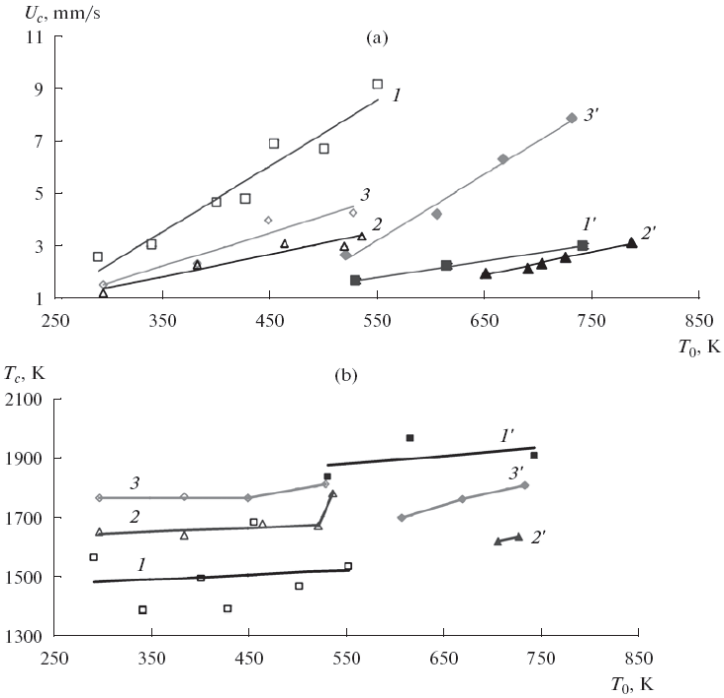

Fig. 10. Dependences of the combustion (a) rate and (b) temperature on the initial temperature of the process for the Cr–B and Ti–Cr–B green mixtures obtained for various MA times. (1, 1') Cr–29.4% B, (2, 2 ') Ti–40% Cr–B, and (3, 3 ') Ti–30% Cr–B. (1–3) Strongly activated (τ_{MA} = 21 min (1) and 18 min (2, 3); (1') slightly activated (τ_{MA} = 1 min) and (2 ', 3 ') nonactivated.

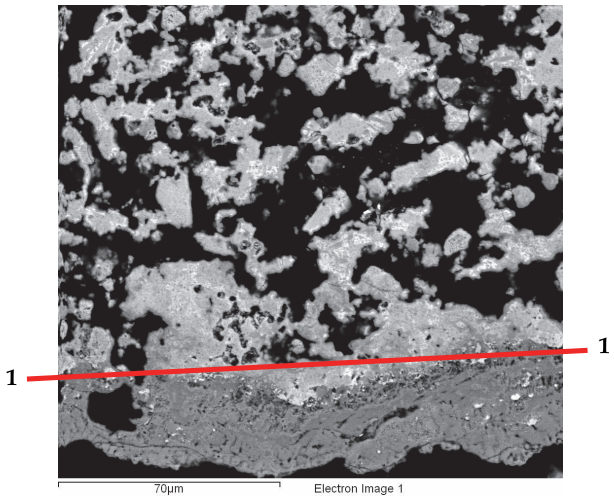

Fig. 11. Quenched combustion front of the Ti–30%Cr–B MA sample.

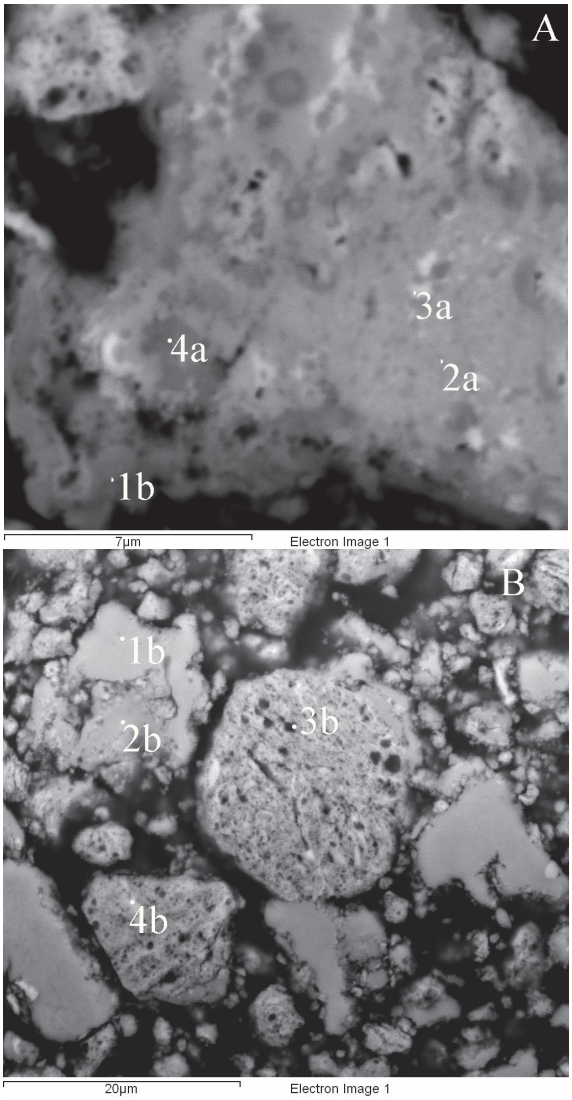

Fig. 12. Stopped combustion front (Fig. 11, the region above line 1–1) of the Ti–Cr–B mixtures. Magnification (a) 5000× and (b) 1500×.

Behind the combustion front, we can also distinguish the regions differing both in color and form. Similarly to those described above, light regions (point 3b) are enriched with chromium, while light gray and dark gray regions are enriched with titanium. Taking into account morphological features of these regions (acicularity or roundness), we can assume their phase composition. The regions with a characteristic needle shape contain titanium and chromium borides, while rounded irregular shapes are characteristic of the starting reagents or a solid solution based on metals. The reagents start to interact at the particle

surfaces. For example, point 1b in Fig. 12b belongs to titanium, while the interaction between Ti, Cr, and B already passed in point 2b. Light needlelike formations correspond to titanium or chromium borides. However, we should note that it is very hard to exactly determine the formation sequence of the phases because of their variety and the similar elemental composition of the intermediate phases. Table 8 shows elemental composition of the Ti–Cr–B sample in each point.

Point № in Fig. 12	B	O	Ti	Cr
1a	16.16	20.58	57.58	5.68
2a	15.42	-	72.62	11.45
3a	22.02	-	65.20	12.42
4a	11.57	-	82.72	5.55
1b	-	-	99.50	0.50
2b	17.89	-	80.64	1.37
3b	56.00	3.66	10.12	29.26
4b	48.15	3.05	15.15	21.63

Table 8. Elemental composition of the Ti–Cr–B sample, wt %

An analysis of possible reactions in the combustion waves of the Ti–Cr–B and Cr–B mixtures under consideration is presented below. Analogously to the Mo–B system [57], the following reactions proceed in the heating zone:

$$B_2O_3(sol) + B \rightarrow 3/2B_2O_2(g) - Q, \quad (4)$$

$$Me + 2B \rightarrow MeB_2 + Q. \quad (5)$$

The solid-phase interaction between chromium and boron in the heating zone is inlikely because of the relatively low diffusion atomic mobility at these temperatures. However, the reversible gas-transport reaction (4) of the formation of volatile boron suboxide occurs on the reagent surface at T = 1100–1250 K. In the combustion wave, it is preceded by the melting of boron oxide B_2O_3 at T = 723 K [57]. Gaseous suboxide is chemisorbed on the surface of the chromium and titanium particles with the formation of the most thermodynamically favorable boride phases, for example, by the reactions:

$$3B_2O_2(g) + 3Ti \rightarrow 2B_2O_3(liq) + TiB_2 + 2Ti + Q \rightarrow 2B_2O_3(liq) + 2TiB + Ti, \quad (6)$$

$$B_2O_2(g) + Cr \rightarrow B_2O_3(liq) + Cr_yB_z + Cr + Q. \quad (7)$$

Thus, the saturation of particles of the reagent metal with boron goes from the surface to the center. Then the product formed in Ti–Cr–B system after combustion zone interact with formation of the ternary boride compounds:

$$TiB + Cr_yB_z \rightarrow CrTi_2B_2 \text{ and } TiB + Cr_yB_z \rightarrow Cr_4Ti_9B \quad (8)$$

as well as the solid solutions and Ti–Cr compounds.

In parallel to mentioned reactions, the endothermic reaction occurs in the heating zone (in front of the combustion front):

$$B_2O_3(sol) + B \rightarrow 3/2B_2O_2(g) - Q, \quad (9)$$

An analysis by oxygen for the Cr–B mixture showed that its fraction is 0.4% in the starting powder chromium, while its fraction is 3.7% in the starting boron. The recalculation for the specified composition of the mixture shows that chromium introduces 0.28% oxygen, boron introduces 1.09% oxygen, and its total content is 1.37%. After MA for 1 min, this characteristic of the charge increases to 2.6% (almost by a factor of 2), and, after 21 min MA, it increases to 3.3%. This excess oxygen increases the concentration of boron and chromium oxides. If we decompose the total amount of oxygen for the mixture reagents, we obtain that, in the case τ_{MA} = 21 min, its fraction in chromium is 0.66%, while its fraction in boron is 2.64%, which corresponds to 3.83% B_2O_3 in the mixture. Thus, boron is the main oxygen carrier in the mixture; 80% of oxygen in the mixture composition is associated with boron, and only 20% is associated with chromium. Such a distribution shows that the contribution chromium oxide to the combustion mechanism and kinetics is not determinative. As the oxygen content in the mixture increases due to MA, the role of the gas-transport boron transfer to the metal surface increases and the reaction diffusion becomes the limiting stage of the interaction between the metal and boron.

We carried out a thermogravimetrical analysis of boron and chromium powders at T = 300–1273 K, as well as the green mixtures mechanically activated for 1 and 21 min. It was established that, in the mentioned temperature range, chromium undergoes no substantial phase transformations accompanied by thermal peaks and a change in weight. The endothermic transformation with an energy of 2.0 kJ/g proceeds in the boron powder at T = 1020–1250 K. Endothermic peaks are also observed for the MA charges. In the case of τ_{MA} = 1 min, this peak is located at T = 1020–1230 K and the thermal absorption is 0.18 kJ/g; at τ_{MA}, this peak is located at T = 900–1020 K and the thermal absorption is 0.9 kJ/g.

The results of qualitative and quantitative X-ray phase analyses of the composition of the synthesized samples showed that, in the case of a strongly activated Cr–29.4% B mixture, as T_0 in the combustion products increases, the fraction of higher chromium borides increases as the amount of boride phases decreases. This occurs during the transition $CrB \rightarrow Cr_3B_4 \rightarrow CrB_2$ by the solid-phase reactive diffusion mechanism; stage I passes almost completely due to the large amount of accumulated energy. However, subsequent stage II has no time to be completed. The product consists of two-phase (CrB_2 and Cr_3B_4) with a small amount of fine pores.

As a result of an X-ray phase analysis of the SHS products in the Ti–Cr–B system under study, previously unknown Cr_4Ti_9B and Ti_2CrB_2 phases were found. In addition, these samples contained TiB and $TiCr_2$ phases. Due to the preliminary MA of the Ti–30% Cr–9.8% B mixture, we succeeded in completely eliminating the $TiCr_2$ intermetallic compound and increasing the content of complex Ti_2CrB_2 boride.

According to the result of our investigations, we synthesized large-scale samples 125 mm in diameter based on chromium borides of compositions Cr–29.4% B, Ti–30%Cr–9.8%B, and Ti–40%Cr–8.4%B. The addition of titanium into the reaction mixture allowed us to decrease the residual porosity from 6% in the Cr–B compact samples to 2% in the Ti–Cr–B synthesis products, which improved the exploitation properties of target materials.

4. Tantalum containing ceramic targets in system Ti-Ta-C

Tantalum finds a wide application in reconstructive surgery, mainly due to its high strength and hardness combined with excellent plastic characteristics, high chemical stability, and

good biological compatibility. Analogously with other carbides and nitrides of transition metals, TaC and TaN possess high hardness, wear resistance, and corrosion resistance. In [66], the macrokinetic features of the combustion of the mixture with the composition (90% – x)(Ti + 0.5C) + x(Ta + C) + 10% $Ca_3(PO_4)_2$, as well as the structure and properties of the synthesis products were investigated depending on mixture parameter x. During these investigations, the temperature profiles of the combustion wave with two peaks of heat release were detected, which indicates that the chemical reactions are staged, and the combustion proceeds in the detached mode. For example, as the charging parameter increases to x = 45% and the initial temperature of heating increases to T_0 = 420 °C, the two peaks merged. The combustion transformed from the detached mode into the coalescence mode, but an increase in x parameter did not lead to a noticeable variation in the combustion rate.

It is known that, in the Ti–C system, the leading SHS stage is the reactive diffusion of carbon into the titanium melt, while it is the diffusion of carbon into tantalum in the Ta–C system [7, 8, 66–69]. Carbon is transported to the surface of tantalum particles through the gas phase via the circulation of CO and CO_2 by the Buduar–Bell cycle [8].

Upon the addition of a certain amount of the Ta + C mixture into the Ti + 0.5C powder mixture, parallel or sequential chemical reactions of the formation of titanium and tantalum carbides occur in the combustion wave. Taking into account the fact that the combustion mechanisms of the mentioned mixtures are different, we should expect that, depending on the amount of the added Ta + C mixture, the moving force of the combustion is either the dissolution of carbon in the titanium melt (after the formation of the reaction surface via the capillary spread of the melt over carbon) or the solid-phase reactive diffusion of carbon into tantalum. In the latter case, the gas transport of the carbon reagent to the surface of the solid Ta particle and the formation of tantalum carbide proceed according to the following scheme: the interaction of the CO_2 molecule with carbon along with two moles of CO being obtained; the gas transport of 2CO to the surface of the Ta particle; the chemisorption of 2CO on the surface; the two-stage interaction between tantalum and carbon with the initial formation of tantalum semicarbide and then tantalum carbide by the scheme Ta + 2CO → TaC + CO_2; the desorption of the CO_2 molecule from the surface of the formed tantalum carbide layer; the transport of CO_2 to the surface of the carbon particle; and the interaction between CO_2 and carbon with the formation of 2CO, etc [7, 66].

In their conclusions, the authors of [66] used the published data on the mechanisms of combustion and structure formation in the Ta–C and Ti–C binary systems, since the mechanism of the phase formation of the SHS products in the Ti–Ta–C ternary system is practically unknown. In connection with the difficulties in interpreting the obtained results, the authors of [66] additionally investigated SHS in the Ti–Ta–C ternary system [69] without the addition of calcium orthophosphate while varying the charging parameter from the minimal (10%) to maximal (50%) value. In this case, powder materials were used, namely, titanium and carbon of the above-mentioned grades and the tantalum TVCh (TU 95-251-83). The compositions of the exothermic mixtures were varied according to the condition (90%–x)(Ti+0.5C) + x(Ta+C), where the mixture parameters corresponded to x = 10, 30, and 50% (Table 9).

The procedure of preparing the sample, the investigation methods, and the equipment are described in detail [64, 69]. The experimental dependences of the temperature and combustion rate on the initial temperature for mixtures with various values of x are shown in Fig. 13.

x, wt %	Mixture composition, wt %			Calculated adiabatic combustion temperature, K	Combustion rate, cm/s
	Ti	Ta	C		
10	80,0	9,5	10,5	1988	0,51
30	62,3	28,1	9,6	2132	0,42
50	44,5	46,9	8,6	2329	0,27

Table 9. Mixture compositions and characteristics of the SHS process

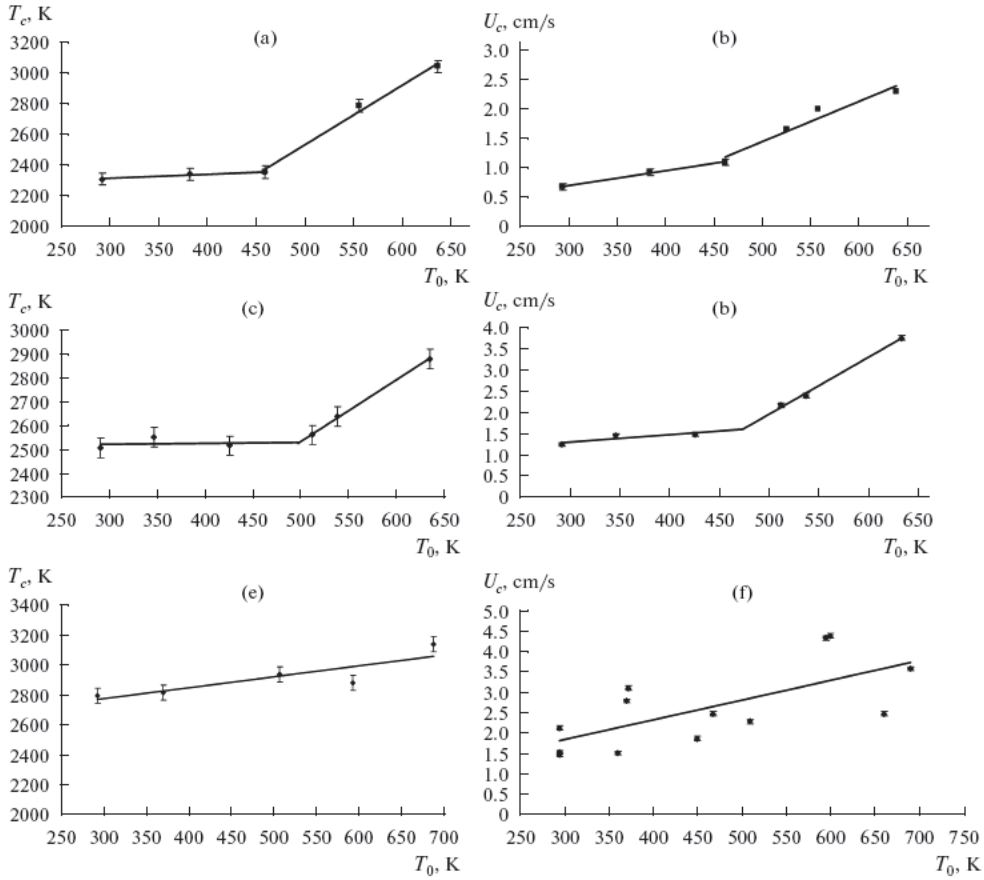

Fig. 13. Dependences of the temperature (a, c, e) and combustion (b, d, f) rate from the initial heating temperature of the mixture at various mixture parameters. x: (a, b) 10, (c, d) 30, and (e, f) 50 wt %.

It is evident from Fig. 13 that in the range of T_0 from room temperature to 450–500 K, the combustion temperature of the under studied mixtures increases linearly. For the compositions with x = 10 and 30%, the combustion rate and temperature abruptly increase at T_0 > 450 K, which indicates the change in the combustion mechanism.

The heating curves of the combustion wave with various charging parameters were analyzed in [66]. It was shown that, at x = 10%, the temperature profile has a complex character, which is associated both with the stage character of the reaction and with microstructural features of the process; namely, the deformation of the medium and the formation of separate hot reaction sources near the thermocouple. In addition, the onset of the reaction is accompanied by an abrupt increase in temperature, which indicates that the first stage of the reaction proceeds rapidly. Then an abrupt drop of T_c follows. Such behavior is typical of cases when the combustion proceeds by the relay race mechanism. Similar results were obtained in [69] when analyzing the profiles of heating curves.

The dependences of T_c and U_c on the initial temperature in the range T0 = 300–700 K for the mixture with x = 50% (Figs. 13e, 13f) are close to linear, which indicates the unique combustion mechanism and that the parallel chemical reactions of the formation of titanium and tantalum carbides proceed in a wide combustion zone. However, with the detailed consideration of the heating curve of combustion (Fig. 14) recorded at various T_0, it is evident that two peaks of heat release with temporal resolution of 0.2 s can be distinguished upon heating to 493 K and above. An analysis of these heating curves confirmed the effect associated with the formation of two peaks established in [66].

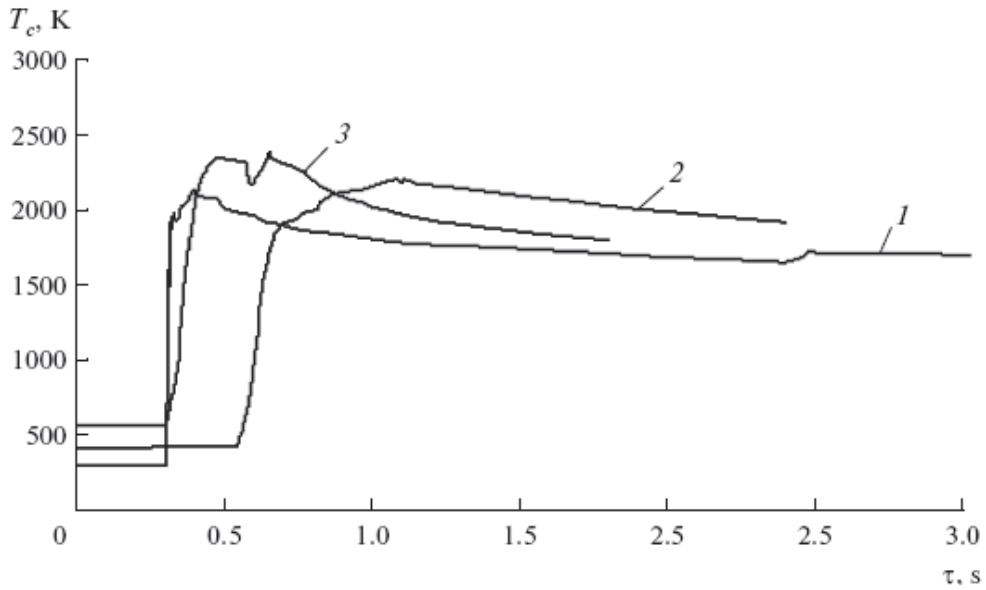

Fig. 14. Temperature profiles for the sample with x = 50%. T_0: (1) 293, (2) 388, and (3) 493 K.

This character of the profile of the combustion wave is possibly associated with the fact that, as T_0 increases, the spatial separation of the chemical reactions proceeding by different mechanisms and having different activation energies takes place. This can be interpreted in the context of the theory of the combustion waves upon two and more parallel or sequential reactions occurring [70–72]. In the mixtures with a low Ta concentration in the combustion front, titanium interacts with carbon through the stage of melting and the capillary spread of titanium over the developed ash surface. In this case, tantalum reacts with carbon in the

afterburning zone. Such combustion mode is usually called the detached mode. As the Ta content increases, the intensity of the second reaction increases, while that of the first reaction (titanium–carbon) substantially drops, and the combustion gradually transforms into the coalescence mode. For the mixture with x = 50%, the contribution of the reaction of the formation of tantalum carbide becomes more noticeable, and, at T_0 > 500 K, the combustion (without a noticeable variation in its average rate) apparently gradually transforms into the detached mode.

It is seen from Fig. 13 that, at T_0 = 300 K, as the mixture parameter increases, the combustion temperature increases from 2250 K at x = 10% to 2600 K at x = 50%, which is in good agreement with the calculated value of the adiabatic temperature of combustion. According to this, due to the higher value of T_c^{ad} of the Ta + C = TaC mixture (2736 K) when compared with the Ti + 0.5C = $TiC_{0.5}$ of the nonstoichiometric composition (2218 K), the integrated combustion temperature of the ternary mixture increases (Table 9).

The presented experimental data on the combustion rate (Fig. 13) illustrate the proportional T_0-dependence of U_c. For each value of x, the combustion rate increases as T_0 increases. It also increases as charging parameter x increases. Based on the available data on average combustion rates of the Ta + C = TaC and Ti + 0.5C = $TiC_{0.5}$ mixtures (0.6 and 2.0 cm/s, respectively [8]), the increase in the combustion rate is explained by the conservation of the leading role that the reaction of titanium carbide formation plays even at the highest tantalum content in the mixture. An increase in x leads to an increase in the carbon concentration in the mixture with respect to titanium. Consequently, by the first stage, more stoichiometric titanium carbide can form. The closer its composition is to stoichiometry, the larger the amount of heat is released, which determines the increase in the combustion rate.

The compositions of the synthesis products and lattice parameters of the obtained complex titanium–tantalum carbide are listed in Table 10.

x, wt %	Mixture composition, wt %	Phase composition of the combustion product	Lattice constant (a), nm
10	Ti- 9,5%Ta-10,5%C	(Ti,Ta)C	A = 0,4304
30	Ti-28,1%Ta-9,6%C	(Ti,Ta)C	A = 0,4316
50	Ti-46,9%Ta -8,6 C	(Ti,Ta)C	A = 0,4331

Table 10. Results of an X-ray phase analysis of the synthesis products depending on the mixture parameter

It is evident that, for all the values of the charging parameter, the product is the (Ti,Ta)C complex carbide. The view of a typical diffraction pattern is invariable for all studied compositions in view of the complete mutual solubility of titanium and tantalum carbides. As the Ta content in the mixture increases, the lattice parameter of carbide increases. The variation in the lattice parameter is close to the calculated one; it completely agrees with the published data [72, 73].

To investigate the dynamics of the phase formation and structure formation of the products of synthesis, experiments on stopping the combustion wave in a copper wedge with the angle at a vertex no larger than 5° with a subsequent electron microscopy investigation and electron probe microstructural analysis of the characteristic segments of the SCF were carried out. This allowed the authors of [69] to show the dynamics of transformations in the

combustion wave of the ternary system under study. The microstructures recorded in different regions of the SCF are shown in Figs. 15 and 16 by the example of a sample with x = 10%. The microstructure of the combustion front is presented in Fig. 15. The heating zone with the initial still unmolten Ti particles 10–80 μm in size (marks 1 and 2 on the light-gray particles) is situated to the left of the visible combustion front. The combustion zone, or the reacting medium after titanium is melted and its capillary is spread over the ash surface, is observed to the right of the combustion front (marks 3 and 4 with the component ratio Ti 90% and C 10%). White Ta particles 40–60 μm in size are also seen (marks 5 and 6).

The primary structure formation, which starts in the combustion zone, can be observed in Fig. 15c. Here, the finest grains of nonstoichiometric titanium carbide are isolated from the supersaturated titanium melt. The primary Ti–C crystals are noticeably smaller than 1 μm. As it goes further from the combustion zone to the zone where the reaction is completed, the Ti–C grains grow to 2–3 μm in size.

It is interesting to follow the regions in which the Ta particles are situated. Particles of the titanium–tantalum solid solution with content up to 6.5% Ti are found near the combustion front. This solid solution was formed due to the dissolution of Ta in the Ti melt and contains almost no carbon. The Ta particles start to react noticeably later, only in the region of where the reaction is completed. Figure 16a shows the reacting Ta particle. The dissolution occurs here, specifically, the diffusion penetration of tantalum (tantalum carbide) into the Ti melt and into the sublattice of nonstoichiometric titanium carbide. In this case, the regions of the diffusion influence of tantalum are more lightly colored.

According to microanalysis data, the composition of white particles corresponds to the initial tantalum powder, and the light-gray regions are enriched with titanium and comprise the agglomeration of titanium carbide grains. However, during a more detailed analysis of the distribution of elements inside these grains (see Fig. 16c), it is seen that the titanium content is higher in the center of the grains, while that of tantalum is higher at their periphery. The formation of a typical ring structure indicates that, initially, titanium carbide grains are formed; their further growth (the secondary structure formation) proceeds due to the dissolution of tantalum or tantalum carbide in them. In this case, the Ta content in the carbide grain depends on the heterogeneity scale. Carbide grains (Ti,Ta)C with an increased Ta content are formed near the places where dissolving Ta particles are arranged (Figs. 16b, 16c). Thus, the structural microinhomogeneity is determined by the size of the Ta particles.

The SCF at x = 30% is also characterized by two structural components, namely, white tantalum particles conserving the shape and sizes and gray regions, which comprise the agglomeration of titanium carbide grains. However, despite the fact that the tantalum content in the mixture is higher, its content in titanium carbide grains is lower than in the sample with x = 10% in this case. This is apparently associated with the fact that the amount of titanium decreases in the reacting system with a large charging parameter and the diffusion transition of tantalum into titanium carbide is retarded. In general, immediately behind the combustion front, the structure consists of two carbides, titanium carbide and tantalum carbide, and a small amount of complex carbide (Fig. 17a, Table 11). Complex carbide is formed due to the complete mutual solubility of titanium and tantalum carbides. Then carbide grains coalesce in the afterburning region due to the fact that they grow as Ti and Ta are dissolved in TiC.

A similar pattern is observed during an investigation of the SCF of the mixture with the largest mixture parameter x = 50% [69]. An expressed structural separation in regards to the

composition of individual regions is noted (Fig. 17b, Table 12). In particular, a larger amount of the regions that comprise either tantalum carbide or titanium carbide is formed. However, the Ta content in the (Ti,Ta)C carbide increases compared with x = 30%.

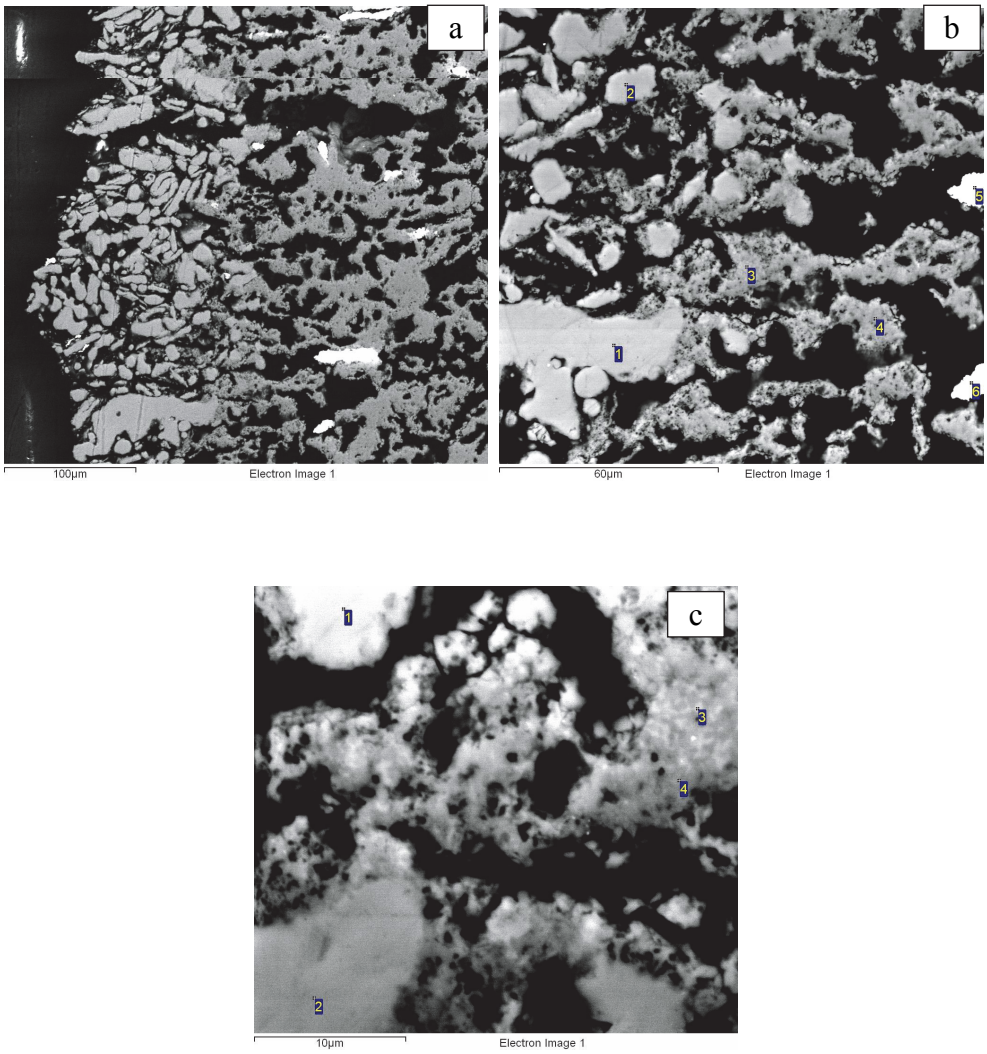

Fig. 15. SCF microstructure at x = 10% near the combustion front. (1, 2) Starting Ti particles in the heating region, and (3, 4) the reacting medium in the combustion zone (after melting Ti and its capillary spread over the surface with the component ratio Ti 90%, C 10%).

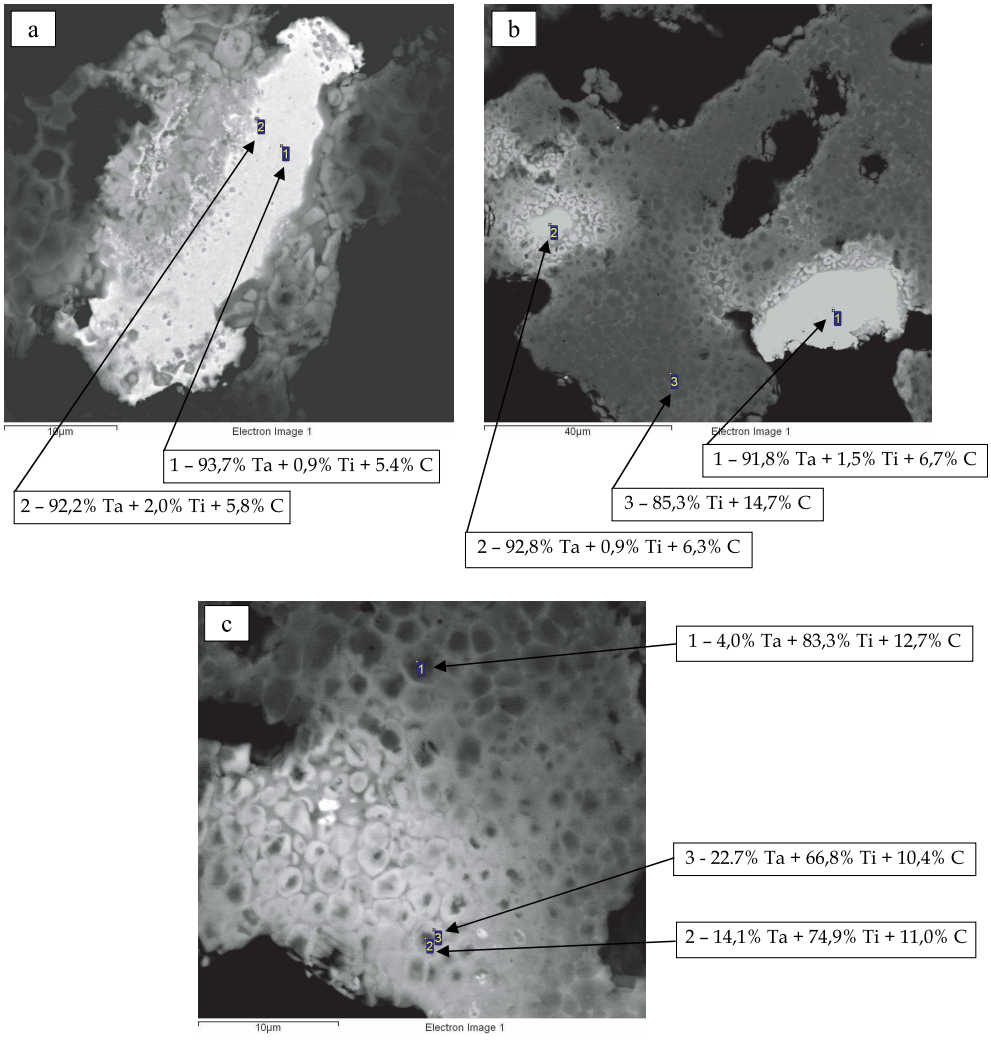

Fig. 16. SCF microstructure at x = 10% in the zone of completing the reaction. (a, b) Reacting Ta particles and (c) formed grains of the (Ti,Ta)C complex carbide, or secondary structure formation.

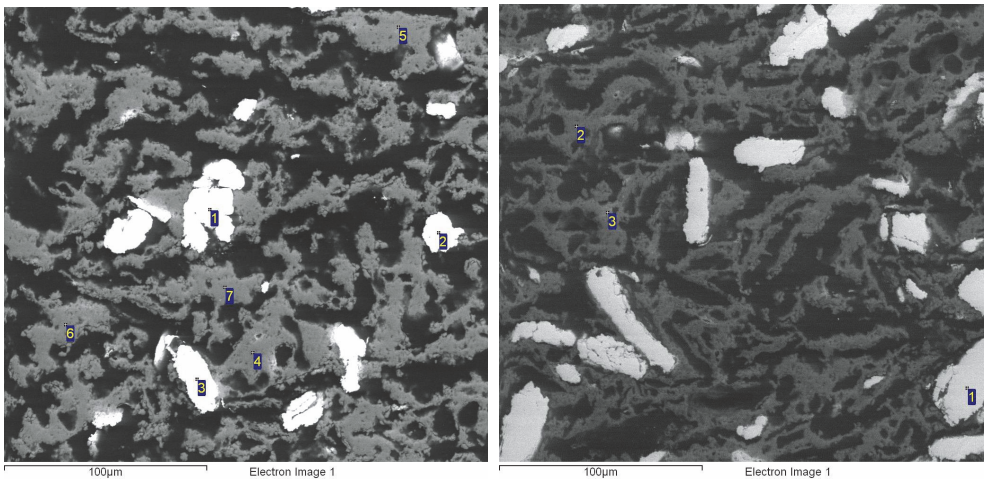

Fig. 17. SCF microstructure at x = 30% (a) and x = 50 % (b).

Point №	Content, wt %		
	C	Ti	Ta
1	4,03	0,00	95,97
2	3,15	0,76	96,09
3	5,07	0,00	94,93
4	15,19	84,81	0,00
5	14,91	84,00	1,09
6	14,43	84,15	1,42
7	13,42	86,58	0,00

Table 11. Results of a microanalysis of various regions at x = 30% in Fig. 17a

Point №	Content, wt %		
	C	Ti	Ta
1	-	-	100,00
2	23,18	76,82	
3	27,12	66,22	6,66

Table 12. Results of a microanalysis of various regions at x = 50 % in Fig. 17b

It follows from an analysis of the microstructures of the products of the synthesis obtained by the technology of the forced SHS pressing that the average size of the carbide grain (Ti,Ta)C decreases from 8 to 4 µm as x increases [69]. This fact can be interpreted only from the viewpoint of the stoichiometry of the formed carbide grains. As x increases, the degree of imperfection of titanium carbide grains by carbon decreases; consequently, the diffusion

mobility of carbon atoms in a more stoichiometric carbide lattice increases [74]. The crystallization and recrystallization of the carbide grains through the liquid phase is retarded. A decrease in the amount of the melt is also the cause of a decrease in the growth rate of the carbide grain.

Obtained materials were tested for high-temperature oxidation resistance at T = 1073 K in air (Fig. 18).

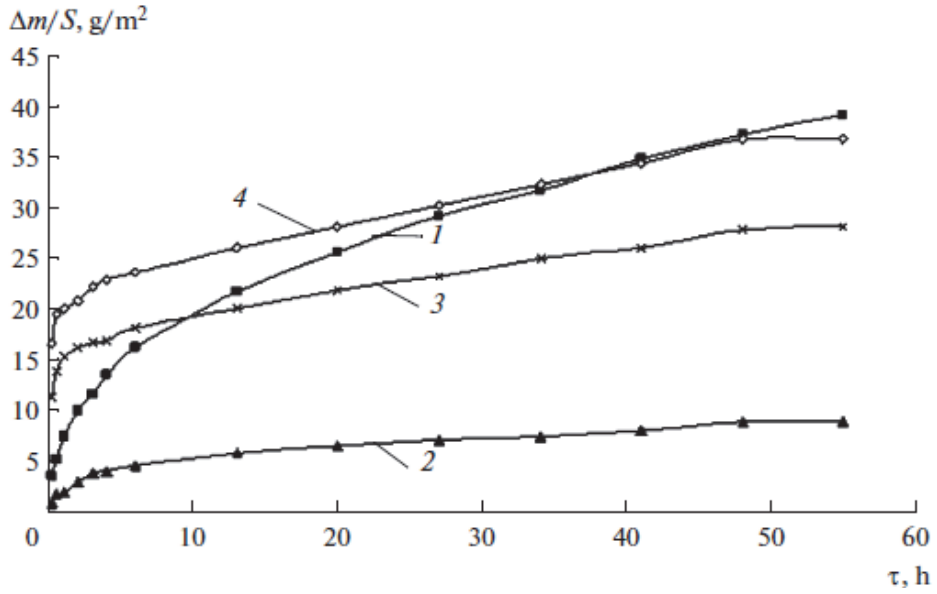

Fig. 18. Oxidation kinetics of the (Ti,Ta)C alloys in air at T = 1073 K. x = 0 (1); 10 (2); 30 (3) , and 50 wt % (4).

The alloy synthesized from the mixture with charging parameter x = 10% showed the highest heat resistance when compared with other ones, including the samples of nonstoichiometric titanium carbide obtained under the same conditions by the SHS compaction technology. The weight increment for this alloy (x = 10%) was < 8 g/m² for 50 h oxidation in air, which exceeds the heat resistance of samples of not only the nonstoichiometric titanium carbide $TiC_{0.5}$, but also stoichiometric TiC and TaC carbides obtained by hot pressing [48]. The alloy with x = 30% under holding > 10 h also has a higher heat resistance than $TiC_{0.5}$. This can be explained by the fact that the samples of nonstoichiometric titanium carbide and complex titanium–tantalum carbide, as a rule, contain a certain amount of α–β-Ti in the first case and β-(Ta,Ti) solid solution possessing higher heat resistance than titanium [75] in the second case.

The higher oxidation rate at short times of holding the samples with a higher tantalum content (x = 30 and 50%) is determined by an increased residual porosity (up to 7%), as well as by the larger extension of grain boundaries due to a decrease in grain size. This facilitates the diffusion of oxygen into the sample depth and increases the weight of formed oxides. The oxidation rate is also affected by protective properties of the oxide film. In our case, oxides appearing on the surface possess strongly differing specific volumes: $V_{Ta_2O_3} / V_{TiO_2} = 1.78$. Therefore, tantalum oxide induces stresses in the oxide film that may lead to a

violation of its integrity, which accelerates oxidation. The tantalum oxide content in the film determines the heat resistance of the alloy. Its small amount affects positively (Fig. 18, curve 2), while heat-resistance drops as it increases (Fig. 18, curves 3, 4). In addition, tantalum carbide is less resistant to high-temperature oxidation than titanium carbide [48].

The oxidation of the alloys follows the logarithmic law: $\Delta m/S = A\ln\tau + B$, where Δm is the difference between the current and initial sample weight, S is the area of the sample surface, and A and B are constant coefficients (Table 13). In this case, the limiting stage of oxidation process is the diffusion through the oxide film.

Generalizing the aforesaid about the Ti–Ta–C system, we can notice that for, compositions with x = 10 and 30 %, an abrupt increase in the combustion rate and temperature is observed at T_0 > 450 K due to the passage from the detached mode to the coalescence mode, which is accompanied by the increment in heat release because of the occurrence of two parallel chemical reactions. For the mixture with x = 50%, the T_0-dependences on T_c and U_c are linear in a wide range of T_0. In the studied range of the mixturing parameter, the products of the synthesis are single-phased and comprise the titanium– tantalum carbide (Ti,Ta)C.

x , wt %	Coefficients of the regression equation	
	A	*B*
0	6.75	7.57
10	1.50	2.32
30	2.90	14.49
50	3.56	19.63

Table 13. Coefficients of the regression equations $\Delta m/S = A\ln\tau + B$

Its lattice constant increases from 0.4304 to 0.4331 nm as x increases from 10 to 50%. The primary structure formation starts in the combustion zone, specifically, submicron grains of nonstoichiometric titanium carbide are allocated from the supersaturated titanium melt. The tantalum particle starts to react only in the aftercombustion zone via the diffusion penetration into the titanium melt and then into the sublattice of nonstoichiometric titanium carbide. The formation of a typical ring structure of grains indicates the primary nucleation of titanium carbide grains and the subsequent dissolution of tantalum (tantalum carbide) in them. An increase in the mixture parameter leads to a decrease in the size and microhardness of the (Ti,Ta)C grains, as well as to a decrease in the relative density of compact synthesis products. The kinetics of high-temperature oxidation is described by the logarithmic equations of the form $\Delta m/S = A\ln\tau + B$. The ceramic obtained at x = 10% has the highest heat resistance.

5. Conclusions

The modern views about the features of the synthesis of few interesting classes of the systems differ in the mechanisms of combustion and structure formation, namely the four-component system $Ti_{2-x}Cr_xAlC$, three-component systems Ti_3AlC_2, Ti_2AlC, Cr_2AlC, the systems based on titanium and chromium borides, and complex titanium–tantalum carbide are considered in this work.

6. Acknowledgment

The experimental works described in the chapter were carried out due to financial support from the Federal Target Program "Scientific and scientific-and-pedagogical personnel of an innovative Russia" for 2009–2013 (State Contracts no. 02.740.11.0133, and 02.740.11.0859), as well as by the Program of creation and development of the National University of Science and Technology "MISIS".

7. References

[1] Levashov, E.A., Shtansky, D.V. (2007). Multifunctional nanostructured films. *Rus. Chem.l Reviews,* Vol. 76, No. 5, p. 463.

[2] Andrievskii, R.A. (2002). Nanomaterials: concept and modern problems. *Ross. Khim. Zh.,* Vol. 46, No. 5, p. 50.

[3] Levashov, E.A., Shtanskii, D.V., Kiryukhantsev-Korneev, F.V., et al. (2009). Mnogofunkcionalnie nanostrukturnie pokritiya: poluchenie, struktura i obespechenie edinstva izmerenii mehanicheskih i tribologicheskih svoistv (Multifunctional Nanostructured Coatings: Preparation, structure and ensuring the measurement of mechanical and tribological properties). *Deform. Razrush.*, No. 11, p. 19.

[4] Shtansky, D.V., Levashov, E.A., Sheveiko, A.N., Moore, J.J. (1999). Optimization of PVD Parameters for the Deposition of Ultra Hard Ti–Si–B–N Coatings. *J. Mater. Synth. Process.*, Vol. 7, No. 3, p. 187.

[5] Musil, J., Jirout, M. (2007). Toughness of Hard Nanostructured Ceramic Thin Films. *Surf. Coat. Technol.,* Vol. 201, p. 5148.

[6] Levashov, E.A., Merzhanov, A.G., and Shtansky, D.V. (2009). Advanced Technologies, Materials and Coatings Developed in Scientific-Educational Center of SHS. *Galvanotechnik,* No. 9, p. 2102.

[7] Sychev, A.E. (2001). *Samorasprostranyayushchiisya vysokotemperaturnyi sintez: teoriya i praktika (Self-Propagating High-Temperature Synthesis: Theory and Practice),* Territoriya, Chernogolovka

[8] Levashov, E.A., Rogachev, A.S., Yukhvid, V.I., Borovinskaya, I.P. (1999). *Fiziko-khimicheskie i tekhnologicheskie osnovy samorasprostranyayushchegosya vysokotemperaturnogo sinteza (Physical-chemical and technological base of the Self-Propagating High-Temperature Synthesis)*, BINOM, Moscow.

[9] Shtansky, D.V., Lyasotsky, I.V., Levashov, E.A., et al. (2004). Comparative Investigation of Ti–Si–N Films Magnetron Sputtered Using Ti_5Si_3 + Ti and Ti_5Si_3 + TiN Targets. *Surf. Coat. Technol.*, Vol. 182, p. 210.

[10] Shtansky, D.V., Kiryukhantsev-Korneev, F.V., Levashov, E.A., et al. (2005) Struktura i svoistva pokritii Ti–B–N, Ti–Cr–B–(N) i Cr–B–(N), poluchennih magnetronnim raspileniem SHS- mishenei (Structure and properties of Ti-B-N, Ti-Cr-B-(N) and Cr-B-(N) coatings, obtained by magnetron sputtering of SHS- targets). *Fiz. Tverd. Tela*, Vol. 47, No. 2, p. 242 [*Phys. Sol. St.* (Engl. Transl.), 2005, Vol. 47, No. 2, p. 252].

[11] Audronis, M., Leyland, A., Levashov, E., et al. (2007). The Structure and Mechanical Properties of Ti–Si–B Coatings Deposited by DC and Pulsed-DC Unbalanced Magnetron Sputtering. *Plasma Process. Polym.*, Vol. 4, p. 687.

[12] Shtansky, D.V., Kulinich, S.A., Levashov, E.A., Moore, J.J. (2003). Osobennosti strukturi i phisico-mehanicheskih svoistv nanostrukturnih tonkih plenok (Features of structure, physical and mechanical properties of nanostructured thin films). *Fiz. Tverd. Tela*, Vol. 45, No. 6, p. 1122 [*Phys. Sol. St.* (Engl. Transl.), Vol. 45, No. 6, p. 1177].

[13] Shtansky, D.V., Levashov, E.A., and Sheveiko, A.N. (1997). Mit einem SHS-Legierungs-Target abgeschiedene Mehrkomponentenschichten Ti–B–N, Ti–Si–B–N, Ti–Si–C–N und Ti–Al–C–N fur unterschiedliche technologische Anwendungen. *Galvanotechnik*, No. 10, p. 3368.

[14] Shtansky, D.V., Kiryukhantsev-Korneev, Ph.V., Levashov, E.A., et al. (2007). Hard tribological Ti–Cr–B–N coatings with enhanced thermal stability, corrosion- and oxidation resistance. *Surf. Coat. Technol.*, Vol. 202, p. 861.

[15] Shtansky, D.V., Lobova, T.A., Levashov, E.A., et al. (2004). Structure and Tribological Properties of WSe_x, WSe_x/TiN, Se_x/TiCN and WSe_x/TiSiN Coatings. *Surf. Coat. Technol.*, Vol. 183, p. 328.

[16] Shtansky, D.V., Sheveyko, A.N., Sorokin, D.I., et al. (2008). Structure and Properties of Nanocomposite and Multilayer TiCrBN/WSe_x Coatings Deposited by Ion Implantation Assisted Sputtering of TiCrB and WSe_2 Targets. *Surf. Coat. Technol.*, Vol. 202, p. 5953.

[17] Kiryukhantsev-Korneev, F.V., Petrzhik, M.I., Levashov, E.A., et al. (2007). Vliyanie Al, Si i Cr na termicheskuyu stabilnost i stoikost k visokotemperaturnomu okisleniyu pokritiy na osnove boronitrida titana (Effect of Al, Si and Cr on the thermal stability and resistance to high temperature oxidation of coatings based on titanium boronitride). *Fiz. Met. Metalloved.*, Vol. 104, No. 2, p. 176.

[18] Paternoster, C., Fabrizi, A., Cecchini, R., et al. (2008). Thermal Evolution and Mechanical Properties of Hard Ti-Cr-B-N and Ti-Al-Si-B-N Coatings. *Sufr. Coat. Technol.*, Vol. 203, p. 736.

[19] Shtansky, D.V., Levashov, E.A., Gloushankova, N.A., et al. (2004). . Structure and Properties of ZrO_2 and CaO-doped TiC_xN_y Coatings for Biomedical Applications. *Surf. Coat. Technol.*, Vol. 182, p. 101.

[20] Shtansky, D.V., Gloushankova, N.A., Bashkova, I.A., et al. (2006). Multifunctional Biocompatible Nanostructured Coatings for Load-Bearing Implants. *Surf. Coat. Technol.*, Vol. 201, p. 4111.

[21] Shtansky, D.V., Gloushankova, N.A., Levashov, E.A., et al. (2006). Multifunctional Ti-(Ca,Zr)-(C,N,O,P) Films for Load-Bearing Implants. *Biomaterials*, Vol. 27, p. 3519.

[22] Shtansky, D.V., Gloushankova, N.A., Levashov, E.A., et al. (2005). Design, characterization and testing of Ti-based multicomponent coatings for load-bearing medical application. *Biomaterials*, Vol. 26, p. 2909.

[23] Shtansky, D.V., Bashkova, I.A., Levashov, E.A., et al. (2008). Bioaktivnie keramicheskie tantalsoderzhashie plenki dlya implantatov (Bioactive ceramic tantal-containing films for implants). *Dokl. Akad. Nauk*, Vol. 418, No. 1, p. 121.

[24] Shtansky, D.V., Gloushankova, N.A., Bashkova, I.A., et al. (2008). Ta-Doped Multifunctional Bioactive Nanostructured Films. *Sufr. Coat. Technol.*, Vol. 202, p. 615.

[25] Zhong, D., Sutter, E., Levashov, E.A., et al. (2001). Mechanical properties of Ti–B–C–N coatings deposited by magnetron sputtering. *Thin Solid Films*. Vol. 398–399, p. 320.

[26] Kulisch, W., Colpo, P., Gibson, P.N., et al. (2004). ICP assisted sputter deposition of TiC/CaO nanocomposite films. *Surf. Coat. Technol.*, Vol. 188–189, p. 735.

[27] Werner, Z., Stanislawski, J., Levashov, E., et al. (2003). New Types of Multi-Component Hard Coatings Deposited by ARC PVD on Steel Pre-treated by Pulsed Plasma Beams. *Vacuum*, Vol. 70, pp. 263.

[28] Kiryukhantsev-Korneev, F.V., Shtansky, D.V., Levashov, E.A., et al. (2004) Struktura i svoistva Ti–Si–N pokritii, poluchennih magnetronnim raspileniem SHS- mishenei (Structure and properties of Ti-Si-N coatings deposited by magnetron sputtering of SHS targets). *Fiz. Met. Metalloved.*, Vol. 97, No. 3, p. 96.

[29] Shtansky, D.V., Levashov, E.A., Sheveiko, A.N., Moore, J.J. (1998). The Structure and Properties of Ti–B–N, Ti–Si–B–N, Ti–Si–C–N and Ti–Al–C–N coatings deposited by magnetron sputtering using composite targets produced by self-propagating High-temperature Synthesis (SHS). *J. Mater. Synth. Process.*, Vol. 6, No. 1, p. 61.

[30] Shtansky, D.V., Sheveiko, A.N., Levashov, E.A., et al. (2005). Hard Tribological Ti–B–N, Ti–Cr–B–N, Ti–Si–B–N and Ti–Al–Si–B–N Coatings. *Surf. Coat. Technol.*, Vol. 200, p. 208.

[31] Shtansky, D.V., Levashov, E.A., Khavskii, N.N., Moore, J.J. (1996). Perspektivi sozdaniya kompozitnih iznosostoikih plenok, poluchaem ih s ispolzovaniem SHS-katodov (Prospects of wear-resistant composite films deposition using SHS cathodes). *Izv. Vyssh. Uchebn. Zaved., Tsvetn. Metall.*, No. 1, p. 59.

[32] Shtansky, D.V., Kaneko, K., Ikuhara, Y., Levashov, E.A. (2001). Characterization of Nanostructured Multiphase Ti–Al–B–N Thin Films with Extremely Small Grain Size. *Surf. Coat. Technol.*, Vol. 148, p. 206.

[33] Kiryukhantsev-Korneev, Ph.V., Pierson, J.F., Levashov, E.A., et al. (2009). Effect of Nitrogen Partial Pressure on the Structure, Physical and Mechanical Properties of CrB2 and Cr–B–N films. *Thin Solid Films*, Vol. 517, p. 2675.

[34] Kiryukhantsev-Korneev, Ph.V, Pierson, J.F, Bauer, J.P., Levashov, E.A., et al. (2008). Structure and Properties of Hard Nanostructured Coatings in Cr-B-N system, *Proceedings of the III France–Russia Seminar "New Achievements in Materials and Environmental Sciences"*, Paris: EDP Sciences, 2008, p. 11.

[35] Shtansky, D.V., Kiryukhantsev-Korneev, F.V., Levashov, E.A., et al. (2010). Multicomponent Nanostructured Films for Various Tribological Applications. *Int. J. Refract. Met. Hard Mater.*, Vol. 28, p. 32.

[36] Shtansky, D.V., Kiryukhantsev-Korneev, F.V., Levashov E.A., et al. (2009). Comparative Investigation of TiAlC(N), TiCrAlC(N) and CrAlC(N) Coatings Deposited by Sputtering of MAX- phase $Ti_{2-x}Cr_xAlC$ Targets. *Surf. Coat. Technol.*, Vol. 203, p. 3595.

[37] Barsoum, M.W. and El-Raghy, T. (2001). The MAX Phases: Unique New Carbide and Nitride Materials. *Am. Sci.*, Vol. 89, No. 4, p. 11.

[38] Eklund, P., Beckers, M., Jansson, U., et al. (2010). The $M_{n+1}AX_n$ phases: Materials Science and Thin-Film Processing. *Thin Solid Films*, Vol. 518, p. 1851.

[39] Tzenov, N.V., Barsoum, M.W. (2000). Synthesis and Characterization of Ti_3AlC_2. *J. Am. Ceram. Soc.*, Vol. 83, No. 4, p. 825.

[40] Wubian Tian, Peiling Wang, Guojun Zhang et al. (2006). Synthesis and thermal and electrical properties of bulk Cr_2AlC. *Scr. Mater.*, Vol. 54. p. 841.

[41] Levashov, E.A., Pogozhev, Yu.S., Shtansky, D.V., Petrzhik, M.I., (2009). Self-Propagating High-Temperature Synthesis of Ceramic Materials Based on the $M_{n+1}AX_n$ Phases in the Ti-Cr-Al-C System. *Russ. J. Non-Fer. Met.*, Vol. 50, No. 2, p. 151.

[42] Zhimei, Sun., Rajeev, Ahuja, Jochen, M. Shnaider. (2003). Theoretical investigation of the solubility in $M_xM'_{2-x}AlC$ (M and M' are Ti,V,Cr). *Phys. Rev. B*, Vol. 68, p. 4.

[43] Zou, Y., Sun, Z.M., Tada, S., and Hashimoto, H. (2006). *Scr. Mater.*, Vol. 55, p. 767.

[44] Levashov, E.A., Kurbatkina, V.V., Rogachev, A.S., Kochetov, N.A. (2007). Mechanoactivation of SHS Systems and Processes. Int. Journal of Self-Propagating High-Temperature Synthesis. *Int. J. SHS, 2007*, Vol. 16, No. 1, p. 46.

[45] Kurbatkina, V.V, Levashov, E.A, and Rogachev, A.S, (2007). Mechnoactivation of SHS. In: *Combustion of Heterogeneous Systems: Fundamentals and Application for Materials Synthesis*, Mukasyan A.S., Martirosyan, K.S., p. 131–143, Transword Research Network.

[46] Kurbatkina, V.V., Levashov, E.A., Patsera, E.I., et al. (2009). Issledovanie macrokineticheskih harakteristic processov goreniya predvaritelno mehanicheski aktivirovannih reakcionnih smesei Cr-B i Cr-Ti-B (Study of the macrokinetic characteristics of combustion processes of previously mechanically activated Cr-B and Cr-Ti-B reaction mixtures). *Khim. Interesakh Ustoich. Razvit.*, No. 6, p. 21.

[47] Kochetov, N.A., Rogachev, A.S., Pogozhev, Yu.S. (2010). The effect of mechanical activation of a reaction mixture on the velocity of the wave propagation of SHS reactions and microstructure of the TiC–Ni hard alloy. *Russ. J. Non-Fer. Met.*, Vol. 51, No. 2, p. 177.

[48] Voitovich, R.F., Pugach, E.A., (1978). *Okislenie tugoplavkikh soedinenii: Spravochnik (Oxidation of Refractory Compounds: Handbook)*, Metallurgiya, Moscow.

[49] Samsonov, G.V., Markovskii, L.Ya., Zhigach, A.F., Valyashko, M.G. (1960). *Bor, ego soedineniya i splavy (Boron, Its Compounds and Alloys)*, Kiev: AN USSR.

[50] Okada, S., Kudou, K., Iisumi, K., et al. (1996). Single-crystal growth and properties of CrB, Cr_3B_4, Cr_2B_3 and CrB_2 from high-temperature aluminum solutions. *J. Cryst. Growth*, Vol. 166, p. 429.

[51] Muetterties, E.L. (1976). *The Chemistry of Boron and Its Compounds*, Wiley, New-York.

[52] Samsonov, G.V., Serebryakova, T.I., and Neronov, V.A. (1975). *Boridy (Borides)*, Atomizdat, Moscow.

[53] Kuz'ma, Yu.B. (1983). *Kristallokhimiya boridov (Crystal Chemistry of Borides)*, Vyshcha Shkola, Lviv.

[54] Kosolapova, T.Ya. (1986). Svoistva, poluchenie i primenenie tugoplavkikh soedinenii: Spravochnik (Properties, Obtaining, and Application of Refractory Compounds: Handbook), Metallurgiya, Moscow.

[55] Serebryakova, T.I., Neronov, V.A., Peshev, P.D. (1991). *Vysokotemperaturnye boridy (High-Temperature Borides)*, Metallurgiya, Chelyabinsk.

[56] Ivanovskii, A.L., Shveikin, G.P. (1998). *Kvantovaya khimiya v materialovedenii. Bor, ego splavy i soedineniya (Quantum Chemistry in Materials Science. Boron, Its Alloys and Compounds)*, UrO RAN, Yekaterinburg.

[57] Levashov, E.A., Kurbatkina, V.V., Patsera, E.I., et al. (2008). Combustion and structure formation in the mechanoactivated Cr-B system. *Int. J. SHS*, Vol. 17, No. 3, p. 189.

[58] Eremina, E.N., Kurbatkina, V.V., Levashov, E.A., et al. (2005). Poluchenie compositsionnogo materiala MoB metodom silovogo SHS- kompaktirovaniya s primenenirm mehanicheskogo aktivirovaniya ishodnoi smesi Mo-10%B (Obtaining of MoB composite material by forced SHS- pressing with using of preliminary mechanical activation of the initial mixture of Mo-10%B). *Khim. Interesakh Ustoich. Razvit.*, Vol. 13, p. 197.

[59] Avakumov, E.G. (2009). *Fundamental'nye osnovy mekhanicheskoi aktivatsii, mekhanosinteza i mekhanokhimicheskikh tekhnologii: Sbornik statei (Fundamental Base of Mechanical Activation, Mechanosynthesis, and Mechanochemical Technologies: Collected Articles)*, SO RAN, Novosibirsk.

[60] Lyakhov, N.Z., Talako, T.L., Grigoreva, T.F. (2008). *Vliyanie mekhanoaktivatsii na protsessy fazo- i strukturoobrazovaniya pri samorasprostranyayushchemsya vysokotemperaturnom sinteze (Influence of the Mechanical Activation on the Structure Formation during the Self-Propagating High-Temperature Synthesis)*, Parallel, Novosibirsk.

[61] Grigoreva, T.F., Barinova, A.P., Lyakhov, N.Z. (2008). *Mekhanokhimicheskii sintez v metallicheskikh sistemakh (Mechanochemical Synthesis in Metallic Systems)* (Avakumov, E.G. edition), Parallel, Novosibirsk.

[62] Novikov, I.I., Rozin, K.M. (1990). *Kristallografiya i defekty kristallicheskoi reshetki (Crystallography and Defects of Crystal Lattice)*, Metallurgiya, Moscow.
[63] Boldyrev, V.V., Tkasova, A.K. (2000). Mechanochemistry of solids: Past, present, and prospects. *J. Mater. Synth. Process*, Vol. 8, No. 3–4, p. 121.
[64] Shelekhov, E.V., Pripisnov, O.N., Rupasov, S.I. (2001). Analiz tonkoi strukturi Cr v processe mehanicheskogo aktivirovaniya smesei Cr-C (Analysis of the thin structure of Cr during mechenical activation of the Cr-C mixtures). *Izv. Vyssh. Uchebn. Zaved., Tsvetn. Metall.*, No. 1, p. 29.
[65] Gorelik, S.S., Rastorguev, L.N., Skakov, Yu.A. (1999). Rentgenograficheskii i elektronno-opticheskii analiz (X-Ray Diffraction and Electron-Optical Analyses), MISiS, Moscow.
[66] Levashov, E.A., Rogachev, A.S., Epishko, Yu.K., Kochetov, N.A. (2007). Samorasprostranyayushiisya visokotemperaturnii sintes katodov-mishenei v sisteme Ti-Ta-C-$Ca_3(PO_4)_2$ dlya ionno-plazmennogo napileniya mnogofunkcionalnih biosovmestimih pokritii (Self-propagating high-temperature synthesis of target cathodes in the system Ti-Ta-C-$Ca_3(PO_4)_2$ for the ion-plasma deposition of multifunctional biocompatible nanostructured coatings). *Izv. Vyssh. Uchebn. Zaved., Poroshk. Metall. Funkts. Pokr.,* No. 1, p. 14.
[67] Mossino, P. (2004). *Ceram. Int.*, Vol. 30, No. 3, p. 311.
[68] Rogachev, A.S., Mukasyan, A.S., and Merzhanov, A.G. (1987). Strukturnie prevrasheniya pri bezgazovom gorenii sistem titan-uglerod i titan-bor (Structural transformations during gasless combustion of titanium-carbon and titanium-boron systems.) *Dokl. Akad. Nauk*, Vol. 297, No. 6, p. 1425.
[69] Levashov, E.A., Kurbatkina, V.V., Rogachev, A.S., et al. (2008). Characteristic properties of combustion and structure formation in the Ti–Ta–C system. *Rus. J. Non-Fer. Met.*, Vol. 49, No. 5, p. 404
[70] Merzhanov, A.G., Mukasyan, A.S. (2007). *Tverdoplamennoe gorenie (Solid-State Combustion),* TORUS PRESS, Moscow.
[71] Levashov, E.A., Senatulin, B.R., Leyland, A., Matthews, A. (2006). *Rus. J. Non-Fer. Met.*, Vol. 47, No. 1, p. 39.
[72] Merzhanov, A.G. (1979). Processi goreniya kondensirovannih sistem. Novoe napravlenie issledovanii (Combustion of condensed systems. The new direction of research). *Vestn. Akad. Nauk SSSR*, No. 8, p. 10.
[73] Pearson, W.B. (1958). *Handbook of Lattice Spacings and Structures of Metals and Alloys*, Pergamon, New York.
[74] Kiparisov, S.S., Levinskii, Yu.V., Petrov, V.M. (1989). *Karbid titana (Titanium Carbide)*, Metallurgiya, Moscow.
[75] Kubashewsky, O., Hopkins, B. (1969). *Okislenie metallov i splavov (Oxidation of Metals and Alloys)*, Mir, Moscow.

2

Advanced Ceramic Target Materials Produced by Self-Propagating High-Temperature Synthesis for Deposition of Functional Nanostructured Coatings - Part 2: Multicomponent Systems

Evgeny A. Levashov, Yury S. Pogozhev and Victoria V. Kurbatkina
National University of Science and Technology "MISIS", Russia

1. Introduction

The introduction of doping elements Al and Si into the coatings allows one to attain a combination of the high characteristics of the hardness and wear resistance with a relatively low friction coefficient. One important factor in increasing of the durability of different products is the provision of thermal stability and oxidation resistance at high temperatures [1, 2]. Therefore, the problem of the development of hard wear-resistant coatings with high thermal stability, heat resistance, and corrosion resistance is very urgent.

In this work, the possibility of synthesizing of promising composite materials based on TiC_yN_z, Ti_5Si_3, and $TiAl_3$ from the reactionary mixtures in the Ti–Al–Si_3N_4–C system is shown. As the initial components of the reactionary mixtures we used powders of titanium, aluminum, technical carbon (ash) of above-mentioned grades, and silicon nitride (TU 88-1-143-88). The mixtures composition was determined from the accounting of the complete transformation of the initial reagents and the formation of the product with phase composition described by the general formula

$$X\times(TiAl_3) + (100\text{-}X)\times(0{,}448TiC_{0,5}+0{,}552(Ti_5Si_3+4AlN)), \quad (10)$$

where x is the mixture parameter taking values in the range from 10 up to 50 wt %.

The experimental compositions of the reactionary mixtures for the synthesis of the composite ceramic materials, depending on the mixture parameter, are presented in Table 1.

x , wt %	Content of the initial components in green mixture, wt %			
	Ti	Al	Si_3N_4	C
10	63,9	17,3	14,3	4,5
20	61,0	22,3	12,7	4,0
28,1	58,6	26,4	11,4	3,6
40	55,1	32,4	9,5	3,0
50	52,1	37,5	7,9	2,5

Table 1. Composition of the initial reaction mixtures in the Ti–Al–Si_3N_4–C system

The values of the adiabatic combustion temperature (T_c^{ad}) of the reactionary mixtures in the Ti–Al–Si_3N_4–C system and the equilibrium composition of the synthesis products at this temperature calculated using the "THERMO" software depending on the mixture parameter are listed in Table 2.

As the mixture parameter increases, the adiabatic combustion temperature decreases monotonically. In this case the content of ceramic phases (titanium carbide, nitride, and silicide) decreases and the fraction of metal melts increases. At x = 40 and 50%, phases of titanium aluminide and aluminum nitride appear. It should be noted that the equilibrium phase composition given in Table 2 shows the state of the system immediately after the combustion under the condition that the combustion temperature equals the adiabatic value. As the sample is cooled, the evolution of the microstructure and the phase composition of the product inevitably take place (the so-called secondary structure formation). For this reason, the composition of the final material should be differing. We can expect the mutual solubility of TiC and TiN with the formation of titanium carbonitride most probably, of the nonstoichiometric composition (taking into account the excess of titanium in the system).

x , wt %	T_c^{ad}, K	Calculated composition of final products at the adiabatic temperature, %							
		Al (l)	TiC (s)	TiN (s)	Ti_5Si_3 (s)	Ti (l)	Ti (s)	TiAl (s)	AlN (s)
10	2309	17,3	22,5	25,3	33,1	1,8	-	-	-
20	2046	22,3	20,0	22,5	29,4	5,9	-	-	-
28,1	1863	26,4	18,0	20,2	26,4	9,0	-	-	-
40	1733	24,6	15,0	11,0	22,0	-	9,04	14,5	3,8
50	1732	19,6	12,5	2,7	18,0	-	3,5	36,3	7,4

Table 2. Thermodynamical calculation of the adiabatic combustion temperature and the phase composition of the synthesis products at a specified temperature

From the results of a thermodynamic calculation, we can make an important conclusion that silicon nitride completely transforms during SHS. It decomposes onto the elements, which react with titanium forming the nitride and silicide phases. Since Si_3N_4 is a refractory compound, this phase is often considered as inert additive not entering into any reactions. However, due to the higher chemical affinity of titanium with nitrogen and silicon, silicon nitride can be used as a reagent.

The experimental values of the combustion parameters for mixtures with x = 10; 20 and 28,1 % at the initial temperature equal to room temperature are presented in Table 3.

x , wt %	T_c, K	U_c, cm/s
10	1906	0,29
20	1823	0,26
28,1	-	0,25

Table 3. Experimental values of the combustion temperature and rate at $T_0 = T_{room}$

At initial room temperature and x = 10, 20, and 28.1%, the combustion proceeds in the self-oscillation mode, while we failed to initiate the combustion at all at higher x (40 and 50%).
It is evident from Tables 2 and 3 that the experimental combustion temperature is lower than the calculated adiabatic temperature by 300–400 K on average, which is associated with heat losses for heating of the surrounding environment. It should be noted that, at T_0 = 293 K (20°C), the sample with x = 28.1% is incompletely combusted, so, it does not allow us to measure the combustion temperature.
The dependence of the combustion rate, measured by photodiode light indicator directly during the process of forced SHS pressing, from the composition of the initial reaction mixtures is shown in Fig. 1. It is seen that U_c is almost invariable while the mixture parameter is varying in the range of 10–28.1 %. With further increase of the parameter X (40 and 50%) the combustion rate decreases significantly.
The combustion rate of the three-layered briquettes under the conditions of the quasi-isostatic compression is considerably higher than the combustion rate of homogeneous cylindrical samples in the reaction chamber. Obviously, that one of the causes of this phenomenon is the additional heat coming from the "chemical heater". We also cannot exclude the influence of the convective heat and mass transfer, which can intensify the heat transmission in the billet pores under the pressing conditions.
The results of an X-ray phase analysis of the compact synthesis products based on TiC_yN_z, Ti_5Si_3, and $TiAl_3$ are presented in Table 4. It can be seen that the phase composition and their quantitative ratio change when the mixture parameter is varied. For x = 10, 20, and 28.1%, the predominant phase is titanium carbonitride TiC_yN_z, which is formed due to the chemical interaction between titanium, carbon and nitrogen, which is evolved during the decomposition of silicon nitride. As the mixture parameter increases, the TiC_yN_z content in the synthesis products decreases from 55 to 48 %. In addition, we identified the phases of the intermetallic compound $TiAl_3$ and titanium silicide Ti_5Si_3.

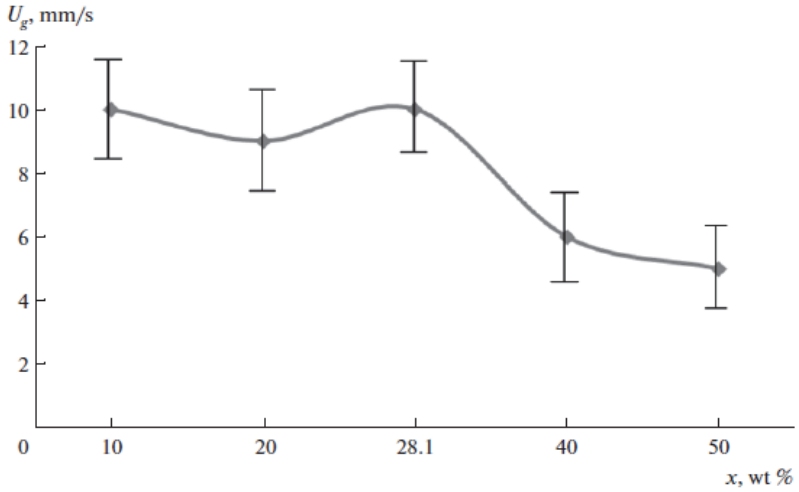

Fig. 1. Dependence of the combustion rate of the samples from the composition of the initial components during forced SHS pressing.

Phase in the samples composition	Mixture parameter x, wt %									
	10		20		28,1		40		50	
	Fraction, wt %	Period a, nm	Fraction, wt %	Period a, nm	Fraction, wt %	Period a, nm	Fraction, wt %	Period a, nm	Fraction, wt %	Period a, nm
TiC_xN_y	55	a=0,4285	50	a=0,4284	48	a=0,4286	9	a=0,4270	-	-
$TiAl_3$	15	a=0,3830 c=0,8584	23	a=0,3848 c=0,8561	21	a=0,3842 c=0,8585	39	a=0,3841 c=0,8582	47	a=0,3848 c=0,8566
Ti_5Si_3	30	a=0,7445 c=0,5175	27	a=0,7444 c=0,5170	21	a=0,7449 c=0,5166	13	a=0,7448 c=0,5158	8	a=0,7451 c=0,5163
Ti_3SiC_2	-	-	-	-	10	a=0,3074 c=1,8144	39	a=0,3043 c=1,8117	-	-
$TiAl_2$	-	-	-	-	-	-	-	-	29	a=0,3971 c=2,4289
β-Si_3N_4	-	-	-	-	-	-	-	-	9	a=0,7765
TiC	-	-	-	-	-	-	-	-	7	a=0,4309

Table 4. Results of a quantitative phase analysis of the synthesized samples

At x = 28.1%, also the Ti_3SiC_2 phase presents in amounts to 10%, while at x = 40 %, its content increases up to 39 %. The phase composition of the products at x = 40 % also includes the $TiAl_3$ intermetallic compound (39%) and the Ti_5Si_3 and TiC_yN_z phases (13 and 9%, respectively).

The phase composition of the synthesis products with x = 50% has the strongest distinctions when compared with other samples under study. The presence of silicon nitride in almost the same amount as in the initial green mixture, as well as the $TiAl_2$ intermetallic compound, indicates the incompleteness of the chemical reactions as a result of the incomplete combustion. The main phase is an intermetallide $TiAl_3$ with a content of 47 %. In addition, a small amount of nonstoichiometric titanium carbide (7%) with a lattice period of 0.4309 nm and titanium silicide Ti_5Si_3 (8%) are found.

Generalization of the data of an X-ray phase analysis allows us to conclude that increase in the mixture parameter from 10 to 50% lead to decrease in the content of the ceramic phases TiC_yN_z and Ti_5Si_3 and to increase in the content of the metallic phase $TiAl_3$.

Figure 2 shows the microstructures of the materials with various mixture parameters (magnification ×10000).

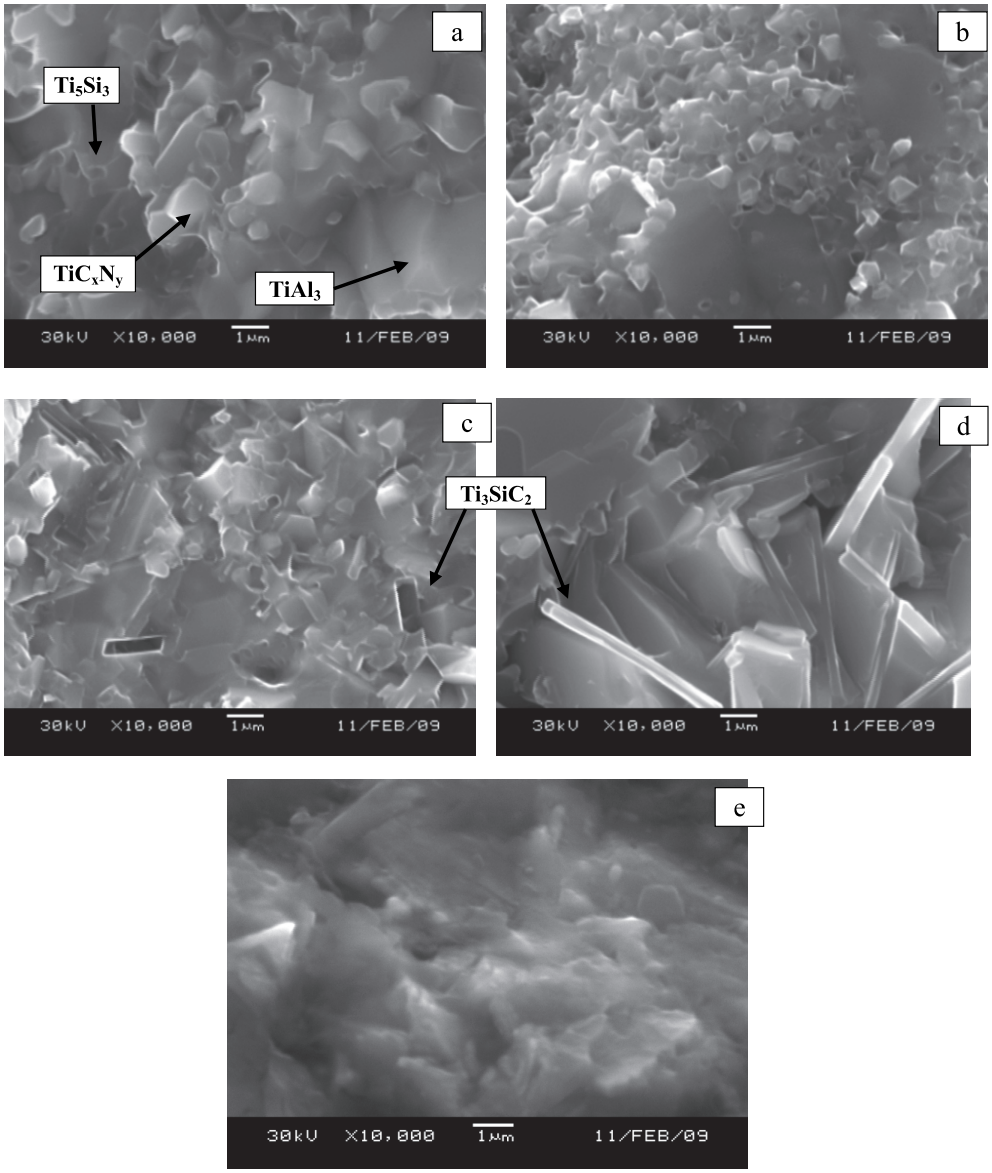

Fig. 2. Microstructures of the samples of compact ceramic materials based on TiC_yN_z, Ti_5Si_3, and $TiAl_3$. x: = 10 (a); 20 (b); 28.1 (c); 40 (d); and 50 wt % (e).

At x = 10%, the structure consists of titanium carbonitride grains (the average size of ~1 μm) and $TiAl_3$ and Ti_5Si_3 binder phases. As x increases from 10 to 20%, the titanium carbonitride grains become finer to 0.5 μm. From a comparison of microstructures of the samples at x = 28.1 and 40 % can be seen that, there is no changing in the grain size of TiC_yN_z due to x increasing. In addition to titanium carbonitride, titanium aluminide and titanium silicide, the structure of this samples also contains the $M_{n+1}AX_n$ phase [3-5] of the Ti_3SiC_2 composition in the form of ~300 nm thick characteristic layers. The phase interfaces in the sample with x = 50 % are strongly spread, this is associated with the incompleteness of the chemical reactions during synthesis.

The physical and mechanical properties of the obtained materials, namely, the hardness, ultimate bending strength, and elasticity modulus, as well as the hydrostatic and true (measured using a helium pyknometer) densities, residual porosity, and ultrasonic rate in the bulk material, are given in Table 5.

x, wt %	$\rho_{hydr.}$, g/cm^3	ρ_t, g/cm^3	P_{res}, %	C, m/s	HV, GPa	σ_{bend}, MPa	E, GPa
10	4,19	4,34	3,7	6263	10,3	169	385
20	4,18	4,27	2,3	5880	10,1	193	521
28,1	4,04	4,06	0,5	6473	8,7	218	456
40	3,76	3,82	1,6	5274	8,3	182	482
50	3,18	3,67	13,4	4237	7,4	-	-

Table 5. Physical and mechanical properties of ceramic materials based on TiC_yN_z, Ti_5Si_3, and $TiAl_3$

At x = 50%, the obtained material has an increased brittleness, so its strength properties were not measured.

It is evident from the measured data of the ultrasonic rate that the sample with the mixture parameter of 28.1 % has fewer defects, while the highest defect concentration is observed for the composition with x = 50 %. These results completely agree with the characteristics of the residual porosity and strength. Since the residual porosity of the sample with x = 28.1 % is 0.5 %, while for other compositions (excluding x = 50%), it varies in the limits 2–4 %.

Based on the results of hardness measurement, we can see that, with increasing X from 10 to 50 % the value of HV decreases from 10.3 to 7.4 GPa. This is associated with a decrease in the content of the hard carbonitride phase. The obtained values of hardness are fully comparable with the hardness of the carbide and nitride based ceramics, as well as of the classic hard alloys [6]. The sample with x = 28.1 % has the highest strength. No direct dependence between the elasticity modulus, residual porosity, and mixture parameter is found.

The results of heat resistance tests for the materials based on TiC_yN_z, Ti_5Si_3, and $TiAl_3$ are presented in Fig. 3. The values of their specific oxidation rate in air at T = 1173 K and τ = 30 h are given in Table 6.

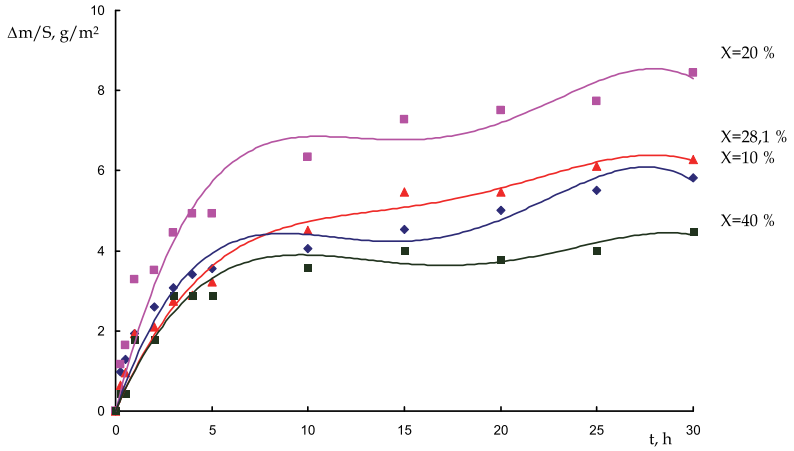

Fig. 3. Variation in the weight of the experimental samples of ceramic materials as a function of the oxidation time at T = 1173 K.

x, wt %	Specific oxidation rate, g/(m²×s)	Δm/S, g/m²
10	$5{,}4\times10^{-5}$	5,8
20	$7{,}8\times10^{-5}$	8,4
28,1	$5{,}8\times10^{-5}$	6,3
40	$4{,}1\times10^{-5}$	4,5
50	$1{,}6\times10^{-3}$	175,2

Table 6. Specific oxidation rate of the samples of ceramic materials based on titanium carbide, titanium silicide, and titanium aluminide at T = 1173 K for τ = 30 h

Oxidation process follows the parabolic law when the growth of the oxide film is limited by the diffusion of oxygen through the oxide layer. The material synthesized at x = 40% has the lowest oxidation rate (4.1×10^{-5} g/(m²×s)), which is explained by a high content of highly heat resistant $TiAl_3$ and Ti_3SiC_2 phases. It should be noted that oxidation rates of other samples in the system under study are very close to this best result, except for the sample with a mixture parameter of 50 %.

Developed ceramic materials based on titanium carbonitride, titanium silicide, and titanium aluminide (except material with X = 50 %) were used for production by forced SHS pressing technology of experimental disc and segmented planar targets for ion-plasma deposition (magnetron sputtering) of multifunctional nanostructured coatings. The disk targets are shown in Fig. 4.

2. Conclusions

The modern views about the features of the synthesis of few interesting classes of the systems based on titanium carbonitride, silicide, aluminides, and $M_{n+1}AX_n$ phase are considered in this work.

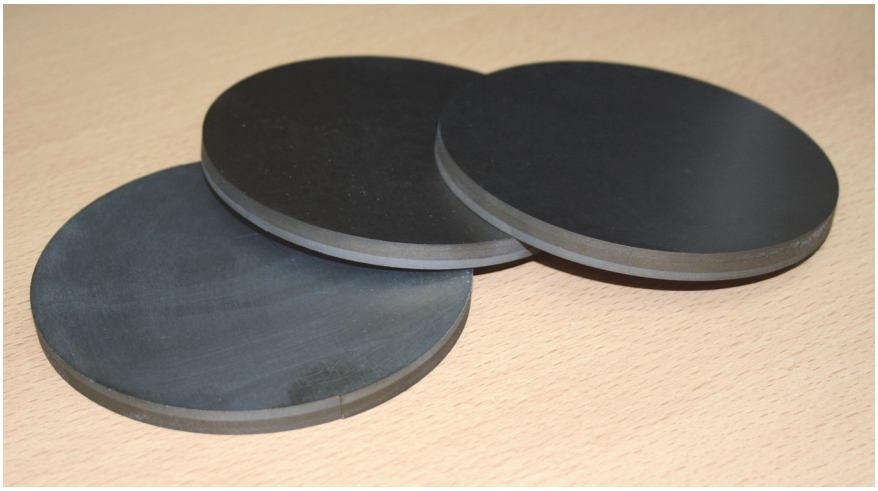

Fig. 4. Disc targets based on titanium carbonitride, titanium silicide, and titanium aluminide.

3. Acknowledgment

The experimental works described in the chapter were carried out due to financial support from the Federal Target Program "Scientific and scientific-and-pedagogical personnel of an innovative Russia" for 2009–2013 (State Contracts no. 02.740.11.0133, and 02.740.11.0859), as well as by the Program of creation and development of the National University of Science and Technology "MISIS".

4. References

[1] Shtansky, D.V., Kiryukhantsev-Korneev, Ph.V., Levashov, E.A., et al. (2007). Hard tribological Ti–Cr–B–N coatings with enhanced thermal stability, corrosion- and oxidation resistance. *Surf. Coat. Technol*., Vol. 202, p. 861.

[2] Kiryukhantsev-Korneev, Ph.V., Pierson, J.F., Levashov, E.A., et al. (2009). Effect of Nitrogen Partial Pressure on the Structure, Physical and Mechanical Properties of CrB2 and Cr–B–N films. *Thin Solid Films*, Vol. 517, p. 2675.

[3] Eklund, P., Beckers, M., Jansson, U., et al. (2010). The $M_{n+1}AX_n$ phases: Materials Science and Thin-Film Processing. *Thin Solid Films*, Vol. 518, p. 1851.

[4] Tzenov, N.V., Barsoum, M.W. (2000). Synthesis and Characterization of Ti_3AlC_2. *J. Am. Ceram. Soc*., Vol. 83, No. 4, p. 825.

[5] Levashov, E.A., Pogozhev, Yu.S., Shtanskii, D.V., Petrzhik, M.I. (2009). Self-propagating high-temperature synthesis of ceramic materials based on $M_{n+1}AX_n$ -phases in Ti-Cr-Al-C system. *Rus. J. Non-Fer. Met.*, Vol. 50, No. 2, pp. 151-160.

[6] Panov, V.S., Chuvilin, A.M. (2001). Tekhnologiya i svoistva spechennykh tverdykh splavov i izdelii iz nikh (Technology and Properties of Sintered Hard Alloys and Articles on Their Base), MISiS, Moscow.

3

Combustion Synthesis of Ceramic Powders with Controlled Grain Morphologies

Guanghua Liu[1], Jiangtao Li[1] and Kexin Chen[2]
[1]*Technical Institute of Physics and Chemistry, Chinese Academy of Sciences, Beijing*
[2]*Department of Materials Science and Engineering, Tsinghua University, Beijing*
China

1. Introduction

Combustion synthesis, which is also known as self-propagating high-temperature synthesis (SHS), is a facile and economic technique to prepare a large variety of advanced materials, such as ceramics, intermetallics, composites, and functionally-graded materials [1-4]. By this technique, new materials are synthesized from self-sustained exothermic chemical reactions instead of long-time heat treatment by furnace. Once the reactants are ignited, a large amount of heat energy is produced to support the reaction to continue. With the propagation of combustion wave through the whole sample, the reactants are converted into products. Because exothermic combustion reactions occur quickly, a non-equilibrium state is usually involved in combustion synthesis and characterized by high temperatures and fast heating or cooling rates. This non-equilibrium reaction state offers an opportunity for controlling the microstructure of products.

Among the extensive applications of combustion synthesis, the fabrication of advanced ceramic powders is an important and successful practice. By combustion synthesis, many kinds of ceramic powders have been prepared, including nitrides (Si_3N_4, AlN, TiN, BN, SiAlON, etc.), carbides (SiC, TiC, ZrC, Ti_3SiC_2, Ti_3AlC_2, Ti_2AlC, etc.), borides (MgB_2, TiB_2, ZrB_2, etc.), silicides (e.g. $MoSi_2$), and oxides (e.g. ferrites, Y-Ba-Cu-O superconductors). The grain size and morphology of the ceramic powders can be manipulated by controlling the processing parameters, such as proportion of diluents, porosity of green compacts, and particle size distribution of raw materials.

This chapter presents some recent results on combustion synthesis of ceramic powders, with an emphasis on the investigation of crystal growth kinetics and control of final grain morphologies. Four kinds of ceramic powders (TiN, SiC, SiAlON, and Ti-Al-C) with different grain morphologies are reported as examples. The grain growth mechanisms involved in combustion synthesis of these ceramic powders are discussed in detail.

2. Combustion synthesis of TiN powders with different grain morphologies

The nitrides of transition metals have received increasing attention because of their unique chemical and physical properties. Among these materials, TiN is particularly interesting due to its superior hardness, good thermal stability, high wear resistance, excellent corrosion resistance, and relatively high electrical conductivity [5]. It can be used as a coating material

on cutting tools, diffusion barrier in microelectronic devices, and protective layer on optical components. For these various applications, the surface roughness, film texture, and crystallization shape of TiN strongly affect its physical properties. Therefore, it is important to understand the nucleation and growth kinetics of TiN for controlling its microstructure. In this aspect, many results have been reported on the epitaxial growth of TiN thin films. In the preparation of TiN powders or bulk ceramics, however, studies on the crystal growth and shape evolution are limited.

Combustion synthesis is an important method to prepare TiN powders. This method can induce high reaction temperature and drastic heating or cooling rate, which offers an opportunity to manipulate the microstructure of the products. By controlling the starting compositions and processing parameters in combustion synthesis, TiN powders can be prepared with different grain morphologies [6].

Using commercial Ti powder (99 % pure, 300 mesh, General Research Institute for Nonferrous Metals, Beijing, China) and high-purity N_2 (99.9 %, Huayuan Gaseous Co., Beijing, China) as major reactants, TiN and NH_4Cl as additives, single-phase TiN can be prepared by combustion synthesis. As shown in Figure 1, no residual Ti or other impurity is detected in the product, indicating that the Ti powder has been fully nitridized into TiN. Figure 2 shows the temperature history during the combustion reaction. It is clear that, once the combustion reaction is triggered, the temperature immediately increases from room temperature to nearly 2000°C in only one second, and the maximum heating rate reaches 6000°C/s. When the combustion reaction is over, the sample quickly cools down with a cooling rate of ~60°C/s. In the short reaction period, the resultant TiN micro-crystals undergo a fast shape evolution process and develop into various morphologies such as quasi-spherical grains, faceted cubic or pyramidal crystals, and dendrites, as shown in Figure 3.

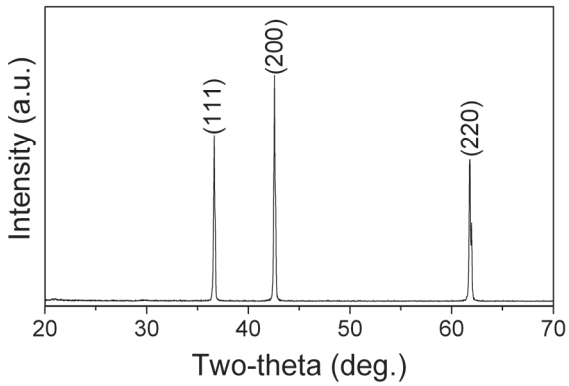

Fig. 1. XRD pattern of TiN powder prepared by combustion synthesis

Generally speaking, the final morphology of a crystal depends on both its intrinsic lattice structure and external conditions for growth. The intrinsic lattice will lead to the equilibrium crystal shape (ECS) with minimum total surface energy, and the external conditions often force the crystal to deflect from its ECS and develop into various morphologies. The actual crystal shape is derived from the competition of internal and external factors. Based on this viewpoint, the formation mechanisms of the observed different morphologies of TiN grains can be discussed.

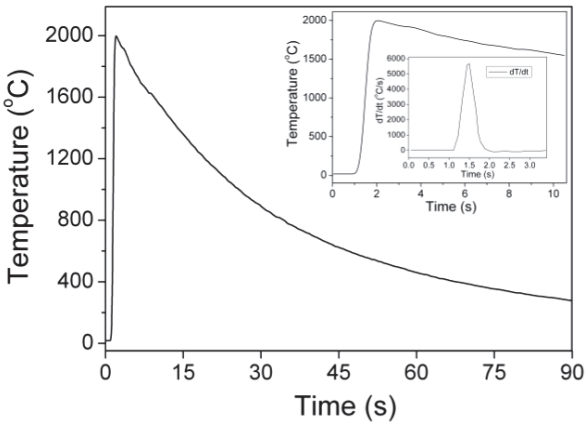

Fig. 2. Temperature history during the combustion synthesis of TiN

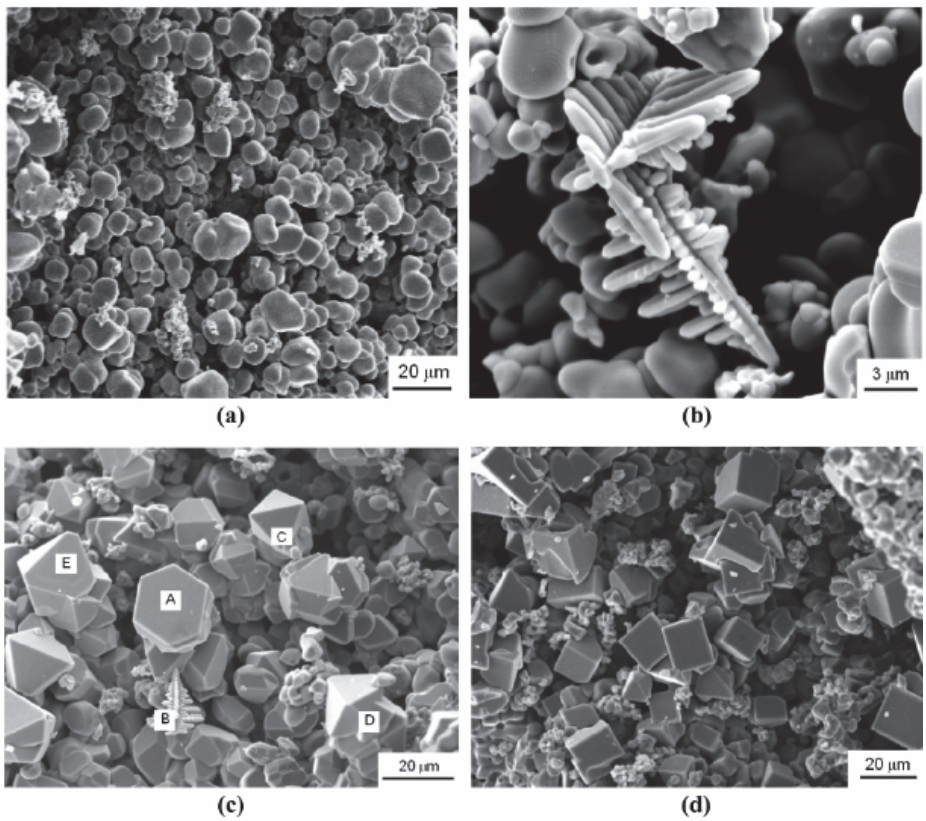

Fig. 3. TiN powders prepared by combustion synthesis with various grain morphologies: (a) quasi-spherical grains; (b) dendrites; (c) faceted pyramidal crystals; (d) faceted cubic crystals

2.1 Quasi-spherical TiN grains

In the combustion synthesis of TiN, the maximum reaction temperature (Figure 2) is much higher than the melting point of Ti. Therefore, in the combustion reaction, TiN is produced mostly by the reaction between Ti melt and N_2. Compared with the gaseous reaction of Ti vapor and N_2, the nitridation of Ti melt has a lower latent enthalpy. In this case, the interface between TiN crystals and Ti melt is thought to be rough and there is no crucial nucleation barrier for the formation of TiN. That is to say, new TiN nuclei can be formed continuously, which then grow isotropically into quasi-spherical grains.

Figure 4 simply illustrates the continuous growth of the quasi-spherical TiN grains. In the N_2 atmosphere at a high pressure, some N_2 molecules or N atoms can dissolve into Ti melt and then react with the latter to produce initial TiN nuclei. These nuclei act as the bases for later heterogeneous nucleation, which is easier than homogeneous nucleation in Ti melt. By diffusion, the dissolved N_2 molecules or N atoms move to the interface and react with Ti via the reaction of Ti(melt) + N_2/[N] → TiN(crystal). Because there is no crucial nucleation barrier, the formation and growth of TiN is limited by the diffusion of N_2 or [N] in Ti melt.

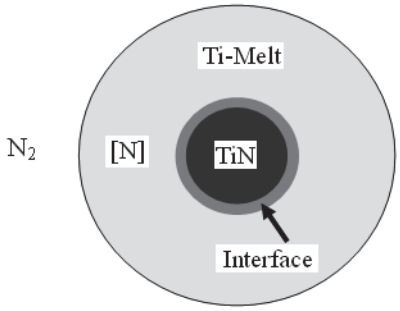

Fig. 4. A simple illustration of diffusion-controlled continuous growth of quasi-spherical TiN grains

2.2 Faceted TiN crystals

As mentioned above, crystals with anisotropic surface energy are inclined to reach the ECS with the minimum total surface energy. Generally, ECS is bounded with the close-packed faces with larger interplanar spacings because they have lower surface energy. Experimental observations have revealed that, the importance (frequency of occurrence) of a crystal face decreases with its interplanar spacing, which is known as the Bravais-Friedel law [7,8]. TiN has a composite face-centered cubic (FCC) lattice like NaCl, and its crystal faces with decreasing interplanar spacings run as {100}, {110}, {111}, {200}, {220}, {222}. In the composite FCC lattice of TiN, the elementary growth layers are {200}, {220} and {222}. According to the Bravais-Friedel law, the importance of these crystal faces should be {200}>{220}>{222}. If only the most important {200} faces are exposed, the ECS of TiN should be a cube.

From kinetic point, crystal growth is such a process that the reactant atoms in fluid phases are attached and bonded at crystal surface. The attachment energy or bonding energy can be used to estimate the difficulty for the formation of a new layer. The crystal faces with higher bonding energies have higher growth rates, which will shrink gradually and finally disappear during crystal growth. On the contrary, the crystal faces with lower binding energies and growth rates will be reserved and exposed in the end.

Now let's consider the binding energy for a new atom at {200}, {220}, and {222} faces in a TiN crystal according to the atom arrangements shown in Figure 5. Although TiN has a lattice structure like NaCl, the bonding ways are different in these two compounds. It is usually accepted that, TiN is not a normal ionic-bonded compound like NaCl, but a Hägg phase bonded with covalent and metallic bonds. The metallic bonds are formed among the *d*-electrons of Ti, and the covalent bonds are formed between the *d*-electrons of Ti and the *p*-electrons of N. The metallic bonds are relatively weak, while the directional covalent bonds are much stronger. In this way, the bonding energy is mainly determined by the covalent bonds between the new atom and its first nearest neighbors, with the distance of *a*. As shown in Figure 5, the number of first nearest neighbors of a new atom is 1, 2, and 3 for {200}, {220}, and {222} faces, respectively. Therefore, crystal faces with decreasing binding energies and thus growth rates run as {222}>{220}>{200}. During crystal growth, the crystal faces with higher growth rates will shrink and those with lower growth rates will expand. Therefore, in the final crystal shape, crystal faces with increasing importance should be {222}<{220}<{200}, which agrees well with the prediction from the Bravais-Friedel law.

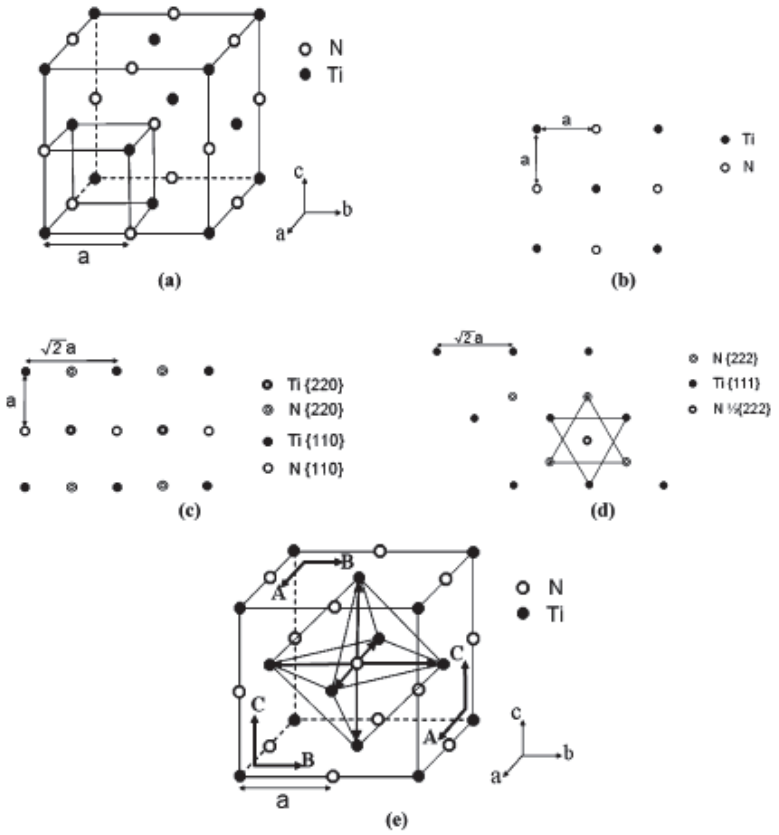

Fig. 5. A schematic illustration showing (a) the FCC lattice structure, (b), (c), and (d) atom arrangements at {200}, {220}, and {222} faces, and (e) PBC vectors in TiN crystals

For the prediction of final crystallization shape of a crystal based on its intrinsic lattice structure, the Periodic Bond Chain (PBC) theory is usually considered. According to PBC theory [7,8], a crystal should be bounded by edges parallel to the directions in which there is a continuous chain of strong bonds between the building units. Such a chain is called a PBC and the crystal can be considered as an array of PBCs. From the numbers of PBCs involved, crystal faces are divided into three categories, F-faces containing two or more PBCs, S-faces containing only one PBC, and K-faces containing no PBC. The three types of crystal faces have different growth rates, F-faces grow slowly and thus are important faces, K-faces grow fast and have least importance, and S-faces have a middle importance. In the lattice structure of TiN, there are three PBCs consisting of continuous strong Ti-N covalent bonds, viz. A//[100], B//[010], and C//[001], as shown in Figure 5. Thus, {200}, {220}, and {222} faces are identified as F, S, and K-faces, respectively. Therefore, {200} faces are most important and exposed, while {220} and {222} faces will shrink during crystal growth and finally degrade to edges and corners. By this means, faceted cubic TiN crystals are produced, as shown in Figure 6 (a).

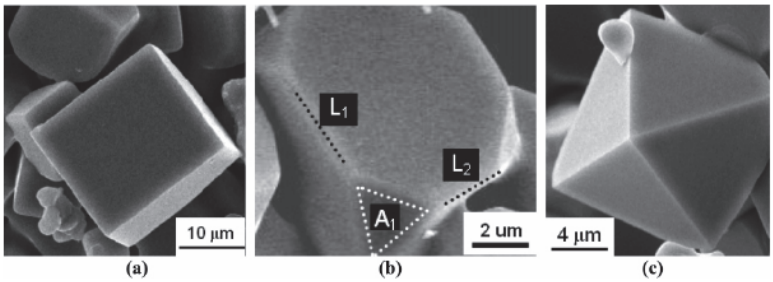

Fig. 6. Several typical shapes of faceted TiN crystals: (a) cube; (b) truncated cube; (c) pyramid

Except for the intrinsic factor, external conditions also affect the growth of TiN crystals and cause a deflection of crystal shape from the ECS. It is reported that, during the growth of TiN thin films, the preferred orientation of TiN crystals depends on the incident ion/metal flux ratio, and the nucleation kinetics of TiN is strongly affected by reaction temperature and the pressure of N_2. In combustion synthesis, however, both the temperature and N_2 pressure can be variable because of the drastic reaction and abrupt heating or cooling rate. This variance in reaction conditions will change the growth kinetics of TiN crystals and result in a diversity of crystal shapes, such as truncated cubic and pyramidal crystals, as shown in Figure 6 (b) and (c).

From the energy viewpoint, the most stable shape of a crystal is the one with the minimum total surface energy, and this shape is ECS as mentioned before. Driven by the reduction of total surface energy, TiN crystals with other shapes have a tendency to transform into the ECS. That is to say, the quasi-spherical TiN grains will undergo a faceting process to become cubic crystals. If this faceting process is not complete, intermediate products including truncated cubic and pyramidal crystals will be obtained (Figure 6). At the surface of some TiN grains, a terraced structure consisting of a series of layered circular plates is observed, as shown in Figure 7. It is proposed that this terraced structure is caused by the faceting process via two-dimensional nucleation. When a layer grows larger than a critical size, new nuclei can form on it. By this means, the outward growth in the normal direction takes place together with the lateral growth of each layer, and finally produces a series of terraces.

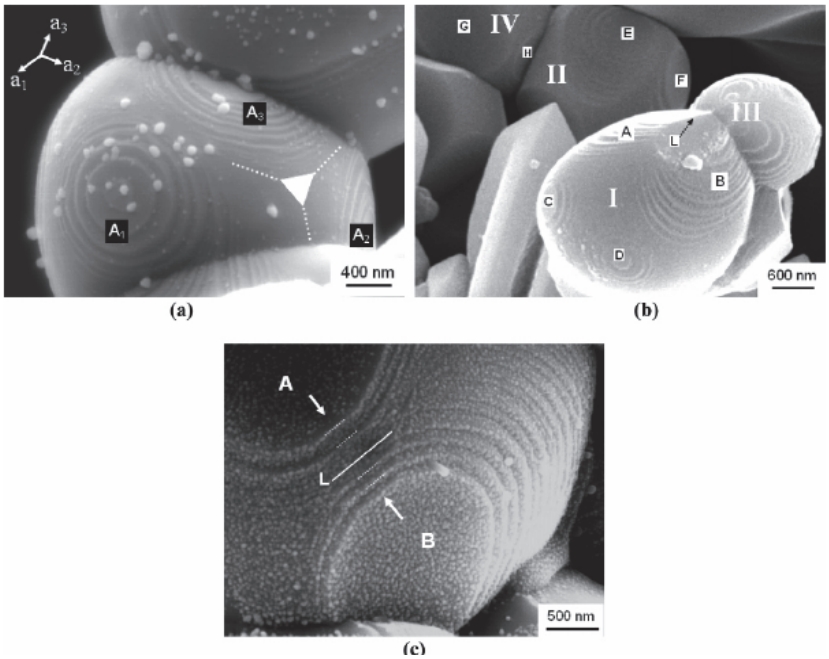

Fig. 7. SEM images showing a terraced structure on the TiN grains

Figure 8 schematically illustrates the transformation of a spherical TiN grain into a faceted cubic crystal by the faceting process. At first, small facets appear on the surface of the spherical grain. Then, the facets grow in both lateral and normal directions by two-dimensional nucleation, and a series of terraces are created. With further growth, two neighboring facets toward different directions will cross and thus an edge forms. At last, nucleation stops and the existing layers expand by lateral growth until they joined at edges. Consequently, a faceted cubic crystal is obtained. The above illustration is supported by SEM observations. For example, Figure 7 (a) shows three series of terraces (A_1, A_2, and A_3) in orthogonal directions, which can develop into three faces of a cubic crystal. Figure 7 (b) shows a faceting grain (II) with a clear tendency to transform into a cubic crystal. Details of the formation edges are shown in Figure 7 (b) and (c).

In the faceting process, the final crystal shape is closely connected with the growth rates of different faces. Variations in growth kinetics can cause different crystal morphologies from the ECS. For example, in the truncated cube shown in Figure 6 (b), {220} faces have degraded to edges but {222} faces still remained as small triangular facets (A_1). This is probably attributed to the retarded growth at {222} faces. As illustrated in Figure 8 (d), only when the ratio of the growth rate of {222} faces (V_T) to that of {200} faces (V_A=V_B=V) is equal or larger than $\sqrt{3}$, {222} faces will completely degrade to corners. Otherwise, when $V_T/V<\sqrt{3}$, {222} faces will be partially reserved and a truncated cube is obtained. If V_T further decreases to be much smaller than V, {222} faces become the most important and the final crystal shape will be an octahedron. The four-fold symmetric pyramidal TiN crystal shown in Figure 6 (c) can be regarded as a half octahedron.

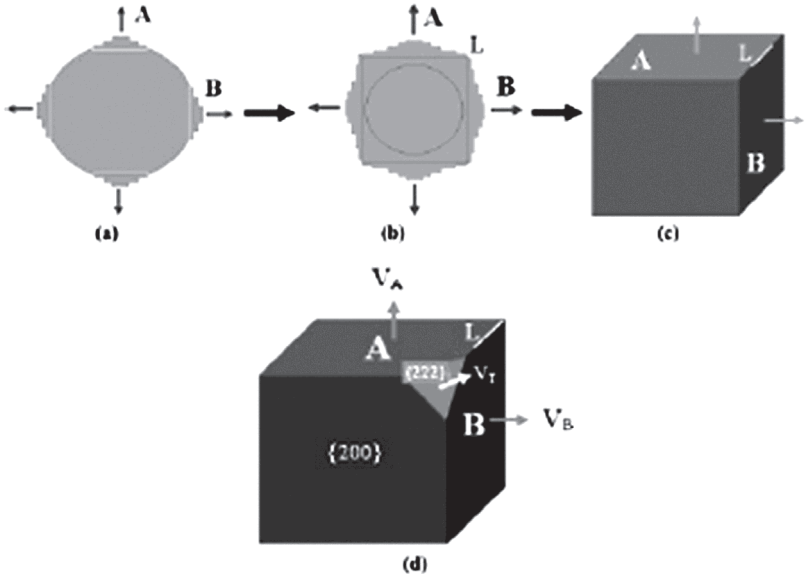

Fig. 8. A schematic illustration of the faceting process of spherical TiN grains

2.3 TiN dendrites

Besides quasi-spherical grains and faceted crystals, TiN dendrites are also observed in the product. Dendrites are usually found in metal ingots from fast cooling of melts, and the formation of TiN dendrites here should be attributed to the fast cooling rate in combustion synthesis. The TiN dendrites exhibit interesting morphologies like bamboos, trees, and flowers, as shown in Figure 9. The bamboo-like dendrite has a wavy shape with sharp tips at its side faces, and with the growth of the tips a teeth-like morphology can be formed. Figure 9 (e) shows some small dendrites with round tips in four directions, which will grow into branches of tree-like dendrites. When several neighboring dendrites grow simultaneously toward different directions, larger flower-like dendrites will be produced. Despite the difference in apparent morphologies, all the TiN dendrites show a four-fold symmetry. In the formation of a dendrite, secondary branches grow perpendicular to a primary truck and smaller twigs perpendicular to a branch. By this means, the TiN dendrites grow in three orthogonal directions. In one direction, several growth units are connected or overlapped, and in the plane normal to this direction each growth unit grows in the other two perpendicular directions.

Based on SEM observation, the growth mechanism of the TiN dendrites is proposed as follows. As shown in Figure 10, in each dendrite, the three orthogonal growth directions are parallel to the reference axes of *a*, *b*, and *c*, respectively, and the four-fold symmetric pyramids are bounded with {222} faces. Figure 10 (c) illustrates a unit growing in the plane normal to *c*-axis. In the directions of *a* and *b*, four horns grow simultaneously, where the final morphology depends on the growth rates in forward (V_N) and lateral (V_R) directions. If $V_R=V_N$, the horns will reserve their initial shape during growth. If $V_R>>V_N$, the horns will grow quickly in forward directions and the lateral growth is limited, thus developing into slim branches finally.

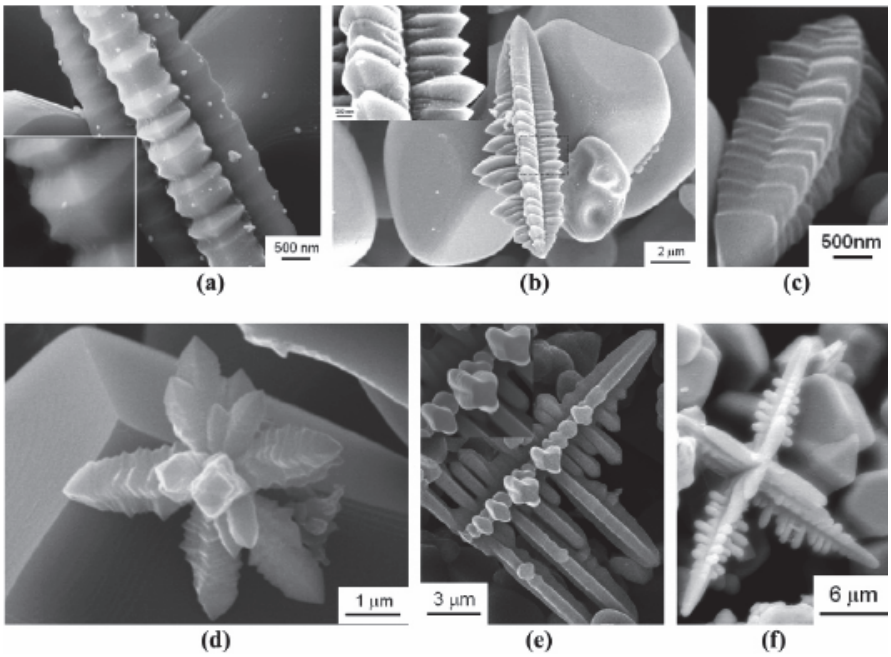

Fig. 9. SEM images of TiN dendrites

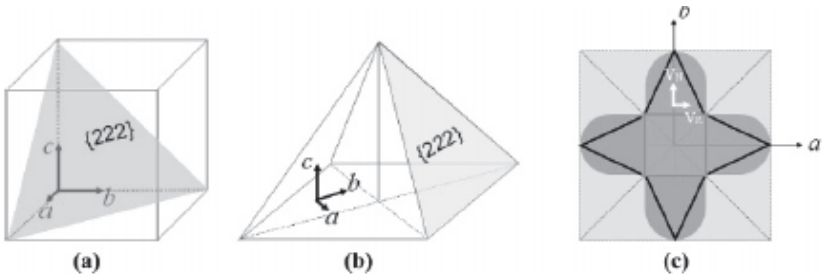

Fig. 10. An illustration of the growth mechanism of TiN dendrites

3. Combustion synthesis of nano-sized SiC powders

SiC ceramics are widely studied for tribological and structural applications, such as abrasives, refractories, bearings, valves, and seals, because of its high elastic modulus and hardness, excellent oxidation and corrosion durability, high strength at elevated temperatures, and good thermal shock resistance. Consolidated SiC ceramics are usually prepared by sintering techniques including liquid-phase sintering, hot-pressing, and spark plasma sintering [9-12]. In these sintering processes, both densification kinetics and microstructure evolution strongly depend on the quality of starting powders. At the same time, the fabrication cost of sintered SiC ceramic components is also largely determined by that of the starting SiC powders.

The most conventional approach to prepare SiC powders is the Acheson method, which is based on the carbothermal reduction of silica at high temperatures above 2000°C. SiC powders produced by this method have large particle size and hence post-treatment by extensive milling is required to improve the sinterability. Such milling process, however, is inevitably accompanied by the contamination of milling media. By pyrolysis or reaction of silane compounds, high-purity and ultrafine SiC powders can be synthesized. A major drawback of this method is the high cost, which limits its application for large-scale industrial production.
From the viewpoint of reducing costs, combustion synthesis is a desirable technique to produce SiC powders. Because (Si+C) system is weakly exothermic, combustion synthesis of SiC requires extra energy input by mechanical activation, preheating, microwave radiation, or electric field activation. Combustion synthesis of SiC can also be carried out in a high-pressure N_2 atmosphere, where nano-sized powders can be obtained [13].
Figure 11 shows the photographs of SiC product prepared by combustion synthesis in N_2.

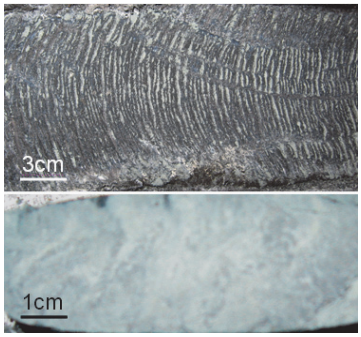

Fig. 11. Photographs of SiC product prepared by combustion synthesis

The product has a color from grey to light green and can be easily pulverized into powder. On the surface of the product, clear veins are found as a result of propagation of combustion wave. XRD analysis (Figure 12) confirms that the product is almost single-phase β-SiC. SEM observation (Figure 13) reveals that the as-synthesized SiC powder is very fine and the average grain size is below 100 nm.
As a weakly exothermic system, the self-sustained reaction of Si+C=SiC is difficult to realize in vacuum or an Ar atmosphere. In this case, in the preparation of SiC powders by combustion synthesis, N_2 plays an important role. Nevertheless, no Si_3N_4 has been found in the products. Moreover, there is no significant decrease in the pressure of N_2 after combustion reaction, which implies that the N_2 has not been consumed. Then, what ever role does N_2 play in the combustion synthesis of SiC and how does it affect the reaction? To solve this problem, an incomplete product gives some instructive information. In the incomplete product, there are several dark areas that have not fully reacted. XRD analysis (Figure 14) reveals that in the partially-reacted areas much Si_3N_4 is present other than the major SiC phase, which is further confirmed by TEM observation shown in Figure 15. From these results, a two-step reaction mechanism is proposed for the combustion synthesis of SiC in N_2. In the first step, Si reacts with N_2 to form Si_3N_4, which decomposes in the second step and the released Si reacts with C to produce SiC. Here, N_2 acts as a catalyst in fact, which is consumed first and released later. In this way, the pressure of N_2 will not decrease after the reaction.

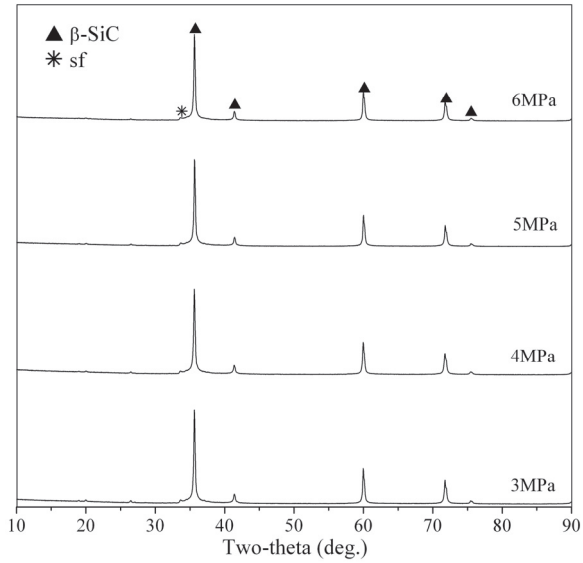

Fig. 12. XRD patterns of SiC powders prepared by combustion synthesis under different N_2 pressures

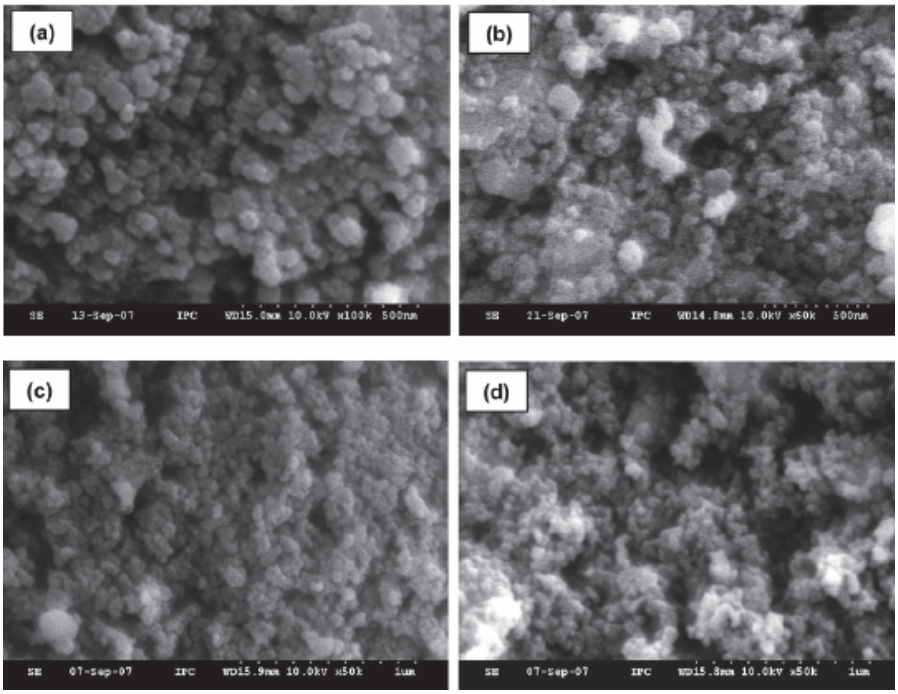

Fig. 13. SEM images of SiC powders prepared by combustion synthesis in high-pressure N_2

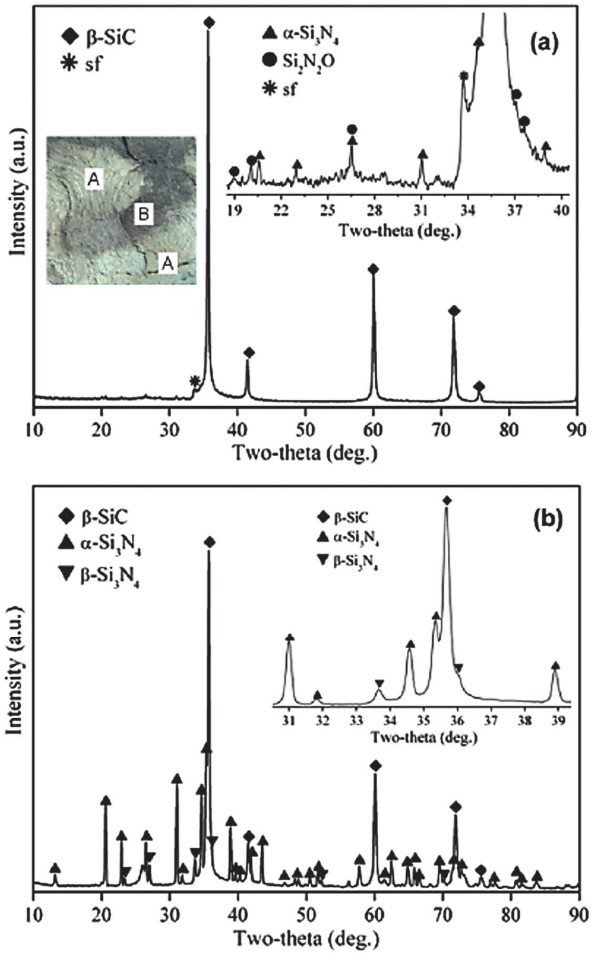

Fig. 14. XRD patterns of (a) fully-reacted and (b) partially-reacted products in combustion synthesis of SiC in high-pressure N_2

For further understanding the chemical reactions in the Si-N-C system, thermodynamical calculation is carried out based on the reaction

$$Si_3N_4\ (s) + 3C\ (s) = 3SiC\ (s) + 2N_2\ (g) \quad (1)$$

According to reported thermodynamic data, the Gibbs free energy change (ΔG) of Reaction (1) can be worked out as

$$\Delta G = 591450 - 314.8T + RT\ln K_R \quad (2)$$

where K_R is the reaction equilibrium constant. Assuming that the activity coefficients of solid reactants equal to 1, the equilibrium constant can be further written as

$$K_R = P^2(N_2) \tag{3}$$

In Equations (2) and (3), the units of ΔG and T are $J \cdot mol^{-1}$ and K, the unit of $P(N_2)$ is P^{θ} ($P^{\theta}=10^5$ Pa), the equilibrium constant of K_R is dimensionless, and R is gas constant equal to 8.31 $J \cdot mol^{-1} \cdot K^{-1}$.
At equilibrium state

$$\Delta G(P, T) = 0 \tag{4}$$

Thus the pressure of N_2 can be expressed as the function of temperature

$$\text{Log } P(N_2) = 7.23 - 15459 / (T+273) \tag{5}$$

where the units of $P(N_2)$ and T are converted to MPa and ^{o}C, for the convenience of discussion.

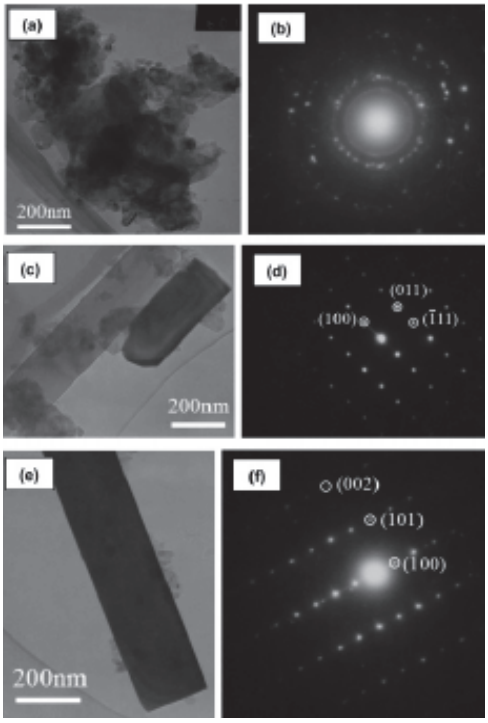

Fig. 15. TEM images and SAED patterns of the phases obtained in the partially-reacted product: (a) and (b) β-SiC; (c) and (d) α-Si_3N_4; (e) and (f) β-Si_3N_4

According to Equation (5), the relationship between $P(N_2)$ and T is plotted in Figure 16. By the $P(N_2)$-T curve, the reference frame is divided into two parts with different phases being stable. The formation of SiC is favored at higher temperature and lower N_2 pressure. For a certain pressure of N_2, there is an equilibrium temperature beyond which Si_3N_4 will decompose and SiC will be formed. With increasing pressure of N_2, the decomposition temperature of Si_3N_4 increases.

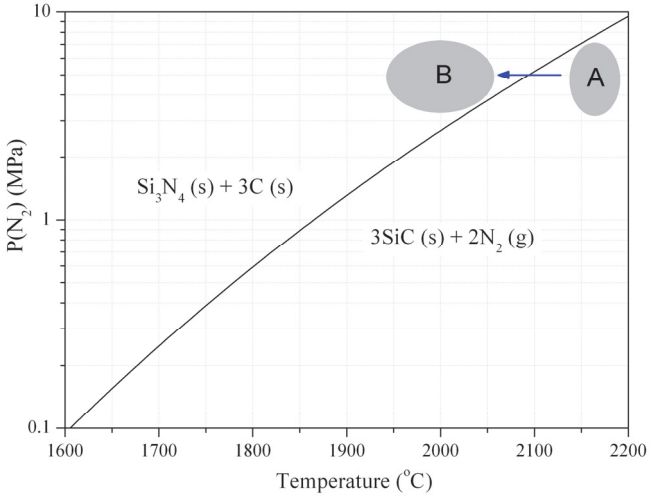

Fig. 16. Thermodynamical evaluation on the stability of possible phases in Si-C-N system

Finally, about the formation of SiC by the reaction between Si and C, several mechanisms have been reported [14-16], with either interface reaction or diffusion being the rate-limiting process. For combustion synthesis of SiC in N_2, most starting Si particles react with N_2 to form Si_3N_4. The Si species directly responsible for the formation of SiC come from the decomposition of Si_3N_4 and can be regarded as regenerate Si. Because the decomposition temperature of Si_3N_4 is much higher than the melting point of Si, the regenerate Si will exist in a melt or vapor state. Carbon particles are coated by Si melt, and SiC forms first at the solid-liquid interface. The continued reaction is controlled by the diffusion of C through the SiC layer. In addition, SiC can be produced by the reaction between C particles with Si vapor, which is also initiated by interface reaction and then limited by diffusion.

4. Combustion synthesis of SiAlON powders with rod-like crystals

As a solid-solution of Si_3N_4, SiAlON ceramics exhibit good mechanical properties such as high hardness, superior wear durability, and excellent thermal shock resistance, making them promising for tribological and high-temperature applications [17,18]. The properties of SiAlON ceramics strongly depend on their chemical compositions and microstructure including grain morphology and size. For example, the fracture toughness of SiAlON ceramics can be greatly improved by developing coarse elongated grains [19,20]. In this aspect, seeding has been proved to be an effective method to induce isotropic growth of SiAlON and formation of elongated grains. The seeds used in this method are usually rod-like SiAlON crystals. For prepare such crystals, combustion synthesis is an effective technique, and by this technique two kinds of rod-like SiAlON crystals have been prepared [21-25], which are known as α-SiAlON and β-SiAlON, respectively.

4.1 Rod-like α-SiAlON crystals

According to the general chemical formula of $R_{m/z}Si_{12-(m+n)}Al_{m+n}O_nN_{16-n}$ (R means the stabilizing cations), from the raw materials of $CaCO_3$, Yb_2O_3, Si, Al, α-Si_3N_4, AlN, SiO_2, and

NH_4F, Ca and Yb-stabilized α-SiAlON can be prepared by combustion synthesis, with chemical compositions of $Ca_{0.8}Si_{8.8}Al_{3.2}O_{1.6}N_{14.4}$ (m=n=1.6) and $Yb_{0.5}Si_{9.5}Al_{2.5}O_{1.0}N_{15.0}$ (m=1.5, n=1.0), respectively. For Ca-stabilized system the product is α-SiAlON with minor AlN and Si, and for Yb-stabilized system almost single-phase α-SiAlON is obtained, as shown in Figure 17.

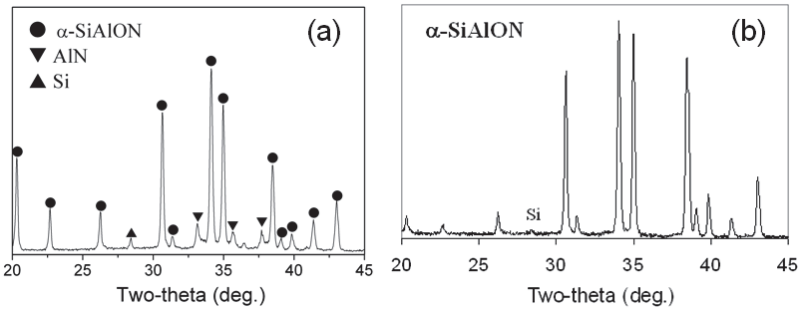

Fig. 17. XRD patterns of α-SiAlON powders prepared by combustion synthesis:
(a) Ca α-SiAlON; (b) Yb α-SiAlON

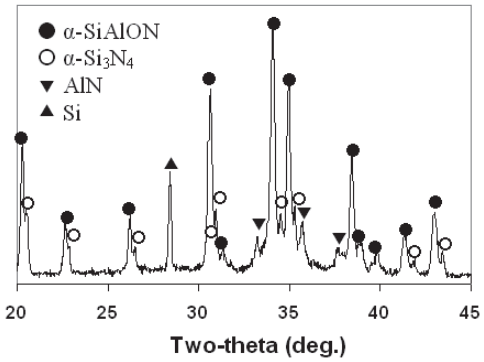

Fig. 18. XRD pattern of the intermediate product during combustion synthesis of Ca α-SiAlON

Since combustion synthesis takes place very quickly, it is difficult to exactly clarify the reaction procedure in detail. In this aspect, the analysis of intermediate product can give some useful information. In combustion synthesis, the reaction at surface layer of samples is usually incomplete because of severe heat loss and as a result some intermediate product is obtained. Figure 18 shows the XRD pattern of the intermediate product in combustion synthesis of Ca α-SiAlON. In the intermediate product, except for α-SiAlON, α-Si_3N_4, AlN, and much residual Si is present. From this result, the reaction procedure during combustion synthesis of Ca α-SiAlON is proposed as follows.

$$2Al + N_2 = 2AlN$$

$$3Si + 2N_2 = \alpha\text{-}Si_3N_4$$

$$CaCO_3 = CaO + CO_2$$

$$CaO + SiO_2 + Al_2O_3 \rightarrow \text{Ca-Si-Al-O liquid phase}$$

$$\text{Ca-Si-Al-O liquid phase} + \alpha\text{-}Si_3N_4 + AlN \rightarrow \text{Ca-Si-Al-O-N liquid phase}$$

$$\text{Ca-Si-Al-O-N liquid phase} \rightarrow \text{Ca } \alpha\text{-SiAlON}$$

It should be pointed out that, this proposition just outlines possible major reactions and the actual combustion reaction is more complicated. The above reactions can take place simultaneously and overlap with each other.

Figure 19 shows the SEM images of as-synthesized α-SiAlON powders, which consist of rod-like crystals. From the low-magnification image, a flower-like morphology is observed, which is caused by simultaneous growth of many rod-like crystals. The formation of the rod-like α-SiAlON crystals is thought to be related with the special reaction condition in combustion synthesis characterized by high temperature and fast heating rate. Under this reaction, a non-equilibrium reaction state will be caused, where the chemical composition of the co-existing liquid phase remarkably deflects from that in equilibrium with the α-SiAlON crystals. In this case, a strong driving force for mass transportation and crystal growth will be created. Hence, the α-SiAlON crystals undergo a rapid anisotropic growth by a dynamic ripening mechanism and develop into a rod-like morphology.

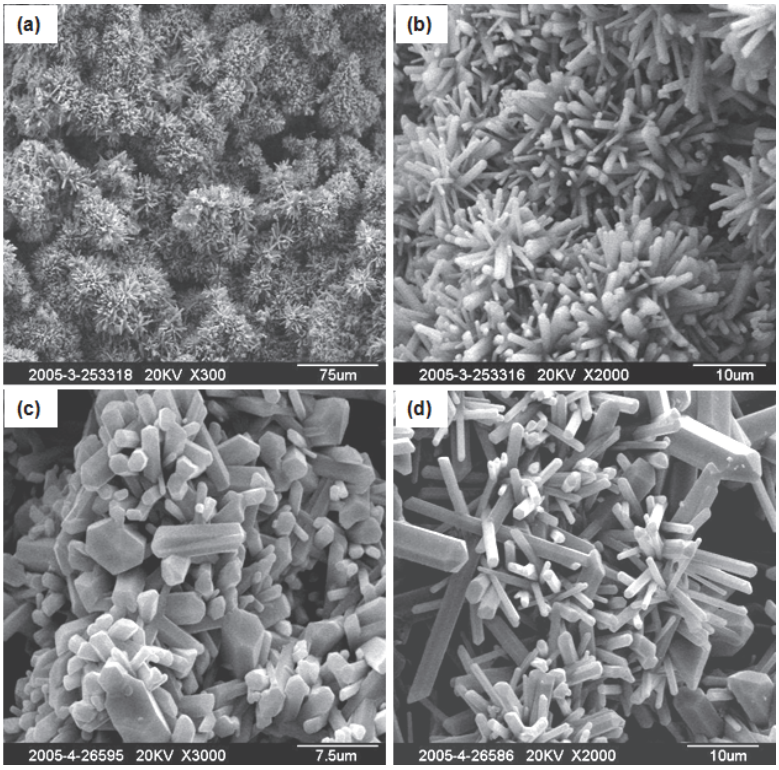

Fig. 19. SEM images of α-SiAlON powders prepared by combustion synthesis: (a) and (b) Ca α-SiAlON; (c) and (d) Yb α-SiAlON

The anisotropic growth of rod-like α-SiAlON crystals in combustion synthesis is further studied by TEM. As shown in Figure 20, the preferred growth direction of rod-like α-SiAlON crystals is [001] and parallel to the c-axis in the hexagonal lattice. This is consistent with the prediction from the intrinsic crystallography characteristics of α-SiAlON. In the hexagonal lattice of α-SiAlON with c/a<1, the basal face has a lower atom packing density and smaller grid distance compared with the prismatic side faces. Accordingly, the basal face has the priority for nucleation and a higher growth rate, leading to the rod-like morphology of α-SiAlON crystals.

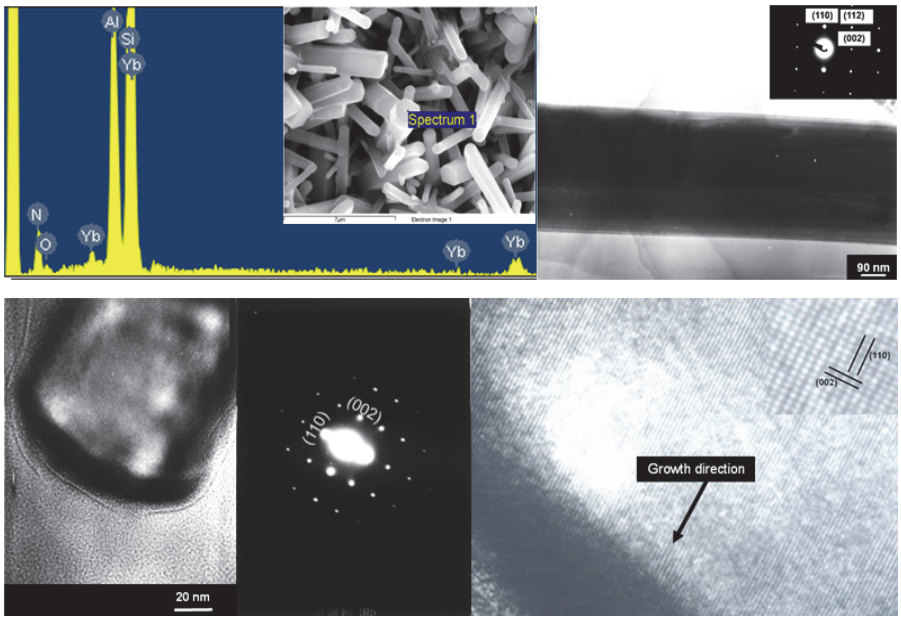

Fig. 20. EDS spectrum and micrographs of rod-like Yb α-SiAlON crystals

Besides the intrinsic lattice structure, reaction conditions also have a strong effect on the growth of α-SiAlON crystals. For example, in most sintered α-SiAlON ceramics, equiaxed grains are more frequently observed than rod-like crystals. This is because that, in the sintering of α-SiAlON, α-Si_3N_4 is usually used as raw materials. The α-Si_3N_4 grains can provide preferred nucleation sites and cause the formation of too much α-SiAlON nuclei. In later growth stage, a large amount of α-SiAlON grains impinge on each other and this steric hindrance suppresses the growth of rod-like crystals. On the other hand, the growth of α-SiAlON generally occurs by Ostwald ripening, where small grains dissolve into a co-existing liquid and the species are transported by diffusion to larger grains and precipitated there. In this dissolution-diffusion-reprecipitation process, fast anisotropic grain growth is often retarded by slow dissolution or mass transportation.

Compared with conventional sintering, combustion synthesis can create a non-equilibrium reaction state and provide a strong driving force for fast growth of α-SiAlON crystals by a dynamic ripening process. At the same time, combustion reaction progresses rapidly and the high heating rate limits the nucleation. In this way, combustion synthesis can offer the opportunity for the growth of rod-like α-SiAlON crystals.

In combustion synthesis of α-SiAlON, the growth of rod-like crystals can be affected by introducing proper additives. For example, with the addition of NH_4F and Fe_2O_3, faceted prismatic rod-like Yb α-SiAlON crystals have been prepared, as shown in Figure 21. The rod-like crystals show different morphologies at their heads, such as facets, pyramids, and incomplete pyramids as a transition from facets to pyramids. In the formation of rod-like α-SiAlON crystals, different nucleation modes can be operative. Nucleation can take place based on the un-dissolved Si_3N_4 grains or on the side and basal faces of present rod-like α-SiAlON crystals. When nucleation occurs on the basal face, a terraced morphology will be produced, where new crystals have a hexagonal shape similar to the substrate crystals with the c-axis and side faces being parallel. It appears that the nucleation and growth of new crystals are not random but epitaxial with strict orientation relations to the substrate crystals. When this epitaxial nucleation occurs on an incomplete pyramidal substrate crystal, a T-like morphology is produced, as illustrated in Figure 22.

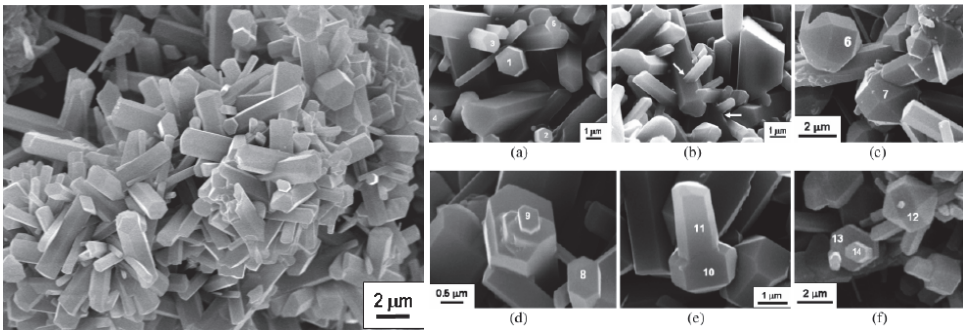

Fig. 21. SEM image of rod-like Yb α-SiAlON crystals with different head morphologies

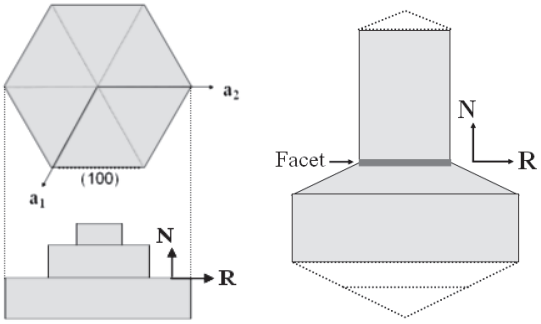

Fig. 22. An illustration of the formation of different head morphologies in rod-like α-SiAlON crystals

4.2 Rod-like β-SiAlON crystals

Besides α-SiAlON, β-SiAlON is another important polymorph in the SiAlON family. β-SiAlON is the solid solution of β-Si_3N_4, where Si-N bonds are partially substituted by Al-O bonds. The composition of β-SiAlON can be represented by a general chemical formula of $Si_{6-z}Al_zO_zN_{8-z}$ ($0<z<4.2$). From the raw materials of Si, Al, Si_3N_4, Al_2O_3, $SrCO_3$, and NH_4F, β-

SiAlON powders can be prepared by combustion synthesis. Figure 23 shows the XRD pattern of β-SiAlON powders prepared by combustion synthesis. It is clear that single-phase β-SiAlON is obtained without any impurities. SEM observation (Figure 24) reveals that the β-SiAlON powders consist of prismatic rod-like crystals. By the addition of $SrCO_3$ and NH_4F, the aspect ratios of the rod-like crystals are increased. It is reported that the anisotropic growth of β-SiAlON crystals is caused by preferential interfacial segregation [26,27]. This segregation is related with the basicity of metallic oxides and more basic oxides result in stronger segregation. Because SrO is more basic than SiO_2 and Al_2O_3, the interfacial segregation will be enhanced by adding $SrCO_3$, which improves the anisotropic growth of rod-like β-SiAlON crystals.

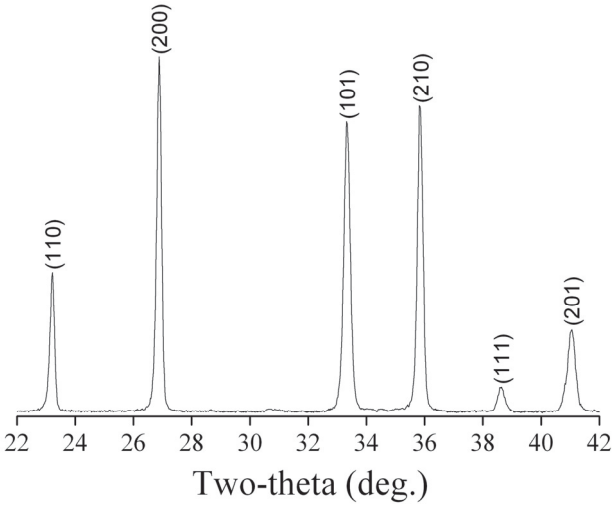

Fig. 23. XRD pattern of β-SiAlON powders prepared by combustion synthesis

In addition to rod-like crystals, micropalings with nanorods are observed in β-SiAlON powders prepared by combustion synthesis, as shown in Figure 25. The nanorods are produced on side faces of the coarse prismatic crystals, and the thickness of most nanorods is in the range of 50-150 nm. In each micropaling, nanorods are aligned around a large prismatic crystal in the direction parallel to the side faces. TEM characterizations (Figure 26) reveal that the preferred growth direction of the nanorods is [001].

The anisotropic growth of β-Si_3N_4 and β-SiAlON crystals has been widely studied and generally attributed to different structures and growth kinetics at the basal and side faces [28-30]. Some studies suggest that, the basal face is atomically rough while the side faces are smooth, and thus the crystal growth rate is controlled by diffusion at the basal face and by interfacial reaction at the side faces. In this case, the basal face has a higher growth rate than the side faces, leading to the anisotropic growth and formation of rod-like crystals. According to the periodic bond chain (PBC) theory, the ideal crystallization shape of β-Si_3N_4 has been theoretically predicted to be an elongated prism bounded by {100} and {101} faces [31]. When a large amount of oxygen is present, the {101} faces can be replaced by {001} ones.

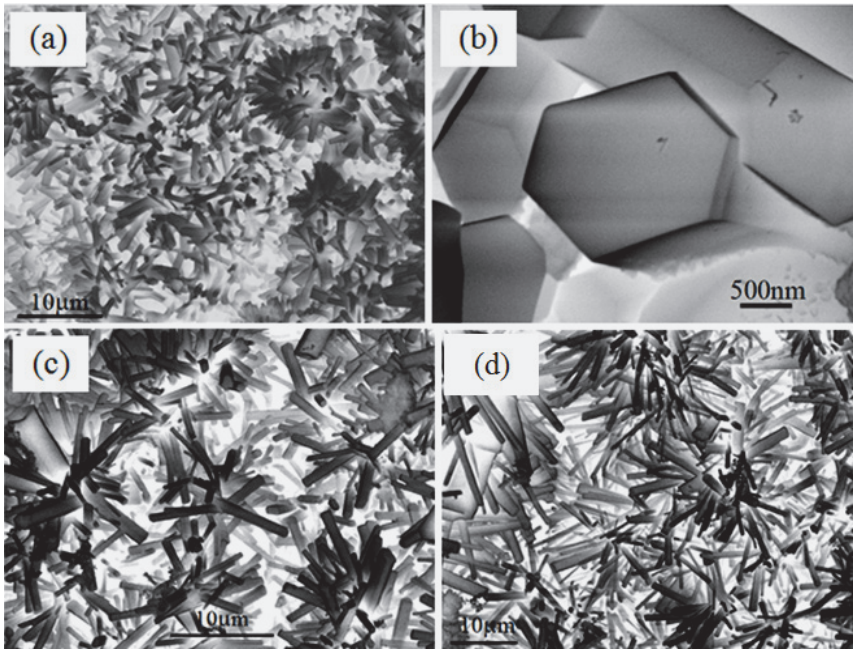

Fig. 24. SEM images of β-SiAlON powders prepared by combustion synthesis: (a) and (b) with no additives; (c) with 4 wt.% $SrCO_3$; (d) with 2 wt.% $SrCO_3$ and 2 wt.% NH_4F

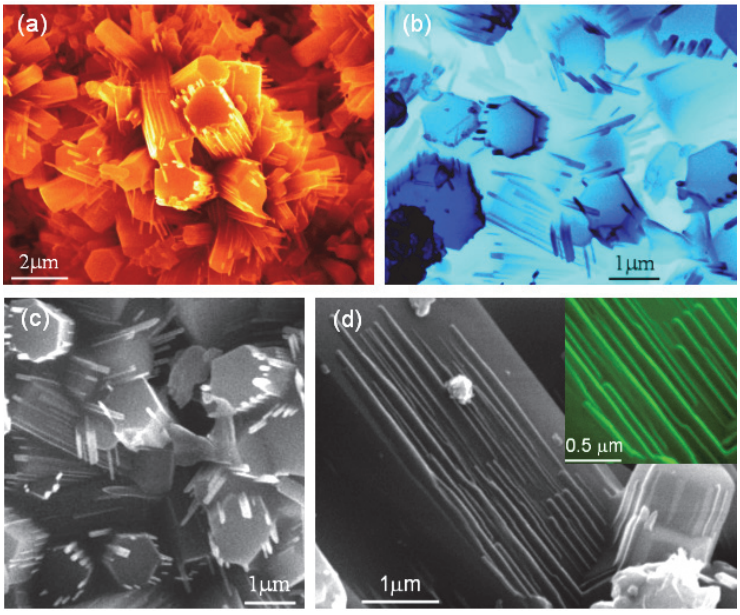

Fig. 25. SEM images of β-SiAlON micropalings with nanorods

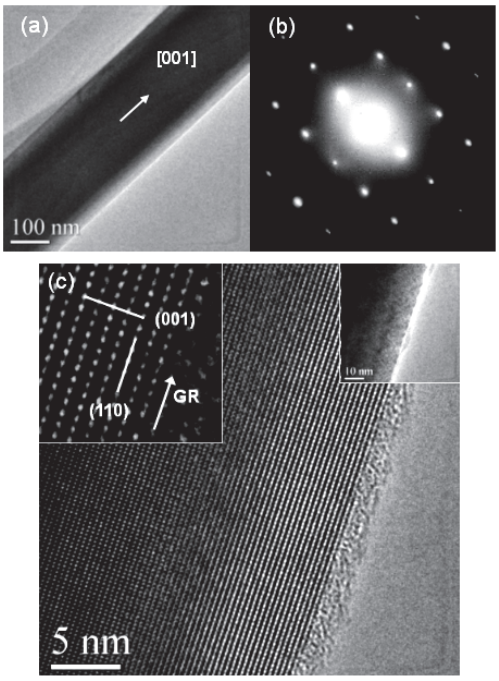

Fig. 26. TEM photographs of β-SiAlON nanorods with SAED pattern

From the above experimental results and discussion, an epitaxial nucleation and anisotropic growth mechanism is proposed to explain the formation of β-SiAlON micropalings. This mechanism includes two primary hypotheses: (1) epitaxial nucleation on side faces of coarse prismatic crystals; (2) anisotropic growth of nanorods in [001] direction. By epitaxial nucleation, a new crystal forms on a side face of a coarse prismatic crystal and then grows in three orthogonal directions, as illustrated in Figure 27. If the growth rate in the preferred direction (V_C) is much higher than those in two lateral directions (V_A and V_B), the new crystal undergoes an anisotropic growth and develop into a slim nanorod. With the formation of more nanorods around the central coarse crystal, a micropaling is produced.

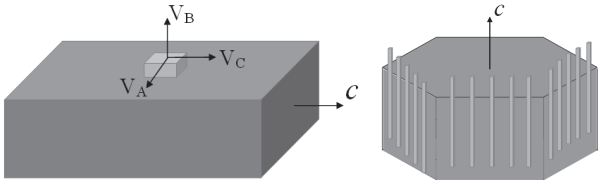

Fig. 27. A schematic illustration of the formation of β-SiAlON micropalings

5. Combustion synthesis of Ti-Al-C powders with lamellar grains

The lamellar ceramics in the Ti-Al-C ternary system have unique physical and mechanical properties, such as high melting point, good thermal and electrical conductivity, and

machinability by both electrical discharge method and conventional cutting tools [32-34]. Among these ceramics, Ti_3AlC_2 and Ti_2AlC are two typical materials that have been mostly studied. For example, it is reported that Ti_3AlC_2 exhibits room-temperature compressive plasticity in contrast to normal brittle ceramics, and Ti_2AlC shows excellent machinability. Ti-Al-C ternary compounds can be synthesized by different methods, such as sintering, mechanical alloying, and combustion synthesis.

From the raw materials of Ti, Al, carbon black, and TiC, both Ti_3AlC_2 and Ti_2AlC can be prepared by combustion synthesis [35-38]. In the synthesized products, TiC is also present other than the Ti-Al-C ternary compounds, as revealed by XRD patterns shown in Figure 28. In the combustion synthesis of Ti-Al-C ternary carbides, two reaction stages are generally involved:

$$Ti + C \rightarrow TiC \text{ and } Ti + Al \rightarrow \text{Ti-Al melt}$$

$$TiC + \text{Ti-Al melt} \rightarrow Ti_3AlC_2/Ti_2AlC$$

In the formation of Ti_3AlC_2 and Ti_2AlC, TiC is involved as an intermediate product, which is produced first and then reacts with Ti-Al melt to form ternary carbides. That is to say, the ternary carbides are produced through a dissolution-precipitation process. Because the combustion reaction occurs quickly, the dissolution of TiC is often incomplete in a limited period, and some un-reacted TiC remains in final products.

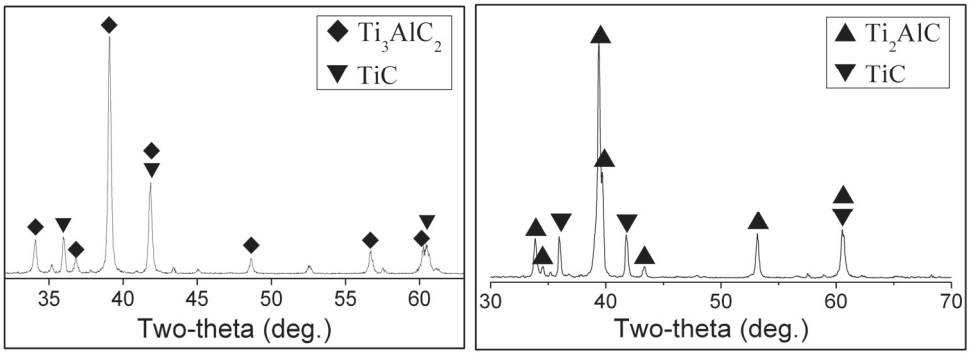

Fig. 28. XRD patterns of Ti_3AlC_2 and Ti_2AlC powders prepared by combustion synthesis

Figure 29 shows the SEM images of Ti_3AlC_2 and Ti_2AlC powders prepared by combustion synthesis, where lamellar grains are observed. More careful observation reveals that most grains exhibit a terraced structure with parallel layers overlapped. This terraced morphology is proposed to be caused by a two-dimensional nucleation and growth mechanism. As illustrated in Figure 30, when a lamellar grain is precipitated from the Ti-Al-C melt and grows larger than a critical size, it can act as a substrate for the nucleation of new grains. The new grains then grow up and form a new layer (the second layer) on the substrate. Similarly, when the second layer become enough large the third layer can form on it. Finally, a terraced structure is produced by continuous stacking of parallel layers. In this process, each layer undergoes a preferential growth, expanding quickly along radial (R) directions in the basal plane but growing slowly in normal (N) direction.

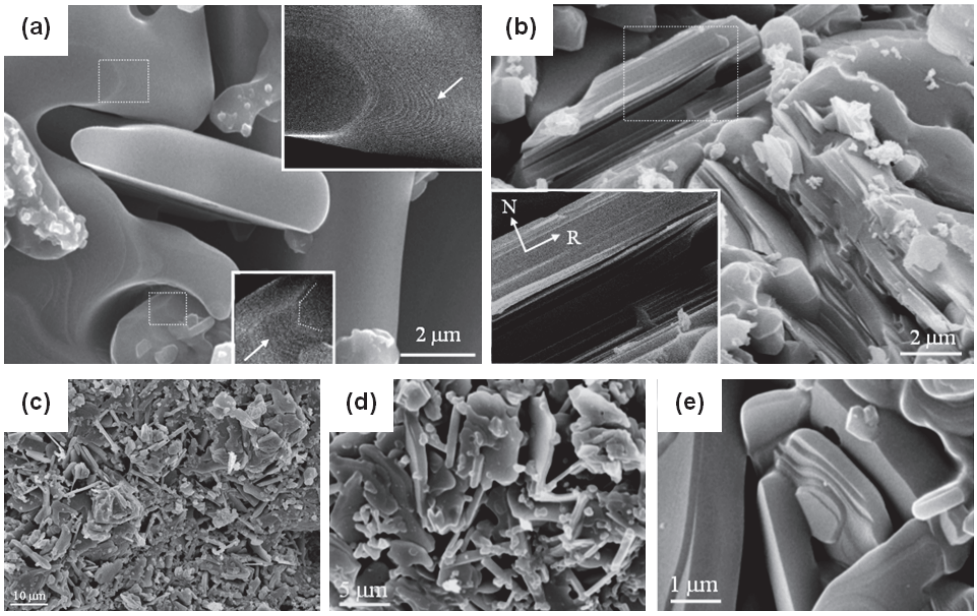

Fig. 29. SEM images of (a) and (b) Ti_3AlC_2 and (c)-(e) Ti_2AlC powders prepared by combustion synthesis

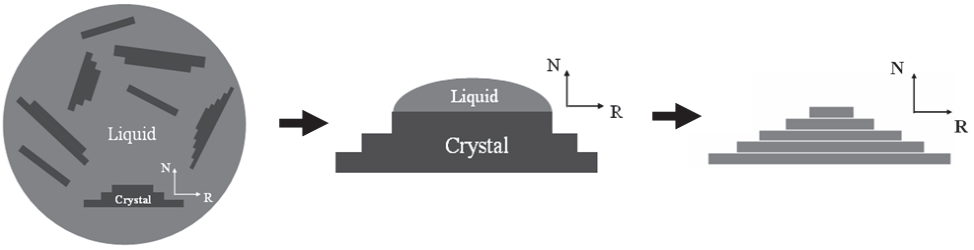

Fig. 30. A schematic illustration of the formation mechanism of the terraced structure in Ti-Al-C ternary carbides prepared by combustion synthesis

Based on the two-dimensional nucleation and growth mechanism, the phase formation and microstructure evolution can be further discussed in detail. At first, Ti_3AlC_2 and Ti_2AlC grains are precipitated from the Ti-Al-C liquid matrix. The ternary carbide grains are separately distributed in a continuous liquid and each grain is surrounded by liquid. At this stage, the material supply for the growth of the lamellar layers is sufficient. With the formation and growth of more ternary carbide grains, the volume proportion of liquid greatly decreases. The ternary carbides become the major phase, and the liquid is not continuous but separately located at the surface of the ternary carbide grains. In this case, the nucleation and growth of new layers take place at the interface between the liquid and the ternary carbide crystals, and the growth of the underlying layers with no contact with liquid is not active. Finally, the liquid phase disappears by severe consumption and with the

decrease in temperature, and the growth of the ternary carbide crystals stops, leaving a terraced structure .

Figure 31 shows TEM images and SAED patterns of Ti_2AlC and Ti_3AlC_2 lamellar crystals prepared by combustion synthesis. For both Ti_2AlC and Ti_3AlC_2, the basal faces of the lamellar crystals are parallel to (001) plane and the normal direction is parallel to the c-axis in the hexagonal lattice. Similar result has been found in Ti_3SiC_2, which is another typical ternary carbide with the same hexagonal structure as Ti_3AlC_2. It is reported that, the linking modes of octahedral Ti_6C units have a strong influence on the growth behavior and morphology of Ti_3SiC_2 grains [39]. In the direction along c-axis, the Ti_6C octahedrons are separated by Si atomic layers, and hence the growth rate is much lower that those in other directions. Therefore, the ideal crystal morphology of Ti_3SiC_2 should be a hexagonal prism bounded with {110} and {001} faces. The above analysis on the growth kinetics of Ti_3SiC_2 is also applicable to Ti_3AlC_2 and Ti_2AlC. That is to say, during the growth of Ti_3AlC_2 and Ti_2AlC lamellar crystals, the growth rate in the direction parallel to c-axis should be lower than those in other directions. In this case, the (001) faces will be exposed most frequently in final crystal shape, resulting in a lamellar morphology.

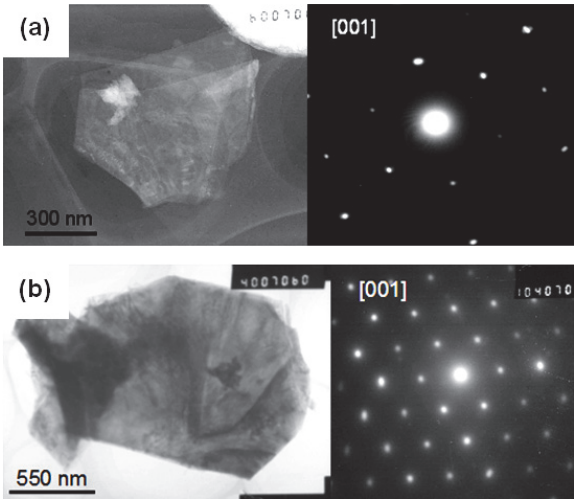

Fig. 31. TEM images and SAED patterns of (a) Ti_2AlC and (b) Ti_3AlC_2 lamellar crystals

6. Conclusions and perspectives

With the progress of theories and development of experimental skills, combustion synthesis has shown an increasing importance in preparing ceramic materials. The unique non-equilibrium reaction state in combustion synthesis offers an opportunity to control crystal growth kinetics. By combustion synthesis, ceramics powders with various grain morphologies can be prepared, including faceted, rod-like, and lamellar crystals. This advantage of combustion synthesis is desirable for both basic research on crystal growth and industrial applications of ceramic powders.

Besides the results presented in this chapter, other new findings have been recently reported related with combustion synthesis of ceramic materials. For example, some nitride ceramic

powders were prepared by combustion synthesis in air instead of high-pressure N_2 atmosphere [40-44]. This enhances the advantage of combustion synthesis as a low-cost technique and shows the possibility to further reduce the production cost of nitride powders. In addition, combustion synthesis was carried out in a high-gravity field to directly fabricate bulk ceramics through melt-casting. By this method, both single-phase translucent ceramics and eutectic ceramic composites have been prepared [45-48]. These new findings expand the field for the application of combustion synthesis and make this versatile technique available for preparing more kinds of ceramic materials.

7. Acknowledgements

This work was supported by National Natural Science Foundation of China (Grant No. 50102002, 50932006, and 51002163).
The first author would like to thank Prof. Zhou Heping, Dr. Ge Zhenbin, and Prof. Guo Junming for their great help and instructive discussions.

8. References

[1] Munir Z A, Umberto A T. *Mater Sci Rep*, 1989, 3:277.
[2] Merzhanov A G. *Ceram Int*, 1995, 21:371.
[3] Moore J J, Feng H J. *Prog Mater Sci*, 1995, 39:243.
[4] Moore J J, Feng H J. *Prog Mater Sci*, 1995, 39:275.
[5] Toth L E. Transition metal carbides and nitrides, Academic Press, New York, 1971.
[6] Liu G H, Chen K X, Zhou H P, Tian J J, Pereira C, Ferreira J M F. *Cryst Growth Des*, 2006, 6:2404.
[7] Pamplin B R. Crystal growth, Pergamon Press Ltd., U. K., 1980.
[8] Hartman P. Crystal growth: an introduction, North-Holland Publishing Company, The Netherlands, 1973.
[9] Padture N P, Lawn B R. *J Am Ceram Soc*, 1994, 77:2518.
[10] She J H, Jiang D L. *Ceram Eng*, 1998, 227:3.
[11] Nagano T, Kaneko K, Zhan G D, Mitomo M. *J Am Ceram Soc*, 2000, 83:2497.
[12] Peng H, Salamon D, Bill J, Rixecher G, Burghard Z, Aldinger F, Shen Z *J. Adv Eng Mater*, 2007, 9:303.
[13] Liu G H, Yang K, Li J T, Du J S, Hou X Y. *J Phys Chem* C, 2008, 112:6285.
[14] Pampuch R, Stobierski L, Lis J, Rczka M. *Mater Res Bull*, 1987, 22:1225.
[15] Gorovenko V I, Knyazik V A, Shteinberg A S. *Ceram Int*, 1993, 19:129.
[16] Narayan J, Raghunathan R, Chowdhurry R, Jagannadham K. *J Appl Phys*, 1994, 75:7252.
[17] Jack K H. *J Mater Sci*, 1976, 11:1135.
[18] Ekstrom T, Nygren M. *J Am Ceram Soc*, 1992, 75:259.
[19] Chen I W, Rosenflanz A. *Nature*, 1997, 389:701.
[20] Shen Z J, Zhao Z, Peng H, Nygren M. *Nature*, 2002, 417:266.
[21] Liu G H, Chen K X, Zhou H P, Ferreira J. *J Mater Res*, 2004, 19:3408.
[22] Liu G H, Chen K X, Zhou H P, Ning X S, Ferreira J. *J Eur Ceram Soc*, 2005, 25:3361.
[23] Liu G H, Chen K X, Zhou H P, Pereira C, Ferreira J. *J Am Ceram Soc*, 2006, 89:364.
[24] Liu G H, Chen K X, Zhou H P, Ren K G, Li J T, Pereira C, Ferreira J. *Scripta Mater*, 2006, 55:935.

[25] Liu G H, Pereira C, Chen K X, Zhou H P, Ning X S, Ferreira J. *J Alloy Comp*, 2008, 454:476.
[26] N Shibata, S Pennycook, T Gosnell, G Painter, W Shelton, P Becher. *Nature*, 2004, 428:730.
[27] A Ziegler, J Idrobo, M Cinibulk, C Kisielowski, N Browning, R Ritchie1. *Science,* 2004, 306:1768.
[28] M Kramer, M Hoffman, G Petzow. *J Am Ceram Soc*, 1993, 76: 2778.
[29] M Kitayama, K Hirao, M Toriyama, S Kanzaki. *Acta Mater*, 1998, 46:6541.
[30] I W Chen, A Davenport, L Wang. *Acta Mater*, 2003, 51:1691.
[31] M Kramer, D Wittmuss, H Kuppers, M Hoffmann, G Petzow. *J Cryst Growth*, 1994, 140:157.
[32] M Barsoum, T Elraghy. *J Am Ceram Soc*, 1996, 79:1953.
[33] M Barsoum, D Brodkin, T Elraghy. *Scr Metall Mater*, 1997, 36:535.
[34] Y C Zhou, Z M Sun. *Phys Rev* B, 2000, 61:12570.
[35] W C Lee, S L Chung. *J Am Ceram Soc*, 1997, 80:53.
[36] A G Zhou, C A Wang, Y Huang. *Mater Sci Eng* A, 2003, 352:333.
[37] Z B Ge, K X Chen, J M Guo, H P Zhou, J Ferreira. *J Eur Ceram Soc*, 2003, 23:567.
[38] Liu G H, Chen K X, Zhou H P, Guo J M, Ren K G, Ferreira J. *Mater Lett*, 2007, 61:779.
[39] K Tang, C Wang, Y Huang, Q Zan. *J Cryst Growth*, 2001, 222:130.
[40] Liu G H, Chen K X, Zhou H P, Ren K G, Jin H B, Ferreira J. *J Am Ceram Soc*, 2007, 90:2918.
[41] Liu G H, Chen K X, Zhou H P, Li J T, Pereira C, Ferreira *J. Mater Res Bull*, 2007, 42:989.
[42] Li J T, Mei L, Yang Y, Lin Z M. *J Am Ceram Soc*, 2009, 92:636.
[43] Mei L, Li J T. *Acta Mater*, 2008, 56:3543.
[44] Yang Y, Lin Z M, Li J T. *J Eur Ceram Soc*, 2009, 29:175.
[45] Z Zhao, L Zhang, Y Song, W Wang. *Scripta Mater*, 2008, 58:207.
[46] R Liang, J Pei, J T Li, K X Chen. *J Am Ceram Soc*, 2009, 92:549.
[47] J Pei, J T Li, G H Liu, K X Chen. *J Alloy Comp*, 2009, 476:854.
[48] L Mei, P Mai, J T Li, K X Chen. *Mater Lett*, 2010, 64:68.

4

Molten Salt Synthesis of Ceramic Powders

Toshio Kimura
Keio University
Japan

1. Introduction

Molten salt synthesis, one of the methods of preparing ceramic powders, involves the use of a molten salt as the medium for preparing complex oxides from their constituent materials (oxides and carbonates). Ceramic powders are prepared from solid, liquid, and gas phases by various methods (Rahaman, 2003). For large-scale commercial production, ceramic powders are fabricated mainly from the solid phase by a conventional powder metallurgical method. Molten salt synthesis is a modification of the powder metallurgical method. Salt with a low melting point is added to the reactants and heated above the melting point of the salt. The molten salt acts as the solvent.

Molten salts have been used as additives to enhance the rates of solid state reactions for a long time. The amount of salt is small, typically a few percent of the total weight. In contrast, in molten salt synthesis, a large amount of salt is used as the solvent to control powder characteristics (size, shape, etc.). In this sense, molten salt synthesis is different from the flux method, which uses the salt as an additive to enhance the reaction rate.

Typical examples of salts used in molten salt synthesis are chlorides and sulfates. In many cases, eutectic mixtures of salts are used to lower the liquid formation temperature. The melting points of NaCl and KCl are 801°C and 770°C, respectively, and that of 0.5NaCl–0.5KCl (eutectic composition) is 650°C. For example, $0.635Li_2SO_4$–$0.365Na_2SO_4$ is the most commonly used salt among sulfates because of its low melting temperature, which is 594°C, whereas that of Na_2SO_4–K_2SO_4 is 823°C. The solubilities of oxides in molten salts vary greatly from less than 1×10^{-10} mole fraction to more than 0.5 mole fraction, typically 1×10^{-3} - 1×10^{-7} mole fraction (Arendt et al., 1979). In many cases, the formation reaction occurs in the presence of solid reactant particles. In this sense, molten salt is somewhat different from ordinary solvents, which dissolve all reactant particles and the product particles precipitate from a homogeneous liquid phase.

Generally, a complex oxide powder is prepared from reactants by the following procedure. A mixture of the reactants and salt is heated above the melting temperature of the salt. At the heating temperature, the salt melts and the product particles form. The characteristics of the product powder are controlled by selecting the temperature and duration of the heating. Then, the reacted mass is cooled to room temperature and washed with an appropriate solvent (typically, water) to remove the salt. The complex oxide powder is obtained after drying. The procedure is the same as that of a conventional powder metallurgical method and is easily scaled up for the fabrication of large quantities of materials.

The use of molten salt is a common method to grow single crystals from solution (Elwell & Scheel, 1975). In this method, the reactant materials are completely dissolved in molten salt

to obtain a uniform liquid. Upon cooling, solid particles nucleate homogeneously in the liquid phase ("homogeneously" means that a nucleus forms somewhere in the liquid phase). A single crystal with a large size can be obtained by limiting the number of nuclei formed during cooling. Therefore, a salt having a high solubility of the reactant materials is required. Conversely, in molten salt synthesis, a large number of nuclei are necessary to obtain powder particles with an appropriate size, typically from a few tenths to about ten micrometers. The surfaces of the reactant particles are utilized as the nucleation sites. In other words, the product particles nucleate heterogeneously on the surfaces of the reactant particles. Therefore, high solubility for all reactants is not desirable. The control of the cooling rate is very important in the single-crystal growth, because the cooling rate determines the number of nuclei and the size of the product crystals. The cooling rate gives a minor influence on the particle sizes in the molten salt synthesis, because a vast number of particles are already present before cooling and the materials dissolved in the molten salt precipitate on the surfaces of the already existing solid particles.

The role of the molten salts is (1) to increase the reaction rate and lower the reaction temperature; (2) to increase the degree of homogeneity (the distribution of constituent elements in the solid solution); (3) to control particle size; (4) to control particle shape; and (5) to control the agglomeration state. The major purpose of employing molten salt synthesis is (1) to prepare powders for sintering and (2) to prepare anisometric particles. In sintering of powders, a good sintered compact is obtained from a powder with grains of submicrometer size and a low degree of agglomeration (Rahaman, 2003). Recently, textured ceramics are prepared by the templated grain growth method, in which anisometric particles with sizes from several to a few tens micrometers are required (Kimura, 2006; Messing et. al., 2004; Tani & Kimura, 2006). The formation of aggregates must be avoided to form green compacts by tape-casting.

The requirements on the salt are that they are stable, readily available, inexpensive, and easily washed away with water. A low melting temperature is desirable, and the eutectic composition or the composition at the minimum liquidus temperature is often used. Other requirements are that they have a low vapor pressure at the heating temperature and do not cause undesirable reactions with either the reactants or the product. One example of unsuitable salt is LiCl, which is used for the preparation of $LiFe_5O_8$ (Wickham, 1971). LiCl accelerates the reaction between Fe_2O_3 and Li_2CO_3 to yield $LiFe_5O_8$, but it is hygroscopic and volatile at the reaction temperature. Furthermore, it is subject to hydrolysis; Li_2O produced by hydrolysis reacts with $LiFe_5O_8$ and converts it to $LiFeO_2$.

This chapter deals with (1) the phenomena occurring during synthesis; (2) the reaction rate; (3) the characteristics of powders with a special emphasis on particle morphology; and (4) the reaction of salt with the reactants and product. This chapter excludes (1) the salts as a reaction promoter; (2) the formation of simple oxides (MO); and (3) the salts as a reactant, such as the formation of $LiCoO_2$ and $LiMn_2O_4$ using Li salts (LiCl, $LiNO_3$, etc.), which is an important application of molten salt synthesis to lithium ion batteries (Han et al., 2003). Furthermore, this chapter does not include nitrate salts, because the reaction mechanisms are different from those of the chlorides and sulfates (Afanasiev & Geantet, 1998).

2. Fundamentals of molten salt synthesis

2.1 Preparation procedure

2.1.1 Formulation

Figure 1 shows the flowchart of the preparation procedure. A reaction batch contains the reactants and the salt. The salt is selected based on the desired powder characteristics. The

relation between the properties of the salt and the powder characteristics is described in this review. Sometimes, a surfactant is added to prepare nano-sized powders (Mao et al., 2003). In general, the mixing ratio of reactants is stoichiometric, i.e., two moles of Bi_2O_3 and three moles of TiO_2 are mixed for $Bi_4Ti_3O_{12}$. Care must be paid when carbonates are used as reactants. The solubility of oxides in the molten salt is generally low but that of carbonates is high, resulting in deviations from stoichiometry in the product phase. In the preparation of $Ba_6Ti_{17}O_{40}$, the Ba/Ti ratio of 6/17 in the reactant mixture results in the inclusion of $Ba_4Ti_{13}O_{30}$ particles in the product and that of 6/15 is employed to obtain nearly single-phase $Ba_6Ti_{17}O_{40}$ (Kimura, et al., 2005). When $KNbO_3$ is prepared from $K_4Nb_6O_{17}$ and K_2CO_3 using KCl, a K_2CO_3/ $K_4Nb_6O_{17}$ ratio of 1.2 or greater is desirable (Saito & Takao, 2007).

A typical amount of salt is 80-120 wt% of the reactant mixture. The amount is determined by the requirement that there is adequate salt to substantially fill the interstices of the reactant particles and to coat the reactant surfaces. In some systems, the amount of salt influences the product particle size (Yoon et al. 1998). When the amount of salt is too small, the effect of the liquid phase is not fully expected. An extremely large amount causes two problems. One is the separation of the reactant particles by sedimentation (Kimura et al., 1980; Wickham, 1971). When the reactant particles have different densities and sizes, they have different sedimentation rates, resulting in the separation of the reactant particles and a reduction in the reaction rate. Another problem is related to difficulties during treatment. When the amount of salt is excessive, the interstices of the reactant particles can never hold all of the molten salt, and a fairly large amount of the molten salt oozes from a gob of reactants. Oozed molten salt never acts as a solvent. Furthermore, the molten salt adheres to the wall of the crucible and changes to a hard lump after solidification. The dissolution of hard salt in the lumps is quite laborious.

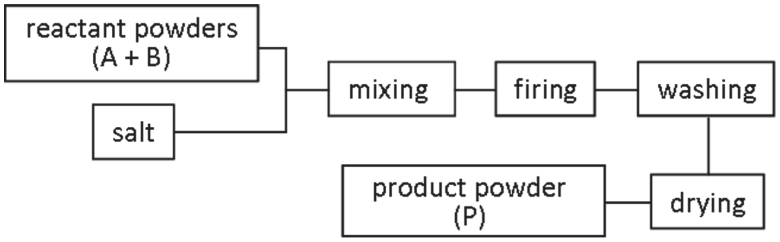

Fig. 1. Preparation procedure in molten salt synthesis.

When all the reactants are dissolved in the molten salt, another problem arises. It is related to the particle size. When Bi_2WO_6 is prepared from Bi_2O_3 and WO_3 using NaCl-KCl, two kinds of platelike particles are obtained depending on the amount of salt and the heating temperature (Kimura & Yamaguchi, 1982). The first kind consists of particles with a diameter of several micrometers, and the second kind of particles has a diameter of about 100 μm. When the amount of salt is small and the heating temperature is low, the system is located in the solid-liquid two-phase region of the phase diagram. The Bi_2WO_6 particles nucleate heterogeneously on the surfaces of the reactants, and a great number of them form. Conversely, when the amount of salt is large and the heating temperature is high, the system is located in the liquid single-phase region. The Bi_2WO_6 particles homogeneously nucleate in the liquid phase. Because the cooling rate is relatively high compared to that employed in the single-crystal growth, many nuclei form but the number of nuclei is less

than that nucleated heterogeneously on the surfaces of the reactants. Thus, quite large-sized particles are obtained.

2.1.2 Heat treatment

The mixture of reactants and salt is put in a covered or sealed crucible and heated in a furnace. A platinum crucible is used in the laboratory experiment. Alternatively, alumina and zirconia crucibles may be used if the chemical interaction between the crucible and the reactants and product is negligible. The heating conditions such as temperature and duration are determined by the desired powder characteristics. In general, the rate of material transport is increased with an increase in the heating temperature. At the same time, the salt evaporation increases as well. The heating duration is determined by the reaction rate and the size and shape of the product particles. Typical conditions are temperatures between 800°C and 1100°C with durations between 30 and 60 min. In a particular system, the heating rate influences the size of the product particles (Yoon et al., 1998).

After heating, the product mass is washed with an appropriate solvent to remove the salt. Ordinarily, this is water, which means that water-soluble salts are typically used in molten salt synthesis. The solubilities of chlorides and sulfates are generally high and washing with water two or three times seems sufficient to remove all the salt. Nevertheless, the ions from the dissolved salt may adsorb on the surfaces of the product particles, and, then, repeated washing is necessary. The chloride ions are sometimes detected by an Ag^+ solution even after ten times of washing. To desorb ions efficiently, the use of hot, instead of cold, water is recommended. After washing, the supernatant water is decanted and the remaining powder is dried. When the formation of hard agglomerates needs to be avoided, the powder is rinsed with a solvent with low surface tension, such as acetone, before drying.

2.2 Formation of product particles

2.2.1 Two stages of particle formation

The product particles are formed in two stages, which are the reaction and particle-growth stages (Kimura & Yamaguchi, 1983). In the reaction stage, the product particles are formed in the presence of solid reactant particles. The reactant particles dissolve in the molten salt and product particles form. When all the reactant particles are consumed, the particle-growth stage starts. There are solid product particles and molten salt in the system. The product particles have a particle size distribution, and the large particles increase their size by Ostwald ripening (Rahaman, 2003); particles smaller than a critical size dissolve in the molten salt and precipitate on the surfaces of particles larger than the critical size. The supersaturation with respect to the product compound is different in the two stages.

2.2.2 Supersaturation

The supersaturation is determined by the concentration of the reactants in the molten salt. When the product (P) is formed by a reaction between reactants A and B ($A + B \rightarrow P$), the solubility of P determines the equilibrium concentration of A and B in the molten salt, i.e., $[A]_e$ and $[B]_e$, respectively. The supersaturation is given by $([A][B]/[A]_e[B]_e - 1)$, where [A] and [B] are the actual concentration of A and B, respectively, in the molten salt. In the reaction stage, the solid reactant particles are present, and [A] and [B] are equal to their solubilities [A]* and [B]*, respectively. Figure 2 shows the relation between the molar free

energy of a liquid phase (G^l) and the composition of A (mole fraction) (Hillert, 1998). The chemical potential of the molten salt is indicated by $\mu_{salt}{}^l$ on the vertical axis at x_A=0, and $\mu_A{}^l$ and $\mu_A{}^s$ on the vertical axis at x_A=1 are the chemical potentials of liquid and solid A, respectively. The contact point of the G^l curve and the tangent line to G^l from $\mu_A{}^s$ (dashed straight line T_A in Fig. 2) gives the equilibrium concentration of A in the molten salt, which is the same as solubility of A ([A]*). Figure 2 does not show the relation for B, but the same relation applies. In the same manner, the equilibrium concentration of A in the molten salt coexisting with P is given as $[A]_e$, where the chemical potential of A in the solid P phase is indicated by $\mu_{A\ in\ P}$ on the vertical axis at x_A=1. The difference between $\mu_A{}^s$ and $\mu_{A\ in\ P}$ corresponds to the free energy change of the reaction Δ_rG, because $\Delta_rG = (\mu_{A\ in\ P} - \mu_A{}^s) + (\mu_{B\ in\ P} - \mu_B{}^s)$. When the reaction proceeds spontaneously, $\Delta_rG < 0$ and $\mu_A{}^s > \mu_{A\ in\ P}$, as shown in Fig. 2, and the solubility of A ([A]*) is larger than $[A]_e$. Therefore, in the reaction stage, the solid reactants A and B are present with molten salt, and the degree of supersaturation with respect to P is high because $[A]=[A]^*>[A]_e$. When the reaction between A and B is complete, the solid phase present in the system is only P, and [A] and [B] are reduced to $[A]_e$ and $[B]_e$, respectively. Therefore, the degree of supersaturation with respect to P decreases to almost zero in the particle-growth stage.

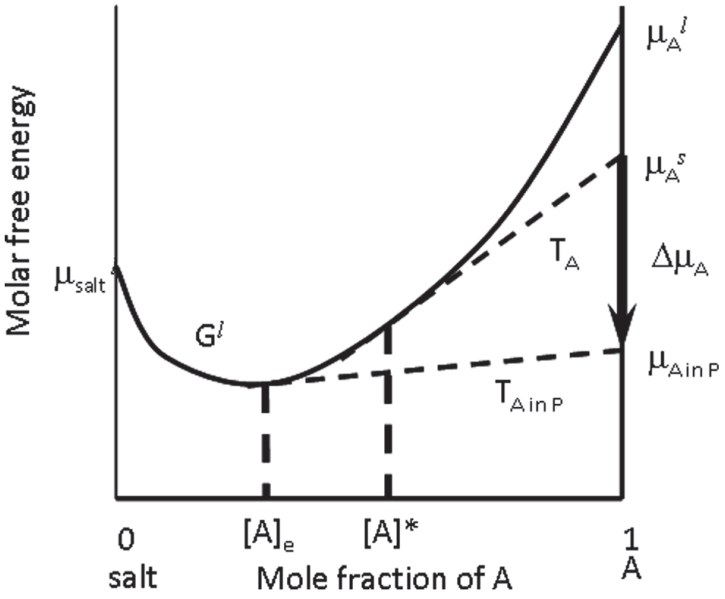

Fig. 2. Relation between the composition and the molar free energy of liquid phase.

Table 1 shows the solubility of $NiFe_2O_4$ and $ZnFe_2O_4$ in the chloride and sulfate salts together with that of NiO, ZnO, and Fe_2O_3. Irrespective of the salt species, the solubilities of ferrites are one order of magnitude smaller than those of the constituent oxides. The solubility is an important property in molten salt synthesis but the solubility data of oxides in molten salts are limited (Janz, 1967).

Oxides	Solubility (mol / g salt)			
	Sulfate salt*	NaCl	0.5NaCl-0.5KCl	KCl
NiO	1.6×10^{-6}	6.7×10^{-7}	6.7×10^{-7}	6.7×10^{-7}
ZnO	1.5×10^{-6}	1.7×10^{-6}	1.2×10^{-6}	9.1×10^{-7}
Fe_2O_3	4.8×10^{-6}	1.9×10^{-6}	2.2×10^{-6}	1.2×10^{-6}
$NiFe_2O_4$	5.1×10^{-7}	7.7×10^{-8}	9.8×10^{-8}	5.1×10^{-8}
$ZnFe_2O_4$	1.6×10^{-7}	2.4×10^{-7}	1.8×10^{-7}	5.0×10^{-8}

*: $0.635Li_2SO_4$-$0.365Na_2SO_4$

Table 1. Solubilities of $NiFe_2O_4$ and $ZnFe_2O_4$ and constituent oxides in salts at 900°C (Hayashi et al., 1986a)

2.3. Reaction rate

2.3.1 Reaction stage

Molten salts increase the reaction rate, and the product formation is completed at lower temperatures than that in solid state reaction. Figure 3 shows the fractional completion of the ferrite formation from the constituent oxides heated at various temperatures for 1 h in the solid state reaction and molten salt synthesis using Li_2SO_4-Na_2SO_4 (Takahashi et al., 1981). The molten salt decreases the temperature range of the reaction. Furthermore, three ferrites (M = Zn, Ni, and Mg) have almost the same temperature range in molten salt synthesis, whereas that largely depends on the chemical species of M in the solid state reaction.

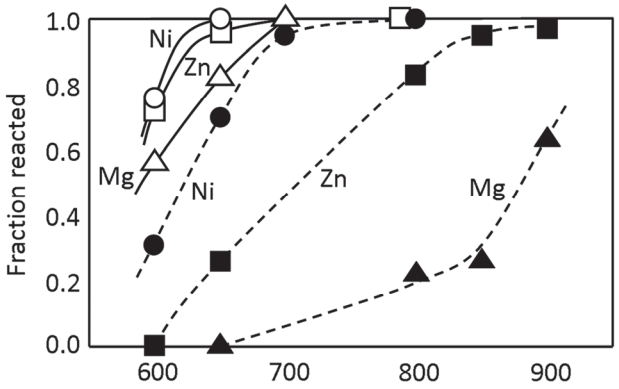

Fig. 3. Formation of MFe_2O_4 (M=Ni, Zn, Mg) with (solid lines) and without (dashed lines) molten Li_2SO_4-K_2SO_4 salt, heated for 1 h (Takahashi et al., 1981).

The promotion of reaction by molten salt has been reported in many systems. The increase in the formation rate is a consequence of (1) an increase in the contact area of the reactant particles and (2) an increase in the mobility of the reactant species in the molten salt (Arendt et al., 1979). The position of the product formation is limited to the contact points of the dissimilar reactants in the solid state reaction, and further increase in the product volume is caused by material transport through the product phase (Schmalzried, 1995). The mobility of material through this route is in the order of 10^{-18} cm^2 sec^{-1}. Conversely, in molten salt

synthesis, the surfaces of the reactant particles are covered with melt and they become available to the reaction. In the molten salt, the mobility of the species ranges from 10^{-5} to 10^{-8} cm^2 sec^{-1}. This is fairly larger than the mobility in the solid state reaction.

2.3.2 Particle-growth stage

After the reactants are completely consumed, the solid phase in the molten salt is only the product particles and the degree of supersaturation drops to almost zero. The prolonged heating increases the average particle size by Ostwald ripening. The rate of Ostwald ripening depends on the diffusion coefficient, the solubility, and the atomic structure of the particle surfaces (Rahaman, 2003). A large diffusion coefficient and solubility enhance the material transport in the molten salt. Therefore, a larger growth rate is expected at higher temperatures. The growth rate of surfaces with well-developed facets is low because of a smooth surface structure at the atomic scale (Kang et al., 2009). The effect of solubility on the growth rate is observed in the ferrite system. Prolonged heating of acicular $NiFe_2O_4$ and $ZnFe_2O_4$ particles in NaCl-KCl at 900°C causes the particles to adopt a somewhat rounded shape (Hayashi et al., 1986a). At this temperature, the formation reaction is complete in 4 min, and the particle shape is acicular. Therefore, the particles deform in the particle-growth stage. The degree of particle deformation is higher in $ZnFe_2O_4$ than $NiFe_2O_4$, for which the higher solubility of $ZnFe_2O_4$ than that of $NiFe_2O_4$ is responsible (Table 1). The same tendency is observed in $ZnFe_2O_4$ particles in NaCl, NaCl-KCl, and KCl. Use of NaCl results in a high degree of particle deformation. The solubility values are 2.4×10^{-7}, 1.8×10^{-7}, and 0.50×10^{-7} mol/g salt in NaCl, NaCl-KCl, and KCl, respectively (Table 1).

2.4 Powder characteristics

2.4.1 Homogeneity of composition

Molten salt enhances the material transport, and it is expected that the product powders are more homogeneous than those prepared by the solid state reaction. To examine the compositional homogeneity in $(Ni,Zn)Fe_2O_4$ powders, $NiFe_2O_4$ and $ZnFe_2O_4$ powders are reacted at 900°C for 4 h by molten salt synthesis using Li_2SO_4-Na_2SO_4 and by the solid state reaction. The compositional fluctuation in the obtained powders is analyzed by measuring the Curie temperature because it is a function of composition (Hayashi et al. 1985). Figure 4 shows the distribution of the Curie temperature for $(Ni,Zn)Fe_2O_4$ powders obtained by molten salt synthesis and solid state reaction. In the absence of molten salt, the distribution curve is broad, indicating a large compositional fluctuation. The molten salt narrows the distribution of the composition.

2.4.2 Agglomeration

During the solid state reaction, sintering (neck growth) of the product particles proceeds concurrently with their formation, which results in the formation of aggregates (Niesz & Bennett, 1978). In contrast, in molten salt synthesis, molten salt covers the surfaces of all particles present and prevents the formation of necks between the product particles. Therefore, it is expected that powders with a low degree of aggregation are obtained. Figure 5 shows the particle size distribution of rod-shaped $BaTiO_3$ particles obtained by the reaction between rod-shaped $TiO_2{\cdot}H_2O$ and $BaCO_3$ (Hayashi et al., 1986b). Heating temperatures are 700°C for the molten salt synthesis using NaCl-KCl and 1000°C for the

solid state reaction; these are minimum heating temperatures needed to complete the reaction within 1 h. The grain size of powder obtained by the molten salt synthesis is smaller than that obtained by the solid state reaction. Because the size of the primary particles is almost the same for both powders as observed with a scanning electron microscope, this size distribution reflects the size of the aggregates in the product powders. Thus, molten salt synthesis produces powders with a low degree of aggregation.

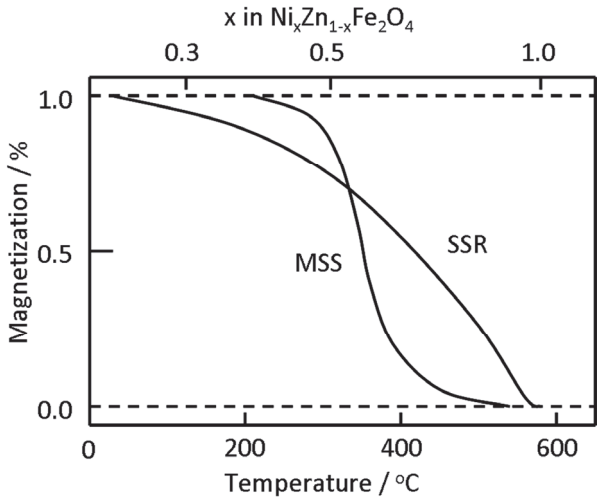

Fig. 4. Distribution of the Curie temperature in $(Ni,Zn)Fe_2O_4$ powders prepared by the molten salt synthesis (MSS) and solid state reaction (SSR), heated at 900°C for 4 h (Hayashi et al., 1985).

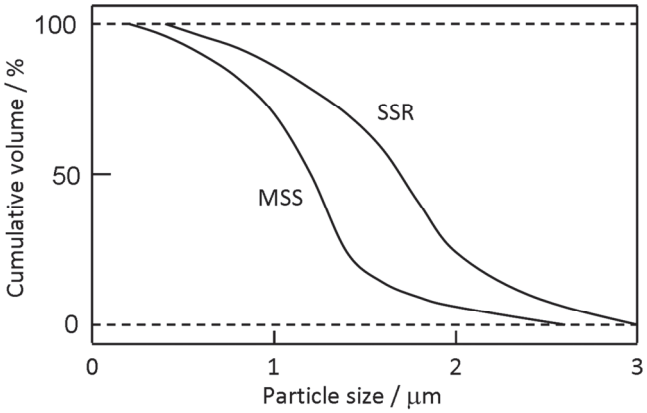

Fig. 5. Particle size distribution of $BaTiO_3$ powders obtained by the molten salt synthesis (MSS) and solid state reaction (SSR), measured by the sedimentation method (Hayashi et al., 1986b).

3. Morphology of powders

3.1 Equilibrium and growth forms

Powders with grains of various shapes are obtained by molten salt synthesis, depending on the chemical composition and reaction conditions. The presence of a liquid phase promotes the facet formation as usually observed in the single-crystal growth from solution (Elwell & Scheel, 1975). Because the crystal structure determines the crystallographic faces (*hkl*) of the stable facets, the particle shape is to some extent determined by the chemical composition. Powder particles are formed in two stages in molten salt synthesis. They are the reaction and particle-growth stages, and the supersaturation is high during the reaction stage and almost zero during the particle-growth stage (see **2.2**). Because the degree of supersaturation determines the growth rate of each crystallographic face, the particle shape is determined by the reaction conditions, such as the chemical species of the salt used, the reaction temperature and its duration, and the powder characteristics of the reactants.

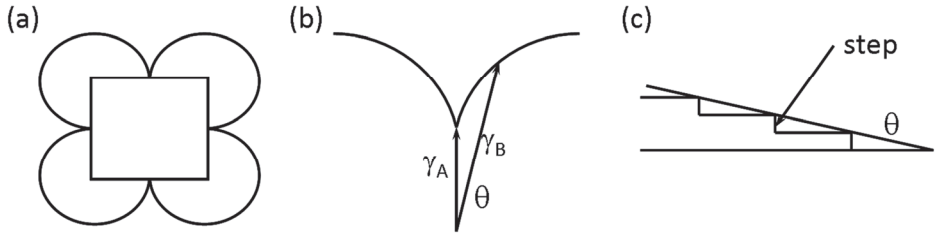

Fig. 6. The equilibrium form is derived from (a) the Wulff plot, (b) the depth of cusp is related to the value of surface free energies (γ_A and γ_B), and (c) the energy of steps on surface A is related to the difference $\gamma_B - \gamma_A$.

In general, the particle shape is determined by two factors, equilibrium and growth forms (Elwell & Scheel, 1975). The equilibrium form is the shape with the minimum surface free energy, and can be derived using the Wulff or γ plot. The Wulff plot is a polar diagram of the specific surface free energy, which is determined by the combination of solid and liquid materials. The equilibrium form is found by drawing all the planes normal to the radius vectors of the surface energy and taking the innermost envelop (Fig. 6(a)). A sharp cusp implies that a certain face has much lower free energy than other faces and the crystal will be facetted. The sharpness of the cusp in the γ plot relates to the roughness of the surfaces at the atomic scale. Figure 6(b) shows a part of the γ plot. Surface A has the lowest surface free energy of γ_A, and surface B is tilted by an angle θ and has a surface free energy of γ_B. The difference between γ_A and γ_B is the energy of the steps on the A surface (Fig. 6(c)). Therefore, a surface with a sharp cusp has high step energy; the density of steps on the surface with a well-developed facet is low.

The growth form is determined by the faces with the lowest growth rate in each direction (Elwell & Scheel, 1975). The growth rate of each face is determined by the structure of the surface at the atomic scale. It is generally anticipated in the crystal growth process that ions in the liquid phase adsorb on the crystal surface, diffuse over the surface, attach to a step on the surface, diffuse along the step, and finally are integrated into the crystal at a kink. When the surface is atomically rough, the density of steps and kinks is high, resulting in a high ion

integration rate into the crystal, and vice versa. Therefore, the surface with a well-developed facet has an atomically smooth structure and a low growth rate. The adsorption of the materials dissolved in a solvent or the solvent itself also influences the growth rate through changing the surface roughness or filling the growth sites.
The particle shape depends on the degree of supersaturation. In many cases, the growth rates of different faces exhibit different dependence on the degree of supersaturation. At a low degree of supersaturation, the difference in the growth rates is large and particles with a distinctive habit form. At a high degree of supersaturation, many faces have almost the same growth rate and particles with an equiaxed, rounded shape form.

3.2 Shape of particles during reaction stage

The degree of supersaturation changes in the course of reaction: it is high during the reaction stage and low during the particle-growth stage. Two mechanisms of particle formation are reported during the reaction stage, and Ostwald ripening is the main mechanism during the particle-growth stage. Powders with the desired morphology (size and shape) can be obtained by the precise control of the reaction conditions in these stages (Tiano et al., 2010).
Figure 7 shows the schematic diagram of the formation of product particle P from reactants A and B. The relative dissolution rate determines the dominant formation mechanism. When the dissolution rates of A and B are comparable (Fig. 7(a)), both reactants dissolve in the molten salt and the product particles precipitate under a high degree of supersaturation (solution-precipitation process: mechanism 1). In this case, particles have a growth form, which is often different from the equilibrium form. Typical examples are Bi_2WO_6 obtained from Bi_2O_3 and WO_3 using Li_2SO_4-Na_2SO_4 (Kimura & Yamaguchi, 1982) and $TiZrO_4$ from TiO_2 and ZrO_2 using KCl (Kimura et al., 1992). The Bi_2WO_6 and $TiZrO_4$ particles have rectangular and irregularly rounded shapes, whereas the equilibrium forms are an oblate an oblate sphere and needle, respectively.

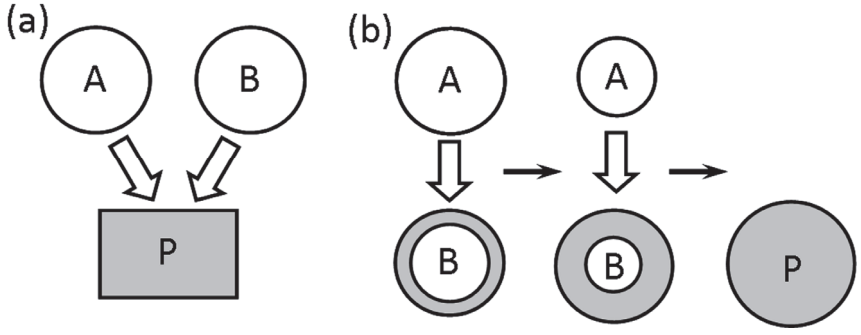

Fig. 7. Schematic diagrams of the formation of product particle P from reactant particles A and B by (a) solution-precipitation and (b) solution-diffusion processes.

When the dissolution rate of A is considerably higher than that of B, and the product layer forms on the surface of particle B (Fig. 7(b)), then another mechanism operates. The product layer prevents the dissolution of B. A large amount of A dissolves in the molten salt before the dissolution of B, diffuses through the molten salt, reaches the surface of particle B, and

reacts with B. The reaction proceeds by the diffusion of A from the interface of the molten salt/product layer to the interface of product layer/particle B and/or by the diffusion of B in the reverse direction, resulting in an increase in the thickness of the product layer. Finally, reactants A and B are completely consumed and the product particle with almost the same shape as that of particle B are obtained (solution-diffusion process: mechanism 2). Sometimes, this mechanism is called templating (Yang et al. 2001).

The relative dissolution rate is important because it determines the mechanism of the particle formation. It is determined by the solubility and particle size of the reactants. In the preparation of $LiFe_5O_8$ by the reaction between Li_2CO_3 and Fe_2O_3 in Li_2SO_4-Na_2SO_4 salt, Li_2CO_3 dissolves completely in the molten salt and $LiFe_5O_8$ particles form by the solution-diffusion process (mechanism 2) (Wickham, 1971). Acicular $NiFe_2O_4$ and $ZnFe_2O_4$ particles are prepared by the reaction between acicular Fe_2O_3 and equiaxed NiO and ZnO using NaCl-KCl and Li_2SO_4-Na_2SO_4 (Hayashi et al., 1986a). The particles obtained in the reaction stage (700°C for 1 h) are divided into two groups; one has the acicular shape and the other has a deformed shape with equiaxed grains of about 0.1 μm and rounded acicular particles. $ZnFe_2O_4$ obtained in NaCl-KCl and Li_2SO_4-Na_2SO_4 and $NiFe_2O_4$ obtained in NaCl-KCl have the acicular shape, whereas $NiFe_2O_4$ obtained in Li_2SO_4-Na_2SO_4 has the deformed one. The effect of the chemical species on the particle shape is explained by the solubility of ferrites in molten salt (Table 1). $NiFe_2O_4$ has the highest solubility in Li_2SO_4-Na_2SO_4 (5.1×10^{-7} mol/g salt) compared to $NiFe_2O_4$ in NaCl-KCl (0.98×10^{-7} mol/g salt) and $ZnFe_2O_4$ in Li_2SO_4-Na_2SO_4 and NaCl-KCl (1.6×10^{-7} and 1.8×10^{-7} mol/g salt, respectively). The possible explanation is that the high solubility of $NiFe_2O_4$ in Li_2SO_4-Na_2SO_4 requires an extensive time for saturation with $NiFe_2O_4$. This gives a greater opportunity for Fe_2O_3 to dissolve, and $NiFe_2O_4$ particles are formed by the solution-precipitation process (mechanism 1).

The relative dissolution rate is also determined by the size of the reactant particles. $NiFe_2O_4$ powders with different shapes are obtained by the reaction of the same Fe_2O_3 powder with two NiO powders with different sizes in Li_2SO_4-Na_2SO_4 (Kimura et al., 1980). In this case, the condition with respect to the solubility is the same, and the origin of the difference in particle shape is explained by the dissolution rate determined by the particle size. Figure 8 shows the shapes of the reactant Fe_2O_3 and product $NiFe_2O_4$ powders. The $NiFe_2O_4$ particles obtained by the reaction with fine NiO particles have almost the same shape as that of Fe_2O_3 particles, and those obtained by the reaction with coarse NiO particles have well-developed {111} facets. The dissolution rate of fine NiO particles is larger than that of Fe_2O_3 and the $NiFe_2O_4$ particles are formed by the solution-diffusion process (mechanism 2). In the case of coarse NiO particles, the solution-precipitation process (mechanism 1) is dominant and {111} facets develop; {111} is the closed packed planes of the spinel structure.

The evidence that the particle size determines the rate of dissolution in molten salt is reported in the formation of $(Ni,Zn)Fe_2O_4$ by the solution-precipitation process from $NiFe_2O_4$ and $ZnFe_2O_4$ with various particle sizes in the presence of Li_2SO_4-Na_2SO_4 (Hayashi et al., 1985). The mixtures of $NiFe_2O_4$ and $ZnFe_2O_4$ with various values of the fractional surface area of $NiFe_2O_4$ (surface area of $NiFe_2O_4$ in the starting mixture/total surface area of $NiFe_2O_4$ and $ZnFe_2O_4$ in the starting mixture) is heated at 900°C for 10 min, and the composition of the $(Ni,Zn)Fe_2O_4$ particles formed at the initial stage of the reaction is determined by the Curie temperature measurement. Figure 9 shows the relation between the fractional surface area of $NiFe_2O_4$ and the composition of the $(Ni,Zn)Fe_2O_4$ particles. A simple relation is observed, indicating that the dissolution rate is determined by the surface area, i.e., the particle size.

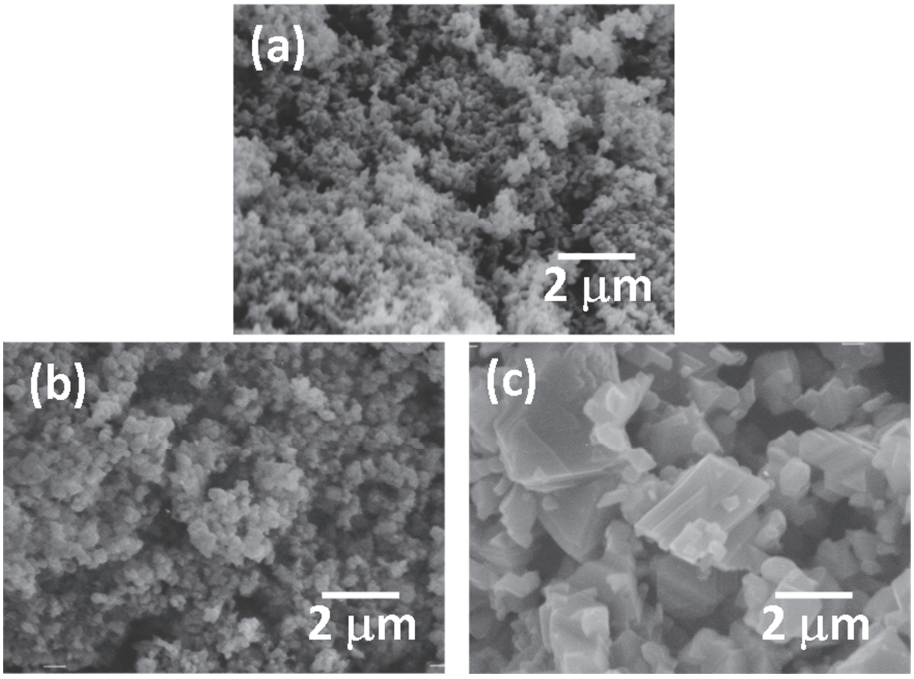

Fig. 8. Equiaxed and faceted $NiFe_2O_4$ particles ((b) and (c), respectively) are obtained from equiaxed Fe_2O_3 particles (a) by the reaction of fine and coarse NiO particles, respectively (Kimura et al., 1980).

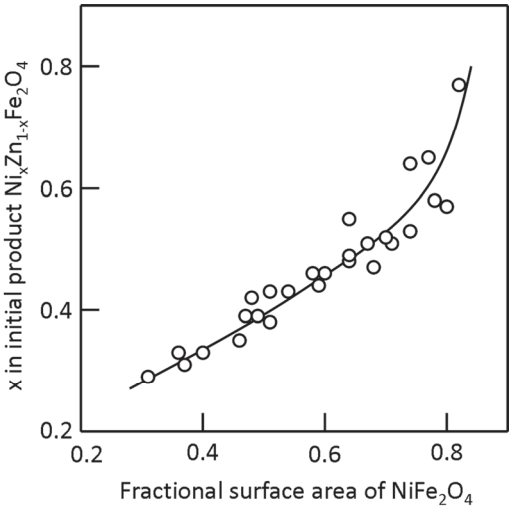

Fig. 9. The relative surface area of $NiFe_2O_4$ particles determines the Ni concentration in $(Ni,Zn)Fe_2O_4$ (Hayashi et al., 1985).

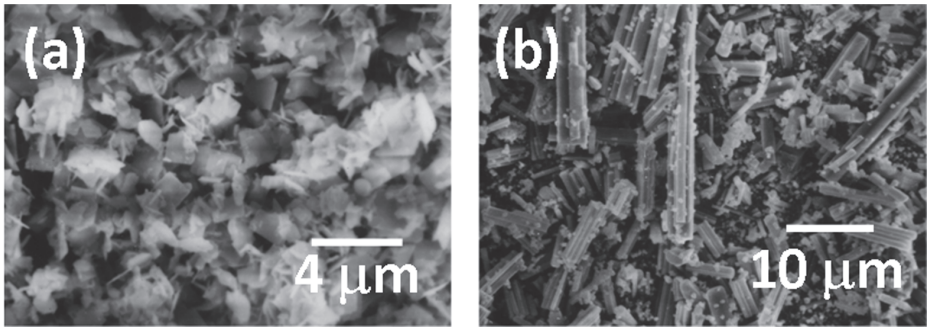

Fig. 10. Morphology of (a) $Bi_4Ti_3O_{12}$ and (b) $PbK_2Nb_5O_{15}$ particles obtained in the reaction stage (Kimura & Yamaguchi, 1983; Kimura et al. 1983a).

The degree of supersaturation is high when the product particles are formed by the solution-precipitation process (mechanism 1) and, consequently, aggregates often form. Figure 10 shows examples of aggregates (Kimura & Yamaguchi, 1983; Kimura et al. 1983a). $Bi_4Ti_3O_{12}$ and $KPb_2Nb_5O_{15}$ have platelike and needle-like shapes, respectively. The $Bi_4Ti_3O_{12}$ aggregates are composed of small platelike particles, and the $KPb_2Nb_5O_{15}$ aggregates have a columnar structure. In the latter case, discrete, needle-like particles are formed in the initial stage of the reaction, and a high degree of supersaturation causes the nucleation of new particles at particle edges as shown in Fig. 11.

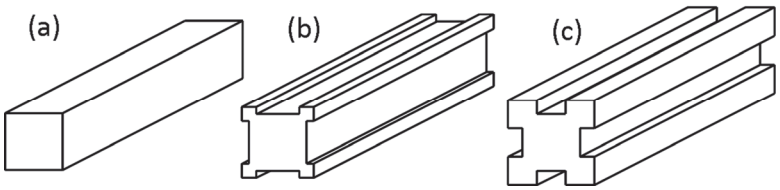

Fig. 11. Formation of the columnar structure by heterogeneous nucleation at the edges of needlelike particle.

3.3 Shape of particles during particle-growth stage

The free energy associated with the particle/molten-salt interfaces decreases during the particle-growth process via two routes. The first is the reduction of the surface area, resulting in particle growth. The second is the disappearance of surfaces with high energy, resulting in a shape change towards the equilibrium form.

The particle growth at this stage is caused by Ostwald ripening, and the growth rate is determined by the solubility and diffusion coefficient of the product oxide (Rahaman, 2003). Therefore, the heating temperature is a decisive factor in determining the particle size. For example, $Bi_4Ti_3O_{12}$ particles in KCl are platelike with the diameter of the plate faces of about 5 μm after heating at 950°C for 1 h and about 25 μm after 1 h at 1130°C, and the size can be controlled by selecting the heating temperature and its duration (Kimura & Yamaguchi, 1983). The exceptions are observed in highly faceted particles. The highly faceted surfaces have a high degree of smoothness at the atomic scale and high step energy, and their growth is sluggish (Kang et al., 2009). For example, platelike $BaBi_4Ti_4O_{15}$ particles in KCl hardly

grow in the particle-growth stage (Kimura & Yoshida, 2006). The top and side faces of the $BaBi_4Ti_4O_{15}$ particles are highly faceted; whereas the side faces of $Bi_4Ti_3O_{12}$ particles are atomically rough. The growth rate of the $BaBi_4Ti_4O_{15}$ particles is substantially zero. Therefore, the control of the particle size by selecting the heating conditions is difficult. Large $BaBi_4Ti_4O_{15}$ particles can be obtained from $Bi_4Ti_3O_{12}$ using the topochemical micro-crystalline conversion (see **3.4.1**) (Kimura & Yoshida, 2006).

If the surfaces of the particles formed in the reaction stage have higher interfacial energy than those of the equilibrium form, the particle shape changes to reduce the total interfacial energy. A typical example is Bi_2WO_6 obtained from Bi_2O_3 and WO_3 in Li_2SO_4-Na_2SO_4 (Kimura & Yamaguchi, 1982). The shape of the Bi_2WO_6 particles in the reaction stage is rectangular and changes to oblate in the particle-growth stage. Bi_2WO_6 has a layered structure and platelike particles form in NaCl-KCl in the reaction and particle-growth stages. The (001) cusp is sharp in NaCl-KCl and shallow in Li_2SO_4-Na_2SO_4, as expected from their shapes in the particle-growth stage. The shallow cusp indicates that the step energy on the (001) face is low and the growth rate of (001) is not different from that of other faces. Thus, the (100), (010), and (001) faces have almost the same growth rate under a high degree of supersaturation (reaction stage), resulting in the rectangular shape. In the particle-growth stage, either the particle shape approaches the equilibrium form or the growth rate of (001) becomes smaller than that of (100) and (010) under a low degree of supersaturation. The dependence of particle shape on the degree of supersaturation is also observed in the cases of $NiFe_2O_4$ (Kimura et al., 1980) and $BaZrO_3$ (Zhou et al., 2007).

The aggregated $Bi_4Ti_3O_{12}$ particles formed in the reaction stage (Fig. 10(a)) change to discrete platelike particles in the particle-growth stage (Kimura & Yamaguchi, 1983). The particle shape is shown in Fig. 12(a). However, the aggregated $KPb_2Nb_5O_{15}$ particles with a columnar structure (Fig. 10(b)) do not change their shape by prolonged heating, because the particle surfaces are highly faceted. Therefore, the discrete needle-like particles are obtained via a different route (Kimura et al. 1983a). The formation of particles with a columnar structure must be avoided. Therefore, the degree of supersaturation must be kept low in the reaction stage. A mixture of PbO, Nb_2O_5, and KCl is heated at 750°C for 1 h. The obtained material is $PbNb_2O_6$ powder composed of aggregates of small equiaxed particles. Then, the material is heated at 1050°C for 3 h. The reaction with KCl change the particles from $PbNb_2O_6$ to $KPb_2Nb_5O_{15}$ (see **4.1**), and the growth at a low degree of supersaturation results in the formation of discrete needle-like particles (Fig. 12(b)).

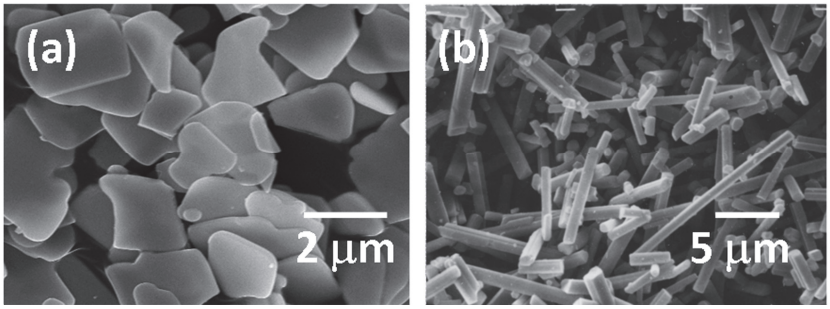

Fig. 12. Morphology of (a) $Bi_4Ti_3O_{12}$ and (b) $PbK_2Nb_5O_{15}$ particles obtained in the particle-growth stage (Kimura & Yamaguchi, 1983; Kimura et al. 1983a).

A change in the particle shape as a function of the heating temperature is reported for $SrO{\cdot}5.5Fe_2O_3$ from Fe_2O_3 and $SrCO_3$ in KCl (Park et al., 1996). Heating at 900°C results in the formation of platelike particles and that at 1200°C produces near-spherical particles. The origin of this shape change is the change in the surface structure from smooth to rough at the atomic scale. The smooth surfaces have high step energy and develop the facets, leading to the platelike shape. The various crystallographic faces on the rough surfaces have almost the same growth rate, resulting in the near-spherical shape. The rate-determining step is also changed from reaction-controlled to diffusion-controlled. The particle size is not largely dependent on the amount of salt for the reaction-controlled case, whereas the mean particle size decreases as the amount of salt is increased in the diffusion-controlled case.
The particle shape obtained via the molten salt synthesis can be predicted from the crystal structure of the product, but the prediction is not always successful because the chemical species of the salt also influence the particle shape, because the γ-plot (Fig. 6(a)) is determined by the combination of the product and salt materials. The particle shape is often determined in the particle-growth stage with a low degree of supersaturation. The growth under a low degree of supersaturation is similar to that in the single-crystal growth from solution. Therefore, the reported shape of single crystals can be used to predict the shape of particles obtained via the molten salt synthesis (Elwell & Scheel, 1975).

3.4 Topochemical micro-crystalline conversion

In materials with low crystallographic symmetry, particles with an anisometric shape can be easily prepared by molten salt synthesis. In contrast, for materials with high crystallographic symmetry, particles with a large aspect ratio (plate or needle) are difficult to prepare directly from the constituent materials, because this shape is far from the equilibrium form. In this case, a precursor particle is used and, subsequently, it is converted to the objective material. The precursor particle must have an anisometric shape and a topotactic relation with the objective material. Molten salt synthesis can easily make the solution-diffusion mechanism dominant (mechanism 2 in Fig. 7); the particles of the objective material are formed by the diffusion of the supplementary material into the precursor particles, thus, preserving the outer shape of the precursor particles. This method is called topochemical micro-crystalline conversion, and is divided into three groups based on the relation between the crystal structures of the precursor and the objective materials; (1) the precursor with a structure similar to the objective material; (2) the precursor with a structure different from the objective material; and (3) the conversion accompanied by by-product.

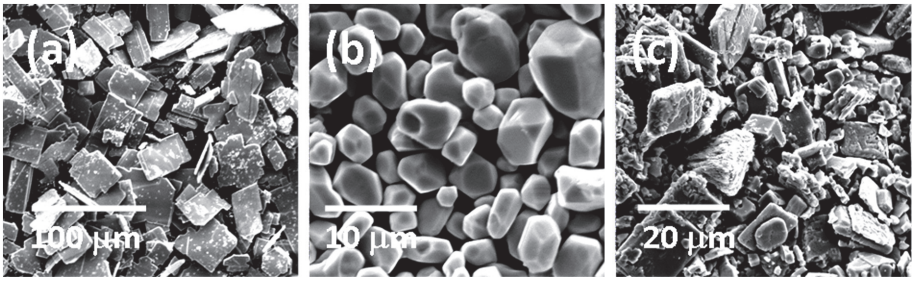

Fig. 13. Morphology of (a) platelike $K_4Nb_6O_{17}$, and (b) equiaxed and (c) platelike KNb_2O_6 particles (Sakurai, 2011).

The shape of the precursor particles must be preserved during the topochemical reaction, which occurs in the reaction stage (see **3.2**). In the reaction stage, two reaction processes are possible; the solution-precipitation and solution-diffusion processes. If the former process is dominant, the precursor particles dissolve and the objective material particles precipitate with an intrinsic shape. Therefore, anisometric particles cannot be obtained. The reaction conditions must be selected to make the solution-diffusion process dominant. Platelike $KNbO_3$ particles are obtained via platelike $K_4Nb_6O_{17}$ particles (Saito & Takao, 2007). Figure 13(a) shows platelike $K_4Nb_6O_{17}$ particles obtained by the reaction between Nb_2O_5 and $(COOK)_2{\cdot}H_2O$ in KCl. $KNbO_3$ is obtained by the reaction of the platelike $K_4Nb_6O_{17}$ particles with $(COOK)_2{\cdot}H_2O$, but the particle shape depends on the particle size of (COOK)2·H2O (Sakurai, 2011). When $(COOK)_2{\cdot}H_2O$ particles of tens of micrometer are used, $KNbO_3$ particles with an equiaxed shape are obtained (Fig. 13(b)). When $(COOK)_2{\cdot}H_2O$ particles of several micrometers are used, then, polycrystalline platelike particles are obtained (Fig. 13(c)). The $(COOK)_2{\cdot}H_2O$ particle size determines the dissolution rate of K_2O in the molten salt and the process of the formation of the $KNbO_3$ particles. Usually, K_2CO_3 is used as the potassium source, but it is hygroscopic and difficult in handling. $(COOK)_2{\cdot}H_2O$ is not hygroscopic and it can be used in the preparation of the particles (Fig. 13); $(COOK)_2{\cdot}H_2O$ decomposes to K_2CO_3 upon heating at about 370°C.

The chemical species of the reactants also determine the reaction process. In the preparation of $PbTiO_3$ in NaCl-KCl, the $PbTiO_3$ particle shape depends on the titanium source (Cai et al., 2007). Needlelike $PbTiO_3$ particles are obtained from needlelike TiO_2 particles, whereas the use of needlelike $K_2Ti_4O_9$ particles results in the formation of cube-shaped $PbTiO_3$ particles. When the needlelike TiO_2 particles are used, the dominant process of the $PbTiO_3$ formation is solution-diffusion (mechanism 2). In the $K_2Ti_4O_9$ case, the needlelike $K_2Ti_4O_9$ particles break-up to small pieces before reacting with PbO, or the reaction in the reaction stage is caused by the solution-precipitation process (mechanism 1). A similar effect of the source of the B-site cation is reported for $ANbO_3$ (A = Na, K, and (Na,K)) (Li et al., 2009). The effect of the barium source is seen in the preparation of needlelike $BaTiO_3$ particles (Huang et al., 2009). $BaCO_3$ gives needlelike $BaTiO_3$ particles via the reaction with the needlelike TiO_2 particles, but BaO produces cube-shaped $BaTiO_3$ particles. $BaCO_3$ has a high solubility and the $BaTiO_3$ particles are formed by the solution-diffusion process (mechanism 1 in Fig. 7), whereas the low solubility of BaO makes the solution-precipitation process dominant (mechanism 2 in Fig. 7).

3.4.1 Similar structures between precursors and products

The Aurivillius structure consists of alternately stacked Bi_2O_2 layers and pseudoperovskite blocks. The number of pseudoperovskite blocks is three in $Bi_4Ti_3O_{12}$ and four in $MBi_4Ti_4O_{15}$ (M = Ca, Sr, and Ba) (Fig. 14). The platelike $Bi_4Ti_3O_{12}$ particles are easily obtained by molten salt synthesis using KCl and their size can be easily controlled by selecting the heating temperature and duration. The growth rate of $BaBi_4Ti_4O_{15}$ is low and it is difficult to obtain platelike $BaBi_4Ti_4O_{15}$ particles with a diameter more than 10 μm (see **3.3**). The reaction of platelike $Bi_4Ti_3O_{12}$ particles with $BaTiO_3$ or $BaCO_3$ + TiO_2 in salt (for example, KCl-$BaCl_2$) results in platelike $BaBi_4Ti_4O_{15}$ particles with almost the same size as that of $Bi_4Ti_3O_{12}$ particles (Kimura & Yoshida, 2006). Because the addition of pseudoperovskite blocks into $Bi_4Ti_3O_{12}$ does not disturb the structure, single-crystalline $BaBi_4Ti_4O_{15}$ particles are obtained.

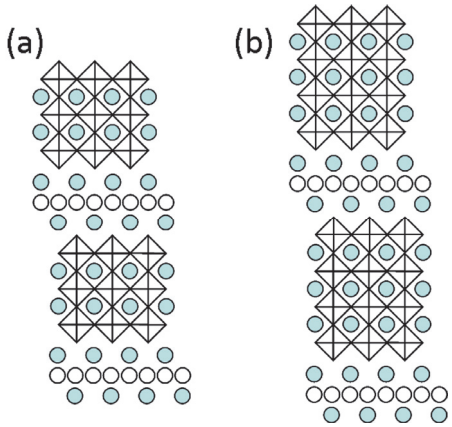

Fig. 14. Crystal structures of (a) $Bi_4Ti_3O_{12}$ and (b) $BaBi_4Ti_4O_{15}$.

3.4.2 Different structures between precursors and products

A material with a different crystal structure from the objective material can be used as a precursor, when the material has a topotactic relation to the objective material. Typical examples are the conversion of the layered perovskite to perovskite (Schaak & Mallouk, 2000) and the preservation of the packing direction of closed-packed layers. The former example is the formation of $SrTiO_3$ from $Sr_3Ti_2O_7$ and the latter of MFe_2O_4 (M = Zn, Ni, Mn, etc.) from α-Fe_2O_3 and of $BaTiO_3$ from $Ba_6Ti_{17}O_{40}$.

Tabular $SrTiO_3$ is obtained via a reaction between tabular $Sr_3Ti_2O_7$ and equiaxed TiO_2 in molten KCl (Watari et al., 2000). $Sr_3Ti_2O_7$ has a Ruddlesden-Popper-type layered perovskite structure, and tabular particles can be obtained by the reaction of $SrCO_3$ and TiO_2 in KCl. $Sr_3Ti_2O_7$ and $SrTiO_3$ have a topotactic relationship, $[001]_{Sr3Ti2O7}//[001]_{SrTiO3}$ and $[100]_{Sr3Ti2O7}//[100]_{SrTiO3}$, as shown in Fig. 15. The diffusion of reactant TiO_2 into the $Sr_3Ti_2O_7$ particles results in the formation of $SrTiO_3$ particles with the shape same as that of $Sr_3Ti_2O_7$ (Liu et al., 2009). Thus, tabular $SrTiO_3$ particles with [001] perpendicular to the tabular faces are obtained. In this case, both $Sr_3Ti_2O_7$ and $SrTiO_3$ particles are single crystals. A similar method is applied to the preparation of platelike $Bi_{0.5}Na_{0.5}TiO_3$ powders from platelike $Na_{0.5}Bi_{4.5}Ti_4O_{15}$ particles by the reaction $Na_{0.5}Bi_{4.5}Ti_4O_{15}+Na_2CO_3+TiO_2$ in NaCl (Zeng et al., 2006). $Na_{0.5}Bi_{4.5}Ti_4O_{15}$ and $Bi_{0.5}Na_{0.5}TiO_3$ have the Aurivillius (Fig. 14(b)) and perovskite (Fig. 15(b)) structure, respectively. In this case, the single-crystalline $Na_{0.5}Bi_{4.5}Ti_4O_{15}$ particles are converted to polycrystalline $Bi_{0.5}Na_{0.5}TiO_3$ particles.

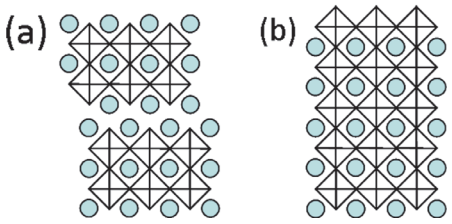

Fig. 15. Crystal structures of (a) $Sr_3Ti_2O_7$ and (b) $SrTiO_3$.

Alfa-Fe_2O_3 and MFe_2O_4 (M = Zn, Ni, Mn, etc.) have the corundum and spinel structure, respectively. They have closed-packed oxygen layers with different sequences; hexagonal (ABAB…) in Fe_2O_3 and cubic (ABCABC…) in MFe_2O_4. The directions perpendicular to these layers are preserved when MFe_2O_4 is formed by the diffusion of MO into Fe_2O_3. When platelike Fe_2O_3 particles prepared by the hydrothermal method are used, platelike MFe_2O_4 particles are obtained in Li_2SO_4-Na_2SO_4 (Kimura et al., 1981). In this case, platelike Fe_2O_3 particles are single crystals but the obtained MFe_2O_4 particles are polycrystalline, and the topotactic relationship is preserved in each grain, i.e., $[0001]_{Fe2O3}//[111]_{MFe2O4}$. Thus, platelike MFe_2O_4 particles with [111] perpendicular to the plate faces are obtained. By a similar process, needlelike (Ni,Zn)Fe_2O_4 particles are obtained from needlelike α-Fe_2O_3 (Hayashi et al., 1986a). Even though the orientation of $MgAl_2O_4$ crystal axes is not reported, platelike $MgAl_2O_4$ particles are obtained from platelike α-Al_2O_3 particles (Jayaseelan et al., 2007).

Similar preservation of the closed-packed layers is observed in titanates. $Ba_6Ti_{17}O_{40}$ and $BaTiO_3$ have closed packed layers containing both barium and oxygen ions. The packing sequences are hexagonal in $Ba_6Ti_{17}O_{40}$ (Hofmeister et al., 1984) and cubic in $BaTiO_3$. Platelike $Ba_6Ti_{17}O_{40}$ particles with the [001] direction perpendicular to the plate face (the crystal structure of $Ba_6Ti_{17}O_{40}$ is monoclinic) are obtained by the reaction of $BaTiO_3$ and TiO_2 in NaCl (Kimura et al., 2005), and they are converted into platelike $BaTiO_3$ particles with [111] perpendicular to the plate face by the reaction with $BaCO_3$ in NaCl (Sato & Kimura, 2008). In this case, the obtained platelike $BaTiO_3$ particles are polycrystals.

A series of topochemical reactions are employed to obtain anisometric particles. An example is needlelike $BaTiO_3$ (Hayashi et al., 1986b). At first, needlelike $K_2Ti_4O_9$ particles are prepared from K_2CO_3 and TiO_2 in K_2MoO_4 flux, converted to needlelike $TiO_2 \cdot nH_2O$ by washing with an HCl solution and to needlelike TiO_2 by heating at high temperatures, and finally reacted with $BaCO_3$ in NaCl-KCl. A similar procedure is employed to prepare needlelike and platelike $KNbO_3$ particles (Li et al., 2009).

3.4.3 Conversion accompanied by by-products

Platelike particles with the perovskite structure are prepared from platelike particles with the Aurivillius structure, as already shown for platelike $Bi_{0.5}Na_{0.5}TiO_3$ particles in **3.4.2** (Zeng et al., 2006). The Aurivillius structure shown in Fig. 14 consists of pseudoperovskite blocks and can be topotactically converted to the perovskite structure (Fig. 15(b)). To extend the method to other perovskite materials, the formation of Bi_2O_3 particles cannot be avoided as shown by the following reaction.

$$Bi_{2.5}Na_{3.5}Nb_5O_{18} + Na_2CO_3 \rightarrow NaNbO_3 + Bi_2O_3 + CO_2$$

Thus, platelike $NaNbO_3$ particles with [001] perpendicular to the plate faces are prepared from platelike $Bi_{2.5}Na_{3.5}Nb_5O_{18}$ particles, which are obtained by the reaction between Bi_2O_3, Na_2CO_3, and Nb_2O_5 in NaCl (Sait et al., 2004). The platelike $Bi_{2.5}Na_{3.5}Nb_5O_{18}$ particles are single crystals but change to polycrystalline $NaNbO_3$ particles. The by-product Bi_2O_3 particles cannot be removed by washing with water. Washing with an acid solution is necessary. Platelike particles such as BaTiO3 (Liu et al., 2007), CaTiO3 (Saito et al. 2008), PbTiO3 (Poterala et al., 2010), $SrTiO_3$ (Saito & Takao, 2006), $Bi_{0.5}Na_{0.5}TiO_3$ (Zhao et al., 2008), etc., can be prepared by the same procedure from appropriate precursors.

The mechanism of the topochemical conversion from the Aurivillius to the perovskite structure has been proposed by Poterala et al. (Poterala et al., 2010). The Aurivillius phase converts directly to the perovskite phase as in $NaNbO_3$ or via an intermediate phase, which is formed by multiple nucleations on the Aurivillius phase, as in $BaTiO_3$ and $PbTiO_3$. The conversion occurs in two sequential stages. The first stage is the multiple topotactic nucleation of the perovskite phase either directly on the Aurivillius phase or on the intermediate phase. The nuclei grow to small crystallites. They are slightly misaligned from the Aurivillius parent structure. At the end of the first stage, the Aurivillius single-crystal particle changes to an aggregate of aligned perovskite crystallites with a slight misorientation. In the second stage, the aligned crystallites in the aggregate grow to form a dense platelike particle. When the growth of the aligned crystallites is complete, the perovskite particles are single-crystals with almost the same shape and size as those of the Aurivillius particles. When the growth is incomplete, the perovskite particles are polycrystalline in nature. The change from single-crystalline, platelike $Bi_4Ti_3O_{12}$ particles to single-crystalline, platelike $Bi_{0.5}Na_{0.5}TiO_3$ particles via poly-crystalline, platelike aggregates is also observed in the stage of the template particle formation in $Bi_{0.5}Na_{0.5}TiO_3$ textured by the reactive-templated grain growth process (Motohashi & Kimura, 2008).

4. Reaction between oxides and salts

4.1 Reaction

It is desirable that salt acts as a pure solvent and does not react with the reactant and product materials. However, many reactions between oxides and salts (chlorides, sulfates, carbonates, etc.) are reported. Therefore, care must be taken to avoid the reaction with the salt in the selection of salt species.

Severe reactions are reported in the molten salt synthesis of niobates with the tungsten bronze structure. In the preparation of $PbNb_2O_6$ from PbO and Nb_2O_5, pure $PbNb_2O_6$ cannot be obtained using NaCl and KCl (Kimura et al., 1983b). When KCl is used as the molten salt, K ions extensively substitute for Pb ions and the product is a solid solution $(1-x)PbNb_2O_6$-$xKPb_2Nb_5O_{15}$ with the tungsten bronze structure. The extent of the substitution, x, is determined by the heating conditions. When NaCl is used, the substitution reaction proceeds to form the $(Na,Pb)NbO_3$ phase as well as $(1-x)PbNb_2O_6$-$xNaPb_2Nb_5O_{15}$. The reaction $PbO+2MCl \rightarrow M_2O+PbCl_2$ (M=Na, K) is responsible for this substitution.

Alkali chlorides cannot be used to prepare MNb_2O_6 (M=alkaline earth metal), and MCl_2 is a candidate for molten salt. When the product phase is the $M_xM'_{1-x}Nb_2O_6$ solid solution and the salt is MCl_2-$M'Cl_2$, then, an interchange reaction is possible. When $Sr_{0.5}Ba_{0.5}Nb_2O_6$ is prepared from $SrCO_3$, $BaCO_3$, and Nb_2O_5 using $SrCl_2$-$BaCl_2$, Sr–rich $(Sr,Ba)Nb_2O_6$ phase forms, for which the reaction $BaO+SrCl_2 \rightarrow BaCl_2+SrO$ is responsible (Furubayashi & Kimura, 2011). $Sr_{0.5}Ba_{0.5}Nb_2O_6$ can be prepared by selecting the $SrCl_2$ to $BaCl_2$ ratio.

The reaction between the Aurivillius phase and chloride is possible (Fuse, 2006). The Aurivillius phase has the general formula $Bi_2O_2(A_{m-1}B_mO_{3m+1})$, and a compound with an m value different form that of the objective material often forms. Figure 16 shows the X-ray diffraction patterns of $Bi_4Ti_3O_{12}$ obtained from Bi_2O_3 and TiO_2. When NaCl is used as the molten salt, the diffraction lines of $Na_{0.5}Bi_{8.5}Ti_7O_{27}$ are detected in the specimen heated at 1130°C. The diffraction lines other than those of $Bi_4Ti_3O_{12}$ are not detected in the specimens

heated at 950°C in NaCl and at 1130°C in KCl. $Bi_4T_3O_{12}$ reacts with NaCl at high temperatures but does not with KCl. The NaCl-KCl salt cannot be used in the preparation of $Bi_4Ti_3O_{12}$ at high temperatures. Because the Aurivillius compounds with different *m* values have similar X-ray diffraction patterns, close examination of the pattern is necessary to ensure the formation of the material with the desired composition (Sanson & Whatmore 2005).

The reactivity of an oxide with the salt often depends on the oxide chemical species. When Li_2SO_4 is used in the preparation of $BaFe_{12}O_{19}$ from $BaCO_3$ and Fe_2O_3, $LiFe_5O_8$ forms by the following reaction; $BaCO_3+5Fe_2O_5+Li_2SO_4 \rightarrow 2LiFe_5O_8+BaSO_4+CO_2$ (Wickham, 1971). The exchange reaction $MgCO_3+Li_2SO_4 \rightarrow MgSO_4+Li_2CO_3$ does not occur and $MgFe_2O_4$ is obtained from $MgCO_3$ and Fe_2O_3 in Li_2SO_4-Na_2SO_4.

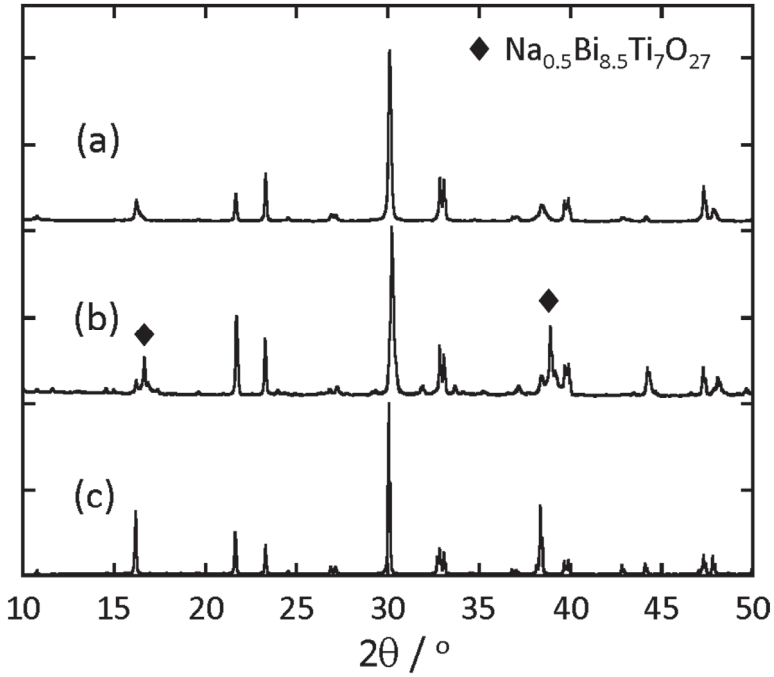

Fig. 16. X-ray diffraction patterns of the products of reaction $2Bi_2O_3+3TiO_2$ after 1 h (a) in NaCl at 900°C, (b) in NaCl at 1130°C, and (c) in KCl at 1130°C.

4.2 Positive uses of exchange reactions

The substitution reaction of alkali ions for alkaline earth ions is positively used for the preparation of needlelike $AM_2Nb_5O_{15}$ particles, where A and M are alkali and alkaline earth ions, respectively. When the $KSr_2Nb_5O_{15}$ particles are prepared from K_2CO_3, $SrCO_3$, and Nb_2O_5 using molten KCl, needlelike particles are obtained, but their size range is limited. The high degree of supersaturation during the reaction stage results in a large number of nuclei and the atomically smooth surfaces make the growth rate substantially zero. If the degree of supersaturation is low during the reaction stage, the number of nuclei is limited

and the formation of large needlelike particles is expected. When $SrCO_3$+Nb_2O_5 or $SrNb_2O_6$(+Nb_2O_5) is used as the reactant and an excessive amount of KCl is used as salt, needlelike $KSr_2Nb_5O_{15}$ particles of large size are obtained (Zhao et al., 2005; Yang et al., 2007).

Interesting ion-exchange reaction between the solid oxide and molten chloride is reported in the preparation of $RbCa_2Nb_3O_{10}$ at 800°C (Geselbracht et al, 2002). The reaction of K_2CO_3, $CaCO_3$, and Nb_2O_5 with a large excess of RbCl produces $RbCa_2Nb_3O_{10}$. K_2CO_3 is a necessary compound to form $RbCa_2Nb_3O_{10}$, because the reaction without K_2CO_3 results in the formation of $CaNb_2O_6$ and $Ca_2Nb_2O_7$. Heating $KCa_2Nb_3O_{10}$ in molten RbCl forms $RbCa_2Nb_3O_{10}$. These results indicate that the ion-exchange reaction is necessary to obtain $RbCa_2Nb_3O_{10}$.

5. Summary

Molten salt synthesis is a simple method for the preparation of ceramic powders. The preparation procedure is quite similar to that used in an ordinary powder metallurgical method. A mixture of reactant and salt powders is heated at temperatures above the melting point of the salt. The reactants interact under the presence of the molten salt. After a pre-determined heating stage, the product mass is cooled, and washed with a solvent (mainly water) to remove the salt. The product powder is obtained after drying.

The product powder is formed in two stages, reaction and particle-growth. In the reaction stage, the molten salt does not dissolve all the reactant powders and the reaction occurs in the presence of solid reactant particles. The product powder is formed by two processes under a high degree of supersaturation. One is the solution-precipitation process; all members of reactants dissolve in the molten salt and the product particles precipitate. Another is the solution-diffusion process; one of the reactants dissolves in the molten salt and reacts with another reactant on the surface of the latter. At the end of the reaction stage, the only solid material in the molten salt is the product particles. Further heating starts the particle-growth stage; the product particles change their size and shape under a low degree of supersaturation.

Powders of various sizes from a few tens nanometers to a few tens micrometers can be obtained by the careful control of the preparation conditions. The particle shape can also be controlled. The size and shape of particles changes in the course of the stages of particle formation. In the reaction stage, two types of particles can be obtained. When the product particles are formed by the solution-precipitation and solution-diffusion processes, the particles have a growth form and a shape similar to that of one of the reactant particles, respectively. The dominant process is determined by the relative dissolution rate of the reactant particles into the molten salt, and the dissolution rate is determined by the solubility and particle size of the reactant. In the particle-growth stage, the particle size is increased and the particle shape approaches the equilibrium form. For the materials with low crystallographic symmetry, anisometric particles can be obtained. When anisometric particles are desired for materials with high symmetry, the topochemical micro-crystalline conversion can be applied.

The application of molten salt synthesis is widely spread since 2005, from ferroelectric and ferromagnetic materials to materials for Li-ion batteries (Santhanam & Rambabu, 2010),

semiconductors (Huang et al, 2010), phosphors (Yan & Lei, 2010), and photocatalysts (Arney et al., 2008), especially with regard to nano-sized materials (Mao et al., 2007). Although this review only deals with complex oxides, the application has been extended to simple oxide powders with specific morphology (Tiano et al., 2010). The preparation of nanoparticles with various shapes (equiaxed, wire, strip, plate) has been reported for a wide variety of materials. Further researches on the formation mechanism from nanoparticles might be necessary, because various phenomena are reported in literatures but their origins are not explained. For example, needlelike $PbTiO_3$ particles are formed by heating of a mixture of equiaxed $PbTiO_3$ particles, NaCl, and surfactant (Cai, et al., 2007) and non-equiaxed $BaTiO_3$ particles are prepared from equiaxed nano TiO_2 particles without a surfactant (Deng et al., 2009). Careful examination of product particles is necessary because the formation of titanium oxide-rich compounds, instead of $PbTiO_3$ and $BaTiO_3$, is possible (Rørvik et al., 2008).

6. Rererences

Afanasiev, P. & Geantet, C. (1998). Synthesis of Solid Materials in Molten Nitrates. *Coordination Chemistry Reviews*, Vol.178-180, Part 2, (December 1998), pp. 1725-1752, ISSN 0010-8545

Arendt, R. H., Rosolowski, J. H., & Szymaszek, J. W. (1979). Lead Zirconate Titanate Ceramics from Molten Salt Solvent Synthesized Powders. *Materials Research Bulletin*, Vol.14, No.5, (May 1979), pp. 703-709, ISSN 0025-5408

Arney, D., Porter, B., Greve, B., & Maggard, P. A. (2008). New Molten-Salt Synthesis and Photocatalytic Properties of $La_2Ti_2O_7$ Particles. *Journal of Photochemistry and Photobiology A: Chemistry*, Vol.199, No.2-3, (June 2008), pp. 230-235, ISSN 1010-6030

Cai, Z., Xing, X., Yu, R. Sun, X., & Liu, G. (2007). Morphology-Controlled Synthesis of Lead Titanate Powders. *Inorganic Chemistry*, Vol.46, No.18, (July 2007), pp. 7423-7427, ISSN 0020-1669

Deng, H., Qiu, Y., & Yang, S. (2009). General Surfactant-free Synthesis of $MTiO_3$ (M = Ba, Sr, Pb) Perovskite Nanostrips, *Journal Materials Chemistry*, Vol.19, No.7, (January 2009), pp. 976-982, ISSN 0959-9428

Elwell, D. & Scheel, H. J. (1975). *Crystal Growth from High-Temperature Solutions*, Academic Press, ISBN 0-12-237550-8, London, UK

Furubayashi, A. & Kimura, T. (2011). Preparation of Needlelike $Sr_{0.5}Ba_{0.5}Nb_2O_6$ Particles Using Molten $SrCl_2$-$BaCl_2$ Salt. *Journal of the Ceramic Society of Japan*, Vol.119, No.4 (April 2011), pp. 282-284, ISSN 0914-5400

Fuse, K. (2006). Mechanisms of Texture Development in $Bi_{0.5}(Na,K)_{0.5}TiO_3$ made by Reactive-Templated Grain Growth Method. *Master Thesis*, Keio University, Japan (March 2006)

Geselbracht, M. J., Walton, R. I., Cowell, E. S., Millange, F., & O'Hare, D. (2002). An Investigation of the Synthesis of the Layered Perovskite $RbCa_2Nb_3O_{10}$ Using Time-Resolved in Situ High-Temperature Powder X-ray Diffraction. *Chemistry of Materials*, Vol.14, Vol.10, (September 2002), pp. 4343-4349, ISNN 0897-4756

Han, C. -H., Hong, Y. -S., & Kim, K. (2003). Cyclic Performances of HT-$LiCo_{0.8}M_{0.2}O_2$ (M=Al, Ni) Powders Prepared by the Molten Salt Synthesis Method. *Solid State Ionics*, Vol.159, No.3-4, (April 2003), pp. 241-247, ISSN 0167-2738

Hayashi, Y., Kimura, T., & Yamaguchi, T. (1985). Mechanism of Flux-Aided Reaction in Ferrite Systems. *Bulletin of the American Ceramic Soc*iety, Vol.64, No.9, (September 1985), pp. 1249-52, ISSN 0002-7812

Hayashi, Y., Kimura, T., & Yamaguchi, T. (1986a). Preparation of Acicular NiZn-Ferrite Powders. *Journal of Materials Science*, Vol.21, No.8, (August 1986), pp. 2876-2880, ISSN 0022-2461

Hayashi, Y., Kimura, T., & Yamaguchi, T. (1986b). Preparation of Rod-Shaped $BaTiO_3$ Powder. *Journal of Materials Sci*ence, Vol.21, No.3, (March 1986), pp. 757-762, ISSN 0022-2461

Hillert, M. (1998). *Phase Equilibria, Phase Diagrams and Phase Transformations, Their Thermodynamic Basis*, Cambridge University Press, ISBN 0-521-56584-7, Cambridge, UK

Hofmeister, W., Tillmanns, E., & Baur, W. (1984). Refinement of Barium Titanate, $BaTi_4O_9$, and Hexabarium 17-Titanate, $Ba_6Ti_{17}O_{40}$. *Acta Crystallographica Section C*, Vol.40, No.9, (September 1984), pp. 1510-1512, ISSN 0108-2701

Huang, K. -C. Huang, T. -C., & Hsieh, W. -F. (2009). Morphology-Controlled Synthesis of Barium Titanate Nanostructures. *Inorganic Chemistry*, Vol.48, No.19, (September 2009) pp. 9180-9184 ISSN 0020-1669

Huang, Z., Li, B., & Liu, J. (2010). Molten-Salt Synthesis of Oxyapatite $La_{9.33}Si_6O_{26}$ Powders as Electrolytes for Intermediate Temperature Solid Oxide Fuel Cells. *Physica Status Solidi A – Application and Materials Science*, Vol.207, No.10, (August 2010), pp. 2247-2251, ISSN 1862-6300

Janz, G. J. (1967). *Molten Salt Handbook*, Academic press, LCCCN 66-30087, New York, USA

Jayaseelan, D. D., Zhang, S., Hashimoto, S., & Lee, W. E. (2007). Template Formation of Magnesium Aluminate ($MgAl_2O_4$) Spinel Microplatelets in Molten Salt. *Journal of the European Ceramic Society*, Vol.27, No.16, (June 2007), pp. 4745-4749, ISSN 0955-2219

Kang, S. -J. L., Lee, M. -G., & An, S. -M. (2009). Microstructure Evolution During Sintering with Control of the Interface Structure. *Journal of the American Ceramic Society*, Vol.92, No.7, (June 2009), pp. 1464-1471, ISSN 0002-7820

Kimura, T., Takahashi, T., & Yamaguchi, T. (1980). Preparation and Characteristics of Ni-Ferrite Powders obtained in the Presence of Fused Salts. *Journal of Materials Sci*ence, Vol.15, No.6, (June 1980), pp. 1491-1497, ISSN 0022-2461

Kimura, T., Takahashi, T., and Yamaguchi, T. (1981). Preparation of Ferrite Powder by Flux Method. *Ferrites, Proceedings of ICF 3,* pp. 27-29, UTP 3055-67543-5149, Kyoto, Japan September 29 – October 2, 1980

Kimura, T. & Yamaguchi, T. (1982). Morphology of Bi_2WO_6 Powders obtained in the Presence of Fused Salt. *Journal of Materials Sci*ence, Vol.17, No.7, (July 1982), pp. 1863-1870, ISSN 0022-2461

Kimura, T. & Yamaguchi, T. (1983). Fused Salt Synthesis of $Bi_4T_{i3}O_{12}$. *Ceramics International*, Vol.9, No.1, (January-March 1983), pp. 13-17 ISSN 0272-8842

Kimura, T., Yamaguchi, T., & Newnham, R. E. (1983a) Phase and Morphology of $PbNb_2O_6$ Obtained by Molten Salt Synthesis. *Particulate Science and Technology*, Vol.1, No.3, (July 1983), pp. 357-364 ISSN 0272-6351

Kimura, T., Machida, M., Yamaguchi, T., & Newnham, R. E. (1983b). Products of Reaction Between PbO and Nb_2O_5 in Molten KCl or NaCl. *Journal of the American Ceramic Society*, Vol.66, No.10, (October 1983), pp. C-195-C-197, ISSN 0002-7820

Kimura, T., Takenaka, A., Mifune, T., Hayashi, Y., & Yamaguchi, T. (1992). Preparation of Needle-like $TiZrO_4$ and PZT Powders. *Journal of Materials Science*, Vol.27, No.6, (June 1992), pp. 1479-1483, ISSN 0022-2461

Kimura, T., Miura, Y., & Fuse, K. (2005). Texture Development in Barium Titanate and PMN-PT using Hexabarium 17-Titanate Heterotemplates. *International Journal of Applied Ceramic Technology*, Vol.2, No.1, (January 2005), pp. 15-23, ISSN 1546-542X

Kimura, T. (2006). Application of Texture Engineering to Piezoelectric Ceramics – A Review. *Journal of the Ceramic Society of Japan*, Vol.114, No.1, (January 2006), pp. 15-25 ISSN 0914-5400

Kimura, T. & Yoshida, Y. (2006). Origin of Texture Development in Barium Bismuth Titanate Made by Templated Grain Growth Method. *Journal of the American Ceramic Society*, Vol.89, No.3, (January 2006), pp. 869-874, ISSN 0002-7820

Li, L., Deng, J., Chen, J., Sun, X., Yu, R., Liu, G., & Xing, X. (2009). Wire Structure and Morphology Transformation of Niobium Oxide and Niobates by Molten Salt Synthesis. *Chemistry of Materials*, Vol.21, No.7, (March 2009), pp. 1207-1213, ISNN 0897-4756

Liu, D., Yan, Y., & Zhou, H. (2007). Synthesis of Micron-Scale Platelet $BaTiO_3$. *Journal of the American Ceramic Society*, Vol.90, No.4, (March 2007), pp. 1323-1326, ISSN 0002-7820

Liu, Y. -F., Lu, Y. -N., Xu, M., Zhou, L. -F., & Shi, S. -Z. (2009). Topochemical Reaction of $SrTiO_3$ Platelet Crystals based on $Sr_3Ti_2O_7$ Platelet Precursor in Molten Salt Synthesis Process. *Materials Chemistry and Physics*, Vol.114, No.1, pp. 37-42, (November 2008), ISSN 0254-0584

Mao, Y., Banerjee, S., & Wong, S. S. (2003). Large-Scale Synthesis of Single-Crystalline Perovskite Nanostructures. *Journal of the American Chemical Society*, Vol.125, No.51 (November 2003), pp. 15718-15719, ISSN 0002-7863

Mao, Y., Park, T. -J., Zhang, F., Zhou, H., & Wong. S. S. (2007). Environmentally Friendly Methodologies of Nanostructure Synthesis. *Small*, Vol.3, No.7, (June 2007), pp. 1122-1139, ISSN 1613-6811

Messing, G. L., Trolier-McKinstry, S., Sabolsky, E. M., Duran, C., Kwon, S., Brahmaroutu, B., Park, P., Yilmaz, H., Rehrig, P. W., Eitel, K. B., Suvaci, E., Seabaugh, M., & Oh, K. S. (2004). Templated Grain Growth of Textured Piezoelectric Ceramics. *Critical Reviews in Solid State and Materials Science*, Vol.29, No.2, (June 2004), pp. 45-96, ISSN 1040-8436

Motohashi, T. & Kimura, T. (2008). Formation of Homo-Template Grains in $Bi_{0.5}Na_{0.5}TiO_3$ Prepared by Reactive-Templated Grain Growth Process. *Journal of the American Ceramic Society*, Vol.91, No.12, (November 2008), pp. 3889-3895, ISSN 0002-7820

Niesz, D. E. & Bennett, R. B. (1978). Structure and Properties of Agglomerates, In: *Ceramic Processing Before Firing*, G. Y. Onoda, Jr. & L. L. Hench, (Ed.), pp. 61-73, John Wiley & Sons, ISBN 0-471-65410-8, New York, USA

Park, J. -H., Lee, D. -H., Shin, H. -S., & Lee, B. -K. (1996). Transition of the Particle-Growth Mechanism with Temperature Variation in the Molted-Salt Method. *Journal of the American Ceramic Society,* Vol.79, No.4, (April 1996), pp. 1130-32, ISSN 0002-7820

Poterala, S. F., Chang, Y., Clark, T., Meyer, Jr, R. J., & Messing, G. L. (2010). Mechanistic Interpretation of the Aurivillius to Perovskite Topochemical Microcrystal Conversion Process. *Chemistry of Materials*, Vol.22, No.6, (February 2010), pp. 2061-2068, ISSN 0897-4756

Rahaman, M. N. (2003). *Ceramic Processing and Sintering* (2nd edition), Marcel Dekker, ISBN 0-8247-0988-8, New York, USA

Rørvik, P. M., Lyngdal, T., Sæterli, R., van Helvoort, A. T. J., Holmestad, R., Grande, T., & Einarsrud, M. -A. (2008). Influence of Volatile Chloride on the Molten Salt Synthesis of Ternary Oxide Nanorods and Nanoparticles. *Inorganic Chemistry*, Vol.47, No.8, (February 2008), pp. 3173-3181, ISSN 0020-1669

Saito, Y., Takao, H., Tani, T., Nonoyama, T., Takatori, K., Homma, T., Nagaya, T., & Nakamura, M. (2004). Lead-Free Piezoelectrics. *Nature*, Vol.432, No.7013, (October 2004), pp. 84-87, ISSN 0028-0836

Saito, Y. & Takao, H. (2006). Synthesis of Platelike {100} $SrTiO_3$ Particles by Topochemical Microcrystal Conversion and Fabrication of Grain-Oriented Ceramics. *Japanese Journal of Applied Physics*, Vol.45, No.9B, (September 2006), pp. 7377-7381, ISSN 0021-4922

Saito, Y. & Takao, H. (2007). Synthesis of Polycrystalline Platelike $KNbO_3$ Particles by the Topochemical Micro-Crystal Conversion Method and Fabrication of Grain-Oriented $(K_{0.5}Na_{0.5})NbO_3$ Ceramics. *Journal of the European Ceramic Society*, Vol.27, No.13-15, (April 2007), pp. 4085-4092, ISSN 0955-2219

Saito, Y., Takao, H., $ Wada, K. (2008). Synthesis of Platelike CaTiO3 Particles by a Topochemical Microcrystal Conversion Method and Fabrication of Textured Microwave Dielectric Ceramics. Ceramics International, Vol.34, No.4, (September 2007), pp. 745-751, ISSN 0272-8842

Sakurai, F. (2011). Mechanism of Texture Development in $(K,Na)NbO_3$-Based Ceramics. *Master Thesis*, Keio University, Japan (March 2011)

Sanson, A. & Whatmore, R. W. (2005). Phase Diagram of the $Bi_4Ti_3O_{12}$-$BaTiO_3$-$(Na_{1/2}Bi_{1/2})TiO_3$ System. *Journal of the American Ceramic Society*, Vol.88, No.11, (August 2005), pp. 3147-3135, ISSN 0002-7820

Santhanam, R. & Rambabu, B. (2010). Research Progress in High Voltage Spinel $LiNi_{0.5}Mn_{1.5}O_4$ Material. *Journal of Power Source*s, Vol.195, No.17, (March 2010), pp. 5442-5451 ISSN 0378-7753

Sato, T. & Kimura, T. (2008). Preparation of <111>-textured $BaTiO_3$ Ceramics by Templated Grain Growth Method Using Novel Template Particles. *Ceramics International*, Vol.34, No.4, (September 2007), pp. 757-760, ISSN 0272-8842

Schaak, R. E. & Mallouk, T. E. (2000). Topochemical Synthsesis of Three-Dimensional Perovskites from Lamellar Precursors. *Journal of the American Chemical Society*, Vol.122, No.12, (March 2000), pp. 2798-2803, ISSN 0002-7863

Schmalzried, H. (1995). *Chemical Kinetics of Solids*, VCH Verlagsgesellschaft mbH, ISBN 3-27-29094-X, Weinheim, Germany

Takahashi, T., Mogushi, N., Kimura, T., & Yamaguchi, T. (1981). Formation Mechanism of Ferrite Powders in Flux. *Bulletin of the Chemical Society of Japan*, Vol.1981, No.9, (September 1981), pp. 1391-1395, ISSN 0009-2673

Tani, T. & Kimura, T. (2006). Reactive-templated Grain Growth Processing for Lead-free Piezoelectric Ceramics. *Advances in Applied Ceramics*, Vol.105, No.1, (February 2006), pp. 55-63, ISSN 1743-6753

Tiano, A. L., Koenigsmann, C., Santulli, A. C., & Wong, S. S. (2010). Solution-based Synthetic Strategies for One-dimensional Metal-containing nanostructures. *Chemical Communications*, Vol.46, No.43, (September 2010), pp. 8093-8130, ISSN 1359-7345

Watari, K., Brahmaroutu, B., Messing, G. L., Trolier-McKinstry, S., & Cheng, S. -C. (2000). Epitaxial Growth of Anisotropically Shaped, Single-Crystal Particles of Cubic $SrTiO_3$. *Journal of Materials Research*, Vol.15, No.4, (April 2000), pp. 846-849, ISSN 0884-2914

Wickham, D. G. (1971). The Preparation of Ferrites with the Aid of Fused Salts. *Ferrites, Proceedings of the International Conference*, pp. 105-107, UTP 3055-67543-5149, Kyoto, Japan, July 6-9, 1970

Yan, B. & Lei, F. (2010). Molten Salt Synthesis, Characterization and Luminescence of $ZnWO_4$:Eu^{3+} Nanoparticles. *Journal of Alloys and Compounds*, Vol.507, No.2, (August 2010), pp. 460-464, ISSN 0925-8388

Yang, Z., Wei, L., Chang, Y., & Liu, B. (2007). Synthesis of Anisometric $KSr_2Nb_5O_{15}$ Particles in the $SrNb_2O_6$-Nb_2O_5-KCl System. *Journal of Materials Sci*ence, Vol.42, No.10, (May 2007), pp. 3627-3631, ISSN 0022-2461

Yang, B., Yuan, X., & Chai, D. (2011). A Rational Self-Sacrificing Template Route to $LiMn_2O_4$ Nanotubes and Nanowires. *Journal of Nanomaterials*, Vol.2011, Article ID 197265, 5 pages, ISSN 1687-4129

Yoon, K. H., Cho, Y. S., & Kang, D. H. (1998). Molten Salt Synthesis of Lead-based Relaxors. *Journal of Materials Science*, Vol.33, No.12, (June 1998), pp. 2977-84, ISSN 0022-2461

Zhao, L., Gao, F., Zhang, C., Zhao, M., & Tian, C. (2005). Molten Salt Synthesis of Anisometric $KSr_2Nb_5O_{15}$ Particles. *Journal of Crystal Growth*, Vol.276, No.3-4, (December 2004), pp. 446-452, ISSN 0022-0248

Zhao, W., Zhou, H., Yan, Y., & Liu, D. (2008). Topochemical Synthesis of Plate-like $Na_{0.5}Bi_{0.5}TiO_3$ from Aurivillius Precursor. *Journal of the American Ceramic Society*, Vol.91, Vol.4, (January 2008), pp. 1322-1325, ISSN 0002-7820

Zhou, H., Mao, Y., & Wong, S. S. (2007). Probing Structure-Parameter Correlation in the Molten Salt Synthesis of $BaZrO_3$ Perovskite Submicrometer-Sized Particles. *Chemistry of Materials*, Vol.19, No.22, (October 2007), pp. 5238-5249, ISSN 0897-4756

Zeng, J. T., Kwok, K. W., Tam, W. K., Tian, H. Y., Jiang, X. P., & Chan, H. L. W. (2006). Plate-Like $Na_{0.5}Bi_{0.5}TiO_3$ Template Synthesized by a Topochemical Method. *Journal of the American Ceramic Society*, Vol.89, No.12, (October 2006), pp. 3850-3853, ISSN 0002-7820

5

Advanced SnO_2-Based Ceramics: Synthesis, Structure, Properties

Mihaiu Maria Susana, Scarlat Oana,
Zuca Stefania and Zaharescu Maria
"Ilie Murgulesc" Institute of Physical Chemsitry of the Romanian Academy
Romania

1. Introduction

Tin dioxide presents specific optical and electrical properties and a good chemical stability which confers special characteristics to the SnO_2 based materials.
SnO_2 belongs to the important class of transparent conductor oxide materials that combine low electrical resistance with high optical transparency in the visible range of the electromagnetic spectrum. These properties are requiered for optoelectronic applications i.g light emitting diodes, electrode materials in solar cells flat panel displays, transparent field effect transistors[Wagner, 2003; Presley et al., 2004]. Tin dioxide is aslo an oxidation catalyst and its activity and selectivity can be substantially improved by incorporation of various additives [Mihaiu et al., 2002]. Another field in which tin dioxide plays a dominant role is in solid state gas sensors. A wide variety of oxides exhibit sensitivity towards oxidizing and reducing gases by a variation of their electrical properties, but SnO_2 was one of the first considered, and still is the most frequently used, material for these applications [Caldararu et al., 1999]. The sensor properties of SnO_2 depend not only on such factors as the oxide's surface stoichiometry, the methodology used to prepare the powder, temperature and atmosphere of calcination but also, and mainly, on the high specific area deriving from the low densification of this oxide. Nowadays, SnO_2 is certainly one of the main polycrystalline ceramic candidates to compete with the traditional multicomponent ZnO-based varistors (voltage-dependent resistor-VDR's), especially because of high electrical stability and its more simple microstructure [Bueno et al., 2007]. High density in polycrystalline ceramics is essential for high varistor properties, since the phenomena involved for good varistor properties occur in the region of the material's grain boundaries. The main restriction in a wider use of this type of material is related to poor sintering ability of the SnO_2-based compositions. This behaviour is related to the low diffusivity of the SnO_2 structure and predominance of the nondensifying mechanisms (surface diffusion and evaporation-condensation). The latter result in grain and pore growth, thus limiting the final density [Varela et al., 1990]. The sintering problem is further complicated by the formation of deleterious intermediate phases above 1273K and high vapor pressurre of SnO [Dolet et al., 1992]. Dense SnO_2-based materials have been obtained either by using sintering additives (e.g.,CuO) to promote densification by liguid-phase mechanism or by applying high pressures (e.g., in hot isostatic pressing technique).

In recent years, aluminium smelters have made great progress in reducing emissions of various gaseous and particulate compounds that may have a negative impact on the global, regional and local environment [Popescu et al., 2007]. The selection of a suitable anode material has proved to be very difficult task. It should be resistant to evolving oxygen and cryolite-alumina melt at ~ 950° C , i.e., in the melt, which is used as solvent for oxides. The maximum allowable wear rate for a commercial use is evaluated as 1.0 cm/year at a current density of 0.8 A/cm^2. The electric conductivity and electrocatalytic activity with respect to oxygen evolution should be high enough to prevent extra losses of electricity. The material should be resistant to mechanical and thermal stress, and its components should not be poisonous for the raw aluminum, to avoid further purification. The only materials that meet these requirements are a number of oxides. Over the years, many materials have been tested on a laboratory scale with mixed success. One such material is tin oxide (SnO_2) doped with different additives which is considered to be a promising material for manufacturing electrodes for melts electrolysis due to their excellent corrosion resistance and heat resistant properties. Studies on the electrical conductivity of SnO_2-based ceramic materials revealed the major influence exerted by the nature of the dopants and the thermal treatment, i.e. the sintering conditions. The electrical resistance is claimed [Zuca et al.,1999] to be decreased drastically (by 4 to 5 orders of magnitude) by the addition of Sb_20_3 as, following its limited solubility in the SnO_2 lattice, the concentration of charge carriers increases. On the other hand, the sintering capacity was found to be greatly improved by the addition of CuO [Dolet et al., 1995]. Although a list of various potential additives has been suggested by Varela, their influence on the sintering properties (namely densification) and electrical conductivity has not been systematically investigated so far [Varela et.al., 1992]. The influence of a series of oxide additives (individual and various combinations), namely Sb_2O_3, CuO, ZnO, Fe_2O_3, Cr_2O_3, TiO_2, MnO_2 and MoO_3 on the sintering capacity and electrical conductivity of the SnO_2-based ceramic materials has been investigated. From among various oxide additives tested, only CuO was found to promote the densification of the composite. The addition of Sb_2O_3, which is claimed to increase the electrical conductivity, is only effective in the presence of CuO addition [Zuca et al., 1991].

During the electrochemical investigations some irregularities were found (it seemed that a small amount of oxygen was consumed on the anode). To understand the causes of these phenomena in order to diminish or remove them it is considered necessary to investigate the chemical processes between the three oxides (SnO_2, Sb_2O_3, and CuO) that take place during the thermal treatment of their mixture.

In this work we propose a review of chemical processes that occur in the SnO_2- Sb_2O_3- CuO system over the whole concentration range of the components. The obtaininig of the sintered materials by conventional ceramic method and spark plasma sintering and the electriacal behaviour of the oxide materials belonging to this system is also approached.

2. Phase formation in the SnO_2-Sb_2O_3-CuO ternary system

A summary of physical characteristics of individual SnO_2, Sb_2O_3, and CuO compound is given in the Table 1.

Based on the experimental data determined under non-isothermal conditions up to 1773K for pure components [Zaharescu et al., 1991], the following has been established:

1. no effects were observed for SnO_2 in the 293-1773 K temperature range;

2. the endothermal reduction of CuO to Cu_2O which starts at 1348 K, is followed by eutectic melting of the two copper oxides;
3. the oxidation of Sb_20_3 to Sb_2O_4, which takes place within a wide temperature interval from 713 to 933 K is accompanied by a well marked exothermal effect and a mass increase; the endothermal effect observed at 1433 K indicates the vaporization of Sb_2O_4.

Physical and structural characteristics	SnO_2	Sb_2O_3	Sb_2O_4	CuO
Mineral	cassiterite	valentinite	cervantite	tenorite
Culour	white	colorless	white	black
Molecular weight	150,69	291,50	307,50	78,54
Symmetry	tetragonal	romboedric	orthorhombic	monoclinic
Space group	D_{4h}^{14} (P4/mnm)	V_h^{10} (P_{ccn})	*Pna*21	C_{dh}^{6C}(c2/c)
Lattice parameters (Å)	a_0=b_0=4,7374 c_0=3,1864	$a_{0=}$ 4,92 b_0=12, 46 c_0= 5,42	a = 5.43 b = 4.79 c = 11.73	$_{0=}$ 4,92 b_0=12, 46 c_0= 5,42 β =99˚29′
Ionic radius (Å)	Sn^{4+}= 0,71		Sb^{3+} =0,76 Sb^{5+} =0,62	Cu^{2+}=0,72
Density (g/cm^3)	6,95	5,67	6.64	6,3- 6,49
Melting point (K)	-O;1800;>2200*		1433 sublimes	1599
Boiling point (K)	2073 sublimes			2273
Refraction index	2⊥ c 2,11// c	2,18 2,35 2,35	2,00	2,63

Table 1. Physical and structural characteristics of SnO_2, Sb_2O_3, CuO [Wyckoff, 1963, 1964]

2.1 Solid state reactions in the component subsystems

2.1.1 SnO_2-CuO binary system

The experimental data on the SnO_2-CuO binary system have been published in several papers [Zaharescu et al., 1991; Scarlat et al., 1999]. The thermal analysis of (1-x)SnO_{2-x}CuO compositions, in non-isothermal conditions, in air, up to 1773 K, underlined that the thermal effects registrated could be assigned exclusively to the presence of CuO in the reaction mixture. The reduction process of CuO to Cu_2O over 1273 K as well as the formation over 1373 K of the liquid phase have been evidenced. No binary compounds were formed.

The results obtained by isothermal treatments at 1173, 1273 and 1473 K of the (1-x)SnO_{2-x}CuO mixtures were also analyzed. Thus, for the samples with 1-10% content of CuO only SnO_2 was identified by X-ray diffraction, no matter of treatment temperature. Although the

ionic radii of the two ions are close (0.71 Å for the Sn^{4+} and 0.72 Å for the Cu^{2+}) due to their different structures and especially their different valence, the formation of a a solid solution between the two oxides is unlikely to occur. The disappearance of characteristic diffraction lines of copper oxide and the sharp contraction of these samples was assigned to its penetration into the liquid phase (eutectic melt), which facilitates rapid rearrangement of the ions [Zaharescu et al., 1991; Dolet et al., 1992]. It was observed that in isothermal condition the reaction of CuO reduction, namely: $CuO \rightarrow Cu_2O$ takes place at substantially lower temperature compared with the non-isothermal measurements. The phase composition of the binary mixtures with a content of CuO >30%, thermally treated at 1273 K consists in a mixture of SnO_2, CuO and Cu_2O. The samples with a CuO content exceeding 10% fused when thermally treated at 1473 K. The shrinkage of the tested samples increased with increasing temperature while the porosity decreased; at 1273 and 1473 K samples with a zero porosity were obtained, apparently owing to the presence of the liquid phase.
As a conclusions, at temperature over 1273 K the SnO_2-CuO initial binary system transforms into the SnO_2- CuO- Cu_2O pseudo-ternary system. In the presence of CuO the sintering ability of SnO_2 is promoted. Below 1173 K, the rate of densification can be explained in terms of viscous flow model [Zaharescu et al.,1993], while at higher temperature a copper-rich liquid is formed and rearrangement is occuring even for short sintering time.

2.1.2 SnO_2-Sb_2O_3 binary system

Widely used as catalysts in catalytic oxidation reactions, the oxide powders belonging to the SnO_2-Sb_2O_3 system are studied by many research groups in this field [Harrison et al., 1999;. Park et al., 1999] especially in the subsolidus domain.
In accordance with the rules of formation of substitional solid solutions (the sizes of two ions differ by less than 15%, have similar valency factor, chemical affinity and structure type) tin dioxide can form a limited solid solution with antimony oxides. Solid solubility limit depends on the method of preparation and treatment temperature. Volta obtained monophasic powders with rutile type structure by coprecipitation of tin (IV) and antimony (V) chlorides and heat treatment at 773 for 16 hours [Volta et al., 1985] of the resulted hidroxides. Similar results have been obtained by Vlasova for the powders with the antimony content of 40% and thermal treatment at 873 K temperature[Vlasova et al.,1990]. At 1273 K the amount of antimony atoms in solid solution decreases to 30% and at 1473 K to 4%. Orel et al. have found that regardless of the initial concentration of antimony, the maximum amount of Sb_2O_4 entered into the SnO_2 lattice is of 2.38 mol at 1473 K [Orel et al., 1995]. The interactions that occur between the two oxides in the whole concentration range in non isothermal (up to 1773 K) and isothermal conditions at 873, 1073, 1273 and 1473 K temperatures were investigated in paper [Zaharescu et al., 1991]. The temperature interval of the exothermal effect corresponding to the oxidation of Sb_2O_3 to Sb_2O_4 is substantially narrowed in the binary mixtures (695-716 K) compared to the pure Sb_2O_3 (713-933 K) which suggests the catalysing effect of SnO_2 in the oxidation process. It may be also assumed that in the reaction with SnO_2, antimony participates as a heterovalent mixture of the $Sb(III)Sb(V)O_4$ type. The endothermal effect observed at high Sb_20_3 concentrations at temperatures above 1423 K which is accompanied by a mass loss, is assigned to the vaporization of Sb_2O_4. The exothermal effect indicates the oxidation of Sb_2O_3 to Sb_2O_4 at 873 K however, the latter oxide has not been identified by X-ray diffraction at concentrations up to 10% (all concentrations are given in mass %). This can be apparently assigned to the

formation of the solid solution owing to the substitution of antimony for tin in the SnO_2 crystal structure. Although the samples with a higher Sb_2O_4 concentration undergo deformation and peeling at higher temperatures which make them unsuited for the subsequent measurements. The concentration of Sb_2O_4 (up to 30%) in the solid solution apparently increases with increasing temperature (up 1273 K) and only SnO_2 is identified in the undeformed samples. The XRD results indicate the displacement of the pure SnO_2 diffraction peaks due to the formation of this rutile type of solid solution. All peaks were slightly shifted to the right after the solid solution was formed (larger angle or smaller both *a* and *c* lattice paramaters) with respect to pure SnO_2.
Taking into account that Sb_2O_3 in the presence of SnO_2 over 773 K in air, completly turns into Sb_2O_4 and the oxidation state of tin ions do not change, the question is what form of antimony ions enter the tin dioxide lattice. Vlasova proposed the following "formula" [Vlasova et al., 1990]:

(a) $Sn^{4+}_{1-2x}Sb^{3+}_xSb^{5+}_xO^{2-}_2$ (b) $Sn^{4+}_{1-2x}Sn^{3+}_xSb^{5+}_xO^{2-}_2$; (c) $Sn^{4+}_{1-x}Sb^{5+}_xe_xO^{2-}_2$;

(d) $Sn^{4+}_{1-5x}Sb^{5+}_{4x}V^0_{kx}O^{2-}_2$ (e) $Sn^{4+}_{1-x}Sb^{3+}_xO^{2-}_{2-x}V_{ax}$; (f) $Sn^{4+}_{1-x}Sb^{3+}_xO^{2-}_{2-x/2}V_{ax/2}$;

(g) $Sn^{4+}_{1-3x}Sn^{2+}_xSb^{5+}O^{2-}_2$;

where e_x = free electrons
and V_k and V_a cation and anion vacancies, respectively
When contents of antimony atoms do not excede 3% in the SnO_2 latice, the following "compounds" were identified by EPR: $Sn^{4+}_{1-x}Sb^{3+}_xO^{2-}_{2-x}V_{ax}$; $Sn^{4+}_{1-x}Sb^{5+}_xe_xO^{2-}_2$;

$$Sn^{4+}_{1-2x}Sn^{3+}_xSb^{5+}_xO^{2-}_2.$$

In the case of higher concentration of antimony embeded in the SnO_2 lattice the most likely the resulted solid solution has the the following composition: $Sn^{4+}_{1-2x}Sb^{3+}_xSb^{5+}_xO^{2-}_2$. By EXAFS it has been established that Sb dopants occupy Sn sites in the rutile structure [Chadwick et al.,1993; Rockenberger et al., 2000]. XANES measurements showed that the largest fraction of Sb has a valency of 5^+, although 3^+ was also observed in nanocrystalline SnO_2. The Sb^{3+} species may be due to a strong tendency of Sb to segregate to the surface [Dusastre et al., 1998; Slater et al., 1999].

2.1.3 Sb_2O_3-CuO binary system

Sb_2O_3-CuO binary system is the most complex subsystems of the SnO_2-Sb_2O_3-CuO ternary system. In this system, the formation of $CuSb_2O_6$ binary compound with pentavalent antimony has been reported. The compound has a tri-rutile structure, short-range and long range magnetic ordering. Under some special conditions, two other binary compounds, having a higher copper content, have been prepared: $Cu_4SbO_{4,5}$ and $Cu_9Sb_2O_{19}$ [Bystrom et al.,1944; Shimada et al.,1982; 1985;1988].Stan et al., have studied the (10-n)CuO + nSb_2O_3mol (n=0;1;….10) mixtures belonging to the Sb_2O_3-CuO binary system at room temperature. According to the thermal analysis results, the following solid state reactions occur [Stan et al.,1998] :

$$\approx 773\ K \quad Sb_2O_3 + 1/2\ O_2 = Sb_2O_4 \tag{1}$$

$$>1023\ K \quad Sb_2O_4 + CuO + 1/2\ O_2 = CuSb_2O_6 \tag{2}$$

$$>1223\ K\ \ CuSb_2O_6+7CuO=(1-r)\ CuSb_2O_6+7(1-r)CuO+2rCu_4SbO_{4.5}+2rO_2 \qquad (3)$$

Where $r \epsilon (0,1)$ is the fraction of $CuSb_2O_6$ that transforms into $Cu_4SbO_{4.5}$.

In order to emphasize an intermediate stage in the compound formation, Fig. 1 shows the relative intensities of the X-ray characteristic lines for the mixtures thermally treated for only one hour.

The same compounds have been obtained in both isothermal treatment (one hour and three hours) and non-isothermal conditions. This points to the high reactivity of the oxides in this system. There is no evidence of $Cu_9Sb_2O_{19}$ compound formation. This compound as reported only for high pressures (see Table 2). Then, in the range of 293-1273 K at normal atmospheric pressure, the following compounds can be found in equilibrium: CuO, Cu_2O, Sb_2O_3, Sb_2O_4, $CuSb_2O_6$ and $Cu_4SbO_{4.5}$.

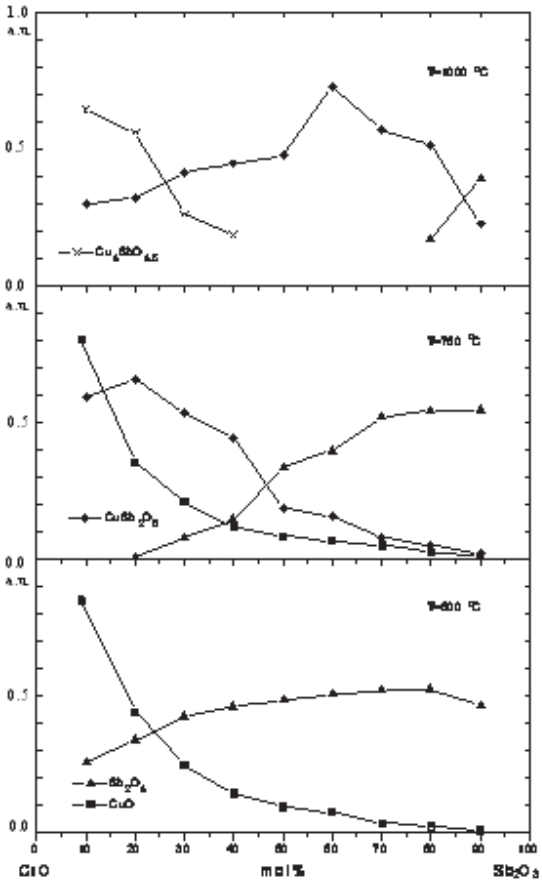

Fig. 1. Relative intensities of the X-ray characteristics lines for the binary mixtures thetmally treated at 773, 823 and 1273 K, one hour

All the experimental evidences show that equations (1), (2) and (3) are suficient to describe the reactions occuring in the Sb_2O_3-CuO binary system with increasing temperature. If the

reactions are considered as completed, including r=1 in equation (3), then the quatity of oxygen that is gained or lost can be calculated for each sample.
The atomic composition modifications during the thermal treatments for the four representative samples is given Fig.2. At room temperature the compositions lay on the Sb_2O_3-CuO line as shown in Fig.2. The composition line moves to Sb_2O_4-CuO at 773 K and changes to Sb_2O_4-$CuSb_2O_6$-CuO over 823 K. Finally, if the reaction (3) is completed at 1273 K, the compositions lay on the CuO- $Cu_4SbO_{4.5}$-$CuSb_2O_6$ - Sb_2O_4 .

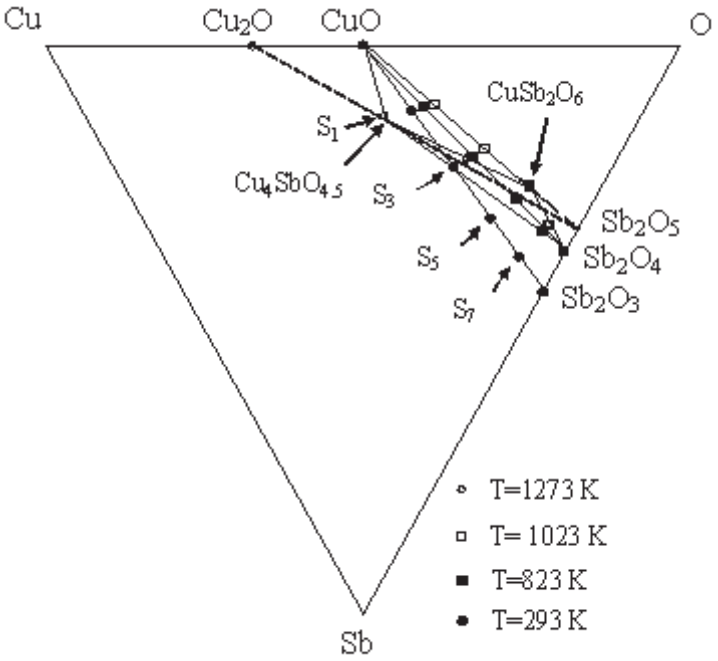

Fig. 2. Atomic compositions after the thermal treatment for the following initial mixtures: S_1 the mixture of 90 mol% of CuO and 10% mol of Sb_2O_3; S_3 the mixture of 70 mol% of CuO and 30% mol of Sb_2O_3; S_5 the mixture of 50 mol% of CuO and 50% mol of Sb_2O_3; S_7 the mixture of 30 mol% of CuO and 70% mol of Sb_2O_3 [Stan et al.,1998]

2.2 Solid state reactions in the SnO_2-Sb_2O_3-CuO ternary system

The SnO_2-Sb_2O_3-CuO ternary system have been investigated in the whole concentrations range isothermal and non-isothermal conditions in[Zaharescu et al.,1991;1993; Mihaiu et al.,1995] .In the Fig.3 experimental ternary compositions are graphically presented.
Equimolecular mixture of CuO and Sb_2O_3 (which leads to $CuSb_2O_6$ formation) determine the next evolution of the mixtures in the system and this ratio affords the classification of sample in three categories:
(I) CuO:Sb_2O_3=1 and the samples lie on SnO_2-equimolecular mixture;
(II) CuO:Sb_2O_3 >1 and the samples are belonging to the CuO-CuO.Sb_2O_3–SnO_2 pseudo-ternary system;

(III) $CuO:Sb_2O_3<1$ and the samples are belonging to the Sb_3O_3-$CuO.Sb_2O_3$–SnO_2 pseudo-ternary system [Zaharescu et al., 1993]

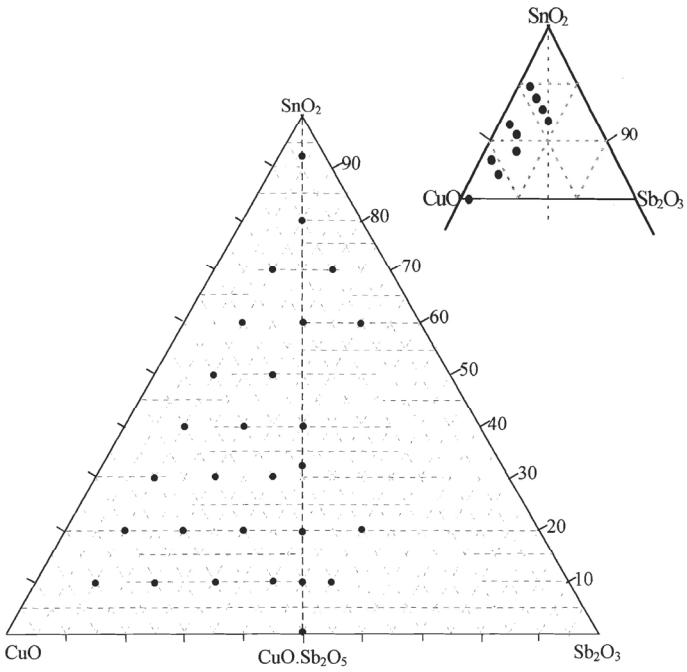

Fig. 3. Domain of the studied compositions in the SnO_2-Sb_2O_3 – CuO system [Zaharescu et al., 1999]

The oxidation of Sb_2O_3 to Sb_2O_4 (and Sb_2O_5), as well as the high temperature interactions of Sb_2O_3 with SnO_2 and respectively with CuO have been discussed in the section 2.1.1 and 2.1.3. The thermal behaviour of Sb_2O_3 in the presence of both mentioned oxides in non-isothermal conditions (up to 1273 K) is summarized in the Table 2 .For the mixtures from (I) categorie ($CuO:Sb_2O_3=1$) on can note that the oxidation of Sb_2O_3 to Sb_2O_5 is total and take place in two steps. The experimental weight increase is in good agreement with the theoretical one. The resulted phase composition of the samples corresponds to a mixture of SnO_2 and $CuSb_2O_6$. Accordigly, in the presence of both SnO_2 and CuO there is a higher tendency of Sb_2O_3 to react with CuO than to form solid solution with SnO_2.

In the ternary mixtures of molar ratio $CuO:Sb_2O_3>1$, a total oxidation of Sb_2O_3 to Sb_2O_5 is obtained; above 1233 K; a weight loss is also observed which is assigned to the reduction of CuO to Cu_2O. After thermal treatment the phase composition consists in SnO_2, $CuSb_2O_6$ and $Cu_4SbO_{4.5}$ mixtures.

In the ternary mixtures of molar ratio $CuO:Sb_2O_3<1$, in the first step Sb_2O_3 entirely oxidize to Sb_2O_4. In the second step the transformation of Sb_2O_4 to Sb_2O_5 is limited to the quantity required by $CuSb_2O_6$ formation.The unreacted Sb_2O_4 dissolves partially into SnO_2 with the formation of a solid solution with SnO_2 crystal structure.

Oxide compositions (%mol.)			Thermal effects (K)		Mass variation (%)		Assignment	Phase composition
SnO_2	Sb_2O_3	CuO	Endo	Exo	Exp.	Calc.		
93	3	4		695,728	+0.34	+0.34	[O] $Sb_2O_3 \longrightarrow Sb_2O_4$	SnO_2
80	10	10		713,733	+0.86	+1.01	[O] $Sb_2O_3 \longrightarrow Sb_2O_4$	SnO_2, $CuSb_2O_6$
					+0.47	+1.00	[O] $Sb_2O_4 \longrightarrow Sb_2O_5$	
70	10	20		713	+0.96	+1.06	[O] $Sb_2O_3 \longrightarrow Sb_2O_4$	SnO_2, $CuSb_2O_6$, $Cu_4SbO_{4.5}$
				1053	+0.96	+1.05	[O] $Sb_2O_4 \longrightarrow Sb_2O_5$	
			1233		-0.41	-0.52	$CuO \longrightarrow Cu_2O$ [-O]	
70	20	10		733	+1.65	+1.86	[O] $Sb_2O_3 \longrightarrow Sb_2O_4$	SnO_{2ss}, Sb_2O_4 $CuSb_2O_6$
					+0.76	+0.92	[O] $Sb_2O_4 \longrightarrow Sb_2O_5$	
60	20	20		748	+1.66	+1.94	[O] $Sb_2O_3 \longrightarrow Sb_2O_4$	SnO_2, $CuSb_2O_6$
				1073	+1.63	+1.91	[O] $Sb_2O_4 \longrightarrow Sb_2O_5$	
33.3	33.3	33.3		761	+3.07	+3.07	[O] $Sb_2O_3 \longrightarrow Sb_2O_4$	SnO_2, $CuSb_2O_6$
				1112	+2.90	+2.89	[O] $Sb_2O_4 \longrightarrow Sb_2O_5$	
10	45	45		713	+3.14	+3.96	[O] $Sb_2O_3 \longrightarrow Sb_2O_4$	$CuSb_2O_6$, SnO_2
				1148	+3.14	+3.89	[O] $Sb_2O_4 \longrightarrow Sb_2O_5$	
10	40	50		713,793	+3.44	+3.73	[O] $Sb_2O_3 \longrightarrow Sb_2O_4$	$CuSb_2O_6$, SnO_2, Cu_4SbO_4.
				1063	+3.55	+3.59	[O] $Sb_2O_4 \longrightarrow Sb_2O_5$	
			1223		-0.30	-0.43	$CuO \longrightarrow Cu_2O$ [-O]	
10	50	40			+3.98	+4.15	[O] $Sb_2O_3 \longrightarrow Sb_2O_4$	$CuSb_2O_6$, SnO_2, Sb_2O_4
					+3.12	+3.18	[O] $Sb_2O_4 \longrightarrow Sb_2O_5$	

Table 2. The results of differential thermal analysis and thermogravimetry of the ternary mixtures

The phase composition consists in SnO_{2ss}, Sb_2O_4, $CuSb_2O_6$ mixtures. In isothermal conditions the ternary mixtures have been themally treated at 873, 1073, 1273, 1373 and 1473 K. Samples thermally treated at lower temperatures (873,1073,1273 K) showed no linear

shrinkage but linear dilatation and high porosity pointing out an inadequate sintering [Zaharescu et al., 1999]. Besides oxide composition in Table 3 the phase components and the ceramic characteristics of studied mixtures thermally trated at 1373 K are given. In the categorie (I) ($CuO:Sb_2O_3$=1) the solid solutions with SnO_2 crystal structure (rutile) includes $CuSb_2O_6$ (tri-rutile structure) up to a limit of about 50 mol%. Below this limit a mixture of SnO_2 and $CuSb_2O_6$ is detected. A similar behaviour has been reported by Kikuchi in the SnO_2–MSb_2O_6 system (M=Zn,Mg) [Kikuchi et al., 1983]. As claimed by the author, $ZnSb_2O_6$ is solved in SnO_2 up to 50 mol% as $Zn_{1/3}Sb_{2/3}O_2$ at 1473K whereas SnO_2 is dissolved in $ZnSb_2O_6$ up to 20 mol% at the same temperature. The lattice parameters decreasd with decreasing SnO_2 contents. Similarly, $MgSb_2O_6$ dissolved in SnO_2 up to 50 mol% at 1523 K but SnO_2 was sparingly solved into $MgSb_2O_6$. In the categorie (II) ($CuO: Sb_2O_3$ >1) the same type of solid solubility has been observed. The compounds $CuSb_2O_6$ and $Cu_4SbO_{4.5}$ have been also identified by XRD for a large range of concentrations. For the mixture containing 10 mol% SnO_2, this compound was not identified. On can assume that SnO_2 dissolves in $CuSb_2O_6$ forming a solid solutin with tri-rutile structure. In the categorie (III) ($CuO: Sb_2O_3$<1) SnO_2-based solid solution and $CuSb_2O_6$ compound have been observed. Although in this system Sb_2O_3 is exceeding the necessary amont required by $CuSb_2O_6$ stoichiometry, it was not identified by XRD. This result suggests that the unreacted Sb_2O_4 dissolves preferentially in SnO_2 and hinders the dissolutions of $CuSb_2O_6$ in the SnO_2 crystal network.

Based on the experimental data, the authors [Stan et al.1997]reported that in SnO_2-Sb_2O_3-CuO ternary system besides the solid state reactions represented by 1-3 equations (section 2.1.3.), at temperature above 1273 K, the following reactions take place:

$$T > 1273\ K: \quad SnO_2 + CuSb_2O_6 \longrightarrow SnO_2(ss) \tag{4}$$

$$T > 1273\ K: \quad SnO_2 + CuSb_2O_6 + Sb_2O_4 \longrightarrow SnO_2(ss) \tag{5}$$

$$T > 1273\ K: \quad CuSb_2O_6 + SnO_2 \longrightarrow CuSb_2O_6(ss) \tag{6}$$

Evolution of the phase composition ofn the SnO_2-Sb_2O_3-CuO ternay system with thermal treatment at 873, 1073, 1273, 1373 K could be better visualized in a guaternary representation (Figure 4).

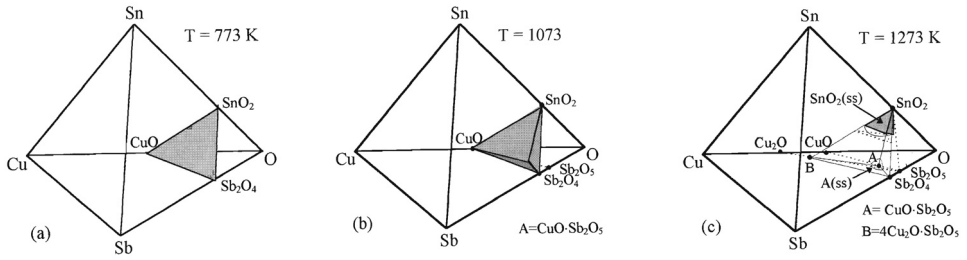

Fig. 4. Evolution of phase composition with thermal treatment temperature

In these representations the experimental ternary mixtures belonging to SnO_2-Sb_2O_4-CuO ternary subsystem at 773K, SnO_2-Sb_2O_4-CuO-$CuSb_2O_6$ pseudo-quaternary system at 1073 K andSnO_2-Sb_2O_4-$CuSb_2O_6$-$Cu_4SbO_{4.5}$ pseudo-quaternary system at temperatures >1273 K.

Crt. No.	Composition (mol.%)			Phase composition	Shrinkage %	Porosity %	Density g/cm^3
	SnO_2	Sb_2O_3	CuO				
(I) CuO: Sb_2O_3 =1							
1.	80	10	10	SnO_2(ss)	10	-	5.815
2.	60	20	20	SnO_2(ss)	10	0.16	5.9237
3.	40	30	30	SnO_2+ $CuSb_2O_6$	2	3.56	
4.	33.3	33.3	33.3	SnO_2+ $CuSb_2O_6$	+5	6.25	
5.	20	40	40	$CuSb_2O_6$ + SnO_2	+1	4.92	
(II) CuO: Sb_2O_3 >1							
1.	70	10	20	SnO_2(ss)	12	0.73	
2.	60	10	30	SnO_2(ss)+ $Cu_4SbO_{4.5}$	12	0.77	
3.	50	10	40	SnO_2(ss)+ $Cu_4SbO_{4.5}$	15	0.79	
4.	50	20	30	SnO_2(ss)+ $Cu_4SbO_{4.5}$	13	0.35	
5.	40	10	50	SnO_2(ss)+ $Cu_4SbO_{4.5}$	20	0.43	6.3018
6.	40	20	40	SnO_2(ss)+ $Cu_4SbO_{4.5}$	12	0.38	
7.	30	10	60	SnO_2(ss)+ $Cu_4SbO_{4.5}$	12	0.58	
8.	30	20	50	$CuSb_2O_6$ + SnO_2+ $Cu_4SbO_{4.5}$	9	0.33	5.9820
9.	30	30	40	$CuSb_2O_6$ + SnO_2+ $Cu_4SbO_{4.5}$	6	0.92	
10.	20	10	70	$CuSb_2O_6$(ss) + $Cu_4SbO_{4.5}$	11	0.31	5.8785
11.	20	20	60	$CuSb_2O_6$ (ss)+ $Cu_4SbO_{4.5}$	6	0.11	6.0248
12.	20	30	50	$CuSb_2O_6$(ss) + $Cu_4SbO_{4.5}$	7	0	5.6297
13.	10	10	80	$Cu_4SbO_{4.5}$ + SnO_2(ss)	12	1.45	
14.	10	20	70	$CuSb_2O_6$(ss) + $Cu_4SbO_{4.5}$	10	0	5.8088
15.	10	30	60	$CuSb_2O_6$(ss) + $Cu_4SbO_{4.5}$	7	0	5.7790
16.	10	40	50	$CuSb_2O_6$(ss)	+5	5.29	
(III) (CuO: Sb_2O_3<1							
1.	70	20	10	SnO_2(ss)	1		
2.	60	30	10	SnO_2(ss) + $CuSb_2O_6$	+2		
3.	20	50	30	$CuSb_2O_6$ + SnO_2(ss)	+3		
4.	10	50	40	$CuSb_2O_6$(ss)	-		

Table 3. Oxide composition, phase composition, ceramic characteristics of the ternary mixtures thermally treated at 1373 K, 1 h

2.2.1 SnO_2–$CuSb_2O_6$ binary system

In the subsolidus domain, the formation of the $CuSb_2O_6$ binary compound was found to be a basic stage in the SnO_2-Sb_2O_3-CuO ternary sistem evolution and, consenquently, SnO_2–$CuSb_2O_6$ binary system was considered to be representative for the study of Sn-Sb-Cu-O quaternary system. In the work [Scarlat et.al., .2002], the high temperature interactions between SnO_2 and $CuSb_2O_6$ have been investigated both in non-isothermal and isothermal conditions. The experimental compositions are expressed as $(1\text{-}x)SnO_2$-x $CuSb_2O_6$, with x= 0, 0.025, 0.04, 0.06, 0.08, 0.1, 0.2, 0.25, ….0.75, 0.8…1, covering the whole concentration range. The thermal treatments in the non-isothermal conditions pointed out that more than one chemical process developed between 1398 – 1723 K which are exclusively a result of the presence in the initial mixture of $CuSb_2O_6$ (see Table 2, section 2.1.3.) according to the following equations:

$$T \approx 1476\ K: \quad 4\ CuSb_2O_6 \longrightarrow Cu_4SbO_{4.5} + 7/2\ Sb_2O_3 + 9/2O_2 \tag{7}$$

$$T \approx 1520\ K: \quad 2\ Cu_4SbO_{4.5} \longrightarrow 4\ Cu_2O + Sb_2O_3 + O_2 \tag{8}$$

This observation suggests that no solid state interactions have occurred between SnO_2 and $CuSb_2O_6$ in non-isothermal conditions.

The isothermal treatements of the binary mixtures at 1273 K (one, three and ten hours) and at 1373 and 1473 K respectively (three hours) have been done. An increase of the temperature value over 1473 K was not possible due to reactions (7) and (8), resulting in the decomposition and partial melting of pure $CuSb_2O_6$ and solid solutions.

Based on the experimental results, the subsolidus phase relations of SnO_2–$CuSb_2O_6$ system are presented in Fig.5.

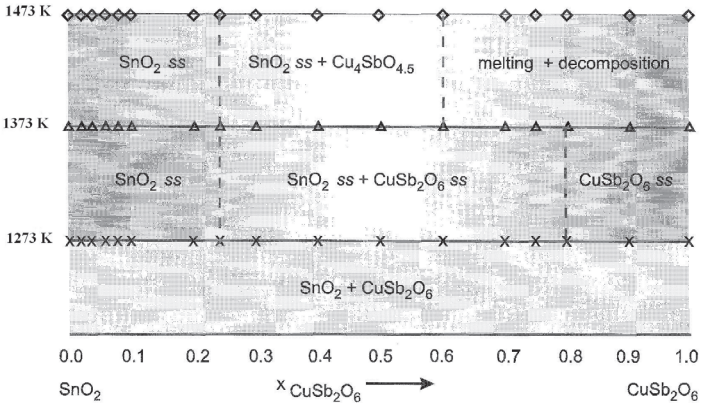

Fig. 5. Subsolidus phase relations in the SnO_2 –$CuSb_2O_6$ system

Accordingly, the system was divided at 1373 K into the following three subsolidus domain:

$$0 < x \leq 0.25 \quad \longrightarrow SnO_{2\ ss} \text{ described as } Sn_{1-x}Cu_{x/3}\ Sb_{2x/3}O_2$$

$$0.25 < x < 0.8 \longrightarrow SnO_{2\ ss} + CuSb_2O_{6\ ss}$$

$$0.8 < x \leq 1 \quad \longrightarrow CuSb_2O_{6\ ss} \text{ described as } Cu_{1-x}Sb_{2(1-x)}\ Sn_{3x}O_6$$

Due to the $CuSb_2O_6$ decomposition and to the presence of the liquid phase extending from the Cu-O system [Scarlat et al.,20020], the phase relationships establishing becomes more difficult over 1473 K.
One has established that SnO_2–$CuSb_2O_6$ is a pseudobinary system with solid solubility limit of the end members.

2.2.2 Solid state solutions

The results previously presented evidenced the formation of large domains of unique phase with rutile as well as tri-rutile structure. The mechanism of their formation was approached in the papers [Mihaiu et al., 1995; Scarlat et al., 2002]. It considers framing the initial ternary mixtures from which the unique phase is formed in the subsystems component of the Sn-Sb-Cu-O quaternary system: (1) SnO_2–$CuO.Sb_2O_5$ pseudobinary system (the ratio $CuO:Sb_2O_3$ =1), (2) SnO_2–$CuO.Sb_2O_5$-CuO pseudoternary subsystem (the ratio CuO: $Sb_2O_3 \geq 1$) and (3) SnO_2 –$CuO.Sb_2O_5$-Sb_2O pseudoternary subsystem (the ratio CuO: $Sb_2O_3 \leq 1$). As has been stated previously, in all cases the formation of the $CuSb_2O_6$ binary compound, which precedes the formation of the SnO_2 solid solution as unique phase, was found to be a basic stage in the interactions at high temperature of the initial components.
In the following, the formation of solid solutions from the ternary mixtures belonging to the SnO_2-Sb_2O_3-CuO system as well as from the SnO_2 and $CuSb_2O_6$ binary mixtures will be presented. The rutile type solid solution unique phase was formed from the ternary mixtures with a SnO_2 molar content of over 70% and a ratio $CuO:Sb_2O_3 \geq 1$, and was thermally treated at 1273K for 3 h. The lattice parameters calculated from X-ray diffraction data decrease due to the inclusion of $CuSb_2O_6$ in the SnO_2 lattice [Mihaiu et al., 1995]. The solid solution which was formed is of $Sn^{4+}_{1-x}Cu^{2+}_{x/3}Sb^{5+}_{2x/3}O_2$ ($0<x<1/2$) type .The excess of copper oxide forms with SnO_2 a liquid phase which is responsible for the sample densification at 1273K. In case of the ternary mixtures with the ratio CuO: $Sb_2O_3 \leq 1$ (molar content of $SnO_2 \geq 70\%$) the formation of the rutile type solid solution as a unique phase takes place in two steps. In the first step, Sb_2O_4 dissolves in the SnO_2 lattice (1273 K), and in the second step $CuSb_2O_6$ is included in the SnO_2 lattice (1273K). The decrease of the parameters is more important than previously mentioned [Mihaiu et al., 1995].
The following formula was proposed: $Sn^{4+}_{1-x}Cu^{2+}_{x/5}Sb^{3+}_{x/5}Sb^{5+}_{3x/5}O_2$, in which $0<x<1/2$
In case of the ternary mixtures with the ratio CuO: Sb_2O_3 =1, the unique phase of rutile type solid solution was obtained up to the composition domain with over 60 mol% SnO_2.
The development of phase composition of the ternary mixture with 60 mol% of SnO_2, 20 mol% of Sb_2O_3 and 20mol% of CuO at different temperature is presented in the Fig.6. [Zaharescu et al., 2001] At 1373 K temperature only SnO_{2ss} solid solution with $Sn_{0.5}Cu_{0.17}Sb_{0.33}O_2$ formula should be observed. To clarify the way $CuSb_2O_6$ is dissolved into SnO_2 lattice to form a solid solution, IR absoption spectra (Fig.7) for the same samples utilized to identify by XRD the formation of SnO_2- based solid solution were recorded.
One can draw the following conclusions:
After thermal treatment, one hour at 873 K the presence of SnO_2 by the 635 cm^{-1} strongest band was identified. One can assume that CuO bands overlap those of SnO_2, whose presence is predicted from the shoulder located at 580 cm^{-1}.The bands group that comes up at 735, 480 and 377 cm^{-1} may be assigned to the presence of α- Sb_2O_4. At 1073 K the SnO_2 typical band (650 cm^{-1}) does not change its position but becomes less clear. The bands of α-Sb_2O_4 come out less outlined in the same wave number domain as at 873 K. The authors

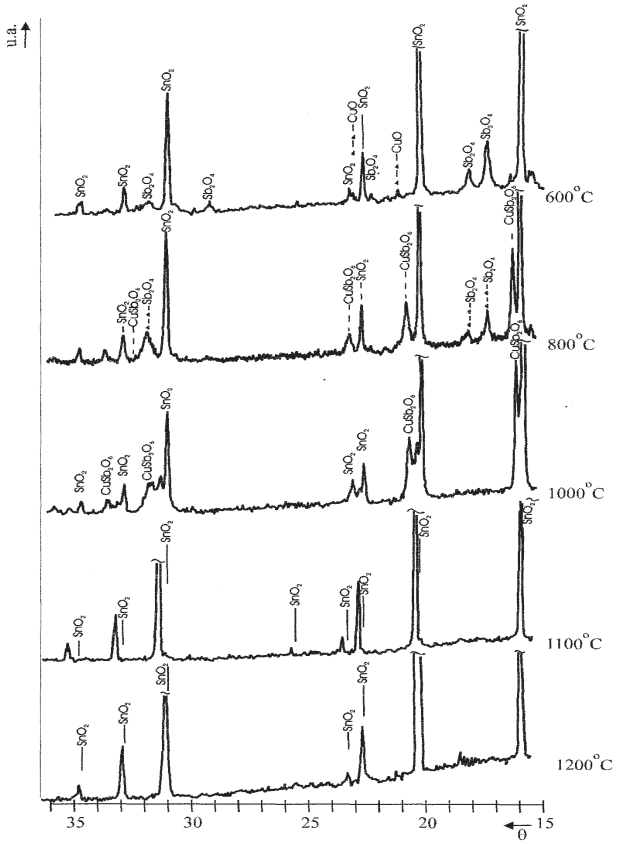

Fig. 6. XRD patterns of the mixture with initial composition: 60mol% of SnO_2, 20 mol% of Sb_2O_3 and 20 mol% of CuO, thermally treated one hour at 873, 1073,1273,1373 and 1473 K.

noted the presence of two extra-bands (located at 575 cm^{-1} and 815 cm^{-1}) and a shoulder at 680 cm^{-1} assigned to $CuSb_2O_6$ presence whose formation started at about 1023K. At 1273 K the SnO_2- based solid solution besides SnO_2 and $CuSb_2O_6$ presence was identified by X-ray diffraction. IR measurements have shown an intensity decrease for the SnO_2 strongest absoption band and its splitting into 682 cm^{-1} and 630 cm^{-1} bands. At this temperature better conditions are offered to $CuSb_2O_6$ formation which can be noticed from its typical bands (575 cm^{-1} and 815 cm^{-1}) those bands intensify and an extra-band at 680 cm^{-1} appears. At >1273 K the typical pure oxides and $CuSb_2O_6$ compound bands disppear and one can note an abnormal decrease of transmission, assigned to the dissolution of $CuSb_2O_6$ into the SnO_2 lattice.

The typical IR bands disappearance of the SnO_2- based solid solution may be explained by the strong interaction between the lattice phonons and a higher charge carrier concentration determined by the solid solution formation. The assumption is sustained by semimetallic behaviour of the sample [Ionescu et al., 1997].

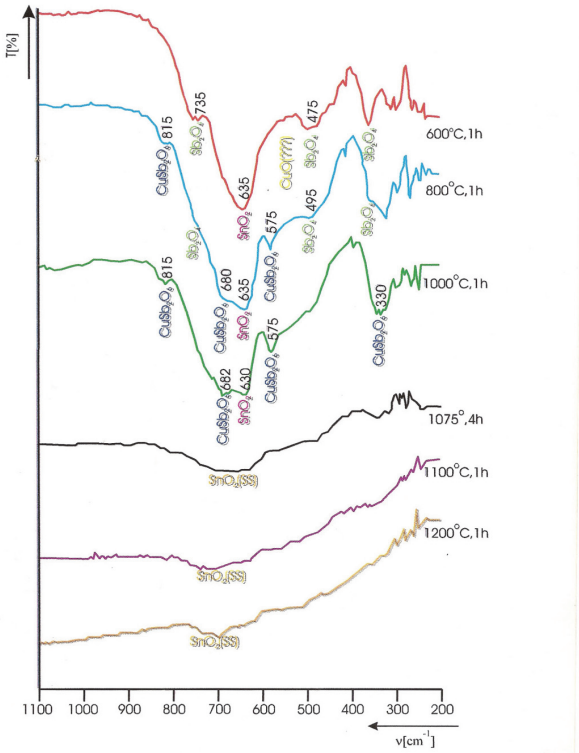

Fig. 7. IR Spectra of the mixture with initial composition:60 mol% of SnO_2, 20 mol% of Sb_2O_3 and 20 mol% of CuO, thermally treated one hour at 873, 1073,1273,1343,1373 and 1473 K

The scanning electron micrograph(SEM) of the $Sn_{0.5}Cu_{0.17}Sb_{0.33}O_2$ solid solution thermally treated at 1373 K (Fig.8) show homogeneous textures with mono-sized grains. No vitreous phase is noticed. According with the results of the chemical microanalysis obtained from SEM a good agreement between initial composition of the mixture and $Sn_{0.5}Cu_{0.17}Sb_{0.33}O_2$ (SS) should be observed.

Tri-rutil type solid solutions occurr at concentration below 20 mol% of SnO_2 at 1273. The cell parameters calculated from the diffraction data show a small variation of the elementary cell as compared to those of $CuSb_2O_6$.

In the papers following [Mihaiu et al., 1999; 2001; Scarlat et al., 2002] the formation of *rutil* (SnO_2) and *tri-rutil* type ($CuSb_2O_6$) solid solutions was studied starting not with the three component oxides (SnO_2, Sb_2O_3, CuO) but with SnO_2 and $CuSb_2O_6$ thermally treated at la 1373 K, 3 hours.

The lattice parameters for $SnO_{2\ ss}$ and $CuSb_2O_6$ ss were calculated from diffraction data.

For the tin rich-end members of the series, which crystallise with the *rutile* type lattice, the measured a_o [Å] and c_o [Å] lattice parameters obey Vegard's Rule:

$$a_o = 4.736 - 0.0016 \cdot x_{CuSb2O6} \pm 0.002 \text{ Å}$$

$$c_o = 3.1865 + 0.016 \cdot x_{CuSb2O6} \pm 0.002 \text{ Å}$$

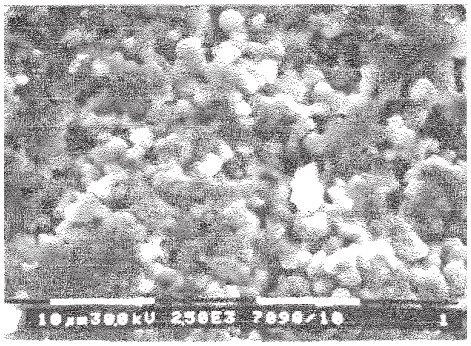

The chemical microanalysis from Scanning electron micrographs (SEM) data for the $Sn_{0.5}Cu_{0.17}Sb_{0.33}O_2$ solid solution thermally treated at 1373 K:

% at.	Exp.	Calc.
Sn	18.23	16.67
Cu	6.77	5.55
Sb	11.11	

Fig. 8. SEM image of the $Sn_{0.5}Cu_{0.17}Sb_{0.33}O_2$ solid solution thermally treated at 1373 K

The solid solubility limit of $CuSb_2O_6$ in SnO_2 was estimated to be at $x_{CuSb2O6}$ = 0.25, in accordance with previous results obtained using the mixture with 60mol% of SnO_2, 20 mol% of Sb_2O_3 and 20 mol% of CuO .The variation of the lattice parameters for the composition which consists from SnO_{2ss} is shown in Fig. 1(a, b)

For the SnO_2 based solid solutions (Fig. 9), a linear decrease of the lattice parameters a and c was noticed up to a 25% mol. CuSb2O6 content in the initial mixture. At higher amount of $CuSb_2O_6$ in the mixture, the lattice parameters remain constant, confirming the assumption that the dissolution of $CuSb_2O_6$ in the SnO_2 matrix take place until half of the Sn^{4+} were substituted with Cu^{2+} and Sb^{5+} in the 1:2 ratio.

In this way the composition of the higher limit of the solid solution formed corresponds to the $Sn_{1/2}Cu_{1/6}Sb_{2/3}O_2$ compound (the same value as when starting with individual tin, antimony, copper oxides). In the case of the sample which contains the highest quantity of $CuSb_2O_6$ incorporated in the SnO_2 matrix, the magnetic susceptibility ($\chi_{g,293K}$) value of $2.5 \times 10^{-6} cm^3/g$ is very close to those obtained in the case of mixture of phases ($\chi_{g,293K} = 2.9 \times 10^{-6} cm^3/g$). That could be a confirmation of the inclusion of the $CuSb_2O_6$ compound in the rutile type structure as a $Cu_{1/3}Sb_{2/3}O_{6/3}$ moiety [Mihaiu et al., 2001].

The $CuSb_2O_6$ based solid solutions were lesser studied [Mihaiu et al., 2001; Scarlat et al., 2002]. It is known that $CuSb_2O_6$ compound crystallizes in a distorted monoclinic trirutile structure in space group $P2_{1/c}$ or $P2_{1/n}$ [2] with folllowing unit cell parameters: a=4.6324Å, b=4.6359 Å, c=9.2967 Å and β°=91.12. The trirutile type structure can be generated from the rutile structure by tripling the c-axis due to the chemical ordering of the divalent and pentavalent cations. The structure consists of a network of edge and corner sharing CuO6 and SbO6 octahedra. The Cu^{2+} and Sb^{5+} cation position are such that the magnetic Cu^{2+} ions are separated from each other by two sheets of diamagnetic ions. In fact, the magnetic cation sublattice is the same as that of the K_2NiF_4 structure, which is the canonical example of a square lattice two-two-dimensional antiferomagnet. Nakua established that $CuSb_2O_6$ compound shows the clearest evidence for the dominance of one-dimensional correlations

in the short range ordered regime with the magnetic susceptibility value $\chi_{g,293K}$=3,7.10^{-6}cm3/g [Nakua et al., 1991].

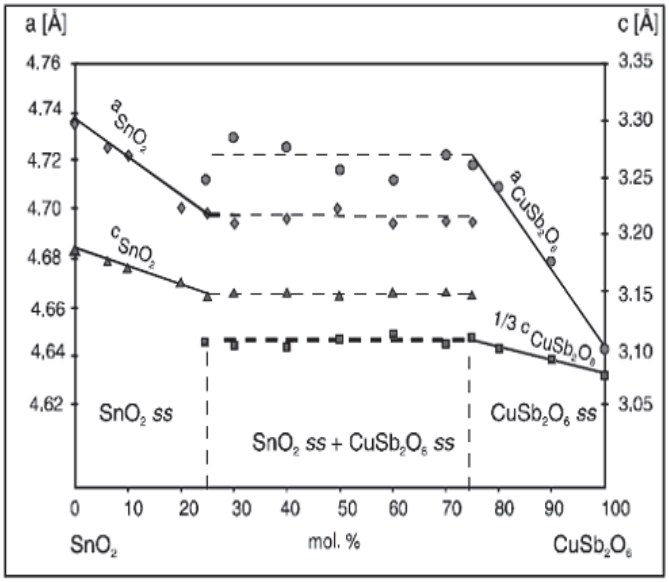

Fig. 9. Variation of the lattice parameters (a, c) for the solid solution SnO_2-$CuSb_2O_6$

Paramagnetic moment values of 1.5, respectively, 1.9 (B.M.) was determinated by Donaldson in the 90-950 K temperature range [Donaldson et al., 1975]. Based upon the cell parameters vs. composition dependence, the solubility limit of SnO_2 in $CuSb_2O_6$ at 1373 K was estimated to be $x_{SnO2} \leq 0.20$. Similarly, for the *trirutile* type solid solution in accordance with Vegard's rule, the lattice parameters varied with the decreasing of SnO_2 content:

$$a_o = 4.679 + 0.0005 \cdot x_{SnO2} \pm 0.002 \text{ Å}$$

$$c_o = 11.065736 + 0.017544 \cdot x_{SnO2} \pm 0.002 \text{ Å}$$

In the case of the $CuSb_2O_6$ solid solution formation, the volume of the unit cell lattice decrease with the decreasing of SnO_2 content. In the same time the β angle value indicates a stabilization of the tetragonal structure of the $CuSb_2O_6$ compound even at room temperature. The magnetic susceptibility($\chi_{g,293K}$) values of about 3.6×10^{-6}cm^3/g obtained for $CuSb_2O_6$ solid solutions was found to lie within the reported limits typical for Cu^{2+} ions It is suggested that the Sn^{4+} incorporation into trirutile lattice take place preferentially on Sb^{5+} sites[Scarlat et al., 2002].

3. Sintered ceramics

For improving properties as thermal and electrical conductivity, translucency and strength it is desirable to eliminate as much of the porosity as possible. For some other application it may be desirable to increase the stregth without decreasing the gas permeability.

The conventional ceramic method, the hot isostatic pressing technique and spark plasma sintering technique are some of the techniques used for the obtaining sintered compacts.
The flow chart of the whole experimental procedure is given in Fig.10.

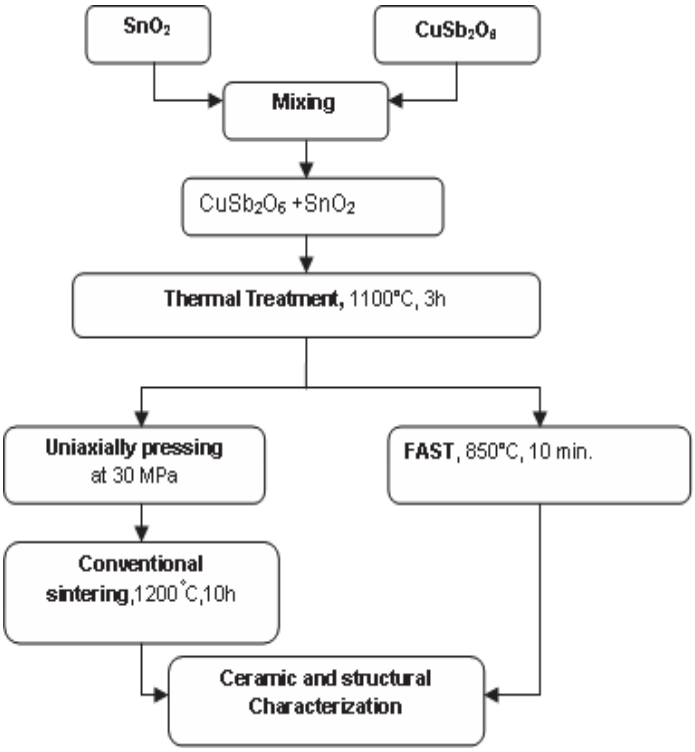

Fig. 10. The flow chart of the whole experimental procedure

3.1 Conventional ceramic method

The usual processing of ceramics, polycrystalline powders are compacted and then thermally treated at temperature sufficient to develop useful properties. During the thermal treatments for the obtaining ceramic compact three major changes commonly occur: (a) an increase in grain size; (b) a change in pore shape; (c) change in pore size and number, usually to give a decreased porosity.
Ceramics belonging to the SnO_2-Sb_2O_3-CuO ternary system thermally treated at lower than 1273K temperatures showed no linear shrinkage but linear dilatation and high porosity pointing out an inadequate sintering[Mihaiu et al., 1999]. The oxide composition that lead to dense ceramics were obtained starting with mixtures with CuO: $Sb_2O_3 \geq 1$ and the SnO_2 content >40 mol% at 1373 K.
Dense ceramics with zero porosity and relative density >94%($d_r = d_{exp}/d_c$).have been reported only in the compositional range with >85mol% SnO_2 and thermal treatment at 1473 K, four hours[Popescu et al.,2002]. For the theoretical density authors [Mihaiu et al., 2005]used the following relation:

$$d_c = \frac{2(1-x)A_{Sn} + 2\frac{x}{3}A_{Cu} + 2\frac{2x}{3}A_{Sb} + 4A_O}{N_A \cdot V_{SnO_{2(ss)}}} \quad (7)$$

in which :A_{Sn}, A_{Cu}, A_{Sb} and A_O are the atomic weights of tin, copper, antimony and oxygen, N_A is Avogadro's number and $V_{SnO2(ss)}$ unit cell volume of the solid solution calculated from the X-ray measured lattice parameters. At 1373 K ceramics formed by the incorporation of the $CuSb_2O_6$ in SnO_2 matrix have not the ability to sinter by conventional sintering method authors [Mihaiu et al., 2005]. Thus, for the $Sn_{0.75}Cu_{0.083}Sb_{0.167}O_2$ composition after thermal treatment three hours, 8.45 % porosity and a relative density of 64.53% have been reported [Mihaiu et al., 2005]. A better sintering capability of the samples with the same compositions was observed from the initial oxides (SnO_2,, CuO and Sb_2O_3) mixtures (72,12% relative density). This difference in the obtained relative density values may be related only to the better sintering capabilities of the sample prepared starting from the initial oxides; as a result of the simultaneously proceeding of the sintering and the formation process of the SnO_2 based solid solution, the latter taking place in stages and thus increasing the whole reactivity of the system. On the other hand, the presence of some un-reacted CuO may develop the formation of a liquid phase at high temperatures. Such a liquid phase rich in CuO was evidenced in the SnO_2–Sb_2O_3–CuO based compositions even for short sintering times[7] and its presence may thus significantly improve the densification properties of the latter sample. The microstructure developed is vizualized by SEM in the Fig.11 (a and b) [Scarlat et al., 2003]

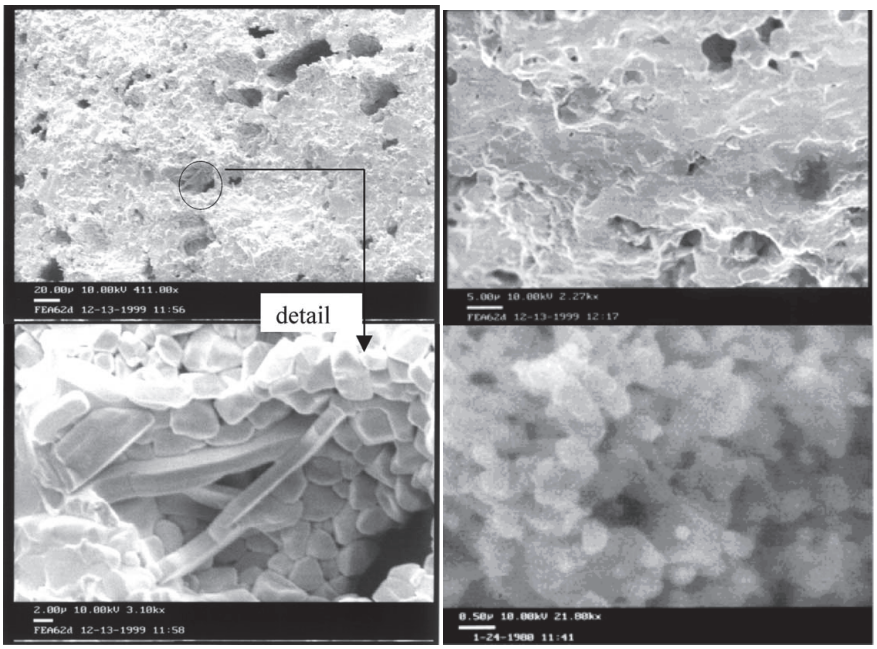

a) b)

a) starting with ternary mixture of 80 mol% of SnO_2, 10 mol% of Sb_2O_3 and 10 mol% of CuO
b) starting with binary mixture 90 mol% of SnO_2 and 10 mol% of $CuSb_2O_6$

Fig. 11. SEM micrographs of the sintered $Sn_{0.75}Cu_{0.083}Sb_{0.167}O_2$ composition at 1373 K, 3 hours

The presence of grains of about the same shape and size with some local and occasional inhomogeneties and a high amount of voids are evidenced.
The SEM images of the $Sn_{0.75}Cu_{0.083}Sb_{0.167}O_2$ composition (binary mixtures) thermally treated at 1373 K , ten hours and at 1473 K three hour are presented in Fig.12(a and b). By prolonged thermal treatment the sintering process is enhanced, but some pores (about 0.5 μm) are still enclosed in the obtained dense ceramics (Fig. 12. a). For the sample Thermally treated at 1473 K (Fig.12 b) the presence both of the primary phase composed of the relative uniform grains with the sizes more of 10 μ, and of the secondary phase with smaller size grains can be observed. However, the supplementary addition of CuO to the $Sn_{1-x}Cu_{x/3}$ $Sb_{2x/3}O_2$ solid solutions did not improve essentially the sintering abilities of the sample [Mihaiu et al., 2003]

3.2 Spark plasma sintering technique(SPS)

The spark plasma sintering technique (SPS) is a nonconventional densification method, which has been succesfully applied to dificult-to-sinter materals. A pulsed low-voltage high current is applied to loose powder loaded into a graphite punch and die unit. The pulsed current promotes electrical discharges at powder particle surfaces, thus activating them for subsequent bonding. A modest pressure (<100MPa) is applied throughout the sintering cycle. Densities in excess of 99% have been reported by SPS sintering of ceramics powders, such as AlN, Al_2TiO_5 or TiN without any sintering additives [Scarlat et al., 2003].

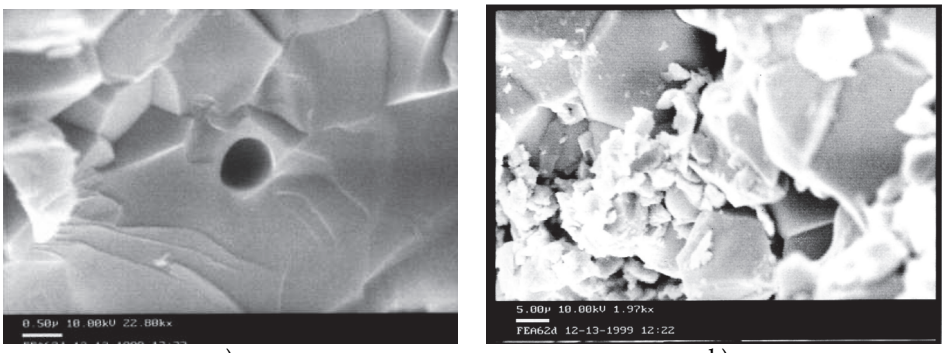

a) b)

Fig. 12. SEM micrographs of the sintered $Sn_{0.75}Cu_{0.083}Sb_{0.167}O_2$ composition starting with binary mixture 90 mol% of SnO_2 and 10 mol% of $CuSb_2O_6$: a) thermally treated at at 1373 K, 10 hours ; and thermally treated at at 1473 K, 3 hours.

The sintering modulus of the SPS machine is presented in Fig.13.
The solid solutions of the $Sn_{0.82}Sb_{0.18}O_2$ composition (prepared after thermal treatment at 1273 K, 3 hour of the tin and antimony oxide mixture) and of $Sn0_{0.75}CuO_{0.083}Sb_{0.167}O_2$ composition have been densified by Spark plasma sintering technique. The sintered compacts with high relative density of 92.44% in the case of $Sn_{0.82}Sb_{0.18}O_2$ composition and 99.6% for $Sn_{0.75}$ $Cu_{0.083}$ $Sb_{0.167}O_2$ composition have been reported by [Scarlat et al., 2003; Mihaiu et al.,2005]. The SEM photographs of the samples $Sn_{0.82}Sb_{0.18}O_2$ and $Sn_{0.75}Cu_{0.083}Sb_{0.167}O_2$ illustrated in Figs.13 (a and b) indicate the obtaining of the consolidated microstructure with the grain sizes lower than 1μ. However, the very fine homogeneous grains of the sample $Sn_{0.82}Sb_{0.18}O_2$ in comparison with the sample $Sn_{0.75}Cu_{0.083}Sb_{0.167}O_2$ could be notice.

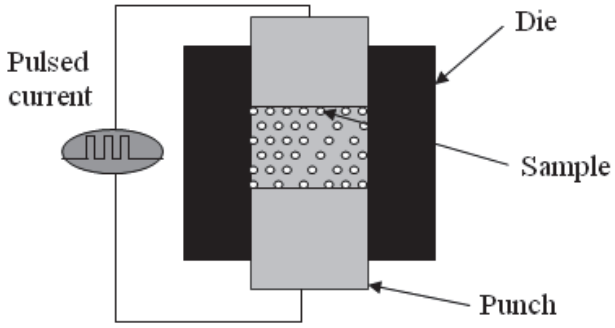

Fig. 13. Sintering modulus of the SPS machine

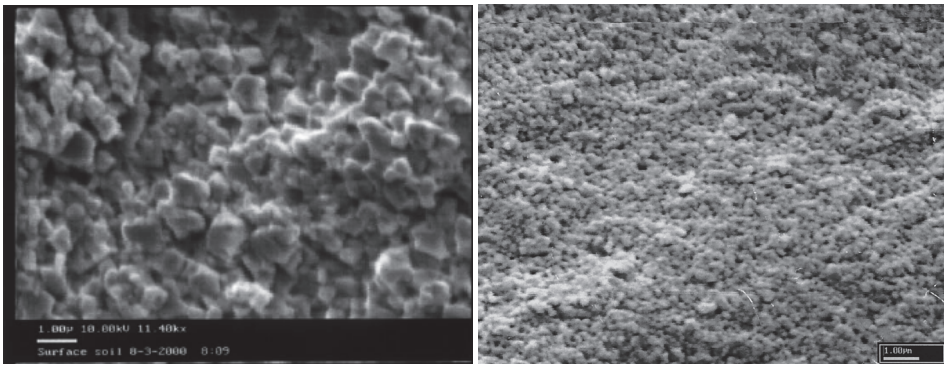

a.) b.)

Fig. 14. SEM micrograph of the compats sintered by Spark plasma sintering technique (SPS): a.) solid solution of $Sn_{0.75}$ $Cu_{0.083}$ $Sb_{0.167}O_2$ composition obtained after thermal treatement at 1373 K , 3 hours[Scarlat et al.,2004]; b.) solid solution of $Sn_{0.82}Sb_{0.18}O_2$ composition obtained after thermal treatement at 1273 K , 3 hours [Scarlat et al., 2003]

Even though the exact mechanism of the enhanced SPS densification is not yet known, it is assumed that the pulsed electrical current creates favorable conditions for the removal of impurities and activation of powder particle surfaces. Some arcing or electrical discharge phenomena at particle- to-particle contacts may be responsible for adsorbate elimination or surface ''cleaning'', thus creating favorable conditions for subsequent particle bonding. This activation explained the high densities obtained in ceramics without additives and direct grain-to-grain contact at atom scale observed by HREM in ceramics and metals. In addition to the little coarsening due to a very short time at high temperatures, the final nanometer grain sizes by SPS sintering also reflect a minimal coarsening during the heating up stage.

4. Electrical behaviour of the SnO_2-based ceramics

The electrical behaviour of the dense ceramic masses in the system was approached a in Sn-Sb-Cu-O papers [Zuca et al., 1995, 1999; Mihaiu et al., 200; ,Scarlat et al., 2003, 2004; Popescu

et al., 2002] Electrical conductivity measurements were effected in the 77-1100 K temperature range on two types of materials with distinct structure:

- SnO_2 monophasic ceramics with rutile type structure
- ceramics consisting of phase mixtures: SnO_2 +$Cu_4SbO_{4.5}$ or

$$SnO_2 + Cu_4SbO_{4.5} + Cu\ Sb_2O_6$$

Measurements in the 300-1100 K temperature range were accomplished in the cell presented in Fig.15

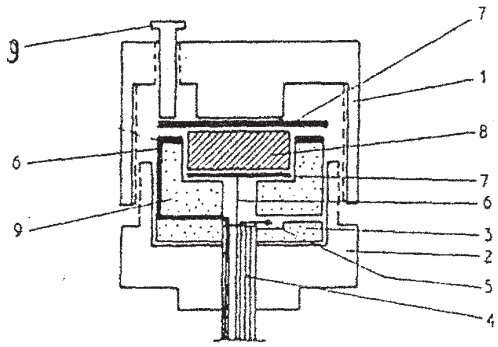

1, 2 refractory steel threated bodies; 3 boron nitride ring; 4 four channel insulator; 5 Pt-PtRh thermocouple; 6 platinum wire; 7 platinum electrodes; 8 semiconductor pellet; 9 boron nitride support; 10 stainless steel screw; 11 platinum ring.

Fig. 15.The pellet holder for conductivity measurements.

An other serie of measurements were realized in the low temperature range between 77-300 K .The dependence of the resistivity on the temperature and the values of Seebeck coefficient for some selected samples is shown in Fig. 16(a) and Tables 4. A small variation of the samples consisting of SnO_2 ss with the temperature was found. The samples consisting of phase mixtures show an important decrease of three orders of magnitude of the resistivity up to 800K. Over this temperature, all the samples have a similar behaviour.
A graphical analysis of the linear of ln k vs.1/T dependence in the two temperature ranges studied(Fig. 16. b) brings about new additional information. According to these data all samples exhibit a n-extrinsic conductivity whose activation energy ranges within 0.04-0.3 eV. As it could be seen in Fig.16 (b-inserted) for the samples composed from a unique phase single Arrhenius line was obtained over the whole 300-1100 K, similar behavoiur of the sample where Sb_2O_3 and CuO act as dopant [Zuca et al., 1991]. However some distinctive tendencies were recorded in Fig.17 for samples consisting of a mixture of phases. As seen a marked change of slope takes place at temperatures exceeding 600K which suggests a possible modification of charge carriers involved in conduction process. Indeed Shimada and Mackenzie identified in the temperature range under discussion, the following chemical reaction [Shimada & Mackenzie, 1982]:

$$Cu_4SbO_{4.5} \leftrightarrow CuSb_2O_6 \qquad (8)$$

Sample	Oxide composition			Phase Composition	Seebeck Coeficient (μV/K)
	SnO_2	Sb_2O_3	CuO		
t_1	95	1	4	SnO_{2ss}	-1.7
A_1	80	10	10	SnO_{2ss}	-1.6
A_2	60	20	20	SnO_{2ss}	-1.7
B_3	50	10	40	$SnO_{2ss}+Cu_4SbO_{4.5}$	-
B_4	50	20	30	SnO_{2ss}	-3
B_5	40	20	40	SnO_{2ss}	-1.8
B_9	30	10	60	$SnO_{2ss}+Cu_4SbO_{4.5}$	+10
B_{10}	20	30	50	$CuSb_2O_6$+ SnO_2 $+Cu_4SbO_{4.5}$	-

Table 4. Oxide composition and phase composition

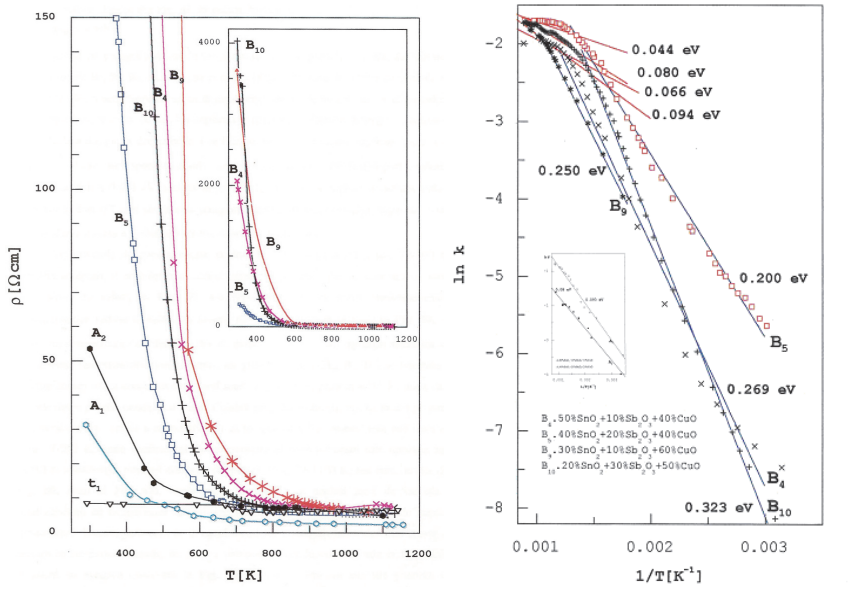

a) b)

Fig. 16. Electrical behavior: a) Dependence ρ plotted against temperature; b) Arrhenius behaviour in 300-1100K temperature range for various samples; solid solutions of $Sn_{0.75}Sb_{0.17}Cu_{0.08}O_2$ and $Sn_{0.5}Sb_{0.33}Cu_{0.17}O_2$ composition are inserted in b.)

Which could generate the behaviour shown in Fig17.b By an additional incorporation of $CuSb_2O_6$in the SnO_2 labilized lattice with increasing temperature[Zuca et al., 1999] The small negative values ofthe Seebeck coeficient confirm the electronic conduction in all samples except the sample which consists of a phase mixture. În this case the existence of Cu4SbO4.5 compound even at 300K temperature can favour a different mechanism of carrier motion (a possible p-type conductivity), which accounts for the Seebeck coefficient which take comparatively high positive value.

5. Conclusions

Discussion on the high-temperature interactions of components in the binary SnO_2-Sb_2O_3, SnO_2-CuO, Sb_2O_3-CuO, SnO_2-$CuSb_2O_6$ systems and in the ternary SnO_2-Sb_2O_3-CuO system was presented. The complexity of phase formation and phase composition evolution with thermal treatment temperature was established.

Results on the sintering capacity and consequently the densification using coventional and spark plasama sintering were presented. The powders sintering behavior depends on the method used. Highly densified ceramics were obtained only by using SPS sintering.

According to the electrical data all samples exhibit n-extrinsic conductivity whose activation energy ranges within 0.04-0.3 eV.

6. References

Bueno, P. R. Varela, J.A. & Longo, E. (2007). Admittance and dielectric spectroscopy of polycrystalline semiconductors *J. Eur. Ceram. Soc.* 27 : 4313–4320

Caldararu, M.. Mihaiu, S. Spranceana, D. Zaharescu, M. Popa, V.T. & Ionescu, N.I. (1999). The role of Hydration-dehydration effects on oxygen adsorption on SnO_2. *R ev.Ruom. Chim*. 44 (11-12) : 1115-1121

Chadwick, A.V. (1993). EXAFS studies of dopant sites in metal oxides. *Solid State Ion*. 63–65: 721-726

Dolet, N. Heintz, J. M. Onillon, M. & Bonet, J. P. (1992). Densification of 0.99SnO2–0.01CuO Mixture: Evidence for Liquid Phase Sintering, *J. Eur. Ceram.Soc.*, 9: 19–25

Heintz, J. M. Rabardel, L. Onillon, M. & Bonnet, J. P. (1995). Sintering Mechanisms of 0.99SnO2–0.01CuO Mixtures. *J. Mater. Sci*., 30 (2): 365–368

Donaldson J. D. Kjekshus, A. Nicholson, D. G.& Rakke, T. (1975). Properties of Sb-compounds with Rutile –like Structures *Acta Chem.Scan.* A29,: 803

Dusastre, V. &Williams, D.E. (1998). Sb(III) as active sites for water adsorption on Sn(Sb)O2, and its effect on catalytic activity and sensor behavior *J. Phys. Chem.* B 102: 6732-6738

Harrison, P.G. Bailey, C.& Azelee, W. (1999). Modified tin(IV) oxide (M/SnO2 M = Cr, LA, Pr, Nd,Sm, Gd) catalysts for oxidation of carbon monoxide and propane. *J. Catal*. 186: 147-151

Kikuchi, T. Watanabe, A. & Uchida. K. (1983). Formation of rutile type solid solutions in Pseudobinary Systems SnO_2-ABO_4 (A=Ga, Cr; B= Nb, Ta, Sb^{5+}) and SnO_2- AB_2O_6 (A=Mg, Zn; B= Sb^{5+}) *Yogyo-Kyokai Shi* 91(3): 110-116

Mihaiu, S. Zaharescu. M., Crişan D., & Zuca, Şt.. (1995). Stucture and Properties of the Solid Solutions in the Sn-Sb-Cu-O System" *Adv.Sci.&Technol.,B3*(Ceramics Charting the Future), pp. 702-710

Mihaiu, S. Scarlat, O. Radovici, C. & Zaharescu M. (2000). Phase Formation Sintering in the SnO_2- $CuSb_2O_6$ Pseudobinary System"Powder Metallurgy Science and Technology, *Proceedings of Second International Conference on Powder Metallurgy RoPM* . Ed. G. Arghir, U.T.Pres, Cluj-Napoca, 1, pp. 73-77

Stanica N. & Zaharescu M. (2001). Oxide Materials with Magnetic Properties in the SnO_2-$CuSb_2O_6$ Pseudobinary System. *J. Optoelect. Adv. Mater.* 3: pp. 913-918

Mihaiu, S. Scarlat O. Aldica Gh.& Zaharescu M. (2001). SnO_2 Electroceramics with Various Additives *J. Eur.Ceram. Society*, 21: pp. 1801-180

Mihaiu, S. Dragan, N. Scarlat, O.; Szatvanyi, A. Crisan, D. & Zaharescu, M. (2002). Structural Characterisation of the SnO_2Ceramics with Various Additives *Rev. Roum. Chim.* 47(9) : pp. 843-849

Mihaiu, S. Scarlat , O. Aldica, Gh. & Zaharescu M. (2003). Electronic Conduction of the $Sn_{1-x}Cu_{x/3}Sb_{2x/3}O_2$ (x<1/2) Rutile Type Structures. *J. Optoelectr. Adv. Mat*., 5,:913-918

Nakua, A. Yun, H. Reimers, J. N. Greedan, J. E. & Stager, C. V. (1991). Crystal Structure, Short Range and Long Range Magnetic Ordering in Cu Sb_2O_6 . *J. Solid State Chem* 91: 105-110

Orel, U. Stangar, L. Opara, U. Gaberscek, M. & Kalcher, K. (1995). Preparation and Characterization of Mo- and Sb:Mo-Doped SnO2 Sol–Gel-Derived Films for Counterelectrode Applications in Electrochromic Devices. *J. Mater. Chem*., 5 (4): 617–624

Park, P.W. Kung, H.H. Kim, D.-W. & Kung, M.C. (1999). Characterization of SnO2/Al2O3 lean NOx catalysts. *J. Catal*. 184: 440-446

Presley, R.E. Munsee, C.L. Park, C.-H. Hong, D.J. Wager, F. & Keszler D.A. (2004). Tin oxide transparent thin-film transistors, *J. Phys. D* 37: 281-287

Popescu, A.M. Mihaiu, S. & Zuca, S. (2002). Microstructure and Electrochemical Behaviour of Some SnO_2-Based Inert Electrodes in Aluminium Electrolysis", *Z.Naturforsch.* 57 a: 71-75

Popescu, A.M. Mihaiu, S. Constantin V.& Zaharescu M. (2007). Processing of oxide advanced ceramics as inert electrodes. *J. Optoelect. Adv.Mater.* 9(7): 2227- 2231

Rockenberger, J. Felde.U. Tischer, M. Troger, L. Haase, M. & Weller, H. (2000). Near edge X-ray absorption fine structure measurements (XANES) and extended X-ray absorption fine structure measurements (EXAFS) of the valence state and coordination of antimony in doped nanocrystalline SnO_2, *J. Chem. Phys*.112: 4296 Scarlat, O. Mihaiu, S.M. & Zaharescu M.(1999). CAS'99 *Proceedings of International Semiconductor Conference*, 22nd Edition, October 5 - 9, Sinaia, Romania., 1: 401

Scarlat, O. Mihaiu, S.& Zaharescu M (2002). Subsolidus Phase Relations in the SnO_2 - $CuSb_2O_6$Binary System". *J Eur Ceram Soc*., 22: 1839-1846

Scarlat, O. Payne, A.C. Mihaiu, S. Aldica, Gh. & Zaharescu, M. (2003). A Study of the SnO_2 and $CuSb_2O_6$ Based Solid Solutions: Electrical and Magnetic Properties. *J. Optoelectr. Adv. Mat*., 5: 997-1002

Scarlat, O. Mihaiu, S. Aldica, Gh. Zaharescu, M. & Groza, J. R. (2003). Enhanced Properties of Tin (IV) Oxide Based Materials by Field-Activated Sintering. *J.Am. Ceram. Soc*. 86: 893- 897

Scarlat, O. Mihaiu, S. Aldica Gh., Groza, J. & Zaharescu, M. (2004). Semiconducting Densified SnO_2- Ceramics Obtained by a Novel Sintering Tehnique. *J. Eur. Ceram. Soc.* 24 : 1049-1052

Slater, B. Catlow, C.R. Gay, D.H. Williams, D.E. & Dusastre, V. (1999). Study of surface segregation of antimony on SnO2 surfaces by computer simulation techniques. *J. Phys. Chem. B* .103: 10644.

Stan, M. Mihaiu, S. Crisan, D. & Zaharescu, M. (1997). Subsolidus Equilibriq in the Sn-Sb-Cu-O System. *Key Engineering Materials*, Ed. Trans. Tech. Publications, Switzerland. p.790 -793

Stan, M. Mihaiu, S. Crisan, D. & Zaharescu, M. (1998). Subsolidus Equilibria in the Sb-Cu-O System. *E. J. Solid State Inorg.Chem* .35: 243-254

Varela, O. J. Whittemore, & M. J. Ball, (1990). Pore Size Evolution during Sintering of Ceramic Oxides. *Ceram. Int.*, 16: 177–189

Varela, O. J. Gouvea, D. Longo, E. Dolet, N. Onillon, M. & Bonnet, J. P. (1992). The Effect of Additives on the Sintering of Tin Oxide. *Solid State Phenom.*, **25** (26): 259–268

Vlasova, M. V. Dıˆsel, D. E. & Kakazei N. G. (1990). Protzesı Formirovania Dispernıh Chastitz pri Terminchеskoi Ogragotke Smesei Ghidroksidov Olova i Surımı. *Neorg.Mater.*, 26 (7): 1486–1490

Volta, J.C. Benaichouba, B. Mutin,I. & Vedrine, J.C (1983). Comparative study of SnSbO and SnSbFeO mixed oxide catalysts in propene mild oxidation. Physico-chemical And catalytic investigation. Appl.Catal. 8: 215-236

Wagner, F. (2003). Transparent electronics. *Science* 300: 1245.

Wyckoff, R.W.G. (1963). Crystal Structures, vol.I-II, Ed. John Wiley & Sons, New York, London, Sidney,1964

Zaharescu, M. Mihaiu, S. Zuca, S. & Matiasovsky, K. (1991). Contribution to the study of SnO_2 -based ceramics.I.High- temperature interaction of tin (IV) oxide with antimony(III) oxide and copper(II) oxide. *J.Mat.Sci.* 26: 1666-1672

Zaharescu, M. Mihaiu**,** S. Crişan, D.& Zuca, Şt (1993). Structure and properties of ceramics in the SnO_2- Sb_2O_3-CuO system.. *The Proceedings of the European Ceramic Society Conference (THIRD ECerS)* Third Euro-Ceramics (Eds. P.Duran and J.F.Fernandez), Faenza Editrice Iberica S.L., Spain, 2: 359-364

Zaharescu, M. Mihaiu, M.S. & Zuca S (1999). Ceramic Properties of the Sintered Materials in the Sn-Sb-Cu-O System. *Advance Science and Technology of Sintering*, Ed.Kluwer Academic/Plen. Publis., N.Y. 251-258.

Zuca, S. Terzi, M. Zaharescu, M. & Matiasovsky ,K. M. (1991). Contribution to the study of SnO2- based ceramics: Part II. Efect of various oxide additives on the sintering capacity and electrical conductivity of SnO2. *J. Mater. Sci*. 26:1673-1676

Zuca, S. Mihaiu, S**.** & .Zaharescu M. (1995). Electrical Properties of the Ceramics în the Sn-Sb-Cu-O System. *Electroceramics,* Ed. Gusmano G. , Traversa E.,5: 373-380

Zuca, S. Aldica, Gh.; Mihaiu, M.S. Zaharescu, M. (1999). Electrical Behaviour vs Temperature of the Ceramics in the Sn-Sb-Cu-O System" Advances in Science and Technology. 13, Ceramics: Getting into the 2000's, Part B, Edited by P.Vincenzini, Italy, TECHNA, Faenza: p.345-352

6

Synthesis and Thermoluminescent Characterization of Ceramics Materials

Teodoro Rivera
Instituto Politécnico Nacional/CICATA-Legaria
México

1. Introduction

The development of novels materials represents a new and fast evolving application of research in physics and medicine. Processing synthesis is critical because it generally controls the final properties of the materials, ceramic forming techniques are generally based on powder processing with powder synthesis, forming and sintering. Moreover, ceramic processing has also to consider other techniques of synthesis and crystal growth, thin films and bulk desirable microstructures and nanostructures architectures. Luminescent of micro and nanostructured ceramics change their luminescent properties, and other topics as well as, temperature sintering process, luminescent properties by diminishing the crystallites size particles. This is closely related to the confinement effects in nano-scale materials. Among the various nano-materials, phosphor powders are attracting considerable attention because of their novel optical properties, which affect emission lifetime, luminescent efficiency. A great variety of different routes for the solution-based preparation of ceramics have been reported in the literature, using a wide range of precursor chemicals (inorganic and metal-organic), media (aqueous or non-aqueous) and methods as chemical precipitation, leading to powder products with a wide range of structure uniform powders. It has been shown that the sol-gel derived ceramics are former in particle size, narrower in particle size distribution, higher in sinterability, and more homogeneous in composition than many of those prepared via other processing routes, then sol-gel method was used to obtain ceramics powder. Precipitation method was the second method used to obtain micro and nanostructured ceramics. When a new luminescent material is proposed as candidate to functional applications, generally, various morphological, structural and functional characteristics is required i.e. crystalline structure, particle sizes, shape geometry, etc. Crystallization treatment is the first routine processes, after this process to perform a sintering processing is necessary in order to stabilize the trap structure. Annealing temperature and time are used to produce the lowest intrinsic background and to obtain the highest efficiency. One field of activities in the field of functional ceramics in luminescence is oriented towards the development of advanced materials and processes for thermoluminescence and functional applications, principally based on radiation physics detection. In this sense, different preparation methods and properties of several TL materials have been studied so far and it was found that metal oxides doped with proper activators constitute a class of promising TL phosphors. In this chapter author try to describes the details of the physics and try to show to different radiation field applications of the ceramics. The TL dosimetry (TLD) technique

offers the advantage of being able to place the dosimeters in outdoor stations for solar radiation monitoring, without requiring any additional special monitoring or logistical considerations, ceramics as well as, undoped and RE doped ZrO_2 and aluminium oxide are suggested by us as a suitable TLD material to accomplish this task.

2. Synthesis and processing of materials and ceramics

Ceramic luminescent is a material that emits light after absorbing external energy (e.g. ultraviolet radiation, X-rays, gamma rays). This kind of material has been widely applied in the fields of illumination, display, X-ray detectors, etc. However, with the development of sciences and technology, lots of the conventional phosphors have been unable to meet the requirements of current luminescent applications. In recent years, researchers have focused their work on the improvement of the luminescence property of traditional phosphors and preparation of new luminescent material. In this sense, different preparation methods and properties of several TL materials have been studied so far and it was found that metal oxides doped with proper activators constitute a class of promising TL phosphors.

2.1 Microstructured materials

Traditionally, $CaSO_4$:Dy thermoluminescent materials are used extensively for the radiation dosimetry purpose due to low cost, high sensitivity, and very high storage stability in ambient climatic conditions (Azorín, 1990). However, the integrated processes of sintering and microstructure development in a crystalline compound are so complex that even after 50 years of research. Over this time, research on luminescence micro and nanocrystalline materials has been greatly accelerated by the advances in the ability to manipulate structures at molecular or atomic level (Rivera et al., 2010a; Salah et al., 2006a). Most of the studies have been directed towards the synthesis, characterization, and application of these systems as structural and optical or electronic materials (Salah et al., 2006b). Many ceramic compounds are most easily prepared in a powder form. Powders-based processing allow the fabrication of ceramics at temperatures that are hundreds of Celsius degrees lower than are possible by the melt processes often used for metals and polymers. Powder processing also results in ceramic components with microstructures that are ideal for luminescent applications. Both chemical and morphological control of many advanced ceramic powders have been achieved at the commercial level, for compounds including aluminium oxide, zirconium oxide polycrystalline, silica, and barium titanate. Research in ceramics processing is extremely diverse, and encompasses all activities which contribute to the science and technology of fabricating ceramic materials in a useful form. Ceramics manufacturing has historically been based primarily on powder processes. The basic fabrication steps in producing such a ceramic component consist of powder synthesis, powder forming, and sintering. An important role of basic research is to address the chemical and physical phenomena involved in each of these steps. A largely qualitative understanding of sintering and microstructure development has evolved over recent years, leading to successful control of the sintered microstructure of many structural and functional ceramics, i.e. translucent alumina, toughened zirconia.

2.2 Nanostructured materials

The integration of powders of controlled size and shape with handling procedures based on principles of colloid and interfacial science has permitted the development of new powder

processing paradigms. For example, the improvement in mechanical properties of structural ceramics has been enabled by better powders and more thoughtful processing to avoid the deleterious effects of aggregates. Powders with particle sizes on the nanometer scale have the potential for further decreasing firing temperatures, and thereby developing new applications. The development of new tools suitable for nanoscale particles such as computational chemistry and improved understanding of colloidal behaviour at the nanoscale are required. Furthermore, there is a need to develop processing schemes that utilize more environmentally-benign aqueous systems rather than organic solvents.

2.3 Routes for solution-based preparation

Various methods to synthesize ceramics materials have been reported based on traditional approaches to modify the band structure of the materials as well as the characteristics of their trapping centres. Interest in synthesizing based ceramics has increased considerably in recent years as possible technological applications triggered a wide variety of research activities on this material.

2.3.1 Precipitation method

Currently, nanotechnology and nanomaterials have attracted several researchers from different fields (Heuer & Hobbs, 1981), especially from the field of luminescence. It has been found that the physical properties of individual nanoparticles can be very different from those of their bulk counterparts. Recent studies on different luminescent nanomaterials have showed that they have a potential application in dosimetry of ionizing radiations for the measurements both of low and high doses using the thermoluminescence (TL) technique, where the conventional microcrystalline phosphors saturate (Kumar et al., 1994; Rivera et al., 2007b). For high doses, the saturation occurs due to the ionized zones overlapping each other in some micromaterial. The TL results of the reported nanomaterials have revealed very imperative characteristics such as high sensitivity and saturation at very high doses. Among the preparation methods of luminescent materials, homogeneous precipitation method not only has the advantages of simple process, convenient for doping and low production cost, but also can prepare uniform and small sized particles, because the precipitants are formed slowly and homogeneously throughout the solution during the precipitation process.

2.3.2 Sol–gel method

The interest in sol-gel synthesis of luminescent materials arises from the relatively low cost of the method; as well as the approach that allows the chemical content and concentration ratio of the elements of the sol-gel derived powders to be tailored, with ready fabrication into different solutions. More specifically, the sol, i.e., the dispersion of colloidal particles of diameter 1 to 100 nm in a liquid (Rivera et al., 2007c), is able to penetrate through the interacting channels of mesoporous matrices, enabling to fabricate a luminescent xerogel located on the surface porous powders of several μm in grain size (Brinker & Scherer, 1990). The idea behind the chemical synthesis of micromaterial is to transform molecular precursors into materials under retention of the structural units, which are inherent to the precursor molecule and also forms and integral part of the solid-state structure. Although, the concept of synthesizing materials from molecule has long been shifted to the synthesis of new materials with novel compositions (Brinker & Scherer, 1989). Among the commonly used precursors to oxides such as halides, nitrates, acetates, carboxylanes, alkyls, alcoxides,

etc., metal alkoxides [M(OR)n] are specially attractive due to the pre-existent metal-oxygen bonds. The sol-gel process based on the hydrolytic decomposition of metal alkoxides has been successfully used for the synthesis of a large number of monometal oxides phases (Al_2O_3, TiO_2, ZrO_2, etc.). However, metal alkoxides [M(OR)n] are preferred precursors to oxides because of their pronounced tendency to associate by forming M.(OR).M´ type bridges. When carefully hydrolyzed, metal alkoxide derivatives produce molecular entities containing oxo-and/or hydroxo-bridges, they can associate themselves via hydrolysis and cross-condensation reactions to form macromolecular networks. In recent decades, zirconia dioxide (ZrO_2) has attracted great interest due to its extensive practical applications as a structural ceramic (Rivera et al., 2007d).

2.4 Ceramic polycrystalline powder

For luminescent materials, this is crucial since the light emission is usually due to crystalline structure or doping ions like rare-earth or transition metals ions. Quenching concentrations are usually found higher for sol-gel-derived materials because of better dispersion of doping ions and thus higher average distance between emitting centres. Several authors have also developed heterometallic precursors associating different elements through chemical bonding and thus providing the highest homogeneity.

2.4.1 Metal alkoxides

In particular, transition metal alkoxides are very reactive because of the presence of highly electronegative OR groups that stabilize the central atom in its highest oxidation state. This in turn makes the metal atom very susceptible to nucleophilic attack. The point where this network extends throughout the reactor is described by the percolation theory and named the gel point. The obtained wet gel can be dried in various conditions leading a xerogel with residual porosity. Further heating of the xerogel in controlled conditions allows obtaining the desired glass or ceramic. Furthermore, the temperatures required for the full densification and crystallization of the desired glass or ceramic are usually lower than the ones required by classical melting or solid-state processes (Aguilar et al., 2001; Petrik et al., 1999). This can be interesting from an economical point of view but also because in some cases, the obtained phases can differ from the one obtained by classical procedures. By this way, new phases can be obtained or high-temperature phases can be stabilized at room.

2.4.2 Zirconium oxides

Zirconium dioxide (ZrO_2), which is also referred to as zirconium oxide or zirconia, is an inorganic metal oxide that is mainly used in ceramic materials. Zirconium dioxide is the most important zirconium compound which due to its properties is used in various products. In nature, ZrO_2 occurs in the mineral form as baddeleyite, a modification in monoclinic crystal lattices. The sol–gel synthesis of ZrO_2 powder involves hydrolysis and condensation of zirconium (IV) propoxide in ethanol solution (Rivera et al., 2007c). The hydrolysis and condensation reactions, which take place as a result of mixing two parts of alcohol solution, can be described as:

$$(RO)_3\text{–Zr-O-R} + H_2O \xrightarrow{H^+} (RO)_3\text{–Zr-O-H} + \text{R-OH} \rightarrow \text{Hydrolysis.} \quad (1)$$

$$2(RO)_3\text{-Zr-O-H} \rightarrow (RO)_3\text{-Zr-O-Zr-}(OR)_3 + H_2O \rightarrow \text{Condensation} \quad (2)$$

Generally, Zr(OPr*n*) (13.3 mmol, 6ml of 70 wt% solution) adding by drops up to 48 ml (2.667 mol) of deionized water acidified with nitric acid to pH 1 in a nitrogen atmosphere. During this step, a white suspension is formed immediately. Then, the suspension is heated for 24 h at 80°C. After this, other 100 ml of deionised water acidified to pH 1 is added to initial suspension, and it is maintained with vigorous stirring at room temperature (RT) for 72 h. The stirring is performing in order to disperse the aggregates into small particles and small aggregates. After this, a-Zr:H powders of different sizes is obtained and then dried at 120°C for 20 h. Finally, powder is submitted thermally at a temperature of 1100 ◦C for 5 h.

2.4.3 Aluminium oxide

Alumina is the most cost effective and widely used material in the family of engineering ceramics. The raw materials from which this high performance technical grade ceramic is made are readily available and reasonably priced, resulting in good value for the cost in fabricated alumina shapes. Aluminium oxide, commonly referred to as alumina, possesses strong ionic interatomic bonding giving rise to its desirable material characteristics (Salah et al., 2011; Sallé et al., 2003). Alpha phase alumina is the strongest and stiffest of the oxide ceramics (Gitzen, 1998). This is the phase of particular interest for luminescent applications. Ceramic oxide of aluminium oxide powder has been obtained using solvent evaporation method (Rivera et al., 1999). The solution is heated at 250°C for half an hour, then evaporation 700°C for half an hour. In order to stabilize the traps, powder obtained is then submitted to thermal treatments of two hours at the following sintering temperature: 500, 700 and 900°C.

2.4.4 Zirconium oxide-aluminium oxide

The uniform dispersion of zirconia particles in the alumina matrix can be controlled by homogeneous powder synthesis techniques. The ZrO_2-Al_2O_3 ceramic composites display different properties depending on the precursors, chemical composition and preparation route. The ZrO_2-Al_2O_3 ceramic composite has been observed that the structure of the matrix material and the zirconia particles dispersed in the alumina matrix are so important in order to produce optimally tough transformation-toughened composite materials that increase the mechanical and thermal properties of the composite (Li et al., 1995; Taavoni et al., 2009; Zhang & Glasser, 1993). Among the preparation methods of zirconium-aluminium luminescent materials, sol-gel method has been the most appropriate synthesizing method. Homogeneous mixtures of pseudoboehmite with average formula $Al_4O_3(OH)_6$ obtained from U.G. Process (Zarate et al., 2005) and t-$ZrO_2(Y_2O_3)$ were prepared by a mechanochemical treatment employing HNO_3 as a peptising agent. The U.G. process is related with the alkaline desulphatation of $Al_2(SO_4)_3$ using an ammonia solution (Rivera et al., 2010b). Suspensions of precursory powders were prepared with pseudoboehmite seeded during mechanochemical treatment with 2.5 mass% a-Al_2O_3 of 0.20 μm (Taimicron, TM10) and tetragonal zirconia powders (TOSOH, TZ-3YS) with average particle size of 0.26 μm were added in adequate proportions for each composition (100, 90, 70, 50, 30, 15 and 0 mass % of ZrO_2). The suspensions were stirred and spray dried using a YAMATO Mini-spray dryer ADL31. The precursory powders were submitted at 1200°C.

2.4.5 Hafnium oxides

The hafnium oxide (HfO_2) is a material with a wide range of possible technological applications because of its chemical and physics properties as high melting point, high

chemical stability, and hardness near to diamond in its tetragonal phase. The large energy gap and low phonon frequencies of the HfO_2 makes it appropriate as host matrix for being doped with rare earth activators. Hafnium oxide (HfO_2) films have been deposited by a variety of techniques; these include atomic layer epitaxy, chemical vapour deposition, and electron beam evaporation. Ultrasonic spray pyrolysis represents an alternative processing method that has been employed for deposition of wide variety of films and coatings and several type of powders production. The HfO_2 films were grown using the ultrasonic spray pyrolysis technique (Guzman et al., 2010). The precursor solution is atomized and goes away to corning glass substrate heating on a tin bath by dry air flow. The starting reagents to HfO_2 films deposition was $HfCl_4$ in deionised water as solvent; the initial solution was prepared to a 0.05 M. Deposition temperatures (Ts) were in the range from 300°C to 600°C. Filter air as carrier gas was used at flow rate of 10 l/min. The deposition time was 10 minutes for all the samples in order to reach almost same films thickness. The films show a deposition of about 2 μm per minute.

2.5 Ceramic thin film

Ceramic thin films are presently used in, and will continue to be developed for, a multitude of devices critical to luminescence and optoelectronics technology. The processing of thin-film ceramics differs from that of many other materials due to the complex microstructures and defect structures that can arise in complex ionic and covalent compounds. The fundamental knowledge base necessary for understanding and predicting the orientation and microstructure of ceramic thin films does not now exist (Agarwal et al., 1997; Asiltürk et al., 2011; Rivera et al., 2005a). The nucleation and growth mechanism of ceramic compounds in thin film form is also poorly understood, as are the mechanical strains that accompany film formation, and the surface morphologies of ceramic thin films. Furthermore, many applications of thin film ceramics require deposition at very low temperatures. The role of nonthermal sources of energy in determining ceramic film microstructure is emerging as a fascinating area for future research, as is the processing of low density (microporous) ceramic films for their ultraviolet dosimetry properties (Deis & Phule, 1992). Bulk processing remains important, while many of the new device applications requires processing in thin film form. Thin film techniques via Spray pyrolysis deposition and sol-gel need to be developed for doped (e.g., with rare earth elements) materials for integrated photonic applications. As the deposition technique, spray pyrolysis is a simple technique that allows obtaining good quality films over extended areas at low cost (Chacon et al., 2008; Guzman et al., 2010). The ceramic thin films generally grow with a crystalline microstructure (Azorín et al., 1998).

2.6 Development of advanced ceramics

The science and engineering of ceramic is rich with fundamental questions related to the synthesis, fabrication, and characterization of physical and luminescent properties. The synthesis approaches and the luminescent materials produced can perhaps be conceptually separated according to the size scale of the microstructure produced (Langlet & Joubert, 1993). Nanostructure processing offers new capabilities for manipulating materials microstructural and compositional variation on the nanometric scale (Rivera et al., 2007c; Shang et al., 2009). Due to their fine grain sizes, ultra high surface-to-volume ratio can be achieved in nanocrystalline materials. Therefore, the large number of atoms located at the edges and on the surfaces of nanocrystallites provides active sites for luminescent surface.

Furthermore, nanocrystallites have unique hybrid properties characteristic of neither the molecular nor the bulk solid state limits (Taavoni et al., 2009). Nanocrystalline processing offers a practical way for retaining the results for appropriate manipulation on the atomic or molecular level, producing novel materials with unique size-dependent behaviour, including quantum confinement effects, greater microstructural uniformity for better optical reliability, and high ductility and super plasticity for advanced ceramics (Nalwa, 2000; Sasikumar & Vijayaraghavan, 2010; Somiya et al., 1988). The ability for producing luminescent materials with the desired microstructure and active component dispersion can bring significant advances in the field of luminescence. This can be accomplished through nanostructural processing of materials (Rivera et al., 2006). Besides their composition, luminescent materials are also characterized by their microstructure: grain size, surface state or interface with their host media and packing of the particles within the material. The optimization of the luminescent properties of phosphors, varying their nanostructure, is a subject which has certainly not been fully investigated up to now. It is nevertheless clear that the excitation energy, the surface defects, the efficiency of light extraction and the interface between the phosphor grains and their environment are parameters which are affected by the nanostructure of the material (Azik et al., 2008; Zhang et al., 2005; Wang et al., 2005). This influence is enhanced for small grain sizes, giving a real motivation for the synthesizing phosphors with dimensions of their microstructure closer to the nanometer size range.
Thermoluminescent nanoparticles with dimensions smaller than or in the order of the size of the bulk exciton show unique optical properties, which depend strongly on the size. These properties have stimulated great interest in luminescent (thermoluminescent) nanoparticles both from a fundamental and from an applied point of view. One of the main problems in understanding variations in the quantum efficiency of nanoparticle luminescence is the large surface area and the role of (surface) defects in the luminescence process. As a result, the luminescence quantum efficiency is extremely importance to the synthesis conditions. Luminescent semiconductors form an important class of phosphors with applications in the thermoluminescent (TL) phenomenon studies (Lochab et al., 2007; Azorín et al., 2007).

3. Temperature effect on ceramic processing

Before using a thermoluminescent (TL) ceramic material for dosimetric proposes, it has to be prepared. To prepare a TL material means to synthesize, crystallizes and perform to luminescent application. In order to prepare a new thermoluminescent material for use, it is needed to perform a thermal treatment process, this thermal treatment consist in four steps, i.e. crystallization treatment, initialization treatment, annealing treatment and post-irradiation treatment (Furetta & Weng 1998).

3.1 Crystallization treatment

Poorly crystallized or truly amorphous material commonly comprises from 10 to 50 volume percent of typical amorphous material. The available phase quantification methods treat this significant fraction of the coating differently (Diaz et al., 1991; Yoshimura et al., 1999).
Rivera et al. (Rivera et al., 2005b) studied crystallization treatment process on hydrogenated amorphous zirconia (a-Zr:H) powder. The first stage of the procedure involves heating materials inside a furnace using different crystallization parameters (temperature and time)

indicated for the luminescent material under test. The ceramic powders are placed in lidded crucible which is placed in the furnace and submitted at different thermal treatment. After each thermal treatment, the powders are cooled in their containers in a reproducible manner. Alternatively, the crucible may be removed from the furnace immediately after the thermal treatment in order to allow the powders to be cooled much faster to room temperature. It is imperative to use always the same cooling procedure and that this is reproducible because the luminescent properties of the material are strongly affected by the cooling. In some case the crystallization thermal treatment procedure consists of two or more subsequent steps. An example is given by zirconium oxide powder form, which needs a first thermal treatment at 600°C during 1 h. After this thermal treatment, ceramic powders are submitted at 800°C during 1 h. Finally, a third thermal treatment is applied, this thermal process consist in a thermal treatment at 1100°C during 5 h. At the end of the thermal procedure the powders are read to check the background signal (see fig. 1). In case thermal treatment is applied at different temperatures, this is finished when the background is very low and constant for the whole powder.

Crystallization thermal treatment temperature affects significantly both the glow curve shape and the TL intensity of ceramics (e.g. ZrO_2, TiO_2, Al_2O_3). Rivera et al. (Rivera 2009, Aguilar 2001) analyze crystallization thermal effect on the ZrO_2 ceramics after thermally stimulation process. They observed, crystalline structure is changing when ceramics are submitted under crystallization temperature. These changes of the glow curve with the crystallization temperature may be correlated with a possible increasing of the oxygen vacancies concentration in the forbidden gap of the material (Hassan et al., 2009).

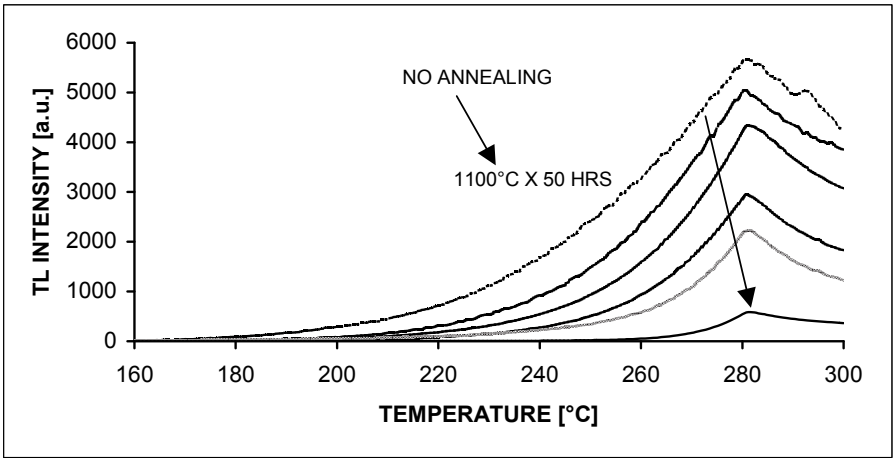

Fig. 1. Background signal of ceramics after crystallization treatment

This correlation indicates that even the powder crystallinity improves, as indicate by X-ray diffraction measurements, the presence of oxygen vacancies is very important for producing the light emission. This emission is probable due to the oxygen vacancies acting as electron trap centres. The shape of the glow curve is finally well defined for 5 hours at 1100°C (see fig. 2). The peak is well defined and centred at around of 190°C.

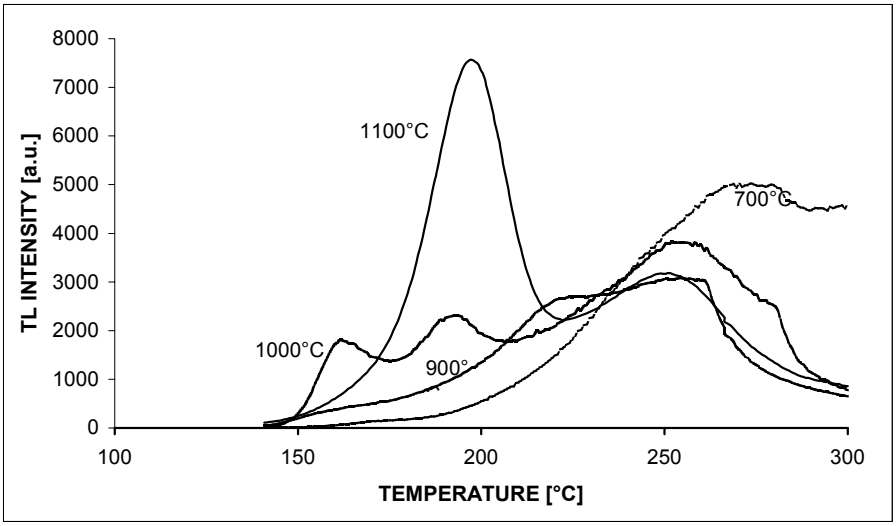

Fig. 2. TL glow curves of ZrO_2 after crystallization treatment process.

3.2 Temperature sintering process

In some cases, although, sintering is an essential process in the manufacture of ceramics, as well as several other functional applications, until now, no single book has treated both the background theory and the practical application of this complex and often delicate procedure. Sintering process is the end of the thermal process of crystallization ceramics (Ferey et al., 2001; Suk, 2005). The sintering process provides the energy to encourage the individual powder particles to bond or "sinter" together to remove the porosity present from the compaction stages. During the sintering process the "green compact" shrinks by around 40 vol % (German, 1996). Sintering process of ceramic materials is the method involving consolidation of ceramic powder particles by heating the green compact part to a high temperature below the melting point, when the material of the separate particles diffuse to the neighbouring powder particles (Chang & Su, 1993). The process of sintering (solid state) can be divided in three stages that phenomenologically appear and can be identified (see fig. 3). These stages differ from the form and transport mechanisms begin to dominate as it evolves during the sintering. There is an initial phase where they join the powders without contraction. In this phase, the surface transport mechanisms are of vital importance. At this stage, the sintering process starts with an aggregation of particles and the disappearance of the border began to produce a neck in the points of contact between the particles. Grain boundaries are formed between two adjacent particles in the contact plane. The centres of the particles are only slightly closer, which means very low shrinkage. Usually, it will reach an equilibrium value in the grain size due to surface tension called intermediate stage. In the intermediate stage the pores have been reduced due to the growth of the neck of the initial stage (Nasar et al., 2004). There is a large contraction in comparison with the other stages; the pores are reorganized in order to leave maximized the contact area of a particle with other particles obtaining a porous structure.

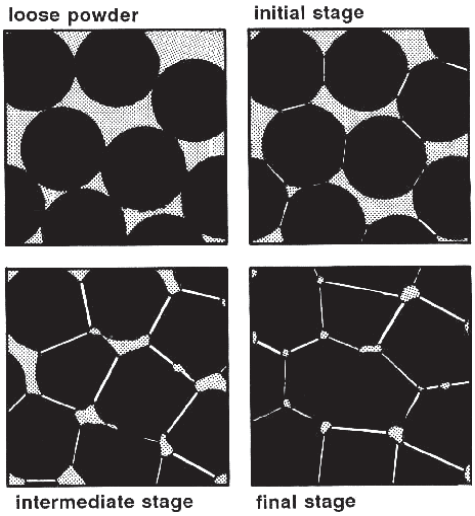

Fig. 3. Sintering process in ceramic powder

Later, when activated further filling processes or mass transport, is beginning to see a larger contraction. Cylindrical forms pores taken to minimize and then come to a final stage where the pores are closed and dispersed. Turning to a final stage, where the pores into a state of instability, they prefer to divide and spread evenly over the material. At the end of the sintering process density of the material is reached between 90 and 95% of the theoretical calculations. The amount of closed porosity increases rapidly and solidifies into spherical isolated pores. The densification is almost zero and takes a strong grain growth
The influence of temperature on the thermoluminescent ceramic powder is very notable, characteristics of the TL glow curve of ceramics polycrystalline powder for different applications is studied. Particularly, luminescent applications polycrystalline powder ceramics is improvement as sintering process is increased.

3.3 Thermal luminescent process

This thermal treatment is used for new (fresh or virgin) thermoluminescent materials which have not been used. The aim of this thermal treatment is to stabilize the trap levels, so that during subsequent uses the intrinsic background and the sensitivity are both reproducible. The time and temperature of the initialization annealing are, in general, the same as those of the standard annealing. Standard annealing process is used to erase any previous residual irradiation effect which is supposed to remain stored in the crystal after the readout. It is carried out before using the TLDs in new measurements. The aim of this thermal treatment is to bring back the traps-recombination centres structure to the former one obtained after the initialization procedure.

3.3.1 Initialization treatment

The first stage of the procedure involves heating dosimeters inside a furnace using the optimum annealing parameters (temperature and time) indicated for the TL material under test. The actual duration of annealing will be longer than the required annealing time in

order to attain thermal equilibrium at the required temperature (Furetta & Weng, 1998). Alternatively, the crucible may be removed from the furnace immediately after the thermal treatment in order to allow the dosimeters to be cooled much faster to room temperature. At the end of the annealing procedure the dosimeters are read to check the background signal. The background depends on the high voltage, applied to the photomultiplier tube, on this age and on the room temperature stability of the TL reader must be checked before and after annealing reading session. The background values determined for each dosimeter have to be collected, which is memorized in a file, so that they can be used for the successive tests. In many cases an average background vale is considered for the whole batch and then subtracted from each individual reading of the irradiated TLDs. This procedure is valid when the background is very low and constant for the whole batch.

3.3.2 Annealing treatment

In order to prepare a thermoluminescent material to be used for dosimetric applications, it is necessary to perform a thermal treatment process, usually called annealing. This process is carried out in oven, heating the TL samples up to a given temperature, keeping them at this temperature for a given period of time and then cooling down the samples to room temperature (Y. Zhang, et al., 2002). Thermal treatments used in this study can be classified into two main different types: (a) Initialization treatment, which was used on virgin ZrO_2 samples. The aim of this thermal treatment is to stabilize the trap levels, so that during subsequent uses both the intrinsic background and the sensitivity should be reproducible. (b) The second class of the thermal treatment corresponds to the pre-irradiation annealing, also called: standard annealing. This treatment is used to erase any previous residual irradiation effect which is supposed to remain stored in the crystal after the readout. The general aim of this thermal treatment is to bring back the trap-recombination center structure to the original one as obtained after the initialization procedure.

When a new TL material is going to be used for the first time, it is necessary to perform at first an annealing study which has two main goals. (i) To find a good combination of annealing temperature and time to stabilize the trap structure; (ii) to produce the lowest intrinsic background and to obtain the highest reproducibility of TL response.

3.3.3 Post-irradiation treatment

This kind of the thermal treatment is used to erase the low temperature peaks, if they are found in the glow curve structure. Such low temperature peaks are normally subjected to a quick thermal fading and many times this value is not been included in the readout to avoid any errors in the dose determination. In all cases, value and reproducibility of the cooling rate after the annealing process are of great importance for the performance of a TLD system. In general, the TL sensitivity is increased using a rapid cool dawn. It seems that the sensitivity reaches the maximum value when a cooling rate of 50-100°C/s is used. It must be noted the thermal procedures listed above can be carried out in the reader itself. But in many times when TLDs are many, TL reader is not enough for each TL materials to avoid spent a lot time an oven is used. Temperature annealing is monitored in step by step in order to care any variation time not listed. This is important for TL materials embedded in plastic cards (personnel dosimetry) or TL materials embedded in plastic medium as agglutinate material (Teflon) as material support for TL chips performing. In fact, the plastic material is not to able to tolerate high temperatures and the in-reader annealing is shortened to a few seconds.

4. Structural and morphological characterization

The requirements for high-quality special ceramics with certain physical and mechanical properties call for a functional characterization of the raw materials after various processing steps. Several methods have been described for determining the phase composition and the amorphous of ceramics (Rivera et al., 2007d). Extremely interesting is the characterization of these ceramic materials from the structural by means of X-ray diffraction and morphological by means of scanning electron microscopy methods, with the aim of fully understanding the reasons for their macroscopic properties, and of being able to examine the possibility of modifying and improving them.

4.1 X-Ray Diffraction method (XRD)

X-ray diffraction (XRD) is an important tool in luminescence for identifying, quantifying and characterizing optical materials in ceramic materials. Its application to photonic ceramics and its transformation products yields information on the ceramic composition of the compounds. Details of synthesizing processes, like firing temperatures and crystallization process as well as applications of ceramics may thus become optimums. X-ray diffraction process its application in luminescent ceramics is relevant. While it is relatively easy to determine which ceramics impurities contains from the positions and rough intensities of the diffraction peaks, which attributed luminescence performance. The identification of crystalline zirconium oxide in ceramics powder by XRD is a fine example where not only the presence of peaks has to be considered, but also their relative intensities need to be taken into account quantitatively, not only if one wishes to determine the zirconium oxide concentration quantitatively, but even to be able to identify zirconium in the ceramic material at all (Hideo et al., 2006). The major problem with zirconium oxide in ceramics is that its best diagnostic peak, the 002 reflection, coincides with the most intense peak 101 of the omnipresent baddeleyite. Determination of structural properties such as crystallite size and lattice distortions leads to a considerably improved characterization of ceramic powders and compacts during processing (Yoshimura et al., 1999). The application of this method to powder metallurgy problems is shown by the example of aluminium oxide or zirconium oxide after different thermal processing steps: quality control of the powders, structural changes, luminescence changes, etc. Complementary morphological investigations may broaden the understanding of the spatial arrangement of the particles in densified ceramic materials. Compacted but still porous Al_2O_3 is used to show the significance of morphological studies of the fracture surface and also studies on structural defects (Thompson et al., 1987).

Keller (Keller, 1995)] has been described a parallel beam XRD method developed for determining the percent crystallinity of fully crystalline and "fully amorphous" powders. Rivera et al (Rivera et al., 2007d) reported of analyzing on structural characterization of ZrO_2 powders, using a Siemens D5000 diffractometer employing nickel-filtered Cu Kα radiation (λ = 1.5406 Å, 40 kV, 30 mA) at 0.020° intervals in the range $20° \leq 2\theta \leq 75°$ with 1s count accumulation per step directly from the catalyst foils.. Their contribution on structural and morphological on X-ray diffraction patterns of ZrO_2 powder obtained by the sol-gel method and submitted to thermal treatment at 700°C for 10 h in air were relevant. The paper shows the diffraction patterns suggested a monoclinic phase of Zirconia. A monoclinic zirconia structure is observed to be predominant when the material is annealed at 1100°C. The strongest peak appeared always at around 2θ = 28.17° corresponding to the (-111)

monoclinic reflection. This spectrum is in excellent agreement with the reference spectrum (Powder Diffraction File # 37-1484) of zirconia. Except for the peak at around 2θ = 31.5 the other peaks with relatively weak intensities are described to the diffractions from the monoclinic structure. The line broadening of the highest peak at 2θ = 28.17° was used to estimate the average grain size of the powder. Assuming the particles to be stress-free, their size was estimated using the equation of Scherrer. Powder materials with average nanopolicrystalline sizes from 8-10 nm up to about 40 nm were obtained.
For the monoclinic phase of the ZrO_2 powder, the intensity is denoted by the (-111) plane; meanwhile, the other individual planes are found to be comparable to those expected for standard ZrO_2 which indicates randomly oriented crystallites in the powder. As thermal annealing is increased the intensity from the (-111) plane starts becoming higher (see fig. 4). However, at 1100°C the ratio exceeds the standard one, showing the preferential orientation to lie along the (-111) plane. For the material annealed at 1100°C, other weak intensity peaks are observed at 2θ = 49.3° (220), 50.2° (which corresponds to the (022) plane), 24.04° (110), 35.3° (002) and (34.2°) (which corresponds to the (200) plane). All these planes show only one preferred orientation. The preferred orientation along (-111) plane has the lowest Gibbs free energy.

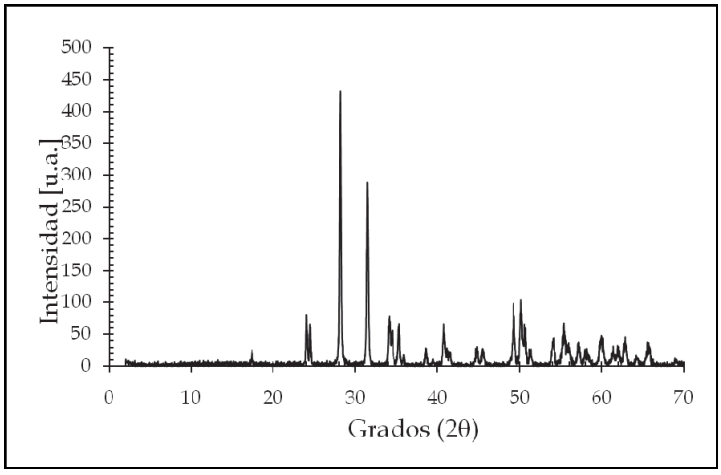

Fig. 4. X-ray diffractogram of zirconium oxide powder submitted at 1100°C

There has been increased interest in fabricating crystalline-textured materials using the influence of an external energy source against the luminescent property of the materials. It is well known that many solid-solution systems can produce semiconducting materials with properties that are useful for electronic and optical applications. One requirement that needs to be considered when using ceramics as luminescent materials is their microstructural properties since those ceramics must be subjected to vibration and strain.

4.2 Scanning electron microscope

The scanning electron microscope (SEM) has proved of great value in the examination of luminescent ceramic materials obtained for two different method preparations (precipitation and sol-gel). In a scanning electron microscope, a tiny electron beam is scanned across the

sample. Simultaneously, the generated signals are being recorded, and an image is formed pixel by pixel. Valuable information about morphology, surface topology and composition can be obtained (De Lange et al., 1995). SEM microscopes achieving resolutions below 1 nm are available now. This technique forms images with electrons instead of light allowing high magnification photographs with excellent depth of field. At 100,000X magnification a penny is roughly a mile in diameter. The EDS detector on this instrument allows identification of the elements present in ceramic matrix as impurity (Hernández et al., 2009). The scanning electron microscope (SEM) is one of the most versatile instruments available for the examination and analysis of microstructural characteristics of ceramics (Hideo et al., 2006). The primary reason for the usefulness of the SEM is the high resolution that can be obtained when bulk objects are examined. Scanning Electron Microscopy (SEM) has been for high magnification imaging and elemental analysis. For morphological ceramic characterization a Jeol JSM-6400 scanning electron microscope equipped with an energy dispersive spectrometer (EDS) has been used. According to figure 5 on micrography of Al_2O_3 ceramics obtained at 1400°C, it can be observe a heterogeneous microstructure with regions of small grains and regions of large grains of irregular shapes and the presence of micropures intergranulares. As sintering thermal process is increase micropures intergranulares decrease in the size still the micropores are overlapping (see fig. 5). This phenomenon is observed as sintering temperature is increased to achieve uniformity in the microstructure and so compact of the powders is observed. Pores distribution and surface area of ceramics can be measured using the SEM techniques and these properties can be correlated with luminescence properties.

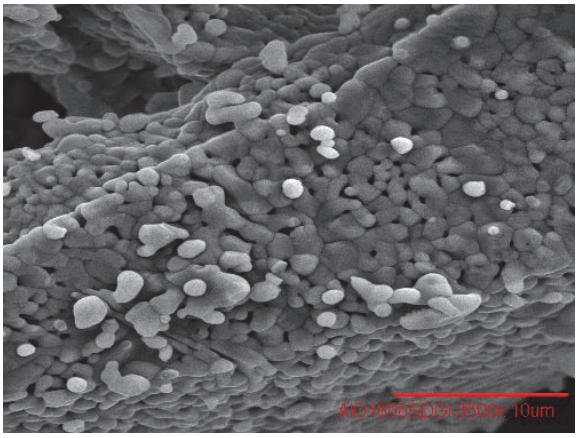

Fig. 5. Scanning electron microscopy micrographs of Al_2O_3 ceramics

5. Luminescent characterization

Enormous progress has been made in recent years in the study of ceramic free surfaces, grain sizes, grain boundaries, and ceramic or metal interfaces. High resolution TEM, analytical electron microscopy, scanning probe microscopies, and surface and interface spectroscopies are amongst the tools which have contributed greatly to developing an atomic level understanding of such phenomena as intergranular film formation, crystalline surface

anisotropy, wetting, and heterogeneous chemical reactions. These tools and approaches should now be brought to bear on ceramic properties for luminescent applications.

5.1 Luminescence process

Luminescence is "cold light" from other sources of energy, which can take place at normal and lower temperatures. In luminescence, some energy source kicks an electron of an atom out of its ground state into an excited state; then the electron gives back the energy in the form of light so it can fall back to its ground state (Mishra et al., 2011). Fluorescence and phosphorescence are two special aspects of luminescence. The phenomenon is fluorescence if emission takes place by one or more spontaneous transitions. If the emission occurs with the intervention of a metastable state followed by return to the excited stated due to addition of energy, then this is called phosphorescence (Furetta & Weng, 1998). There are varieties of luminescence phenomena observed in the nature or in manmade articles. The nomenclature given to these is invariably related to the exciting agent, which produces the luminescence. i.e. (i) Photoluminescence is distinguished in that the light is absorbed for a significant time, and generally produces light of a frequency that is lower than, but otherwise independent of, the frequency of the absorbed light. (ii) When excitation is done by electron beams generated at the electrical cathodes, the emission produced is called cathodoluminescence. (iii) Chemiluminescence is not a common accompaniment in chemical reactions, because the amount of energy released even in the exothermic reactions is not sufficient to cause electronic excitation, which needs a couple of eV energy. (iv) Bioluminescence is luminescence caused by chemical reactions in living things; it is a form of chemiluminescence. (v) A large number of inorganic and organic materials subjected to mechanical stress, emit light, which is called triboluminescence. (vi) Thermoluminescence is phosphorescence triggered by temperature above a certain point. In thermoluminescence, heat is not the primary source of energy, only the trigger for the release of energy that originally came from another source.

5.2 Photoluminescence in ceramics

Photoluminescence (PL) is generally taken to mean luminescence from any electromagnetic radiation. The principles of PL are very simple an exciting light source is focused on to the sample under observation. The energy of the light normally exceeds the band gap energy of the ceramic (Nakajima & Mori, 2006; Song et al., 2002). The light sent out by the ceramic is collected and focused onto the slit of a monochromator. In the monochromator the light is dispersed by gratings and the monochromatic light is detected by a light sensitive detector. By rotating the gratings, different wavelengths may be detected and if the signal from the detector is simultaneously recorded one will obtain a spectrum. The differences in the PL intensities observed are generally attributed to the dopants or optical defects localized into ceramics. This, characterization techniques ha recently emerged as powerful tools for developing and monitoring the fabrication of high efficiency luminescent ceramics.

Optical and electronic properties of nanocrystalline materials strongly depend on their composition, structural and morphological characteristics, but also on the presence of defects. For crystallite size comparable to Bohr exciton radius of particular materials the quantum size effects become important, the band gap grows, and the optical and electronic properties of nanomaterial differ significantly from its bulk counterpart. On the other hand, presence of intrinsic defects and impurities may introduce different electronic levels within

the band-gap, which can cause the various electronic transitions mediated by these levels and variation of the optical band gap energy as well (Jacobsohn et al., 2010). The luminescence is a process of emission of optical radiation from a ceramic from causing other than heating it to incandescence.

Rivera et al. (Rivera et al., 1999) studied and obtained the PL emission spectrum of ZrO_2 prepared by the sol-gel method obtained by using an excitation wavelength of 270 nm. This spectrum exhibits a single peak with its maximum emission centred at 370 nm. Figure 6 shows the excitation spectrum of ZrO_2 obtained by using exciting light of 480 nm. Both emission and excitation spectra were obtained at room temperature. In figure 6, it can be seen that luminescent intensity of the beta-irradiated samples is higher than the luminescent intensity obtained from unirradiated samples. The PL excitation spectrum exhibits several peaks centred at around 390 nm when the samples were excited with light of 525 nm wavelength. However, the PL excitation spectrum consists of a single maximum emission centred at around 380 nm when the samples are excited with light of 480 nm wavelength.

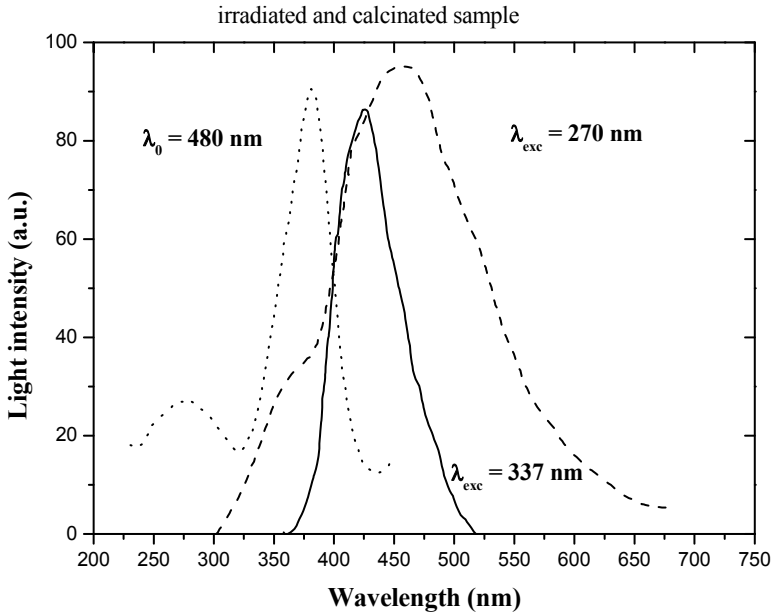

Fig. 6. Excitation spectrum of the intrinsic emission of polycrystalline ZrO_2 at RT described by dotted line (····). PL emission spectra of polycrystalline ZrO_2 powder samples for excitation wavelength of 270 nm described by dashed line (---). PL emission spectra of polycrystalline ZrO_2 powder samples for excitation wavelength of 337 nm described by solid line (—) beta-irradiated samples.

This result suggests that the PL excitation peak of 337 nm is insight of the broad structure composed by the highest emission. Thus, taking into account these results, it can be

suggested that the emission excitation obtained is almost independent of the excitation wavelength used. Therefore, excitation wavelengths of 480 and 525 nm produce the emission peaks at 380 and 390 nm, respectively. Using these emission maxima the PL emission peaks centred at 370 and 430, respectively, can be obtained. These results indicate that ZrO_2 has two absorber centres and that the PL emission comes from ZrO_2 network. There are oxygen vacancies in ZrO_2 powder, which can induce the formation of new energy levels in the band gap. Then, the emission spectra can be divided into two broad categories. The first is due to those energy levels created by oxygen vacancies and the second broad peak is due to the deep level. For the TL phenomenon, this property is very important because the TL emission could be correlated to PL emission. Moreover, the TL glow curve of ZrO_2 exhibits two peaks. Thus, the defects responsible for the 370 nm emission might be correlated to the second TL peak at around 260°C. Meanwhile, the 400 nm emission could be correlated to the first TL emission peak. Thus the TL emission of the second peak could be a result of the electrons retrapped by deeper traps or because of the electrons already present in the deeper traps. This property is very important for the TL phenomenon because the TL emission could be correlated to photoluminescence emission.

5.3 Thermoluminescence in ceramics

Thermoluminescence (TL) or thermally stimulated luminescence (TSL) is the light emission after removal of the source of exciting energy light, x-rays, or other radiation; the free electrons may be trapped at an energy level higher than their ground state by application of thermal energy. The transition of electrons directly from a metastable state to ground state is forbidden (McKeever, 1985). The metastable state represents a shallow electron trap and electrons returning from it to the excited state require energy. This energy can be supplied in the form of optical radiation (photo stimulation) or as heat (thermal stimulation). The probability p per unit time that a trapped electron will escape from a metastable state to an excited state is governed by the Boltzmann equation.

$$p = s.\ \exp(-E/\ kT) \tag{3}$$

where s is the frequency factor (sec-1), depending on the frequency of the number of hits of an electron in the trap which can be considered as a potential well, E is the thermal activation energy required to liberate a trapped charge carrier called trap depth (eV), k is Boltzmann's constant and T is the absolute temperature (K). First, the intensity of thermoluminescent emission does not remain constant at constant temperature, but decreases with time and eventually ceases altogether. Second, the spectrum of the thermoluminescence is highly dependent on the composition of the material and is only slightly affected by the temperature of heating. In the usual thermoluminescence experiments, the system is irradiated at a temperature at which the phosphorescence intensity is low, and later heated through a temperature range where the phosphorescence intensity is bright, until a temperature level at which all the charges have been thermally excited out of their metastable levels and the luminescence completely disappear (Chen & McKeever, 1997). The thermoluminescence emission mainly is used in solid state dosimetry for measurement of ionizing radiation dose.

5.3.1 Mechanism of thermoluminescence

The details of the mechanisms of thermoluminescence phenomena with result in recombination luminescence are still not completely understood. The mechanism of

luminescence in semiconductor involves at least two steps: (i) first ionizing radiation (IR) induced defects both electron traps (ET) and hole traps (HT) which are created and, (ii) free electrons and holes are created in the conduction band and the valence band, with the subsequent emission of photons in the visible region spectrum. Thermoluminescence is the thermally stimulated emission of light from an insulator or a semiconductor following the previous absorption of energy from ionizing radiation.
The thermoluminescence process can be understood in terms of the band structure model of semiconductor. In a semiconductor there are two relevant energy bands: (i) an almost completely filled valence band (VB) and (ii) an almost empty conduction band (CB). The two energy bands are separated by a forbidden band gap (FB), which means that between these two bands there are no electronic energy levels. Transitions of electrons between the valence band and the conduction band are allowed and they produce free electrons in the conduction band and free holes in the valence band. The energy difference between the two bands is denoted by the band-gap energy Eg (see fig. 7).

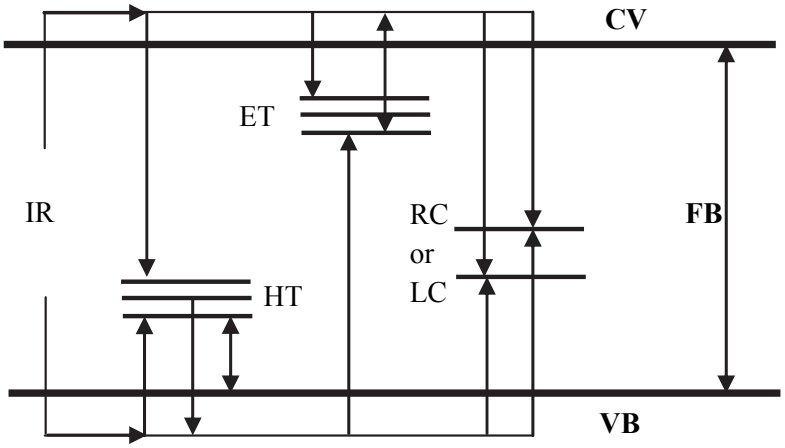

Fig. 7. Mechanism of the thermoluminescence process in a semiconductor

Due to ionizing radiation electrons are transferred from the valence band to the conduction band, which leads to the presence of significant concentrations of free electrons (in the conduction band) and free holes (in the valence band), in this case of electron-hole pairs case is created. To maintain electroneutrality of the crystal, for each electron, which is trapped at an electron trap a hole is produced, which might be trapped at a hole trap. During irradiation free electrons and holes can migrate in the crystal until they are trapped by impurities, luminescent centres and other imperfections in the crystal. Then the electrons and holes are (re-)distributed continuously over the available electron and hole traps (McKeever, 1985). After irradiation, the trapped electron or hole can be released is liberated from the trap by heating the crystal to moderate temperatures (optimum amount of thermal energy); it crosses a certain potential-energy barrier and when the electron recombines with a hole trapped at a recombination centre light is emitted ($h\nu$) in the recombination process. A similar reasoning holds for the case of luminescence produced by recombination of free holes at the electronic recombination centres.

5.4 Ceramic luminescence material

Phosphors for luminescent displays are commonly used in the form of powders. However, the role of particle size, shape, and crystallographic habit on excitation, quenching and emission is not understood. Fundamental studies which examine the fundamental luminescent characteristics of model particle systems of controlled purity, size and shape are necessary. The optical property has common applications in photochromic and colloid colored glasses (Wilkinson et al., 2004; Zhifa et al., 2010). Ceramics have found extensive applications in many important fields, such as thermal barrier coatings, laser coatings and hard overcoats. It is also considered a promising candidate for ionizing radiation dosimeter by means thermoluminescence phenomena (Brown et al., 1994).

5.5 Thermoluminescence materials

Thermally stimulated luminescence or better known as thermoluminescence (TL) is a powerful technique extensively used for dosimetry of ionizing radiations. TL dosimeter (TLD) materials presently in use are inorganic crystalline materials (McKeever et al., 1995). They are in the form of chips, single crystals or microcrystalline size powder. The most popular are LiF:Mg,Ti, LiF:Mg,Cu,P, CaF_2, $Li_2B_4O_7$, $CaSO_4$:Dy, CaF_2:Dy (Azorín et al., 1993; Bhatt et al., 1997; Fox et al., 1988; Madhusoodanan & Lakshmanan, 1999). All materials described above are in microcrystalline sizes. However, with the use of very tiny particles such as nanoscale TLD materials, this problem is overcome to a major extent. The TL results of the recently reported nanomaterials have revealed very imperative characteristics such as high sensitivity and saturation at very high doses (Noh et al., 2001; Sahare et al., 2007; Salah et al., 2011). However, recent studies on different luminescent ceramic micro or nanomaterials showed that they have a potential application radiation dosimetry using TL technique (Azorín et al., 2007).

These materials spread over various applications such as medical imaging, high energy physics, and nondestructive testing. During the last two decades, numerous ceramic materials have been proposed to be used as radiation detectors. Among them, a lot of oxides materials have successfully been developed up to luminescent applications. In order to provide efficient dosimeters for X or γ rays, the choice of the oxide matrix is crucial. Since the first step of the detector mechanism involves absorption of energy photon, photoelectric absorption, Compton dispersion and creation pairs effect has to be favoured. Then, materials with high $\rho.Z^4_{eff}$ could be are suggested. In this formulation, ρ is the density of the material and Z_{eff} is the effective atomic number defined as (Van Eijk, 1997).

$$Z^4_{eff} = \Sigma_i w_i Z^4_i \quad (4)$$

where w_i is the mass fraction of atom i and Z_i is its atomic number.

More recently, research focused more on improving the performances of known radiation detectors rather than developing new materials. It appears that a good way to improve detectors is to get a control of the material on a nanometric scale. It is indeed very important to control the dispersion of doping ions in the matrix and to control the size of the grains in case of powders. The possibility to prepare nanocrystalline powder could allow the preparation of ceramics that could replace traditional thermoluminescent material. Another very attractive solution is the direct preparation of radiation detecting thin films. Thin detecting films are particularly valuable in fundamental spectroscopic studies when the

absorption coefficient of the material is high or when the excitation energy is close to the absorption edge. They are also very interesting for high-resolution imaging where the film is required as a homogeneous coating. Both solutions provide low-cost substitutions for single crystals. The use of sol-gel processes for the preparation of luminescent ceramics seems to be a very interesting way to reach these objectives. In effect, the use of molecular precursors is the guarantee of very high chemical homogeneity which is usually also observed in the final material. Furthermore, the high versatility of the sol-gel process allows to reach various compositions and to vary the nature and the concentration of the doping ion easily.

6. Luminescent ceramic application

The nature and applications of optical luminescent ceramics have evolved rapidly in recent years. Their role as passive optical elements has been emerged by so-called photonic systems. These can have many active components oscillators, amplifiers, frequency and so on, most of which rely, to some degree, on optical field confinement (Kirm et al., 2005). The design of appropriate materials for this new technology involves progress on two separate levels. There is a need both for the optimization of microscopic electronic properties and for the separate control of bulk optical parameters on the scale of optical wavelengths (Lee & Rainforth, 1994). In the last years most of the work done in the Flat Panel Displays (FPD) area has been focused to the development of luminescent films based oxides of high quality, that can be applied as optically active layers in photoluminescent, cathodoluminescent and luminescent devices, for this purpose it is necessary to obtain flat and transparent films in order to obtain a device with a good resolution, contrast and efficiency characteristics (Chacon et al., 2008; Zhang et al., 2005). The optical ceramic preparing techniques were successfully developed in past years; the production of the transparent ceramic from ceramic nanopowders has high importance (Garcia et al., 1997; Gutzov & Lerch, 2003). ZrO_2 (zirconia) is a widespread material due to large number of different applications, e.g., material for sensors, semiconductor devices, biocompatible material, and luminescent material. The luminescence of ZrO_2 ceramics has been studied mainly for yttria-stabilized zirconia containing rare earth dopands and for mixed zirconia–alumina ceramics (Rivera et al., 2010b). The range of optical ceramic application is extended significantly since the transparent ceramic was sintered. The ceramic materials have some advantages over single crystals: easy fabrication, lower cost, large homogenous samples, and possibility to doping with rare earths elements.

Ceramic materials have been suggested for medical imaging in X-ray Computed Tomography (Moses, 1999; Van Eijk, 1997). The studies and developments of ceramic materials for detectors and scintillators are essential for many radiation dosimetry applications. Transparent ceramic materials with fast luminescence decay, low afterglow, high density (or radiation stopping power) and luminescence response in the visible region are required for technological applications. One of the promising materials for X and gamma rays detection is ZnO mainly for medical imaging. Another of the promising ceramic material for ionizing radiation and non ionising radiation dosimetry is ZrO_2. The luminescence results of ZrO_2 is in spectral region obtained at room temperature, this spectrum covers the wide range (190–370 nm) of the TL excitation spectrum (Rivera et al. 1998), which in turn resembles the activation spectra of most of the UV-induced biological effects.

6.1 Ceramics in medicine

In recent years, bioceramics have helped improve the quality of life for millions of people. These specially designed materials (e.g. polycrystalline alumina or hydroxyapatite or partially stabilized zirconia, bioactive glass or glass-ceramics and polyethylene-hydroxyapatite composites) have been successfully used for the repair, reconstruction and replacement of diseased or damaged parts of the body, including bone (Roriz et al., 2010). Applications include orthopaedic implants (vertebral prostheses, intervertebral spacers, bone grafting), middle-ear bone replacements and jawbone repair (Chun et al., 2004; Emerich & Thanos, 2003,). For instance, alumina has been used in orthopaedic surgery for more than 20 years as the articulating surface in total hip prostheses because of its exceptionally low coefficient of friction and minimal wear rates. Microporous bioceramics based on calcium phosphate, with pores >100 to 150 microns in diameter, have been used to coat metal joint implants or used as unloaded space fillers for bone ingrowth (Kokubo, 2008). Ingrowth of tissue into the pores occurs, with an increase in interfacial area between the implant and the tissues and a resulting increase in resistance to movement of the device in the tissue. As in natural bone, proteins adsorb to the calcium phosphate surface to provide the critical intervening layer through which the bone cells interact with the implanted biomaterial (Flach et al., 1994).

Zirconia is used as a femoral head component in hip implants. High strength and high toughness allow the hip joint to be made smaller which allows a greater degree of articulation. The ability to be polished to a high surface finish also allows a low friction joint to be manufactured for articulating joints such as the hip. The chemical inertness of the material to the physiological environment reduces the risk of infection. Nanosized zirconium oxide should be is an ideal ceramic for dental applications because of its strength and transparency to light, but it is opaque to x-rays, making it an excellent material for UV-cured dental fillings (Studart et al., 2007). The need for understanding of ceramic biological interfaces obviously extends to other applications of bioceramics (e.g., joint replacements, implants), although the specific needs are not addressed here. It should be stressed that collaboration with those in the dental and medical fields is essential for effective research in these areas.

6.2 Ceramics in radiation dosimetry

Since the discovery of X-ray by Rontgen and the concomitant use of the first dosimeter, research directed towards materials that can convert energy radiations (X-rays, γ-rays) into visible light, easily detectable with conventional detectors, is in constant development (Bhatt et al., 1997). A current interest of synthesizing and processing of advanced materials. The sol-gel technique is a low temperature method which uses chemical precursors to produce ceramics and glasses with better purity and homogeneity than the conventional high temperature processes. The sol-gel technique has been used to produce a wide range of compositions (mostly oxides) in various forms, including powders, fibbers, coatings and thin films, monoliths and composites, and porous membranes (Somiya et al., 1988). The sol-gel process to produce zirconia involves the hydrolysis and condensation of alkoxides. By controlling the synthesis conditions carefully, the sol morphology can be directed towards branched polymeric systems. Control of relative rates of hydrolysis and polycondensation, and the respective mechanisms of these reactions are the main tools for this difference

(Rivera et al., 2007c). This new preparation method of nanophosphors has been recently strongly developed for producing high efficiency luminescent materials. For the preparation of ZrO_2 it is important to retain a high degree of crystallization and its possible correlation with the concentration of defects should be well-known. For this purpose new techniques to prepare well defined nanopowders have been used. A recent study on nanocrystalline ZrO_2 obtained from amorphous zirconia demonstrated several unique features of nanocrystalline processing (Rivera et al., 2006).

Thermoluminescence (TL) is a very common technique used for dosimetry of ionizing radiation (Azorín, 1990). During TL, the energy absorbed by a phosphor previously exposed to ionizing radiation is released as light during the heating of the material. The intensity of light emitted by the phosphor is proportional to the irradiation dose given to it. Different preparation methods and properties of several TL materials have been studied so far and it was found that metal oxides doped with proper activators constitute a class of promising TL phosphors (Rivera et al., 2007a). The TL dosimetry (TLD) technique offers the advantage of being able to place the dosimeters in outdoor stations for solar radiation monitoring, without requiring any additional special monitoring or logistic considerations. ZrO_2 is suggested by us as a suitable TLD material to accomplish this task. The luminescence of zirconia ceramics was not studied in detail and the comparison of single crystal, ceramic and nanopowder luminescence could be fruitful.

6.2.1 Ceramics for UV dosimetry

Pushing the limits of transparency in ceramic materials further into both the UV and the IR is of extreme importance in many applications. The humanity is constantly exposed to ultraviolet (UV) natural radiation reaching the surface of the earth. An important part of the UV spectrum is considered to be low energy ionising radiation. One of the former materials studied for possible use as a dosimeter is aluminium oxide (Al_2O_3) (Colyott et al., 1997). Recently, for monitoring the ultraviolet radiation (UVR) different materials have been employed using the thermoluminescence (TL) method (Chang & Su 1992; Driscoll, 1996, Colyott et al., 1999). This technique has an advantage over other methods owing to the simplicity of the sample readout. Another advantage of this method and these phosphors include their small size, portability, lack of electrical power requirements, and linear response to the increasing radiation dose and high sensitivity (Van Dijken et al., 2000; Wang et al., 2005). ZrO_2 was firstly proposed in 1990 as a TL material showing good dosimetric performances under the ultraviolet and visible light (Hsieh & Su, 1994; Rivera et al., 1998). Since then, several additional studies have been reported (Rivera et al., 2005a; 2005b; Azorín et al., 1999). Zirconium oxides have recently received considerable attention in view of its possible use as a TL dosimeter (TLD), if doped with suitable activators. These authors have been studied and developed thermoluminescent characteristics of various ceramics. Some of them were introduced into every day practice. For example, TLD pellets based on aluminium oxide are accepted and practically used in all applications. TLD pellets based on zirconium oxide and zirconium oxide doped with manganese and copper is developed to ultraviolet radiation dosimetry.

Pure oxides both monoclinic zirconia and α-alumina have been studied after ultraviolet irradiation, before and after the thermal treatment at 1400°C under oxygen. TL glow curve of α-alumina presents two peaks 260 nm after UV irradiation centred at 180°C and 350°C respectively. The monoclinic zirconia, which is discussed in mayor forms during this

chapter, the maximum peak is observed a change of positions, depending on the method preparation, when these are exposed to ultraviolet radiation. Thus, co-precipitation method gives the maximum at about 160°C. Sol-Gel method shows two peaks centred at 150°C and 230°C, respectively, with a maximum at about in 150°C. When compared by light output sum, the luminescent ceramic obtained by co-precipitation method demonstrate about one half efficiency of one obtained by Sol-Gel. In the case of alumina-zirconia mixtures is not response under UV irradiation.

6.2.2 Ceramics for ionising radiation dosimetry

The scientific study of thermoluminescence phenomena has an extremely rich history spanning many centuries and interacting with many other fields of endeavour: archaeology, geology, medicine, solid-state physics, biology and organic chemistry, to name just some of the mainstream areas of study. Many research groups are interested in thermoluminescence application to ionising radiation dosimetry as well as in the development of radiation response materials for solid state systems (Akselrod et al., 1990). These areas of endeavour are of major importance in fundamental questions of radiation medicine, which in turn can have great impact on questions concerning the future of radiation safety and the effects of interaction of radiation in matter, both beneficial and harmful, with the human organism. Although various thermoluminescent materials have been heretofore developed, practical uses of such materials has been limited due to numerous limitations in the materials themselves. For example, some materials require a relatively high energy input (light used to excite electrons) in order to trap a sufficient number of electrons to provide a relatively low afterglow effect. On the other hand, materials which are more efficient at trapping electrons may have trap depths which preclude room temperature level thermal energy from releasing the electrons and causing the light emission. Although the latter materials may be useful for other phenomena, such trap depths are not desirable or suitable for thermoluminescent material. Materials which have a very low electron trap depth do not store electrons sufficiently securely to allow an afterglow effect to last for an appreciable time after removal of the light or other energy used to excite the electrons. That is, the afterglow effect might be noticeable for a relatively short period of time (under one second), but the emission of light due to room temperature level of thermal energy may not be at all noticeable in such materials after a slightly longer period of time (10 seconds). The above and other limitations were disadvantageous of previously available thermoluminescent material has greatly limited the possible applications for using the phenomena of thermoluminescence. Additionally, the range of possible uses for thermoluminescent material has been limited by the restrictions in form of various thermoluminescent materials. As used herein, thermoluminescent material, shall refer to material having an afterglow which is perceptible by an unaided human eye and having a time duration depended upon the temperature. The large interest in TL as a technique for radiation dosimetry in environmental, personal and clinical applications pushes the research for producing new and high-performance TL materials. Zirconium oxides have recently received considerable attention in view of its possible use as a TL dosimeter (TLD), if doped with suitable activators.

The Thermoluminescent (TL) glow curve of zirconium oxide obtained by sol-gel method shows main maximum also was observed at different positions, depending on the source irradiation (see fig. 8). Thus, zirconium oxide beta irradiated (dashed line (---) gives the

maximum at about 180°C. Zirconium oxide exposed to X-ray diagnostic beam (solid line (—)) shows two peaks centred at 160°C and 260°C, respectively, with a maximum at about in 260°C. In the figure, the second peak is the most prominent one and its amplitude is about 1.5 times that of the first peak.

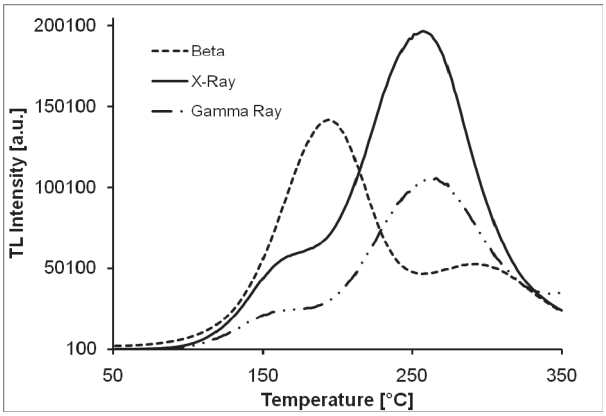

Fig. 8. TL response of ZrO_2 exposed to photons and particles beams.

The shape of the glow curve remains almost the same for exposures between 2 and 100 Gy, but the relative heights of the two peaks change as a function of beta-absorbed dose; and zirconium oxide gamma irradiated (dashed and dotted line (-..-..-..) shows a TL glow curve very similar than obtained than that obtained by X-ray exposed. When compared by light output sum, the luminescent ceramic gamma irradiated demonstrate about one half efficiency than that one in X-ray exposed. TL sensitivity of zirconium oxide under beta irradiated demonstrates less sensitivity than those ZrO_2 X-ray photon beams irradiations. The width of the main peak suggests that the activation energies of the traps form a continuous distribution. Thermoluminescent technique has an advantage over other methods owing to the simplicity of the sample readout. Other advantages of this method and these phosphors include their small size, portability, lack of electrical power requirements, linear response to the increasing radiation dose and high sensitivity. The large interest in TL as a technique for radiation dosimetry in environmental, personal and clinical applications pushes the research for producing new and high-performance TL materials.

Thermoluminescent (TL) response of ceramics as a function of ionising radiation absorbed dose depends on several factors. The simplest case is obvious: no side recombination and storage process, and the only kind of trapped state is involved into the energy storage. Nevertheless, side recombination processes are sometimes linear, and hence, can be present without affecting the linearity of the dose response. Then, the development of convenient thermoluminescent material with a good linearity requires very pure starting materials and rigidly controlled method preparation. Ceramics oxides (both aluminium oxide and zirconium oxide) are a good material for environmental dosimetry. They have a high sensitivity and linear dose dependence in a wide range of radiation doses for environmental monitoring. These ceramics show also good application for ionising radiation dosimetry in medical applications due to their wide range dose linearity. Rivera et al. (Rivera et al., 2007a) determined TL response of zirconium oxide as a function of ionising radiation absorbed

dose (e.g. gamma absorbed dose and beta absorbed dose). These authors obtained a good linearity in a wide range dose (see fig. 9). As it can be seen in figure, ZrO_2 showed a linear response from 2 to 100 Gy denoted by full black square figures (■) after gamma irradiations. Meanwhile, ZrO_2 under beta also exhibited a linear response at the same range dose which denoted by full black triangle (▲).

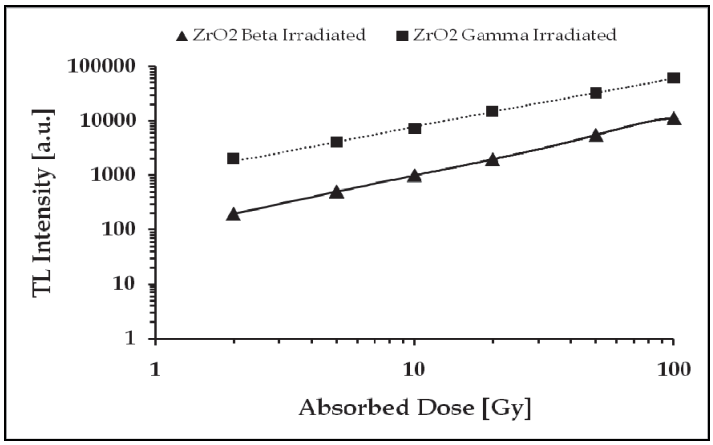

Fig. 9. TL response of ceramics as a function of IR absorbed dose

Reusability is one of the most important characteristics and another very useful property that a TL material should possess in order to be used in practical dosimetry. The Standard guide suggests reusability better than 5% standard deviation for those phosphors proposed to be used as TL dosimeter. In order to perform this test, the samples were exposed to 10 Gy of gamma absorbed dose; the TL glow curve recorded heating the samples up to 350°C at a heating rate of 10°C/s and then annealed. Several such cycles of exposure, glow curve recording and annealing were performed. No significant change in the intensity of both 160 and 260°C peaks were observed. Experimental results are shown in figure 10, confirming that reusability characteristics after 10 cycles of reading–irradiation was ±2.5% S.D. (see fig. 10).

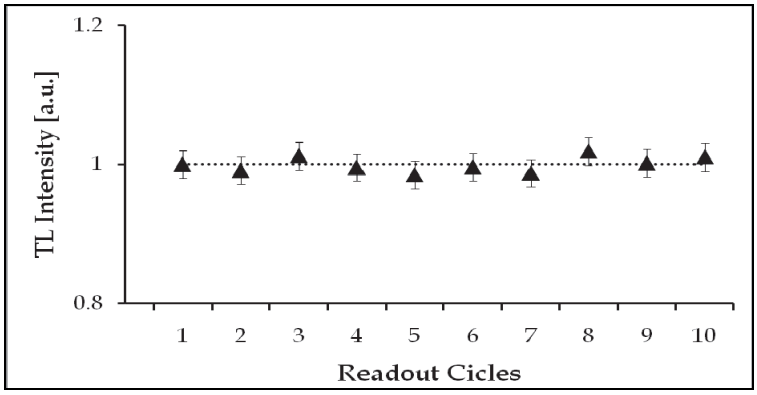

Fig. 10. Reproducibility of polycrystalline ZrO_2 powder

If the samples have to be used in radiation dosimetry, their TL response must be stable and not fade appreciably upon storage after exposure. In order to check the stability characteristics of ZrO_2, several samples were irradiated and subsequently stored at RT in a dark place for a month. After storage it was found that the 260°C glow peak was quite stable. ZrO_2 lost 30% of its information during the first 2 h after irradiation. After that, only 3% fading was observed during the next 30 days, indicating no serious fading problem for dosimetric applications.

6.2.3 Dopant effect on ceramics

Solid-state band theory provides a way to explain the luminescence phenomenon. This explanation consist in an insulating solid material with forbidden gap, in this there are metastable states where electrons are trapped when insolate is excited. If the energy lost when the electrons are vacated from the traps is emitted in the appropriate energy or wavelength range, luminescence will result. There are several possible kinds of the traps can to produce luminescence. If the luminescence is produced by structural imperfections which are characteristics of the host lattice is called intrinsic luminescence (Asiltürk et al., 2011; Bourgoin & Lannon, 1983; Li et al., 1995). Extrinsic luminescence is another kind of luminescence which results from impurities in the structure. The impurities generate luminescent centres and are most commonly transition elements, rare earth elements and actinide elements (due to the occurrence of valence electrons in either "d" or "f" orbital). These impurities are generally the most common source of luminescence in ceramics (Bao et al., 2007; Ekambaram, 2005; Jung et al., 2005). Some of these impurities are trace elements that promote luminescence in a ceramic material (substitutional). In general, the intensity and wavelength of the luminescence is dependent on the electron configuration of the activator ion and the nature of the lattice that holds the ion luminescence (Ming & Tang, 2011). These dopants present in thermoluminescent phosphors induce higher luminescence efficiency either due to better incorporation of activator ions or due to improvement in energy transfer processes (Rivera et al., 1999). Doping with ion activators of the thermoluminescent phosphors resulted in increasing the TL sensitivity from 1.2 to 3.4 times, when compared with that of the TL phosphors without ion dopant (Rivera et al., 2007d; J. Zhang et al., 2002). It is observed that the addition of ion dopant induces in some TL phosphors enhancement of the higher temperature peak which is correlated with the increase of TL sensitivity. The high TL output of these TL phosphors could be used in dosimetric practice for special short-term measurements.

The substitution of impurities ions into insulating host crystals introduces lattice strains and, for non-trivalent sites, a need for charge compensation. Such effects alter the site symmetry and this is reflected in properties such as the wavelength, line width, lifetime and relative intensity of the ion transitions. The ions are variously incorporated as substitutional ions, pairs, clusters, or even as precipitates of new phases, but the detailed modelling is often speculative. There are numerous differences in glow peak temperature, for nominally the same defect sites, which are thought to indicate charge trapping and recombination within coupled defect sites, or within a large complex. Size and cluster effects can be modified by heat treatments (Rivera et al., 2007b). Other impurities inhibit or eliminate thermoluminescence in a material intensity; this effect is known as quenching. The fact can be seen that both TL glow peaks reach the maximum when the activators Cu is introduced into ceramic matrix, and the TL intensity is reduced still 3 times than that obtained with the

ceramic without impurity as well as reported by Rivera et al (Rivera et al., 2007b). This effect may is attributed a lattice distortion. When the dopant atoms with large radio come into matrix lattice, the lattice will be distorted. The fact can be found out in Figure 11 that the intensity of low energy emission band is reduced and that of high energy emission band is enhanced with the presence of copper ion (Cu+); on the contrary, the intensity of low energy emission band is enhanced and that of the high energy one is reduced with the presence dopant Mg. Lattice distortion effect is showed by Rivera when ZrO_2 ceramics were exposed to UV radiation. They reported their results and plotted in figure 11. In this figure, as it can be seen TL glow curve of ZrO_2 exhibited two peaks at around 90 and 160°C denoted by line solid (—). The TL glow curve of ZrO_2 doped with cooper (Cu) and magnesium (Mg) showed a single peak. ZrO_2:Mg ceramics exhibited a main peak centred at around in 130°C denoted by dotted line (····). Meanwhile, ZrO_2:Cu exhibited one peak centred at around of 180°C denoted by dashed line (---). The position peak is shifted for about 50°C.

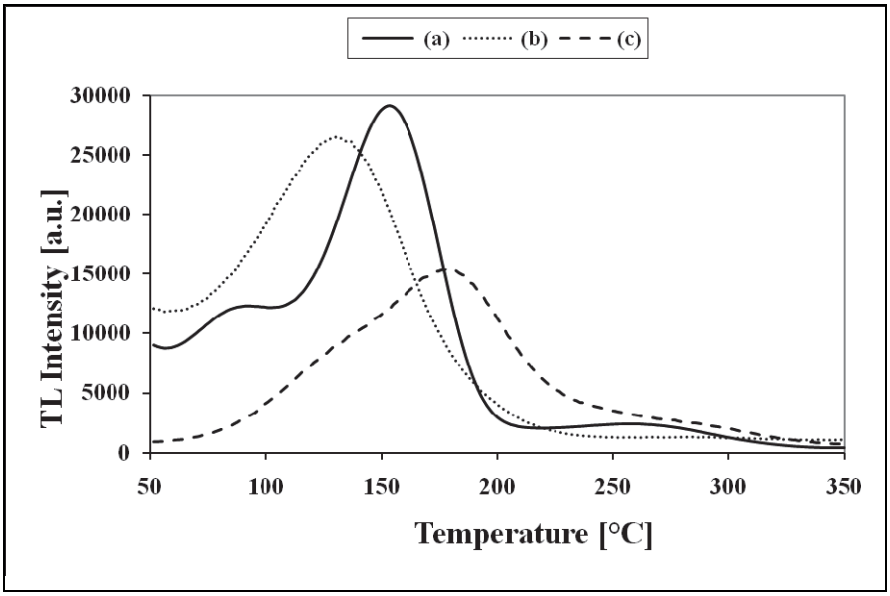

Fig. 11. Effect of dopant in ZrO_2 ceramics exposed to UV radiation

Ceramics oxides doped with impurities are a good material for environmental dosimetry. They have a high sensitivity and linear dose dependence in a wide range of ultraviolet radiation doses for UV monitoring; this effect was confirmed by Rivera et al. (Rivera et al., 2007b). They obtained experimental results zirconium oxide doped with various dopants (ZrO_2:VD) as a function of UV radiation analyzed by thermoluminescence phenomena (see fig. 12). In this figure shows this TL response as a function of spectral irradiance. It can be seen, ZrO_2:Mg showed a linear response from 50 to 4600 mJ/cm² denoted by full black square figures (■). Meanwhile, ZrO_2:Cu exhibited a linear response from 20 to 2400 mJ/cm² denoted by full black circle (●).

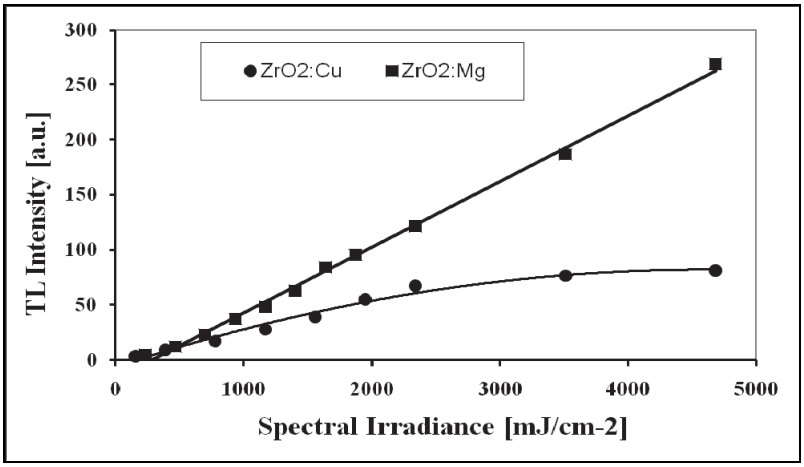

Fig. 12. TL response of ZrO_2 as a function of spectral irradiance of UVR

The same authors also studied the dopants effect in ceramics when are submitted under ionising radiation field. They concluded glow peak shifted is correlated of kind of dopant in ceramics matrix (see fig. 13). In this figure zirconium oxide doped with cooper and magnesium was irradiated with beta radiation. As it can be seen in figure 13, TL glow curve of ZrO_2 denoted by dotted line (····) exhibits two peaks centred at around of 160 and 260°C respectively, when this is submitted to an absorbed dose up to 10 Gy. As absorbed dose is increased up to 10 Gy a second peak appeared at around 260°C.

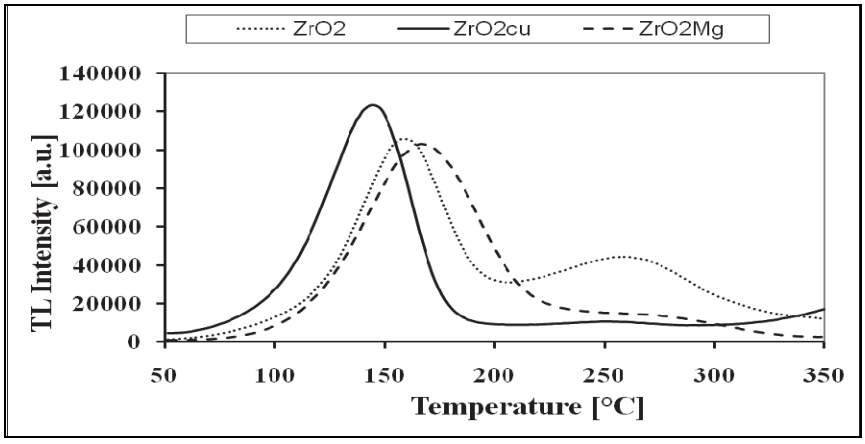

Fig. 13. Effect of dopants in ceramics beta irradiated

The TL glow curves of ZrO_2:Mg denoted by dashed line (---) has just one peak centred at around of 180°C. Ceramic of zirconium oxide doped with cooper ions (ZrO_2:Cu) denoted by solid line (—) also show one main peak centred at around 130°C. As absorbed dose is increased a second peak appeared at around 250°C. The first peak of the zirconium oxide doped with dopants is shifted for about 50°C; this effect is attributed to the dopant ions. The

TL glow curves can be conceived as composed by many closely spaced peaks resulting in a broad TL curve in which individual peaks cannot yet resolved. The shape of the glow curve for all samples remains almost the same for all irradiation exposures; however, the relative peak heights change as a function of radiation dose.
TL response as a function of beta absorbed dose is also analyzed by Rivera et al. They show zirconium oxide doped with cooper (ZrO_2:Cu) exhibits a linear response from 2 to 35 Gy (see fig. 14) which is denoted by solid line (—) and TL response of zirconium oxide doped with magnesium (ZrO_2:Mg) as a function of beta irradiation, which exhibited linearity from 2 to 35Gy. Each experimental data point represents the average response over five irradiated pellets.

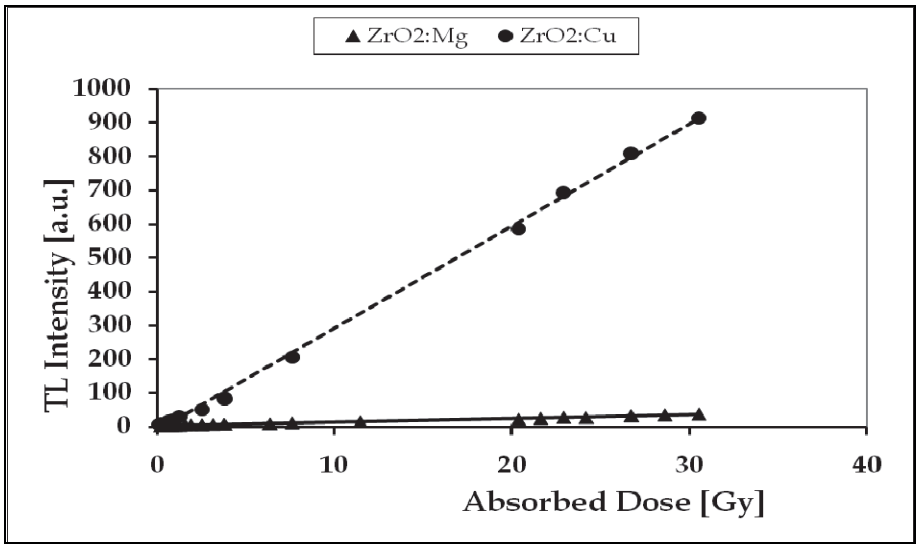

Fig. 14. TL response of ZrO_2 as a function of beta dose

6.3 Ceramic material for the 21th century

Nanotechnology can be defined as the science and engineering involved in the design, synthesis, characterization and luminescent application of ceramic materials and devices whose smallest functional organization in at least one dimension is on the nanometer scale (Emerich & Thanos, 2003). The genesis of nanotechnology can be traced to be promise of revolutionary advances across in medicine, medical physics, biomedical, and robotics.
Nanotechnology covers a broad range of fundamental and applied topics in the field of oxide ceramics, such as novel processing techniques and equipment; solidification and crystal growth; analysis and characterization; structural ceramics; mechanical properties and applications; defect transport and related phenomena; modelling of processes and properties; advances in electro-ceramics; oxide based ceramics for energy applications; applications and development of porous ceramics; nano-structured oxide ceramics; functional oxides and applications; transparent and luminescent ceramics. In semiconductor area, nanostructured semiconductors will be developed ceramics with non-linear optical properties, with quantum confinement effects which may lead to special properties, like the

luminescence in silicon powders and silicon germanium quantum dots as infrared optoelectronic devices. Nanotechnology optoelectronics will be the most attractive nanophosphors development for high-definition television and flat panel displays. This, opening the way for optoelectronic chips and possibly new type of colour displays. Also efficient light-emitting diodes based on quantum dots with a voltage-controlled, tuneable output colour. In optics glass ceramics will acquire importance in graded refractive index (GRIN) optics for developing of special plastic lenses or inexpensive colored glasses and optical filters.

Applications of ceramics in medicine are specially promising and areas as diagnosis imaging treatment of tumours. In biomedical, nanostructural ceramic materials with sizes 1 to 100 nm can act as new and effective constituents of bone materials. Besides the ceramic applications in medical diagnostic instruments, the field of bioceramics for bone replacement and chemotherapy release capsules is here. As ceramic materials improve in terms of strength, nonreactivity, compatibility, longevity, porosity for tissue growth, and lower costs, more use of ceramic devices will be seen. Several studied have reported improved osseointegration on nanostructure surfaces created from ceramics (Chun et al., 2004). Noninvasive imaging techniques have had a major impact in medicine over the past 25 years or so. The current drive in developing techniques such as functional magnetic resonance imaging (MRI) is to enhance spatial resolution and contrast agents. Computed tomography (CT) is a medical imaging technique that has become an important medical diagnostic tool over the last 15 years. This technique reconstructs cross-sectional images of the body and head by scanning the patient with X-rays. Body tissues and bones intersected by the X-ray beam can be imaged. In addition to medical applications, CT is being used for industrial inspection of aircraft engine components. At the heart of a CT system is the detector, consisting of a number of scintillator elements (Kirm et al., 2005). A scintillator is made out of a solid state luminescent material that converts high energy radiation into useful visible light. A ceramic material based on a combination of rare earth oxides (e.g. Eu^{3+}, Tb^{3+}, Ce^{3+}, Dy^{3+}) has been suggested that meets these requirements. In addition to being transparent, the material has an absorption efficiency of 99%, scintillation efficiency three times that of conventional detector materials. The afterglow property of this material is very low in crisp edge definition that is maintained between acquired views during scanning. This property is necessary in order to produce smoother, sharper images and superior low contrast detection without the risk of increased radiation dose to the patient. Thus, a more accurate and safer diagnosis can be made. Further research will lead to ceramic scintillators with higher X-ray stopping power, faster speeds and lower costs that can be tailored to specific applications. Whether used for imaging the human body or aircraft parts, such improvements can only result in more saved lives.

The radiation dosimetry in medical physics applications will be revolutionized with the development of optic fibres. Development of optical fibres luminescent technique and microminiaturization of components will come the incorporation of optical luminescent ceramics to real time in vivo dosimetry. Nanocrystalline ceramics developing and enhancement luminescent properties promise as a good candidate for high dose measurements. Crystalline ceramics will be used in nuclear accident where retrospective dosimetry is urgently required in order to advance epidemiological studies of the population.

7. Conclusion

In this chapter synthesis and luminescent characterization properties of ceramics using thermoluminescent phenomena were analyzed. In this chapter an enhancement of luminescence property in ceramics is attributed to dopant ions effect. The position change of the TL glow peaks is attributed to preparation method. It changes observed in many nanostructured materials that the energy level bands are altered or reorganized to the dopant ions effect could be due to the creation vacancy into the crystal field effects. The change of the position of the main peaks as function excitation energy (e.g. UV radiation, X-rays or gamma rays) is observed in these ceramics. It changes observed in many nanostructured materials that the energy level bands are altered or reorganized to the particle size effect could be due to the absence of crystal field effects. This change may be attributed to creation of vacancy effect due to radiation energy, trap distribution and cross section of the absorber materials. It is known that on decreasing the particle size to nanoscale, the band gaps are widened. Due to the widening of the bandgap, the energy levels of the host of ceramics doped with dopant might also get reorganized. On irradiation to high-energy radiation, the population of the trapping or luminescent centers (TC or LC) get change, this effect should be reflected on the occurrence of different intensities for the TL glow peaks. According to this effect, the number of traps generated by the high-energy radiation in the traps depends not only on the cross-section of the traps but also on the deep of the traps inside the matrix. It is evident that in the case of a single crystal or a microcrystalline powder, high-energy radiation (such as gamma rays or x-ray beams accelerated having energy of the order of MeV) could generate a track of approximate length equal to dimensions of the crystal or crystallites while penetrating through it. This could be of the order of several mm. But in the case of nanocrystallites, the length of such tracks will be only of the order of few tens of nanometers (dimensions of the nanoparticles). If it, therefore, compares the number of TC or LC generated in the nanocrystalline it would be much less than that in the case of a single crystal or microcrystalline powder sample for low doses. However, as the dose increases, more overlapping tracks occur, which might not give extra TL and saturation occurs in the case of a single crystal or microcrystalline powder material. However, in the case of nanoparticles, there still exist some particles that would have been missed while being targeted by the high-energy radiation, due to the very tiny size of the particles. Other, advantages of the nanoparticles is the slow down the process of generating the competing traps at different levels, giving rise to a somewhat low sensitivity but a good linearity over a very wide range of doses. From the application point of few, the easy method of preparation, good sensitivity, simple glow curve structure and TL response over a wide range of exposure are some of the good characteristics of the presented luminescent ceramic nanopowders. Therefore, it might be used as a dosimeter for low as well as high doses of ionizing radiations that has several applications such as medical physics.

8. References

Agarwal, M.; De Guire, M. R. & Heuer, A. H. (1997). Synthesis of ZrO_2 and Y_2O_3-doped ZrO_2 thin films using self-assembled monolayers. *American Ceramics Society.* Vol. 80, pp. 2967-2981.

Aguilar, D. H.; Torres, L. C.; Torres, L. M.; Lopez, T.; Quintana, P. (2001).A Study of the Crystallization of ZrO_2 in the Sol–Gel System: ZrO_2–SiO_2. *Solid State Chemistry.* Vol. 158, No. 2, pp. 349-357.

Akselrod, M. S.; Kortov, V. S.; Kravetsky, D. J. & Gotlib, V. I. (1990). Highly Sensitive Thermoluminescent Anion Defect a-Al_2O_3:Single Crystal Detector. *Radiation Protection Dosimetry.* Vol. 32, pp.15–20.

Asiltürk, M.; Burunkaya, E.; Sayılkan, F.; Kiraz, N.; Arpaç E. (2011). Structural and optical properties of thin films prepared from surface modified ZrO_2. *Journal of Non-Crystalline Solids.* Vol.357, No. 1, pp. 206-210.

Azik, P.; Głuchowski, R.; Hreniak, P.; Strek, D.; W., Ro´s, M., Fedyk, R. & Łojkowski,W. (2008). Fabrication and luminescence studies of Ce:$Y_3Al_5O_{12}$ transparent nanoceramic. *Optical Material.* Vol. 30, pp. 714–718.

Azorín, J.; Khaidukov, N.M.; Sánchez, A.; Rivera, T. (2007). Thermoluminescence properties of TiO_2 nanopwder. Radiation Measurement. Vol. 42, pp. 613-616

Azorín, J.; Rivera, T.; Falcony, C.; Martínez, E. & García, M. (1999). Ultraviolet Thermoluminescent Dosimetry Using Terbium-doped Zirconium Oxide Thin Films. *Radiation Protection Dosimetry.* Vol. 85, pp. 317-319.

Azorín, J.; Rivera, T.; Martínez, E; & García, M. (1998).Thermoluminescence of Eu-doped Zr_2O thin films to Ultraviolet and Visible Light. *Radiation Measurements.*Vol. 29, pp. 315-317.

Azorin, J.; Furetta, C.; Scacco. A. (1993). Preparation and properties of thermoluminescent materials. *Physica Status Solidi (a).* Vol. 138, No. 1, pp. 9-46

Azorín, J. *Luminescence Dosimetry. Theory and Applications*. (Ediciones Técnico Científicas, México 1990)

Bao, A.; Tao, C.; Yang, H. (2207). Synthesis and luminescent properties of nanoparticles $GdCaAl_3O_7$:RE^{3+} (RE=Eu, Tb) via the sol–gel method. *Journal of Luminescence.* Vol. 126, No. 2, pp. 859-865.

Bhatt, B.C.; Sanaye, S.S.; Shinde, S.S.; Srivastava, J.K. (1997). A Comparative Study of the Dosimetric Characteristics of $BaSO_4$:Eu and $CaSO_4$:Dy Teflon TLD. Discs. *Radiation Protection Dosimetry.* Vol. 105, pp. 105-110.

Bourgoin, J. & Lannon, M. (1983). *Points Defects in Semiconductors Experimental Aspects*. Springer, Berlin, Heidel berg, NewYork.

Brinker, C.J. & Scherer, G.W. (1990). Sol-Gel Science: *The Physics and Chemistry of Sol-Gel Processing*, Academic Press, inc. San Diego, CA.

Brinker, C.J. & Sherrer, G. (1989). *Sol–Gel Chemistry, the Physics and Chemistry of Sol–Gel Processing*. Academic Press, San Diego.

Brown, C.K.; Bolch, W.E. & Porton, J.W. (1994). Characterization of Al_2O_3:C Thermoluminescent Dosimeter Response to Beta-Radiation. *Radiation Protection Managment*. Vol. 11, pp. 30-40

Chacon C.V., Guzman, J.; Aguilar, M.A.; Garcia, M.; Alvarez, O. & Falcony, C. (2008). Characterization of luminescent samarium doped H_fO_2 coatings synthesized by spray pyrolysis technique. *Journal of Physics D: Applied Physics*. Vol. 41, No. 1, pp. 15104.

Chang, S.C. & Su, C.S. (1992). Direct thermoluminescence of sintered ZrO_2 pellets induced by ultraviolet. R*adiation Nuclear Trakcs Radiation Measurement. Vol.* 20, No. 3, pp. 511-516.

Chang, S.C. & Su, C.S. (1993). Influence of the sintering process of ZrO_2 pellets on thermoluminescence induced by ultraviolet radiation. *Radiation Protection Dosimetry*. Vol. 47, No. 1–4, pp. 689–692.

Chen, R. & McKeever, S.W.S. (1997). *Theory of Thermoluminescence and Related Phenomena*. World Scientific Publications Singapore.

Chun, A.L.; Moralez, J.G.; Fenniri H.; Webster, T.J. (2004). Helical rosette nanotubes: a more effective orthopedic implant material. Nanotechnology Vol. 15. pp. s1-s6

Colyott, L.E.; Akselrod, M.S.; McKeever, S.W.S. 1997. An integrating ultraviolet-B dosimeter using phototransferred thermoluminescence from Al_2O_3:C. *Radiation Protection Dosimetry.* Vol. 72, No. 2, pp. 87–94.

Colyott, L.E.; McKeever, S.W.S.; Akselrod, M.S. 1999. An integrating UVB dosimeter system. *Radiation Protection Dosimetry.* Vol. 85, No. 1–4, pp. 309–312.

Deis, T.A. & Phule, P.P. (1992). Preparation of oriented lithium tantalate thin films using molecularly modified tantalum(V) ethoxide and lithium acetate. *Materials Science Letters.* Vol. 11, pp.1353-1355.

De Lange, R.S.A.; Hehhink, J.H.A.; Kelzer, K.; Burggraaf, A.J. (1995). Synthesis and characterization with SAXS *Journal of Non-Crystalline Solids.* Vol. 191, pp. 1-16.

Diaz, M.A.; Luff, B.J.; Townsend P.D. & Wirth, K.R. (1991). Temperature dependence of luminescence from zircon, calcite, Iceland spar and apatite. *Radiation Applications and Instrumentation. Part D. Nuclear Tracks and Radiation Measurements*. Vol. 18, No. 1-2, pp. 45-51

Driscoll, C.M.H. 1996. Solar UVR measurements. *Radiation Protection Dosimetry*. Vol. 64, No. 3, pp.179–188.

Ekambaram, S. (2005). Effect of host-structure on the charge of europium ion. *Journal of Alloys and Compounds*. Vol. 390, No. 1-2, P. L1-L3.

Emerich, D.F. & Thanos, C.G. (2003). Nanotechnology and medicine. Expert Opin Bio Ther. Vol. 3, P. 655-63

Ferey, F.; Grosseau, P.; Guilhot, B.; Iacconi, P.; Benabdesselam, M. (2001).Thermoluminescence and sintering of high purity α-alumina doped by Zr, Th and Ca. *Solid State Ionics.* Vol. 141-2, pp. 567-74

Flach, J.S.; Shimp, L.A.; Blitterswijk, C.A. & Groot, K. (1994). A calibrated method for crystallinity determination of hydroxylapatite coatings for implants. Characterization and performance of calcium phosphate coatings for implants, ASTM STP 1196, Emanuel Horowitz and Jack E. Parr, ASTM, Philadelphia. pp. 25-32.

Fox, P.J.; Akber, R.A.; Prescott, J.R. (1988). Spectral Characteristics of Six Phosphors Used in Thermoluminescence Dosimetry. *Journal of Physics. D.* Vol. 21, pp. 189-194.

Furetta, C. & Weng P.S. (1998). *Operational Thermoluminescence Dosimetry*. World Scientific Publishing Co.

Garcia, M. A.; Paje, S. E. and Llopis, J. (1997). Luminescence of ZTA ceramics. *Journal of Luminescence.* Vol. 72-74, pp. 662–663.

German, R. M. (1996). *Sintering Theory and Practice*. John Wiley & Sons, Inc. USA.

Gitzen, W. H. (1998). *Alumina as a Ceramic Material*. The American Ceramic Society, Special Publication No. 4, Westerville Ohio.

Gutzov, S. & Lerch, M. (2003). Optical properties of europium containing zirconium oxynitrides. *Optical Material*. Vol. 24, pp. 547–554.

Guzmán, J.; Aguilar, M.A.; Alarcón, G.; García, M.; Azorín, J.; Rivera, R.; Falcony C. (2010). Synthesis and characterization of hafnium oxide films for thermo and photoluminescence applications. *Applied Radiation and Isotopes*. Vol. 68 pp. 696–699.

Hassan, F.; Abdel, S.; Abdel, M.; Abd, N.; Ahmed, S-; Kato, S.; Kojima, T. (2009). Crystallization behaviour and hardness of glass ceramics rich in nanocrystals of ZrO_2. *Ceramics International*. Vol. 35, No. 3, pp. 1133-1137.

Hernández, J.M.; Cortez, L.A.; García, R.; Castillo, A.; Sandoval, G.; García, L.A. (2009). Synthesis and characterization of mesoporous and nano-crystalline phosphate zirconium oxides. *Journal of Alloys and Compounds*. Vol. 483, No. 1-2, pp. 425-428.

Heuer, A.H. & Hobbs, L.W. (Eds.), (1981). *Science and Technology of Zirconia, Advances in Ceramics*. Vol. 3, American Ceramic Society, Columbus OH.

Hideo, T.; Yoshimura, M.; Somiya, S. (2006). Calibration Curve for Quantitative Analysis of the Monoclinic-Tetragonal ZrO_2 System by X-Ray Diffraction *American Ceramic Society*. Vol. 67, No. 6, pp. 119-121

Hsieh, W.C. & Su C.S. (1994). UV Induced Thermoluminescence in $Zr0_2$ Doped by Er_20_3. *Journal of Physics D: Applied Physics*. Vol. 27, pp. 1763-1768

Jacobsohn, L.G.; Tornga, S.C.; Bennett, B.L.; Muenchausen, R.E.; Ugurlu, O.; Tseng T.K.; Choi, J.; Holloway, P.H. (2010). Annealing effects on the photoluminescence yield of Gd_2O_3:Eu nanoparticles produced by solution combustion synthesis. *Radiation Measurements*. Vol. 45, No. 3-6, pp. 611-614.

Jung, K.Y.; Woo, H.; Chan, Y.; Bin, S. & Suk, Y. (2005). Luminescent Properties of (Ba,Sr)$MgAl_{10}O_{17}$:Mn,Eu Green Phosphor Prepared by Spray Pyrolysis under VUV Excitation. *Chemistry of Materials*. Vol. 17, No.10, pp. 2729-2734.

Keller, L. (1995). X-ray Powder Diffraction Patterns of Calcium Phosphates Analyzed by the Rietveld Method. *Biomedical Materials Research*. Vol. 29, pp. 1403-1413.

Kirm, M.; Aarik, J.; Jurgens, M. & Sildos, I. (2005).Thin films of HfO_2 and ZrO_2 as potential scintillators. *Nuclear Instruments Methods in Physics Resesearch A*. Vol. 537, pp. 251–255.

Kokubo, T. (2008). *Bioceramics and their clinical applications*. Woodhead Publishing, Cambridge, U.K.

Kumar, P.M.; Borse, P.; Rohatgi, V.K.; Bhoraskar, S.V.; Singh, P.; Sastry, M. (1994). Synthesis and structural characterization of nanocrystalline aluminium oxide. *Materials Chemistry and Physics*. Vol. 36, No. 3-4, pp. 354-358.

Langlet M. & Joubert J.C. (1993). *Chemistry of Advanced Materials*, edited by C.N.R. Rao (Blackwell Science,Oxford, UK.

Lee, D. & Rainforth W.M. (1994). *Ceramic microstructures property control by processing*, Chapman & Hall, 3

Li , C.; Chen, Y.W.; Yen, T.M. (1995) The effects of preparation method on the characteristics of alumina–zirconia powders. *Sol–Gel Science Technology*. Vol. 4, pp. 205–10.

Lochab, S.P.; Pandey, A.; Sahare, P.D.; Chauhan, R.S.; Salah, N.; Ranjan, R. (2007). Nanocrystalline MgB_4O_7:Dy for high dose measurement of gamma radiation. *Physica Status Solidi. A*. Vol. 204, pp. 2416-2425.

Madhusoodanan, U. & Lakshmanan, A.R. (1999).Development of $BaSO_4$:Eu thermoluminescence phosphor. *Radiation Measurements*. Vol. 30, pp. 65-72.

McKeever, S. W. S.; Moscovitch, M. & Townsend, P. D. (1995). *Thermoluminescence Dosimetry Materials: Properties and Uses* (Ashford: Nuclear Technology Publishing).

McKeever, S.W.S. (1985). *Thermoluminescence of Solids*. (Cambridge University Press, Cambridge)

Ming, Y. & Tang, Y. (2011). Effect of Dy Ions on Optical Properties of $Sr_{0.985-X}$ Al_2O_4: $Eu^{2+}_{0.015}Dy^{3+}_x$ Phosphors. *Materials Science Forum*. Vol. 663-665, pp. 84-87.

Mishra, K. C.; Di Bartolo, B.; Collins, J. M. (2011). Luminescence Process of Optically Active Ions in Solids. *Science and Technology of Atomic, Molecular, Condensed Matter & Biological Systems*. Elsevier Science Publishing.

Moses, W. (1999). Scintillator requirements for medical imaging. In *Proceedings of the 5th International Conference on Inorganic Scintillators and their Applications. P*. 11–21.

Nakajima, H. & Mori,T. (2006).Photoluminescence excitation bands corresponding to defect states due to oxygen vacancies in yttria-stabilized zirconia. *Journal Alloys and Compounds*. Vol. 408–412, pp. 728–731.

Nalwa, H.S. (2000). *Handbook of Nanostructured Materials and Nanotechnology*. Vol. 1–5, Academic, CA, San Diego.

Nasar, R. S.; Cerqueira, M.; Longo, E.; Varela. J. A. (2004). Sintering mechanisms of ZrO_2·MgO with addition of TiO_2 and CuO. *Ceramics International*. Vol. 30, No. 4, pp. 571-577.

Noh, A.M.; Amin, Y.M.; Mahat, R.H.; Bradley. D.A. (2001). Investigation of some commercial TLD chips/discs as UV dosimeters. *Radiation Physics Chemistry*. Vol. 61, pp. 497-500.

Petrik, N. G.; Taylor, D. P. & Orlando, T. M. (1999). Laser-stimulated luminescence of yttria-stabilized cubic zirconia crystals. *Journal Applied Physics. Vol*. 85, pp. 6770–6776.

Rivera, T.; Roman, J.; Azorín, J.; Sosa, R. Guzmán, J.; Serrano*, A.K.; García M. & Alarcón G. (2010a). Preparation of $CaSO_4$:Dy by precipitation method to gamma radiation dosimetry. *Applied Radiation and Isotopes*. Vol.68, pp. 623–625.

Rivera, T.; Sosa, T.; Azorín, J.; Zarate, J.; Ceja, A. (2010b).Synthesis and luminescent characterization of sol-gel derived zirconia-alumina. *Radiation Measurements*. Vol. 45, pp.465-467.

Rivera, T.; Azorin, J.; Barrera, M.; Soto, A.M. & Furetta, C. (2007a). Thermoluminescence (TL) of europium-doped ZrO_2 obtained by sol-gel method. *Radiation Effects and Defects in Solids*. Vol. 162, No. 5, pp. 378-383.

Rivera, T.; Olvera, L.; Martinez, A.; Molina, D.; Azorin, J.; Barrera, M.; Soto, A.M.; Sosa, R. & Furetta, C. (2007b). Thermoluminescence properties of copper doped zirconium oxide for UVR dosimetry. *Radiation Measurement*. Vol. 42, pp. 665-667

Rivera, T.; Azorín, J.; Barrera, M.; Soto, A.M. (2007c). Nanostructural processing of advanced thermoluminescent materials. *Radiation Effects and Defects in Solids*. Vol. 162, No. 10-11, P. 731-736.

Rivera, T.; Azorín, J.; Barrera, M.; Soto, A.M.; Sosa, R.; Furetta, C. (2007d). Structural characteristics of nanocrystalline ZrO_2 powder sol-gel derived to luminescent applications. *Radiation Effects and Defects in Solids*. Vol. 162, No. 7-8, pp. 597-603.

Rivera, T.; Olvera, L.; Azorin, J.; Sosa, R.; Soto, A.M.; Barrera M. & Furetta, C. (2006). Preparation of luminescent nanocrystals started from amorphous zirconia prepared by sol-gel technique. *Radiation Effects and Defects in Solids*. Vol. 161, No. 2, pp. 91-100.

Rivera, T.; Furetta, C.; Azorín, J. (2005a). Ultraviolet induced thermoluminescence in gadolinium-doped zirconium oxide films. *Materials Science Forum*. Vol. 480-481, pp.145-148.

Rivera, T.; Olvera, L.; Azorín, J.; Soto, A.M.; Barrera, M. & Furetta, C. (2005b). Thermoluminescence (TL) characteristics of hydrogenated amorphous zirconia. *Radiation Effects and Defects in Solids*. Vol. 160, No. 5, pp. 181-186.

Rivera, T.; Azorín, J.; Martínez, E. & García, M. (1999). Thermoluminescent and Optical Properties α-Al_2O_3:C and ZrO_2:Eu exposed to ultraviolet light. *Revista Mexicana de Fisica.* Vol.45, No.1, pp. 68-70.

Rivera, T.; Azorín, J.; Martínez, E. & García, M. (1998). Termoluminiscencia inducida por la luz ultravioleta y visible en ZrO_2:TR. *Revista Mexicana de Fisica*. Vol.44, No. 3 pp. 240-243.

Roriz, V.M.; Rosa, A.L.; Peitl, O.; Zanatto, E.D.; Panzeri, H; De Oliveira, P.T. (2010). Efficacy of bioactive glass-ceramic (Biosilicate) in the maintenance of alveolar Ridges and in osseointegration of titanium implants. *Clinical Oral Implants Research*. Vol. 21, pp. 148-55

Sahare, P.D.; Ranjan, R.; Salah, N.; Lochab, S.P. (2007). $K_3Na(SO_4)_2$:Eu nanoparticles for high dose of ionizing Radiation. *Journal of Physics. D*. Vol. 40, pp.759-765.

Salah, N.; Zishan H.K.; & Habib, S.S. (2011). Nanoparticles of Al_2O_3:Cr as a sensitive thermoluminescent material for high exposures of gamma rays irradiations. *Nuclear Instruments and Methods in Physics Research Section B: Beam Interactions with Materials and Atoms*. Vol. 269, No. 4, pp. 401-404.

Salah, N.; Sahare, P.D.; Lochab, S.P.; Kumar, P. (2006a). TL and PL studies on $CaSO_4$:Dy nanoparticles. *Radiation Measurements*. Vol. 41, pp. 40-47.

Salah, N.; Sahare, P.D.; Rupasov, A.A. (2006b). Thermoluminescence of nanocrystalline LiF:Mg,Cu, P. *Journal of Luminescence*. Vol. 124, pp. 357-364.

Sallé, C.; Ferey, F.; Grosseau, P.; Guilhot, B.; Iacconi, P.; Benabdesselam M. and Fantozzi, G. (2003). Detection of foreign phases in doped a-alumina powders by Thermoluminescence. *Thermal Analysis and Calorimetry*. Vol. 73, No. 1, P. 25-33.

Sasikumar, S. & Vijayaraghavan, R. (2010). Synthesis and Characterization of Bioceramic Calcium Phosphates by Rapid Combustion Synthesis. *Materials Science & Technology*. Vol. 26, No. 12, pp. 1114-1118.

Shang, C.; Horng, L.; Ding, L.; Jow, H. (2009). Processing and physical properties of Al_2O_3/aluminum alloy composites. *Ceramics International*. Vol. 35, No. 1, pp. 7-12.

Somiya, S.; Yamamoto, N.; Yanagina, H. (Eds.). (1988). *Advances in Ceramics*, vol. 24A, American Ceramic Society, Westerville, OH.

Song, C. F.; Meng, K. L.; Ping, Y.; Feng, G.; Dong, X.; Duo, R.Y. (2002). A potential blue photoluminescence material: ZrO_2–SiO_2 glasses. *Materials Science and Engineering B*. Vol. 94, No. 2-3, pp. 181-185.

Studart, A. R.; Filser, F.; Kocher, P. & Gauckler, L.J. (2007). In vitro lifetime of dental ceramics under cycling loading in water. *Biomaterials*. Vol. 28, pp. 2695–2705.

Suk, L.K. (2005). *Sintering, Densification, Grain, Growth & Microstructure*. ED. Elsevier, 2005.

Taavoni, A.; Taheri, E.; Akhondi, H. (2009). The effect of zirconia content on properties of Al_2O_3–ZrO_2 (Y_2O_3) composite nanopowders synthesized by aqueous sol–gel method. *Journal of Non-Crystalline Solids*. Vol. 355, No. 4-5, pp. 311-316.

Thompson, P.; Cox, D.E. & Hastings, J.B. (1987). Rietveld Refinement of Debye–Scherrer Synchroton X-ray Data from Al_2O_3, *Journal Applied Crystalography*. Vol. 20, pp. 79–83.

Van Dijken, A.; Meulenkamp, E. A.; Vanmaekelbergh, D. & Meijerink, A. (2000). The luminescence of nanocrystalline ZnO particles: the mechanism of the ultraviolet and visible emission. *Journal of Luminescence*. Vol. 87–89, pp. 454–456.

Van Eijk, C.W.E. (1997). New scintillators, new light sensors, new applications. *Proceedings of the international conference on inorganic scintillators and their applications*. Shangai Branch Press, Shangai, China. pp. 3.

Wang, Z.; Yang, B.; Fu, Z.; Dong, W.; Yang, Y. & Liu,W. (2005). UV-blue photoluminescence from ZrO_2 nanopowders prepared via glycine nitrate process. *Applied Physics A. Vol.* 81, pp. 691–694.

Wilkinson, J.; Ucer, K.B. & Williams, R.T. (2004). Picosecond excitonic luminescence in ZnO and other wide-gap semiconductors. *Radiation Measurements*. Vol. 38, pp. 501–505.

Yoshimura, M.; Sung, O.; Sando, M.; Niihara, K. (1999). Crystallization and microstructural characterization of ZrO_2 (3 mol% Y_2O_3) nano-sized powders with various Al_2O_3 contents. *Journal of Alloys and Compounds*. Vol. 290, No. 1-2, pp. 284-289.

Zárate, J.; Juárez, H.; Contreras, M.E. & Pérez, R. (2005). Experimental design and results from the preparation of precursory powders of ZrO_2(3%Y_2O_3)/(10–95)% Al_2O_3 composite. *Powder Technology*. Vol. 159, No. 3, pp. 135-141

Zhang, H.; Fu, X.; Niu, S.; Sun, G. & Xin, Q. (2005). Synthesis and characterization of ZrO_2:Eu nanopowder by EDTA complexing sol–gel method. *Materials Chemistry and Physics*. Vol. 91, No. 2-3, pp. 361-364.

Zhang, J.; Zhang, Z.; Tang, Z.; Tao, Y.; Long, X. (2002). Luminescent Properties of the $BaMgAl_{10}O_{17}:Eu^{2+},M^{3+}$ (M = Nd, Er) Phosphor in the VUV Region. *Chemistry Materials*. Vol.14, pp. 3005-3008.

Zhang, W. & Glasser, F.P. (1993). The structure and decomposition of Al_2O_3–ZrO_2 gels. *Journal European Ceramic Society*. Vol.11, pp.149–54.

Zhang, Y.; Jin, S.; Yang, Y.; Chunsheng, Y. (2002). Annealing effects on the phase and microstructure transformations of nanocrystalline $(ZrO_2)_{1-x}(Sc_2O_3)_x$ (x=0.02–0.16) thin films deposited by sol–gel method. *Solid State Communications*. Vol. 122, No. 7-8, pp. 439-444.

Zhifa, S.; Chen, D.; Yu, Y.; Huang, P.; Lin, H. & Wang, Y. (2010). Luminescence in rare earth-doped transparent glass ceramics containing GdF_3 nanocrystals for lighting applications. Journal of Materials Science. Vol. 45, No. 10, pp. 2775-2779

7

Synthesis and Characterizations of $Ba(Mg_{1/3}Nb_{2/3})O_3$ Powder

Wanwilai Vittayakorn and Rachanusorn Roongtao
Department of Physics and Materials Science,
Faculty of Science, Chiang Mai University
Thailand

1. Introduction

A microwave communication system is important applications in the communication industry such as global communication satellites, cellular phones, radar detectors and wireless communication of the demands are rapidly rising in the present. Microwave dielectric ceramics were applied to the operation of filters and oscillators in several microwave systems as a small ceramic component. The general formula $Ba(B'_{1/3}B''_{2/3})O_3$ (B′ = Mg, Zn, Ni or Co; B′′ = Ta or Nb) ceramics are one of microwave dielectric which have attracted a great deal of attention and are currently being used for microwave devices due to its very high quality factors. Barium magnesium niobate ($Ba(Mg_{1/3}Nb_{2/3})O_3$: BMN) compound is one of candidate materials of relative cheap and exhibits high performance microwave dielectric. Firstly, a high dielectric constant (ε_r = 32) is needed, so that the materials can be miniaturized (because the size of a dielectric resonator $\alpha\ 1/\varepsilon_r^{1/2}$). Secondly, a high quality factor (Q = 5600) is very important for radio frequency system to keep a better selectivity and noise reduction, and a small temperature coefficient of resonance frequency (τ_f = 33 ppm/°C) is also required so that the microwave circuits remain stable (Dias et al., 2001; Lin et al., 2006; Lian et al., 2004; Lian et al., 2005; Chen et al., 2006; Zhong-qing et al., 2004; Tian et al., 2009). So far, there have been only a few studies on BMN system and most of them prepared by chemical route due to its high purity and small particle size. However, it's expensive and complicated technique. Therefore, in this paper, BMN were prepared by conventional mixed-oxide technique which is the most economical and very simply consists of wet milling the individual oxides or other compounds that decompose to the oxides during calcining (Haertling, 1999). The characterizations of the phase formation, particle shape and particle size of all powders were investigated and experimental results are then discussed.

2. Experimental

The BMN powder was prepared by the convention mixed-oxide method. The reagent grades of $BaCO_3$ (Fluka, >98.5% purity), MgO and Nb_2O_5 (Aldrich, >99% purity) were used as raw materials in this system. The raw materials were weighed and mixed by ball milling technique with alumina balls in ethanol for 24 h. The mixtures were then dried into mixed powder. The powder processing was shown schematically in Fig. 1.

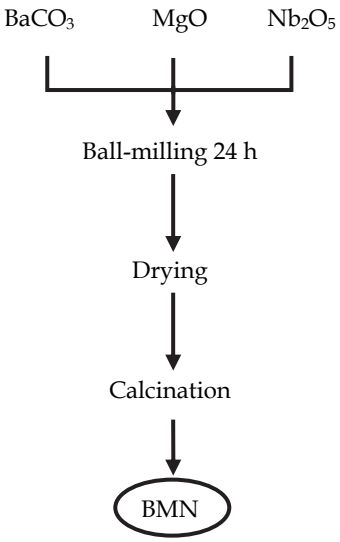

Fig. 1. Preparation route for the BMN powders.

The phase characterization process for all samples was examined using X-ray diffraction analysis (XRD) at room temperature in order to monitor phase evolution obtains calcination conditions that result in single phase BMN powder. The particle shape and particle size of powders were also observed using scanning electron microscopy (SEM).

3. Results and discussion

The TG-DTA curves of the BMN powders prepared by mixed-oxide method are illustrated in Fig. 2. In the temperature rang from room temperature to ~1250°C. The TG curve shows two distinct weight losses. The first weight loss occurs at ~300°C and the second one between 600-1000°C. The both small endothermic and exothermic peaks are observed in the DTA curve which is related to the first weight loss (~1.0%). These DTA peaks can be attributed to the decomposition of the organic species from the milling process (Wongmaneerung et al., 2006; Ananta, 2004). After the first weight loss demonstrate a much sharper fall in specimen weight with increasing temperature from ~600-1000°C. This precursor also exhibits a significantly larger over all weight loss (~14.2%). Corresponding to the second fall in specimen weight by increasing the temperature up to ~1000°C the solid-state reaction occurs the formation of some crystalline phase associated with BMN. A moderate exothermic peak at 930°C could be related to the crystallization of BMN phase as indicated in XRD patterns shown in Fig. 3. The broad exothermic characteristic in the DTA curve is found at the temperature range of 1000-1250°C, which has a maximum at ~1018°C. It has been considered as the process of further crystallization in BMN phase (Lian et al., 2004). No further significant weight loss was observed for the temperatures above 1000°C in the TG curve, indication that the minimum firing temperature

to obtain BMN compound is in good agreement with XRD results (Fig. 3). These data were used to define the range of calcination temperatures for XRD investigation.

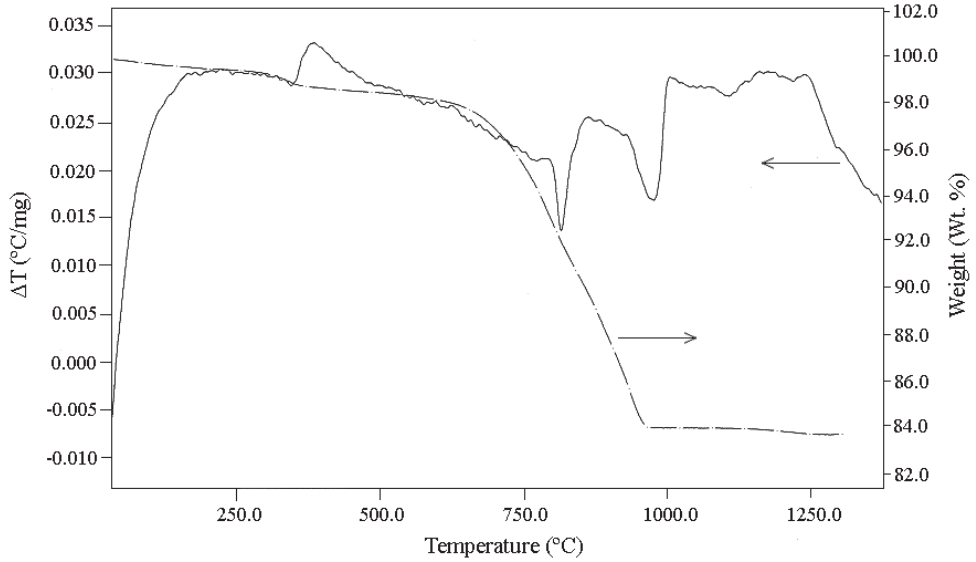

Fig. 2. TG-DTA curves for the mixture of BMN powders.

The XRD patterns of the BMN powder calcined in the temperature range of 800-1400°C for 4 h in air are shown in Fig. 2. The uncalcined powder show only X-ray peaks of $BaCO_3$, MgO and Nb_2O_5 precursors, which could be matched with JCPDS file no. 05-0378 (Powder Diffraction, 2000) 71-1176 (Powder Diffraction, 2000) and 80-2493 (Powder Diffraction, 2000), respectively. This result confirmed that no reaction had been initiated during the milling process. After calcination at 800°C, the crystalline phase of $Ba(Mg_{1/3}Nb_{2/3})O_3$ was developed accompanying with $BaCO_3$, MgO and Nb_2O_5 as separated phases. This observation agrees well with those derived from the TG-DTA results. As the temperature increased to 900°C, the intensity of the BMN peaks was further enhanced. Whereas the traces of minor phases of unreacted Nb_2O_5 could not be completely eliminated at 1100°C. This could be attributed to the poor reactivity of niobium species (Ananta et al., 1999). The peak of precursors gradually disappeared with increasing calcination temperature and reached to single BMN phase after calcination at 1200°C. This perovskite BMN powder can be matched exactly with JCPDS file no. 17-0173 for the hexagonal phase, in space group P3m1 with cell parameters of a = 5.77 pm and c = 7.08 pm (Powder Diffraction, 2000).

The morphological evolution of the calcined BMN powders was also revealed by SEM and showed Fig. 3. In general, the particles are agglomerated and basically irregular in shape with a substantial variation in particle size. The smallest and the biggest particle size of powders were estimated from SEM micrographs and listed in Table 1. From the results, it is seen that average particle size increases with increasing calcination temperature of BMN which can be attributed to the occurrence of hard agglomeration with strong inter-particle bond within each aggregates resulting from firing process.

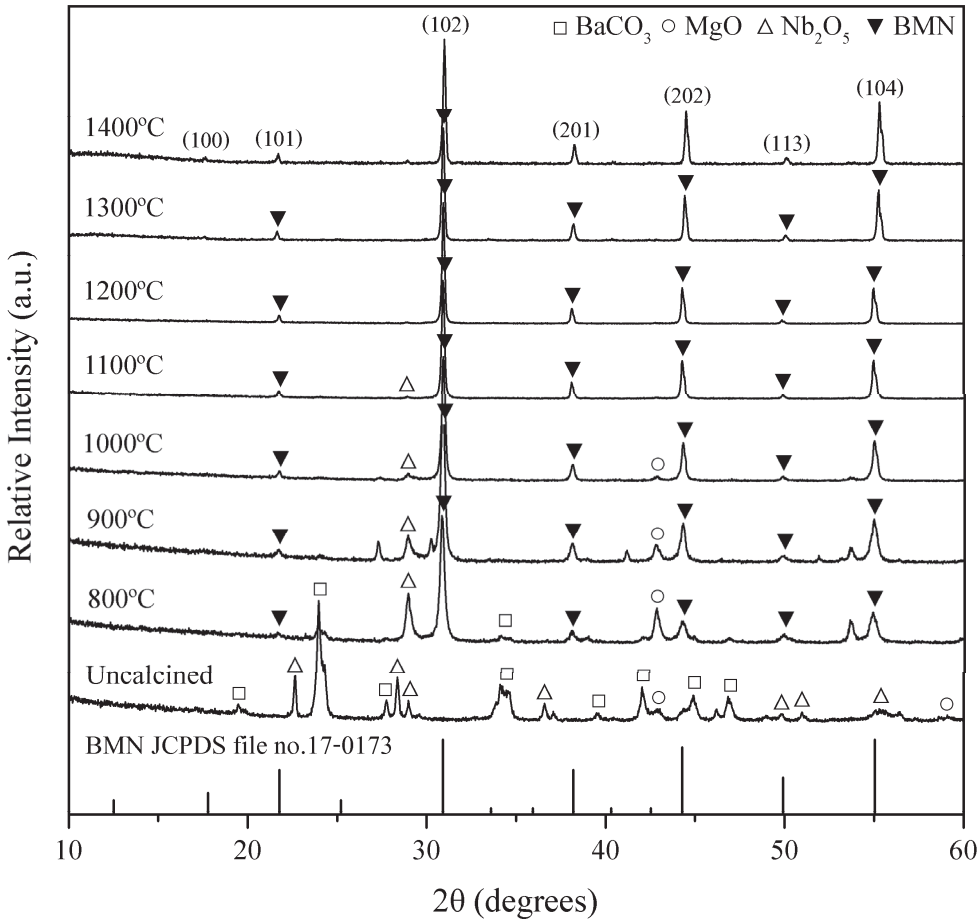

Fig. 3. XRD patterns of BMN powder calcined at various temperatures for 4 h with heating rates of 5°/min.

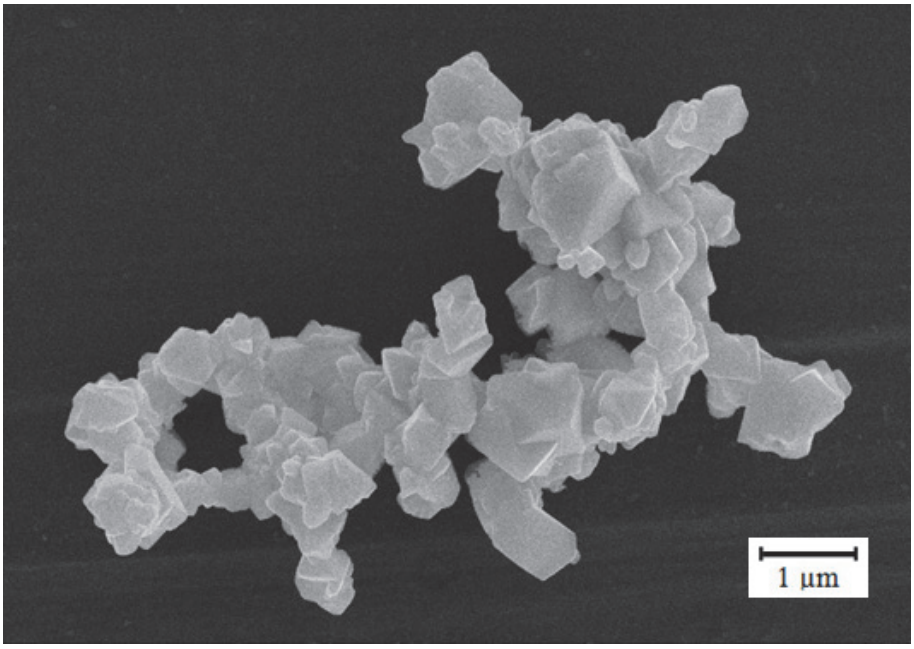

(a)

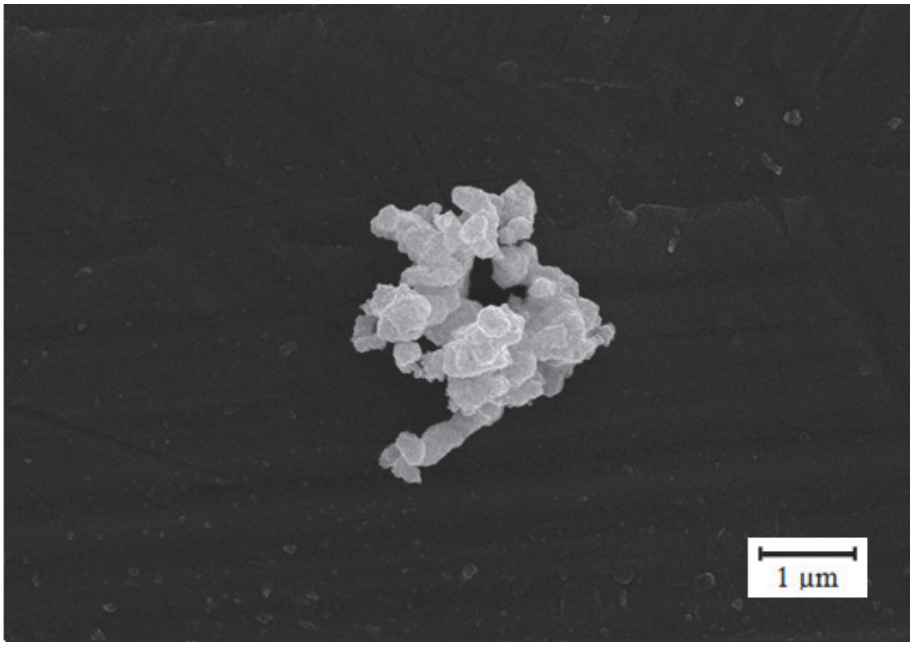

(b)

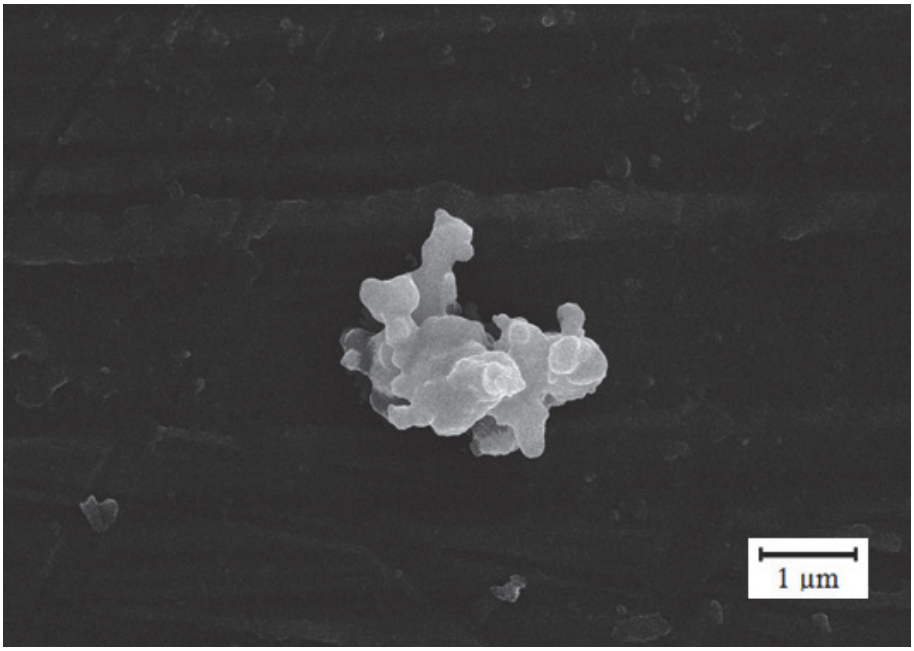

(c)

Fig. 4. SEM micrographs of BMN powder at different a calcination temperature of (a) 1200°C (b) 1300°C and (c) 1400°C for 4 h with heating rates of 5°/min.

Calcination temperature (°C)	Particle size rang (µm)	Average particle size (µm)
1200	0.21 – 1.45	0.65
1300	0.29 – 2.00	1.19
1400	0.35 – 4.00	1.56

Table 1. Particle size range and average particle size of BMN powder calcined at various temperatures for 4 h with heating rates of 5 °C/min.

4. Conclusion

The compound $Ba(Mg_{1/3}Nb_{2/3})O_3$ powders were successfully prepared by the conventional mixed-oxide technique. The effect of calcination condition on the phase formation and microstructural evolution of this system was investigated via X-ray diffractometer (XRD) and scanning electron microscope (SEM), respectively. From the results, it can be concluded that single phase of $Ba(Mg_{1/3}Nb_{2/3})O_3$ powder has been obtained by using a calcination temperature of 1200°C for 4 h with heating rates of 5°C/min with particle size ranging from

0.21 to 1.45 μm. Moreover, average particle size increases with increasing calcination temperature.

5. Acknowledgement

This research was conceived by the support from the Thailand Research Fund (TRF), the Commission on Higher Education (CHE), the Synchrotron Light Research Institute (Public Organization), the Faculty of Science and Graduate School of Chiang Mai University.

6. References

A. Dias, V.S.T. Ciminelli, F.M. Matinage, R.L. Moreira (2001). Raman scattering and X-ray diffraction investigations on hydrothermal barium magnesium niobate ceramics. Journal of the European Ceramic Society, Vol. 21, pp. 2739-2744

Chen-Fu Lin, Horng-Hwa Lu, Tien-I Chang, Jow-Lay Huang (2006). Microstructural characteristics and microwave dielectric properties of $Ba[Mg_{1/3}(Nb_{x/4}Ta_{(4-x)/4})_{2/3}]O_3$ ceramics. Journal of Alloys and Compounds, Vol. 407, pp. 318-325

Fang Lian, Lihua Xu, Fushen Li, Hailei Zhao (2004). A new sol-gel process for preparing $Ba(Mg_{1/3}Nb_{2/3})O_3$ nanopowders. Journal of University of Science and Technology Beijing, Vol. 11, pp. 48-51

Fang Lian, Lihua Xu, Xhi Fu, Ning Chen (2005). Electronic structure Calculations of $Ba(Mg_{1/3}Nb_{2/3})O_3$ and its dielectric properties analysis. Key Engineering Materials,Vol. 280-283, pp. 39-42

Gene H. Haertling (1999). Ferroelectric ceramics: History and technology. J. Am. Ceram. Soc, Vol. 82, pp. 797-818

M.-Y. Chen, C.-T. Chia, I.-N. Lin, L.-J. Lin, C.-W. Ahn, Shan Nahm (2006). Microwave properties of $Ba(Mg_{1/3}Ta_{2/3})O_3$, $Ba(Mg_{1/3}Nb_{2/3})O_3$ and $Ba(Co_{1/3}Nb_{2/3})O_3$ ceramics revealed by Raman scattering. Journal of the European Ceramic Society, Vol. 26, pp. 1965-1968

Powder Diffraction File No. 05-0378. International Centre for Diffraction Data, NewtonSquare, PA, 2000.

Powder Diffraction File No. 71-1176. International Centre for Diffraction Data, Newton Square, PA, 2000.

Powder Diffraction File No. 80-2493. International Centre for Diffraction Data, Newton Square, PA, 2000.

Powder Diffraction File No. 17-0173. International Centre for Diffraction Data, Newton Square, PA, 2000.

R. Wongmaneerung, T. Sarakonsri, R. Yimnirun, S. Ananta (2006). Effects of magnesium niobate precursor and calcination condition on phase formation and morphology of lead magnesium niobate powders. Materials Science and Engineering, Vol. 132, pp. 292-299

R. Wongmaneerung, T. Sarakonsri, R. Yimnirun, S. Ananta (2006). Effects of milling method and calcinations condition on phase and morphology characteristics of $Mg_4Nb_2O_9$ powders. Materials Science and Engineering, Vol. 130, pp. 246-253

S. Ananta, R. Brydson, N.W. Thomas (1999). J. Eur. Ceram. Soc, Vol. 19, pp. 355

S. Ananta (2004). Phase and morphology evolution of magnesium niobate powders synthesized by solid-state reaction. Materials Letters, Vol. 58, pp. 2781-2786

TIAN Zhong-qing, LIU Han-xing, Yu Hong-tao, OUYANG Shi-xi (2004). Molten Salt Synthesis of $Ba(Mg_{1/3}Nb_{2/3})O_3$ powder. Mater. Sci. Ed., Vol. 19, pp. 17-19

Zhongqing Tian, Lin Lin, Fancheng Meng, Weijiu Huang (2009). Combustion synthesis and characterization of nanocrystalline $Ba(Mg_{1/3}Nb_{2/3})O_3$ powders. Materials Science and Engineering, Vol. 158, pp. 88-91

8

SiC_f/SiC Composite: Attainment Methods, Properties and Characterization

Marcio Florian[1], Luiz Eduardo de Carvalho[2]
and Carlos Alberto Alves Cairo[3]
[1]*R&D Department, Angelus – Dental Products Industry*
[2]*Department of Materials Engineering – Federal Technological University of Paraná*
[3]*Department of Materials - Instituto de Aeronáutica e Espaço,*
Science Department and Aerospace Technology
Brazil

1. Introduction

Silicon carbide exists in several polymorphic forms (over 150) and in each case, the bond between the Si and C is always tetrahedral. The simplest form is silicon carbide (SiC) in a cubic zinc blend structure, also called 3C-SiC or β-SiC. The other polymorphs are a hexagonal network and are known as 2H-SiC, 4H-SiC, 6H-SiC shown in Figure 1, and all are listed as α-SiC (Ching et al., 2006; Camassel, 2000).

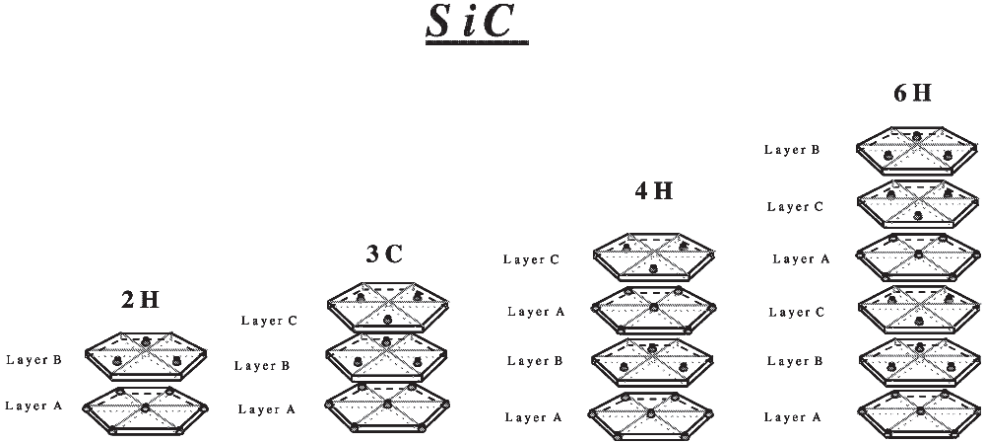

Fig. 1. Illustration of the stacking of successive layers of Si and C to represent the polytypes of SiC (Ching et al., 2006).

The four polytypes shown are the most widely used: 2H and 4H-SiC in the electronics area; 6H-SiC as a nitride substrate for optoeletronics; and 3C-SiC for use at high temperatures (Camassel, 2000).

2. SiC_f/SiC composite

Ceramic silicon carbide (SiC) has received wide attention because of its excellent oxidation resistance, corrosion resistance, and low density even at high temperatures. These materials have been widely used in the engineering industry, chemistry, energy resources and military projects (Xu, 2001). Thus, this material has been used in advanced ceramics, as it combines the advantages of traditional ceramics, such as high hardness, heat resistance, and chemical inertness, with the ability to withstand a considerably tensile strength (Kubel Jr, 1989; Roman & Stinton, 1997) together with high specific hardness and chemical inertness at high temperatures (Kubel Jr, 1989).

Ceramic matrix composites (CMC) materials, based on SiC, containing continuous or woven fibers show potential for many applications such as structural materials at high temperatures in the aerospace (Davies et al., 2001; Ferraris et al., 2000) and automotive fields, as well as, high-performance machines and turbines (Davies et al., 2001).

The SiC_f/SiC silicon carbide fiber reinforced silicon carbide composite studied in this chapter is part of the class of ceramic matrix composites in which a SiC fiber preform is infiltrated and densified by a matrix of SiC, thus improving its properties. Compared to monolithic SiC, SiC_f/SiC composite exhibits a high increase in fracture toughness, making it non-catastrophic. (Ortona et al. 2000; Goto & Kagawa, 1996). Therefore, SiC_f/SiC composite is being considered as a structural material (Young et al., 2000), with potential applications in a wide spectrum of activities, ranging from aerospace and fusion reactors up to filters for pollution control for high temperature and corrosive environment because it is lightweight, tough, and maintains antioxidant stability even at high temperature (Interrante et al., 1997).

The first SiC fibers developed were obtained by deposition via chemical vapor on a tungsten or carbon support. Its large diameter, more than one hundred microns, prevented the weaving of preforms, and only in the early 80's, did small diameter (≅10μm) "ex-polymer" SiC fibers appear, obtained from polycarbosilane (PCS). This polymer of linear formula -$(CH_2SiHMe\text{-}CH_2)_n$-is reliable in the molten state (≅200 °C), after being crosslinked in three directions, before finally being converted into ceramics by pyrolysis under nitrogen, argon and hydrogen. The methyl groups (Me) show an excess of carbon (and hydrogen), which is not prejudicial where the mixture of SiC/C is stable up to 2500 °C. Its great nanostructural homogeneity gives "ex-polymer" SiC fibers good mechanical properties. (Gouadec, 2001).

2.1 Mechanical properties

When ceramic fibers are embedded in the ceramic matrix composite, mechanical properties are quite different from monolithic ceramics because of the reinforcement fibers, which act so that the mechanical stress received by the matrix is transferred to the fiber, increasing the flexural resistance and fracture toughness. For example, the fracture toughness and thermal shock resistance of the composites are superior when compared to monolithic materials. The fracture toughness of monolithic SiC is close to 5 $MPa.m^{1/2}$, while the SiC_f/SiC composite is in the order of 20-30 $MPa.m^{1/2}$. Moreover, the properties of ceramic matrix composites (CMC) can easily be adapted, varying, for example, the architecture of the fibers, fiber types, interfacial layers of materials and thickness of composites.

Due to the efficiency of the CVI process to fill between the fibers, and the purity and crystallinity of the matrix material, it is expected that the mechanical properties of composites obtained by CVI are better than those of composites obtained by other techniques. However, no major difference in the values of flexural strength and fracture is

observed. The average flexural strength of SiC composite with Nicalon fiber obtained by different methods is 300 MPa with a fracture toughness of 15 MPa.$m^{1/2}$ (Roman & Stinton, 1997).

2.2 Chemical properties

SiC_f/SiC composite is considered a structural material when in contact with liquid materials, such as $Li_{16}Pb_{84}$ and Li_2BeF_4, which are used as refrigerants, tritium producers ($^3H_1$) and protective materials for fusion reactors whose compatibility of SiC_f/SiC with molten materials is studied. According to thermodynamic assessments, the β-SiC crystalline phase is stable against lithium metal saturated with oxygen. For the alloy $Li_{16}Pb_{84}$, SiC can be more stable because the activity of lithium in the alloy is 4-5 times lower than lithium pure (Yoneka, et al., 2001). The predominant chemical reactions between SiC and liquid metals are those which result in carbon exchange. SiC is quickly eroded when in contact with liquid lithium ($2SiC + 2Li \rightarrow 2Si + Li_2C_2$) at temperatures above 600 ^oC. At high temperatures, SiC_f/SiC composites are stable when exposed to corrosion of $Li_{17}Pb_{83}$ at 800 ^oC for 1500 hours.

Corrosive factors found in the atmosphere (H_2O, NO_x, NaCl), or derived from kerosene (sulfides, Na_2SO_4, K_2SO_4) will necessary accelerate the corrosion process. This phenomenon is difficult to anticipate, since the combustion atmospheres vary strongly according to the kind of the fuel and temperatures, typically in the order of 1400 °C in combustion chambers. SiC is inert under N_2, H_2 or in the H_2-H_2S mixture but particularly vulnerable to oxidation by hot steam and corrosion by molten alkali salts. SiC fibers have good resistance to oxidation at temperatures up to 1300 °C for the Hi-Nicalon fiber and even higher temperatures for the quasi-stoichiometric fibers. However, the ceramic matrix component of the CMC, for which are designed for extreme conditions, can limit its lifetime (<10,000 hours required for civil construction) (Gouadec, 2001).

2.3 Thermal properties

The thermal conductivity of ceramics is strongly influenced by structural defects, impurities, grain size and porosity; in the specific case of ceramic matrix composites (CMC) the fiber-matrix interface also significantly influences the thermal conductivity. The SiC single crystal with high purity has a thermal conductivity of about 5000 $W.m^{-1}.K^{-1}$ at 50 K and decreases to about 500 $W.m^{-1}.K^{-1}$ at room temperature (298K). SiC_f/SiC composite, because of its high porosity, inherent in the manufacturing process has low thermal conductivity in the direction perpendicular to the fibers. SiC_f/SiC composites exhibit advanced thermal conductivity of 73 $W.m^{-1}.K^{-1}$, at room temperature and 35 $W.m^{-1}.K^{-1}$, at 1000 ^oC, approaching the sintered monolithic SiC. The thermal conductivity varies with the orientation of fibers within the composite (Sharafat et al., 1995).

3. SiC_f/SiC composite fabrication

The most common methods for the production of SiC matrix reinforced with high strength SiC are: chemical vapor infiltration, chemical vapor deposition, impregnation and liquid pyrolysis with reaction sintering and chemical vapor reaction, the latter being, the method used in this study (Roman & Stinton, 1997).

3.1 Chemical vapor infiltration

The chemical vapor infiltration appears to be one of the most promising techniques for preparing CMC currently available, for several reasons: the SiC crystal matrix with high purity and density, can be introduced into complex preforms at relatively low temperatures. Damage to the fiber and the interdiffusion between the matrix and fibers are avoided and densification requires no additional mechanical load, and finally, the application of a layer at the interface is part of the process. The first information about the CVI technique for the preparation of ceramic materials was patented in 1964. In the CVI process, a porous preform is heated and reactive gases are passed through its pores. Most commonly, this preform is made of woven carbon or fibers SiC.

There are reports of the use of tungsten carbide substrate, where the material is infiltrated into thin β-SiC crystals, preferably oriented in the tungsten parallel plane (111). The problem is that the SiC formed reacts with the substrate after a prolonged use at temperatures above 1000 °C, forming W_2C and W_5Si_3, affecting and consequently degrading their properties (Matthews & Rawlings, 2000). One of the most common precursors of silicon carbide is methyltrichlorosilane. The reaction via chemical vapor infiltration to form the SiC matrix is given in Equation 1.

$$SiCH_3Cl_{3(g)} \xrightarrow{H_2} SiC_{(s)} + 3HCl_{(g)} \quad (1)$$

At first, a variety of matrices can be produced using other gaseous precursors. The modification process via chemical vapor infiltration differs in process conditions, that is, temperature and pressure (around 850 – 1200 °C and between 1 to 1000 mbar). Ortona (Ortona et al., 2000), Interrante (Interrante et al., 1997) and Nechanicky (Nechanicky et al., 2000) have suggested that this process requires, complex and expensive equipment and typically produces gaseous hydrochloric acid as a byproduct, in addition to the difficulty of infiltrating into thick layers (≥ 4mm). Pochet (Pochet et al., 1996) also studied some limitations of the chemical vapor infiltration technique: exhaust from the gas phase, which results in a high growth rate of the substrate layer, nodular deposits and variation of the deposit thickness in the substrate.

3.2 Infiltration and polymer pyrolysis

Another way to manufacture SiC_f/SiC composite can be by the route of infiltration of polymer precursors or the sol-gel method. The advantages of this method are related to low processing temperatures, effective mixture of the components of the composite, therefore, greater homogeneity and potential for the formation of multiphase matrices. The liquid precursor for the formation of the ceramic is infiltrated into fibers or particles to produce the matrix. The precursor is converted by hydrolysis in the sol-gel and thermal decomposition of the polymer precursor method. The result is a densified matrix and the process can be repeated several times to achieve an increase in the density. The major disadvantages of the sol-gel process are: low yield of the reaction, high shrinkage and low rate of gelation of polymers. (Nechanicky et al., 2000).

The alternative to this process is polymer precursor infiltration and subsequent pyrolysis of matrix (Nechanicky et al., 2000), making the technique economically attractive (Ortona et al., 2000). For the infiltration process and pyrolysis of polymer to be successful, the following parameters must be optimized:

- High efficiency for impregnation;
- Applicable to manufactured components with complex sizes (Ortona et al., 2000);
- Quality of the precursor (high yield, chemical purity after the pyrolysis and controlled microstructural evolution) (Nechanicky et al., 2000);
- Porosity (minimum porosity or completely open in the green compact and during processing);
- Microstructure (controlled densification with minimal grain growth during sintering) (Nechanicky et al., 2000).

For the manufacturing of SiC matrix, two routes were developed using polycarbosilane (PCS), which maintains the stoichiometry Si:C 1:1, when pyrolysis is carried out. The first route involves the synthesis of linear PCS $[SiH_2CH_2]_n$, which has all the desirable characteristics for an ideal matrix of SiC, but presents high costs and low yield. The precursor of this study allows a detailed understanding of cross-links and pyrolytic conversion processes occurring in the PCS system containing Si-H to produce a high yield of SiC. The second route employs a different organosilane, chloromethyltrichlorosilane ($ClCH_2SiCl_3$) as starting material (lower cost) and obtains a final product which differs in terms of structure with, however present approximately the same compositional formula $[SiH_2CH_2]_n$. In this case, either the properties of the precursor as well as projected costs are calculated in the application of SiC matrix (Interrante et al., 1997).

One drawback of this technique is that the matrix of SiC obtained after pyrolysis, has lower purity and an amorphous glassy phase, resulting in decreased thermal and mechanical properties compared to composites obtained by chemical vapor infiltration. (Lin et al., 1995).

Kotani (Kotani et al., 2001) proposed a process for fabrication of SiC_f/SiC composite using PIP, which provides highly efficient impregnation and control of the microstructure, with reaction sintering to obtain a dense SiC matrix without hot pressing. The impregnated fibers were prepared by polymeric densification intra-fiber with four options in the process: (a) pyrolysis of the SiC precursor, (b) pyrolysis of carbon precursor and subsequent reaction sintering of polymer-derived carbon and silicon particles; (c) reaction sintering between particles of silicon and carbon and (d) reaction sintering between particles of carbon and impregnation of liquid silicon. Process optimization was performed by adjusting the ratio in the mixture and formation conditions in order to reduce porosity.

3.3 Chemical vapor reaction

The chemical vapor reaction method was first introduced in 1985 and patented in 1992. In this process, particles or grains of SiC are formed from gaseous precursors via chemical vapor deposition and deposited on a hot graphite substrate, resulting in a coating. Having attained sufficient thickness, the graphite is removed by oxidation (Roman & Stinton, 1997).

The chemical vapour reaction method is based on the carbothermal reduction process, in which an intermediate phase of SiC is formed during the reduction process of silica and carbon. The chemical reaction between silica and carbon is applied to the formation of a SiC layer on carbon materials and synthesis of powders of SiC and Si. The carbothermal reduction process can be classified into two steps. The first step is the reduction of silica by carbon, this step consists of the formation of SiO, CO, and the formation of SiC (intermediate phase) between SiO and carbon. The second step is the reduction of silica by SiC, this step consists of the formation of SiO and CO from SiC and silica, and the formation of SiC from SiO and CO (Yun et al., 2005).

First Step

$$SiO_{2(s)} + C_{(s)} \rightarrow SiO_{(g)} + CO_{(g)} \quad (2)$$

$$SiO_{(g)} + 2C_{(s)} \rightarrow SiC_{(s)} + CO_{(g)} \quad (3)$$

$$SiO_{2(s)} + 3C_{(s)} \rightarrow SiC_{(s)} + 2CO_{(g)} \quad (4)$$

Second Step

$$2SiO_{2(s)} + SiC_{(s)} \rightarrow 3SiO_{(g)} + CO_{(g)} \quad (5)$$

$$SiO_{(g)} + 3CO_{(g)} \rightarrow SiC_{(s)} + 2CO_{2(g)} \quad (6)$$

$$SiO_{2(s)} + CO_{(g)} \rightarrow SiO_{(g)} + CO_{2(g)} \quad (7)$$

The transformation of carbon into β-SiC (zinc blende structure) can be driven by the following steps: at high temperatures, graphitic materials show an appreciable expansion of the C-axis, in which case the prismatic planes have a great reactivity. Moreover, it is thought that conversion of the graphite substrate is obtained by the interaction of SiO gas and planes of crystalline carbon (or atomic sites), which are more reactive than other planes. Probably, the process includes the decomposition of SiO and the insertion of Si in the structure between the carbon layers. As a result, carbon crystalline units are converted into SiC tetrahedral units.

During the conversion of carbon into SiC, some SiC whiskers could be formed. This occurs because the formation of SiC leads to a decrease in the SiO/CO ratio during the conversion process. It is suggested that the two reactions may occur following competition with one another in the conversion process. The notable difference in the two reactions is the type of phase reactant, a vapor-vapor reaction (Equation 8), in contrast to a solid-vapor reaction (Equation 9). It is known that the reactant SiO and CO should be provided for the production of SiC whiskers, so the formation of SiC whiskers is likely (Yun et al., 2005), according to the equations:

$$SiO_{(g)} + 3CO_{(g)} \rightarrow SiC_{(s)} + 2CO_{(g)} \quad (8) \text{ Formation of Whiskers}$$

$$SiO_{(g)} + 2C_{(s)} \rightarrow SiC_{(s)} + CO_{(g)} \quad (9) \text{ Formation of Polycrystrals}$$

Kowbel (Kowbel, 1997, 2000) transformed only the carbon fibers into SiC fibers from a carbon cloth through the process of chemical reaction via vapor at high temperatures, which used SiO gas as the reactive gas. The conversion of carbon to SiC was controlled by the gas generation and temperature of operation. The level of conversion was measured by direct oxidation of the converted fibers and by scanning electron microscopy of a cross section of fibers converted. After observation, it was found that 100 per cent of the fibers were converted into SiC after being subjected to this treatment.

In order to obtain the composite the chemical vapour infiltration technique was used following four different routes: (a) SiC powder consolidation and densification by chemical vapor infiltration, (b) SiC powder consolidation and densification via hot-pressing; (c) PCS consolidation and densification by chemical vapor infiltration and (d) consolidation and densification via chemical vapor infiltration, achieving high purity crystalline β-SiC.

Ohsaki (Ohsaki et al., 1999) produced the SiO gas, using a powder mixture of Si and SiO_2, with a ratio of 1:1 (%weight), which was heated from 1200 to 1400 °C, varying 1 to 10 hours (in a vacuum of 1.5 $x10^{-2}$ Torr) to obtain β-SiC from activated carbon.
With this reaction mixture, it is necessary to heat the system at temperatures below the eutectic point to cause a process of oxidation-reduction in the mixture, where silicon oxides and SiO_2 reduce, according to the reaction shown in Equation 10:

$$Si_{(s)} + SiO_{2(s)} \rightarrow 2SiO_{(g)} \quad (10)$$

Tang (Tang et al., 2000) grew SiC nanotubes from carbon nanotubes in an oxidizing atmosphere of SiO. From this growth, it was expected that SiC nanotubes would have a diameter have diameter equal to carbon nanotubes, however, nanotubes have an epitaxial growth on the surface of SiC due to the reaction between gaseous SiO and CO as shown by Equation 6. Furthermore, the CO_2 gas generated can react with carbon nanotubes still present, reducing the initial diameter of carbon nanotubes, thus mitigating the SiC nanotubes, consequently, presenting a more widespread diameter, as shown in Equation 11.

$$C_{(s)} + CO_{2(g)} \rightarrow 2CO_{(g)} \quad (11)$$

Rogers (Rogers et al., 1976) covered the C/C composite with a silicon carbide layer using the "*pack-process*" technique which was used in a powder mixture consisting of 60% SiC, Si 30% and 10% Al_2O_3, in which the first stage is controlled by the liquid phase, where the molten metallic silicon reacts with carbon to form SiC and the second stage is controlled by the vapor phase, where silicon vapors react with carbon. The SiC formed on the carbon surface is presented in cubic form (β-SiC).

4. Conversion of C/C composite into SiC_f/SiC composite

Powders and materials utilized in this conversion process are:

- Carbon fiber twill, T-10 EKHO (Ural, Ukraine), obtained by carbonization of a PAN precursor;
- Phenolic resin Resafen 8121, manufactured by Reichhold– Resana Ind. Quim. S/A (Mogi das Cruzes, SP, Brazil), in the form of a liquid resin soluble in water, used as carbon matrix precursor;
- Silicon powder from Elektroschmeltzwerk Kempten GMbH, (Kempten, Germany), 99.9% purity and mean size particle 10 μm;
- SiO_2 powder manufactured by Mineração Jundu, (Descalvado, SP, Brazil), 99% purity and mean size particle <2 μm;
- α Al_2O_3 SG A-16 manufactured by Alcoa, 99% purity and sub-micron particles.

The first step in the preparation is the fabrication of a primary C_f/C composite by a PIP method. A first carbon/resin (C_f/R) composite is made out of eight carbon fabric layers impregnated with phenolic resin. The resulting laminate was heated in an autoclave with a heating rate of 5°C/min and a pressure of 0.3 MPa up to 130 °C. The C_f/R composite was carbonized at 1000 °C in an argon atmosphere, with a heating rate of 60 °C/h. The resulting C_f/C material was dried for 12 h at 180 °C.
The second step involves the transformation of the C_f/C into SiC_f/SiC by Chemical Vapor Reaction (CVR). The source of gaseous silicon monoxide was produced by two different

powder mixtures. First by a reaction among 60%SiC + 30%Si + 10%Al_2O_3 (%weight) (Rogers et al., 1976) (called Mixture 1) and the second by the reaction of 50% SiO_2 + 50% Si (%weight) (called Mixture 2), both of which were prepared by co-milling in a planetary mill for 30 min and drying for 12 h at 180 °C. The mixture 1 powder was put in a carbon crucible and the C_f/C was placed inside the powder mixture. The mixture 2 powder was placed in an alumina crucible and the C_f/C composite was located above the mixture without contact with the powder. Mixture 1 was placed in a furnace in vacuum atmosphere and heated at temperatures from 1400 °C to 1800 °C for 3 h in a with a heating rate of 10 °C/min. Mixture 2 was placed in a furnace in a vacuum atmosphere and heated at 1400 °C for 3 h in a with a heating rate of 10 °C/min. Total conversion of the material was verified by X-ray diffraction and scanning electron microscopy.

5. Results

5.1 Results from Mixture 1 (60%SiC, 30%Si e 10%Al_2O_3)

Figure 2 shows the photomicrographs obtained by scanning electron microscopy of the cross section of converted SiC_f/SiC composites. At the temperature of 1400 °C, the composite was not fully converted, because a difference can be observed a difference in the fiber color. Since the images are taken by electron backscattering, is possible to obtain contrast due to the atomic weight of elements (the heaviest appear brighter), we can say that the light outside corresponds to the carbon converted into SiC and the inside dark carbon not converted. This partial conversion can be proven by an X-ray diffractogram of the composite surface, which reveals a band of carbon, as shown in the Figure 3.

At the temperature of 1600 °C, the composite is fully converted as shown in the Figure 4. Because thefiber and matrix of the composite show a homogeneous contrast (carbon converted into SiC). This conversion is shown by an X-ray diffractogram of the composite surface not revealing the presence of carbon as shown in Figure 5, indicating a complete conversion.

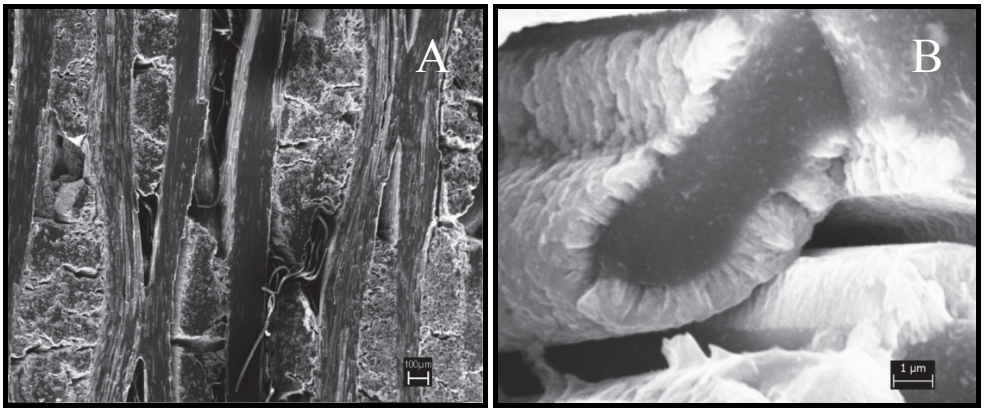

Fig. 2. (a) Scanning electron micrographs of SiC_f/SiC composite converted at 1400°C for 3 hours and (b) Fibers not fully converted into SiC.

At the temperature of 1800 °C, the composite, in addition to being totally converted, showed a growth of SiC grains, altering the shape of the fiber and causing cracks in the grain boundaries as shown in the Figure 6. This conversion is shown by X-ray diffractogram of the composite surface.The presence of silicon is also observed, from the silicon melting of the mixture, as shown in Figure 7, because the composite is in contact with the powder mixture during the conversion. Transformation at this temperature is harmful to the integrity of the composite, despite theincrease in crystallinity of the β-SiC phase, as shown by the decreased background and increased intensity of characteristic peaks in the X-ray diffractogram.

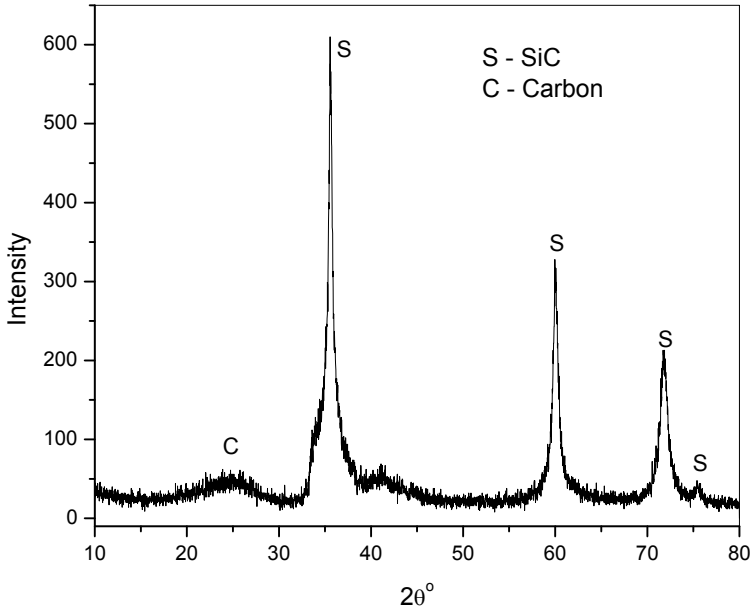

Fig. 3. X-Ray diffractogram of phase transformation of carbon into SiC at 1400ºC for 3 hours.

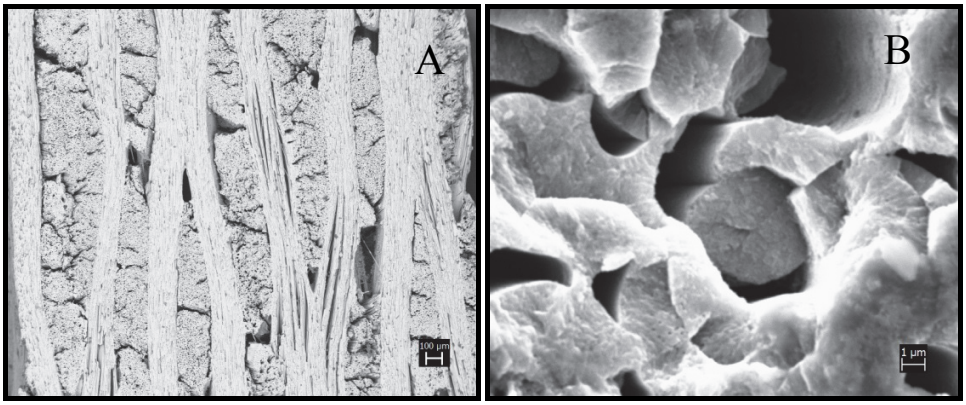

Fig. 4. (a) Scanning electron micrographs of SiC_f/SiC composite converted at 1600ºC for 3 hours and (b) Fibers fully converted into SiC.

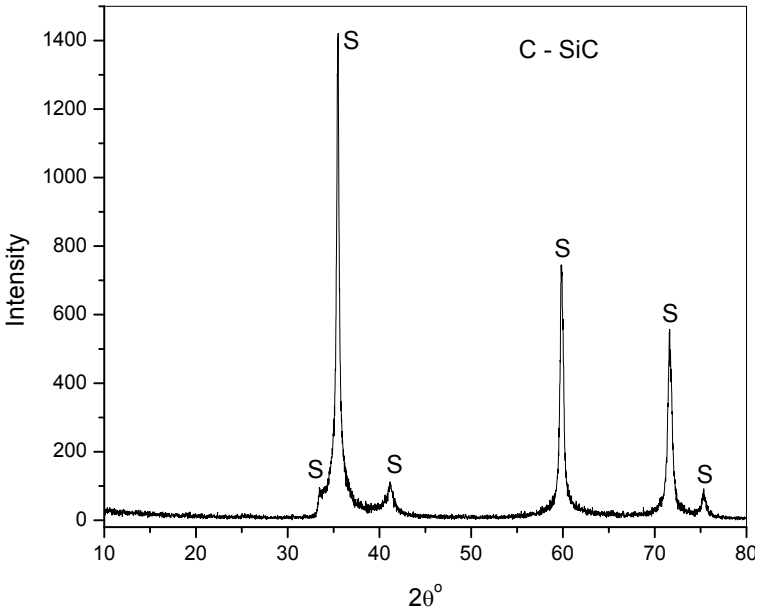

Fig. 5. X-Ray diffractogram of phase transformation of carbon into SiC at 1600ºC for by 3 hours.

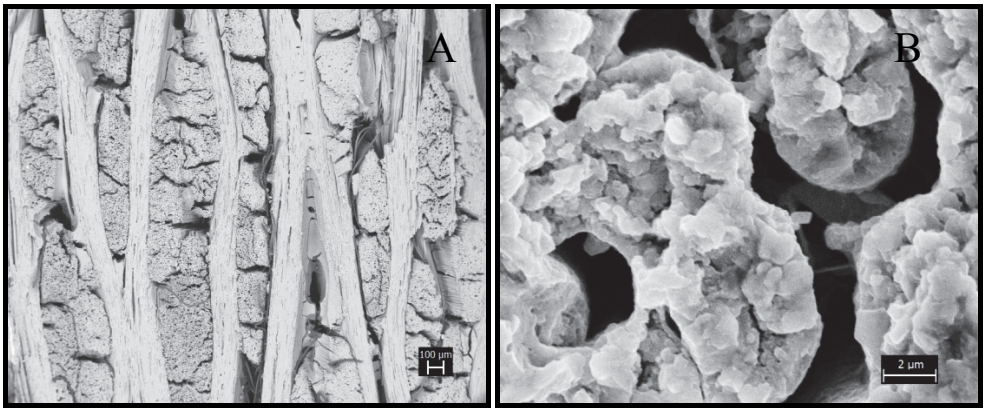

Fig. 6. (a) Scanning electron micrographs of SiC_f/SiC composite converted at 1800ºC for 3 hours and (b) Fiber totally converted into SiC with the grain growth.

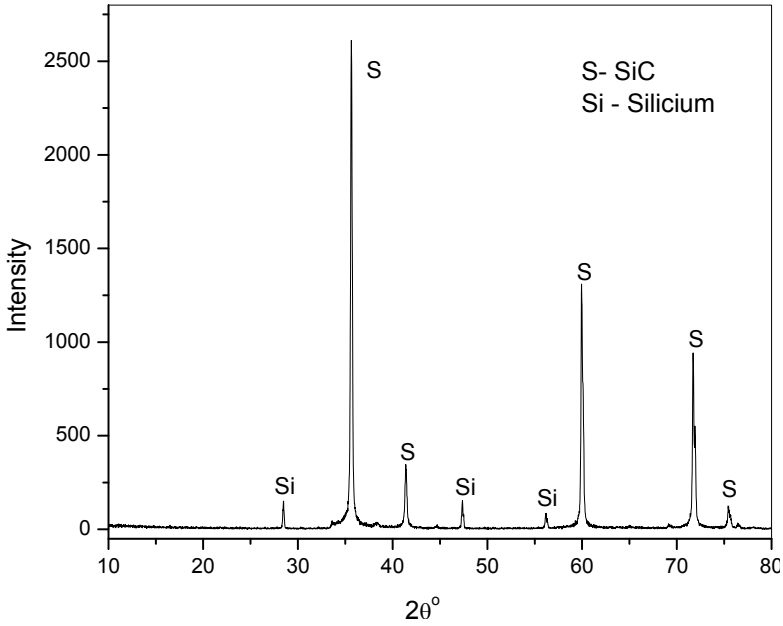

Fig. 7. X-Ray diffractogram of phase transformation of carbon into SiC at 1800ºC for 3 hours.

From the results presented of the microstructure analyzed by scanning electron microscopy (SEM) and X-ray diffractogram (XRD), the best fit to convert the composite was at a temperature of 1600 °C, since we obtained a SiC_f/SiC composite fully converted and intact without fracture of the fibers. The analysis by energy dispersive spectroscopy (EDS), performed to determine the constituents of the composite, revelead the presence of aluminum from alumina used in the mixture, as shown in Figure 9.

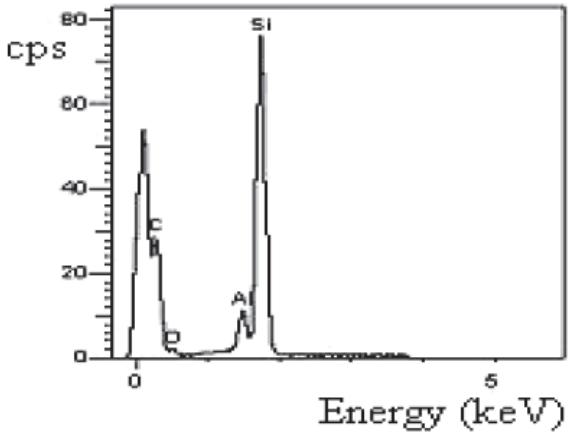

Fig. 8. Elemental analysis by energy dispersive spectroscopy in the SiC_f/SiC composite processed at 1600 °C, showing the presence of Si, C and Al.

The presence of aluminum in the SiC_f/SiC composite is harmful because it reduces the values of mechanical strength at high temperatures, and increases the values of conductivity/thermal diffusivity (Itatani et al., 2006).

5.2 Results from Mixture 2 (50% SiO_2 + 50% Si)

Figure 9 presents photomicrographs by scanning electron microscopy of the SiC_f/SiC composite converted by the Mixture 2.

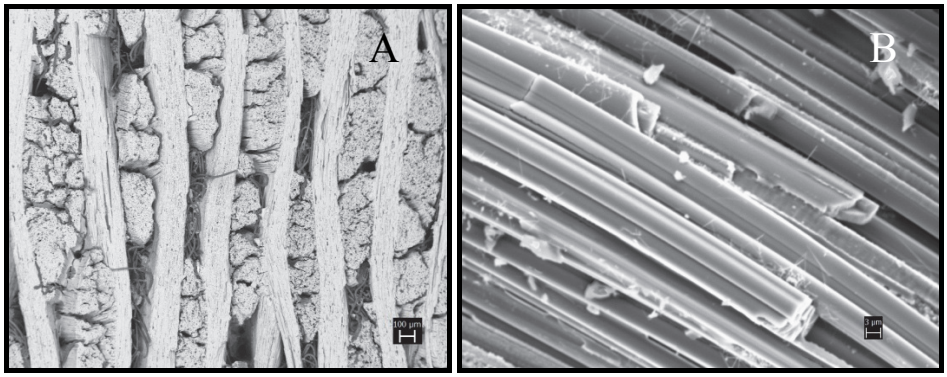

Fig. 9. (a) Scanning electron micrographs of SiC_f/SiC composite converted at 1400°C for 3 hours. (b) Fibers fully converted into SiC.

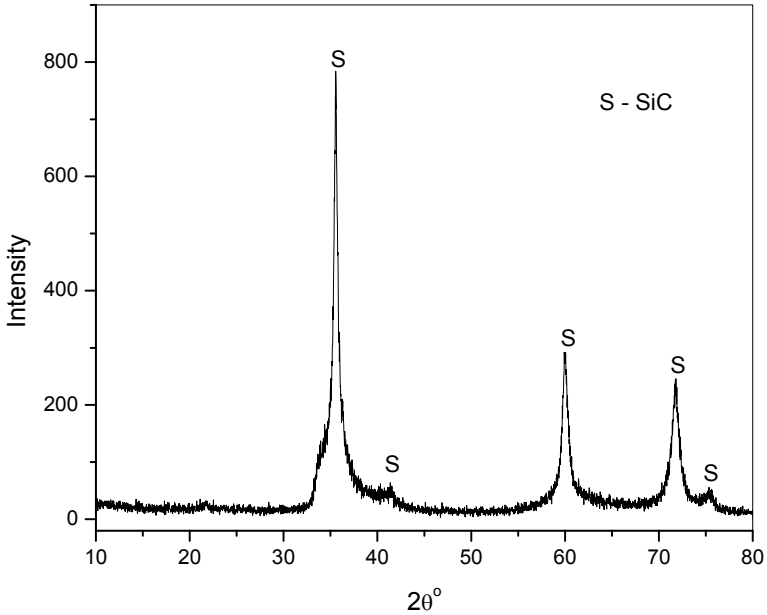

Fig. 10. X-Ray diffractogram of phase transformation of carbon into SiC at 1400°C for 3 hours.

The composite was fully converted into SiC. The fibers showed a smoother texture than those obtained in the conversion at 1600 °C using mixture 1. Only the β-SiC phase was identified by X-ray diffraction in the composite, as is shown in Figure 10. In the energy dispersive spectroscopy analysis, the converted composite shows only the peaks corresponding to silicon and carbon, as illustrated in Figure 11.

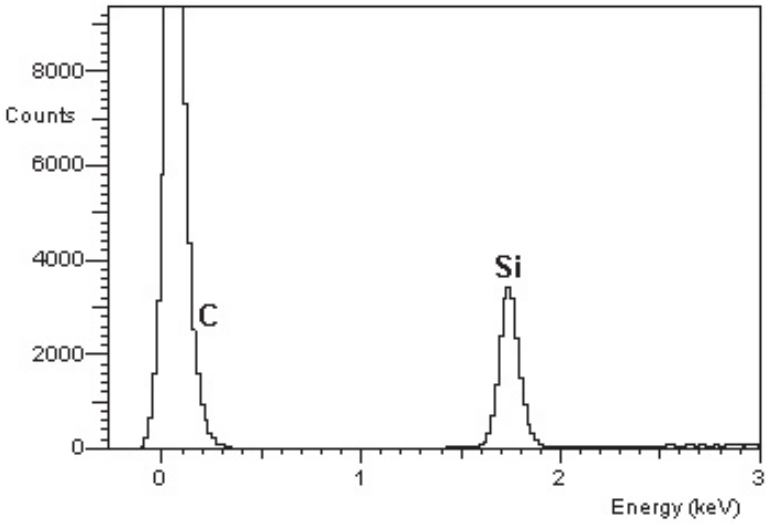

Fig. 11. Elemental analysis using energy dispersive spectroscopy in the SiC_f/SiC composite processed at 1400 °C, showing the presence of Si and C.

Since the conversion method utilizing the Mixture 2 was carried out at a lower temperature, and avoided the contamination by aluminum with a mixture containing only the powders of SiO_2 and Si, this process was chosen to obtain samples of SiC_f/SiC in order to carry out a study using the plasm torch test.

5.3 Plasma torch test

Figure 12 shows the sequence of the test procedure performed in plasma torch.

Figure 13 shows the mass variation versus time of exposure to the plasma torch. The temperature of the plasm attack was 1450 ° C with a distance of 8 cm between the nozzle and the sample. The larger decrease in mass of the composite, the greater was the exposure time of the plasma.

As exposure time increases a reduction in the mass of the composite occurs. This mass variation is associated with mechanical erosion caused by the flow of plasma over the surface of the composite, but this value is low compared to the total mass. The mass was decreased by 0.017% per 100 seconds.

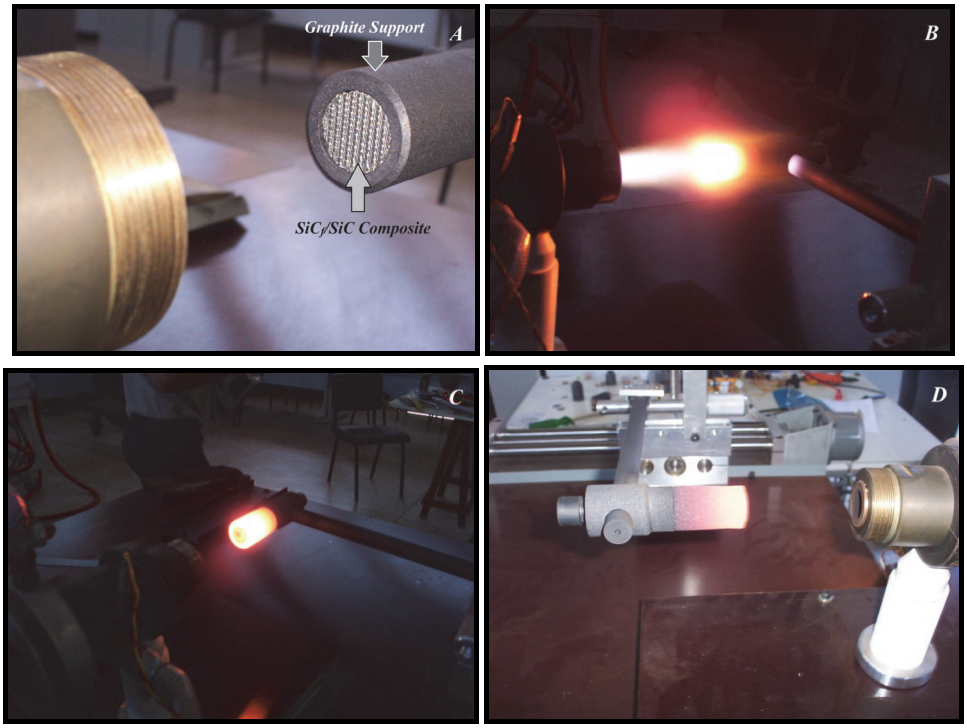

Fig. 12. (a) View of the SiC_f/SiC composite before the plasma attack, (b) Beginning of the plasma attack on the SiC_f/SiC composite, (c) End of plasma attack, the SiC_f/SiC composite and (d) Cooling support assembly of SiC_f/SiC composite and graphite.

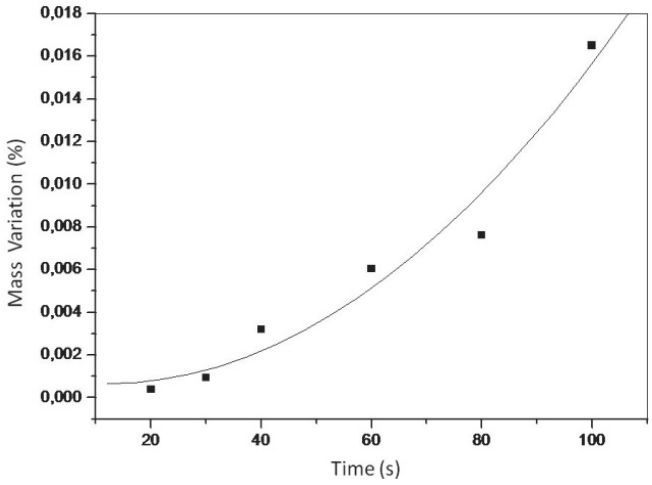

Fig. 13. Mass variation of the SiC_f/SiC composite as a function of exposure time to plasma at a temperature of 1450 ° C.

Figure 14 shows an overview of the surface of the SiC_f/SiC composite before and after the plasma attack.

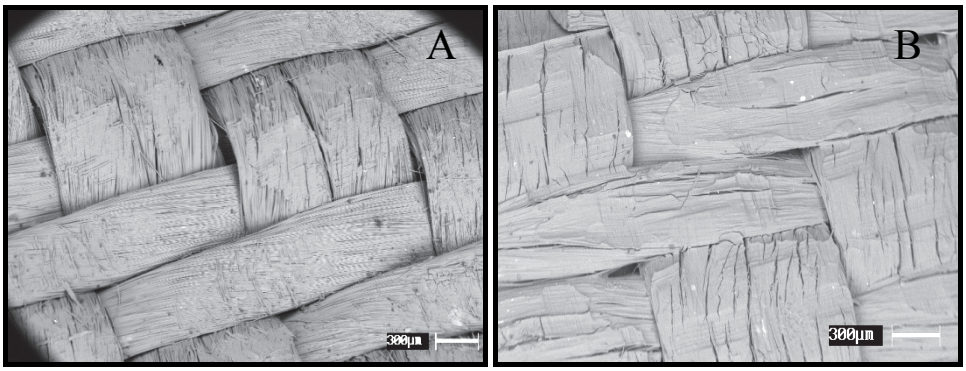

Fig. 14. (a) General view of the SiC_f/SiC composite before the plasma attack and (b) General view of the SiC_f/SiC composite after a 60 seconds plasma attack.

It can be observed that the composite showed no microstructural difference, keeping the same arrangement and morphology of the fibers before and after the plasma attack. In Figure 15, it is possible to see that in the fractured surface, after the plasma attack, only the ends of the fibers that were exposed SiC are oxidized with a glassy aspect, with the formation of SiO_2.
This is possible because at temperatures above 600 °C, SiC begins to suffer oxidation, transforming itself into SiO_2, as shown in Equation 12 (Opila & Jacobson, 1995). This new phase forms a thin film on the surface, which acts as a protective layer in the composite, preventing further penetration of oxygen into the composite avoiding higher oxidation of the composite. This can be observed by X-ray diffraction carried out on the matrix surface after the plasma attack, indicating the presence of both the β-SiC phase and the SiO_2 phase, as shown in Figure 16.

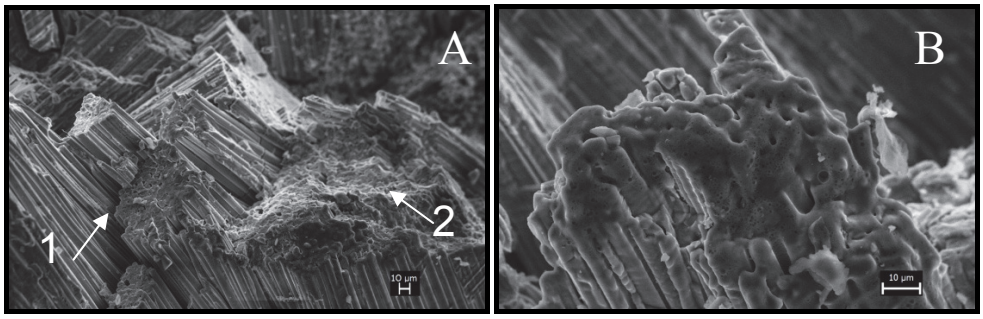

Fig. 15. View of the fiber bundles attacked by the plasma beam. (1): Region oxidized with formation of SiO_2 and (2): Region fractured by mechanical erosion. (b) Detail of a fiber bundle attacked by the plasma beam.

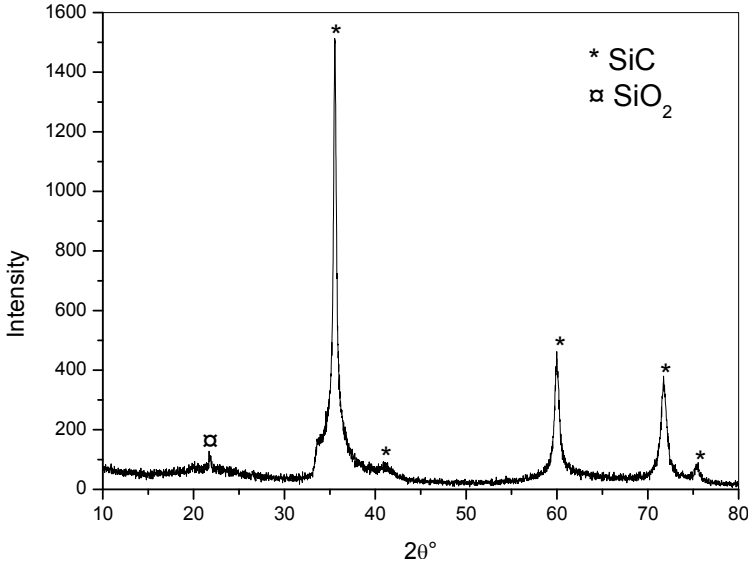

Fig. 16. X-ray diffractogram of the SiC_f/SiC composite after plasma attack.

6. Conclusion

1. It is possible to obtain SiC_f/SiC composite by conversion reactions at high temperatures, starting from C/C composite, by the reaction between carbon and $SiO_{(g)}$ from pack mixtures composed of 60 SiC + 30 Al_2O_3 + 10 Si and 50 Si + 50 SiO_2 (wt%). Using the mixture 50 + 50 Si SiO_2, the appropriate temperature for conversion is 1400 °C, lower compared to the former 1600 °C, which produces a composite with fibers of a fine texture, with submicrometric grains and purity of the β-SiC phase.
2. The method makes it possible to obtain CVR composite SiC_f/SiC with the same microstructure of C/C precursor and avoids any dimensional variation or changes in the original distribution voids.

7. Acknowledgment

The authors would like to thanks to CNPq and FAPESP due to the grants for performed this study.

8. References

Camassel, J. Contreras, S. Robert, J. L. (2000). SiC materials: a semiconductor family for the next century. *Comptes Rendus de l'Académie des Sciences - Series IV - Physics* Solids, Vol.1, Issue 1, (March 2000), pp. 5-21, ISSN 1296-2147

Ching, W. Y., Xu Y-N., Rulis, P., Ouyang, L. (2006). The Eletronic Structure and Spectroscopic properties of 3C, 2H, 4H, 6H, 15R and 21R polymorphs of SiC. *Materials Science and Engineering A*, Vol.422, Issues 1-2, (April 2006), pp. 147-156, ISSN 0921-5093

Davies, I. J., O., Toshio, I., Takashi and N. Suzuki. (2001). Case study of failure in a glass-sealed SiC/SiC-based composite creep tested at 1100°C in air. *Materials Letters*, Vol.48, Issues 3-4, (April 2001), pp. 205-209, ISSN 0167-577X

Ferrraris, M., Montorsi, M., Salvo, M. (2000). Glass coating for SiC_f/SiC composites for high-temperature application. *Acta Materialia*, Vol.48, Issues 18-19, (December 2000), pp. 4721-4724, ISSN 1359-6454

Goto, K.; Kagawa, Y. (1996). Fracture behaviour and toughness of a plane-woven SiC fibre-reinforced SiC matrix composite. *Materials Science and Engineering A*, Vol.211, Issues 1-2, (June 1996), pp. 72-81, ISSN 0921-5093

Gouadec, G. (2001) Analyse (Micro)-Mécanique Et (Nano)-Structurale De Solides Hétérogènes Par Spectroscopie Raman. 197 pages, PhD Thesis – Materials Science University of Rennes, Retrieved from http://www.ladir.cnrs.fr/pages/theses/Corps_du_texte.pdf

Interrante, L.V., Whitmarsh, C.W., Sherwood, W. (1997). Fabrication of SiC Matrix Composites by Liquid Phase Infiltration with a Polymeric Precursor, *Proceedings of Material Research Society Symposium*, San Francisco, California (U.S.A.), April 1997

Itatani, K., Tanaka, T., Davies I.A. (2006). Thermal properties of silicon carbide composites fabricated with chopped Tyranno® Si Al C fibres. *Journal of the European Ceramic Society*, Vol.26, Issues 4-5, pp. 703-710, ISSN 0955-2219

Kotani, M., Kohyama, A., Katoh, Y. (2001). Development of SiC/SiC composites by PIP in combination with RS. *Journal of Nuclear Materials*, Vol.289, Issue 1-2, (February 2001), pp. 37-41, ISSN 0022-3115

Kowbel, W., Bruce, C.A., Tsou, K.L., Patel, K., Withers, J.C. (2000). High thermal conductivity SiC/SiC composites for fusion applications. *Journal of Nuclear Materials*, Vol.283-287, Part1, pp.570-573, ISSN 0022-3115

Kowbel, W., Kyriacou, C., Gao, F., Bruce, C.A., Withers, J.C. Properties of SiC-SiC composites Produced Using CVR converted graphite cloth to SiC, *Proceedings of Material Research Society Symposium*, San Francisco, California (U.S.A.), April 1997

Kubel Jr., E.J. (1989). Advanced high-performance ceramics often are the only materials suitable for many critical applications. *Advanced Materials and Process*, Vol.136, Issue 3 (September 1989) pp. 55-60 ISSN: 0882-7958

Lin, H.T., Becher, P.F., Tortorelli, P.F. Elevated Temperature Static Fatigue of a Nicalon Fiber-Reinforced SiC Composite, *Proceedings of Material Research Society Symposium*, San Francisco, California (U.S.A.), April 1995

Matthews, F.L. Rawlings, R.D. (2000) Composite Materials: Engineering and Science. *CRC Press*, ISBN 084930251X, Boca Raton FL

Nechanicky, M.A., Chew, K.W., Sellinger, A., Laine, R.M. (2000). α-Silicon Carbide/β-Silicon carbide particulate composite via polymer infiltration and pyrolysis (PIP) processing using polymethylsilane. *Journal of European Ceramic Society*, Vol.20, Issue 4, (April 2000), pp. 441-451, ISSN 0955-2219

Ohsaki S., Cho D.H., Sano H. (1999). Synthesis of β-SiC by the reaction of gaseous SiO with activated carbon. *Key Engineering Materials*, Vol.159-160, pp.89-94

Opila, E.J., Jacobson, N.S. (1995). SiO(g) Formation from SiC in Mixed Oxidizing-Reducing Gases. *Oxidation of Metals*, Vol.44, No.5-6, pp.527-544, ISSN 1573-4889

Ortona, A., Donato, A., Filacchioni, G., De Angelis, U., La Barbera, A., Nannetti, C. A., Riccardi, B., Yeatman J. (2000). SiC–SiC_f CMC manufacturing by hybrid CVI–PIP

techniques: process optmization. *Fusion Engineering and Design,* Vol.51-52, (November 2000), pp.159-163, ISSN 0920-3796

Pochet, L.F., Howard, P., Safaie, S. (1996). Practical aspects of deposition of CVD SiC and boron silicon carbide onto high temperature composites. *Surface and Coatings Technology*, Vol.86-87, Part1, (December 1996), pp. 135-141, ISSN 0257-8972

Rogers, D.C., Scott, R.O., Shuford, D.M. (1976). Material Development Aspects of an Oxidation Protection System for a Reinforced Carbon-Carbon Composite, *Proceedings of the 8th National SAMPE Technical Conference*, Seattle, Washington

Roman, Y.G., Stinton, D.P. (1997) The Preparation and Economics of Silicon Carbide Matrix Composites by Chemical Vapor Infiltration. *Proceedings of Material Research Society Symposium*, San Francisco, California (U.S.A.), April 1997

Roman, Y.G., Stinton, D.P. The preparation and economics of silicon carbide matrix composites by chemical vapor infiltration. *Materials Research Society Symposium Proceedings*, Vol. 365, p.343-350, 1997.

Sharafat, S., Jones, R.H., Kohyama, A., Fenici, P. (1995). Status and prospects for SiC-SiC composite materials development for fusion applications, *Fusion Engineering and Design*, Vol.29 p.441-420, 1995, ISSN 0920-3796

Tang, C.C., Fan, S.S., Dang, H.Y., Zhao, J.H., Zhang, C., Li, P., Gu, Q. (2000). Growth of SiC nanorods prepared by carbon nanotubes-confined reaction. *Journal of Crystal Growth*, Vol.210, Issue 4, (March 2000), pp. 595-599, ISSN 0022-0248

Xu, Y., Cheng, L., Zhang, L., Yin, X., Yin, H. (2001). High performance 3D textile Hi-Nicalon SiC/SiC composites by chemical vapor infiltration. *Ceramics International*, Vol.27, Issue 5, (June 2001) pp. 565-570, ISSN 0272-8842

Yoneka, T., Tanaka, S., Terai, T. (2001). Compatibility of SiC/SiC Composite Materials with Molten Lithium Metal and Li16-Pb84 Eutetic Alloy. *Materials Transactions*, Vol.42, No.6, (March 2001), pp. 1019-1023, ISSN 0916-1821

Youngblood, G.E., Senor, D.J., JONES, R.H., GRAHAM, S. (2002). The transverse thermal conductivity of 2D-SiCf/SiC composites. *Composites Science and Technology*, Vol.62, Issue 9, (July 2002), pp. 1127–1139, ISSN 0266-3538

Yun, Y.H., Choi, S.C., Chang, J.C., Kim J.C. (2005). The conversion mechanism of SiC conversion layers on graphite substrates by CVR (Chemical Vapor Reaction). *Journal of Ceramic Processing Research*, Vol.2, No.3, pp. 129-133, ISSN 1229-9162

9

Ceramic Preparation of Nanopowders and Experimental Investigation of Its Properties

Sergey Bardakhanov, Vladimir Lysenko,
Andrey Nomoev[1] and Dmitriy Trufanov
Khristianovich Institute of Theoretical and Applied Mechanics of Siberian Branch of Russian Academy of Science, Novosibirsk,
[1]Buryatian State University, Ulan Ude,
Russia

1. Introduction

Particles of the sizes less than 100 nm (nanoparticles) provide new properties to the materials. For example, the quantum confinement of carriers within small nanocrystals enables the tuning of optical properties with a particle size that led to the demonstration of nanostructured light emitting diodes (Colvin et al., 1994). Metal nanopowders obtained in an electron accelerator (Lukashov et al., 1996), (Bardakhanov et al., 2008) through the evaporation of initial materials exhibit high catalytic properties (Korchagin et al., 2005) and silicon nanopowders exposed to ultraviolet radiation reemit in the visible blue–green spectral range (Efremov et al., 2004).

The design and preparation of nanoceramics from nanopowders is one of the directions of modern nanotechnology. Special effort has been directed toward retaining the smallest possible grains in the final product. It is known that the development of dislocations is terminated at the grain boundaries. Hence, it follows that the smaller the size of grains in the ceramics and the more developed the grained structure, the higher strength of the ceramic material. It is assumed that nanoceramics will have some other unique characteristics (for example, superplasticity (Zhou Xinzhang et al., 2005). The preparation of fine-grained ceramics with a homogenous structure has opened up new possibilities for wide application of these materials in many fields, for example, in structural elements of engines, cutting tools, bioceramics (as coatings for implants), corrosion-resistant and wear-resistant coatings, insulators with high dielectric properties, and so on.

The purpose of the present work was to prepare dense high-strength ceramics with a small grain size (of the order of several microns) from nanopowders.

2. Experimental procedure

The nanopowders of different manufacturers were used as raw material, including the ones obtained by evaporation at the electron beam accelerator with the subsequent condensation of substance as nanosize particles (Lukashov et al., 1996), (Bardakhanov et al., 2008). Ceramic compositions were both pure, and constituted of several components. The nanosize powders of the following chemical components were used: silica SiO_2, alumina Al_2O_3,

titania TiO_2, aluminium nitride AlN, tungsten carbide WC, gadolinium oxide Gd_2O_3 and yttrium oxide Y_2O_3.

In our experiments we reproduced the main stages of the ceramic production: (i) the preparation of the initial materials in the form of nanopowders, (ii) their granulation, (iii) molding of raw pellets from powder materials, (iv) heat treatment, and (v) analysis of the ceramic samples. In the main stage of the compression molding, we used steel molds 25 mm in diameter. The preliminary heat treatment of nanopowders and their sintering were performed in furnaces with air atmosphere (for all oxides), nitrogen atmosphere (for AlN) and in vacuum (for WC).

The properties of the ceramic samples thus prepared were investigated using scanning electron microscopy (JSM-6460 LV (Jeol) electron microscope, Japan), transmission electron microscopy (JEM-100CX, Japan) and X-ray powder diffraction (HZG-4 diffractometer, monochromatic Co radiation). The specific surface area was determined with the use of an Quantachrome Autosorb-6B-Kr automated adsorption analyzer (United States) with nitrogen as an adsorbing agent. The optical properties were evaluated on an SF-56 spectrophotometer. The microhardness was determined using PMT-3 device. Ultimate compression strength was determined using the machine for material strength test Zwick/Roell Z005 (Germany).

3. Results and discussion

3.1 Silicon dioxide SiO_2

The nanopowders of two groups were used: (1) tarkosil (Lukashov et al., 1996), (Bardakhanov et al., 2008) with the specific surface of 50-220 m^2/g and the average size of particles 13÷60 nm, (2) aerosil hydrophilic powders (Degussa, Germany) with the specific surface of 90 and 380 m^2/g. All the powders under investigation were X-ray amorphous without impurities of a crystalline phase (reflections in the X-ray diffraction patterns are absent).

At the maximum temperature T_{max}=1000°÷1620°C the sintered tarkosil samples had greater strength, than aerosol samples, but less shrinkage. It seems, it is due to distinctions in ways of tarkosil and aerosil production. One can assume also, that greater aerosil samples shrinkage (sometimes it was about 40%, and for tarkosil it usually was 20-25%) is caused by different shape of agglomerates, although TEM images of tarkosil and aerosil have shown that they are similar (see Fig. 1(a,b)).

The tarkosil powders of SiO_2 initially were subjected to dry pressing and then were sintered. Dry pressing directly resulted in the formation of relatively high-strength pellets only with the use of step-by-step loading. However, with excess of a particular thickness of the raw pellet, it underwent separation into layers. Apparently, the reason for this separation is the existence of elastic agglomerates in the initial powders.

Nonetheless, the pressed samples of tarkosil were subjected to heat treatment, during which they began to be sintered already at the temperature of 1000°C without a change in the white or grayish (depending on the powder type) color of the surface and fracture. The heat-treated samples were not destroyed during moistening. The examination of these samples with a scanning electron microscope revealed the formation of aggregates of sintered particles. The samples obtained at the temperature of 1500°C exhibited indications of the onset of the vitrification on the surface. The heat treatment at the temperature T_{max} = 1620°C in all cases resulted in the formation of ceramic materials that either were separated along the layers into fragments, or were substantially deformed.

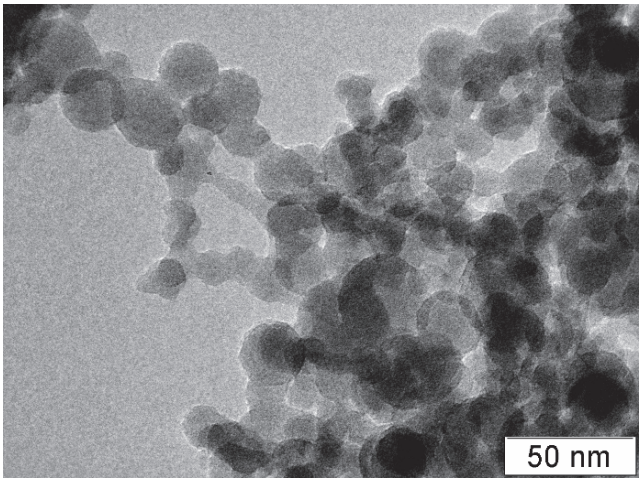

(a)

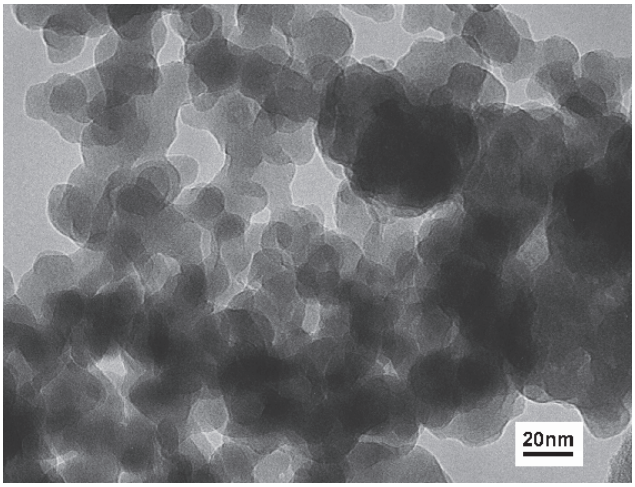

(b)

Fig. 1. TEM image of SiO_2 nanopowders: tarkosil T-25 (obtained with using electron accelerator) (a), aerosil A-380 (Degussa, Germany) (b).

At the next stage, the tarkosil powders were subjected to dispersion in distilled water until the formation of a creamy substance, which was dried for several days at room temperature. The grains obtained after drying were passed through sieves. The fraction with sizes larger than 1 mm and smaller than 2 mm was subjected to step-by-step pressing. This procedure resulted in the formation of non-layered raw pellets with a strength high enough to transfer them to the furnace. These pellets were sequentially sintered under specified temperature–time conditions with isothermal exposure at the temperature T_{max} = 1600°C. As a result, the samples retained their shape without separation into layers. Their ultimate compression

strength was 0.2 GPa about, and microhardness – 2 GPa about. Their surface was vitrified; however they had a different internal structure.

Fig. 2 displays the scanning electron microscope image of the cleavage of the sample sintered from 1- to 2-mm grains of the T-15 tarkosil nanopowder (primary particles size of 25 nm) after the preliminary heat treatment and isothermal exposure at the temperature of 1600°C for 5 h. It can be seen from this figure that the ceramics prepared has the fine-grained nonporous internal structure (with the grain size of the order of 10–20 μm). Although the process of grain transformation requires further investigation, the comparison with the data obtained from analyzing the scanning electron microscope image of the sample surface gives grounds to believe that a more prolonged isothermal exposure should result in the formation of the glassy state throughout the volume of the sample. In particular, the glassy state with a relatively high transparency has already been obtained in thin fragments of some samples after their pressing and sintering.

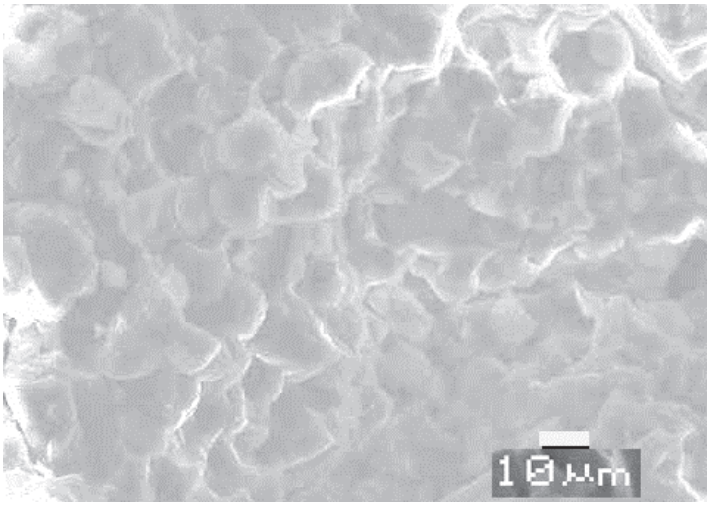

Fig. 2. SEM image of the sample sintered from 1-2 mm grains of the T-15 tarkosil (silicon dioxide) nanopowder with exposure at a temperature of 1660^0C.

For one of the glassy samples (tarkosil T-20, sintered at 1620°C), we evaluated the optical properties. The transparency of this sample for waves with a length of more than 330 nm in the visible spectrum was below the corresponding value for a commercial window glass. However, for waves with a length of 270–330 nm (in the ultraviolet range), the transparency of the prepared glass was higher than that in the case of the window glass.

It can be expected that, apart from ceramics, tarkosils can serve as initial components for the preparation of silica glasses and quartz fibers. For the latter purpose, the T-05 tarkosil powder (specific surface area, 50 m^2/g) with an extremely low content of OH groups on the surface and inside the particles can prove to be especially useful, although the method used for treatment of this powder, certainly, should differ from that described above. We note also that the use of different modifiers (see (Iler, 1979), for example), apparently, will make it possible to obtain a wide variety of glasses based on tarkosils

3.2 Aluminium oxide Al_2O_3

Powders of alumina were processed as pure, as in compositions. The powders AKP-50 (with average size of primary particles d_{av}~200 nm) and AM-21 (d_{av}~4 μm) (Sumitomo Chemicals, Japan), Aluminum Oxide *C* (d_{av}=13nm (Bode et al.), Degussa, Germany), plasma-chemical *A* (d_{av}~300 nm, Siberian Chemical Plant) and *B*, obtained by the method[2,3] (d_{av}=33 nm) were used as basis. The powders of magnesia SG (d_{av}=73 nm, Sukkyoung Co, Republic of Korea) and silica A-380 (d_{av}=7 nm, Degussa) were used as modifiers.

Past experiments on dry pressing pure powders showed that the strength of pressed samples increases in the following course: *A* (300 nm), Aluminum Oxide *C* (13 nm), AM-21 (4 μm), *B* (33 nm), AKP-50 (200 nm). It seems that the strength of pressed samples is determined not by the size of primary particles, but by the kind of agglomerates, which are the consequence of method to obtain powders. One can assume, that compressibility (as well as the form of agglomerates) is determined by phase of substance, and it directly influences the bonding of particles.

The investigation of powders had shown that in plasma-chemical powder *A* the alumina phases δ- and θ- are present in about equal quantities. While Aluminum Oxide *C* and powder B entirely consist of the phase γ-, and AM-21 and AKP-50 almost entirely consist of the phase α-. It can be assumed that the structure and form of agglomerates and phase composition of powders affect the level of particles adhesion during loading, which ultimately determines the strength of pressed samples.

In accordance with the above sequence the microhardness and strength of sintered samples varied – the microhardness: *A* (0.4 GPa), Aluminum Oxide *C* (1.5 GPa), AM-21 (2.8 GPa), *B* (3.1 GPa), AKP-50 (9 GPa), the ultimate compression strength, beginning with AM-21, exceeds 0.3 GPa, and for the most strong ceramics from AKP-50 the strength was more 1 GPa.

The strength and microhardness of sample from the powder B (33 nm, obtained in an electron accelerator) was found to be rather unexpectedly high, because, on X-ray investigation data, this powder initially almost entirely consists of the phase γ-Al_2O_3 of boehmite row. Fig. 3 shows the particle size distribution for Al_2O_3 nanopowder obtained with using electron accelerator.

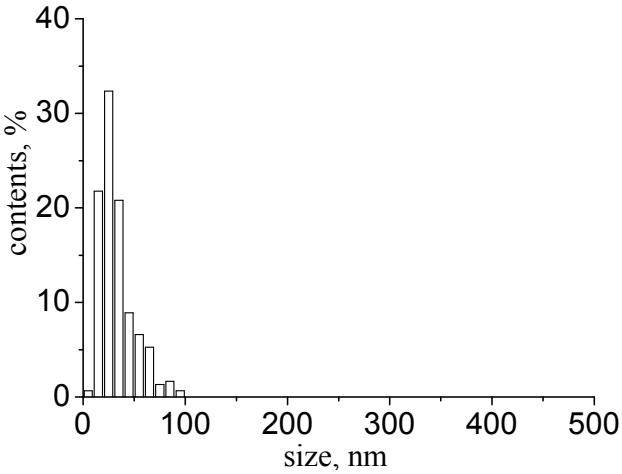

Fig. 3. Particle size distribution for Al_2O_3 nanopowder obtained with using electron accelerator.

The task of preparation of hard and dense electroceramics on the basis of alumina with additives was set. Different compositions were used. Sintering was done at T_{max}=1500°C. The greatest density, strength and microhardness was reached in samples of such composition: AKP-50 (Sumitomo Chemicals, Japan, the average size of primary particles d~200 nm) – modifier SG (magnesia, d=73 nm, Sukkyoung Co, South Korea) – Aluminum Oxide C (d=13 nm, Degussa, Germany). The samples had microhardness of 16-18 GPa, and shrinkage, in relation to initial pellet, was 21-22%.

The radiographic investigation of phase structure of this ceramics (Al_2O_3 (200 nm) – 95%, MgO (73 nm) – 2%, Al_2O_3 (13 nm) – 3%)) showed that it consists of two phases: the main phase is α-Al_2O_3 (46-1212), and as admixture (not more than 1 percent) there is the second phase – cubic phase $MgAl_2O_4$ (10-62) (spinel) with a cell parameter a=8.077 Å. SEM image of such ceramics sample is presented in Fig. 4. It is shown that this ceramics is really dense, its grain size don't exceed 3-5 μm. The formation (even in small quantity) of spinel promotes to high strength and hardness of ceramics.

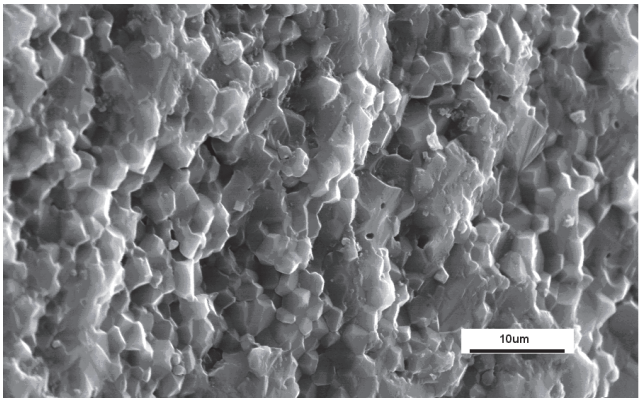

(a)

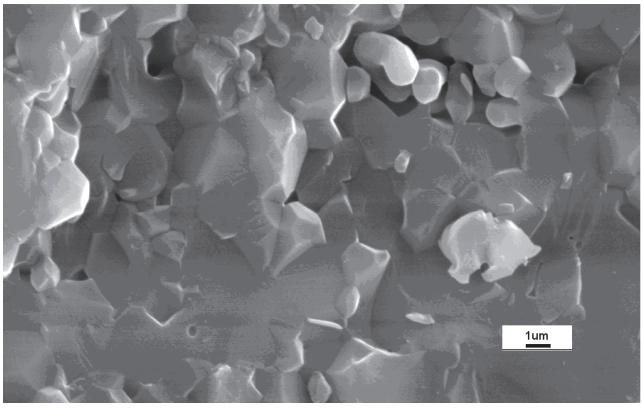

(b)

Fig. 4. SEM image of ceramics sample prepared from such components: Al_2O_3 (200 nm, 95%), MgO (73 nm, 2%), Al_2O_3 (13 nm, 3%) (a, b – different scale).

The phase structure of ceramics samples obtained from the mixture of powders, Al_2O_3 (200 nm) – 95%, MgO (73 nm) – 2%, SiO_2 (7 nm) – 3%, was analogous: the main phase is α-Al_2O_3 (46-1212), and as admixture there is the second phase – spinel $MgAl_2O_4$ (10-62). SEM image of such ceramics sample is presented in Fig. 5. It is shown that this ceramics is more porous and less dense, than in Fig. 4, and less hard.

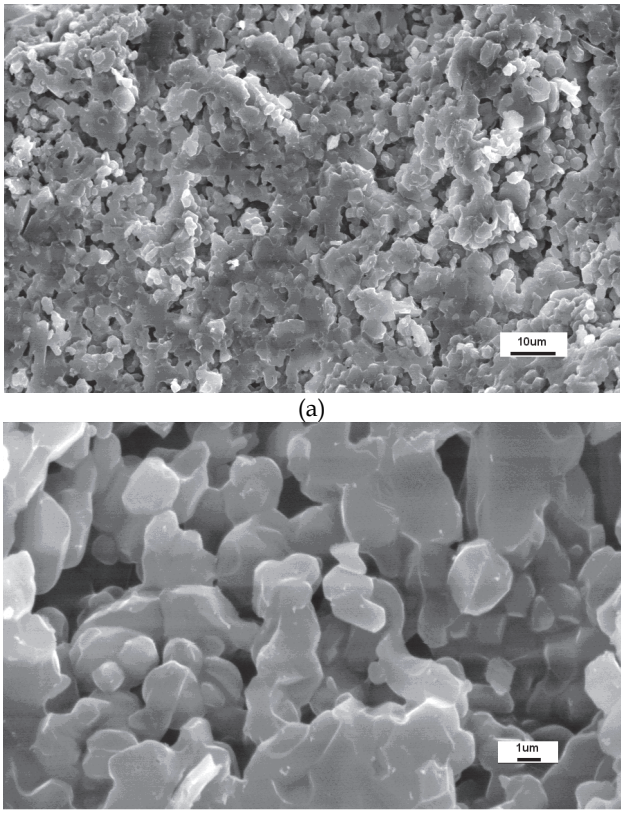

(a)

(b)

Fig. 5. SEM image of ceramics sample prepared from such components: Al_2O_3 (200 nm, 95%), MgO (73 nm, 2%), SiO_2 (7 nm, 3%) (a, b – different scale).

The powders on basis of 4 μm particles powder (AM-21) had more worse (in comparison with 200 nm powder) characteristics – the continuous samples have not been obtained even at temperature T_{max}=1500°C. The important detail is that in composition AKP-50 – SG – Aluminum Oxide C – A-380 (0.05 %) the amorphous phase was showed. The similar effect took place at replacement of A-380 powder by T-20 powder. Thus samples in respect of strength, density and microhardness remained close to samples without SiO_2. Such property can be useful in some cases, for example, at metallization of electrotechnical ceramics.

Besides from plasmachemistry powder (d~300 nm, the Siberian chemical plant) the compact porous tablets of different open porosity, which depends on temperature of sintering, have been obtained.

3.3 Titanium dioxide TiO_2

As is well known, titanium dioxide is widely used as a basis for obtaining ceramics, while it may have photocatalytic properties. In this part of research the task was put to investigate the sintering ability of TiO_2 nanopowder obtained by the method (Lukashov et al., 1996), (Bardakhanov et al., 2008). On the data of X-ray analysis, the titania powder consisted of mainly the metastable X-ray-amorphous phase, probably, this is the fine-grained brookite (29-1360). Fig. 6 presents transmission electron microscopy image of TiO_2 nanopowder and its particle size distribution. The powder has the average size of primary particles of 78 nm.

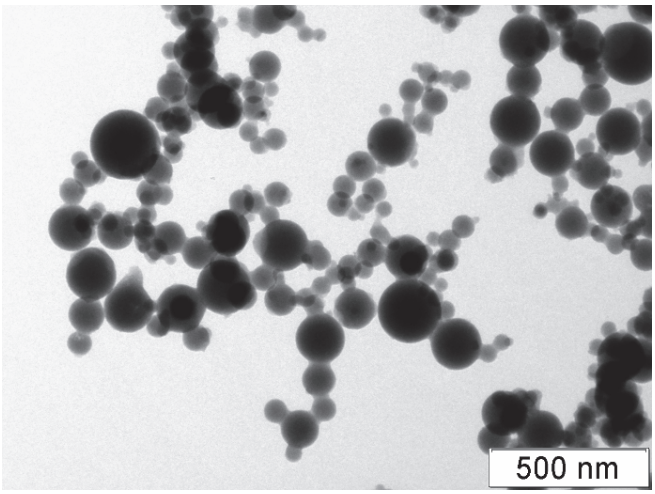

(a)

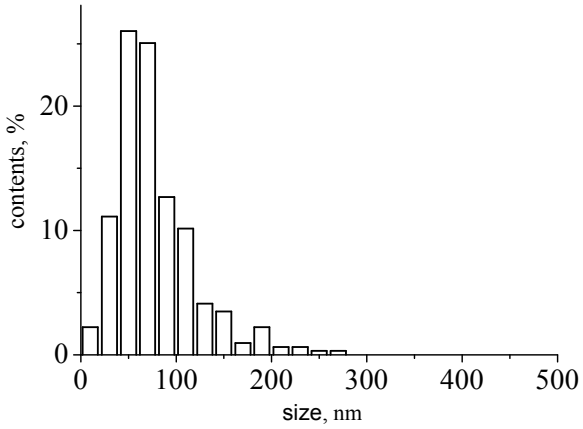

(b)

Fig. 6. TEM image of TiO_2 nanopowder (a) and its particle size distribution (b).

The powder first was pressed, then the pressed samples sintered at temperatures of 1100°, 1200°, 1300°, 1500° and 1600°C. The higher temperature was, the higher samples strength became.

At T_{max}>1300°C the sufficiently strong (microhardness value was about 9 GPa) samples, but with big shrinkage (about 40%), have been obtained. At the same time they were of the bright yellow colour. Powders of titania, prepared at the electron beam accelerator, had high reaction activity.

3.4 Aluminium nitride AlN

As is well known, aluminium nitride possess semi-conductor properties and has been widely used in microelectronics in the form of sprayed films; ceramics from it has high thermal conductivity.

In the present work AlN obtained on the method (Lukashov et al., 1996), (Bardakhanov et al., 2008) was used for ceramics preparation. X-Ray study has shown the next phase structure of AlN powder: the phase of hexagonal AlN (25-1133) (60-70% approximately) and the phase of metal aluminium Al (4-787). The specific surface of this powder is 7 m^2/g, that corresponds to the average particles size of about 250 nm. SEM image of this AlN nanopowder is presented in Fig. 7. It is shown that the powder consists of different fine-grained formations, including ones with the sizes greatly less than 250 nm.

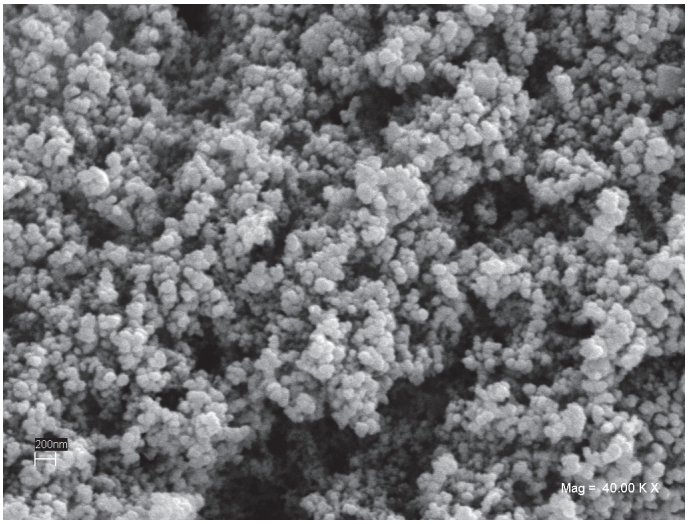

Fig. 7. SEM image of AlN nanopowder obtained with using electron accelerator (scale 200 nm on the left below).

The results of these experiments were found the next. At pressed-samples sintering of aluminum nitride in an atmosphere of air at T_{max}=1600°C the sample was almost completely oxidized to α-Al_2O_3. At sintering in the induction furnace in an atmosphere of air-CO-CO_2 at temperature ~1300°C the sample surface for a large depth was oxidized to α-Al_2O_3, but within the sample the powder partially sintered to the cubic phase (34-679). With sintering in the vacuum furnace at T_{max}≈1800°C the dense nonporous strong sample with crystal structure of aluminium nitride had been produced.

X-Ray study has shown, that this sample contains the phases: main phase AlN (34-679) (with cubic structure, more than 70 wt. %), the phase of hexagonal AlN (25-1133) and traces of the α-Al_2O_3 (corundum). Hence, at sintering of nanosize powder of aluminium nitride, the change of phase structure in comparison with the initial powder (transition from hexagonal structures to cubic) has occured, thus shrinkage of the sample was less than 20%.

3.5 Tungsten carbide WC

Ceramics based on tungsten carbide is widely used in the industry of hardmetal tools. At the same time, in some problems of atomic physics there is a need for targets on the basis of hardmetal carbides of heavy elements which have fine-grained and, at the same time, porous structure.

In these studies the WC powder (TaeguTec, South Korea) with the average particles size of 0.8 μm (800 nm) was exploited. As the source of cobalt, the coarse grain industrial WC8 powder of WC-and-Co alloy was used. The samples, structure of which contains large quantity of WC8, had the greatest strength and density. Their porosity was practically absent. At the same time the samples obtained from mixtures with low WC8 content, and also with latex, possessed a little smaller strength, but had the essential open porosity.

3.6 - 3.7 Gadolinium oxide Gd_2O_3 and yttrium oxide Y_2O_3

The particular interest is to obtain the ceramics from nanopowders of oxides of rare-earth elements, in particular, gadolinium and yttrium. Areas of application of materials on the basis of these substances widen constantly, at that in directions determined the technological progress (alloys of unique properties, nuclear energy, electronics, etc.).

Nanopowders of gadolinium oxide (Gd_2O_3) and yttria oxide (Y_2O_3) produced through technology of raw material evaporation by electron beam (Lukashov et al., 1996), (Bardakhanov et al., 2008) were used for preparation of submicrograin (of several micrometers) dense ceramics. These powders of gadolinium oxide and yttria oxide have the average size of primary particles of 54 nm и 32 nm and chemical purity of 99 percent.

The powders of gadolinium oxide and yttrium oxide were processed in the form of monocompositions. The ceramic samples from them were obtained in a steel press mould by the method of dry pressing (without use of any binding agent and additives) at several loading-unloading cycles (at the maximum pressure 40 MPa) with subsequent sintering in the same sequence of temperature routines, thus T_{max} was 1500°C.

Radiographic research has shown that Gd_2O_3 powder enclosed monocline phase of Gd_2O_3 (JCPDS card number 42-1465), and ceramics from it enclosed (more than 75 %) cubic phase of Gd_2O_3 (43-1014). The powder of Y_2O_3 represented the mix of two phases – monocline phase of β-Y_2O_3 (47-1274) (the basic phase) and monocline phase of Y_2O_3 (44-399), and the ceramics from this powder contained only cubic phase of Y_2O_3 (43-1036).

In Fig. 8(a) there are presented the results of transmission electronic microscopy of the powder of gadolinium oxide which show that powder particles are basically united to agglomerates of chains type. As a whole it is visible that the given powder is nanosize one, that is confirmed by its particle size distribution [Fig. 8(b)]. It is visible that the main part of particles has the size less than 200 nm. The average size of primary particles is 54 nm. It is necessary to notice that many particles have facets though as a whole their form is close to sphere.

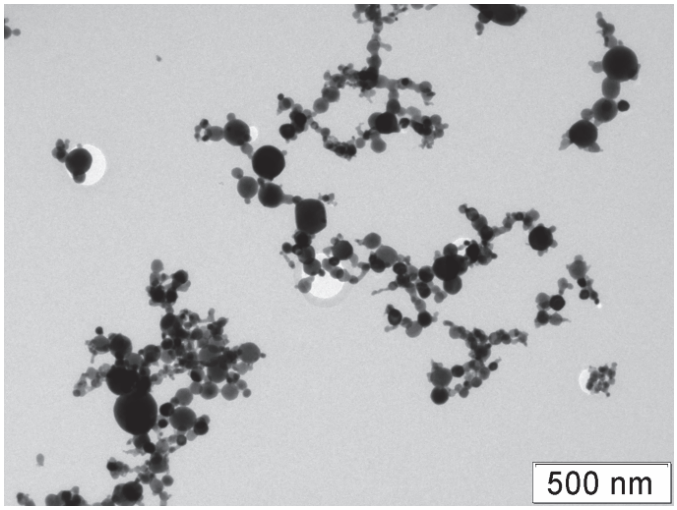

(a)

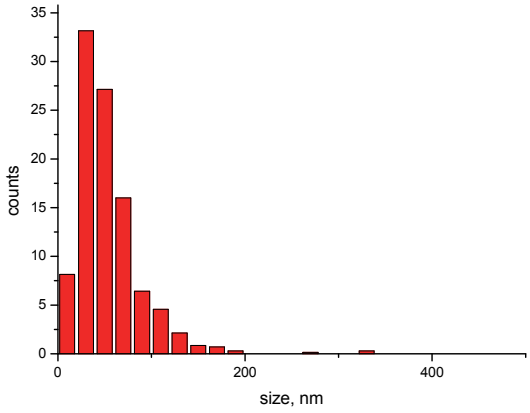

(b)

Fig. 8. TEM image of Gd_2O_3 nanopowder (a) and its particle size distribution (b).

The similar data are presented in Fig. 9 for the powder of yttrium oxide. It is visible that, in comparison with gadolinium oxide, in the powder of yttrium oxide an agglomeration is expressed more poorly, and the form of particles of yttrium oxide also is close to the spherical. The given powder also is nanosize one that is confirmed by the particle size distribution [Fig. 9(b)]. The main part of particles has the size less than 100 nm. Their average size is 32 nm.

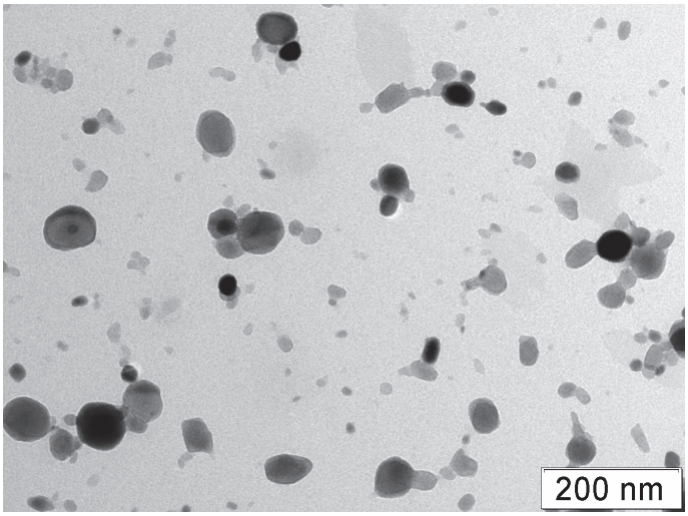

(a)

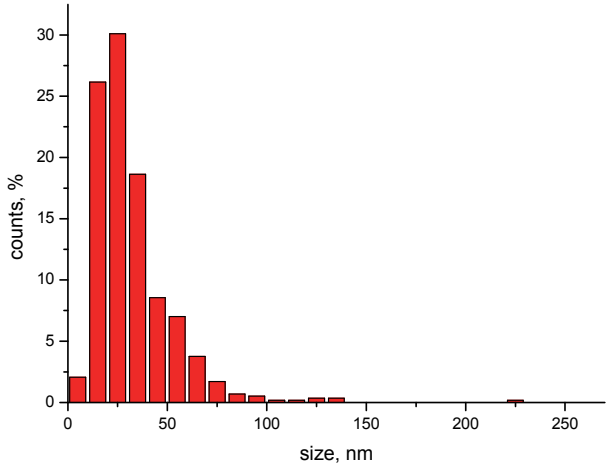

(b)

Fig. 9. TEM image of Y_2O_3 nanopowder (a) and its particle size distribution (b).

In Fig. 10 the structure of ceramics samples of Gd_2O_3 and Y_2O_3 is shown. This figure displays the scanning electron microscope images of chip of ceramics samples prepared from Gd_2O_3 [Fig. 10(a)] and Y_2O_3 [Fig. 10(b)] nanopowders. From comparison of these figures it follows that grains of ceramics of gadolinium oxide are more isolated from each other, than grains of ceramics of yttrium oxide, and the last are good enough sintered among themselves. The size of grains of gadolinium oxide is more, and the forms of grains

of ceramics from gadolinium oxide and yttrium oxide differ. The estimation on survey photos of electronic microscopy of samples has allowed to ascertain that the maximum size of grains of gadolinium oxide is 20–25 μm, and for yttrium oxide – 10–15 μm.
As measurements of microhardness of the obtained samples have shown, for ceramics of gadolinium oxide it was approximately 6–7 GPa, and for ceramics of yttrium oxide – about 11 GPa.

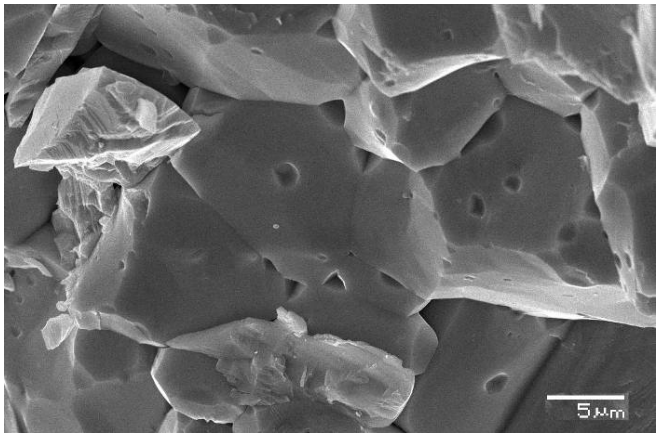

(a)

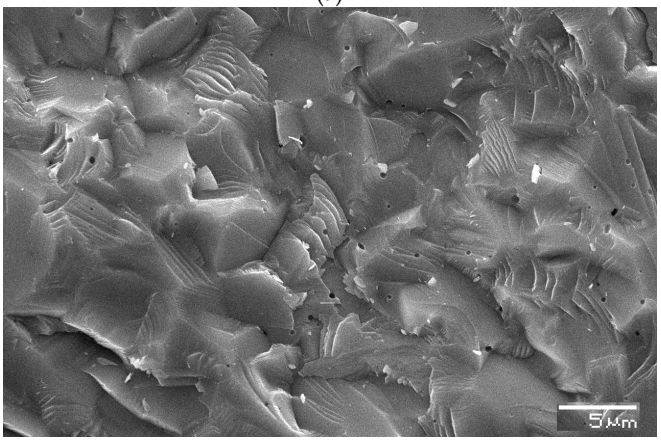

(b)

Fig. 10. SEM images of ceramics samples prepared from Gd_2O_3 nanopowder (a) and Y_2O_3 nanopowder (b).

Ultimate compression strength for ceramics of Gd_2O_3 equaled approximately 0.3 GPa, for ceramics of Y_2O_3 – about 0.4 GPa (it is possible to assume that, besides other reasons, it is explained by difference in ceramics structures).
The study of the data on fluorescence of ceramics from nanopowders of gadolinium oxide and yttrium oxide has shown the following. If radiation of the eximer KrF laser with wave length of 248 nm excites in ceramics of Gd_2O_3 the very weak reddish luminescence which

intensity is insufficient for fixing of a spectrum of fluorescence, then ceramics from Y_2O_3 is shone much more intensively. For ceramics of Y_2O_3 the radiation of wave length of 248 nm in the ultra-violet range excites phosphor in the spectrum visible range with maximum of fluorescence at about 460 nm.
It was shown that the ceramics of yttria irradiate visible light being excited by ultraviolet lasers.

4. Conclusions

Thus, the possibility of ceramics preparation from nanopowders (including powders obtained by authors in their electron accelerator) was investigated. It was confirmed that the sintering process and the resulting ceramics depend on size and shape of particles of the powders used. The sintering temperatures of nanopowders (for example, tarkosil with an amorphous structure) are lower than those of crystalline quartz powders. The ceramic material with the fine-grained structure (with grain sizes of the order of 10–20 μm) was synthesized. The data about the shape-formation and sintering of ceramic samples of different powders combination were obtained. The dense strong samples with the microhardness of 16-18 GPa and size of several micrometers had been produced.

5. Acknowledgements

This study was partly financially supported by Grant RO RNP.2.1.2.3370.

6. References

Bardakhanov, S.P.; Volodin, V.V.; Efremov, M.D.; Cherepkov, V.V.; Fadeev, S.N.; Korchagin, A.I.; Marin, D.V.; Golkovskiy, M.G.; Tanashev, Yu.Yu.; Lysenko, V.I.; Nomoev, A.V.; Buyantuev, M.D. & Sangaa, D. (2008). *Japan. J. Appl. Phys.,* Vol.47, p.7019.

Bode, R.; Ferch, H. & Fratzscher, H. (2006). *Degussa Tech. Bull,* No.11, p.70.

Colvin, V. L.; Schlamp, M.C. & Alivasatos, A.P. (1994). *Nature,* Vol.370, p.354.

Efremov, M.D.; Volodin, V.A.; Marin, D.V.; Arzhannikova, S.A.; Goryainov, S.V.; Korchagin, A.I.; Cherepkov, V.V.; Lavrukhin, A.V.; Fadeev, S.N.; Salimov, R.A. & Bardakhanov, S.P. (2004). *JETP Lett.,* Vol.80, p.544.

Iler, R. (1979). *Chemistry of Silica,* Wiley, New York, Vol.2.

Korchagin, A.I.; Kuksanov, N.K.; Lavrukhin, A.V.; Fadeev, S.N.; Salimov, R.A.; Bardakhanov, S.P.; Goncharov, V.B.; Suknev, A.P.; Paukshtis, E.A.; Larina, T.V.; Zaikovskii, V.I.; Bogdanov, S.V. & Bal'zhinimaev, B.S. (2005). *Vacuum,* Vol.77, p.485.

Lukashov, V.P.; Bardakhanov, S.P.; Salimov, R.A.; Korchagin, A.I.; Fadeev, S.N. & Lavrukhin, A.V. (1996). *Russia Patent,* 2067077.

Zhou Xinzhang, Hulbert, D.M.; Kuntz, J.D.; Sadangi, R.K.; Shukla, V.; Kear, B.H.; Mukherjee, A.K. (2005). *Mater. Sci. Eng. A,* Vol.39, p.353.

Part 2

Topics in Processing of Advanced Ceramic Materials

10

Last Advances in Aqueous Processing of Aluminium Nitride (AlN) - A Review

S.M. Olhero[1], F.L. Alves[1] and J.M.F. Ferreira[2]
[1]*Department of Mechanical Engineering and Industrial Management, FEUP, University of Porto, Porto,*
[2]*Department of Ceramics and Glass Engineering, CICECO, University of Aveiro, Aveiro, Portugal*

1. Introduction

Aluminium nitride (AlN) is a ceramic material that has been intensively studied in the last years due to its good thermal conductivity (319 W/mK, theoretical value), low dielectric losses (8.8), small dielectric consumption (≈4x10^4), a thermal expansion coefficient matching that of silicon, together with other physical properties that make AlN to be the most interesting substrate material for highly integrated microelectronic units (Greil et al., 1994; Iwase et al., 1994; Knudsen, 1995; Prohaska and Miller, 1990; Sheppard, 1990). The most recent breakthroughs were achieved in the processing science field of the AlN, namely on: (i) replacing of the traditionally used organic solvents by water; and (ii) decreasing the sintering temperatures AlN powder compacts through appropriately selecting the sintering additives and process optimization.

Aqueous colloidal processing has been pursued by many authors along the most recent years as an alternative to alcoholic or other flammable and costly dispersion media. The advantages of aqueous processing are the healthier and more environmentally friend production at lower and more competitive costs, which enables to increase and diversify the applications for the nitride-based ceramics. However, nitride powders are susceptible to hydrolysis, what is particularly true in the case of aluminium nitride (AlN) (Bellosi et al., 1993; Osborne & Norton, 1998; Reetz et al., 1992). In fact, when AlN powder is hydrolysed by water, undesirable aluminium hydroxydes are formed on the surface of particles, with a concomitant increase of the oxygen content and the production and release of ammonia. Accordingly, an amorphous layer composed by AlOOH is initially formed at the surface of AlN particles, which then transforms to bayerite, $Al(OH)_3$, according to the following reactions:

$$AlN(s) + 2H_2O(l) \rightarrow AlOOH\ (amorph) + NH_3(g) \quad (1)$$

$$AlOOH\ (amorph) + H_2O(l) \rightarrow Al(OH)_3(gel) \quad (2)$$

$$NH_3(g) + H_2O(l) \rightarrow NH_4{+}(aq) + OH{-}(aq) \quad (3)$$

The resultant hydroxyl ions (OH-) tend to raise the pH of the suspension. The increasing rate of pH is dependent on temperature and initial pH value. Under strong acidic conditions (pH≤3), some authors have even reported the need of a certain incubation time for hydrolysis to start, while accelerated hydrolysis can be expected for pH>7 (Fukumoto et al., 2000; Krnel et. al. 2000; Oliveira et al., 2003; Reetz et al., 1992; Shan et al, 1999). According to this, recently Kocjan (Kocjan et al., 2011) presented a detailed study about the reactivity of AlN powder in diluted aqueous suspensions in the temperature range 22–90◦C in order to better understand and control the process of hydrolysis. The authors conclude that hydrolysis rate significantly increased with higher starting temperatures of the suspension, but was independent of the starting pH value; however, the pH value of 10 caused the disappearance of the induction period. Furthermore, the authors shown that the chemical reaction at the product-layer/un-reacted-core interface was the rate-controlling step for the second stage of the hydrolysis in the temperature range 22–70 ◦C, for which the calculated activation energy is 101 kJ/mol; whereas at 90 ◦C, the diffusion through the product layer became the rate-controlling step. Since there is a continuous formation of ammonia during the hydrolysis, the as created basic conditions approach the isoelectric point (pH_{iep}) of the aluminium hydroxides rich surfaces promoting flocculation. Finally, gelling of the $Al(OH)_3$ reaction product gives rise to a rigid network. Therefore, for a successful aqueous processing one must overcome the hydrolysis of powders' surface that degrades the nitrides by forming hydroxides and releasing ammonia gas bubbles in the suspension and increase the pH of the dispersing media. The gas bubbles trapped in the suspension and in the green bodies act like strength-degradation flaw populations, reducing the density and the general properties of the ultimate products. Other consequences of hydrolysis reactions include an increase of pH and the destabilization of the suspensions leading to structural and compositional inhomogenieties.

On the other hand, the natural enrichment of the surface of nitride particles in oxides may be deleterious for sintering ability and, consequently, for their most characteristic properties, such as the thermal conductivity of AlN. Considering these difficulties, the processing of nitride-based ceramics traditionally involves a previous homogenization of the powders in organic media, followed by consolidation of the green parts via uniaxial and/or isostatic pressing, which have strong limitations in terms of the ability to form complex shapes and achieving a high degree of homogeneity of particle packing. Contrarily, colloidal shaping techniques have the capability to reduce the strength-limiting defects when comparing with dry pressing technologies (Lewis, 2000). Besides traditional processing methods, such as slip casting, tape casting, pressure casting and injection moulding, some new colloidal forming technologies have been developed in the past decade for the near-net-shape forming of complex ceramic parts, including gel-casting, freeze forming, hydrolysis assisted solidification, direct coagulation casting, temperature induced forming, etc. The possibility of application of such performing techniques on the processing of AlN ceramics would broaden their field of application, while keeping ceramics quality higher than those produced by the traditional pressing techniques, turning the materials more commercially competitive. The key controlling factor for the production of reliable ceramic components through colloidal processing is the obtaining of high concentrated and low viscous suspensions. Thus, the work here presented was focused on the preparation of these proper suspensions facing the solid/liquid interfacial reactions and the mutual interactions between the dispersed particles in the suspending aqueous media. The suspensions obtained could then be used for the consolidation of complex-shaped bodies by different

techniques, which could be pressureless sintered at relatively low temperatures. The main goals achieved were the obtaining of standard nitride-based aqueous suspensions that could be used to consolidate homogeneous and high dense green bodies by colloidal techniques, such as slip casting, tape casting, gel casting or to produce high packing ability granulated powders for dry pressing technologies. This enabled obtaining high density ceramic bodies using simpler and less expensive procedures while keeping the high standard valued for the desired final properties. Such achievements are expected to have a tremendous positive impact at both scientific and technological levels, enabling to replace the organic based solvents used in colloidal processing, which are much more volatile and require the control of emissions to the atmosphere, by the incombustible an non-toxic water. Therefore, many efforts have been made to protect AlN powder against hydrolysis, in order to facilitate storage and to make it possible to process and consolidate green bodies from aqueous suspensions (Egashira et al., 1991; Ehashira et al., 1994; Fukumoto et al., 2000; Kosmac et al., 1999; Krnel et. al, 2000, Krnel et al, 2001; Shimizu et al., 1995; Uenishi et al., 1990). Most treatment processes involve coating the surface of AlN particles with long chain organic molecules, such as carboxylic acids, particularly stearic acid, or through use of cetyl alcohol, n-decanoic acid, dodecylamine acid and so on (Egashira et al., 1991; Ehashira et al., 1994). These organic substances are characteristically hydrophobic and thus prevent water from coming into contact with the surface of the protected particles, therefore hindering a good dispersion in water to be achieved even in the presence of organic or inorganic wetting agents, which cause the suspensions to foam. Another disadvantage of this process is that it involves the use of organic solvents that are flammable and dangerous to health, therefore, just transferring the use of this kind of solvents to an earlier step of the processing. Therefore, it is not surprising that more attractive approaches have been attempted to protect AlN surface powders by chemisorbing hydrophilic anions from acidic species such as phosphoric, H_3PO_4, or silicic acids from aqueous media (Kosmac et al., 1999; Oliveira et al., 2003; Uenishi et al, 1990). The efficiency of H_3PO_4 in protecting aluminium from corrosion through anodization was already known to result on impermeable and low soluble phosphate complexes, preventing the reaction. H_3PO_4 also revealed to be very effective in protecting AlN powders dispersed in aqueous solutions for periods of days or even weeks (i.e., long incubation times for hydrolysis to occur). However, besides hydrolysis suppression, another important condition for successfully processing AlN ceramics from aqueous suspensions is the achievement of a high dispersion degree to enable the preparation of stable and highly concentrated suspensions. Such suspensions can then be used to consolidate AlN-based ceramics by different processing techniques such as tape casting and slip casting, or to granulate powders by freezing or spray drying for dry pressing technologies. A proper colloidal processing is essential for enhancing the reliability of the final components and decreasing their production costs.

It is known that the covalent bonds in AlN confer to the material a low diffusivity, which, in turn, demands for high sintering temperatures (1900-2000ºC). The use of sintering aids is a common approach to enhance AlN densification at relatively lower temperatures (Baranda et al., 1994; Boey et al., 2001; Buhr & Mueller, 1993; Hundere & Einarsrud, 1996; Hundere & Einarsrud, 1997; khan & Labbe, 1997; Qiao et al., 2003a; Qiao et al., 2003b; Virkar et al., 1989; Watari et al., 1999; Yu et al., 2002). Y_2O_3 and CaO are the most frequently used sintering additives for aluminium nitride, which provide low-melting point liquids on reacting with Al_2O_3 existing on the surface of AlN particles. These liquids crystallize on cooling to calcium aluminates for CaO or CaC_2 additives and yttrium aluminates for the Y_2O_3 additive.

However, considering the deleterious effects of oxygen on sintering ability and on the thermal conductivity of AlN, many efforts have been made towards finding alternative oxygen-free sintering aids. Moreover, other sintering conditions such as atmosphere, furnace, sintering schedule are also of crucial importance. The appropriate manipulation of these factors could eliminate major structural defects and, consequently, improve the thermal conductivity, which is the more important property of this material. In fact, the thermal conductivities of aluminium nitride often differ extremely from the theoretical value, because structural defects, such as pores and grain boundary segregations, as well as point defects within the AlN lattice all cause a considerable decrease of the thermal conductivity.

This chapter is a review of the last advances on processing AlN-based ceramics in aqueous media, which includes the methodologies for surface coating of the powder against hydrolysis, the preparation of high concentrated suspensions, the consolidation of ceramic parts by different colloidal shaping techniques, the characterization of the green samples and their sintering ability as a function of sintering aids under different atmospheres, including the analysis of the thermo dynamical aspects, and the characterization of the sintered samples.

2. Stability of AlN powders against hydrolysis

The hydrophobic treatment processes firstly used to protect the surface of the AlN particles prevent water from coming into contact with the surface of the protected particles (Binner et al., 2005; Egashira et al., 1991; Ehashira et al., 1994; Fukumoto et al., 2000; Zhang, 2002). However, such approaches present serious disadvantages as follows: (i) their involve the use of organic solvents that are flammable and dangerous to one's health; (ii) the protected hydrophobic powder cannot be dispersed in water without adding organic or inorganic wetting agents, which cause suspensions to foam; (iii) finally, the effectiveness of hydrolysis suppression was shown to depend on the thickness and solubility of the induced protection layer. Low concentrations of some weak to poorly dissociated acids, such as phosphoric, H_3PO_4, or silicic acids in aqueous media, are known to result in a high protection efficiency of the surface of AlN powders for some days or even weeks (i.e., long incubation times) (Koh et al., 2000; Kosmac et al., 1999, Uenichi et al,, 1990). In the particular case of H_3PO_4, aluminium protection through anodisation is known to result on impermeable and low soluble phosphate complexes, preventing the reaction. However, this protection of the AlN is not stable for a long time and the powder does not stand water resistant after an energetic milling procedure or even under relatively high temperatures. In order to overcome these disadvantages another kind of pre-treatments involving a stronger temperature-induced chemical bond between the AlN surface and the phosphate species is most promising. A process for protecting AlN powders against hydrolysis reported by Krnel and Kosmac (Krnel & Kosmac, 2001) appeared to be very promising for these purposes. This protection process involves the use of aluminium phosphate groups to coat the surface of the AlN particles. The protection efficiency of phosphoric acid, acetic acid and a thermochemical treatment with aluminium dihydrogenophosphate solutions in shielding AlN particles from hydrolysis could be described by the evolution of the pH of the AlN aqueous suspensions, as well as, by the crystallinity of AlN particles after hydrolysis, as presented in Figure 1 (Oliveira et al., 2003; Olhero et al., 2004).

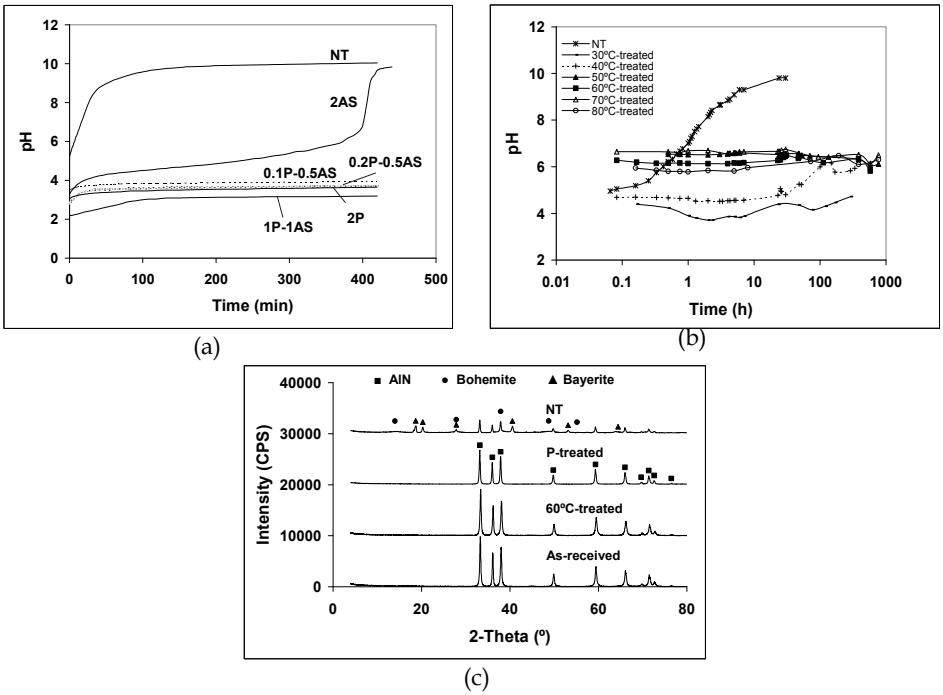

Fig. 1. Evolution of the pH as a function of time for 5-wt.% AlN aqueous suspensions after pre-treatment with: (a) H_3PO_4 and CH_3CO_2H (NT, non-treated; P, H_3PO_4-treated; AS-CH_3CO_2H-treated); (b) $Al(H_2PO_4)_3$, varying the treatment temperature, (c) XRD patterns of AlN powders (as-received and protected by the different described methods) after hydrolysis tests.

In the case of aluminium dihydrogenophosphate, the influence of the treatment temperature is also presented in Fig. 1(b). The suspension prepared from a non-treated AlN powder, NT, suffered a fast pH increase with time (Fig. 1a), concomitant with a strong interfacial reaction leading to the formation of bayerite and amorphous boehmite as shown in Fig. 1(c). The protection of AlN surface with acetic, AS, and phosphoric, P, acids, resulted differently. Adding acetic acid was seen to retard the AlN hydrolysis reaction of the powder, but it did not efficiently avoid the reaction between particles' surface and water and pH steeply increased after about 6 and half hours. Adding H_3PO_4 alone resulted in good protection of the AlN powder particles toward water, as confirmed by the AlN-P-treated spectra that shows pure crystalline AlN. Although a good protection of the surface of the AlN particles could be assured by H_3PO_4 alone, the combination of H_3PO_4 and CH_3CO_2H enhanced the dispersing behaviour of the protected powders, as will be shown in the next section. The effect of $Al(H_2PO_4)_3$ on protecting the AlN particles surface was quite similar to that of H_3PO_4 and CH_3CO_2H, regarding the low pH of the suspension (Fig. 1b) and the resulting pure crystalline AlN powders (Fig. 1c). A treatment temperature as low as 60ºC was seen to result on a stronger bonding of the phosphate groups to the particles' surface, enabling

reliable protection over time. Above this temperature phosphate groups are more weakly bonded to the surface of the AlN particles and, as a result, their partial release into the solution will increase the ionic strength of the dispersing media, therefore decreasing the zeta potential. Due to that, 60ºC was the temperature used to thermochemicaly treat the AlN powder for further investigation.

In order to better understand the interaction between the AlN powder and both H_3PO_4 and $Al(H_2PO_4)_3$ species the fully dried powders were analyzed by FT-IR in the 400–4000 cm^{-1} range (Fig. 2).

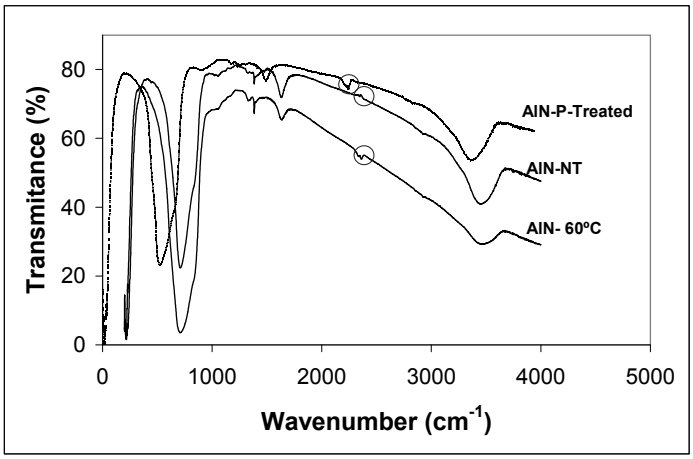

Fig. 2. FT-IR spectra of the AlN powder non-treated (NT), treated with H_3PO_4 (P-treated) and treated with $Al(H_2PO_4)_3$ at 60ºC (AlN-60ºC).

Normally, AlN powder exhibits a large transmittance band at 400–1000 cm^{-1} and two small transmittance bands at 1300–1350 cm^{-1} and 1400–1450 cm^{-1} due to different stretching vibrations of AlN (Nyquist et al., 1997). The peaks observed in the spectra at the wave numbers of 1652 and 3485 cm^{-1} are known to be related with the C-O and H-O bonds vibration due to the surface adsorption of CO_2 and water vapour from the atmosphere, respectively. Pure H_3PO_4 normally reveals a small transmittance band at 500–550 cm^{-1}, a large transmittance band at 1500–1800 cm^{-1}, and a low intense band at 2000–3200 cm^{-1} due to different vibrations of phosphate molecule. Further, the spectrum of the AlN-non treated powder (AlN-NT) shows a transmittance peak located at 2366 cm^{-1}. This peak is characteristic of both Al-N and Al-O bond vibrations (Nyquist et al., 1997). Curiously, the H_3PO_4-treated and $Al(H_2PO_4)_3$-treated powder presents an absorption peak at the same wave number. This absorption peak is characteristic of the aluminum metaphosphate $[Al(PO_3)_3]_x$ (Richard et al., 1997). All of these results support the hypothesis that phosphate ions have been adsorbed at the AlN powder surface, although the chemical bonds involved cannot be stated unambiguously.

Since FT-IR was not conclusive and in order to check if $Al(H_2PO_4)_3$ is strongly attached than phosphoric acid, NMR and was evaluated. Figure 3 shows ^{31}P MAS NMR spectra obtained from H_3PO_4-treated and $Al(H_2PO_4)_3$-treated AlN powders. ^{31}P MAS NMR spectra displayed

a peak at *ca.* –10.7 ppm, consistent with the presence of P-O-Al environments, for example of the type $P(OAl)(OH)_3$ and, thus, supporting the covalent bonding of phosphate species to the AlN particles surface. The large full-width-at-half-maximum of this peak may arise due to the dispersion of other types of local ^{31}P environments, for example $P(OAl)_2(OH)_2$ or even $P(OAl)(OP)(OH)_2$. The shorter dislocation of the large peak to more negative ppm values and the smoothness of the line spectra (less noisy) observed for the thermo-chemically AlN-$Al(H_2PO_4)_3$ treated powder suggests that stronger Al-O-P bonding has occurred, probably involving a higher amount of phosphates species attached at the AlN surface, such as $P(OAl)_3(OH)$ or $P(OAl)_4$. This enhanced the stability of the AlN powder treated with $Al(H_2PO_4)_3$, in comparison to the H_3PO_4-treated one.

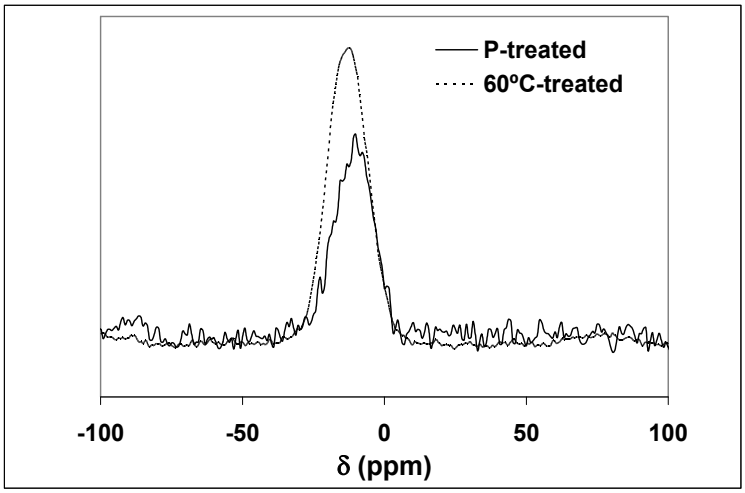

Fig. 3. ^{31}P MAS NMR spectra obtained from the H_3PO_4 (P-treated) and $Al(H_2PO_4)_3$-treated (60ºC-treated) AlN powders.

Based on these results, Ganesh (Ganesh et al., 2008) used the combination of H_3PO_4 and $Al(H_2PO_4)_3$ to passivate AlN powder against hydrolysis. The authors reported that the surface hydroxyl groups play a vital role in the formation of a protective layer against hydrolysis when the AlN powder is treated with H_3PO_4 and $Al(H_2PO_4)_3$. The reaction of an AlN surface with H_3PO_4 was expressed as follows:

$$Al(OH)_3+H_3PO_4+n[Al(H_2PO_4)_3] \rightarrow (n+1)\ Al(H_2PO_4)_3+3H_2O \quad (4)$$

In fact, the reaction occurs between $Al(OH)_3$ and H_3PO_4, and the $Al(H_2PO_4)_3$ is expected to perform a seeding action as $Al(OH)_3$ ultimately converts into $Al(H_2PO_4)_3$ by reacting with H_3PO_4 under the mild reaction conditions employed. It has been reported that approximately 1.1 mg of $H_2PO_4^-$ is required to form a continuous single unimolecular monolayer on a square meter surface of AlN powder (Ganesh et al., 2008). Based on the results obtained a schematic representation of the monolayer coverage of $H_2PO_4^-$ on the surface of an AlN particle was draw and shown in Fig. 4.

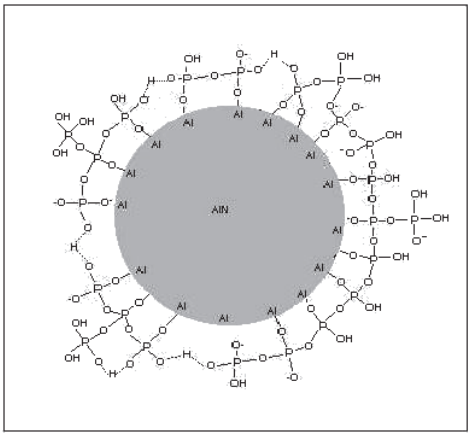

Fig. 4. Schematic representation of the phosphate layer chemisorbed onto the surface of an AlN powder particle.

Besides FT-IR and NMR, the authors (Ganesh et al., 2008) used XPS technique to confirm the presence of the protecting phosphate layer on the surface of AlN treated powder. The authors used four different powders to compare: A-AlN, AlN powder without treatment; T-AlN, AlN powder treated with H_3PO_4 and $Al(H_2PO_4)_3$; A-AlN-72h, AlN powder without treatment after 72 h immersion in water and T-AlN-72h, AlN powder with treatment after 72 h immersion in water. Figures 5 (a, b, c and d) shows the XPS photoelectron peaks of O 1s, N 1s, Al 2p, and P 2p, respectively, and the corresponding binding energy (BE) values are presented in Table 1. All these Figures and Table 1 clearly indicate that XPS bands are highly influenced by the powder surface treatment history, and the observed binding energy value for each element is in agreement with the literature reports (Perrem et al., 1997; Vassileva et al., 2004; Wang & Sherwood, 2002). The O 1s profiles (Figure 5a), are due to the surface hydroxyl groups in the case of the non treated powder (A-AlN) and to the overlapping contribution of oxygen from $H_2PO_4^{1-}$ in the case of treated powder (T-AlN) and treated after 72 h immersion in water (T-AlN-72 h) or of the hydroxyl groups from $Al(OH)_3$ in the case of the non treated AlN powder immersed in water (A-AlN-72 h). Very interestingly, among all the powders investigated, the A-AlN powder exhibits the lowest oxygen concentration, whereas the A-AlN-72 h powder revealed the highest one. The increase in oxygen concentration for the T-AlN and T-AlN-72 h powders is due to the coating $H_2PO_4^{1-}$ layers and partial hydrolysis upon prolonged (72 h) contact with water. The highest oxygen concentration of A-AlN-72 h powder is the result of AlN hydrolysis with the formation of aluminium hydroxide.

Table 1 and Fig. 5 (b) show the binding energy of N 1 sphotoelectron peaks for A-AlN, T-AlN, and T-AlN-72 h at 396.9, 397.1, and 397.1 eV, respectively, which agree well with the values reported in the literature (Perrem et al., 1997). The following trend is observed for the N surface concentration: T-AlN > T-AlN-72h > A-AlN > A-AlN-72 h. The amount of N detected in the A-AlN-72 h powder is negligible. This is due to the occurrence of extensive hydrolysis and to the fact that the soft X-rays (1–3 keV) used in the XPS analysis do not penetrate more than a 30Å depth from the surface of the sample. Because of the high thickness of the aluminium hydroxide layer formed on the surface of AlN particles, the soft

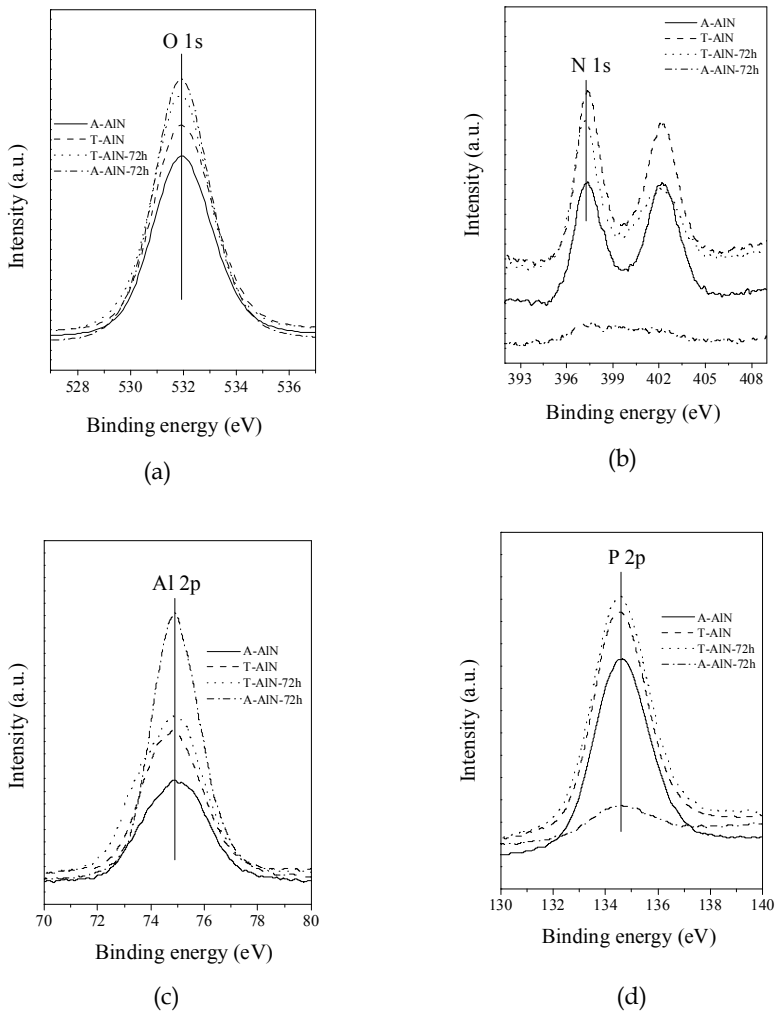

Fig. 5. XPS of the (a) O 1s, (b) N 1s, (c) Al 2p and (d) P 2p binding energy regions for various AlN powder samples: A-AlN (non treated), T-AlN (treated), T-AlN-72h (AlN treated after 72 h in aqueous media), A-AlN-72h (non-treated AlN powder after 72h in aqueous media).

X-rays could not reach the core of AlN particles, whereas hard X-rays used in the XRD study could detect some remaining AlN crystals. Figure 5 (c) and Table 1 shows also XPS peaks and BE values of Al 2p core levels belonging to four AlN powders. No appreciable chemical shifts could be seen in the BE values of Al for all analyzed powders, and the values match very well with those reported in the literature (Wang & Sherwood, 2002). The absence of noticeable chemical shifts in the BE of Al atoms is not surprising since all of them possess a +3 oxidation state. The small differences in the BE values reported in Table 1 are within the allowed range and could be due to the minor changes in the experimental conditions. The

concentration of Al detected in different powders is as follows: A-AlN-72 h > T-AlN-72 h > T-AlN > A-AlN. As a result of the formation of $Al(OH)_3$ upon hydrolysis of AlN, the surface concentrations of Al and O increase at the expenses of nitrogen, which escapes as NH_3 gas. Very interestingly, the A-AlN powder exhibited the lowest Al concentration and highest N concentration among the four powders. This indicates that the A-AlN powder has relatively low oxygen concentration, in good agreement with the technical data sheet from the supplier. Fig. 5 (d) shows the P 2p photoelectron peaks of four different AlN powders and the BE values recorded (Table 1) are according to the literature reports (Perrem et al., 1997; Wang & Sherwood, 2002). In the case of P also, no chemical shift is seen in BE values because of the availability of only a +3 oxidation state for the P atom. As expected, T-AlN and T-AlN-72 h reveal higher P concentrations than the other two powders, confirming the adsorption of a phosphate layer onto the surface of treated AlN particles. Surprisingly, even the A-AlN powder exhibits a small amount of P that can be regarded as an impurity.

Sample	Binding energy (±0.3 eV)				Peak range (eV)			
	O 1s	N 1s	Al 2p	P 2p	O 1s	N 1s	Al 2p	P 2p
A-AlN	532.5	396.9	74.9	134.6	527.0 to 538.9	393.8 to 407.0	68.0 to 80.6	128.0 to 141.1
T-AlN	532.4	397.1	74.8	134.6	527.0 to 538.9	393.8 to 407.0	68.0 to 80.6	128.0 to 141.1
T-AlN-72h	532.6	397.1	75.0	134.8	527.0 to 538.9	393.8 to 407.0	68.0 to 80.6	128.0 to 141.1
A-AlN-72h	531.9	-	74.9	134.6	527.0 to 538.9	393.8 to 407.0	68.0 to 80.6	128.0 to 141.1

Table 1. Binding Energies and Peak Range and XPS Intensity Ratios of Different Powders.

3. Optimisation of aqueous suspensions of pre-treated AlN powders for slip casting

Although several studies present the passivation of AlN powder against hydrolysis, the preparation of high concentrated suspensions using the treated powders is not strongly reported. Some authors present some attempts, however the solids loading achieved is to low to obtain good green and sintered samples (Groat & Mroz, 1994, Shimizu et al.., 1995; Xiao et al., 2004; Wildhack et al., 2005). In fact, dispersing ability is negatively affected by the state of powders agglomeration, which needs to be minimised in order to obtain high degrees of green packing density and homogeneity and enhanced sintering behaviour. Using H_3PO_4 mixed with CH_3CO_2H (Oliveira et al., 2003) it was found that relatively fluid suspensions containing a solids volume fraction as high as 50-vol.% could be prepared by adding a suitable combination both, namely 0.2-wt.% and 0.5-wt.%, respectively. The flow curves presented in Fig. 6 reveal the starting suspension exhibits a strong shear thickening behaviour, which then tends to decrease as deagglomeration time increases, presenting a near Newtonian behaviour up to about 300 s^{-1} after 120 min of ball-milling. The presence of coarser agglomerates/particles population and the predominance of the electrostatic stabilization mechanism were believed to be the main responsible factors for the accentuated shear thickening behaviour of the starting or the poorly deagglomerated suspensions. From these suspensions, AlN compacts with a green density as high as 71% of the theoretical density, could be obtained. However, the obtaining of well deagglomerated suspensions (Fig. 6) required a careful milling procedure with additional increments of H_3PO_4 at each 30min. milling time, in order to keep the coating integrity or to reform it onto

the new exposed surfaces resulting from deagglomeration. Therefore, this procedure to prepare the suspensions might not be so reliable in terms of surface protection and may originate unpredictable and non-reproducible suspensions characteristics. Conversely, the stronger bonding of phosphate species to the surface of AlN particles achieved by the thermo-induced phosphate protection of AlN powders seems more promising and the more resistant protection layer should better outstanding the milling stresses during the deagglomeration step.

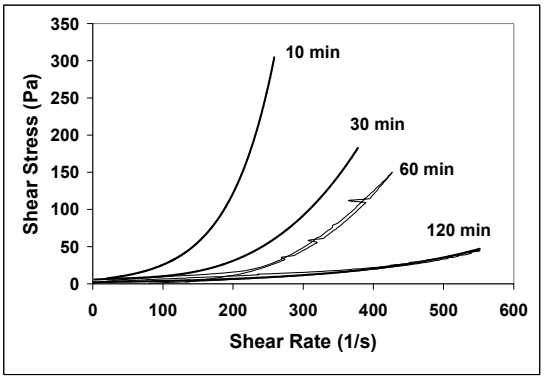

Fig. 6. Flow behaviour of the H_3PO_4-treated AlN aqueous suspension with 50-vol.% solids concentration after different ball-milling times.

Fig. 7 shows the electrophoretic characterization of the thermo-chemical treated AlN powders at 60ºC, in absence and in the presence of different dispersants. The aim was to gather useful data for selecting the most efficient dispersion conditions to stabilize the particles. The amounts used were previously selected as the most proper.

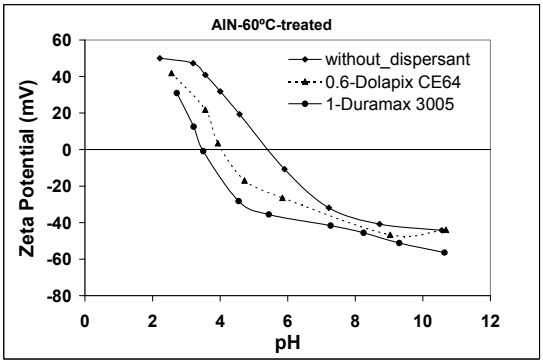

Fig. 7. Electrophoresis curves of thermochemically treated AlN at 60ºC in the absence and in the presence of 0.6-wt.% of Dolapix CE 64 or 1-wt.% Duramax 3005.

From these results it can be concluded that Duramax 3005 is better suited to shift the pH_{iep} of the thermo-chemically treated AlN particles at 60ºC towards the acidic direction, and to increase the negative zeta-potential values in the pH range of interest (near neutral or

slightly alkaline). Moreover, the results of electrophoresis measurements suggest that the stabilization mechanism might be predominantly of an electrostatic nature. It is important to note that in the presence of the Duramax 3005, a good dispersion could be achieved in the pH range from 8 to 9. Thus, for the preparation of well stabilised AlN-based suspensions, Duramax 3005 seems to be the most suitable dispersant. The evolution of rheological behaviour along deagglomeration time of concentrated suspensions containing 50-vol.% of solids loading dispersed with the selected type and amount of dispersant, 1%-wt Duramax 3005, is presented in Fig. 8.

All the suspensions exhibited a shear thinning behaviour within the lower shear rate ($\dot{\gamma}$) range (up to ≈ 200 $\dot{\gamma}$ s^{-1}), followed by near-Newtonian plateau, ending with an apparent shear thickening trend for the highest $\dot{\gamma}$ values. The presence of some coarser particles and/or agglomerates, which would cause a higher resistance to flow, or the relatively large interaction size of the dispersed particles that one would expect when the electrostatic stabilisation mechanism predominates, might account for the shear thickening effect in the highest shear rate range.

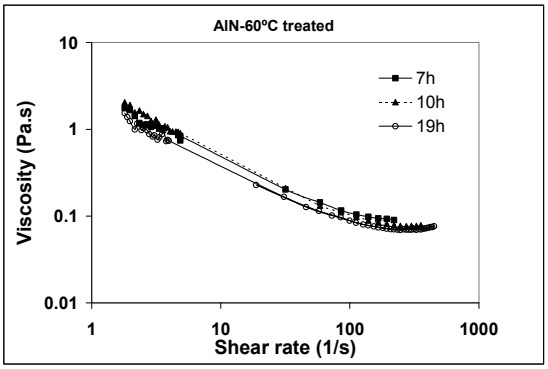

Fig. 8. Evolution of the flow behaviour along deagglomeration time of an aqueous AlN suspension containing 50-vol.% of solids.

Using this well deagglomerated AlN suspension in aqueous media it was possible to prepare green samples with green densities around 59% (percentage of theoretical density (TD) after 19 h deagglomeration time, as it can be seen in Table 2. Using the thermochemical treatment with aluminium phosphate species, the suspension is stable during all the time necessary for deagglomeration and casting, confirming the strong connection of these species to the AlN surface powder, investigated before.

50-vol.% solids	**Green density (% TD)**	
AlN sample	10 h	19 h
	57.7±0.07	59.1±0.2

Table 2. Green densities of slip-cast samples, obtained from 50-vol.% solids-loaded suspensions after deagglomeration for two different periods (10 and 19 h).

Examples of several crucibles obtained by the same suspension are also presented in Fig. 9.

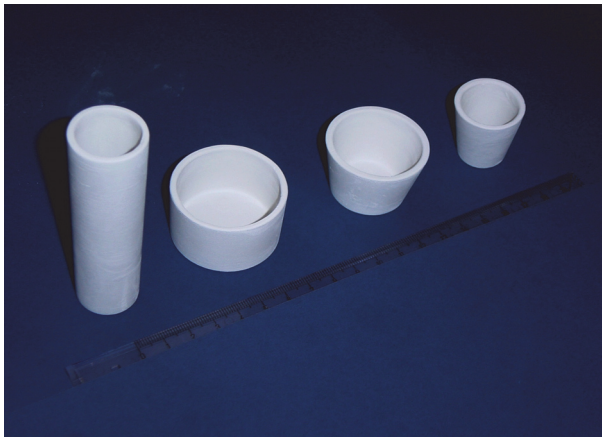

Fig. 9. AlN crucibles obtained by slip casting with an aqueous suspension containing 50-vol.% solids.

3.1 Densification studies of slip casted AlN samples

The quality of ceramic processing based on powder technology, including many steps from preparation of raw materials to sintering of shaped components is a key point. Each step is, in different ways, crucial for the ultimate material properties. The quality of the starting powders, particle size, particle size distribution and particle shape are crucial factors which in an integrated way influence the final material properties (Komeya et al., 1969).

Using the green slip casted samples obtained above with aqueous treated AlN suspensions with 50-vol.% solids, full dense aluminium nitride (AlN) ceramics were obtained after sintering for 2 h at 1750ºC and characterised for Vickers hardness (1000 Hv), flexural strength (200 MPa), and thermal conductivity (115 W/mK) (Olhero et al., 2006a). YF_3 and CaF_2 were used as sintering additives in total amounts ranging from 5 to 7-wt.%, in ratios of 1.25; 1.5 and 2. The sintering additive compositions seem to affect the mechanical properties, density and thermal conductivity through the amount of intergranular phases formed, the volume fraction of porosity, the grain size and grain size distribution, as Table 3 and Fig. 10 suggest. The codes, A, B, C, D, E and F refers the different amounts of sintering aids used as follows: **A**- 5-wt% CaF_2; **B**- 3-wt.% YF_3; **C**- 2-wt.% YF_3 + 1-wt.% CaF_2; **D**- 3-wt.% YF_3 + 3-wt.% CaF_2; **E**- 4-wt.% YF_3 + 2-wt.% CaF_2 and **F**- 4-wt.% YF_3 + 3-wt.% CaF_2.

Samples	Sintered density (%TD)	Thermal conductivity W m^{-1} K^{-1}	Hardness (Vickers)	Mechanical Strength (MPa)
A	99.01± 0.74	93.7 ± 4.68	962.3 ± 28.16	128.5 ± 15.9
B	99.6 ± 0.76	75.0 ± 3.75	1062.1 ± 64.03	135.5 ± 14.0
C	99.8 ± 0.56	77.9 ± 3.89	1100.1 ± 51.37	157.5 ± 20.9
D	100.1 ± 0.08	113.0 ± 5.65	971.3 ± 38.90	178.7 ± 22.8
E	99.9 ± 0.21	115.0 ± 5.75	950.2 ± 27.30	218.8 ± 18.7
F	99.5 ± 0.18	108.0 ± 5.40	908.9 ± 47.18	203.1 ± 21.3
Without additives	99.01± 0.74	93.7 ± 4.68	962.3 ± 28.16	128.5 ± 15.9

Table 3. Final properties (sintered density, thermal conductivity, hardness, and flexural strength) of the AlN samples.

Except the pure AlN samples that presented a relatively low sintered density (≅80%) and the sample with added 5-wt.% CaF_2 (composition A, ≅97%), all the other compositions exhibit high densification levels (>99.5%TD), which tend to increase with an increase in the total amount of sintering additives. Nearly fully dense materials were obtained for compositions with higher total amounts of sintering aids (D and E). However, compositions B and C with the lowest total amount of sintering additives (3-wt.%) are denser (>99.5% TD) than composition A (99% TD) with 5-wt.%, the same total amount as in the fully dense composition D (100% TD). For composition F with the highest amount of sintering additives, the sintering density decreased (99.5 wt% TD), probably caused by an excess of secondary phases. In the system CaF_2–YF_3, the latter component is clearly the most effective one. Incomplete densification might be caused by the incomplete oxygen consumption at the grain boundaries and an insufficient amount of liquid phase formed. The increasing amount of intergranular phases and the concomitant increase in sintered density enhanced the flexural strength of the AlN. This is according to the microstructural observations on fracture surfaces (Figure 10) that clearly showed a number of transgranularly fractured

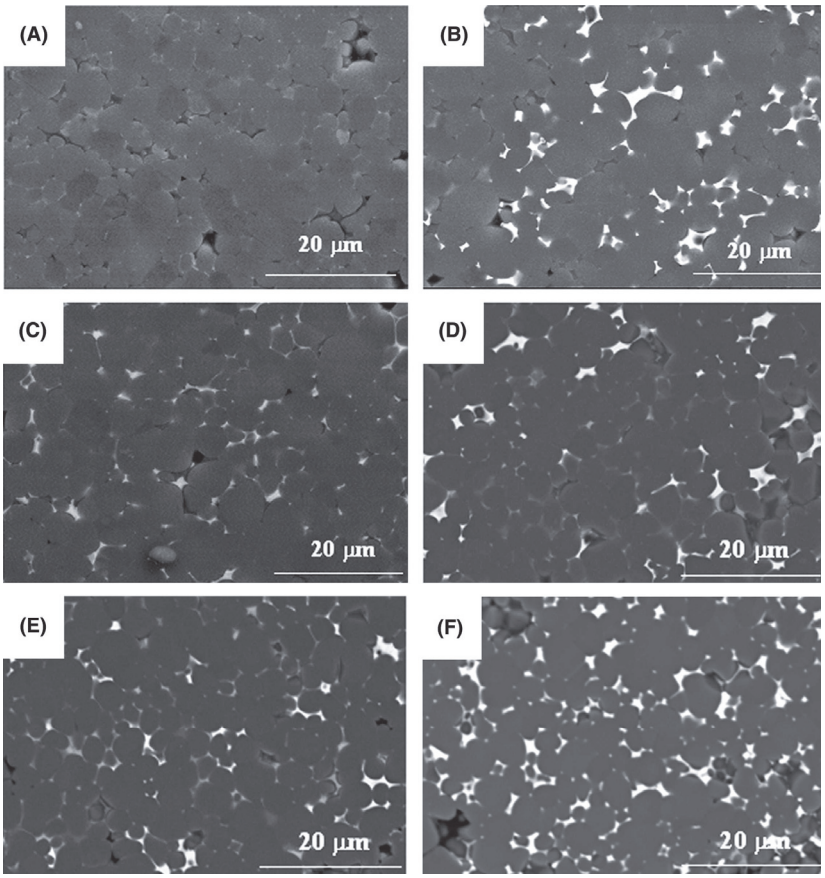

Fig. 10. Backscattering images of the polished AlN samples (A, B, C, D, E, and F) after sintering at 1750°C for 2 h.

grains, indicating strong bonding and high strength of the intergranular phase. The increase in the amount of sintering additives resulted in a decrease of microhardness due to the lower hardness of the secondary phases between AlN grains in comparison to that of crystalline AlN grains (Olhero et al., 2006a).
Therefore, the amount and ratio of the sintering additives play important roles in the microstructural development and in determining the final physical properties of the sintered bodies. These results were explained afterwards, as it will be shown in the next sections.

4. Application of the AlN aqueous suspensions in other colloidal processing techniques

From the technological point-of-view, the inhibition of hydrolysis at the AlN particles surface, a good dispersion of the protected powders and the control of the rheological behaviour of highly concentrated AlN-based suspensions, are the key factors to extend the application of aqueous AlN suspensions to other fields of ceramic processing. Examples include the use of other colloidal shaping techniques such as tape tasting, gel casting and so on, or the production of granulated powders (freeze granulation) for the dry pressing technologies. As stated above, from the rheological point-of-view, a shear thinning behaviour is desirable for the highly concentrated aqueous suspensions of the protected AlN powder, especially if the suspensions have to undergo relatively high shear rates in a given processing step. Such requirements are therefore of major importance in the particular cases of tape casting or freeze granulation due to the high shear rates achieved when the suspension passes under the blade or through the spray nozzle. The compatibility between dispersants, binders and plasticizers and their specific interactions with the AlN protected-surface and water must be also taken into account, since they affect the sintering density and the final properties of the AlN-based ceramics, such as the required excellent thermal conductivity.

4.1 Freeze granulation

Granulation is a size enlargement operation by which a fine powder is agglomerated into larger granules to generate a specific size and shape to improve flowability and appearance and, in general produce a powder with specific properties such as granule strength, apparent bulk density and compacting ability. Compared to the conventional powder granulation technique by spray drying, freeze granulation has the advantage of obtaining granules without inner cavities and with a higher degree of homogeneity, due to the absence of binder segregation during drying or the migration small particles (Nyberg et al., 1993; Nyberg et al., 1994). The density and other physical properties of the freeze dried granules can be controlled by varying the solids content of the slip, the particle size distribution and a proper combination of processing additives to confer the suspension the desired shear thinning behaviour and avoiding pumping difficulties and/or clogging of the spray nozzle that divides the suspension into small droplets. The presence of the binder and plasticizer is essential for confer to the forming granules the required physical properties and the compacting ability, therefore eliminating the possibility of using suspensions without processing additives. Fig. 11 shows general microstructural aspects as well as details of the granules obtained after spraying and freezing suspensions with 50-vol.% solids containing 5-wt.% binder + 2.5-wt.% plasticizer (P200). The high homogeneity of the

binder and plasticizer in the starting suspensions was determinant for the reproducibility of granules characteristics after spraying and freezing, namely: (i) granules size (≈100-800 μm), (ii) wide granule size distribution, and (iii) perfectly round shaped and smooth granule surface. Varying the amounts of binder and plasticizer the aspect of the granules is similar although higher binder amounts affect the compacting ability of the granules in dry pressing. In fact, the increased plasticity of the granules containing the highest content on the polymeric additives binder and plasticizes would account for the higher density values in the greens obtained after uniaxial pressing.

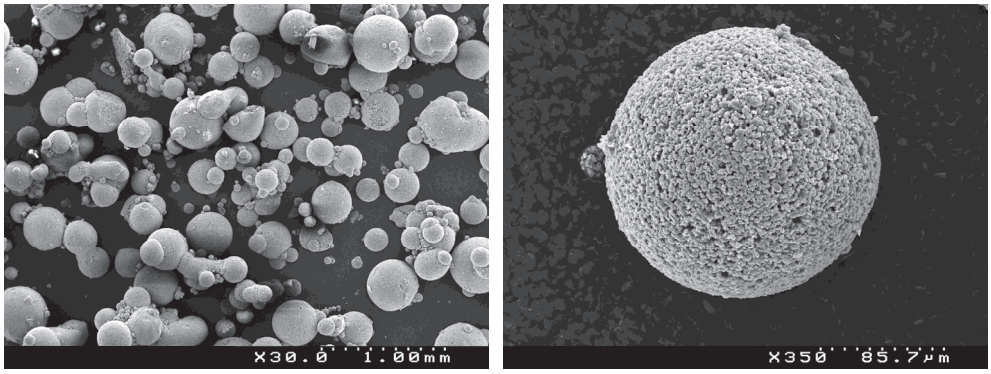

Fig. 11. Size, size distribution and microstructure of the granules obtained by freeze granulation from AlN aqueous suspensions containing 50-vol.% solids and 3-wt% binder + 1.5-wt% plasticizer (P200).

4.2 Tape casting

Oppositely to freeze granulation, tape casting process using AlN suspensions in aqueous media was already reported by other authors (Chartier et al., 1992; Hotza & Greil, 1995; Xiao et al., 2004). As in other forming methods, the arrangement and packing of the AlN particles in the green body influences the sintering behaviour and the final properties. The green microstructure depends on the system to be consolidated and the forming technique employed. Assuming well-dispersed starting slurry, the microstructure of the casting tapes will be determined by two key processing factors: (i) particles' arrangement during the casting process and the shrinkage during drying; (ii) the shear stress generated when the slurry passes under the blade. Due to all of these reasons, the rheological behaviour of the suspensions is of paramount importance in the tape casting process. The rheology determines the flow behaviour in the casting unit, which is dependent on the type and concentration of powder, binder, solvent and other organic additives such as dispersants and wetting agents. In order to obtain aqueous AlN-based suspensions with suitable viscosity for tape casting, and tapes with good mechanical properties (strength and flexibility) the same processing additives used for freeze granulation were also added but in larger amounts: 10- and 15-wt.% of binder and 5- and 10-wt.% of P200 (Streicher et al., 1990a). In same formulations the plasticizer P200 was replaced by a higher molecular weight one, P400, added in the same proportions. All the viscosity curves presented a first shear thinning that is a desired behaviour for the tape casting process, enabling structural

decomposition when the suspension passes under the blade and its level out, as well as, the structural regeneration after passing the blade, avoiding particles segregation and unwanted post-casting flows. Therefore, it is important to mention that no evident incompatibility between binder and plasticizers was observed. From all the suspensions tested, it was possible to obtain un-cracked green tapes, presenting smooth and uniform surfaces, as those shown in Figure 12 (Olhero & Ferreira, 2005). The minimum amount of binder required to produce flexible tapes with a thickness value as high as 1.5 mm was seen to be 15-wt.%. Thicker tapes could be obtained by increasing the solids loading in suspensions through partial evaporation of the excessive water introduced with the emulsion binder.

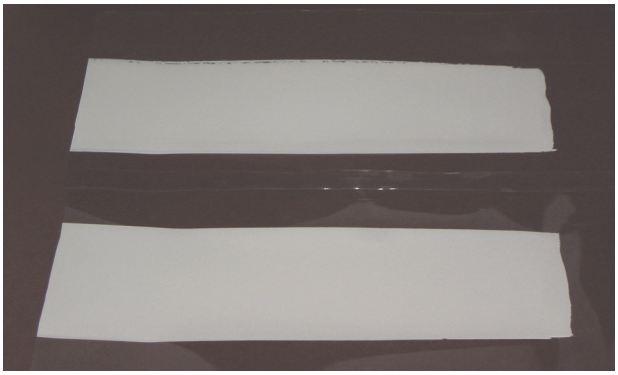

Fig. 12. Green tapes obtained by tape casting from the aqueous AlN-based suspensions.

5. Influence of de-waxing atmosphere on the AlN properties

High-performance advanced electronic packaging for high-density circuits and high-power transistors needs to have high thermal conductivity to dissipate the heat generated during functioning in order to have lower operational temperatures and improved reliability and performance. In the last 10 years, AlN ceramics have been intensively studied for substrates applications due to the high thermal conductivity, non-toxicity and low dielectric constant among other properties (Collange et al., 1997; Enloe et al., 1991; Jackson et al., 1997; Raether et al., 2001). The thermal conductivity was found to depend on several factors, namely intrinsic and extrinsic. The intrinsic ones are material dependent such us the oxygen content (total and lattice dissolved), the microstructure, lattice defects among others, while the extrinsic ones are sintering conditions (atmosphere, furnace), sintering temperature, time and sintering additives. Hence, to achieve excellent properties of AlN, namely high thermal conductivity, it is important to know how to optimize the extrinsic factors, which in turn influence the intrinsic ones. One factor that promotes deleterious sintering is the presence of oxygen at the grain boundaries. In fact, along the sintering period, impurities such as oxygen are solid-dissolved in AlN crystal lattices or form a composite oxide, such as Al-ON, which hinders the propagation of the thermal oscillations of the lattice. During firing, these impurities are incorporated into the AlN lattice by substitutional solution in the nitrogen site, creating aluminium vacancies, according to the following reaction (5):

$$Al_2O_3 \rightarrow 2Al_{Al} + [\cdot]_{Al} + 3O_N \quad (5)$$

where [·]Al denotes an aluminium vacancy.

Mass and strain misfits caused by the vacant aluminium site increase the scattering cross section of phonons, which decreases the phonon mean free path, thereby lowering the thermal conductivity. Taking into account the reasons exposed above, numerous efforts have been done aimed at lowering the oxygen content within the AlN grains and grain boundaries to decrease the temperature of densification and consequently to reduce the costs of the AlN substrates (Jarrige et al., 1993; Liu et al., 1999; Qiao et al., 2003b; Streicher et al., 1990b; Thomas et al., 1989). The use of sintering aids has been the approach more extensively studied to enhance AlN densification and thermal conductivity (Baranda et al., 1994; Boey et al., 2001; Buhr & Mueller, 1993; Hundere & Einarsrud, 1996; Hundere & Einarsrud, 1997; khan & Labbe, 1997; Qiao et al., 2003a; Qiao et al., 2003b; Virkar et al., 1989; Watari et al., 1999; Yu et al., 2002). If oxygen impurities in raw powders react with sintering aids to form stable alumina compounds at the grain boundaries of sintered AlN, oxygen impurities do not diffuse into AlN lattice and crystal defects are not produced (Hyoun-Ee & Moorhead, 1994). The thermodynamics and kinetics of oxygen removal by the sintering aids determine both the microstructure and the impurity level of AlN ceramics. Therefore, besides adequate selection of sintering aids, suitable sintering conditions are very important to prevent further increase in the oxygen content of the AlN powder (Lavrenko & Alexeev, 1983; Wang et al., 2003). A higher thermal conductivity is achieved if the grain boundaries are clean from sintering additives and the system is free of oxygen. This is accomplished by heat treatments that lead to liquid removal by evaporation or migration to concentrate at grain-boundary triple points. Recently, Lin (Lin et al., 2008) studied the effect of reduction atmosphere and the addition of nano carbon powder to enhance deoxidation of AlN parts.

The viability of using aqueous media for processing AlN at industrial level is strongly dependent on the final properties, namely thermal conductivity and mechanical properties. The achievement of comparable properties using water to disperse the powders (AlN + sintering aids) and aqueous suspensions to consolidate green bodies by colloidal shaping techniques or to granulate powders for dry pressing, will have enormous benefits in terms of health, economical and environmental impacts. Further benefits will be obtained if the AlN ceramics processed from aqueous suspensions can be sintered at lower temperatures than those usually used (>1850^{o}C) to densify AlN ceramics processed in organic media without jeopardizing the final properties (high thermal conductivity, mechanical strength, etc.). As exposed above, aqueous processing of AlN needs a surface protection of the particles to avoid hydrolysis, turning the system more complex. Therefore, transposing the findings of sintering studies using AlN samples prepared in organic media to samples processed in aqueous media is not straightforward. The coating layer composed of oxygen and phosphorous might turn the sintering behaviour ambiguous, and further studies were necessary. In fact, the surface layer used to protect the AlN particles could be a trouble for the sintering process, due to the rising amount of oxygen content at the surface of AlN particles supplied by the protection layer (Olhero et al., 2004). Moreover, when binders and plasticizers are used as processing additives, such as in tape casting or powder granulation, it is necessary to remove these organic species prior to densification. Due to the easy oxidation of aluminium nitride in presence of oxygen and the residual carbon supplied by the organic species during burnout, the de-waxing atmosphere is a critical parameter (Olhero et al., 2006b).

Table 4 presents the amounts of carbon, oxygen, phosphorous, aluminium and nitrogen measured for the different AlN powders, without treatment (AlN), after thermochemical treatment (AlN-T), and for the samples A, B and C after de-waxing under different atmospheres (air or N_2). A, B, and C are samples that presents different amounts of sintering aids and binders as follows: **A**: 3-wt.% YF_3 + 2-wt.% CaF_2 and 4.5-wt.% organic binders; **B**: 4-wt.% YF_3 + 2-wt.% CaF_2 and 4.5-wt.% organic binders; **C**: 4-wt.% YF_3 + 3-wt.% CaF_2 and 4.5-wt.% organic binders. The ratios between the different elements, O/Al, N/Al and C/Al are also shown. Comparing the results for AlN and AlN-T powders, it is clear that there was an important surface enrichment in oxygen (≈9–10 wt.%) and P (≈8 wt.%) elements attributed to the phosphate species of the protective layer against hydrolysis, and a concomitant depletion of N and Al elements, confirming the results of the earlier report (Olhero et al., 2004). The decrease of the amount of aluminium at the surface of the AlN-T might also be partially due to a possible reaction between the oxygen and the aluminium to form aluminium oxide and oxynitride (Bellosi et al., 1993; Ichinose, 1995; Osborne & Norton, 1998).

Elements	Content (at %)							
	AlN	AlN-T	Sample A		Sample B		Sample C	
			O_2	N_2	O_2	N_2	O_2	N_2
C (1s)	12.61	12.91	13.79	20.96	12.81	21.63	13.96	21.68
N (1s)	16.99	9.35	6.05	6.21	6.19	6.54	6.14	6.38
O (1s)	35.75	44.97	45.86	40.84	45.91	40.84	45.98	40.68
Al (2p)	34.65	24.97	26.06	23.79	26.52	23.44	25.73	23.08
P (2p)	---	7.80	8.24	8.20	8.58	7.55	8.18	8.19

Table 4. Comparison of surface composition measured by XPS of the AlN powder without treatment and AlN treated powder (AlN-T) before and after de-waxing under different atmospheres (air or nitrogen).

Comparing the results for AlN-T and the compositions A, B and C after de-waxing in air atmosphere, it can be concluded that the surface of AlN particles becomes about 1-wt.% rich in oxygen after the burnout step. On the other hand, de-waxing in N_2 atmosphere results in significant decrease of the amount of oxygen (≈4 wt.%) and a concomitant increase in the carbon content (≈8–9 wt.%). The analysis of the atomic ratios between the different elements reveals that O/Al ranges from 1.73 to 1.79 for the samples de-waxed in air, and between 1.72 and 1.76 for the specimens de-waxed in N_2. On the other hand, the N/Al is 0.23–0.24 for the first set and 0.26–0.28 for the latter one. However, differences in the C/Al atomic ratio are the largest: 0.48–0.54 in air, and 0.88–0.94 in N_2. These results are in good agreement with the findings of other authors (Nakamatsu et al., 1999; Yan et al., 1993). Therefore, the binder burnout process left a significant amount of residual carbon on the AlN surface, which is larger in the case of the samples heat treated in nitrogen. By analysing the C1s peak, Yan (Yan et al., 1993) concluded that the first layer of carbon is bound to oxygen atoms at the AlN surface while additional carbon is bound to carbon itself, forming amorphous graphitoid carbon clusters which covered the powder surface uniformly. In spite of carbon increasing after binder burnout, oxygen content seems to be the most abundant element at

the surface of all AlN powders. Therefore, the use of proper amounts of sintering aids is of crucial importance to help releasing the excess of oxygen. Recently, Robinson and co-workers found that oxygen distribution was not continuous along thickness direction of the oxidized AlN (Robinson & Dieckmann, 1994; Robinson et al., 1994). They suggested that additives enhancing densification may be critically important to the oxidation kinetics of AlN polycrystals and the oxidized structure as well. Wenjea Tseng (Wenjea et al., 2004) also supported this proposition by showing that the additive chemistry and the doping level both play crucial roles in determining the oxidation behaviour of fully sintered AlN. Using different amounts and proportions of sintering additives did not affect the surface chemistry of AlN particles after de-waxing, but influenced the thermal properties after sintering.
The results of density and thermal conductivity of the different AlN-based compositions after de-waxing (in air or nitrogen) and sintering at 1750ºC for 2 h are reported in Table 5. Considering that the standard deviation of sintered density is ±0.1%, one can conclude that full densification was obtained for all the compositions tested, independently of the de-waxing atmosphere used. The values of thermal conductivity are also reported in Table 5, with a standard deviation of ±5%. Since all samples reached full density, the observed differences in thermal conductivity cannot be attributed to the densification degree. The nature and concentration of sintering aids and the de-waxing atmosphere are the most relevant factors determining thermal conductivity, which in turn depends on the microstructural features and on the crystalline phases formed. Significant differences (increases of 22%) in thermal conductivity are observed when comparing the data of samples sintered in air and in nitrogen. These differences might be related to the secondary intergranular crystalline phases. Yttrium aluminium monoclinic (YAM-$Y_4Al_2O_9$) is present when nitrogen atmosphere was used, while yttrium aluminium perovskite (YAP-$YAlO_3$) or $YCaAl_3O_7$ were formed when de-waxing was made in air.

	Sintered densities (%TD)		Thermal conductivity (W/m.K)	
Samples	De-waxing in air (O_2)	De-waxing in N_2	De-waxing in air (O_2)	De-waxing in N_2
A	100	100	111	125
B	100	100	111	136
C	99.8	99.9	119	136

Table 5. Density and thermal conductivity values of the sintered AlN samples

The origin of these secondary crystalline phases in the sintered samples is postulated to be as follows. The surface of AlN treated powder contains significant amounts of oxygen and phosphorous coming from the protective layer against hydrolysis. XPS analysis revealed that the phosphorous element still present at the surface of AlN powders after de-waxing at 500ºC (Table 4) could no more be detected after heat treating the samples at temperatures ≥1400ºC (temperature of liquids). This means that P element volatilizes upon heating up to 1400ºC. The formation of liquid phase is expected to occur at ≈1400ºC, according to the phase diagram (Roth et al., 1983). The oxygen remaining at particles' surface reacts with the sintering additives (YF_3 and CaF_2) to form a low melting point eutectic phase. This liquid phase assists the densification process and gives rise to crystalline phases, such as YAM or

YAP, either precipitated during sintering or on solidification. It is worthwhile to note that the yttrium-richer second phases were formed when the de-waxing was made in nitrogen atmosphere. Therefore, a correlation between the C/O atomic ratio at the AlN powder surface and the Al/Y/Ca in the second phase of the sintered material can be found. In fact, secondary intergranular phases became yttrium-richer ($Y_4Al_2O_9$) as surface C/O ratio increases, consequently enhancing the thermal conductivity. The change of the secondary intergranular phases from aluminium-rich to yttrium-rich can be understood based on carbon de-oxidation during sintering, which removes oxygen impurities from the grain boundaries according to the following chemical reaction:

$$Al_2O_3 + 3C + N_2 \rightarrow 2\ AlN + 3CO \quad (6)$$

The above results are in good agreement with those reported by other authors who defended that when $Y_4Al_2O_9$ is formed in AlN-Y_2O_3 ceramics instead of $Y_3Al_5O_{12}$ or $YAlO_3$, the highest thermal conductivity can be achieved (Nakano et al., 2003; Virkar et al., 1989). The distribution of the secondary phases in the samples, which may contribute to the increase in thermal conductivity, was also found to be dependent on C/O ratio (Yan et al., 1993). The effect of de-waxing atmosphere on microstructural features of fracture surfaces of sintered samples A and C can be observed in Figure 13 and Fig. 14, for the samples de-waxed in air and nitrogen, respectively. It can be seen that AlN grains are separated by grain-boundary films, the thickness of which depend on the type of de-waxing atmosphere. The results of EDS analysis of the inter-granular films revealed that they consist of different proportions of Y, O, Al and N, being more yttrium-rich when de-waxing was in N_2. In samples A and C de-waxed in air, the inter-granular films extend along the whole grain boundaries showing good wetting properties. The presence of these grain boundaries films disrupts the connections between grains and consequently decreases the thermal conductivity. Contrarily, the inter-granular film in sample A and C de-waxed in N_2 atmosphere is thinner and the secondary phases are apparently less abundant and appear preferentially located at the triple points. These differences can be related to the surface composition of the AlN grains. The higher C/Al atomic ratios (see Table 4) of the samples sintered in N_2 atmosphere will decrease the ratio between the grain-boundary energy (γss) and the solid–liquid interfacial energy (γsl), γss/γsl, leading to the isolated structure of the second phase observed in these specimens and increasing the thermal conductivity.

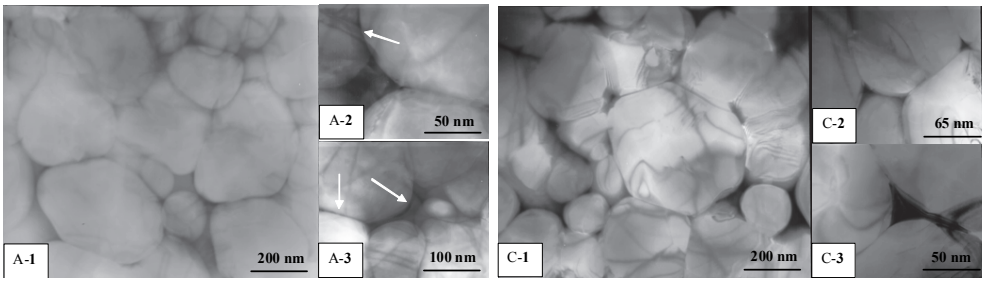

Fig. 13. TEM images of samples A (3-wt.% YF_3 + 2-wt.% CaF_2 and 4.5-wt.% organic binders) and C (4-wt.% YF_3 + 3-wt.% CaF_2 and 4.5-wt.% organic binders) sintered at 1750ºC for 2h after de-waxing in Air.

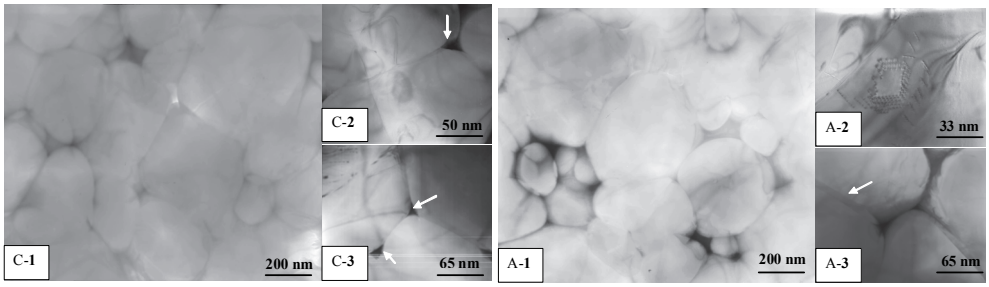

Fig. 14. TEM images of samples A (3-wt.% YF_3 + 2-wt.% CaF_2 and 4.5-wt.% organic binders) and C (4-wt.% YF_3 + 3-wt.% CaF_2 and 4.5-wt.% organic binders) sintered at 1750ºC for 2 h after de-waxing in Nitrogen.

Table 5 shows that increasing the total amount of sintering additives and the YF_3/CaF_2 ratio enhances thermal conductivity. It is suggested that the formation of Y-richer secondary phases de-wets the grain boundaries and segregates the interganular phases preferentially to the triple points leading to a more effective AlN–AlN grain-boundary contact.
Practically full dense AlN ceramics having thermal conductivities varying from 110 to 140 W/mK have been successfully produced from granulated powders processed in aqueous media. De-waxing atmospheres, sintering aids and firing conditions were identified as key processing parameters in controlling density and thermal conductivity. The burnout of organic additives in N_2 atmosphere left a significant amount of residual carbon at the AlN powder surface that partially removes the excess oxygen. The reaction between the remaining excess oxygen and the sintering additives (CaF_2 and YF_3) leads to the formation of yttrium-richer ($Y_4Al_2O_9$) secondary phases preferentially located at the triple points that enhance thermal conductivity. Contrarily, de-waxing in air favours the formation of more abundant alumina-richer yttrium aluminates that better wet the AlN grains and spread along the whole grain boundaries, increasing the density of structural defects, such as dislocations, therefore decreasing thermal conductivity.

6. Thermodynamic studies on the AlN sintering powders treated with phosphate species

Because AlN is a covalently bonded material, pressureless sintering of low oxygen-containing AlN is usually carried out by liquid-phase sintering, where the liquid provides rapid mass transport and therefore rapid densification at low temperatures (Jarrige et al., 1993; Khan & Labbe, 1997; Liu et al., 1999; Streicher et al., 1990b; Thomas & Nicholson, 1989). Chemical reactions between the ceramic powder, sintering aid, and the atmosphere during firing are important for successful sintering. The key elements are those that form volatile species, either directly or by reactions with the atmosphere (Sonntag et al., 2003). The additives typically used to promote the sintering of AlN are alkaline-earth oxides, rare-earth oxides, or mixtures of oxides and carbides (Boey et al., 2001; Buhr & Muller, 1993; Hundere & Einarsrud, 1997; Kurokawa et al., 1988; Qiao et al., 2003a; Molisani et al., 2006; Terao et al., 2002; VanDamme et al., 1989; Watari et al., 1999; Wang et al., 2001; Yu et al., 2002). The sintering aids of the CaF_2–YF_3 system are interesting due to the absence of oxygen

and the low liquidus temperatures. The eutectic points in the CaF_2–YF_3 system occur at 60 and 91 mol% CaF_2 at 1120º and 1106ºC, respectively (Seiranian et al., 1974). The studies on the thermodynamics taking place during sintering of AlN have been reported for AlN samples processed in organic media, therefore involving a residual amount of alumina at the surface of the AlN particles and the sintering additives (Buhr et al., 1991; Gross et al., 1998; Hagen et al., 2002; Hundere & Einarsrud, 1996; Medraj et al., 2005; Virkar et al., 1999).
For samples processed in aqueous media, the presence of a protecting surface layer against hydrolysis makes the system more complex. If the surface layer adds extra oxygen to the surface of the AlN particles as it is demonstrated above, it might have a negative impact on sintering. Therefore, the contribution of this surface layer, phosphate based, to the AlN sintering needs to be investigated in order to choose the best conditions (sintering temperature, amount of sintering additives, etc.) to improve the final properties of AlN ceramics. Therefore, the aim of this part is to make a review of the kinetic effects of the phosphate-based surface layer used to protect AlN powder against hydrolysis on the sintering behaviour of AlN in the presence of YF_3 and CaF_2 as sintering aids, and consequently on the final properties of the samples processed in aqueous media. For that, AlN samples with different amount of sintering aids, in absence or in presence of binders and plasticizers (organic species) were analysed. Table 6 presents the compositions of the samples tested and the respective codes.

Sample codes	Phosphate species (wt.%)	Binder and plasticizer (wt.%)	YF_3 (wt.%)	CaF_2 (wt.%)
AlN-P	2	---	---	---
AlN-P-B	2	4.5	---	---
AlN-P-B-Y	2	4.5	3	---
AlN-P-Ca	2	---	---	5
AlN-P-B-YCa (3/2)	2	4.5	3	2
AlN-P-2B-YCa (3/2)	2	6.0	3	2
AlN-P-2B-YCa (4/2)	2	6.0	4	2

Table 6. Sample codes and the respective compositions of the AlN samples tested.

Firstly the samples were submitted to thermal analysis from room temperature to 1600ºC in order to analyse the weight loss. Figs. 15 (a) and (b) show the weight loss of the AlN samples in presence of the phosphate surface layer and with different amounts and ratios of sintering additives (Table 6), obtained at two different heating rates, 2°C /min and 10°C /min, respectively. Table 7 summarizes the percentage of weight loss of the Aluminium Nitride (AlN) samples measured within certain temperature ranges at a heating rate of 2ºC/min.

	Weight loss (%)					
Sample codes	**25-300**	**300-400**	**980-1030**	**1025-1100**	**1250-1600**	**Total**
AlN-P	0.87	-0.44	0.08	----	-0.81	-0.30
AlN-P-B	2.80	1.06	----	0.51	----	4.37
AlN-P-B-Y	2.51	1.11	0.31	----		3.93
AlN-P-B-Ca	0.70	-0.41	0.17	----	3.70	4.16
AlN-P-B-YCa (3/2)	2.71	1.07	0.36	----	2.43	6.57
AlN-P-2B-YCa (3/2)	2.71	2.42	----	0.43	2.56	8.12
	•Water evaporation •Binder burnout (short chains)	•Binder burnout (long chains)			• Calcium evaporation	

Table 7. Percentage of Weight Loss of the Aluminium Nitride (AlN) samples measured within certain temperature ranges at a heating rate of 2°C/min.

The AlN powder coated with the phosphate species (AlN–P) showed a slight weight decrease up to 300°C, from where a small weight increase was observed up to 1300°C. Above 1300°C, a second weight gain was observed. The addition of the processing aids (binder and plasticizer) to the phosphate-treated AlN powder (AlN–P–B) resulted in significant differences in the weight loss. A first weight loss of about 3.9 wt.% was observed in the temperature range from room temperature up to ≅ 400°C due to the burnout of the organic species, while a second weight loss of about 0.7 wt.% was observed between 1030° and 1060°C, followed by a small weight increase above 1200°–1300°C. The weight loss of the phosphate-treated AlN samples in the presence of the sintering aids (AlN–P–B–Y, AlN–P–B–Ca, AlN–P–B–YCa (3/2)) was practically the same from room temperature till 1300°C. Above this temperature, the samples containing CaF_2 (AlN–P–Ca and AlN–P–B–YCa (3/2)) showed a significant weight loss, while the sample with YF_3 (AlN–P–B–Y) showed a slight weight increase as in the samples with phosphates only (AlN–P and AlN–P–B). In order to investigate the effects of carbon residuals on the weight loss during sintering, TG analysis of the sample with a mixture of the two sintering additives, with two different amounts of binder and plasticizer, was carried out (AlN–P–B–YCa (3/2) and AlN–P–2B–YCa (3/2)). The TG curves presented the same behaviour along the entire temperature range, however, with higher percentages of weight loss (about 2% more) for the sample with a larger amount of binder, as expected. On the other hand, the mass loss observed at around 1000°C started at a lower temperature for the powder with a larger amount of binder (AlN–P–2B–YCa (3/2)). Moreover, the weight loss around this temperature was more gradual in the AlN–P–2B–YCa (3/2) powder, occurring more abruptly in the presence of lower amounts of processing aids (i.e., less amounts of residual carbon).

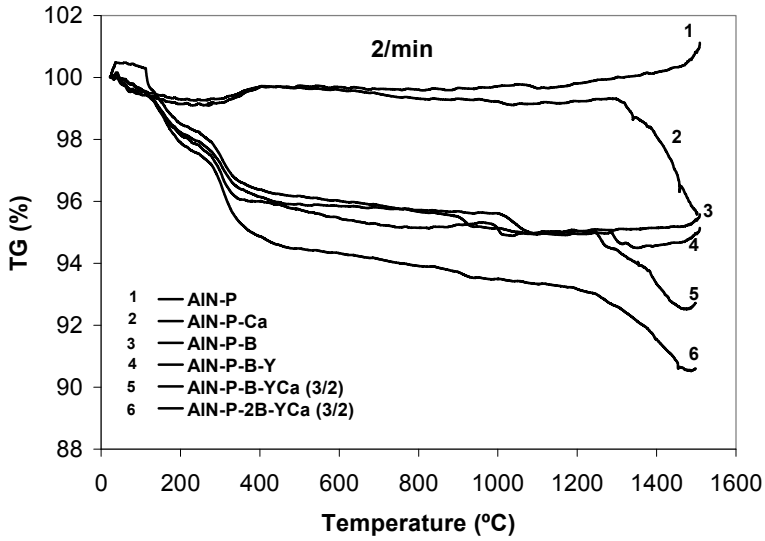

(a)

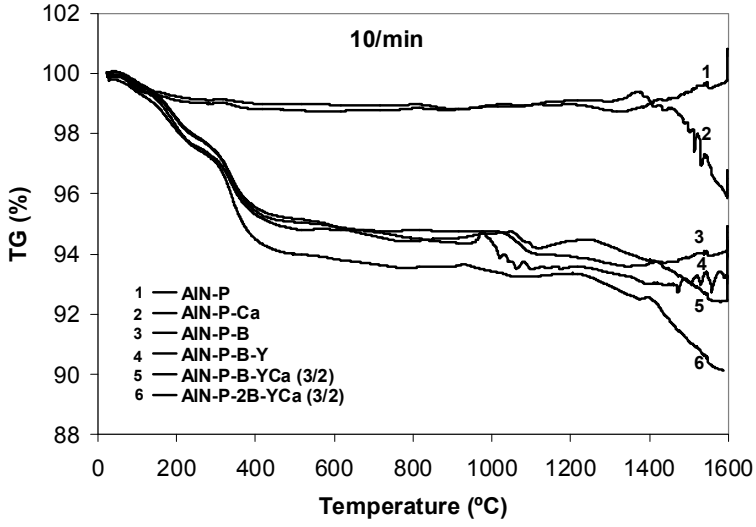

(b)

Fig. 15. Thermogravimetric curves of the AlN samples in the absence or in the presence of phosphates species with different added amounts of sintering aids and organic species (binders and plasticizer): (a) obtained at a heating rate of 2ºC/min; (b) obtained at a heating rate of 10ºC/min.

During heating of the protected AlN powders with a dihydrogenphosphate surface layer (AlN–P), the small mass loss measured within the temperature range of 100º–150ºC, could be attributed to the water evaporation and release of adsorbed gases on the powder surface, according to the following reaction:

$$Al(H_2OP_4)_3 \rightarrow AlPO_4+P_2O_5+3H_2O(g) \quad (7)$$

The water vapour produced by reaction (7) may also react with AlN, leading to the following reaction:

$$Al(H_2PO_4)_3 + 2\ AlN \rightarrow 3\ AlPO_4 + 2\ NH_3(g) \quad (8)$$

which only predicts weight loss due to evaporation of ammonia at low temperatures instead of water. Reaction (8) leads to higher relative oxygen content in the powder mixture. The removal of oxygen from the AlN lattice during sintering is beneficial for enhancing thermal conductivity (Buhr et al., 1991; Gorzawski et al., 1995; Hundere & Einarsrud, 1996; Rang-Rong Lee, 1991; Virkar et al., 1999;). However, oxygen should not be removed during an early stage of the sintering process because Al_2O_3 is needed in the formation of a liquid phase. The weight gain observed for the same sample (AlN–P) at ≅250ºC at a slow heating rate (2ºC/min) could be attributed to the formation of alumina due to the hydrolysis of AlN, according to:

$$2AlN + 3H_2O\ (g) \rightarrow Al_2O_3 + 2NH_3(g) \quad (9)$$

The weight gain at ≅250ºC was only observed for the samples AlN–P and AlN–P–Ca without addition of processing aids.

However, this reaction could also occur in the presence of the processing aids, but the corresponding weight gain due to hydrolysis is masked by the high weight loss derived from the burnout of the organic species. The weight loss corresponding to the burnout of the organic species is divided into two stages: one from 100º to 300ºC, corresponding to the burnout of the organic species with shorter chains, and another one from 300º until ≅ 400ºC, derived from the burnout of the organic species with longer chains. Thermodynamic calculations using Factsage program (Bale et al., 2002) were carried out in order to predict the changes in the phase composition of the powder mixture during sintering and after the removal of water. The program calculates the chemical equilibrium in a closed system as a function of temperature and pressure. The input to the program is the chemical composition and we provided equilibrium calculations in the temperature range of 1200º–1800ºC at constant total pressure 1 bar using the following initial compositions:

i. $10AlN + 0.1AlPO_4 + 0.01(P_2O_5)_2 + 10N_2$
ii. $10AlN + YF_3 + CaF_2 + 0.1AlPO_4 + 0.05(P_2O_5)_2 + 10N_2$
iii. $10AlN + 0.1YF_3 + 0.1\ CaF_2 + 0.01AlPO_4 + 0.005\ (P_2O_5)_2 + 0.2Al_2O_3 + 10N_2$
iv. $10AlN + 0.1\ YF_3 + 0.1CaF_2 + 0.1Al_2O_3 + 10N_2$

The surface coating, $Al(H_2PO_4)_3$, was represented by $AlPO_4$ and P_2O_5 in the calculations because the loss of water, reaction (7), is expected to occur before the initial stage of sintering. Fig. 16 (a & b) present the minority condensed phases (a=1, AlN not present) between 1200º and 1800ºC, and the dominating volatile species within the same temperature range for the system in the absence of phosphate species: $10\ AlN + 0.1\ CaF_2 + 0.1\ YF_3 + 0.1\ Al_2O_3 + 10\ N_2$, respectively. The presence of phosphate species did not change the minority volatile phases presented in Fig. 16 (a & b). These species, in the presence of AlN, are unstable and will react to form alumina, PN(g), and N_2(g) even at low temperatures. The reaction between AlN and phosphate species can be written as follows:

$$5AlN + AlPO_4 + P_2O_5 \rightarrow 3Al_2O_3 + 3PN(g) + N_2(g) \quad (10)$$

Reaction (10) could not be confirmed by thermogravimetry. However no phosphate species could be detected in the sintered samples and supporting the evaporation of phosphorous. The reducing condition in the graphite furnace as discussed further below will contribute to the thermodynamic instability of the phosphate species.

The sintering additives YF_3 and CaF_2 used melt between 1000 and 1200°C (Seiranian et al., 1974). Therefore, the reaction of the fluorides with alumina present in the AlN during sintering is important. Firstly, the reaction of YF_3 with the surface alumina is considered. Based on the XRD data YF_3 is converted to Y_2O_3, which reacts to ternary oxides such as YAP, YAM and YAG. During heating of the green bodies, Y_2O_3 was presumably formed according to reaction (11) as Y_2O_3 is formed according to Fig. 16(a):

$$2\ YF_3(l) + Al_2O_3(s) \rightarrow 2\ AlF_3(g) + Y_2O_3(s) \quad (11)$$

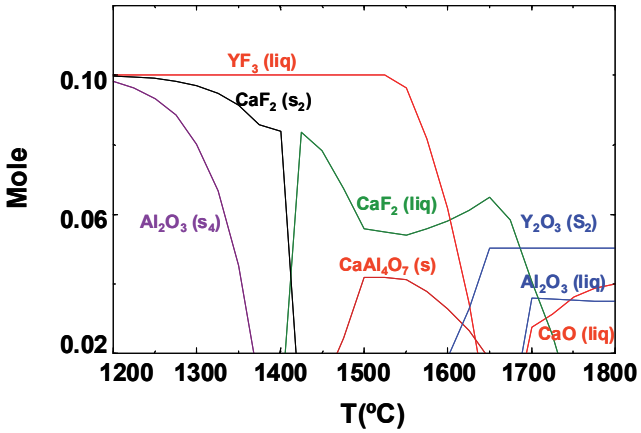

(a)

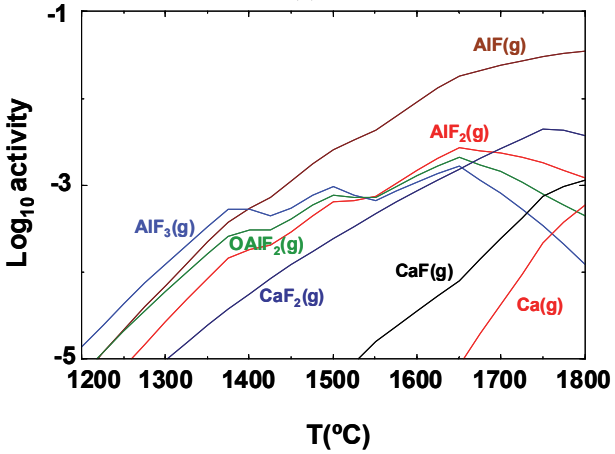

(b)

Fig. 16. **(a)** Minority condensed phases (a=1, AlN not present); **(b)** volatile species between 1200°C and 1800°C for the system 10 AlN + 0.1 CaF_2 + 0.1 YF_3 + 0.1 Al_2O_3 + 10 N_2.

Y_2O_3 is predicted to be formed in the thermodynamic calculations since the thermodynamic data for the ternary oxides is not included in the Factsage database. The melting point of YF_3 is reported to be 1155°C (Barin, 1989). Although some YF_3 might evaporate, most of YF_3 is assumed to react with Al_2O_3 and form $AlF_3(g)$, which sublimes at temperatures higher than 1200°C, as can be observed in Fig. 16(b). CaF_2 can also react with alumina impurities present at the surface of the AlN, forming calcium aluminates (here simplified by CaO) and $AlF_3(g)$, according to:

$$3CaF_2 + Al_2O_3 \rightarrow 2AlF_3(g) + 3CaO \quad (12)$$

The presence of CaO containing species in the sintered materials using CaF_2 as sintering aid confirmed the conversion of CaF_2 to CaO. No fluoride species could be detected after sintering in agreement with the thermodynamic predictions.

Liquid phase sintering of AlN with CaF_2 at elevated temperatures (>1300°C) results in a significant weight loss (Table 7) due to high vapour pressures generated by chemical reactions between AlN and the surface oxides as shown in equations (13) and (14) (Hagen et al., 2002).

$$CaAl_2O_4(s) + 6AlN(s) \rightarrow Ca(g) + 4Al_2O(g) + 3N_2(g) \quad (13)$$

$$CaAl_2O_4(s) + 2/3AlN(s) \rightarrow Ca(g) + 4/3Al_2O_3(s) + 1/3\ N_2(g) \quad (14)$$

Ca(g) involved may react further with Al_2O_3 on the surface of AlN in the powder bed, for example, according to the following reaction:

$$Ca(g) + Al_2O_3 = CaAl_2O_4 + Al_2O(g) \quad (15)$$

6.1 Effect of powder bed on densification, thermal conductivity and microstructure

The thermal conductivity, nature and amount of secondary phases were found to depend on powder bed composition and on the amount of processing aids, which probably introduce different amounts of carbon into the samples (Olhero et al., 2007). Two different compositions of powder bed were tested: 100-wt.% of AlN (100AlN) and 80-wt.% of AlN + 20-wt.% BN (80AlN/20BN). The weight loss of the AlN samples due to thermal decomposition of AlN(s) is considered to be negligible since the protecting embedding was used. However, the Al_2O_3 layer existing at the surface of AlN grains or further formed due to reaction with phosphates might react with AlN according to equation (16) resulting in a weight loss due to removal of oxygen (Hundere & Einarsrud, 1996):

$$Al_2O_3(s) + 4AlN(s) \rightarrow 3Al_2O(g) + N_2(g) \quad (16)$$

For this reaction to proceed, the $Al_2O(g)$ formed has to diffuse through the protective powder bed and react with the carbon residue from the processing aids burn-out, the furnace itself or the outer graphite crucible to reform AlN according to reaction (17).

$$Al_2O(g) + C(s) + N_2(g) \rightarrow 2AlN\ (s) + CO(g) \quad (17)$$

Hence, a more open powder bed will give the highest loss of $Al_2O(g)$ species from the sample giving AlN ceramics with less oxygen content and therefore higher thermal conductivity (Hundere & Einarsrud, 1996). Since the 100AlN powder bed gave a material

with higher thermal conductivity in comparison to 80AlN/20BN, it might be suggested that the former powder bed has a more open structure.
When a sufficient CO(g) pressure is generated due to reaction (16), the $Al_2O(g)$ might be nitrided inside the sample according to:

$$Al_2O(g) + CO(g) + N_2(g) = 2AlN(s) + CO_2(g) \quad (18)$$

However, the CO_2 (g) formed in this reaction will further react with carbon in the surroundings forming more CO(g):

$$CO_2(g) + C = 2CO(g) \quad (19)$$

The change of the secondary phases from aluminium-rich to yttrium-rich using 80AlN/20BN or 100AlN as powder beds, respectively, can be understood based on the reactions given above, which remove alumina from the grain boundaries.
According to the results presented about influence of de-waxing atmosphere, a correlation observed between the C/O atomic ratio at the AlN powder surface and the Y/Ca in the sintering aids can be the reason for the differences in secondary phases. It was verified an important AlN surface enrichment in O_2 (≈ 9-10 at.%) and P (≈ 8 at.%) elements after treatment, attributed to the phosphate species of the protective layer against hydrolysis. Furthermore, the surface carbon amount in the AlN-treated samples is around 12-13 at% and increases about 8-9%, after binder burnout in N_2 atmosphere. In fact, based on the results obtained and according to Hundere (Hundere & Einarsrud, 1996) secondary intergranular phases became yttrium-richer ($Y_4Al_2O_9$) as surface C/O ratio increases, consequently enhancing the thermal conductivity. This explains the higher thermal conductivity values obtained for the AlN samples in the presence of larger amounts of processing aids when compared with the ones in presence of smaller amounts of binders and plasticizers. The smaller amounts of secondary phases present in the AlN sintered in 100AlN powder bed could also be explained by the higher weight loss measured for this sample.
According to the results obtained is possible to summarize that the phosphate species used to protect AlN form $AlPO_4$ and NH_3(g) during firing of the ceramics giving weight losses at temperatures lower than the liquid formation. Further, during liquid phase sintering with fluoride additives, chemical reactions take place between AlN and the sintering aid resulting in weight losses due to the formation of AlF_3 and Al_2O gas species. Evaporation of the Al_2O (g) reduces the oxygen content of the ceramics. The weight loss and the evaporation rate depend on the sintering temperature, the amount of the sintering aids and the embedding or surrounding atmosphere. The presence of reducing species (Carbon or CO(g)) further reduces the oxygen content of the AlN samples. Highest thermal conductivity was achieved using pure AlN as the powder bed and a large amount of processing aids giving carbon residue during firing (Olhero et al., 2007).

7. Conclusions

According to the main findings reported in the reviewed literature works on this subject it is possible to draw the following conclusions:

1. Soaking AlN powders in an aqueous solution of aluminium dihydrogenphosphate at temperatures around 60 °C offers the possibility of preparing water-resistant AlN

powders. Well-dispersed and high concentrated suspensions could be prepared from the protected AlN powder with added CaF_2 and YF_3 as sintering aids by using a commercial dispersant, Duramax 3005. The high degree of homogeneity obtained in the slip-cast green bodies made it possible to achieve relatively high sintered densities, similar to those usually obtained with organic-based suspensions after sintering at higher temperatures. The possibility to prepare high stable AlN suspensions in aqueous media opened the possibility to consolidate AlN samples by other colloidal shaping techniques, such as, freeze granulation and tape casting.

2. Fully dense and relatively high thermal conductive AlN ceramics can be consolidated by slip casting from aqueous suspensions and pressureless sintering at a temperature as low as 1750ºC for a short time period of 2 h. This means that the organic solvents typically used to process this material can definitely be replaced by water. It was also shown that both the amount and ratio of the sintering additives play important roles in the microstructural development and in determining the final physical properties of the sintered bodies. The mixture of 4 wt.% YF_3 + 2 wt.% CaF_2 was the most appropriate combination to obtain AlN samples with relatively good properties.
3. Practically full dense AlN ceramics having thermal conductivities varying from 110 to 140 W/mK have been successfully produced from granulated powders processed in aqueous media. De-waxing atmospheres, sintering aids and firing conditions were identified as key processing parameters in controlling density and thermal conductivity. The burnout of organic additives in N_2 atmosphere left a significant amount of residual carbon at the AlN powder surface that partially removes the excess oxygen. The reaction between the remaining excess oxygen and the sintering additives (CaF_2 and YF_3) leads to the formation of yttrium-richer ($Y_4Al_2O_9$) secondary phases preferentially located at the triple points that enhance thermal conductivity. Contrarily, de-waxing in air favours the formation of more abundant alumina-richer yttrium aluminates that better wet the AlN grains and spread along the whole grain boundaries, increasing the density of structural defects, such as dislocations, therefore decreasing thermal conductivity.

8. Acknowledgments

S.M. Olhero wishes to thank to Foundation for Science and Technology of Portugal for the financial support under the grant SFRH/BPD/27013/2006 and the financial support under the project PTDC/CTM/099489/2008. The authors would also like to thank CICECO (University of Aveiro, Portugal), Institute of Josef Stefan (Ljubljana, Slovenia) and Norwegian University of Science and Technology (Trondheim, Norway) for the experimental work done.

9. References

Bale, C.; Chartrand, P.; Degterov, S.; Eriksson, G.; Hack, K.; Ben, R.; Melanon, J.; Pelton A. & Petersen S. (2002). FactSage Thermochemical Software and Databases. *Calphad*, Vol. 26, No.2, pp.189–228.

Baranda, P.; Knudsen, A. & Ruh, E. (1994). Effect of yttria on the thermal conductivity of aluminium nitride. *J. Am. Ceram. Soc.*, Vol.77, No.7, pp. 1846-1850.

Barin, I. (1989) Thermochemical Data of Pure Substances Part I & 2. VCH VerlagsgesellschaftmbH, Weinheim.

Bellosi, A.; Landi, E. & Tampieri, A. (1993) Oxidation behaviour of aluminium nitride. *J. Materials Research*, Vol.8, No.3, pp.565.

Binner, J. & Yongheng, Z. (2005) Surface chemistry and hydrolysis of a hydrophobic-treated aluminium nitride powder", *Ceramics International*, Vol.31, pp.469-474.

Boey, F.; Cao, L.; Khor, K. & Tok, A. (2001). Phase reaction and sintering behaviour of a Al_2O_3-20wt.%AlN-5wt.% Y_2O_3 system. *Acta Materialia*, Vol.49, pp.3117-3127.

Buhr, H.; Muller, G. & Wiggers, H. (1991). Phase composition, oxygen content and thermal conductivity of AlN (Y_2O_3) ceramics. *J. Am. Ceram. Soc.*, Vol.74, No.4, pp. 718-723.

Buhr, H. & Muller, G. (1993). Microstructure and thermal conductivity of AlN (Y_2O_3) ceramics sintered in different atmospheres. *J. Europ. Ceram. Soc.*, Vol.12, pp. 271-277.

Chartier, T.; Streicher, E. & Boch, P. (1992). Preparation and characterization of tape cast aluminum nitride substrates. *J. Europ. Ceram. Soc.*, Vol.9, pp. 231-242.

Collange, A.; Grosseau, P.; Guilhot, B.; Disson, J. & Joubert, P. (1997). Thermal conductivity of compacted AlN samples. *J. Europ. Ceram. Soc.*, Vol. 17, pp. 1897-1900.

Egashira, M.; Shimizu, Y. & Takatsuki, S. (1991). Chemical surface treatments of aluminium nitride powder suppressing its reactivity with water. *Journal of Materials Science Letters*, Vol.10, pp. 994-996.

Egashira, M.; Shimizu, Y.; Takao, Y.; Yamaguchi, R. & Ishikawa, Y. (1994). Effect of carboxylic acid adsorption on the hydrolysis and sintered properties of aluminium nitride powder. *J. of Am. Ceram. Soc.*, Vol.77, No.7, pp. 1793-1798.

Enloe, J.; Rice, R.; Law, J.; Kumar, R. & Lee, S. (1991). Microstructural effects on the thermal conductivity of polycrystalline aluminium nitride. *J.Am. Ceram. Soc.*, Vol.74, No.9, pp. 2214-2219.

Fukumoto, S.; Hookabe, T. & Tsubakino, H., (2000). Hydrolysis behavior of aluminum nitride in various solutions. *Journal of Materials Science*, Vol. 35, pp. 2743-2748.

Ganesh, I.; Olhero, S.; Branca, A.; Correia, M. & Ferreira, J. (2008). "Chemisorption of phosphoric acid and surface characterization of passivated AlN powder against hydrolysis", *Langmuir*, Vol.24, No.10, pp. 5359-5365.

Gorzawski, G.; Sternitzke, M.; Muller, W.; Berger, A. & Muller, G., (1995) Oxygen enrichment at inversion domain boundaries in aluminium nitride- influence on thermal conductivity. *J. Europ. Ceram. Soc.*, Vol.15, pp. 95-99.

Greil, P.; Kulig, M. & Hotza D. (1994). Aluminium nitride ceramics with high thermal conductivity from gas-phase synthesized powders. *J. Eur. Ceram. Soc.* Vol. 13, pp. 229.

Groat, E. & Mroz, T., (1994). Aqueous slip casting of stabilized AlN powders. *Am. Ceram. Soc. Bull.*, Vol.73, No.11, pp.75-78.

Gross, G.; Seifert, H. & Aldinger, F. (1998). Thermodynamic assessment and experimental check of fluoride sintering aids for AlN. *J. Europ. Ceram. Soc.*, Vol.18, pp. 871-877.

Hagen, E.; Yingda, Y.; Grande, T.; Høier, R. & Einarsrud M.-A. (2002). Sintering of AlN using CaO-Al_2O_3 as a sintering additive: chemistry and microstructural development. *J. Am .Ceram. Soc.*, Vol.85, No.12, pp. 2971-2976.

Hotza, D. & Greil, P. (1995). Review: aqueous tape casting of ceramic powders. *Materials Science and Engineering*, Vol.A202, pp. 206-217.

Hundere, A. & Einarsrud, M.-A. (1997). Microstructural development in AlN (YF_3) ceramics. *J. Europ. Ceram. Soc.*, Vol.17, pp. 873-878.

Hundere, A. M. & Einarsrud M. A. (1996). Effects of reduction of the Al-Y-O containing secondary phases during sintering of AlN with YF_3 additions. *J. Europ. Ceram. Soc.*, Vol.16, pp.899-906.

Hyoun-Ee, K. & Moorhead, A. (1994). Oxidation behaviour and flexural strength of aluminium nitride exposed to air at elevated temperatures. *J. Am .Ceram. Soc.*, Vol.77, No.4, pp. 1037-1041.

Ichinose, N. (1995). Effect of carbon-reducing atmosphere on the properties of aluminium nitride (AlN). *Materials Chemistry and Physics*, Vol.42, pp. 176-180.

Iwase, N.; Ueno, F.; Yasumoto, T.; Asai, H. & Anzai, K. (1994) AlN substrates and packages. *Advancing Microelectronics*, *Vol.*1-2, pp. 24-25.

Jackson, T.; Barrett; Virkar, A.V.; More, K.; Dinwiddie, R. & Cutler, R. (1997). High-thermal-conductivity aluminium nitride ceramics: the effect of thermodynamic, kinetic and microstructural factors. *J. Am. Ceram. Soc.*, Vol.80, No.6, pp. 1421-1435.

Jarrige, J.; Bouzouita, K.; Doradoux, C. & Billy M. (1993). A new method for fabrication of dense aluminium nitride bodies at temperatures as low as 1600ºC. *J. Europ. Ceram. Soc.*, Vol.12, pp. 279-285.

Khan, A. & Labbe, J. (1997). Aluminium nitride-molybdenum ceramic matrix composites, influence of molybdenum addition on electrical, mechanical and thermal properties. *J. Europ. Ceram. Soc.*, Vol.17, No.15/16, pp. 1885–1890.

Knudsen, A. (1995). Aluminum nitride. *Am. Ceram. Soc. Bull.*, Vol.74, pp. 97.

Kocjan, A.; Dakskobler, A.; Krnel, K. & Kosmaˇc, T. (2011). The course of the hydrolysis and the reaction kinetics of AlN powder in diluted aqueous suspensions. *J. Europ. Ceram. Soc.*, Vol.31, pp. 815-823.

Koh, Y.-H.; Choi, J.-J. & Kim, H.-E., (2000). Strengthening and prevention of oxidation of aluminum nitride by formation of a silica layer on the surface. *J. Am. Ceram. Soc.*, Vol.83, No.2, pp. 306-310.

Komeya, K. & Inoue, H. (1969). Sintering of aluminium nitride: particle size dependence of sintering kinetics. *J. Mat. Science*, Vol.4, pp. 1045-1050.

Kosmac, T.; Krnel, K. & Kos, K. (1999). Process for the protection of AlN powder against hydrolysis. *Internacional Patent* N. WO 99/12850, 18.03.1999.

Krnel, K. & Kosmac, T. (2000). Reactivity of aluminum nitride powder in dilute inorganic acids. *J. Am. Ceram. Soc.*, Vol.83, No.6, pp. 1375-1378.

Krnel, K. & Kosmac T. (2001). Protection of AlN powder against hydrolysis using aluminum dihydrogen phosphate. *J. Europ. Ceram. Soc.*, Vol.21, pp. 2075-2079.

Kurokawa, Y.; Utsumi, K. & Takamizawa, H. (1988). Development and microestrutural characterization of high-thermal-conductivity aluminum nitride ceramics.*J. Amer. Ceram. Soc.*, Vol. 71, No.7, pp. 588-594.

Lavrenko, V. & Alexeev, A. (1983). Oxidation of sintered aluminium nitride. *Ceramics International*, Vol.9, No.3, pp. 80-82.

Lewis, J. (2000). Colloidal Processing of Ceramics. *J. of Am. Ceram. Soc.*, Vol.83, No.10, pp. 2341-2359.

Lin, K.-H.; Lin, Y.-C. & Lin, S.-T. (2008). Effects of reduction atmosphere and nano carbon powder addition on the deoxidization of injection molded aluminum nitride parts. *Journal of Materials Processing Technology*, Vol. 201, pp. 701-705.

Liu, Y.; Zhou, H.; Qiao, L. & Wu, Y. (1999). Low-temperature sintering of aluminium nitride with YF_3-CaF_2 binary additive. *Journal of Materials Science Letters*, Vol.18, pp. 703-704.

Medraj, M.; Baik, Y.; Thompson, W. & Drew R. (2005). Understanding AlN sintering through computational thermodynamicas combined with experimental investigation. *J. Materials Process. Technology*, Vol.161, pp. 415-422.

Molisani, A.; Yoshimura, H.; Goldenstein, H. & Watari, K. (2006). Effects of $CaCO_3$ content on the densification of aluminum nitride. *J. Europ. Ceram.Soc.*, Vol.26, pp. 3431–40.

Nakamatsu, T.; Pomar, F. & Ishizaki K. (1999). The effect of carbon coating of AlN powder on sintering behaviour and thermal conductivity. *Journal of Materials Science*, Vol.34, pp. 1553-1556.

Nakano, H.; Watari, K. & Urabe K. (2003). Grain boundary phase in AlN ceramics fired under reducing N_2 atmosphere with carbon. *J. Europ. Ceram. Soc.*, Vol.23, pp. 1761-1768.

Nyberg, B.; Carlstrom, E. & Carlsson, R. (1993). Granulation of ceramic powders for pressing by spray-freezing and freeze-drying. Euro-ceramics II, Vol.1 - Basic Science and Processing of Ceramics, ed. by G. Ziegler and H. Hausner, Deutsche Keramische Gesellschaft, pp. 447-451.

Nyberg, B.; Carlstrom, E. & Carlsson R. (1994). Freeze granulation of liquid phase sintered silicon nitride. Ceramic Transactions, , Silicon Based Structural Ceramics, ed. by B.W. Sheldon and S.C. Danforth, American Ceramic Society, Vol. 42, pp. 107-113.

Nyquist, R.; Ronald O. & Kagel, (1997). Infrared spectra of Inorganic compounds, 3800-45 cm^{-1}, Handbook of Infrared and Raman Spectra of Inorganic Compounds and organic salts, Vol.4, Academic Press, San Diego-EUA.

Oliveira, M.; Olhero, S.; Rocha, J. &. Ferreira J. (2003). Controlling hydrolysis and dispersion of AlN powders in aqueous media. *J. of Colloid and Interface Science*, Vol.261, pp. 456-463.

Olhero, S.M., Novak, S., Krnel, K., Kosmac, T. & Ferreira, J.M.F., "Thermo-chemical Surface Treatment of AlN Powder Towards Aqueous Processing of AlN Ceramics". Journal of Materials Research, 19[3], 746-751, 2004.

Olhero, S. & Ferreira, J. (2005). Rheological Characterisation of water-based AlN slurries for the tape casting process. *Journal of Materials Processing Technology*, Vol.69, No.2, pp. 206-213.

Olhero, S.; Miranzo, P. & Ferreira, J. (2006a). Characterization of AlN ceramics processed by aqueous slip casting. *Journal of Materials Research,* Vol.21, No.10, pp. 2460-2469.

Olhero, S.; Miranzo, P. & Ferreira, J. (2006b). Influence of the de-waxing atmosphere on the properties of AlN ceramics processed from aqueous media. *J. Europ. Ceram. Soc.*, Vol.26, pp. 2475-2483.

Olhero, S.; Morten, S.; Einarsud, M-A.; Grande, T. & Ferreira, J. (2007). Thermodynamic studies on the AlN sintering powders treated with phosphate species. *Journal of American Ceramic Society,* Vol.90, No.11, pp.3589.

Osborne, E. & Norton, M. (1998). Oxidation of aluminium nitride. *J. Mat. Science*, Vol.33, pp. 3859-3865.

Perrem, R.; Henry, F.; Peraudeau, G.; Armas, B. & Berjoan, R. (1997). An XPS and thermogravimetric study of oxidized AlN and AlN–Si_3N_4 layers deposited by liquid-phase chemical vapour deposition. *J. Mater.Sci.*, Vol.32, pp. 1305.

Prohaska, G. & Miller, G. (1990). Aluminium nitride: a review of the knowledge base for physical property development. *Mat. Res. Soc. Symp. Proc.* Vol.167, pp. 215-227.

Qiao, L., Zhou, H. & Fu, R. (2003a). Thermal conductivity of AlN ceramics sintered with CaF_2 and YF_3. *Ceramics International*, Vol.29, pp.893-896.

Qiao, L.; Heping, Z.; Xue, H. & Wang, S. (2003b). Effect of Y_2O_3 on low temperature sintering and thermal conductivity of AlN ceramics. *J. Europ. Ceram. Soc.*, Vol.23, pp. 61-67.

Raether, F.; Klimera, A.; Thimm, A.; Ruska, J.; Mussler, B. & Brunner, D. (2001). High strength and high thermal conductivity of aluminium nitride ceramics by microstructural design. Symposium K5 multifunctional ceramics, Materials Week, Munich, Germany.

Ran-Rong Lee (1991). Development of high thermal conductivity aluminium nitride. *J. Am. Ceram. Soc.*, Vol.74, No.9, pp. 2242-2249.

Reetz, T.; Monch, B. & Saupe, M. (1992). Aluminum nitride hydrolysis. *Cfi/Ber*. DKG, Vol.69, No.11/12, pp. 464-465.

Robinson, D. & Dieckmann, R. (1994). Oxidation of aluminium nitride substrates. *J. Mater. Sci.*, Vol.29, pp. 1949–1957.

Robinson, D.; Yin, G. & Dieckmann, R. (1994). Oxide film formation on aluminium nitride substrates covered with thin aluminium layers. *J. Mater. Sci.*, Vol.29, pp. 2389–2394.

Roth, R.; Negas, T. & Lawrence, P. (1983). In *Phase diagrams for Ceramists, Vol. 5*, ed. G. Smith. American Ceramic Society. pp. 97 (figures) and 5793.

Shan, H.; Zhu, Y. & Zhang, Z. (1999). Surface treatment and hydrolysis kinetics of organic films coated AlN powder. *British Ceramic Transactions*, Vol.98, No.3, pp. 146-150.

Seiranian, K.; Fedorov, P.; Garashina, L.; Molev, G.; Karelin ,V. & Sobolev, B., (1974). Phase Diagram of the System CaF_2–YF_3. *J. Crystal Growth*,Vol.26, pp. 61–64.

Sheppard, L. (1990). Aluminium nitride: A versatile but challenging material. *Am. Ceram. Soc. Bull.* Vol.69, pp. 1801.

Shimizu, Y.; Kawanabe, K.; Taky, Y.; Takao, Y. & Egashira, M., (1995). AlN ceramics prepared by aqueous colloidal processing. in Ceramic Processing Science and Technology, Ceramic Transactions, Edited by H. Hausner, G. L. Messing and S. Hirano, (American Ceramic Society, Westerville, OH, vol.51, pp. 403-407.

Sonntag, R.; Borgnakke, C. & Wylen G. (eds.) (2003). Fundamentals of Thermodynamics. John Wiley & Sons, New York.

Streicher, E.; Chartier, T. & Boch, P. (1990a). Influence of organic components on properties of tape-cast aluminum nitride substrates", *Ceramics International*, Vol.16, pp. 247-252.

Streicher, E.; Chartier, T.; Boch, P.; Denanot, M. & Rabier, J. (1990b). Densification and thermal conductivity of low-sintering-temperature AlN materials. *J. Europ. Ceram. Soc.*, Vol.6, pp. 23-29.

Terao, R.; Tatami, J.; Meguro, T. & Komeya K. (2002). Fracture Behaviour of AlN Ceramics with Rare Earth Oxides. *J. Eur. Ceram. Soc.*, Vol.22, pp. 1051–1059.

Troczynski, T. & Nicholson, P. (1989). Effect of additives on the pressureless sintering of aluminium nitride between 1500º and 1800ºC. *J. Am. Ceram. Soc.*, Vol.72, No.8, pp. 1488-1491.

Uenishi, M.; Hashizume, Y. & Yokote, T. (1990). Aluminum nitride powder having improved water resistance. *Unites States Patent* N. 4.923.689, 08.05.1990.

VanDamme, N.; Richard, S.; Winzer S., (1989). Liquid-phase sintering of aluminum nitride by Europium oxide additives", *J. Amer. Ceram. Soc.*, Vol.72, No.8, pp. 1409-1414.

Vassileva, P.; Krastev, V.; Lakov, L. & Peshev, O. (2004). XPS determination of the binding energies of phosphorus and nitrogen in phosphazenes. *J. Mater. Sci.*, Vol.39, pp. 3201.

Virkar, A.; Barret, J. & Cutler, R. (1989). Thermodynamic and kinetic effects of oxygen removal on the thermal conductivity of aluminium nitride. *J. Am. Ceram. Soc.*, Vol.72, No.11, pp. 2031-2042.

Wang, M.-C.; Yang, C.-C.; & Wu, N.-C. (2001). Densification and Structural Development in the Sintering of AlN Ceramics With $CaCN_2$ Additives. *J. Eur. Ceram. Soc.*, Vol.21, pp. 2185–2192.

Wang, M.-C.; Yang, C.-C.; & Wu, N.-C. (2003). Grain growth and electric properties of liquid phase sintered AlN. *Materials and Engineering*, Vol.A343, pp. 97-106.

Wang, Y. & Sherwood, P. (2002). *Surf. Sci. Spectra,* Vol.9, No.1–4, pp. 159.

Watari, K.; Hwang, J.; Toriyama, M. & Kanzaki, S. (1999). Effective sintering aids for low-temperature sintering of AlN ceramics. *Journal of Materials Research,* Vol.14, No.4, pp. 1409-1417.

Wenjea, J.; Tseng & Tsai, C. (2004). Microporous layer structure in oxidized aluminium nitride polycrystals. *J. Mater.*

Process. Technol., Vol.146, pp. 289–293.

Wildhack, S.; Rixecker, G. & Aldinger F., (2005). Processing of aqueous aluminum nitride suspensions with high solid loading. *J. of Am. Ceram. Soc.*, Vol.88, No.9, pp. 2391-2395.

Xiao, J.-L.; Zhang, B.-L.; Li, W.-L. & Zhuang L.-R. (2004). Characteristic and dispersion of a treated AlN powder in aqueous solvent. *Materials Science and Engineering*, Vol.A368, pp. 126-130.

Xiao, J.-L.; Zhang, B.-L.; Li, W.-L. & Zhuang, L.-R. (2004). Preparation of aluminium nitride green sheets by aqueous tape casting. *Ceramics International*, Vol.30, pp. 2099-2103.

Yan, H.; Cannon, R. & Shanefield, D. (1993). Evolution of carbon during binder burnout and sintering of tape-cast aluminium nitride. *J. Am. Ceram. Soc.*, Vol.76, No.1, pp. 166–172.

Yu, Y.-D.; Hundere, A.; Hoier, R.; Dunin-Borkowski, E. & Einarsrud, M.-A. (2002). Microstructural characterization and microstructural effects on the thermal conductivity of AlN (Y_2O_3) ceramics. *J. Europ. Ceram. Soc.*, Vol.22, pp. 247-252.

Zhang Y., (2002). Effect of surfactant on depressing the hydrolysis process for aluminum nitride powder. *Materials Research Bulletin*, 37, 2393-2400.

11

Advanced Design and Fabrication of Microwave Components Based on Shape Optimization and 3D Ceramic Stereolithography Process

N. Delhote[1], S. Bila[1], D. Baillargeat[1], T Chartier[2] and S Verdeyme[1]
[1]*XLIM, UMR 6172, Université de Limoges/CNRS*
[2]*SPCTS UMR 6638, Université de Limoges/CNRS*
Limoges,
France

1. Introduction

The design of advanced components for space and terrestrial telecommunication systems requires both sophisticated design methodologies and manufacturing technologies for improving current component characteristics. In particular, optimizing the shape and the size of a component is a problem of primary importance for microwave engineers. Moreover, for designing RF and microwave components or antennas, the use of ceramic materials is preferable in order to satisfy both electrical and dimensional constraints.
The main objective of this chapter is to demonstrate that it is possible to jointly improve the design and fabrication procedures of ceramic based advanced RF components. In this context, a ceramic 3D stereolithography based rapid prototyping technique is applied for fabricating 3D ceramic structures. As presented next, theoretical and experimental approaches are complementary and innovative components with excellent electrical performances have been designed, manufactured and characterized. Then the contribution demonstrates how an original CAD design approach based on shape optimization methods can be applied for improving electrical performance and integration of microwave and millimeter-wave devices.
The chapter is organized as follows:

- In the first section of this chapter we will focus on the explanation of the ceramic 3D stereolithography (SLA) process. A particular attention on the process developed by the SPCTS UMR 6638 (Limoges, France) and now available at the Centre de Transfert de technologies Ceramiques (CTTC, Limoges, France) will be paid here. This process has been developed in recent years, in the context of rapid prototyping techniques. More generally three dimensional (3-D) fabrication processes have recently emerged as enabling technologies for the design of compact devices and interconnects, and for packaging needs. For these purposes, polymer (Liu, 2004) and ceramic (Brakora et al., 2007; Delhote et al,2007) stereolithography methods are really promising since they do not require the use of moulds and cutting tools. They are relatively fast and reliable techniques capable of building truly 3-D structures with a high aspect ratio and accuracy.

- The second section is devoted to the description of several test structures. As demonstrated here, the applications concern several areas of microwave engineering, from very complex 3D periodic structures, to advanced millimeter wave antenna and bandpass filters. All the devices were designed applying a 3D electromagnetic software, and were fabricated and tested successfully. The satisfying agreement between theoretical and experimental studies allows us to validate the use of our rapid prototyping technique for fabricating millimeter wave devices.
- The third section is dedicated to the description of shape optimization methods that can be used for computer-aided design of microwave components. Two techniques have been implemented and coupled to an electromagnetic solver based on a finite element method and have been used successfully for the design of ceramic-based microwave components. Several examples are described.

2. 3D ceramic stereolithography process

2.1 Rapid prototyping process

The stereolithography process, commonly referred as layer-by-layer or SLA, can be attached to a more general class of process called rapid prototyping process. One general definition of the fast prototyping fabrication technique is a manufacturing process capable of producing a prototype with a minimum of time and resource (no need for mould for example). The SLA process is an additive process in comparison with traditional substractive shaping techniques like cutting, milling or drilling. The principle of this manufacturing technique can be summarized in Figure 2.1.

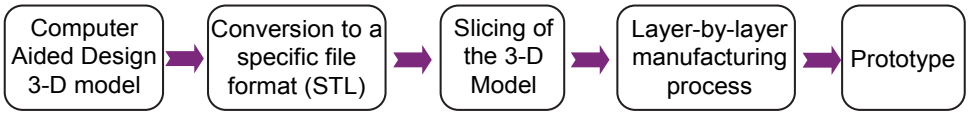

Fig. 2.1. Principle of a layer-by-layer manufacturing process

The starting point of this fabrication chain is the creation of the initial drawing with a Computer Aided Design (CAD) software. This drawing represents the future prototype to build. Then, a conversion software is applied to convert this model into a very specific format called STL. Initially developed for the stereolithography process, it has become the standard format for additive process. This format turns the 3-D model surface into a set of triangles, a rather simple geometry to work with. Then the 3D-model, once converted, is sliced into fixed height slices. The core of this kind of manufacturing technique is to build slice after slice ("layer-by-layer") the whole 3-D objet. The fabrication can now begin and the prototype, with the geometry and dimensions defined in the initial CAD model is finally retrieved.

One can mention the most common 3-D additive techniques like the Selective Laser Sintering (SLS) and a version more dedicated to the fabrication of metal and ceramic parts called Direct Metal Laser Sintering (DMLS), the Laminated Object Manufacturing (LOM) process, Fused Deposition Modelling (FDM), 3D Printing (3DP) and the Inkjet Printing. Among theses techniques, the stereolithography has been the first and most common 3D manufacturing process for the creation of prototypes.

2.2 Stereolithography

The principle now described is the most widely used by research teams and commercial devices. As mentioned earlier, the point of this process is to build the slices of the 3D model one by one, from the bottom of the object to its top. It is based on the polymerisation of a photosensitive resin by a laser, most of the time being in the Ultraviolet wavelength range (Hull, 1986). The Figure 2.2 gives an overview of the device.

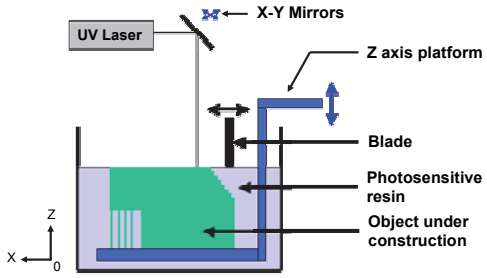

Fig. 2.2. Principle of the SLA manufacturing process

The resin disposed in a tank needs to be very fluid and is composed of photosensitive monomers. These elements can turn into polymers if enough energy is given through a laser beam and constitutes the very heart of 3D additive process (Hull, 1986). Indeed, once polymerised, the resin is quite solid and can be easily separated from the liquid monomers. In the tank containing the photosensitive resin, a platform moving along the vertical (z) axis is placed in order to support the part during its fabrication. Its position is monitored by a computer with a very high positioning accuracy (typically a few micrometers).
For the fabrication of the first slice (layer) of the object, the platform is initially place close to the surface of the resin: the distance between the surface and the platform is more precisely equal to the thickness of the slice. A blade, also monitored by a computer, then goes at a defined speed along the surface of the liquid to make it as flat as possible.
The surface of the liquid will now be selectively exposed to the UV laser thanks to two mobile mirrors according to the pattern of the first slice. These mirrors are illuminated by a fixed laser beam and monitored by computer. With this process, the slice of the object is physically drawn at the surface with the laser polymerising the resin on its path. The polymerisation reaction depth (see Figure 2.3) is also dependant on the amount of power transported by the laser beam.

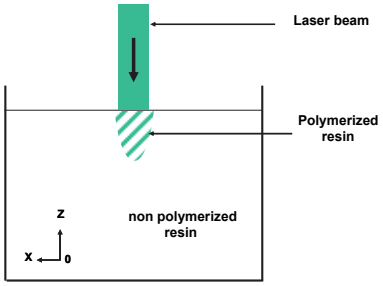

Fig. 2.3. Thickness of polymerisation

The laser beam is slightly scattered at the surface of the resin because of the refractive index difference between the air and the resin. Thus, the laser spot at the resin surface is larger than the initial beam diameter.
After the first slice is done, the Z axis platform goes down with a distance equal to the object second slice thickness and the process is repeated until all the slices are completed.
As seen on Figure 2.3, the polymerised amount of resin has an oblong shape with a diameter becoming smaller as the polymerising depth goes higher. The energy transported by the laser beam has to be very precisely calibrated because it directly defines the thickness of polymerised resin (Chartier, 2002). Indeed, the power transported by the laser beam has to be enough to trigger the polymerisation process but also has to polymerise a sufficient thickness to make the slice under construction attached to the previous layer. If not, the slices are not glued together and the whole part will be delaminated.
At the end of the process, the fabricated part, i.e. the solid polymerised part can be easily retrieved from the liquid resin bath. If needed, a post UV curing can be done in order to fully polymerise the whole part. The accuracy of this process is mainly driven the diameter of the laser beam and very high accuracy close to 5µm can achieved with the appropriate laser (Monneret, 2005).
Many research teams have then tried to use this technique to manufacture 3D object made out of ceramic materials (Bertsch, 2003) by adding a volume percentage of ceramic particles into the photosensitive resin. The term ceramic suspension or paste is in this case more appropriate.

2.3 Evolution to ceramic stereolithography

In order to use the process describe in 2.2, the resin, now with ceramic particles, has to remain very fluid. If the compound is too viscous, the blade cannot ensure anymore a proper flatness at the surface of the resin bath and critical deformations are observed during fabrication. To do so, the logical way is to limit the total volume percentage of ceramic particles because the overall viscosity of the paste is directly related to this parameter (Hinczewski, 1998). However in order to obtain ceramic objects with appropriate properties et mechanical strength and to limit cracks during the necessary firing step, the volume percentage of ceramic particles has to be more than 50% in volume (Hinczewski, 1998).
There is here a deep contradiction because for high percentage, the compound is very viscous. This very high viscosity can also lead to a very high UV exposition time to trigger the polymerisation reaction. In certain circumstances, the critical energy required to polymerise the compound can even not be reached.
Based on such considerations, Thierry Chartier (SPCTS UMR 6638, Limoges, France) in collaboration with the technological transfer centre CTTC (Centre de Transfert de Technologies Ceramiques, Limoges, France) proposed a different approach (Doreau, 2000). Instead of developing a mix, called more specifically a suspension, which should be as fluid as possible, T. Chartier has developed a suspension with a high volume percentage (~65%) of ceramic particles and highly selective photosensitive resin (Doreau, 2000). The obtained suspension is in such configuration thick and viscous.
This composition has then been used by many research teams (Bertsch, 2003).

2.4 Preparation of a ceramic suspension

Adding such amount of ceramic particles in the suspension increases the complexity of its preparation. As its quality is directly dependant on the homogeneous mixing of all its chemicals elements, a very precise protocol has to be followed.

The first step is to sift the ceramic powder in order to keep only particles with a very precise diameter from one to a few micrometers. Their diameter, size distribution and geometry have to be precisely controlled because they directly have an impact on the suspension properties and those of the ceramic part which will be made (Hinczewski, 1998).
These ceramic particles naturally tend to agglomerate together and this behaviour has to be avoided as much as possible. Thus the ceramic particles are mixed with ethanol and a dispersal agent. This latter modifies the interaction forces between the particles by playing on electrostatic repulsion forces for example. Thanks to them, a global homogeneity is ensured within the suspension. This mix is then grinded by highly hard ceramic balls from less than one hour to many hours.
After this grinding step, the mix is placed in an oven to evaporate the ethanol. The obtained very thin particles are then mixed with other elements:

- A photosensitive resin composed of reactive monomers which can be polymerised under UV light exposition
- A photo-initiator which absorbs the UV light and helps the polymerisation process of the resin
- A binder: the goal of this chemical is the keep the particles together enough to ensure a mechanical strength of the ceramic part before the firing step. This part is called a green part.
- A plasticizer which helps the green part to be rigid enough to endure the fabrication process
- A fluidifier which brings the suspension fluidity to a required level
- A wetting agent which helps to control the adhesion between the powder and the binder, making the whole suspension homogeneous

The obtained suspension then goes through rollers to break agglomerates if they still exist.
After that the obtained viscous paste has to remain still for some hours for its outgassing and is now ready to be used for the manufacturing steps.
Because of its high viscosity, a very specific sweeping system has to be used with it.

2.5 Ceramic stereolithography manufacturing process

The next Figure 2.4 shows the manufacturing platform of the stereolithography process.

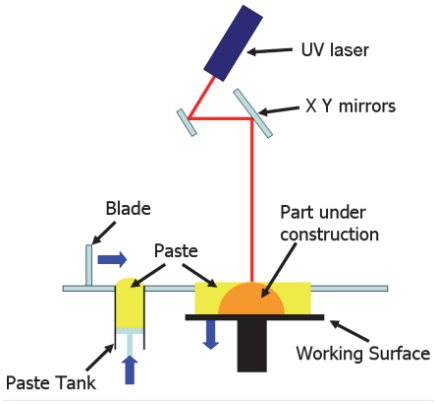

Fig. 2.4. Principle of the stereolithography 3D process

This technique shares many common points with the standard stereolithography process described in part 2.1.
A Ultraviolet (UV) (λ~350 nm) laser is still commonly used to selectively polymerise layers of the prepared suspension to build a 3D object. However because of the high viscosity of the paste used for the fabrication, the manufacturing device needs some modifications.
The paste is put in a paste fed container and a piston delivers the right amount of paste for one layer. Then a specifically profiled blade spreads uniformly the paste on the working surface.
After the first layer is spread, (10 to 15 seconds), this latter is selectively exposed to the UV laser beam thanks to X-Y monitored mirrors within seconds to physically draw the first slice of the 3-D object. The typical diameter of the beam is about 100 μm. After that, the working surface goes down for a distance equal to the thickness of a layer. Another layer of paste is then spread at the top of the previous one and the process continues in the same way for every layer.
The working surface of the device used to manufacture the ceramic parts presented in part 2 is 25 cm by 25 cm. The maximum height which can be obtained is also 25 cm. For a 1 cm thick part composed of 100 μm thick layers, the manufacturing time is close to 1 hour. Thinner layers of 25 μm can be reached with this system.
At the end of the fabrication, because of the paste viscosity, the polymerised part has to be retrieved from the amount of non-polymerised paste. The part is then cleaned by going through different chemical baths. Because of the cleaning step, the part can not have closed volumes and if the part is closed, it needs at least holes to evacuate the non-polymerised paste.
The obtained cleaned part is called the green part and will need to be fired to obtain its final dimensions and properties. Because of the manufacturing process specificities, the suspension has to show specific properties.

2.6 Properties of the suspension

2.6.1 Mechanical strength

The paste has to be viscous enough to be correctly spread by the blade on top of working surface. The spread layer has to keep a defined thickness and a uniform aspect during the process. Because of the blade, a meniscus grows at its bottom but this phenomenon can be limited by refining the suspension composition. Thus, no extra time between the spreading of each layer is required to let the meniscus disappear. The suspension used by Chartier *et al*. (Chartier 2002) is about 10 times more viscous than the suspension used by other research teams (Bertsch, 2003). This high viscosity as explained in part 2.4 is mainly due to the high volume percentage of ceramic particles. Thanks to this viscosity, a layer of non-polymerised paste can generally support the other layers spread on top of it.
However in some cases in order to avoid deformations of the part because of the blade movement, it can be necessary to add some construction supporting elements. These elements are polymerised parts made during the manufacturing. A typical case is shown in the next Figure 2.5.
Typically some pillars acting as supporting elements can be added in critical points where the main part required extra strength during the fabrication process.

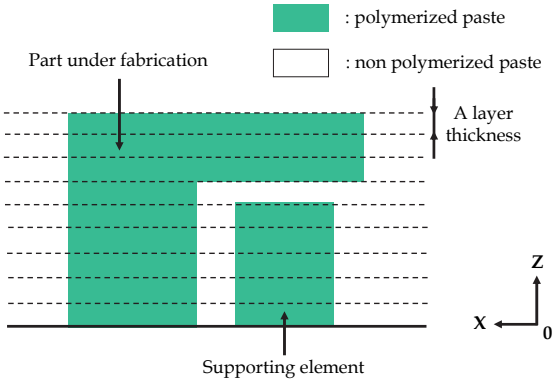

Fig. 2.5. Supporting elements added during manufacturing of the main part

2.6.2 Light scattering and absorption

Adding ceramic particles in the initial photosensitive resin modifies the thickness and width of the polymerised zone exposed to the UV laser beam. The ceramic particles indeed create a combined light scattering and absorption phenomenon as shown in Figure 2.6.

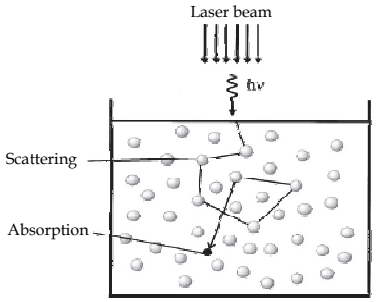

Fig. 2.6. Light scattering and absorption phenomena in a media charged in ceramic particles

The laser beam spot at the surface of the suspension layer is thus 1.5 to 2.5 times wider than its original width. The resolution obtained is consequently lower than with a non charged resin and typical manufacturing tolerances are about 100 µm. This value can however be decreased with refinements on every aspects of the process.
The ceramic particles also absorb a part of the energy provided by the laser beam and tend to limit the polymerisation thickness which will be called *Ep* in the equation 2.1.

$$E_p = D_p \ln(\frac{DE}{DE_c}) \text{ in meters} \tag{2.1}$$

DE is the energy density given to the resin defined by the equation 2.2.

$$DE = \frac{2P}{\pi . w_0 . v} \text{ in J.m}^2 \tag{2.2}$$

With P, the insulation power (in J. s^{-1}), w_0 the radius of the laser beam in meters and v the speed of the laser beam in m.s^{-1}.
DE_c is the critical energy density which is the minimal energy to trigger the polymerisation process in J. m^2.
Dp is finally the laser beam depth of penetration in meters.
The polymerisation thickness Ep is thus directly proportional to the depth of penetration of the laser beam Dp. For suspension charged with ceramic particles, Dp is defined by the equation 2.3:

$$D_p = \frac{2}{3}\frac{d_{50}}{Q.\phi} \text{ in meters} \tag{2.3}$$

with d_{50} the average diameter of the particles in meters, ϕ the volume percentage of particles and Q is a coefficient defined by equation 2.4:

$$Q = \frac{h}{\lambda}.\Delta n^2 \tag{2.4}$$

with h the average inter-particular distance in meters, λ the wavelength of the laser in meters and Δn^2 the difference between the refractive index of the ceramic powder and the resin defined by the equation 2.5:

$$\Delta n^2 = (n_{powder} - n_{resin})^2 \tag{2.5}$$

The higher the ceramic particles percentage is the less the laser beam depth of penetration is. In the same way, high refractive index ceramic powders or low diameter ceramic particles can also strongly decrease this penetration depth.
The equation 1 also indicates that the less Dp is, the less Ep will be.
Remembering the shape of the polymerised paste under the action of the laser (Figure 2.3), Dp has also a significant impact on the polymerization width at the surface of a layer of paste. The higher Dp is the less the lateral definition will be. A compromise has thus to be find between a polymerisation depth high enough to fully polymerised a layer thickness but not too high to not lose too much lateral definition.
As shown in (Chartier, 2002), there is a relation between the polymerisation depth (and lateral definition) and the concentration of the photo-initiator in the suspension. High concentration levels of this element indeed increase the energy density received by the paste without a need of high Dp values. Refining the photo-initiator concentration level can thus lead to the required polymerisation depth without sacrificing the definition.
At the end, the concentration of every constituent in the suspension has to be finely defined to obtain the right compromise between high volume percentage of ceramic particles, acceptable definition and polymerisation depth.

2.6.3 Shrinkage during firing

In the previous part it has been seen that high volume percentages of ceramic particles within the suspension decrease the definition of the stereolithography process. However these high levels of concentration are highly interesting because they will help to decrease the ceramic part deformations during its fabrication. Indeed, the green part retrieved at the end of the process has to go through two final firing steps which will put more mechanical stress on it.

The first firing step is called debinding. This step will burn out organic materials which are still in the part like the polymers, binders… The part is fired while constantly increasing the temperature up to about 600°C. This last temperature is then maintained for a few hours. During this step, the organic elements within the green part slowly move to the outside of the part. Deformations and even cracks can appear if the temperature goes too fast to the maximum value. The temperature has to be increased very slowly, typically less than a Celsius degree per minute.
During the second step, the temperature keeps increasing up to more than 1600°C with a higher ramp of many Celsius degrees per minute. This step called sintering gives the ceramic part its final density with typical values equal or more than 97% of the theoretical value. The part finally presents its final density and size.
During these two steps, the green part shrinks and the shrinkage percentage is directly related to the volume percentage of ceramic particles in the initial suspension. The Figure 2.7 gives an example of a ceramic part before and after firing (debinding and sintering), this part being fabricated with a ceramic suspensions charged at 65% (CTTC, Limoges, France).

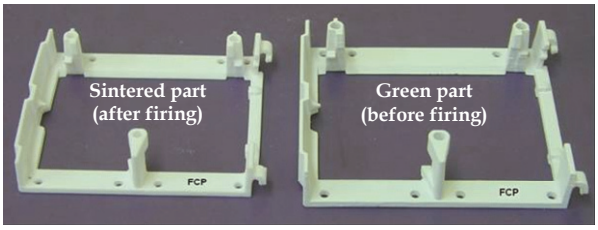

Fig. 2.7. Ceramic part made by ceramic stereolithography before and after firing; courtesy of the CTTC (Limoges, France)

Low percentage of ceramic particles (less than 50%) leads to a shrinkage of typically more than 25%. In such configurations, the sintered part shows high deformations if not cracks.
As a consequence every suspension will lead to a specific shrinkage. This value has to be precisely known in order to fabricate a bigger green part and to have a sintered part at the right size and shape. This initial oversizing is a very delicate step because the shrinkage, for complex geometries, may not be isotropic. The shrinkage is however identical from one fabrication to another.

2.7 Conclusion

Every element in the ceramic suspension used for the fabrication by ceramic stereolithography is very important because it sets all the future properties of the final fired ceramic part. Regarding the mechanical strength of the green part during the fabrication process itself, the fabrication definition, the final part density, its shrinkage during debinding and sintering, …, every suspension has to be very precisely studied in order to obtain a successful compromise between all these parameters.
One major key is to go to high volume percentage of ceramic particles in the suspension because this will lead to highly dense ceramic part (high strength) and low shrinkage during the firing steps (low deformation). The drawbacks of this high percentage are a loss in lateral definition mainly because of the light scattering phenomena due to the presence of the ceramic particles.

However by refining enough all these parameters and with a small diameter laser, a manufacturing accuracy close to 50 µm can be reached. Combining this accuracy and the ability to manufacture dense ceramic parts with a very complex geometry, this technology gives a very high level of freedom for the design of high performances millimetre wave components.

3. Advanced components for millimetre wave applications

In this section, we now focus on advanced RF components fabricated by stereolithography process. Theoretical and experimental structures are compared for validating our approach.

3.1 D ceramic woodpile crystal

One of the most complex devices we fabricated is a ceramic woodpile (layer-by-layer) crystal. Such device is representative of the capabilities of the 3D stereolithography process. We describe two test structures based on the woodpile crystal.

The first one is a waveguide located in the woodpile (Delhote et al., 2007a). The geometrical sizes, shape and location of the waveguide into the ceramic woodpile have been optimized in order to maximize its bandwidth and the matching between this guide and the Input/Ouput feeding WR waveguides. The 3D Electromagnetic Band Gap (EBG) crystal has been designed, optimized and manufactured in one monolithic piece with Zirconia (εr=31.2 at 30GHz) by the 3D ceramic stereolithography process. It experimentally exhibits a very large bandgap superior to 30% and the waveguide located in such woodpile provides a measured 20% bandwidth around 26GHz while keeping a return loss inferior to –10dB. This work focused on the improvement of the electrical performances of the waveguide by enhancing two major points. First, a close attention was paid to maximize the matching between an input standard WR waveguide and the EBG one without any taper by optimizing the configuration of the default. Then, the waveguide bandwidth has been improved simply by enlarging the EBG material complete bandgap. This last purpose has been reached by having recourse to high permittivity ceramic for the manufacturing and optimizing the filling factor, height and width of the woodpile's rods. Of course these different parameters have to agree the constraints imposed by the waveguide geometry. The lattice constant of the woodpile in the horizontal (x0y) plane is refereed as a, the rod width $w(=a/4)$, the rod height h. Considering the chosen configuration, the h/w ratio has to be equal to 0.9 and the filling factor, representing the percentage of dielectric in a unit cell, equal to 25%. The chosen dielectric is the Zirconia ceramic known to present a permittivity of 31.2 at 30GHz. Such EBG material provides a 33% complete bandgap around the normalized frequency af/c (f being the central frequency of the complete bandgap (Hz) and c the speed of light in vacuum) of 0.474. By taking into account the manufacturing tolerances of the 3D ceramic stereolithography, the w parameter has been chosen equal to 790µm, making the complete bandgap appearing between 25 and 35 GHz in the Ka band (26 – 40 GHz). All the dimensions of the EBG crystal were first defined by computing its band diagram and its first Brillouin zone (see Figure 3.1) applying the plane wave method. Then, the dimensions were optimized applying 3D electromagnetic simulations based on a Finite Element Method (FEM)

Fig.3.2 (a) presents the fabricated woodpile. This structure was fabricated in only one monolithic piece. In order to measure its transmission (S21) and reflexion (S11) parameters, it was inserted in a measurement support as shown in Figure 3.2 (b).

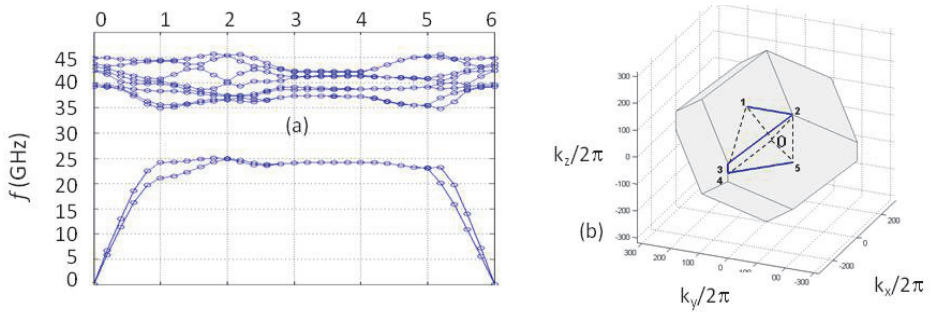

Fig. 3.1. (a) Band diagram of the proposed photonic crystal. (b) First Brillouin zone: the 6 high symmetry points used for the calculation are also displayed.

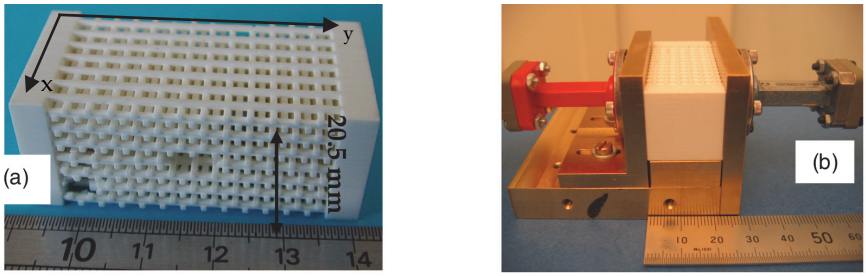

Fig. 3.2. (a) Monolithic waveguide located in a woodpile manufactured with Zirconia by ceramic stereolithography. (b) Woodpile waveguide inserted in its support feeded by two WR28 waveguides.

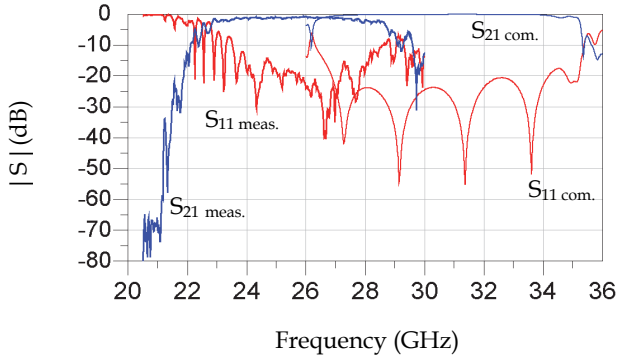

Fig. 3.3. Monolithic waveguide located in a woodpile manufactured with Zirconia by ceramic stereolithography. Experimental (meas.) and computed (com.) scattering parameters.

Figure 3.3 compares the theoretical and experimental scattering parameters of the waveguide. The waveguide band pass appears to be theoretically equal to 29.4% around

30.85GHz while keeping a return loss inferior to –10dB. This waveguide takes advantage of almost the entire complete band gap provided by the woodpile. As presented in Figure 3.3, the experimental waveguide bandpass appeared to be centered around 26GHz instead of 30.85GHz. This shift is due to fabricating discrepancies. Some misshapes have occurred, making the y axis and x axis rods respectively 800 and 500 µm high instead of 710 µm. The rod width is also closer to 800 µm. However the experimental structure presents an interesting 19.6% bandpass around 26 GHz for a return loss inferior to –10 dB. The insertion losses appear very acceptable with the measured values from 0.8 to 1.7dB in the band pass.

The second example concerns a 3D crystal millimetre resonant cavity (Delhote et al., 2007b). Electromagnetic properties of the previous ceramic woodpile structure are exploited in order to design an air resonant cavity. For creating such a cavity, we consider a defect inside the woodpile. The unloaded quality factor of the resonator depends on the dielectric material performances and on the crystal efficiency for limiting as much as possible the leakage through the crystal periods. The cavity dimensions obviously fix its working frequency and have to be precisely taken into account in order to adjust the chosen frequency inside the crystal frequency band gap. As said previously, the leakage can greatly reduce the unloaded Q. It can only be limited by adding a large number of crystal periods surrounding the cavity but this choice also heavily increases its volume as compared to the cavity size. Moreover, this larger number of period increases the losses provided by the dielectric material. Shielding the whole structure with metal allows for efficiently eliminating the leakage issue but can reduce the unloaded Q by adding extra losses due to the metal itself. It has also to be considered that the closer the metal is to the air cavity, the higher the metallic losses are. However the radiative are very high and high unloaded quality factor can not be reached without a metal shield surrounding the whole structure. We investigated the best compromise between the size of a shielded 3D crystal and the unloaded quality factor value in order to manufacture and test such cavity. Two types of test structures were fabricated with success using zirconia and alumina. A specific low loss alumina has been developed with our partners. It presents a very challenging loss tangent of 5 10^{-5}. Figure 3.4 describes the zirconia crystal. The computed E field distribution at the resonant frequency is described. As we can see, it is well confined in the air cavity.

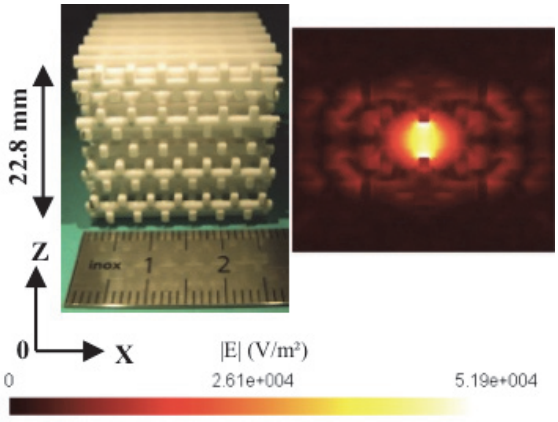

Fig. 3.4. Manufactured Zirconia layer-by-layer crystal. |E| field at f_0

Figure 3.5 (a) displays the measured transmission parameter for the zirconia crystal. The working frequency is 31.5 GHz and the unloaded quality factor is 990, which is very close to the value predicted by computations. Figure 3.5 (b) presents the measured transmission parameter for the alumina crystal air resonant cavity. The measured unloaded Q is about 4000. Due to the very low loss tangent, a theoretical value of the unloaded Q equal to 30000 could be reached. But for measuring such value, the experimental set up needs to be improved.

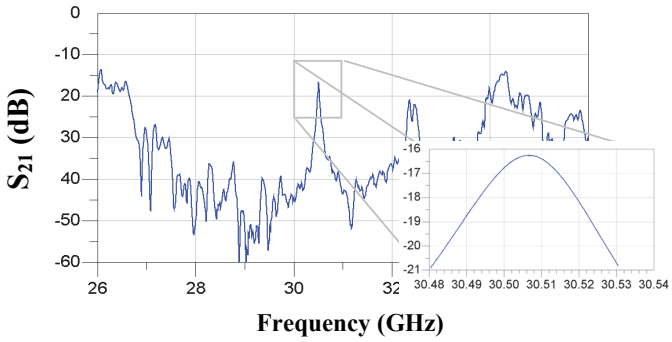

(a)

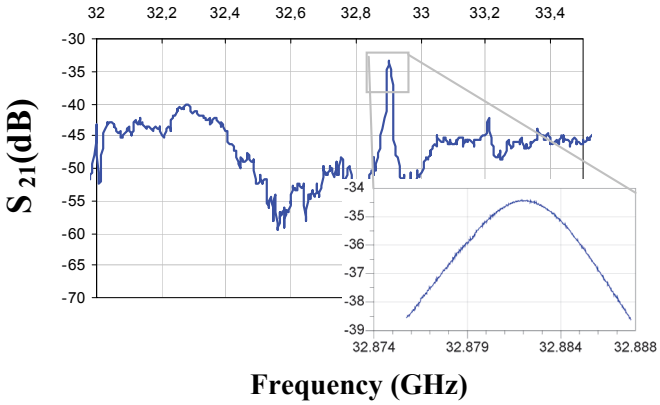

(b)

Fig. 3.5. (a) Measured transmission parameter for the zirconia 3D crystal air cavity. Close view around the working frequency. (b) Measured transmission parameter for the alumina 3D crystal air cavity. Close view around the working frequency

3.2 Alumina lens antennas

In collaboration with IETR UMR CNRS 6164, University of Rennes 1, Rennes, France, we designed, fabricated and characterized integrated lens antennas made in Alumina (Nguyen et al., 2010). They are built through ceramic stereolithography. The operating frequency is in the 60-GHz band. Linear corrugations are integrated on the lens surface to reduce the effects

of multiple internal reflections and improve the antenna performance. The antenna geometry is described in Figure 3.6. It consists of a synthesized elliptical lens made in Alumina; the dielectric characteristics of Alumina have been measured at 10 GHz using a resonant cavity: $\varepsilon_r = 9.0$, $\tan\delta = 5\times10^{-5}$. The same values are chosen at 60 GHz. The antenna is excited by a rectangular waveguide with an integrated impedance matching taper. Three antenna prototypes have been fabricated using the stereolithography process. The first one ($ILA_{\#1}$, Fig. 6a) and second one ($ILA_{\#2}$) have corrugations of different size: their widths equal 300 µm for $ILA_{\#1}$ and 400 µm for $ILA_{\#2}$. The other corrugation dimensions depth and spacing equal 700 µm and 1200 µm respectively. The third lens antenna ($ILA_{\#3}$) has a smooth surface, i.e. no corrugation. Considering two different corrugation widths and depths allows assessing the fabrication limitations in terms of resolution and minimum size of small 3-D objects, whereas comparing ILA configurations with and without corrugations enables one to highlight the impact of these corrugations upon the antenna performance. Here all lenses have the same total diameter and height, and are fed by the same impedance matching taper.

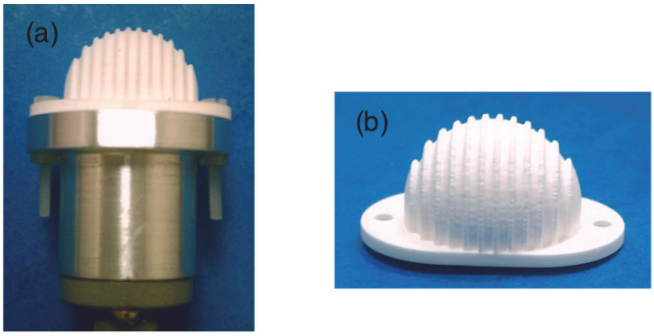

Fig. 3.6. Synthesized elliptical ILA ($ILA_{\#1 \text{ and } 2}$) fabricated by ceramic stereolithography. (a) Antenna prototype (after assembly). (b) Cross-section view of the Alumina lens alone.

The measured reflection coefficients of the three lens antennas are smaller than -10 dB from 55 GHz to 65 GHz. The radiation patterns measured at 60.5 GHz are represented in Figure 3.7 They are in good agreement with the FDTD simulations. The slight asymmetry observed on the measured beams probably comes from lens deformation. Additional experimental results have confirmed that these patterns are very stable between 55 GHz and 65 GHz.
The antenna gains are plotted in Figure 3.8. They have been measured with the comparison method using a 20-dBi standard gain horn in *V*-band. As expected this figure confirms that the gain variations versus frequency are smaller when using fine corrugations ($ILA_{\#1}$). At 60 GHz the gain and directivity of $ILA_{\#1}$ equal 19 dBi and 19.9 dBi, respectively.
This study demonstrates that the stereolithography process can be used to fabricate specific antenna lens with high performances. Measurements have shown that the antenna performances are very stable over the 55-65 GHz band. The agreement between the experimental and numerical results is very satisfactory despite some fabrication issues (mechanical stress observed along the dielectric tapers and lens bases). In particular, for 19-dBi gain antennas, the total amount of loss at the center frequency (60.5 GHz) is lower than 0.9 dB, corresponding to a radiation efficiency of 80%.

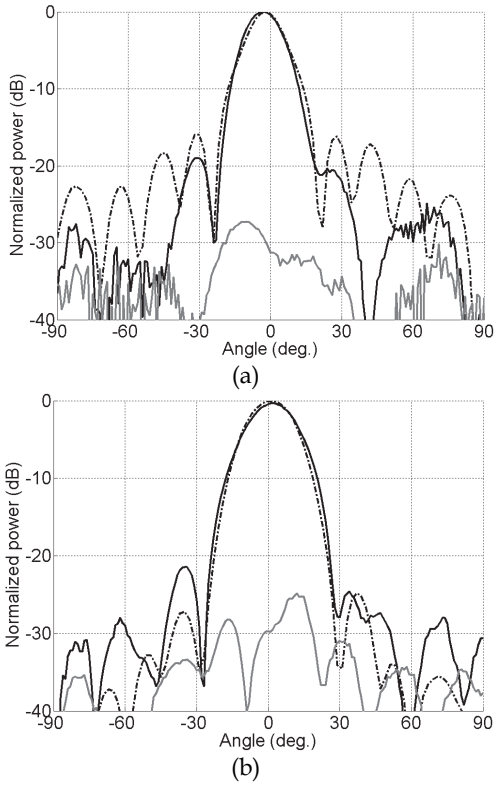

Fig. 3.7. Radiation patterns of $ILA_{\#1}$ at 60.5 GHz. (a) E-plane. (b) H-plane. ——: Measured co-polarization component. -·-·-: Computed co-polarization component. ——: Measured cross-polarization component.

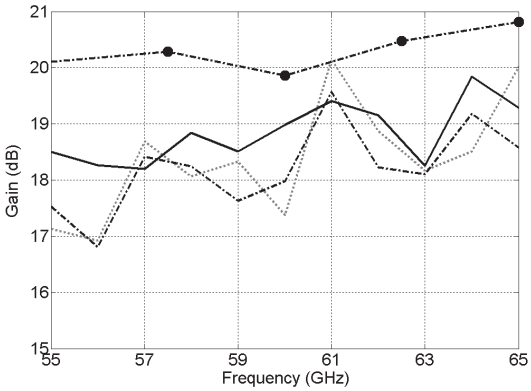

Fig. 3.8. Measured gain of the three lens antennas. ——: ILA#1 (300 μm-thick corrugations). -·-·-: ILA#2 (400 μm-thick corrugations). ·····: ILA#3 (no corrugation). The line with symbols (-●-) represents the theoretical directivity of ILA#1.

3.3 Ceramic bandpass filters

3.3.1 Bandpass filter based on periodic structure

Several bandpass filters have been designed and fabricated applying the stereolithography process. The first example concerns the design of a high unloaded Q factor (Q_u factor) bandpass filter working in the Ka band (Delhote et al., 2007c). Such filter is based on periodic structures and made of Zirconia and high performance $Ba_3ZnTa_2O_9$ (BZT) ceramics. To our knowledge, BZT is mainly used for the manufacturing of simple cylinder-shaped resonators by standard processes such as pressing or molding. It is the first time 3D ceramic stereolithography has been used to manufacture complex innovative filtering devices based on periodic arrangements with high performance ceramics. Figure 3.9 describes the filter under test. It consists of a resonant air cavity surrounding by Bragg reflector as shown in Figure 3.9 (a). Along the x axis, four period reflectors are placed to strongly contain the field in the cavity. The fourth exterior wall of these four period reflectors is $3\lambda g/4$ thick to provide an extra mechanical robustness for this wall which remains in free space.

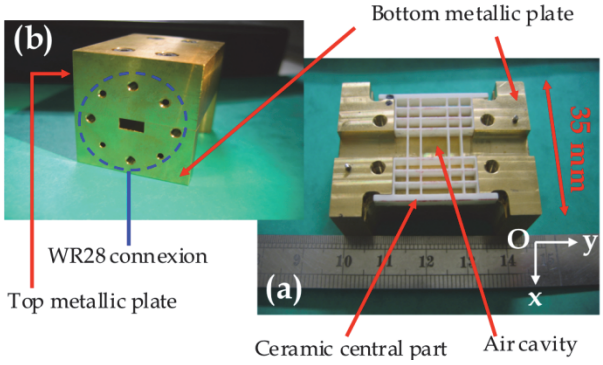

Fig. 3.9. (a) Manufactured single cavity central ceramic part on its brass metallic support (bottom metal plate). (b) The front/rear view of the whole structure is shown in the upper left corner

The air cavity is excited by standard WR28 waveguide placed on each side of the central part along the y axis, and only two period reflectors are placed along this axis to excite the resonant mode of the cavity. The other parts of the structure are metallic plates put on the bottom and on the top (Figure 3.9(b)) of the ceramic central part. The whole structure can be easily connected to standard WR 28 waveguides on its front and rear faces for its measurement (see Figure 3.9(b)). The main interest of this structure is that its performances not only depend on the metallic losses but also on the dielectric ones, making it possible to reach high unloaded quality factor with the proper dielectric material.

During this study, we considered two ceramic: Zirconia with a relative permittivity of 31.2 and a loss tangent (tanδ) of $1.8\ 10^{-3}$ at 30GHz, and the Temex Ceramics© BZT with a relative permittivity of 30.2 and a loss tangent of f(GHz)/173600, that means a loss tangent of $1.9\ 10^{-4}$ at 33GHz. In order to demonstrate the proof of concept of the device described in Figure 3.9, a test structure was fabricated using zirconia. The fabricated dimensions are as follow: the cavity is 7mm by 5.86mm by 3.5mm. Dielectric walls are 0.47mm thick and separated by 2.45mm, making the average manufacturing accuracy close to 50µm. The outside dimensions are 27.2mm by 26.4mm by 3.5mm. It represents a 0.95% manufacturing

discrepancy compared to the theoretical values. This structure was specifically designed for measuring the Q_u factor. The structure, measured with a Hewlett Packard 85107A network analyzer, exhibits a f_0 working frequency of 33.564 GHz (1.7% shift compared to the theoretical value of 32.99 GHz) and a –3dB bandwidth (Δf_{-3dB}) of 42 MHz. The scattering parameters at 33.564 GHz are measured as follow: S_{21} = -6.48dB, S_{11} = -9.91dB and S_{22} = -9.46dB. The unloaded quality factor appears to be about 2400 whereas the theoretical value is 2800 (see Figure 3.10) However this value is less than the 3000 Q_u given by a standard brass shielded air cavity having the same dimensions as the air cavity of the central ceramic part.

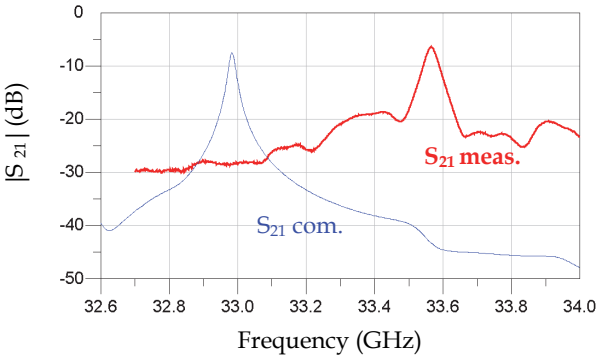

(a)

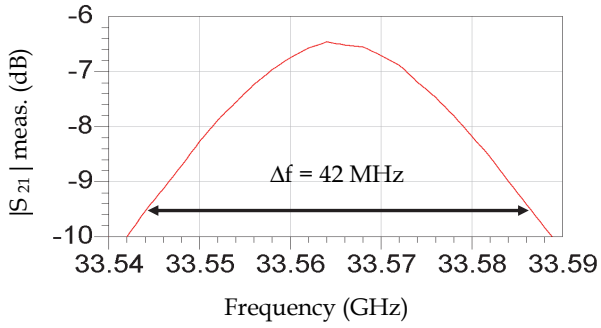

(b)

Fig. 3.10. (a) Computed (thin line) and measured (thick line) transmission parameter of the hybrid single cavity. (b) Close view of the measured (meas.) S21 parameter.

In order to increase the unloaded Q factor and consequently decrease the insertion losses, the Zirconia can be replaced by the BZT. In this case, the Q_u factor is equal to 7000. Such value cannot be reached by a classical metallic cavity at this frequency. As shown in Figure 3.11, several pieces of BZT were fabricated by stereolithography with an average manufacturing accuracy close to 80 µm. New tests and fabrication procedure are currently under consideration in order to improve the fabrication accuracy with BZT.

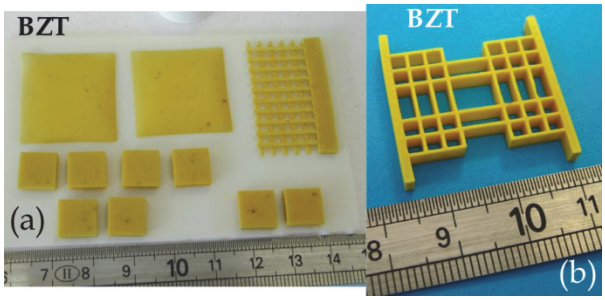

Fig. 3.11. Manufactured pieces out of BZT made to verify its compatibility with the ceramic stereolithography process. (a) Three different parts are presented: 100µm thick plates, parallelepipeds and complex structure composed of crossed bars. (b) Manufactured single cavity resonant structure out of BZT

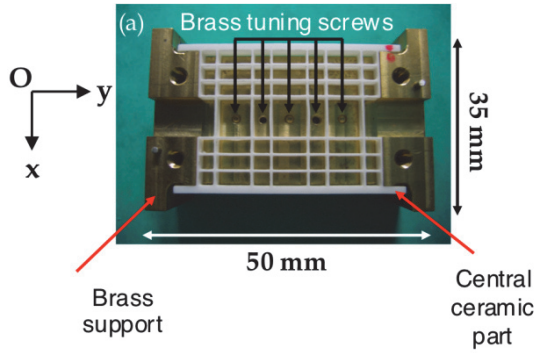

(a)

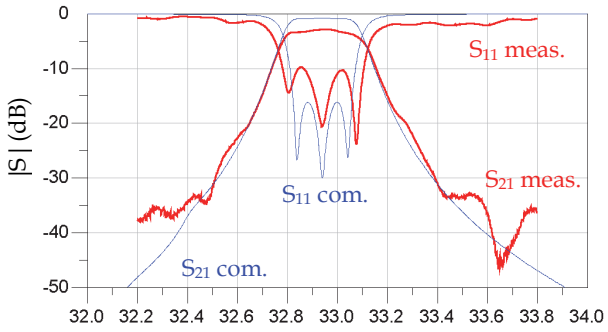

(b)

Fig. 3.12. (a) Manufactured three pole central ceramic part in its brass support (i.e. bottom metallic plate). (b) Measured (thick line) and theoretical (thin line) responses of the three pole filter.

Finally, a narrow bandpass three pole filter was fabricated using Zirconia because of better manufacturing accuracy and its sufficient characteristics to provide a narrow bandwidth in the Ka band. The three cavities required for the three pole filter are placed along the y axis. The coupling distance between them were dimensioned to provide about 1% bandwidth at 33GHz and a ripple of 0.1dB. So, cavities have the same dimensions as the previous ones and the spacing between the cavities is 2.85 mm. The outside dimensions are 27.48mm by 39.75mm by 3.56mm. Brass tuning screws are placed above each cavity and each coupling spacing to refine the different coupling coefficient between the cavities. The three pole filter is described in Figure 3.12 (a) and its S parameters in Figure 3.12 (b). As we can see, experimental (after tuning) and theoretical behaviors are in satisfying agreement.

3.3.2 Alumina resonator shielded in a alumina cavity

The second example of resonant structure dedicated to RF filtering applications, concerns the fabrication of an alumina resonator shielded in a alumina cavity (Delhote et al., 2007d). This device is described in Figure 3.13. It is composed of two parts: a main structure containing the dielectric resonator (DR), its support and the surrounding cavity manufactured in one alumina piece, and a alumina plate placed on the top of the main part in order to close the cavity.

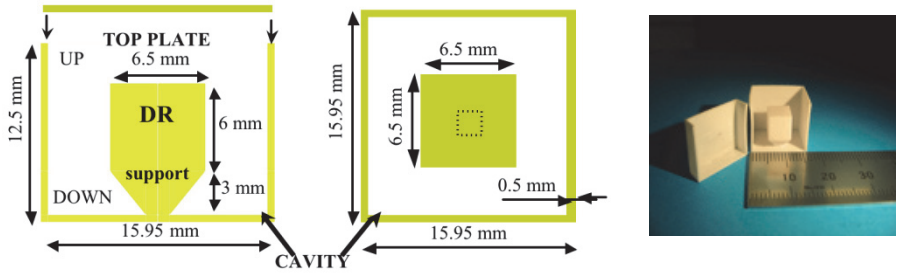

Fig. 3.13. Design of the alumina resonant structure with its main dimensions: inside side view, top view and fabricated structure

The dielectric resonator is parallelepiped because of its manufacturing simplicity and made out of low dielectric loss alumina. This ceramic has been characterized with a permittivity of 9.1 and a low dielectric los tangent of 1.3 10^{-4} .The DR support is also designed taking into account technological constraints, and inversed pyramidal shape is chosen considering this criteria. The surrounding alumina walls are 500-µm thick. This thickness permits to avoid spurious resonant modes inside the ceramic walls and to ensure overall mechanical robustness. As we mentioned, the resonator, its support and the cavity are manufactured in only one piece. During the process, this piece needs to remain open on its top in order to correctly clean the monomer surplus. Then, an alumina plate, having the same outside dimensions as the main part, is centered and glued on top of it in order to close the cavity. The DR resonant mode is the TM111 mode and the working frequency is fixed at 12.57GHz. The DR dimensions are 6 mm x 6 mm x 6.5 mm and the cavity is 15.95 mm x 15.95 mm x 13.5 mm. The DR support height is 3 mm. The surrounding cavity is dimensioned to provide a good compromise between frequency isolation and high unloaded Q. Its external faces are metalized with Epotek E202 epoxy silver glue (conductivity close to 6.6 10^5 S/m).

This method has been chosen for its simplicity to quickly provide good metallic shielding. The top and bottom faces of the cavity are first polished with 10µm grit size diamond polishing discs and Heraeus KQ500 etchable gold is applied on them, in order to provide a 5µm thick layer in gold after baking. Input/output (I/O) RF coplanar excitation accesses are then etched on the top or bottom face of the structure. It is suitable to demonstrate the feasibility of such structure. Figure 3.14 (a) presents the final structure with the coplanar test probes. The experimental transmission parameter is presented in Fig.3.14 (b). It is compared to EM simulations. The two electrical behaviors are in very good agreement. That permits to validate both the numerical approach and the experimental process. The DR resonant frequency (f_0) is equal to 11.87 GHz and unloaded Q factor is extracted by measuring the frequency bandwidth Δf at -3dB from the maximum transmission level (-31dB). Then by considering this weak transmission level, the unloaded Q factor is estimated by the usual formula $Q_u=f_0/\Delta f$. Its experimental value is close to 3900 as expected by numerical computation.

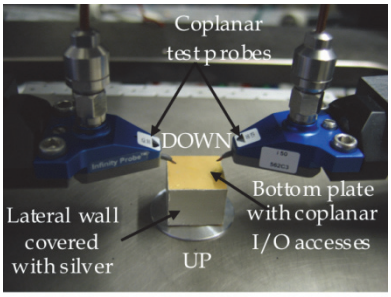

(a)

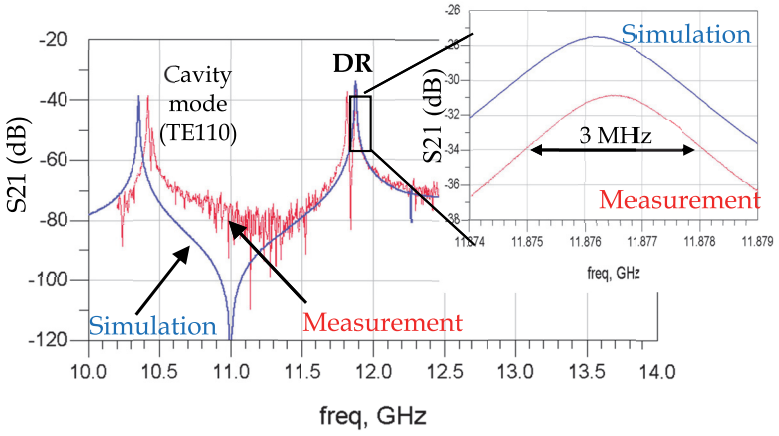

(b)

Fig. 3.14. (a) Final structure under test. The structure is upside down comparing to Fig.3.13 (a). (b) Measured and computed results of the structure: wide band and close view of the S21 parameter around DR resonant frequency at 11.876GHz.

High unloaded Q (~3900) is reached with the presented shielded DR made out of alumina. Its compactness and its ability to be reported on a substrate carrier by standard means (flip-chip or bumps) make this dielectric resonator very interesting for many applications. By providing better metallization (such as gold) instead of silver glue on the lateral walls, unloaded quality factor could theoretically raise to 7000.

3.3.3 3-D pyramidal and collective Ku bandpass alumina filters

The last example described in this book chapter concerns a 3-D pyramidal and collective Ku bandpass filters made in Alumina by ceramic stereolithography (Khalil et al., 2011). The objectives of this work are to propose alternative technologies for the manufacturing of low insertion loss and compact (footprint less than 15 mm by 15 mm) band pass filters in the upper Ku band (17.5 GHz) for space applications. This filter has to remain flat (thickness less than 2.5 mm) and need coplanar input/output accesses to be connected inside a communication module by gold wire bonding or with the flip-chip technology. Temperature stability is a plus and the Alumina has interesting properties in this field. Based on these considerations, the chosen technology for this purpose has been the 3D ceramic stereolithography because of its ability to fabricate 3D compact and low loss Alumina resonators. These resonators will also be shielded with high conductivity metals such as Gold, Silver or Copper. Finally, wet chemical etching or laser ablation techniques will be considered for the etching of the coplanar accesses in the shielding. Nine low footprint Alumina filters are manufactured in one single fabrication by a 3D ceramic stereolithography process. Thank to this technology, high unloaded quality factor resonator (above 1000) have been fabricated and associated to create a low footprint 4-pole Chebyshev filter. Its shielding has been created with a Copper and Gold sputtering technique and its input and output coplanar accesses have been etched by a laser ablation technique. The association of these 3D technologies for the collective manufacturing of many filters in one ceramic part, has led to a low insertion loss filter working around 17.5 GHz. Figure 3.15 displays the shape of the selected 4-pole filter as well as its main dimensions in millimeter.

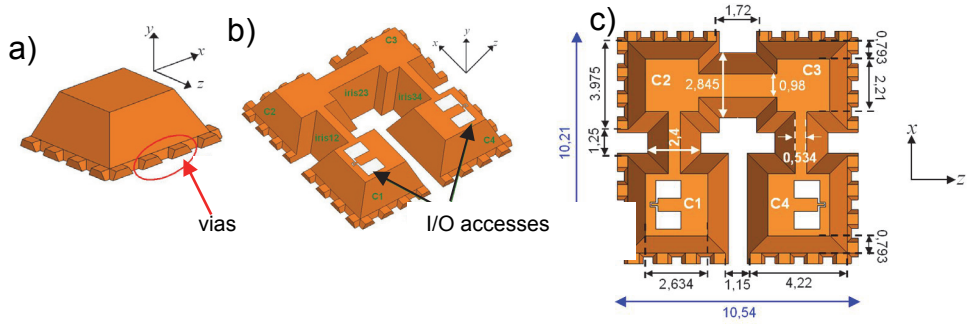

Fig. 3.15.(a) Pyramidal vias integrated at the bottom of the resonator. (b) Final 4-pole filter geometry integrating the pyramidal resonators and vias. (c) Main dimensions of the filter in millimeter (mm).

Figure 3.16 presents the ceramic part before and after metallization and etching of the coplanar accesses. For cost reason, the sputtering of Copper instead of Gold has been preferred. However a Gold coating of 1µm has been put on top of the 5µm thick Copper layer to avoid the oxidization of this layer. The etching step has been performed with a 1080nm YAG laser ablation system. This technology has been chosen because of its sufficient accuracy, its capability of removing all ceramic particles on its path and because of its ability to work with 3D parts.

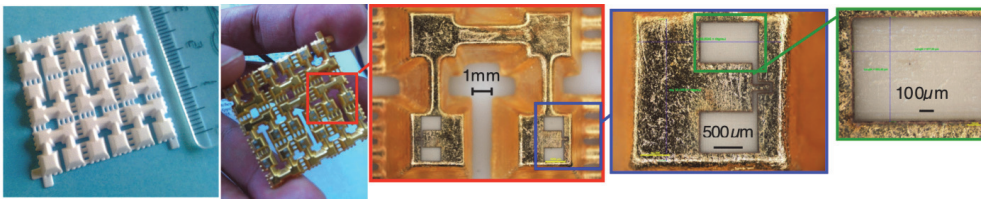

Fig. 3.16. Different view of the filters before and after their metallization with Copper and Gold and their etching with a YAG laser.

Figure 3.16 also shows a close view of the etched accesses. The dimensions of these patterns have been very accurately drawn with a measured accuracy of less than +/- 5 µm. The nine filters have been measured with 50 Ohms coplanar probes on an HP vectorial network analyzer. The experimental S parameters of a typical response are displayed on Figure 3.17 as well as the filtering specifications.

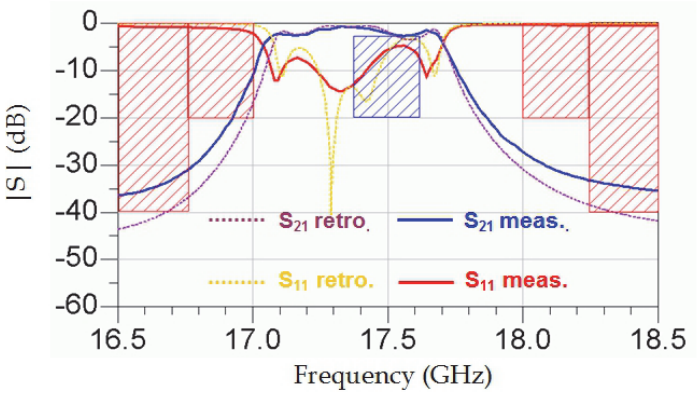

Fig. 3.17. Measured S parameters (solid line) and retro-computations (dashed line).

The experimental results are a central frequency of 17.36 GHz and an equi-ripple band pass of 560 MHz. The insertion loss is 0.7 dB, showing that the Q factor of each resonator is indeed close to 1000 but the in band ripple is about 2 dB. The return loss is only 5dB and the rejection is not sufficient, especially in the lower out of band frequency region. These values coming from a very first fabrication are not satisfying. In order to determine the causes, the manufactured filters main dimensions have been measured. It has appeared that most dimensions present a +/-100µm variation from the theoretical values. Retro-computations have been performed with these dimensions and, as seen on the Figure 3.17, the

experimental behavior has been fully explained. It appears that the inaccurate irises between cavities are mainly responsible of the degraded frequency behavior. Another refined manufacturing of the ceramic part is already ongoing, taking into account the experimental data extracted from this trial. The insertion loss are however acceptable for the filtering specifications (less than the required 3 dB) and the next refinements will be mainly dedicated on obtaining the right pass band, return loss and frequency isolation. The design itself, the overall part geometry, metallization and etching steps have shown that they are compliant with the objective of a small footprint and low insertion loss filter dedicated to space applications. Many 3D technological challenges have thus already been addressed. The proof of concept has been demonstrated.

4. Shape optimization methods

The last section focuses on advanced design of microwave and millimeter-wave components applying shape optimization techniques. These techniques are utilized for optimizing the shape of dielectric components and optimized structures are fabricated using ceramic 3D stereolithography process.

4.1 Shape optimization in the context of electromagnetic problems

Shape optimization methods reside in determining the optimal shape of an object in order to satisfy given specifications. Several approaches have been developed in the context of computer aided-design (CAD), particularly for solving mechanical problems (Sokolowski & Zochowski, 1999; Allaire & Jouve, 2002; Suri et al., 2002), and some of them can be adapted to electromagnetic (EM) problems (Mader et al., 2001; Kozak & Gwarek, 1998; Byun et al., 2004). Considering an initial object embedded in a more global domain, shape optimization strategies can be classified into two categories: boundary optimization, which modifies the contour of the object; and topology optimization, which introduces local perturbations within the domain.

Compared to the classical parameter optimization strategy, which transforms the object with respect to its geometrical dimensions, shape optimization strategies allow accessing to a wider variety of shapes, *i.e.* of solutions, for the object to be optimized.

In the context of electromagnetic computer-aided design, numerical methods based on finite-elements or finite-differences have been extensively developed in the microwave engineer's community. Among boundary optimization techniques, the level-set (LS) method appears well-suited for solving electromagnetic problems (Kim et al., 2009), particularly with such discretized models; while on the other hand, the topology gradient (TG) method can be easily implemented as a topology optimizer for EM problems (Mader et al., 2001).

In both case, optimization of the numerical model is achieved thanks to a gradient evaluation calculated for a cost function related to the model behavior. The optimization strategy consists then in modifying the boundary or the topological elements iteratively in order to minimize the cost function.

Such numerical problems are generally constrained ones, which require the resolution of an adjoint problem, similarly to a geometrical design sensitivity approach (Akel & Webb, 2000). However, considering shape optimization methods, the essential difference lies in the number of variables, which is often huge.

The level-set method (Allaire et al., 2003) is known for modeling propagating fronts and is based on the shape derivative, moving the boundary along the gradient direction during the optimization process. LS methods have been applied very successfully in many areas of scientific modeling and optimization.

The topology gradient method evaluates a gradient concerning a small modification of the domain, translated into adding or removing material very locally. TG optimization was originally developed for mechanics design problems, and it has been recently adapted to other types of design problems, such as electrical and electronic devices.
The topology gradient and level-set methods coupled with a finite element method for optimizing microwave components have been demonstrated in 2-D (Assadi-Haghi et al., 2006) for optimizing the distribution of metal upon the surface of microstrip components and in 3-D (Khalil et al., 2008, 2009, 2010, 2011) for optimizing the distribution of a dielectric material within waveguide components.

4.2 Topology-gradient (TG) and level-set (LS) methods coupled with finite elements

4.2.1 Finite element method (F.E.M)

For analyzing a microwave component with a numerical method such as finite elements, the electromagnetic model is discretized into small elements before solving Maxwell's equations. Applying the finite element method, the following matrix equation is solved:

$$A(\eta)E(\eta) = B \tag{4.1}$$

where A is a square symmetric matrix (Maxwell's operator) representing the geometrical and material properties of the discretized model, B is the column vector of imposed sources, and E the unknown field vector, solution of equation (4.1). Both A and E depend on η, a parameter characterizing the shape.

4.2.2 Topology gradient (TG) method

The topology gradient (TG) optimization procedure starts from an initial configuration of the domain and converges iteratively to the optimum shape using the gradient calculation. The later gradient is calculated at the first order by analyzing the sensitivity of the cost function with respect to a small perturbation of the domain Ω.
We consider η as the reference perturbation centered at origin. The perturbation centered at point x and of size h, is characterized by:

$$\eta_{x,h} = x + h\eta \tag{4.2}$$

For calculating the gradient, the principle of topological asymptotic is utilized. The approach gives then a more precise expression of this gradient.

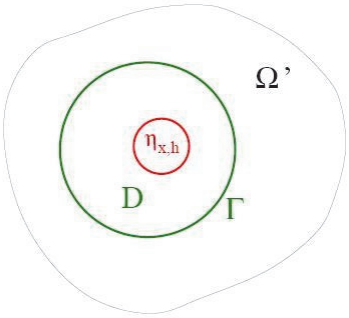

Fig. 4.1. Perturbation in the fixed domain D.

The main idea is to isolate the perturbation in the fixed domain D (Figure 4.1). The interest of this approach is to reduce the domain of problem to $\Omega' = \Omega \setminus D$. The perturbation becomes a surface condition on the contour Γ. A^0 is the initial Maxwell's operator (without perturbation) and $A^{x,h}$ the perturbed operator. A similar notation is utilized for the electric field E.
The perturbation does not depend on the imposed sources, so the problem in (4.1) can be divided into two parts:

$$\begin{aligned} A^0_{\Omega'} E^{x,h}_{\Omega'} &= B^0 - B^{x,h}_{\Gamma} \\ A^{x,h}_{D} E^{x,h}_{D} &= B^{x,h}_{\Gamma} \end{aligned} \tag{4.3}$$

assuming on contour Γ that:

$$E^{x,h}_{D\ /\Gamma} = E^{x,h}_{\Omega'\ /\Gamma} \tag{4.4}$$

When the perturbation is negligible ($h \to 0$), the perturbed field on contour Γ equals the initial field (without perturbation):

$$E^{x,h}_{\Omega'\ /\Gamma} = E^{0}_{\Omega'\ /\Gamma} \tag{4.5}$$

A classical approach for solving this class of problems is to minimize the cost function J applying the Lagrange method where L, the Lagrangian function, is defined by:

$$L\left(Y, \eta_{x,h}, P\right) = J\left(E^{x,h}\right) + Re\ \ Tr\left(P^*\left(A^{x,h}Y - B\right)\right) \tag{4.6}$$

In our case, Y is replaced by E, solution of (1):

$$J\left(E^{x,h}\right) = L\left(E, \eta_{x,h}, P\right), \quad \forall\ P \tag{4.7}$$

P is the vector of Lagrange multipliers, an independent parameter that converts the constrained problem into an unconstrained one. The topology gradient is calculated by the difference between the perturbed cost function and the initial cost function (without perturbation):

$$g_{x,h} = J\left(E^{x,h}\right) - J(E^0) + Re\ \ Tr\ \left(P^*\left(A^{x,h}E^{x,h} - A^0E^0\right)\right) \tag{4.8}$$

If J is a linear function of field E, one can write:

$$\begin{aligned} g_{x,h} &= Re\left(\left(\partial_E J\left(E^0\right)\right)^T + P^* A^0\right)\left(E^{x,h} - E^0\right) \\ &+ Re\ \ Tr\left(P^*\left(A^{x,h} - A^0\right)E^{x,h}\right) \end{aligned} \tag{4.9}$$

P is then the solution of an adjoint problem:

$$\left(A^0\right)^* P = -\partial_E J^* \left(E^0\right) \tag{4.10}$$

The topology gradient can be finally calculated as follows:

$$g_{x,h} = Re\ Tr\left(P^* \left(A_D^{x,h} - A_D^0\right) E_D^{x,h}\right) \tag{4.11}$$

One can note that, in the previous equations, superscripts T and * denote respectively the transposition and conjugation operators.
After solving the direct and adjoint problems successively, the topology gradient is calculated for each element in the fixed domain D, then all topological elements with a negative gradient can be modified to minimize the cost function, and the topology gradient can be then evaluated with the new configuration. The procedure is repeated iteratively until a local minimum is attained.

4.2.3 Level-set (LS) method

The variables are defined on the contour of the object Ω. It suffices to mesh Ω and to deform the contour η according to the descent direction θ. Let a bounded domain $D \subset \mathbb{R}^d$ (d=2 or 3) be the working domain in which all admissible shapes Ω are included, $\Omega \subset D$. In numerical practice, the domain D will be uniformly meshed once and for all. The boundary of Ω is parameterized by means of a level-set function, following the idea of Osher and Sathian (Osher & Sethian, 1988; Osher & Santosa, 2001; Sethian & Wiegmann, 2000). This level-set function ψ is defined in D such that:

$$\begin{cases} \psi(x) = 0 & \Leftrightarrow \quad x \in \partial\Omega \cup D, \\ \psi(x) < 0 & \Leftrightarrow \quad x \in \Omega, \\ \psi(x) > 0 & \Leftrightarrow \quad x \in \left(D \backslash \bar{\Omega}\right). \end{cases} \tag{4.12}$$

In order to minimize J, a shape derivative is computed so that:

$$J'(\Omega)(\theta) = \int_{\partial\Omega} f\left(E, P, \eta\right) \theta . n ds \tag{4.13}$$

where $f(E,P,\eta)$ is a scalar function, which depends on E, P and η.
Therefore, we can define a descent direction in the whole domain D by:

$$\theta = -f . n \tag{4.14}$$

where n is the normal to the shape Ω.
The evolution of the LS function is governed by the following Hamilton-Jacobi transport equation:

$$\frac{\partial \psi}{\partial t} - f\left|\nabla \psi\right| = 0 \tag{4.15}$$

Transporting ψ by (4.15) is equivalent to move the boundary of Ω (the zero level-set of ψ) along the descent gradient direction $-J'(\Omega)$.

4.3 Application to the design of dielectric resonator filters

This sub-section presents the application of shape optimization techniques (LS and TG) coupled with a finite element method for optimizing, in 3D, the shape of microwave components composed of ceramic objects in order to improve their electrical properties.
More precisely, these components are dielectric resonator filters and, traditionally, their design consists of optimizing the geometrical dimensions of resonators and coupling elements in order to achieve the desired function. One can use typical shapes of resonators and optimize their dimensions as a trade-off between quality factor and isolation (Fiedziusko & Holme, 2001). The quality factor is related to the achievable insertion losses while the isolation is related to the stop-band characteristics. In order to relax this compromise, shape optimization methods (in our case TG and LS methods) can be utilized in order to improve a reference design obtained with a classical approach, *i.e.* based on a dielectric resonator with a regular shape.

4.3.1 Improvement of unloaded quality factor

A single pole filter can be constructed with a dielectric resonator inserted in metallic cavity and excited with two metallic irises connected to rectangular waveguides as shown in Figure 4.2. The unloaded quality factor of the dielectric resonator can be estimated by simulation or measurement of scattering parameters. Consequently, a shape optimization of the DR can be conducted for improving its unloaded quality factor.
Applying the level-set method, the unloaded Q is increased by more than 50% as shown in Table 4.1. The optimal shape is depicted in Figure 4.2 (b). The dielectric resonator has been processed by ceramic stereolithography. The dielectric material is characterized by a relative permittivity (ε_r) equal to 9 and a loss tangent ($\tan\delta$) equal to $4.5\ 10^{-5}$.

	Simulation	Measurement
Reference resonator	2000	900
Optimized resonator	3340	1910

Table 4.1. Simulated and measured unloaded quality factors

4.3.2 Improvement of stop-band performance

A two-pole filter is derived from Figure 4.2(a) by cutting a corner in the dielectric resonator and rotating the output iris and waveguide as shown in Figure 4.3(a). Stop-band performance is altered by spurious transmissions due to higher-order modes.
For reducing the impact of spurious transmissions, the shape of the dielectric resonator is optimized applying the topology gradient technique in order to attenuate S21 parameter above the passband. The optimized resonator is shown in Figure 4.3(b) and scattering parameters obtained with reference and optimized resonators are compared in Figure 4.4.

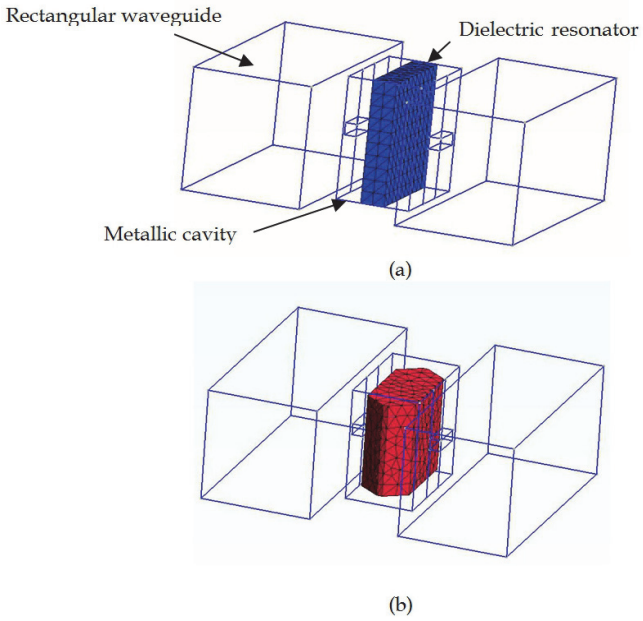

Fig. 4.2. Improvement of unloaded quality factor: (a) reference resonator, (b) optimized resonator

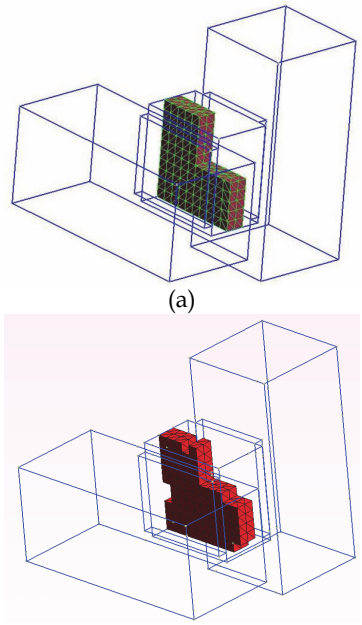

Fig. 4.3. Improvement of stop-band performance: (a) reference resonator, (b) optimized resonator

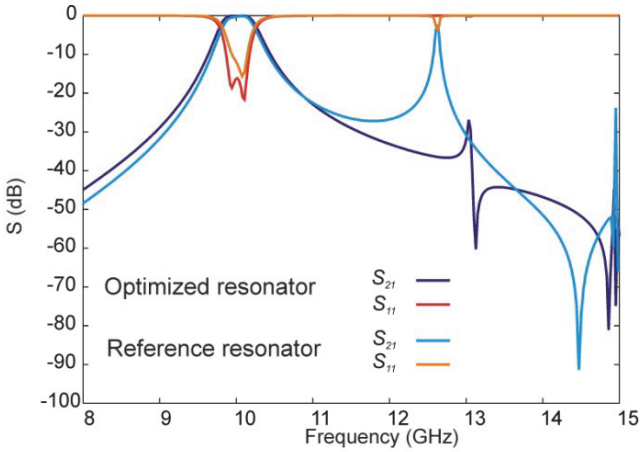

Fig. 4.4. Scattering parameters obtained by simulation of reference and optimized resonators.

4.3.3 Design of dielectric resonator filters

A four-pole dual-mode filter is constructed using two dual-mode resonators assembled together with a metallic cross-iris, as shown in Figure 4.5(a). One can optimize the functionality of the filter by adjusting the dimensions of both, the corners of the dual-mode resonators and the two arms of the metallic cross-iris.

A first shape-optimized design is conducted for replacing the metallic cross-iris by a ceramic coupling element in order to obtain a similar behavior in the pass-band and close out-of-band regions. Optimized resonator is shown in Figure 4.5(b) and scattering parameters are compared in Figure 4.6.

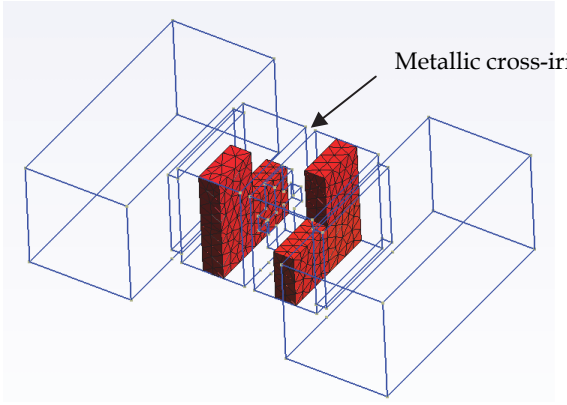

(a)

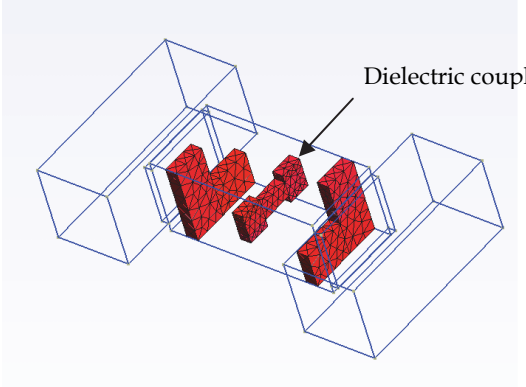

(b)

Fig. 4.5. Four-pole DR filter: (a) with a metallic cross-iris (reference) and (b) with a dielectric coupling element

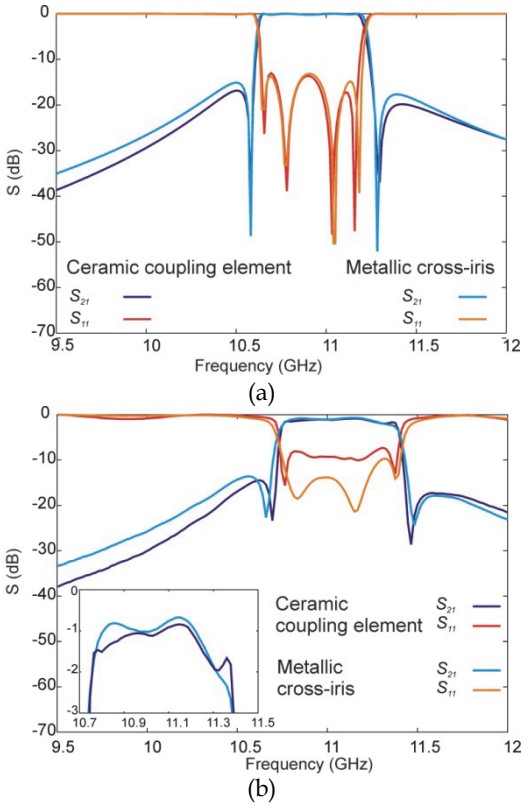

(a)

(b)

Fig. 4.6. S-parameters obtained by simulation (a) and measure (b) of reference and optimized coupling elements.

A second design is performed on the basis of the previous optimization for improving the out-of-band performance of the filter. The initial and final resonators are shown in Figures 4.7(a) and 4.7(b). The simulation and measure of each resonator are compared in Figures 4.8(a) and 4.8(b).

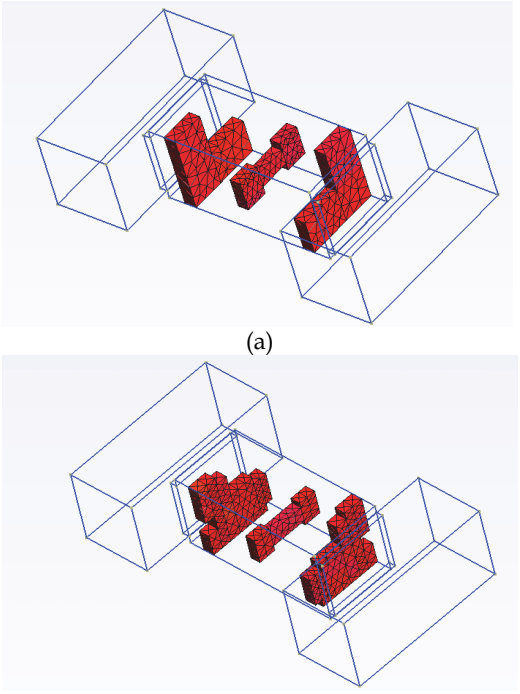

(a)

(b)

Fig. 4.7. Four-pole DR filter: (a) with reference resonators and (b) with optimized resonators.

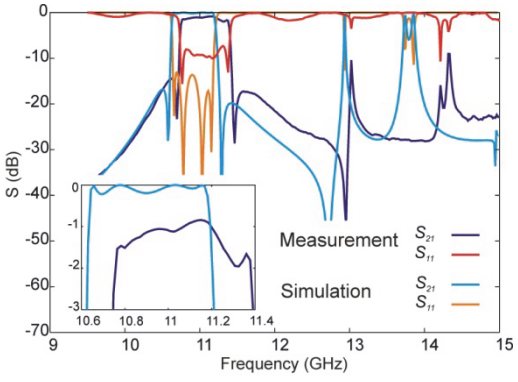

(a)

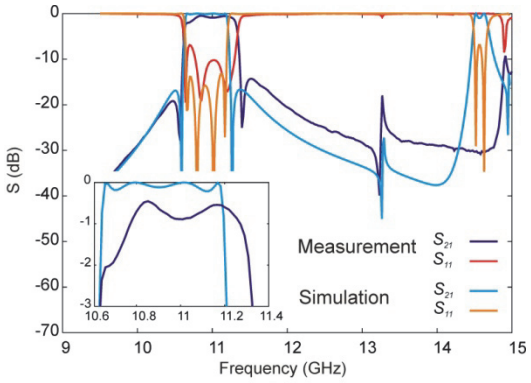

(b)

Fig. 4.8. S-parameters obtained by simulation and measure of reference (a) and optimized (b) resonators

5. Conclusion

This chapter is focused on advanced design and fabrication techniques for ceramic-based microwave and millimeter-wave components. Complementary theoretical and fabrication approaches have been coupled in order to design innovative RF components successfully. As shown, the theoretical approaches are based on 3D electromagnetic and shape optimization methods whereas the rapid prototyping is based on 3D ceramic stereolithography process.

Moreover, the high electrical performances of these components and their geometrical and physical properties demonstrate that ceramic materials are suitable for such microwave applications with high constraints (geometrical, mechanical, thermal and electrical).

At last, this work proves that the 3D ceramic stereolithography process will be in the next future an interesting alternative technological process for the fabrication of 3-D monolithic all-dielectric devices at millimeter wavelengths.

6. References

Akel, H. & Webb, J.P. (2000). Design sensitivities for scattering-matrix calculation with tetrahedral edge elements. *IEEE Transactions on Magnetics*, Vol. 36, No. 4, pp. 1043-1046, 2000.

Allaire, G. & Jouve, F. (2002). Optimal design of micro-mechanisms by the homogenization method. *European Journal of Finite Elements*, Vol. 11, pp.405-416, 2002

Allaire, G.; De Gournay, F.; Jouve, F. & Toader, A.M. (2003). Structural optimization using topological and shape sensitivity via a level set method. *International Series of Numerical Mathematics*, Vol. 147, pp.1-15, Birkhauser, Basel 2003.

Assadi-Haghi, A.; Bila, S.; Durousseau, C.; Baillargeat, D.; Aubourg, M.; Verdeyme, S.; Rochette, M.; Puech, J. & Lapierre, L. (2006). Design of microwave components using topology gradient optimization. *Proceedings of the 36th European Microwave Conference*, pp. 462-465, 2006.

Bertsch, A.; Jiguet, S., Renaud, P. (2003). Microfabrication of ceramic components by microstereolithography, *J. Micromech.*, Vol. 14, pp. 197-203, 2003

Brakora, K. F.; Halloran, J.; Sarabandi, K. (2007). Design of 3-D monolithic MMW antennas using ceramic stereolithography. *IEEE Trans. Antennas Propagat.*,Vol. 55, No. 3, pp. 790–797, March 2007

Byun, J.K; Park, I.H.; Nah, W.; Lee, J.H. & Kang, J. (2004). Comparison of shape and topology optimization methods for HTS solenoid design. *IEEE Transactions on Applied Superconductivity*, Vol. 14, No. 2, pp. 1842-1845, 2004

Chartier, T.; Chaput, C., Doreau, F., Loiseau, M. (2002). Stereolithography of structural complex ceramic parts, *J. Mat. Sci.*, Vol. 37, pp. 3141-3147, 2002

Delhote, N.; Baillargeat, D.; Verdeyme, S.; Thevenot, M.; Delage, C. & Chaput, C. (2007a). Large experimental bandpass waveguide in 3D EBG woodpile manufactured by layer-by-layer ceramic stereolithography. *IEEE/MTT-S International Microwave Symposium*, Honolulu, Hawaï, USA, pp 1431-1434, 2007

Delhote, N.; Baillargeat, D.; Verdeyme, S.; Delage, C.; Chaput, C.; Duterte, C.; Abouliatim, Y. & Chartier, T. (2007b). Electromagnetic band gap millimeter and submillimeter 3D resonators manufactured by ceramic Stereolithography. *Asia-Pacific Microwave Conference*, Bangkok, Thaïlande, pp 1-4, 2007

Delhote ,N.; Baillargeat, D.; Verdeyme, S.; Delage, C. & Chaput, C. (2007c). Ceramic layer-by-layer stereolithography for the manufacturing of 3D millimeter wave filters. *IEEE Transactions on Microwave Theory and Techniques,* Vol. 55, No. 3, pp. 548-554, 2007.

Delhote, N.; Baillargeat, D.; Verdeyme, S.; Delage, C. & Chaput, C. (2007d). Innovative Shielded High Q Dielectric Resonator Made of Alumina By Layer-By-Layer Stereolithography. *IEEE Microwave and Wireless Component Letter*s, volume 17, issue 6, pp 433-435, 2007.

Doreau, F.; Chaput, C.; Chartier, T. (2000). Stereolithography for manufacturing ceramic parts, *Adv. Eng. Mater.*, Vol. 2, pp. 493-496, 2000

Fiedziuszko, J.S. & Holme, S. (2001). Dielectric resonators raise your high-Q. IEEE Microwave Magazine, Vol. 2, No. 3, pp. 50-60, 2001.

Hinczewski, C. (1998). Ph. D., Institut National Polytechnique de Lorraine, France, 1998

Hull, C.; (1986). Apparatus for production of three dimensional objects by stereolithography, U.S. Pat. No. 4575 330, 1986

Khalil, A.H.; Delhote, N.; Pacchini S.; Claus, J.; Mardivirin, D.; Baillargeat, D.; Verdeyme, S.; Leblond, H. (2011). 3-D pyramidal and collective Ku band pass filters made in Alumina by ceramic stereolithography. *IEEE/MTT-S International Microwave Symposium*, Baltimore, USA, 2011

Khalil, H; Delhote, N.; Bila, S.; Aubourg, M.; Verdeyme, S.; Puech, J.; Lapierre, L.; Delage, C. & Chartier, T. (2008). Topology optimization applied to the design of a dual-mode filter including a dielectric resonator. *IEEE MTT-S International Microwave Symposium Digest*, pp. 1381-1384, 2008.

Khalil, H.; Bila, S.; Aubourg, M.; Baillargeat, D.; Verdeyme, S.; Puech, J.; Lapierre, L.; Delage, C. & Chartier, T. (2009). Topology optimization of microwave filters including dielectric resonators. *Proceedings of the 39th European Microwave Conference*, pp. 687-690, 2009

Khalil, H.; Bila, S.; Aubourg, M.; Baillargeat, D.; Verdeyme, S.; Jouve, F.; Delage, C. & Chartier, T. (2010). Shape optimized design of microwave dielectric resonators by

level-set and topology gradient methods. *International Journal of RF and Microwave Computer-Aided Engineering*, Vol. 20, No. 1, pp 33-41, 2010

Khalil, H.; Bila, S.; Aubourg, M.; Baillargeat, D.; Verdeyme, S.; Jouve, F. & Chartier, T. (2011). Shape optimization of dielectric resonators for improving their unloaded quality factor. *International Journal of RF and Microwave Computer Aided Engineering*, Vol. 21, No. 1, pp 102-126, 2011

Kim, Y.S.; Byun, J.K & Park, I.H. (2009). A level set method for shape optimization of electromagnetic systems. *IEEE Transaction on Magnetics*, Vol. 45, No. 3, pp. 1466-1469, 2009.

Kozak, A. & Gwarek, W. (1998). Unrestricted arbitrary shape optimization based on 3D electromagnetic simulation. *IEEE MTT-S International Microwave Symposium Digest 1*, pp. 17-20, 1998

Li, B.; Xu, Y. & Choi, J. (1996). Applying Machine Learning Techniques, *Proceedings of ASME 2010 4th International Conference on Energy Sustainability*, pp. 14-17, ISBN 842-6508-23-3, Phoenix, Arizona, USA, May 17-22, 2010

Lima, P.; Bonarini, A. & Mataric, M. (2004). *Application of Machine Learning,* InTech, ISBN 978-953-7619-34-3, Vienna, Austria

Liu, B.; Gong, X.; Chappell, W.J. (2004). Applications of layer-by-layer polymer stereolithography for three-dimensional high-frequency components. *IEEE Trans. Microwave Theory Tech.*, Vol. 52, No. 11, pp. 2567–2575, November 2004

Mader, P.; Masmoudi, M. & Mangenot, C. (2001). Topological asymptotic for waveguide optimization. *IEEE Antennas and Propagation Society, AP-S International Symposium (Digest 1),* pp 616-619, 2001.

Monneret, S. (2005). La microstereolithographie et ses applications," *Méc. & Ind.*, Vol. 6, pp. 457-462, 2005

Nguyen, N.T.; Sauleau, R.; Delhote, N.; Baillargeat, D. & Le Coq, L. (2010). Design and Characterization of 60-GHz Integrated Lens AntennasFabricated Through Ceramic Stereolithography. *IEEE Transactions on Antennas and Propagation*, Vol. 58 No. 8 , pp 2757 – 2762, 2010.

Osher, J.S. & Sethian, J.A. (1988). Fronts propagating with curvature dependent speed: algorithms based on Hamilton-Jacobi Formulations. *Journal of Computational Physics,* Vol. 79, No. 1, pp. 12-49, 1988.

Osher, J.S. & Santosa, F. (2001). Level set method for optimization problems involving geometry and constraints I. Frequencies of a two-density inhomogeneous drum. *Journal of Computational Physics*, Vol. 171, pp. 272-288, 2001.

Sethian J.A. & Wiegmann, A. (2000). Structural boundary design via level set and immersed interface methods. *Journal of Computational Physics*, Vol. 163, No. 2, pp. 489-528, 2000.

Sokolowski, J.S. & Zochowski, A. (1999). On the topological derivative in shape optimization. *SIAM Journal on Control and Optimization*, Vol. 37, No. 4, pp. 1251-1272, 1999.

Suri, J.S.; Liu, K.; Singh, S.; Laxminarayan, S.N.; Zeng, X. & Reden, L. (2002). Shape recovery algorithms using level sets in 2-D/3-D medical imagery - A state-of-the-art review. *IEEE Transactions on Information Technology in Biomedicine,* Vol. 6, No. 1, pp. 8-28, 2002.

12

Sinterability and Dielectric Properties of $ZnNb_2O_6$ – Glass Ceramic Composites

Manoj Raama Varma, C. P. Reshmi and P. Neenu Lekshmi
Materials and Minerals Division,
National Institute for Interdisciplinary Science and Technology
[NIIST],Thiruvananthapuram,
India

1. Introduction

In the new era of communication technology there are revolutionary developments in satellite communication, global positioning systems and mobile communication systems, which has helped the developments in multilayer technologies like low temperature cofired ceramics (LTCC). The microwave electronic devices have achieved significant miniaturisation, light weight and became very cost effective using LTCC. The characteristic properties required for dielectric materials which are used in multilayers are (a) high dielectric permittivity(ε_r), (b) high quality factor (Q×f) and (c) low temperature coefficient of resonant frequency (τ_f). The size of the resonator is inversely related to the $\sqrt{\varepsilon_r}$. Dielectric materials should posses near zero temperature coefficient of resonant frequency (τ_f) for thermally stable electronic devices [1-7].

Generally most of the dielectric ceramic materials are known to posses the above said properties but will sinter at temperatures above 1000 ^oC. Zinc niobates, $ZnNb_2O_6$ (ZN) is a low loss dielectric material with columbite structure having excellent dielectric permittivity, high quality factor and low temperature coefficient of resonant frequency. Sintering temperature of ZN is comparatively lower (~1200 ^oC) [8]. Hence it is widely used as dielectric resonators in microwave communication devices. In multilayer ceramic structures, the low melting electrodes such as Ag (melting point ~961 ^oC), Cu (melting point ~1083 ^oC) and Au (melting point ~1064 ^oC) are co-fired with these ceramic materials [9,10]. In the case of Ag electrodes, processing temperature of the material must be below 950 ^oC.

There are several approaches to reduce the sintering temperature of the ceramics viz. (i) usage of ultra-fine particles/powders as synthesized by wet chemical methods as starting materials (ii) addition of low melting glasses to obtain a low temperature sintering composite [11-14]. Glass addition is known to be the most popular and least expensive method and hence ZN is widely used in ceramic technology.

Even though the ZN ceramics prepared by conventional ceramic route [1-6] shows excellent properties, high sintering temperature preclude its application potential in the LTCC. Usage of nano sized ZN powders (instead of micron size powders) in multi layer technology can bring down the sintering temperature to a lower value. Hence the procedure for preparing

ZN ceramic powder as both micron size powders and nanosized powders and the sinterability of pure materials as well as the glass added ceramics are described in this chapter. The structural characterisation of the materials can be done using XRD and the microwave dielectric properties (in the frequency range 2-6 GHz) can be studied and compared to highlight the effect of particle size on sinterability and microwave dielectric properties of these materials.

2. Materials and methodologies

ZN ceramic powders can be synthesized using two different well established preparation techniques such as solid state ceramic method and polymer complex techniques [15-17].

2.1 Synthesis of $ZnNb_2O_6$ using solid state synthesis technique

Single phase ZN can be prepared using oxides of Zn (ZnO 99.9+%) and pentoxide of Niobium (Nb_2O_5 99.9+%) as raw materials. These oxides can be weighed in stoichiometric proportion and mixed for 24h in a ball mill, using zirconia balls and distilled water as the milling medium. The slurry can be dried at 80 ^oC and the dried powder can be calcined at 850 ^oC/4h, to get the phase pure ZN ceramics.

2.2 Preparation of $ZnNb_2O_6$ using polymer complex method

Zinc acetate [$Zn(CH_3COO)_2$ 99.99%,] and niobium ethoxide [$Nb(OC_2H_5)_5$, 99.95% metal basis] can be used as the starting material for preparing ZN using polymer complex method. The flow chart, in Fig. 1 shows the various steps involved in the synthesis. 3 mol equivalent of citric acid can be dissolved in 12 mol of ethylene glycol with continuous stirring for 1h to form a clear solution. 1 mol of zinc acetate can then be added and stirred for several hours at 80^oC to dissolve it completely. 2 mol of $Nb(OC_2H_5)_5$ can be added to this clear solution with a stirring speed of 500 rpm until it results in the formation of a thick white gel. The gel can be sonicated for 2h to obtain the uniform distribution. After sonication the polymeric precursor can be recovered by desalting with acetone. The dried polymeric precursor can be calcined at 600^oC/4h to obtain the $ZnNb_2O_6$ nanopowders.

2.3 Preparation of $60ZnO\text{-}30B_2O_3\text{-}10SiO_2$ (ZBS) glass

High purity ZnO, B_2O_3 and SiO_2 (99.9%) can be used as the raw materials for the preparation of $60ZnO\text{-}30B_2O_3\text{-}10SiO_2$ (ZBS, sintering temperature is <800 ^oC). The raw materials weighed accurately in the stoichiometric proportion are mixed well in distilled water medium using zirconia balls for 24 h in a ball mill. The slurry can be dried and the powder can be melted in a platinum crucible at 1000^oC for 2h, and the melt can be quenched into cold distilled water and powdered. This glass powder can be used for the preparation of glass ceramic composites.

2.4 Preparation of ZN-ZBS glass composites

Appropriate amounts of ZN and ZBS glass (1,3,5,10 wt%) can be mixed using an agate mortar for 2 hours in distilled water medium and the slurry can be dried and powdered. 3wt% PVA solution can then be added to this mixture as a binder. The dried powder can be uniaxially pressed using a tungsten carbide (WC) die in the form of cylindrical discs of

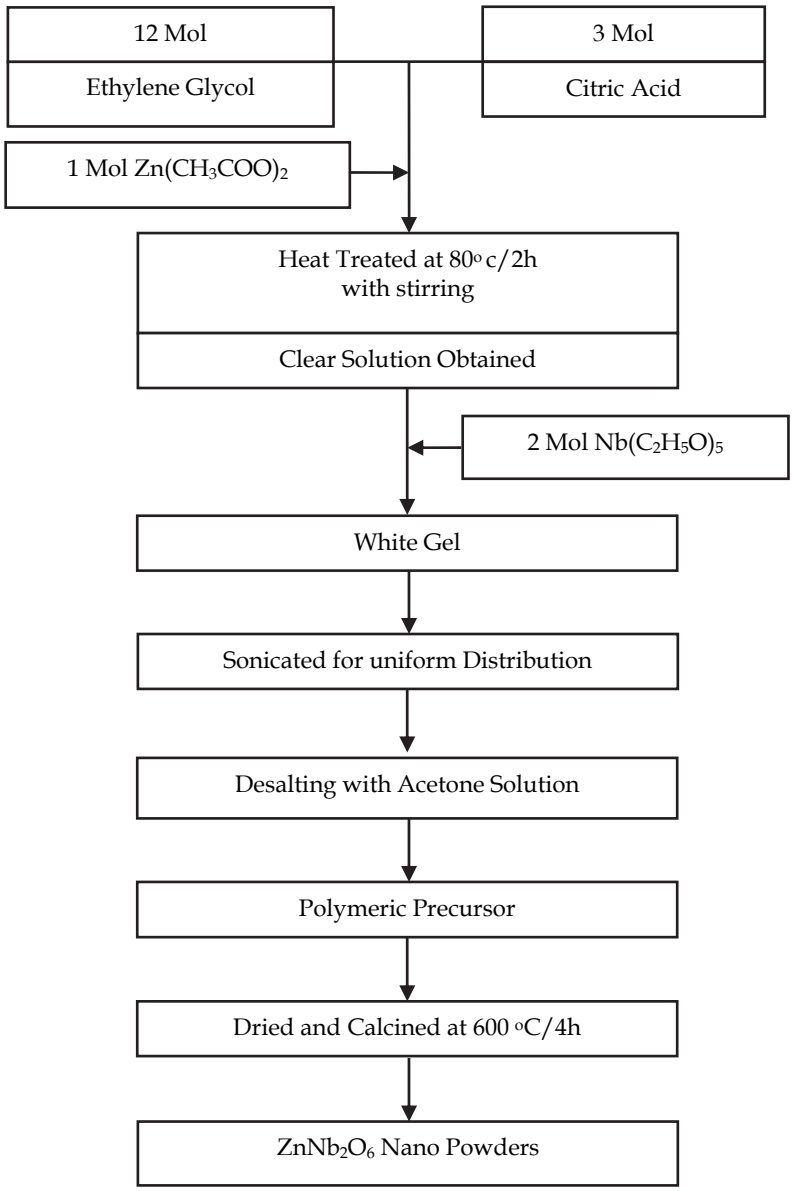

Fig. 1. Flow chart for the preparation of $ZnNb_2O_6$ nano powders

diameter 14 mm and about 7 mm height at a pressure of 150 MPa. The green compact can be heat treated at different temperatures and the dimension changes are recorded. The density can be determined each time and the sintering temperature can be optimised as the temperature which gives the maximum densification.

The sintered pellets of all the compositions can powdered and the crystalline phase of the powders are identified by the XRD analysis using Cu-Kα radiation of wavelength (λ) 1.54056Å for 2θ range 10-80°. The recorded patterns are compared with standard ICDD Data file with the help of Philips X'pert High Score plus software. The ZN nano particles can be characterised using transmission electron microscopy (HRTEM) FEI Technai G² 30S-TWIN high resolution electron microscope operated at 300 KV. The crystallite size, lattice parameter and the selected area diffraction patterns can be recorded using TEM. The crystallite size (d) of the nano-ZN was determined from the XRD patterns using Debye Sherrer formula [18,19],

$$d = \frac{0.9\lambda}{\beta \cos\theta} \tag{1}$$

where λ is the wavelength of the x-ray, β is the FWHM of the maximum intense peak and θ is the glancing angle.

The microstructure analysis of the sintered polished and thermally etched samples can be carried out using scanning electron microscope (SEM, JEOL-JSM, 5600LV, Tokyo, Japan). The bulk densities of the sintered pellets can be measured by the Archimedes method. The dielectric constant can be measured using the post resonator method of Hakki and Coleman modified by Courtney. The unloaded quality factor can be measured by a resonant copper cavity whose interiors are coated silver and the ceramic composites are placed on a low loss quartz spacer which reduces the effect of losses due to surface resistance of the cavity using a Vector Network Analyser. The temperature coefficient of resonant frequency (τ_f) can be measured by noting the temperature variation of the same using $TE_{01\delta}$ mode in the transmission configuration over a range of temperature 20-80°C. The temperature coefficient of the resonant frequency can be calculated using the following relation in a fixed interval of temperature [20-22],

$$\tau_f = \frac{f_2 - f_1}{f_1 (T_2 - T_1)} \tag{2}$$

where, f_1 and f_2 are the resonant frequencies at temperatures T_1 and T_2 respectively and the average value can be calculated and reported.

3. Observations and analysis

Fig 2(a) is the powder XRD diffraction pattern of $ZnNb_2O_6$ synthesized using solid state ceramic route. All the peaks are compared with the ICDD file card for ZN (Number 76-1827) and indexed. Fig 2 (b) depicts the XRD pattern of $ZnNb_2O_6$ with 5wt% of zinc borosilicate glass (ZBS). The addition of ZBS glass did not produce any additional phases, as evident from Fig. 2 (b).

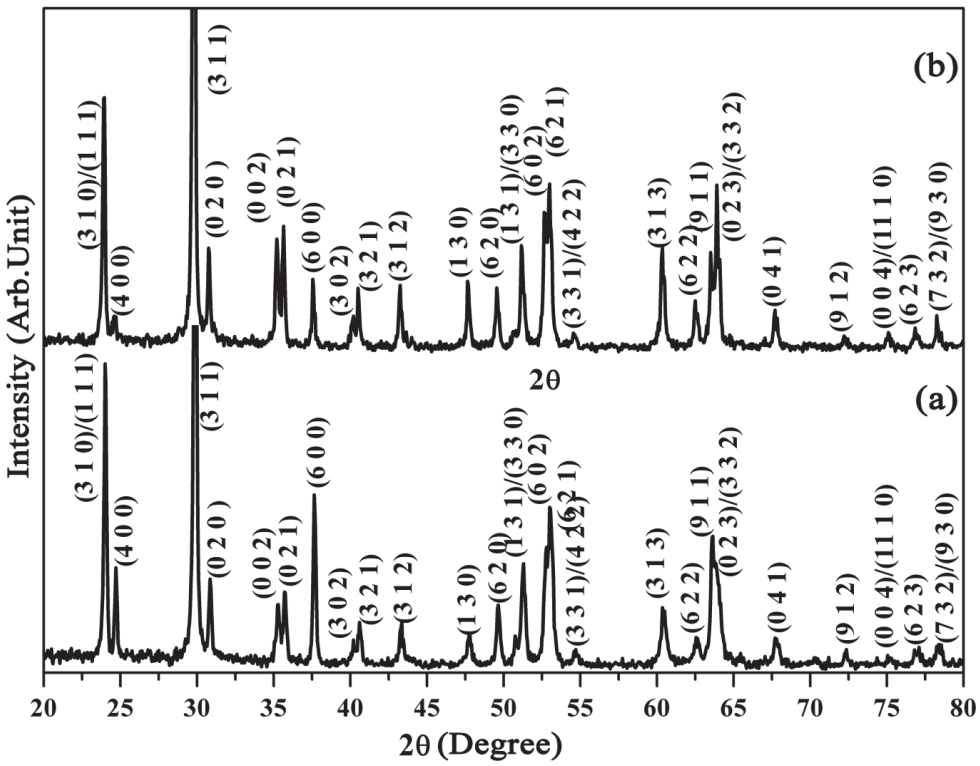

Fig. 2. XRD pattern of $ZnNb_2O_6$ (a) sintered at 1200°C/2h and (b) $ZnNb_2O_6$ + 5Wt%

The powder XRD patterns of the calcined $ZnNb_2O_6$ nanopowders are depicted in the fig 3. Fig 3(a) shows the XRD pattern of $ZnNb_2O_6$ calcined at 600°C/4h and fig 3 (b) is that of $ZnNb_2O_6$ powder sintered at 950 °C/2h. The figures clearly indicate that the powder patterns are in well accordance with ICDD data card (76-1827). The average crystallite size of the nanostructured ZN calcined at 600 °C/4h can be estimeted from the X-ray diffraction pattern. The fig 4 depicts the maximum intense peak obtained from XRD of ZN ceramics. Using Gaussian fit (as seen in the fig 4), the FWHM and centre of the peak can be determined. Employing Debye Sherrer formula (equation 1) the average crystallite size can be calculated as ~17 nm.

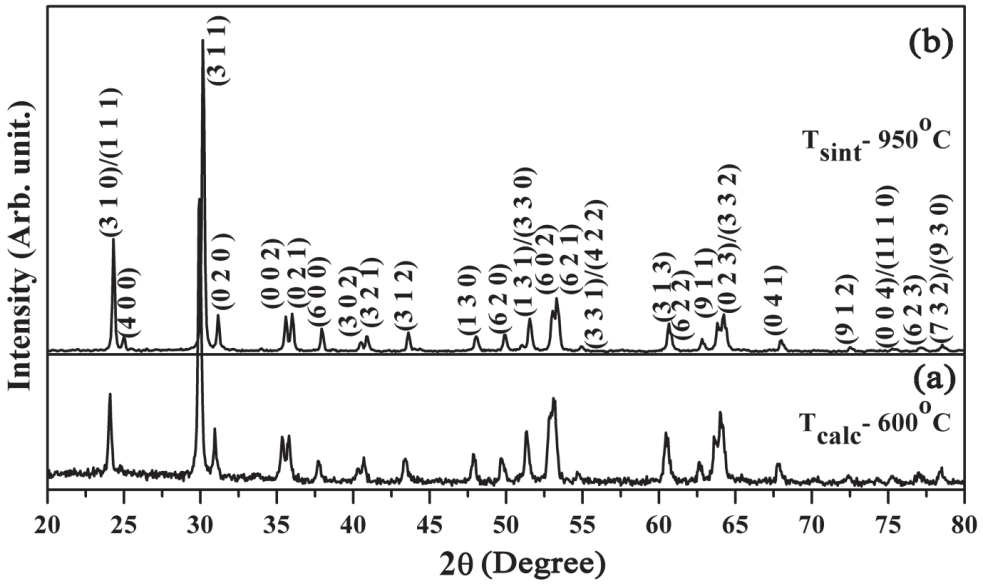

Fig. 3. XRD pattern of $ZnNb_2O_6$ (a) calcined at 600°C/4h and (b) calcined at 950°C/2h.

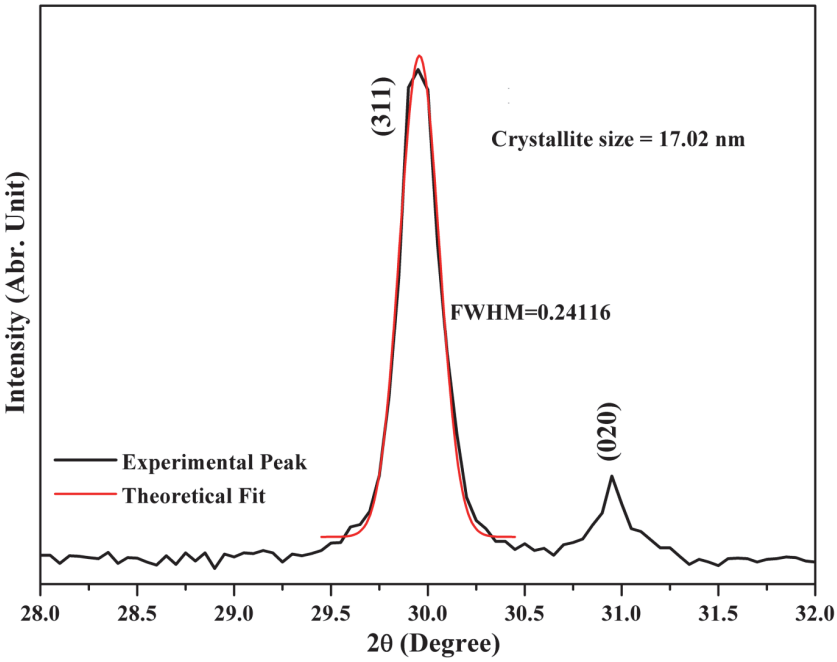

Fig. 4. Maximum intense peak in XRD pattern of nanostructured ZN ceramics with theoretical Gaussian Fit

Fig 4 shows the various TEM images of ZN nanocrystallites. Fig 5 (a), (b) and (c) are the TEM images of the ZN nanocrystallites at two different regions. It can be seen that in both images the nanocrystallites have same characteristics and mostly of spherical in shape. The fig 5 (c) establishes the crystallite size at low magnification; they are well separated and have uniform size distribution. A histogram is shown in fig 5 (d), indicates the crystallite size obtained from the images both fig 5 (a) and (b). In order to obtain particle size distribution, a Gaussian function is fitted for the experimental data. The average particle size is obtained and found that it is lies between 18-20 nm. This is in good agreement with the crystallite size obtained from XRD using Debye Scherrer formula.

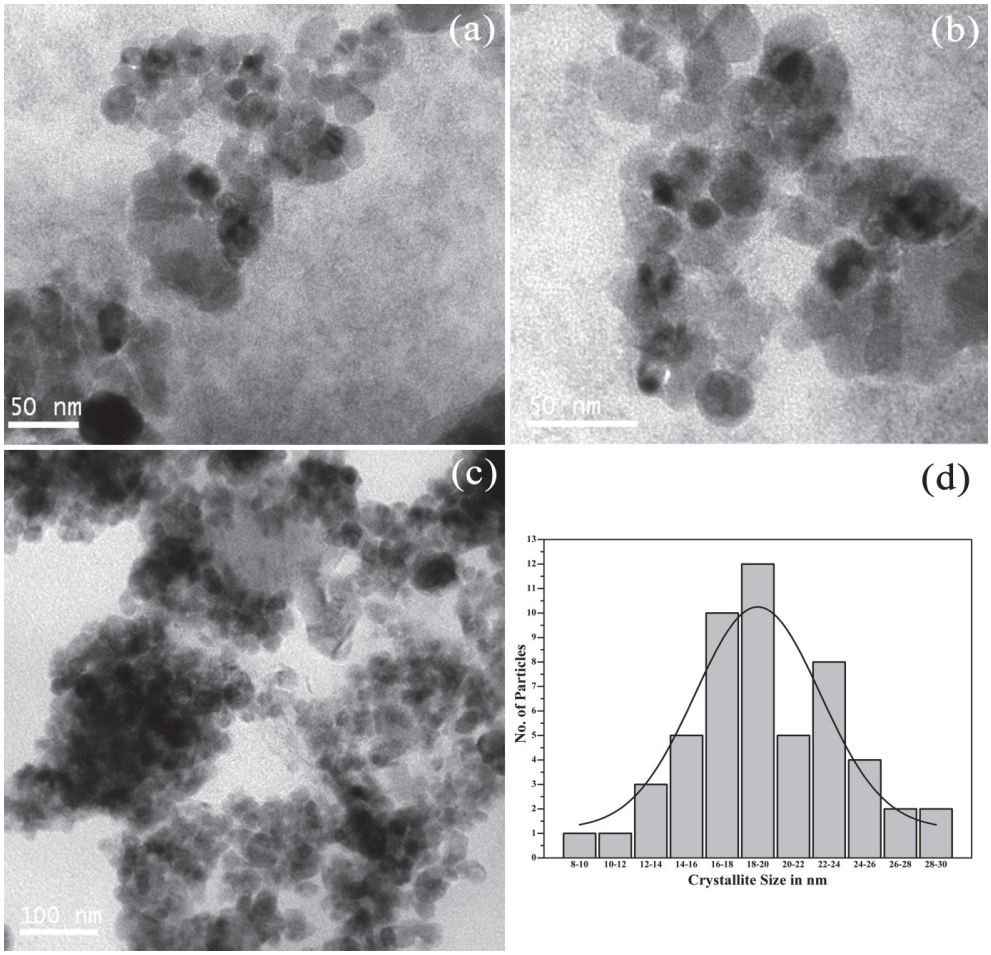

Fig. 5. TEM images of nano $ZnNb_2O_6$ (a), (b) 50 nm scale, (c) 100 nm scale and (d) histograph of particle size distribution obtained from image (a) and (b).

The high resolution TEM (HRTEM) image and the selected area diffraction pattern (SADP) of ZN nanocrystallites are shown in the fig 6 (a) and (b) respectively. Lattice plane of ZN nanoparticles are clearly visible in the HRTEM image. Inter planar spacing 'd' of several planes were determined using set of Fourier Transforms of lattice fringe images. TEM image analysis software (Digital Micrograph - Gatan) was used for the determination of interplanar spacing. The average d values were determined and the plane corresponding to each set of fringes are duly indexed, shown in the fig 6 (a). Interplanar spacing obtained from TEM and XRD are tabulated in table 2. Comparing the d values from the X-ray diffraction pattern, the planes corresponding to each ring was identified and indexed.

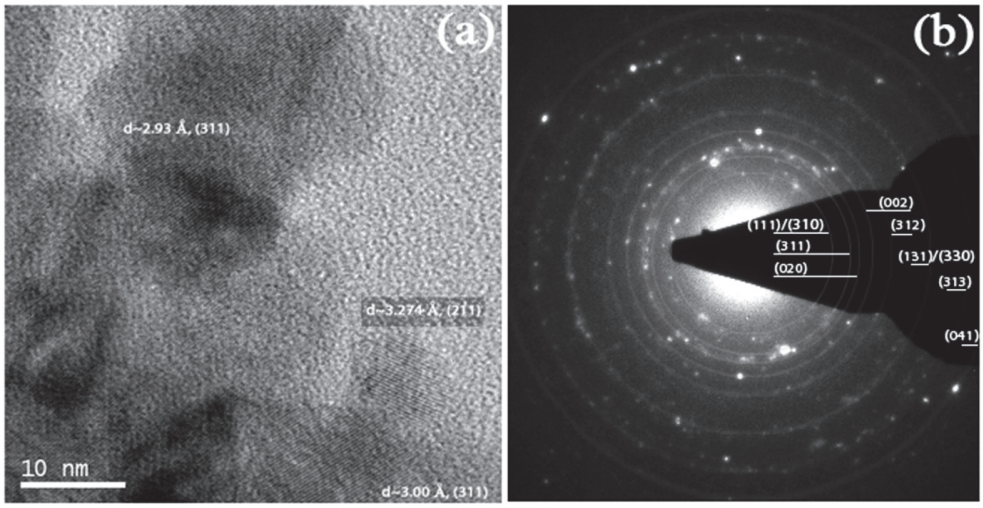

Fig. 6. (a) HRTEM of nanostructured ZN ceramic (b) SAD patterns of ZN ceramics.

In fig 7, variation of bulk density of pellets, synthesised by solid state ceramic route and heat treated at 975^{o}C with different wt% of ZBS is shown. From the fig 7, ZN ceramics with 5 wt% of ZBS has maximum density. Hence 5 wt% of ZBS is taken as the optimized glass addition amount for the composite. Fig 8 illustrates the variation of the bulk density of ZN and ZN-ZBS glass composites with varying sintering temperatures. From Fig. 8 it can be seen that nanostructured ZN with 5 wt% of ZBS glass has greater density at lower sintering temperatures (925^{o}C/2h). Comparison of densification of pure (nano and micron sized) ZN ceramics shows that the densification is faster for nano powder compacts at lower temperatures, however at temperature above 1100^{o}C for micron sized powder compacts synthesised by solid state ceramic route has higher absolute density. Since the nano powders of ZN have higher sinterability, the growth during the sintering process will be more rapid. Hence more finer intergranular porosities will be formed in the case of nano powder compacts than micron sized powder compacts. This will results in the reduction in the values of absolute densities of sintered powder compacts. Similar effects were noticed for sintered nano sized powder compacts of BZT by Manoj Raama Varma et al. [23] In nanostructured ZN ceramics the grain boundary area per unit volume will be more than that of the solid state synthesised ZN ceramics [24]. This deteriorates the densification of

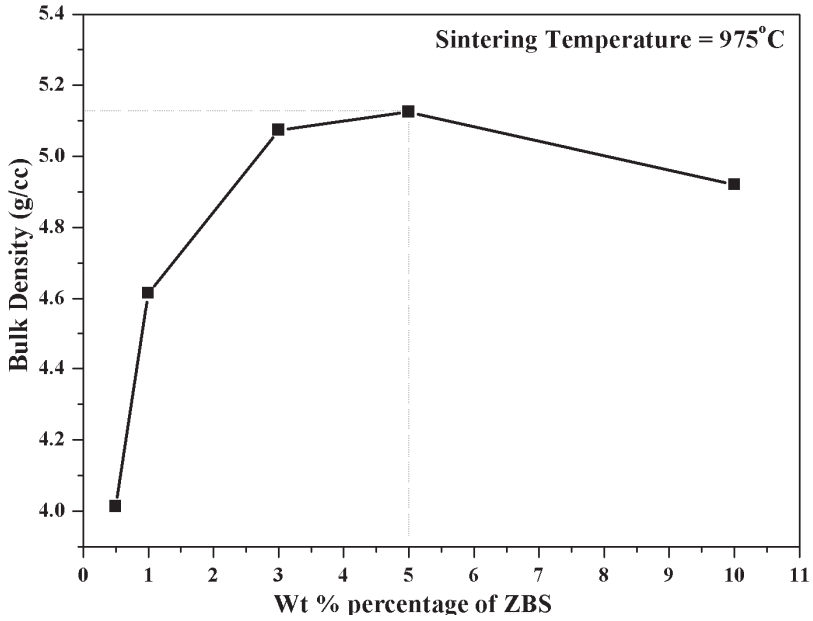

Fig. 7. Variation of bulk density of ZN ceramics (solid state synthesis) with different wt% of ZBS glass

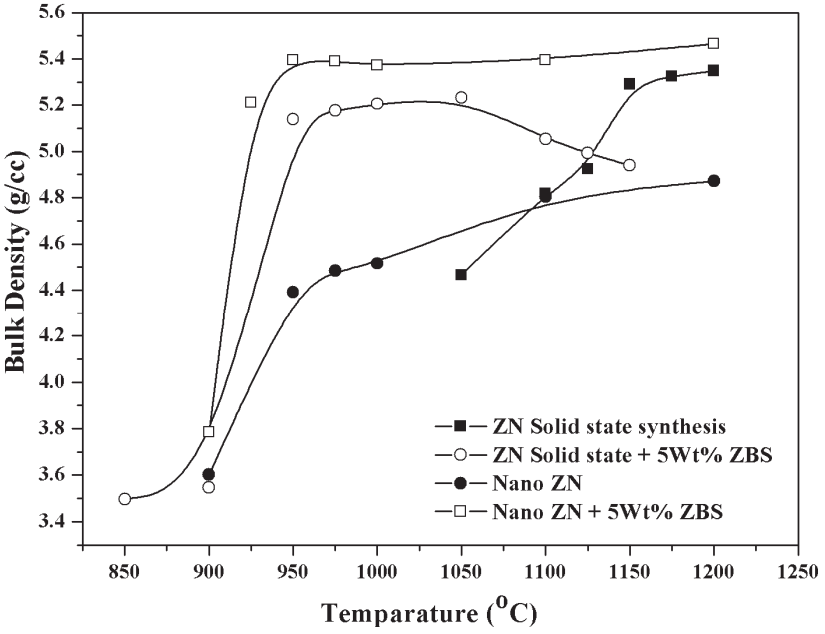

Fig. 8. Variation of the bulk density of ZN ceramics and ZN-glass composites with different temperature

nano sized ZN ceramics. In the case of glass addition, low melting glasses such as ZBS enhances the sinterability of the ZN ceramic powders due to the liquid phase sintering [25,26]. The glasses start melting at lower temperatures and the molten glasses flows through the porosity between the grains and fill the porosity and the gap between the grain Boundaries [27]. This enhances the sinterability *i.e.* the composite gets densified at lower sintering temperatures. Hence the ZN composite with 5 wt% ZBS glass shows higher density than that of the pure materials. The effect of liquid phase sintering is clearly seen in the SEM micrographs (Fig. 9) as molten glass melted at low temperatures.

Fig 9 shows the SEM micrographs of the sintered ZN. Fig 9 (a) and (b) are SEM micrographs of ZN synthesised using solid state ceramic route. Large grains having average grain diameter of ~4.2 μm were observed for pure ZN. Though the sintering has taken place,

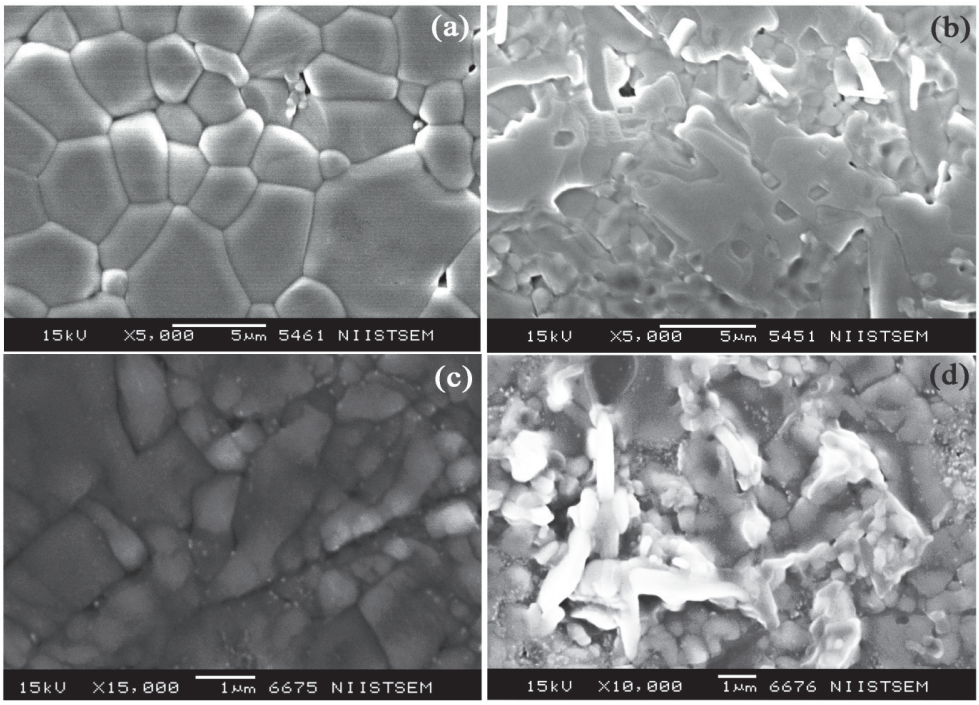

Fig. 9. SEM micrograph images of ZN ceramics and ZN-glass composites

Fig. 9 (b) shows a highly densified microstructure with large amount of molten glass phases for glass-ZN composites. It is observed that by the addition of ZBS glass the grain growth decreases. In fig 9 (b) the grains have an average diameter of about 1 to 2 μm only. Fig 9 (c) shows the SEM images of the sintered nano structured ZN (obtained via chemical synthesis) which are sintered at 925 ^{o}C for 2h. The SEM micrograph exhibits highly dense grains. Average grain size obtained from the micrograph images ranging from about 1-2 μm. It reveals fine sintered grains are obtained by sintering of nano ZN powder. Fig 9 (d) shows micro structure of the nanostructured ZN ceramic powders with 5wt% of ZBS glass. Comparatively smaller grains are obtained for the glass added nano powder compacts of ZN. The densification is very high for a much lower sintering temperature viz 925^{o}C/2hrs.

Comparing all images in Fig. 9 the nanostructured ZN with 5wt% of ZBS shows very high packing with a minimum porosity at 925 °C/2h.

The density and the dielectric properties viz dielectric constant ε_r, Qxf, and τ_f, of ZN ceramics are tabulated in table 2. Comparison of these properties of the materials synthesised by different preparation techniques reveals that the solid state synthesised shows greater values for dielectric constant and Qxf. This can be correlated with the effect of grain size. In ceramic materials the increase in the grain size deteriorates the dielectric loss. Reduction in the number of grains per unit volume, decreases of grain boundaries per unit volume and it would result in a material with a lower dielectric loss and better polarisability which improves both ε_r and Q×f [28,29]. From the SEM micrographs (Fig. 9) it can be concluded that the nanostructured ZN has more grain boundaries than solid state synthesised ZN and hence had a low ε_r and Q×f. However the glass addition to these compounds, due to liquid phase sintering the nanostructured ZN has greater densification at lower sintering temperature. The dielectric properties of micron sized ZN cermic with 5 wt% of ZBS are: density =5.48, ε_r = 21.3, τ_f = -66 ppm/°C and with Q×f ~38,000, sintered at 975 °C/2h. Dielectric properties of sintered nano sized ZN with 5 wt% of ZBS have density = 5.21, ε_r = 22.5, τ_f = -69.6 ppm/°C and with Q×f ~12,800, sintered at 925 °C/2h [30]. Since $ZnNb_2O_6$+5wt%ZBS can be identified as one of the potential LTCC materials sintering at 925°C, co sintering studies were done with silver. $ZnNb_2O_6$+5wt%ZBS was mixed with 20wt% metallic Ag (99.99%) and sintered at 930°C/2h. SEM pictures with EDAX was recorded after sintering and found that Ag is not reacting or melting during the sintering. Hence the co sintering of $ZnNb_2O_6$+5wt%ZBS+20wt%Ag was successful as can be seen in fig.10.

hkl Plane	d spacing from TEM (Å)	d spacing from ICDD file(Å)
111/310	3.6494	3.3602
311	2.9559	2.8455
020	2.8630	2.6789
002	2.5200	2.3098
312	2.0736	1.9918
131/330	1.7703	1.5676
313	1.5260	1.3099
041	1.3770	1.1561

Table 1. d spacing of major reflecting planes determined from TEM analysis

Materials	Sintering temperature (°C)	Density (ρ) (g/cc)	ε_r	Qxf (GHz)	τ_f (ppm/° C)
$ZnNb_2O_6$ – solid state synthesis	1200	5.32	23.3	12,800	-77.9
$ZnNb_2O_6$ + 5wt% ZBS	975	5.48	21.3	38,000	-66.0
$ZnNb_2O_6$ – polymer complex synthesis	1200	4.87	19.2	77,900	-66.4
$ZnNb_2O_6$ + 5wt% ZBS	925	5.21	22.5	12,800	-69.6

Table 2. Density and microwave dielectric properties of ZN and ZN-glass composites

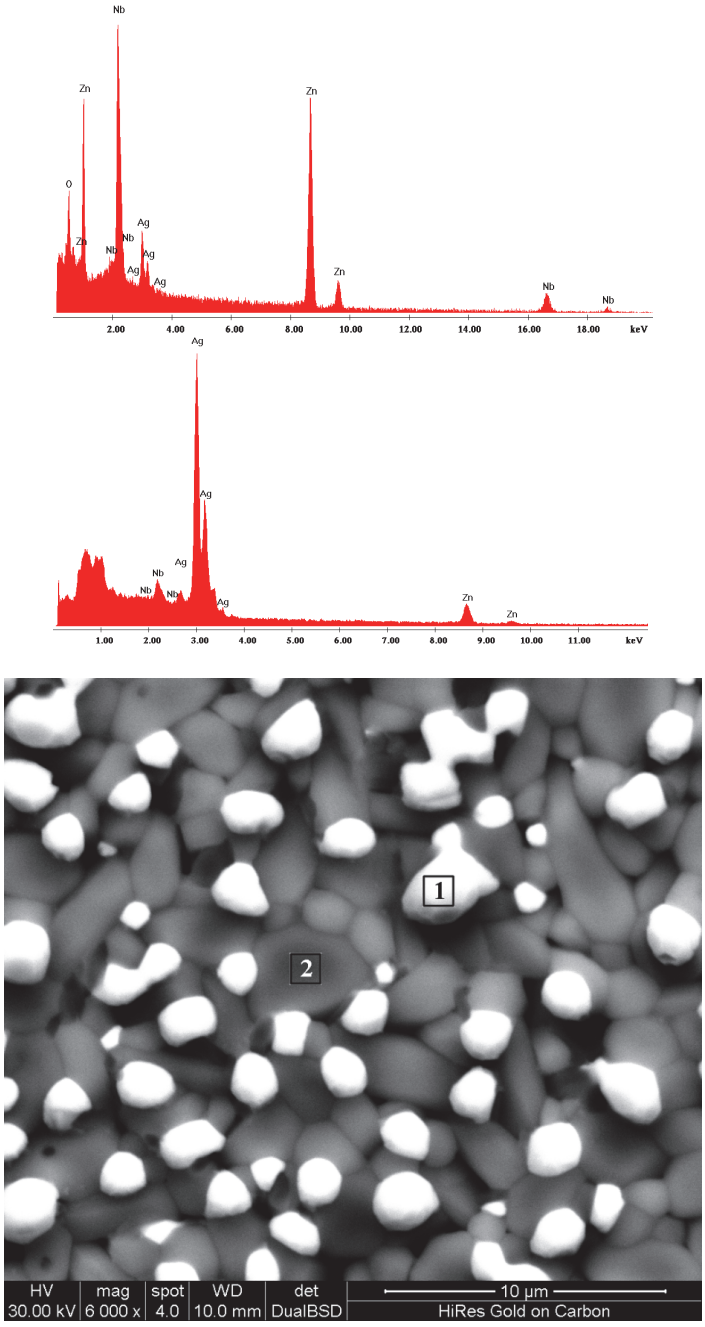

Fig. 10. SEM with EDAX micrographs of $ZnNb_2O_6$+5wt%ZBS+20wt% metallic Ag-Sintered at 930°C/2h

4. Conclusions

Zinc Niobates ceramics were prepared in phase pure powder form using solid state ceramic technique and polymer complex method. Particle size of the ZN ceramics is determined using TEM and it is found most of the particles are in the range 18-20 nm, the particle size obtained from XRD pattern using Debye Sherrer formula is 17 nm. Effect of particle size on the sinterability and the microwave dielectric properties were studied. Micro structure shows that a high density ZN ceramics can be obtained by sintering nanopowder of ZN with 5wt% of ZBS glass at 925 ^oC for 2h. Optimized sintering of nano sized powder at 925 ^oC/2h give microwave dielectric properties of ε_r =22.5, Qxf~12,800 and τ_f= -69.6 ppm/^oC. These composites were successfully co sintered with silver.

5. References

The influence of $ZnNb_2O_6$ on the microwave dielectric properties of $ZrTi_2O_6$ ceramics,Parinaz RiaziKhoei, Feridoon Azough, Robert Freer, J.Am. Ceram. Soc. 89[1] 216-223 (2006).

Characterization and Microwave Dielectric Properties of $M^{2+}Nb_2O_6$ Ceramics, Robert C. Pullar, Jonathan D. Breeze, Neil McN. Alford, J. Am. Ceram. Soc., 88 [9] 2466–2471 (2005)

Influence of Copper(II) Oxide Additions to Zinc Niobate Microwave Ceramics on Sintering Temperature and Dielectric Properties, Dong-Wan Kim, Kyung Hyun Ko, Kug Sun Hong, *J. Am. Ceram. Soc.*, 84 [6] 1286–90 (2001).

Low sintering ceramic materials based on Bi_2O_3-ZnO-Nb_2O_5 compounds, E. A Nenasheva, N.F Kartenko, J. Eur. Ceram. Soc 26, 1929-1932 (2006)

Low temperature sintered $ZnNb_2O_6$ microwave dielectric ceramics doped with ZnO-V_2O_5 additions, Jin Wang, Zhenxing Yue, Zhilun Gui, Longtu Li, J. Mater. Sci. 40, 6581-6583 (2005)

Synthesis and Microwave dielectric properties of $Zn_{1+x}Nb_2O_{6+x}$, A.G Belous, O. V Ovchar, A. V Kramarenko, B. Jancar, J Bezjak, D. Surnov, Inorg. Mater. 43, [3] 227-280, (2007).

Synthesis, characterization and microwave dielectric properties of $ATiO_3$ (A=Co, Mn, Ni) ceramics. P.S. Anjana and M T Sebastian. J. Am. Ceram. Soc. 89 (2006) 2114-2117.

Effects of $ZnCl_2$ addition on the $ZnNb_2O_6$ powder synthesis through molten salt method, Guo Liangzhai. Dai Jinhui, Tian Jintao, Zhu Zhibin, He Tian, Qu Xiaofei, Liu Zhongfang, Mater. Chem. and Phys. 105, 148-150 (2007).

H. Jantunen, R. Rautioaho, A. Uusimaki, S. Leppavuori, J. Eur. Ceram. Soc., 20 (2000), 2331-36.

M. T. Sebastian, H. Jantunen, Int. Mater. Rev., 53, (2008), 57-90.

M Laren, C. B. Ponton, J. Mater. Sci., 33 (1998), 17-22.

O. Renoult, J. P.Boilot, F. Chaput, R. Papiernik, L. G. Hubert-Pfalzgraf, M. Lejeune, J. Am. Ceram. Soc. 75 [12] (1992), 3337-40.

C. L. Huang, C. L. Pan, J. Mater. Sci. Lett. 21, (2002), 149-151.

H. Jantunen, R Rautioho, A. Uusimäki, S. Leppävuori, J. Eu. Ceram. Soc. 20 (2000), 2331-2336.

Synthesis of rare-earth orthoaluminates by a polymer complex method, Hirofumi Takata, Misako Iiduka, Yoshihiko Notsu, Masaaki Harada, J.Allys. Compd. 408-412,p 1190-1192 (2006).

Direct chemical synthesis of high coercivity air-stable SmCo nanoblades, C.N. Chinnasamy, J.Y. Huang, L.H. Lewis, B. Latha, C.Vittoria, V. G. Harris, Appl. Phys. Letts. 93, 032505 (2008).

Low temperature powder synthesis of $LaAlO_3$ through *in situ* polymerization route utilizing citric acid and ethylene glycol, Masato Kakihana, Toru Okubo, J. Allys. Compds. 266 (1998) 129–133.

Nanocrystalline materials and coatings, S.C. Tjong, Haydn Chen, Mater. Sci. Engg. R 45 (2004) pp 1-88.

Sintering and Characterization of Nanophase Zinc Oxide, Anne P. Hynes, Robert H. Doremus, Richard W. Siegel, J. Am. Ceram. Soc. 85[8] (2002) 1979-87.

C. L Huang, M. H Weng, Mater. Res. Bull. 36 (2001) 2741–2750.

C. L. Huang, J. L. Hou, C. L. Pan, C. Y. Huang, C.W. Peng, C. H. Wei, Y. H. Huang, J. Alloys Comp. 450 (2008) 359–363.

C. L Huang, C. H. Shen, C. L Pan, Mater. Sci. Eng. B 145 (2007) 91–96.

Sinterability studies and microwave dielectric properties of sol–gel synthesized $Ba(Zn_{1/3}Ta_{2/3})O_3$ nanoparticles, Manoj Raama Varma, P. Nisha and P.C. Rajath Varma, Journal of Alloys and Compounds, 457, 2008,422-428

Progress on grain growth dynamics in sintering of nano-powders, LIU Chunjing , Wang Xin , Jiang Yanfei , Wang Yongming , Hao Shunli, Rare Metal, Vol. 25, Spec. Issue , Oct 2006, P .471

V. K. Singh, J. Am. Ceram. Soc. 64 (1981) C 133-135.

J. H. Jean, S. C. Lin, J. Mater. Res. 14 (1999) 1359-1363.

Forsterite-based ceramic–glass composites for substrate applications in microwave and millimeter wave communications, T.S. Sasikala, M.N. Suma, P. Mohanan, C. Pavithran, M. T. Sebastian, J. Alloys Comp. 461 (2008) 555–559.

Microwave dielectric loss of titanium oxide, Alan Templeton, Xiaoru Wang, Stuart J. Penn, Stephen J. Webb, Lesley F. Cohen and Neil. McN. Alford, J.Am Ceram Soc. 83 (1) 95-100 (2000).

Effect of porosity and grain size on the Microwave Dielectric properties of Sintered Alumina, Stuart J Penn, Neil McN. Alford, Templeton, Xiaoru Wang, Meishing Xu, Michael Reece, and Kelvin Schrapel. J.Am Ceram Soc. 80(7) 1885088(1997)

Finite size effect on Sinterability and Dielectric Properties of $ZnNb_2O_6$ – Glass Composites, Mukkuttiparambil Ayyappan Sanoj, Chalappurath Pattelath Reshmi and Manoj Raama Varma, J. Am. Ceram. Soc. 92(11):2648-2653;Nov 2009

13

Net-Shaping of Ceramic Components by Using Rapid Prototyping Technologies

Xiaoyong Tian[1], Dichen Li[1] and Jürgen G. Heinrich[2]
[1]*Xi'an Jiaotong University, Xi'an,*
[2]*Clausthal University of Technology, Clausthal-Zellerfeld,*
[1]*China*
[2]*Germany*

1. Introduction

The application of rapid prototyping (RP) in ceramics was motivated by the advances in engineering ceramics and traditional ceramics where methods of creating complex shapes are limited (Cawley, 1997). Ceramics have many outstanding physical and chemical properties and attract lots of researchers' attentions to find new industrial applications for this kind of material such as components resistant to the high temperature, piezoelectric sensor and actuators (Safari et al., 2006; Miyamoto, 2004). But ceramics often cause high machining costs for products in limited quantities and high tooling costs in injection molding of large batches. Moreover, ceramic components with complicated structures cannot be shaped by the conventional forming processes such as casting, forging and machining. High temperature ceramics are also hard and difficult to machine. Even for the simple geometries which can be produced by the traditional fabrication process, the time needed for the mould preparation drastically enlarges the period between the design and the first prototyping verification of the new production. Industrial applications of ceramic materials especially for the jobbing work and complicated components are largely restricted by the lack of the net-shaping capability for the components with complex structures.

Rapid prototyping came into being at the end of last century when the first Stereolithography Apparatus (SLA) was invented as the first RP machine in 1984 by 3D Systems (Hul, 1984). It begins with a CAD model, usually a solid or a surface model which can be designed by the users. The CAD model is imported into the rapid prototyping system in which there is special software slicing the solid model to define a group of layers. The layer information including the process route, parameters and material properties is read by the computer. A computer controlled laser scanner realizes the laser scanning process to form each layer according to the respective layer information. Since the object grows layer by layer, it is possible to realize material and process combinations which are impossible to achieve with conventional methods. The general purpose is just to make prototypes in order to reduce the time of products development by shortening the period between design and test and then cut the development cost of new products.

In recent years a pronounced method diversification has resulted in a large variety of different rapid prototyping techniques allowing for the generation of prototypes made of polymers, metals and ceramics. Now functional components, specially using metal or

ceramic materials, are manufactured using rapid prototyping process by lots of researchers and companies all over the world. There are several processes to realize the net or near-net shaping of the ceramic functional components such as stereolithography of the ceramic slurry, extrusion of ceramic paste, fused deposition of using ceramic loaded polymer filament, selective laser sintering of ceramic powder and 3D printing et al. In this chapter, these typical ceramic net-shaping processes are briefly reviewed. Then, direct laser sintering of ceramics by using Layer-wise Slurry Deposition (LSD) process and Lost Mould combined with Reaction Formed Silicon Carbide process will be described in details. At last, all the processes will be compared according to the raw material, efficiency, fabrication accuracy and et al.

2. Net-shaping of ceramics by RP technologies- a review

2.1 Stereolithography (SL) of ceramic slurry

Photocuring is the basis of SL, one of the most popular and most accurate SFF techniques. Commercial SL machines (3D system, CA) produce plastic prototypes from epoxy resins by photo-polymerization of a liquid monomer with a UV laser. For the 3D-fabrication of ceramics via stereolithography the liquid monomer is replaced by "ceramic resin", a suspension of ceramic powder dispersed in a UV-curable resin, first demonstrated by Gritffith and Halloran (Griffith & Halloran, 1996). As shown in Fig. 1, the first step is curing a thin layer (150~200μm) by laser scanning the cross section on the surface of the ceramic resin. The part is attached by supports to an elevator platform beneath the surface of the ceramic resin. After curing the layer, the elevator platform dips into the suspension allowing the liquid ceramic resin to flow over the cured portion of the part. A doctor blade sweeps over the surface leaving a layer of fresh ceramic suspension which becomes the next cured layer after the laser curing process. Repeating this process building up the three dimensional green body of the ceramic components. And then after post sintering in furnace, dense ceramic objects are obtains. Lasers used in current practice are helium cadmium gas lasers, argon ion gas laser and more recently solid state Nd-YVO4 lasers.

T. Chartier et al have investigated the ceramic suspension suitable for the SL process (Chartier et al., 2002; Hinczewski et al., 1998). To achieve a sufficiently high green density in the part, the solid volume fraction should be in the range of 0.50-0.65. On the other hand, a low viscosity is necessary for a proper flow during recoating of the next layer. Alumina and silica powders have been used to prepare the ceramic suspension (Griffith & Halloran, 1996; Chartier et al., 2002; Hinczewski et al., 1998; Tay et al., 2003). Final mechanical strength similar with that of the uniaxial pressed samples has been achieved.

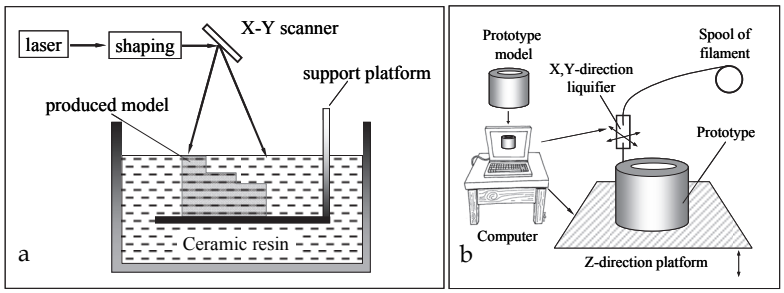

Fig. 1. a) Stereolithography of ceramic powder loaded liquid resin (Griffith & Halloran, 1996), b) Schematic for the extrusion fabrication process (Bandyopadhyay et al., 1997)

2.2 Extrusion forming techniques

The Fused Deposition Manufacturing of Ceramics (FDMC) was developed firstly by Ahmad Safari (Bandyopadhyay et al., 1997; Lous et al., 2000). Filaments were fabricated with a ceramic powder loaded of 50-55vol% in a six-component thermoplastic binder system that contained polymer, elastomer, pacifiers, wax, surfactant, and plasticizer. The filament with a diameter of about 1.8 mm passes through a heated liquefier (140-200^{o}C) and acts thereby as a piston to extrude a continuous bead, or "road' of molten material through a nozzle with a diameter of 0.254-1.5mm (Fig.1 b). The bead is deposited on a platform that indexes down after the first layer is completed. Bonding of neighboring beads and previous deposited layers takes place due to adhesiveness of partly molten material. The 3D components were fabricated by repeat this deposition process layer by layer. After the green part was fabricated, the part was removed from the substrate for further heat treatment processing to remove the organic additives.

Another extrusion forming process of ceramic components, extrusion free forming, developed at the Advanced Research Center (Tucson, AZ, USA) (Lombardi & Calvert, 1999; Vaidyanathan et al., 2000), was equipped with a high pressure extrusion head. This technology has been used for different ceramic materials dispersed in wax-based binders. The fabrication of silicon nitride parts by extrusion of suspensions with as ceramic loading of 55vol% was reported by Baidyanathan et al. [12]. Thermoplastic suspensions of 55vol% zirconia in a wax-based vehicle were extruded through a range of fine nozzles with diameters from 76 to 510μm (Gridal & Evans, 2003). Heat transfer considerations show that the use of thermoplastic suspensions was not ideal for fine (<100μm in diameter.) filament work because the fibers solidified before folding and welding. That means that the use of solid-liquid change materials in extrusion techniques is limited for microfabrication, because the filament solidifies too quickly in ambient air. Solvent-based extrusion freeforming was also developed to build complex ceramic 3D structures. The principle for this technique was transition of the paste from liquid to solid by solvent evaporation (Lu et al., 2010). The drawbacks of solid-liquid change material were overcome.

2.3 Three-dimensional printing

There are two kinds of 3D printing fabricating processes. One is the three-dimensional printing which uses layered ceramic powder and organic binder. Another is the direct ceramic ink-jet printing which uses ceramic powder loaded ink.

Powder based three-dimensional printing was developed at Massachusetts Institute of Technology, USA in 1992 as a method to create preforms from powdered metals and ceramics (Sachs et al., 1992). An individual two-dimensional layer is created by adding a layer of powder to the top of a piston and cylinder which contain a powder bed and the part being fabricated. A new layer of the being built component is to be formed by "ink-jet" printing of a binder material. And then, the piston, powder bed and part are lowered and new layer of powder is spread out and selectively joined. This layering process is repeated until the part is completely printed. After removing the unbound powder, a heat treatment process is following to densify the fabricated part. The sequence of operations is illustrated in Fig.2 a.

Direct ceramic ink-jet printing (DCIJP) makes use of ink-jet printers to create components by multilayer printing of a colloidal suspension dispersed with ceramic powder. This process has the potential to produce a wide range of fine ceramic contours with high resolution enabling miniature components to be manufactured. Functional gradients and multi materials components can be fabricated by this printing method according to the multi

nozzles. By adjusting the aperture of the printing head and by controlling the spreading phenomenon of the droplet, one can expect to reach a standard definition of around 50µm and ultimately of 10µm, taking into account the tremendous evolution in the printing field (Cappi et al., 2008; Lejeune et al., 2009).

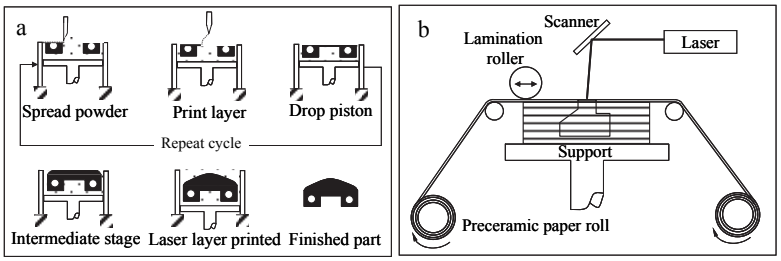

Fig. 2. a) Sequence of operations in the three-dimensional printing process (Sachs et al., 1992), b) Schematic setup of laminated object manufacturing (Travitzky et al., 2008)

2.4 Laminated objective manufacturing

Laminated object manufacturing (LOM) generates three-dimensional ceramic components by sequential stacking, laminating, and shaping of preceramic paper or ceramic green tape (Fig.2 b). It can be considered as a hybrid between additive and subtractive processes: a part is built up in a layer-by-layer lamination approach. Each layer is individually cut by a knife or laser beam according to the cross section of the part defined by the CAD model. Each layer is bonded to the previous layer with a thermoplastic adhesive coating on the bottom side of the paper sheet, which is activated by heat and pressure during the LOM processing. Al_2O_3 and SiC preceramic papers have been prepared for the LOM process (Travitzky et al., 2008). Commercial Low Temperature Co-fired Ceramic (LTCC) green tapes were also used to fabricate complicated ceramic components by Cold Low pressure Lamination [CLPL] process (Schindler & Roosen, 2009). Research on the use of a non-planar LOM process has also been carried out to build curved layer parts to overcome the restriction of flat layers (Klosterman et al., 1999).

2.5 Selective laser sintering

A thin layer powder is spread by a roller from the powder container to the platform, as shown in Fig.3 a. The new powder layer is then selectively sintered by a laser via a scanner controlled by a computer according to the pattern of the cross section in the CAD model. Non-sintered powder is left to serve as a support for the following layers. The laser sintered part is obtained by removing the unsintered powder. For ceramic powders, post treatment is always required to densify the microstructure and achieve a high mechanical property. Oxide ceramic powders, such as alumina and silica, have been selectively sintered by ND: YAG-laser (1064 nm) (Regenfuss et al., 2008). Pure yttria-zirconia powder was also sintered by a fiber laser with a wavelength of 1.064um. But the density and the mechanical properties of the produced samples can not meet the requirement for their potential medical application as dental bridges (Bertrand, 2007). Lower melting point constitutions, such as metal and organic powder were added into the ceramic powder to lower the sintering temperature and then form composite components.

Silicon carbide cannot be reversibly transferred to a liquid state under normal pressure conditions. It decomposes at around 2800-3000^{o}C. The mixed powder of 51% SiC, 41% Si

and 8% C were used for laser micro sintering. The appearance of silicon decreases the sintering temperature because silicon has a melting point around 1420°C. During laser sintering process, melt silicon reacts with carbon and the reaction-formed silicon carbide and residual silicon bind initial silicon carbide powder together (Regenfuss et al., 2008).
Polymer derived ceramic parts with complex shapes were fabricated by selective laser curing (SLC). The ceramic parts were produced by sequentially sintering of SiC loaded polysiloxane powder with a CO_2-laser beam (λ = 10.6um), which locally induces curing reaction of the polymer phase at moderate temperatures around 400°C. The laser-cured bodies were converted to Si-O-C/SiC ceramic parts in a subsequent pyrolysis treatment at 1200°C in argon atmosphere. A post-infiltration with liquid silicon was carried out in order to produce dense parts. The bending strength was only 17MPa before infiltration as a result of both micro cracks in the Si-O-C matrix and a pronounced porosity, while an average value of 220MPa was achieved after post-infiltrating with Si (Friedel et al., 2005).

2.6 Indirect rapid fabrication process

Polymer and wax moulds were produced by using rapid prototyping process, such as SL (Wu et al., 2009; Yin et al., 2004), FDC (Stampfl & Prinz, 2002), and SLS (Guo et al., 2004; Cai et al., 2003) et al., and used for the gel-casting of ceramic slurry to fabricate ceramic components with complex structures. The basic process for the lost mould application of rapid prototyping is shown in Fig.3 b. First, the negative model of the ceramic part was designed in CAD software. Then the negative model was fabricated into a wax or polymer mould by using rapid prototyping process. This polymer mould was used for the gel casting of ceramic slurry which contains monomer, cross linker, imitator, and ceramic powder. After drying, the ceramic slurry was polymerized to form a macromolecular network which binds the ceramic powder together. Enough mechanical strength of the green ceramic body can be achieved for the following treatments. Optimized thermal cycle was applied to the polymerized ceramic green bodies to get the final dense ceramic parts.

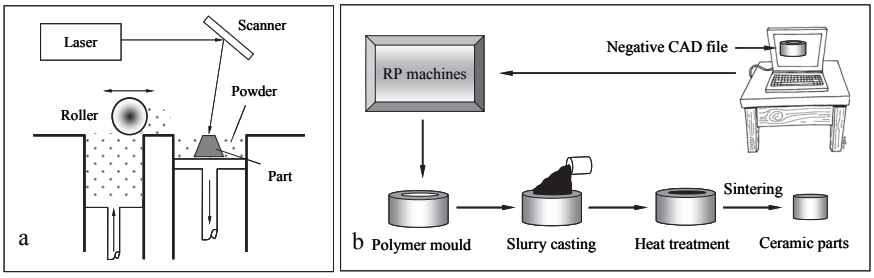

Fig. 3. a) Schematic process of Selective laser sintering, b) Schematic diagram of the steps in the lost mould approach for fabricating ceramic parts

3. Direct laser sintering and layer-wise slurry deposition (LSD)

3.1 Fabrication process

Direct laser sintering using LSD belongs to the selective laser sintering processes except that the starting material in LSD process is ceramic slurry instead of ceramic or polymer-ceramic mixed powders. Layer-wise slurry deposition has been utilized to produce a dense ceramic tape for the following laser sintering process by J. G. Heinrich and colleagues (Sadeghian et

al., 2004; Guenster et al., 2003; Gahler et al., 2006; Heinrich et al., 2007; Krause et al., 2004; Tian et al., 2009). Slurry used in this process is aqueous ceramic suspension with organic additive less than 2% (by the TG analysis). Ceramic tapes can be achieved by evaporating the water in the deposited ceramic slurry layers. These ceramic tapes have a dense microstructure and higher green density than the powder matrix which is used in the conventional selective laser sintering processes. Higher green density will improve the sinteractivity of the ceramic powder and produce a dense laser sintered ceramic body.
The principle of layer-wise slurry deposition (LSD) based direct laser sintering process are illustrated in the Fig. 4. Ceramic slurry is pumped through a doctor blade and deposited on a pre-heated ceramic tile. After drying, the ceramic tape is sintered by a laser beam, which is controlled by a computer via a scanner according to the pattern of the cross sections in the CAD model. Repeat this process until all the layers are finished. The unsintered area is removed by putting the whole part into the water since aqueous ceramic slurries were used. Finally, the laser sintered body is obtained.

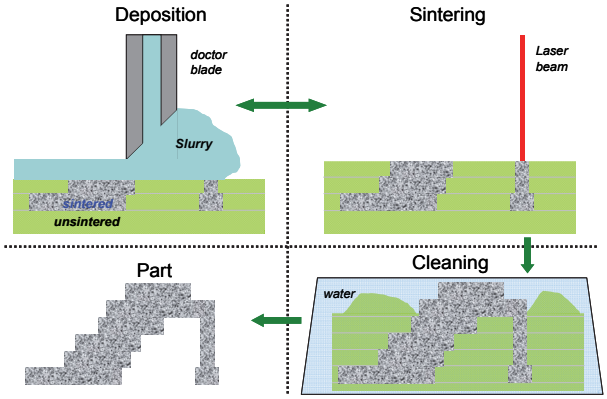

Fig. 4. Fabrication process of ceramic components by using Layer-wise Slurry Deposition and direct laser sintering (Gahler et al., 2006)

3.2 Temperature in heat affected zone (HAZ)

Temperature in HAZ has a significant influence on the microstructure, density and mechanical strength of the laser sintered ceramic bodies. Whereas the temperature in HAZ is affected by the laser sintering process parameters, the relationships between the laser sintering parameters and the sintering temperature become crucial in order to improve or optimize the properties of the laser sintered bodies.
In LSD based laser sintering process, four parameters should be investigated, laser power, scan speed, hatch spacing and layer thickness. However the thickness of newly deposited layer is a constant value of 0.1mm for all experiments in the present research. There are only three factors left to be studied. Laser energy density (LaserED) applied on the surface of the dried slurry is defined as

$$LaserED = \frac{P}{D \times V}(J / cm^2) \tag{1}$$

where P is the laser power, D is the diameter of the laser beam (0.6 mm in diameter) and V is the laser scan speed. The values of P and V are adjustable in the laser sintering process.

A pyrometer was installed in the laser sintering equipments to simultaneously detect the temperature in the heat affected zone (HAZ). The specimens with different sintering temperature were investigated according to the delamination of two adjacent layers or cracks on the surface. An isothermal map of sintering temperature on hatch spacing and laser energy density is plotted in Fig.5. It shows that large laser energy density and small hatch spacing will produce high sintering temperature in the HAZ.

In the inadequate sintering region of Fig. 5 (T<1050ºC), the green bodies delaminated due to the low temperature and the consequent low penetration depth. In the inordinate sintering region of Fig. 5 the cracks (Fig. 6b) appeared on the surface of the sintered bodies due to the high temperature (T>1400ºC). On the contrary, in the appropriate laser sintering temperature range (around 1050 ºC~1400ºC in Fig. 5), the laser sintered surface are homogenous and there are no cracks being observed (Fig. 6 a).

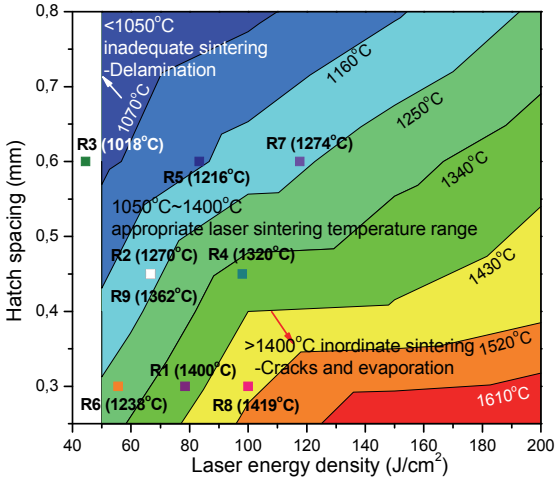

Fig. 5. Influence of laser energy density and hatching space on the temperature in the laser sintering zone, and simulated temperature (average value) for each experimental group

Simulation of the temperature in the HAZ has also been conducted by using the model which has been put forward in the literature (Tian et al., 2010). To validate the feasibility and accuracy of this numerical model, the average laser sintering temperature for each experimental group has been simulated and compared with the experimental results, as shown in Fig. 5. The positions of each experimental group are marked in this isothermal map with the simulated temperature in the following round brackets. The difference between simulated temperature and experimental results is less than around 5%. It can be concluded that simulated temperatures basically match the experimental results. Moreover, the objective of the simulation is a qualitative investigation instead of a quantitive one. It means that this model is reasonable to simulate the laser sintering process of porcelain samples and can be used for the further investigation.

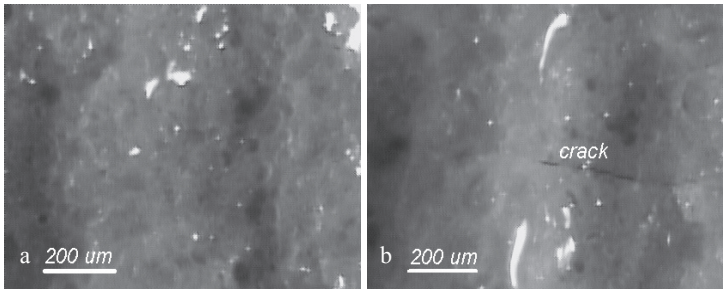

Fig. 6. Optical micrographs of laser sintered surface treated with different laser energy density: a. 125 J/cm²; b. 250 J/cm²

The influence of laser sintering parameters on the average sintering temperature is shown in Fig. 7. With large hatch spacing and low laser energy density (low laser power, and high scan speed) the temperature in the sintering zone decreases. This simulation results are entirely consistent with the experimental results which are shown in Fig. 5.

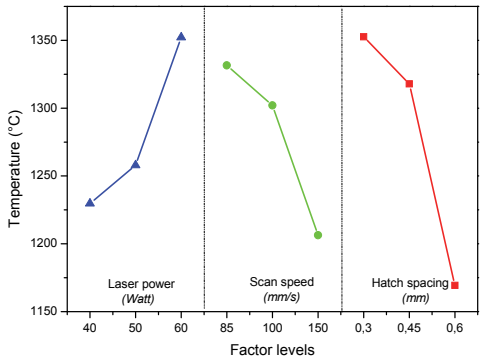

Fig. 7. Average effect of laser sintering parameters on the temperature (statistical results from simulation)

3.3 Residual stresses in the laser sintered bodies

After the laser sintering process is finished, the model is cooled down to room temperature. Transient thermal stresses will be partially released during the cooling process. But there are still residual internal stresses remaining in the model which plays an important role considering the final mechanical strength of ceramic parts after being post sintered in the furnace.

According to the simulation results, distribution patterns of residual internal stresses in x, y, and z directions are shown in Fig. 8 (left). Residual tensile stress appears in the upper part of the model and residual compressive stress appears in the bottom part of the model. This stresses distribution pattern will significantly influence the final mechanical strength of ceramic components. In the real experimental procedure, laser sintered ceramic samples will be post-sintered in a furnace after laser sintering process. In the post sintering process, the stresses with two opposite directions will be released and cause creeps and consequent delamination between two adjacent layers. In the present research, the thickness of the

model is 2mm which is much thicker than one single layer (0.1mm) in the real experiments. Analogy can be made between the simulation model and real experimental situation after 200 layers (2mm in depth) have been deposited on the ceramic tile.

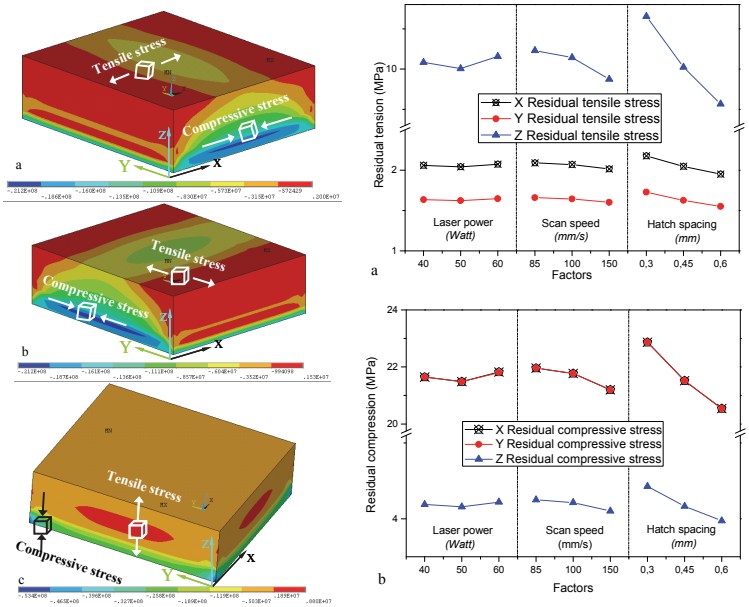

Fig. 8. **Left**, Residual internal stress profiles (Pa) with fully constrained bottom surface, R3, a) X component, b) Y component, c) Z component; **Right**, Average effect of laser sintering parameters on the maximum residual stress, a) tension; b) compression (statistical results from simulation)

Average effects of laser sintering parameters on the maximum residual stresses are shown in Fig. 8 (left). Residual tensile stresses (Fig. 8 (right) a) in z direction (around 10MPa) are much higher than those in x (around 2MPa) and y (around 1MPa) directions. With high laser power and low scan speed, the residual tensile stresses are slightly increased. Hatch spacing has a significant influence on the residual stresses. With large hatch spacing, low residual tensile stresses are present especially for the Z component, as shown in Fig. 8 (right) a. The influence of laser sintering parameters on the residual compressive stresses is similar to that of the residual tensile stresses. X and Y components (around 22MPa) are much higher than the Z component (around 4MPa). Moreover, X component is almost equal to Y component, as shown in Fig. 8 (right) b. In practice, the relationships between laser sintering parameters and residual stresses are more critical than the exact quantity of the stresses. These relationships are very helpful to build up a connection between residual stresses and final mechanical strength of the post sintered ceramic samples.

3.4 Microstructure

In order to understand how the different changing trends of the shrinkages appeared, it is useful to investigate the development of microstructures before (Fig. 10) and after post sintering process (Fig. 9).

The morphology of post sintered specimens was carefully investigated on the fracture cross sections by SEM (Fig. 9). Obvious delaminations are found in R1 and R8 (Fig. 9). The common feature of these two groups is the same hatch spacing of 0.3mm. The laser energy densities of R1 and R8 are 78.43 J/cm^2 and 100 J/cm^2, respectively. These two groups of experiments fall into the inordinate sintering region in Fig. 5 where the sintering temperature is higher than 1400^{o}C. The delamination between two adjacent layers is probably due to the residual thermal stress produced by the laser inordinate sintering. The residual stress couldn't be freely released during the post sintering process. The accumulation of the stresses finally causes the delamination between adjacent layers in the laser sintered body.

On the contrary, the densest microstructure in Fig. 9 is R3 which has a hatch spacing of 0.6 mm and laser energy density of 44.44 J/cm^2 belonging to the inadequate sintering region in Fig. 5. The samples in this group actually delaminated after the laser sintering (Fig. 10a) and it is consistent with the description of Fig. 5. The cross section microstructure in the laser sintered body of R3 is shown in Fig. 10a. There are lots of unsintered regions between two adjacent layers and the binding of the two adjacent layers is relatively loose due to the inadequate laser sintering. When these samples are being post sintered, these remained loose regions could freely release the residual stresses and then tightly combine the adjacent layers together to produce a densified microstructure (Fig. 9 R3). In contrast to the loose binding of the samples in group R3 (Fig.10 a), the microstructure of R5 is more compact (Fig. 10 b). But the post sintered samples in group R3 have a more homogeneous and dense microstructure than the samples in group R5, as shown in Fig. 9. This is consistent with the stress release function of the loose unsintered regions between two adjacent layers.

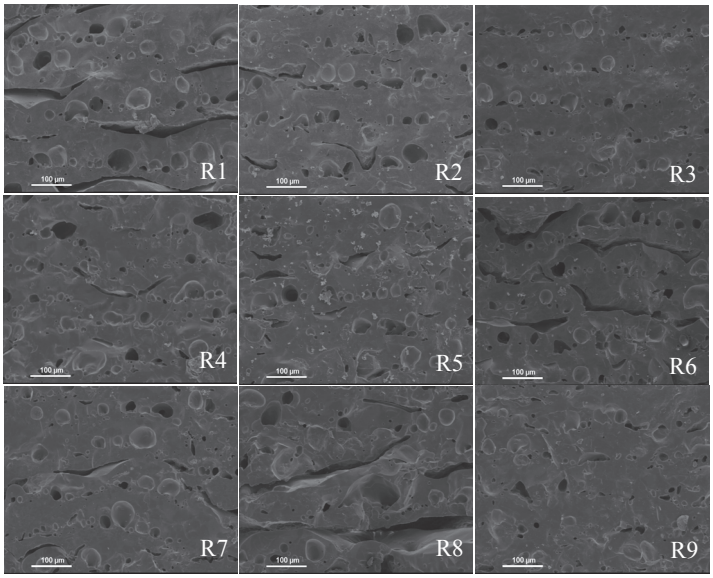

Fig. 9. Microstructure in the fracture cross sections of laser sintered samples after post sintered in a furnace at 1425^{o}C for 2 hours (SEM). The parameters (laser energy density and hatch spacing) used for each group are following:
R1) 78.43J/cm^2, 0.3mm; R2) 66.67J/cm^2, 0.45mm; R3) 44.44J/cm^2, 0.6mm;
R4) 98.04J/cm^2, 0.45 mm; R 5) 83.33J/cm^2, 0.6mm; R6) 55.56J/cm^2, 0.3mm;
R7) 117.65J/cm^2, 0.6mm; R8) 100.0J/cm^2, 0.3mm; R9) 66.67J/cm^2, 0.45mm

A stress relief mechanism was put forward to interpret the changes of the microstructure during the post sintering process and theirs influence on the bending strength (Tian et al., 2010). It has been experimentally proved in the present research that small hatch spacing and high laser energy density will produce high sintering temperature in the HAZ. High transient or residual stress will arise because of the high sintering temperature as well as the large temperature gradient. The post sintering process could be considered as a stress relief process in which residual stress will be released and induce delamination in the ceramic samples. Consequently, the bending strength is reduced by the appearance of delamination which will be discussed in the next section.

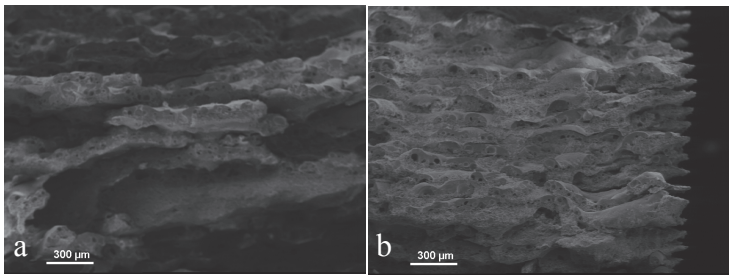

Fig. 10. Microstructures of fracture cross sections in the laser sintered samples (a. R3, b.R5) (SEM)

3.5 Density and mechanical properties

Bulk density and bending strength were measured to study the influence of laser sintering parameters on the properties of final ceramic components. The average effect of laser sintering parameters upon the bending strength is shown in Fig. 11 a. Large hatch spacing and low laser energy density (low laser power and high scan speed) produce high bending strength of the ceramic specimens. The changing pattern of bending strength is consistent with the microstructures shown in Fig. 9. The bulk density is shown in Fig. 11 b. With increasing bulk density the bending strength increases.

The maximum value of bending strength is 29.3±1.0MPa in group R3 which has a most densified microstructure (Fig. 9 R3). However the laser sintered bodies in group R3 delaminated and had a low green strength. The laser sintering parameters in this group cannot be adopted in the following experiments. By comparison with R3, samples in R5 have relatively densified microstructure in the green bodies (Fig. 10b) and relative high bending strength (23.8±1.6MPa, higher than R9 19.5±2.5MPa, as shown in Fig.12) after post sintering. So the laser sintering parameters of group R5, laser power of 50 W, scan speed of 85 mm/s and hatch spacing of 0.6mm, are more appropriate than others.

The relationship between laser energy density and bending strength of the samples post sintered in furnace at 1425^{o}C is shown in Fig. 12. The relation between laser energy density and bending strength is not obvious because bending strength is greatly influenced by hatch spacing. However the maximum bending strength was still achieved when the laser energy density got a minimum value (44.44 J/cm^2, R3). The bending strength was directly measured using the post sintered samples without surface polishing. So the value of the bending strength could be higher after surface treatment.

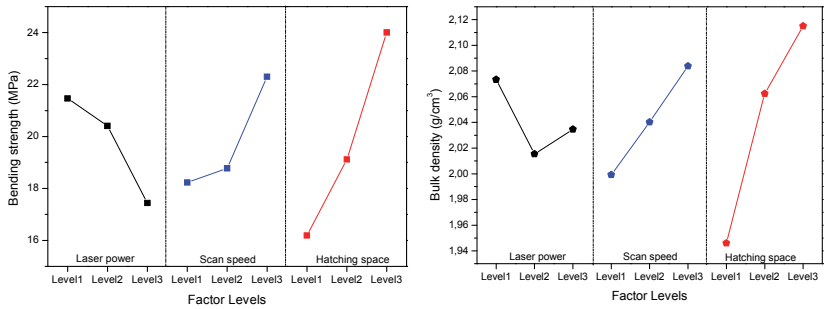

Fig. 11. a) Average effect of each laser sintering factor upon the bending strength of the ceramic samples, b) Average effect of each laser sintering factor upon the bulk density of the ceramic samples

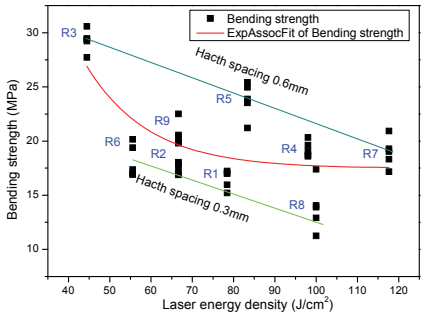

Fig. 12. Relation between laser energy density and the bending strength of the ceramic samples post-sintered in furnace at 1425°C

3.6 Accuracy

The manufacturing accuracy of the direct laser sintered ceramic samples consists of dimensional accuracy in three directions and the surface accuracy. The dimensional accuracy in the laser sintered surface (X, Y plane) depends on the scanning accuracy of the scanner which is controlled by the computer software and can be adjusted or controlled. In Z direction, the dimensional accuracy is affected by the thickness of the deposited slurry layer and the solid content in the slurry, which will be discussed in Section 3.6.1. The surface roughness of the laser sintered plane is controlled by the laser sintering parameters. It's no just an accuracy issue due to the interrelationship between laser sintering parameters and mechanical properties. So, only the influence of surface angle on its roughness will be presented in Section 3.6.2.

3.6.1 Layer thickness

In the fabrication process, a 3D software is used to slice the three-dimensional CAD model from STL files into a series of two-dimensional cross sections. When the layer thickness is

assigned during the slicing process, the cross sections are derived at the increments of that layer thickness. The actual layer for the part is deposited by the stepping of the working table in the same increments. This converts the two-dimensional cross sections into the three-dimensional layers of the actual prototype. The real layer thickness which can be produced by the layer-wise slurry deposition depends on the particle size and the solid content.
The slurry thin film deposited on the preheated ceramic tile will shrink due to the loss of water. Thus the real thickness of each dried layer is different when the preset layer thickness is fixed. The real thickness can be calculated by the following formula,

$$T_l(n) = H(1 - a^n) \tag{2}$$

where $T_l(n)$ is the thickness of the n-th layer after drying, H is the preset slurry deposition thickness (0.1mm in the present research) and a is the shrinking ratio of slurry layer during drying process.
The shrinking ratio (a) of the deposited thin slurry film depends on the volume content of water in the used slurry. The slurries used in the LSD process normally have water content in volume less than 50%. Thus the possible shrinkage ratios for the slurry are less than 50%. The influence of shrinkage ratio on the thickness of dried layers is illustrated in Fig. 13 derived from the Equation x.2. The real thickness is changing at the first few layers and approaching the preset ideal layer thickness, 0.1mm in the present research. More layers are needed to approach the preset thickness for the slurry with large shrinkage ratio. For example, the slurry with a shrinkage ratio of 50% takes 10 layers to achieve 99.9% preset thickness and for shrinkage ratio of 0.1 just 3 layers are needed.
In the fabrication process, supporting layers are always necessary before the laser sintering process starts. The number of supporting layers can also be determined by the shrinkage ratio, i.e. the water content of the slurry. Enough supporting layers can produce homogeneous layer thickness and better quality of the final products.

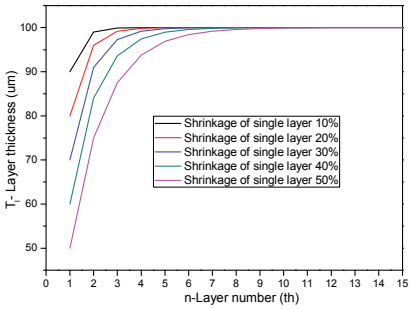

Fig. 13. The development of real layer thickness due to the shrinkage of deposited ceramic slurry

3.6.2 Surface roughness

Surface roughness is quantified by the vertical deviations of a real surface from its ideal form. Roughness is often a good predictor of the performance of a mechanical component, since irregularities in the surface may form nucleation sites for cracks or corrosion.

Ladder effect has a critical influence on the surface roughness of components produced by rapid prototyping. Roughness of curved surfaces is particularly affected by the ladder effect which is the inherent character of layer-wise manufacturing process and can not be avoided. There are two key factors influencing the degree of ladder effect, i.e. surface roughness, layer thickness, and the angle between the slice axis (fabrication direction) and tangent plane of a curved surface, named as surface angle.

In the present research, layer thickness is fixed to 0.1mm. Thus, the dependence of surface roughness on the surface angle will be studied in this section. Ten models with surface angles from 0o to 90^o have been designed, as shown in Fig. 14 a. All the models were input into the rapid prototyping machine (LSD100, Yb-fiber laser system) to fabricate the laser sintered components. Surface roughness measurements were conducted on these samples by using a profilometer along the measuring direction shown in Fig. 14 a. The scan length is 5000μm. Two of them are special, the 0^o surface and 90^o surface. The former is the laser sintered surface and latter is vertical side surface of the component.

Linear profiles of surfaces with different surface angles are shown in Fig. 14 b. Ladder effect is obvious especially for the surface with a small angle (10^o). The vertical side surface with 90^o angle has the smoothest surface because ladder effect has no influence on this surface. The laser sintered surface with 0^o angle has a relative smooth surface because the textured surface was produced by the laser sintering and there was no ladder effect on this surface.

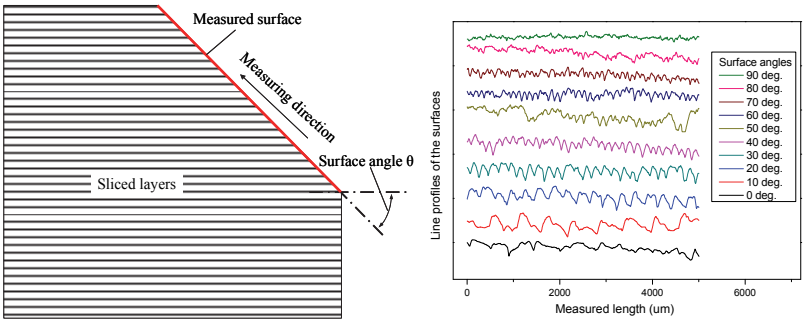

Fig. 14. a) Schematic of the surface angle θ from 0 to 90^o , b) Surface profiles with different surface angles

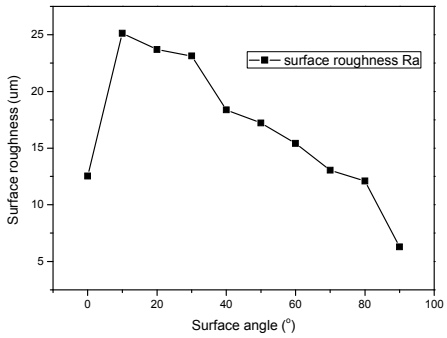

Fig. 15. Surface roughness vs. surface angle

The influence of surface angle on the Ra is shown in Fig. 15. Ra is decreasing from 25.12µm to 12.09µm with an increasing surface angle from 10° to 80° due to the ladder effect. The laser sintered surface hold a Ra of 12.71µm and the vertical side surface has the minimal value of Ra 6.28µm. According to these results from the profilometer, the Ra is variable in the different regions on a curved surface and causes an inhomogeneous surface quality. Post treatment such as surface polishing, and glazing could be used to improve the surface accuracy if necessary.

3.7 Potential applications

3.7.1 Prototypes of porcelain products

Prototypes of the porcelain products are required for evaluation before introducing a new or customized design into the market. The ability to deliver such prototypes in a reasonable time and at an acceptable price can be a decisive factor in a competitive market. However conventional ceramic fabrication processes have the disadvantage that they are normally suitable for the mass production instead of fast and economical manufacturing of prototypes or small-scale series. Porcelain slurry especially for the conventional slip casting process can be taken from ceramic factories and directly used in the present LSD process to produce prototypes of a new design. The cost and lead time for the prototypes can be reduced drastically due to the needless of moulds which are always used in the conventional processes. A bowl model has been fabricated on the LSD 100 machine, as shown in Fig. 16 (left). Certainly, customized ceramic artworks with a complex design like the double-heart in Fig. 16 (right) were also produced by using this LSD process. It probably provides a new method for the artists to transfer their ideas into real ceramic artworks in a very short time.

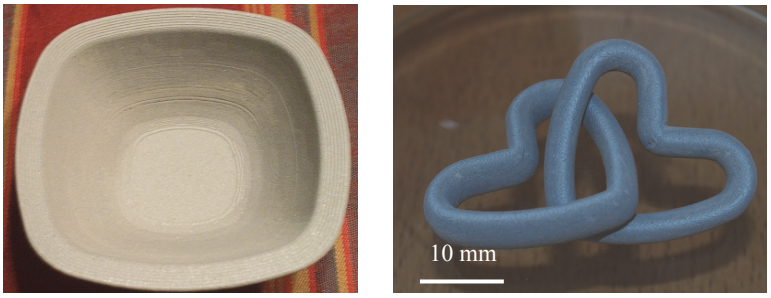

Fig. 16. Porcelain products produced by the LSD-based direct laser sintering process, a bowl (left) and double-heart (right)

3.7.2 Miniature ceramic devices

Several attributes of ceramics make them recognized members in the circles of materials for current and future micro systems. In severe environments, such as high temperature, high pressure, and chemical corrosion, ceramics show very good physical and chemical properties. Moreover, the unique magnetic, piezoelectric, and electro-optical properties make ceramics very popular in the fabrication field of sensors and actuators.

Miniature ceramic parts with a feature size of 500µm have been fabricated by using the LSD-based direct laser sintering process, as shown in Fig. 17. In the following work, high

dielectric constant material can be used by this process to fabricate photonic crystal devices for the microwave application of directional antenna. Piezoelectric ceramics will be used to produce sensors and actuators integrated into a micro system. Laser sinterability of KNN material has already been studied in this thesis. Related research work will continue in the future.

Fig. 17. Miniature ceramic parts by LSD-based direct laser sintering process, photonic crystal, blade wheel, and stationary blade

3.7.3 Biotechnology

The ideal bone implant is a material matrix that will form a secure bond with the tissues by allowing, and even encouraging new cells to grow and penetrate. The used materials should be osteophilic and porous so that new tissue and ultimately new bone can grow into the pores and help to prevent loosening and movement of the implant. As a consequence, a great deal of effort has been placed in the development of porous scaffolds for bone replacement and tissue engineering.

A porous scaffold (Fig. 18) has been fabricated by using porcelain slurry to demonstrate the possible application of our ceramic rapid prototyping machine in biotechnology fields. The model could be reconstructed using the image data from the CT machine. Bioceramics such as hydroxyapatite could be used by the LSD-based direct laser sintering process to produce scaffold for the tissue engineering and bone implants in the future.

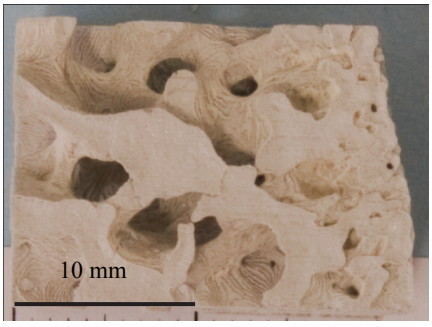

Fig. 18. Porous bone scaffolds

4. Brief comparison of fabrication processes

A simple comparison of these ceramic net-shaping processes will be made according to the following aspects: starting material, energy consumption, efficiency, manufacturing

accuracy, functionality of produced components, and the possibility of materials modification.

4.1 Starting materials

Ceramic slurries are used in stereolithography, direct ink-jet printing, and LSD based laser sintering. For different fabrication process, the content and functions of each composition in the slurry are different. The solid content and viscosity of the ceramic slurry should be optimized according to different process characters. Ceramic powder is used in the three dimensional printing and selective laser sintering process. The powder qualities, such as particle size distribution, morphology, and purity have a great influence on the fabrication processes and properties of produced components. Ceramic tape is used in the LOM process and can be prepared by using the conventional tape casting process. Therefore, it is easy to be adopted by the traditional ceramic factories that have substantial experience on the ceramic tape preparation. Ceramic pastes or filaments are utilized in the extrusion process. The composition and fluidity are important and should be optimized to improve the properties of the ceramic parts. In summary, it is easy to access the ceramic powders as the starting material. Other starting materials, slurry, paste et al, need sequent preparation processes. Aqueous ceramic slurry is widely used in the conventional ceramic manufacturing processes like slip casting and can be directly used by the LSD process. However, the rest slurries, pastes as well as filaments should be prepared carefully by using the ceramic powders.

4.2 Energy consumption

Almost all the rapidly manufactured ceramic parts need post treatment in furnace to further densify the microstructures. So, the difference in energy consumption for each process depends on the characteristics of the material (melting point) and methods used in the shaping processes. Laser employed processes (SL, SLS et al) always consume more energy than the electrical heating process due to the high energy consumption of the laser equipment. Among the laser employed fabrication process, the direct laser sintering of ceramics which always have high densification temperature consumes more energy than the rest processes. In the non-laser processes, the extrusion of ceramic paste consumes less energy than the rests.

4.3 Efficiency

The elemental units in the rapid fabrication process are point, line, face and volume. Different elemental unit causes the diversity of manufacturing efficiency for each fabrication process. “Point” unit is utilized in SL, 3D printing and SLS. “Line” unit is employed in the extrusion process. And LOM process adopts “face” unit as the starting point of the fabrication process. Indirect ceramic forming processes which combine rapid modeling and gel casting use “Volume” as the basic unit. But the efficiency of mould fabrication process should be included into the indirect ceramic forming process. So, LOM process by using “Face” as the basic unit possesses the highest efficiency according to the category of elemental fabrication units. The strategy of the movements in the apparatus also has an influence on the efficiency. Optical movement (laser beam controlled by scanner) has a much higher efficiency than the mechanical movement, such as a knife used to cut the sheets in LOM process.

4.4 Functionality of produced components

Even though there are lots of rapid manufacturing processes focused on the fabrication of ceramic components, functional ceramic parts are still difficult to be produced by most of these processes. Until now, only the indirect rapid manufacturing of ceramic parts by using rapid modeling and gel casting have been used to prepare ceramic parts, such as ceramic shells for the casting. Dense microstructure, high manufacturing accuracy, and good mechanical properties should be achieved before the rapid manufactured ceramic parts can be directly put into the real engineering applications.

4.5 Manufacturing accuracy

Surface accuracy of rapid prototyping depends on the ladder effect which is induced by the principle of fabrication process, slicing and layer-wise deposition. The most important factor influencing the surface accuracy is the layer thickness. Large layer thickness will cause significant ladder effect, especially for the surface with a high curvature. Reducing the layer thickness probably decreases the ladder effect and increase the surface accuracy. But the minimal layer thickness depends on the raw material characters, such as powder size distribution, viscosity of slurry and paste.

Most rapid manufactured ceramic parts need to be post treated in the furnace to densify the microstructure and improve the mechanical strength. Shrinkage in the post treatment process dominates the final dimensional accuracy, which is effected by the different solid content of the starting material in each rapid prototyping process. Dimensional compensation can be used to achieve the ceramic components with the desired size. The information about the shrinkage in the post treatment should be obtained before the accurate compensation can be executed.

4.6 Materials modification

Among all the ceramic solid freeform fabrication processes, only direct laser sintering can manipulate the material properties due to the rapid heating and cooling rate. In the present research, porcelain and $K_{0.5}Na_{0.5}NbO_3$ were both sintered by a laser beam. Dense and textured microstructure has been obtained on KNN samples, which was expected to improve the final piezoelectric properties.

5. Conclusion

In this chapter, net-shaping processes of ceramic components were briefly reviewed. The LSD based direct laser sintering process has been elaborated in details. Temperature distribution in the HAZ was investigated experimentally and by simulation to study its influence on the properties of the produced ceramic components. Microstructure, density and mechanical properties were measured to evaluate and optimize the process parameters. A stress relief mechanism was proposed to explain the relationships between the sintering temperature, residual stresses and microstructure as well as the final mechanical properties. Manufacturing accuracy, including dimensional accuracy and surface roughness, was also studied in order to obtain the desired ceramic components. Some potential applications of the LSD process were also put forward for the future possible researches. A brief comparison has been conducted among all the ceramic net-shaping process at the end of the chapter to help the readers choose appropriate process for their applications.

6. References

Bandyopadhyay, A.; Panda, R. K.; Janas, V. F.; Agarwala, M. K.; Danforth, S. C. & Safari, A. (1997). Processing of piezocomposites by fused deposition technique, *J. Am. Ceram. Soc.*, 80, 1366–72.

Bertrand, Ph.; Bayle, F.; Combe, C.; Goeuriot, P. & Smurov, I. (2007). Ceramic components manufacturing by selective laser sintering, *App. Surf. Sci.*, 254, 898-992.

Cai, K. Guo, D. Huang, Y. & Yang, J. (2003). Solid freeform fabrication of alumina ceramic parts through a lost mould method, *J. Euro. Ceram. Soc.*, 23, 921–925.

Cappi, B.; Oezkol, E.; Ebert, J. & Telle, R. (2008). Direct inkjet printing of Si_3N_4: Characterization of ink, green, bodies and microstructure, *J. Euro. Ceram. Soc.*, 28, 2625–2628.

Cawley, J. D. (1997). *Proc. Int. Gas Turbine and Aeroengine Congress and Exhibition*, Orlando, FA, 1-6, American society of Mechanical Engineering, New York

Chartier, T.; Chaput, C.; Doreau, F. & Loiseau, M. (2002). Stereolithography of structural complex ceramic parts, *J. Mater. Sci.*, 37, 3141-3147.

Friedel, T.; Travitzky, N.; Niebling, F.; Scheffler, M. & Greil, P. (2005). Fabrication of polymer derived ceramic parts by selective laser curing, *J. Euro. Ceram. Soc.*, 25, 193–197.

Gahler, A.; Guenster, J. & Heinrich, J. G. (2006). Direct laser sintering of Al_2O_3-SiO_2 dental ceramic components by layer-wise slurry deposition, *J. Am. Ceram. Soc.* 89, 3076-3080.

Grida1, I. and Evans, J. R.G. (2003). Extrusion free forming of ceramics through fine nozzles, *J. Euro. Ceram. Soc.*, 23, 629–635.

Griffith, M. L. & Halloran, J. W. (1996). Freeform fabrication of ceramics via stereolithgraphy, *J. Am. Ceram. Soc.*, 79, 2601-2608.

Guenster, J.; Engler, S. & Heinrich, J. G. (2003). Forming of complex shaped ceramic products via layer-wise slurry deposition (LSD), *Bul. Eur. Ceram. Soc.*, 1, 1-4.

Guo, D.; Li, L.; Cai, K.; Gui, Z. & Nan, C. (2004). Rapid prototyping of piezoelectric ceramics via selective laser sintering and gel casting, *J. Am. Ceram. Soc.*, 87, 17-22.

Heinrich, J. G.; Gahler, A.; Guenster, J.; Schmuecker, M.; Zhang, J.; Jiang, D. & Ruan, M. (2007). Microstructural evolution during direct laser sintering in the Al_2O_3-SiO system, *J. Mater. Sci*, 42, 5307-5311.

Hinczewski, C.; Corbel, S. & Chartier, T. (1998). Ceramic suspensions suitable for stereolithogiaphy, *J. Euro. Ceram. Soc.*, 18, 583-590.

Hul, C.H. (1984). Apparatus for production of 3D objects by stereolithography, 3D Systems, US Pat. 4,575,330.

Klosterman, D. A.; Chartoff, R. P.; Osborne, N. R.; Graves, G. A.; Lightman, A.; Han, G.; Bezeredi, A. & Rodrigues, S. (1999). Development of a curved layer LOM process for monolithic ceramics and ceramic matrix composites, *Rapid Prototyping J.*, 5, 61–71.

Krause, T.; Engler, S.; Günster, J. & Heinrich, J. G. (2004). Process and a device for producing ceramic molds. *US Patent Appl.*, 6,827-988

Lejeune, M. & Chartier, T.; Dossou-Yovo, C. & Noguera, R. (2009). Ink-jet printing of ceramic micro-pillar arrays, *J. Euro. Ceram. Soc.*, 29, 905–911.

Lombardi, J.L. and Calvert, P. (1999). Extrusion freeforming of nylon 6 materials, *Polymer*, 40, 1775–1779.

Lous, G. M.; Cornejo, I. A.; McNulty, T. F.; Safari, A. and Danforth, S. C. (2000). Fabrication of piezoelectric ceramic/polymer composite transducers using fused deposition of ceramics, *J. Am. Ceram. Soc.*, 83, 124–28.

Lu, X.; Lee, Y.; Yang, S.; Hao, Y.; Evans, J. R.G. & Parini, C. G. (2010). Solvent-based paste extrusion solid free forming, *J. Euro. Ceram. Soc.*, 30, 1–10.

Miyamoto, Y.; Kirihara, S.; Kanehira, S.; Takeda, M. W.; Honda, K.; & K. Sakoda, (2004). Smart processing development of photonic crystals and fractals. *Int. J. Appl. Ceram. Technol.*, 1, 40-48.

Regenfuss, P.; Streek, A.; Ullmann, F.; Suess, T.; Hartwig, L.; Horn, M.; Kuehn, Ch.; Ebert, R. & Exner, H. (2008). Laser micro sintering of ceramics- reaction models and results, *cfi/Ber. DKG*, 85, 65-72.

Regenfuss, P.; Streek, A.; Ullmann, F.; Kuehn, C.; Hartwig, L.; Horn, M.; Ebert, R. & Exner, H. (2008). Laser micro sintering of ceramic materials, *Part 2, Interceram*, 57, 6-9.

Sachs, E.; Cima, M.; Williams, P.; Brancazio, D. & Cornie, J. (1992). Three dimensional printing: rapid tooling and prototyping directly from a CAD model, *J. Eng. Ind.*, 114, 481-488.

Sadeghian, Z.; Heinrich, J. G. & Moztdarzadeh. F. (2004). Direct laser sintering of hydroxyapatite implants by layer-wise slurry deposition (LSD), *cfi/Ber. DKG*, 82, E1-E5.

Safari, A.; Allahverdi, M. & Akdogan, E. K. (2006). Solid freeform fabrication of piezoelectric sensors and actuators. *J. Mater. Sci.*, 41, 177-198.

Schindler, K. & Roosen, A. (2009). Manufacture of 3D structures by cold low pressure lamination of ceramic green tapes, *J. Euro. Ceram. Soc.*, 29, 899–904.

Stampfl, J. & Prinz, F. B. (2002) Rapid prototyping and manufacturing by gelcasting of metallic and ceramic slurries, *Mater. Sci. and Eng. A*, 334, 187–192.

Tay, B. Y.; Evans, J. R. G. & Edirisinghe, M. J. (2003). Solid freeform fabrication of ceramics, *Int. Mat. Rev.*, 48, 341-370.

Tian, X.; Sun, B.; Heinrich, J. & Li, D. (2010). Stress relief mechanism in layer-wise laser directly sintered porcelain ceramics, *Mater. Sci. Eng. A*, 527, 1695-1703.

Tian, X.; Günster, J.; Melcher, J.; Heinrich, J. & Li, D. (2009). Process parameters analysis of direct laser sintering and post treatment of porcelain components using Taguchi's method, *J. Euro. Ceram. Soc.*, 29, 1903-1915.

Tian, X. (2010). *Rapid* prototyping *of ceramics by direct laser sintering, Papierflieger Verlag GmbH*, ISBN 978-3-86948-107-4, Clausthal-Zellerfeld, Germany.

Travitzky, N.; Windsheimer, H.; Fey, T. & Greil, P. (2008). Preceramic paper-derived Ceramics, *J. Am.* Ceram. *Soc.*, 91, 3477–3492.

Vaidyanathan, R.; Walish, J.; Lombardi, J. L.; Kasichainula, S.; Calvert, P. & Cooper, K. C. (2000). The extrusion free forming of functional ceramic prototypes, *JOM – J. Min. Met. Mat. Soc.*, 52, 34–37.

Wu, H.; Li, D.; Tang, Y.; Sun, B. & Xu, D. (2009). Rapid fabrication of alumina-based ceramic cores for gas turbine blades by stereolithography and gelcasting, *J. Mater. Proc. Tech.*, 209, 5886-5891.

Yin, H.; Kirihara, S. & Miyamoto, Y. (2004). Fabrication of ceramic photonic crystals with diamond structure for microwave applications, *J. Am. Ceram. Soc.*, 87, 598–601.

14

Optimization of Ceramics Grinding

Eduardo Carlos Bianchi, Paulo Roberto de Aguiar,
Anselmo Eduardo Diniz[1] and Rubens Chinali Canarim
Sao Paulo State University,
[1]State University of Campinas
Brazil

1. Introduction

Grinding is the most common designation used to define the machining process which uses a tool consisting of abrasive particles to promote material removal. It is traditionally considered as a finishing operation, capable of providing reduced surface roughness values along with narrow ranges of dimensional and geometrical tolerances (Lee & Kim, 2001; Malkin, 1989).

The interactions between abrasive grains and workpiece are highly intense, causing the required energy per unit of volume of removed material to be almost consummately transformed in heat, which is restricted to the cutting zone. The temperatures generated can be deleterious to the machined part, causing damages such as surface and subsurface heating, allowing also for surface tempering and re-tempering. Formation of non-softened martensite may also occur, generating undesirable residual tensile stresses and reducing thus the ultimate fatigue strength of the component.

Moreover, uncontrolled thermal expansion and contraction during grinding contribute to dimensional and shape errors, leading mainly to roundness errors. The grinding severity used is limited by the maximum permissible temperatures during the process. When these are exceeded, they may lead to deterioration of the final quality (Liao et al., 2000; Silva et al., 2007).

In order to optimize the process, aiming for the control of thermal conditions, an increasing focus on proper tool selection emerges, for each material to be ground. Also, the lubri-refrigeration method and types of cutting fluid applied have the main roles of reducing friction and heat, being responsible, as well, for expelling the removed material (chips) from the cutting zone. Adopting those procedures, it can be possible to machine with high material removal rates, as well as to obtain products with high dimensional and shape quality, and also ensuring the abrasive tool a greater life (Webster, 1995).

Cutting fluids in machining have the specific function of providing lubrication and cooling, thus minimizing the heat produced due to friction during cutting. Its drastic reduction or even complete elimination can undoubtedly lead to higher temperatures, causing reduced cutting tool life, loss of dimensional and shape precision and even variations in the machine thermal behavior. An important and often forgotten function, which plays a decisive role in practice, is the ability to expel chips. When abrasive tools are used, a reduction in cutting fluid may render it difficult to keep the grinding wheel pores clean, favoring the tendency for clogging and thus contributing further to the aforementioned negative factors. However,

it is noteworthy that the relative importance of each function also depends on the material being machined, the type of tool employed, the machining conditions, the surface finish and the dimensional quality and shape required (Tawakoli & Azarhoushang, 2008).

1.1 Grinding of ceramics

Ramesh et al. (2001) mention that, during the process of sintering of ceramics, there is a shrinking of material, which cannot be completely avoided. Therefore it is needed to machine the material properly, in order to achieve the shape and geometrical tolerances required for the component.

Mamalis et al. (2002) explain that the material removal mechanism during grinding of ceramics differs considerably from classical grinding theory. In the latter case, in so-called ductile-type grinding, chip removal is accomplished by elasto-plastic change. In the brittle-type grinding of ceramics, material removal is carried out by crack formation (Figure 1), separation, and spalling of the material.

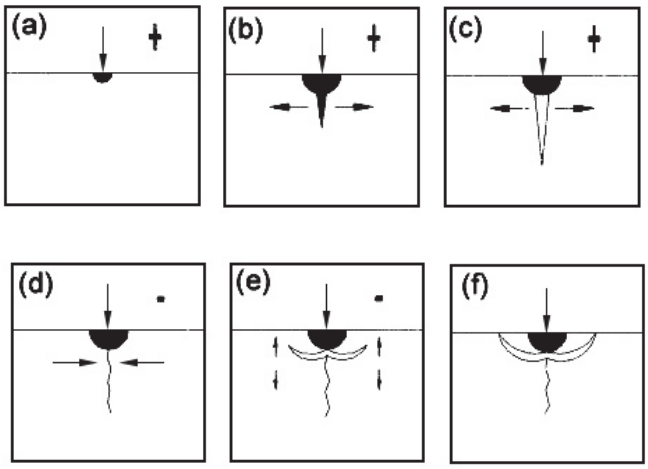

Fig. 1. Stages of crack formation under point indentation (Malkin & Hwang, 1996)

The six characteristic phases of crack formation can be seen in the same figure above. Initially, a plastic zone of small diameter is developed near the surface (Figure 1(a)), whereas subsequently, due to the developed tensile stress field, a small longitudinal crack initiates (Figure 1(b)), and propagates as the indentation goes on and increases in size (Figure 1(c)).

Decreasing the applied load results in the size reduction and/or closing of the longitudinal crack, where compressive stresses prevail (Figure 1(d)). Subsequent load decrease results in the formation of transverse cracks, due to lateral stresses (Figure 1(e)). After unloading, since the tensile residual stress field is developed, the size of the lateral cracks increases, leading to possible separation and/or spalling of the materials in form of chips (Figure 1 (f)).

Malkin & Hwang (1996) also reported that the metal removal mechanism with spall formation may be the governing chip formation mechanism in precision grinding of ceramics; the particular effect on a precision ground ceramic is indicated in Figure 2:

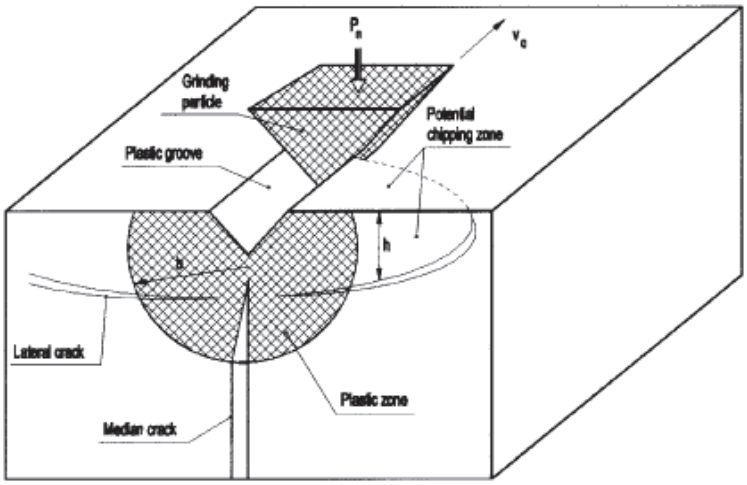

Fig. 2. Plastic zone and crack formation due to scratching by an abrasive grain. (Malkin & Hwang, 1996)

Note, also, that, when grinding ceramics, it must be taken into account that the real depth of cut is larger than the assumed value, because the movement of grains causes additional splintering, leading to a larger depth of cut (Figure 3).

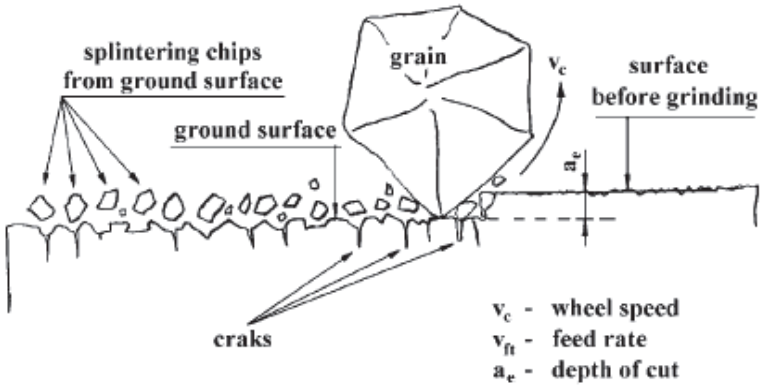

Fig. 3. Model of chip formation in grinding of advanced ceramics.

The main task in grinding ceramics is to define the conditions under which they can be ground economically, with minimal crack formation, thus assuring the part final quality.

1.2 Minimum quantity of lubrication (MQL)

Some limitations of dry machining can be overcome, in many cases, through the introduction of minimum quantity lubrication (MQL) method, whose action is based on the application of 10 to 100 ml/h of cutting fluid on a compressed air jet, under pressures

usually ranging from 4.0 to 6.5 kgf/cm² (Silva et al., 2007). In this technique, the function of lubrication is ensured by the oil, while that of cooling is mainly by the air. Although these advantages allow the foresight of a growing range of MQL applications, the influencing variables to be considered and its effects on the results have been the subject of very few studies (Klocke & Eisenblätter, 1997; Kocke et al., 2000; Silva et al., 2007).

Minimum quantity lubrication systems usually employ mainly non-water-soluble cutting fluids, especially mineral oils. It should be considered that, due to the reduced amounts of coolants used, the costs should not impede the use of high technology compositions in the field of basic and additives oils. It is not recommended to use fluids which are designed for conventional systems, in virtue of the occurrence of atomization and vaporization, deleterious to human health. Higher cutting speeds (which along with temperature, cause problems of this kind), makes indispensable the use of basic oils, with higher viscosity, and adaptations in terms of additives (anti-mist). The used lubricants should be environmentally correct (free of solvents and fluorated materials) and capable of high heat removal. (Heisel et al., 1998.

From a comparison with conventional cooling, many advantages follow (Heisel et al., 1998; Klocke & Eisenblätter, 1997; Kocke et al., 2000):

The ratio between the amount of fluid used and the machined part volume is many times lower than for conventional lubri-refrigeration;

Low consumption of fluid and elimination of a fluid circulation system;

Filtering materials and devices along with maintenance recycling can be avoided;

Low amount of oil remaining along with the machined chips does not justify its recovering;

Machined parts are removed almost dry, so in many cases it is unnecessary an ensuing washing;

The application of biocides and preservatives can be eliminated, due to only the quantity to be used in a work shift should be added to the MQL system reservoir.

Regarding economical aspects, in comparison with conventional cooling, MQL causes additional costs concerning air pressurization and technological supports, which are intrinsically required to overcome its restrictions. For example, special techniques or devices for chip removal could be necessary, and maybe the productivity would be reduced due to the thermal impacts on the machined components.

The oil vapour, mist and smoke generated during the use of minimum quantity lubrication can be considered undesired byproducts, for they contribute to increase the air pollution of the workplace, and thus becoming a factor of concern (being necessary, perhaps, an exhaustion system near the contact area). In pulverization, it is used a compressed air line which functions intermittently during the process. These lines generate a level of noise that usually surpasses the limits allowable by legislation. Therefore, beyond affecting human health, the noise also pollutes the environment and prejudices the communication (Klocke et al., 2000).

1.2.1 MQL in grinding

A relatively small amount of research has been conducted regarding the application of MQL in grinding. Some researchers investigated the effects of grinding parameters on AISI 4340 steel grinding using conventional lubrication and MQL. They found that the surface roughness, diametric wear, grinding forces and residual stress improved when using the latter, due to optimum lubrication of the grinding zone, providing rather grain slipping at

the contact zone (Silva et al., 2005; Silva et al., 2007). Brunner showed that the MQL grinding with a 4 ml/min ester oil (comparing to 11 ml/min mineral oil), when machining 16MnCr5 (SAE-5115) steel with microcrystalline aluminum oxide reduced the process normal and tangential forces to one third, however increasing the surface roughness by 50% (Tawakoli et al., 2009).

Investigations by Brinksmeier confirmed these results and showed in addition that the type of coolant used during MQL grinding (ester oil or emulsion) can considerably influence the process result (Tawakoli et al., 2009). Hafenbraedl and Malkin found that MQL provides efficient lubrication, reduces the grinding power and the specific energy to a level of performance comparable or superior to that obtained from conventional soluble oil (at a 5% concentration and a 5.3 l/min flow), while at the same time it significantly reduces the grinding wheel wear. However, it presented slightly higher surface roughness values (Ra) (Hafenbraedl & Malkin, 2001; Silva et al., 2005; Silva et al., 2007).

The performance was also assessed when applying dry grinding. The results with the minimum quantity lubrication technique were obtained in the internal cylindrical plunge grinding of an AISI 51200 steel (quenched and tempered, detainer of an average hardness of 60 HRc), using conventional alumina wheels.

For MQL technique, a precision dozer providing ester oil at a specific flow rate (12ml/h) was attached to the grinder. A nozzle mixed the oil with compressed air at a pressure of 69 kPa, aiming to form a thin mist. The application of ester oil for internal grinding was unsatisfactory, in virtue of the restricted area to the nozzle access. Its design was optimized to stay as close as possible to the inlet of grinding zone. Also it was used a cold air gun, in an attempt to supply some cooling to the workpiece. The cold air (-2°C) left the nozzle at a flow rate of 3l/s and a pressure of 7.6 bar. It was evaluated, subsequently, that the available amount of cold air would not be capable of providing significant cooling. However, the main disadvantage of MQL was the poor cooling, resulting in high temperatures and the thermal dilatation of the workpiece.

Still in this line of thought, Baheti and others (1998) made some experiments using ester oil (10ml/h) with cold air (-10ºC at outlet) on surface grinding of carbon steel worpieces, using a conventional wheel. The authors proved that MQL technique presented lesser values of partition energy, temperature and specific energy, when compared to conventional cooling. When a comparison with soluble oil was made, MQL with cold air reduced the specific energy by a rate of 10 to 15%, the workpiece temperature by a rate of 20 to 25% and the partition energy to the piece (fraction of grinding energy which is received as heat) by a rate of 15 to 20%.

Tests were made in different lubri-cooling conditions: liquid nitrogen; soluble oil (5% concentration); dry; ester oil; cold air (-10 °C) at a flow rate of 990l/min and pressure of 690kPa, and cold air along with ester oil. Dry condition presented higher partition energy values, which was already expected. On the other hand, the application of liquid nitrogen provided higher specific energy values.

The researchers concluded that is possible to eliminate or reduce the cutting fluid use, contributing to clean manufacturing. Environmentally safe, ester oil was capable of providing good lubrication and, when applied along with cold air, the cooling was more effective than with soluble oil. Ester oil is classified as an unhazardous and noncarcinogenic substance. At the same time, MQL proves that is a promising alternative to cutting fluids in grinding. Despite the liquid nitrogen provided better cooling, it presents weak lubricity, which results in high values of specific energy (Baheti et al., 1998).

Klocke and collaborators presented the behavior of normal and tangential specific forces in external cylindrical plunge grinding when comparing the cooling by a shoe nozzle (24l/min) and MQL technique (215ml/h), the latter resulting in a reduction on these forces. In what refers to microstructure, they revealed that no modifications happened, whatever the conditions employed. On the other hand, MQL application presented the worst surface roughness values (R_z) when compared to wet grinding. The researches proved that, by several results with defined geometry tools, MQL can be used prosperously in grinding processes (Klocke et al., 2000).

However, extensive studies are necessary before this technology is applied industrially, mainly concerning to the lubricant employed. In this context, they are needed in order to verify the benefits and damages caused by this process, enabling it to become viable in industrial scale. These researches include optimization of lubrication composition along with modifications on the design of grinders, abrasive tools and monitoring strategies, to adapt to different conditions of machining.

According to Tawakoli, in order to make the MQL system proper to grinding, certain developments are necessary on the following: satisfactory systems for chip removal; optimized systems to supply cutting fluids in low flow rates; adjustment of the machining parameters, based on the complete understanding of MQL technology, for the chip thickness reach an optimum value; reduction of friction and optimized use of tools (Tawakoli, 2003).

The results obtained by several researches, until the present, using the MQL technology with defined geometry tools, show the possibility of its advantageous application in many cases, contributing to a clean manufacturing without harm to the environment and to human health. They proved that MQL systems result in increased tool life, higher cutting speeds, better surface finishing quality and lesser damages to the workpiece. MQL technology is perfectly qualified for manufacturing processes; however, it is indispensable to have aggregation of effort between users, tool and machine tools fabricants, to obtain better results. It should be remembered that, however, despite all optimistic results with defined geometry tools, in relation to grinding, MQL is still far from its decisive implementation (Tawakoli, 2003).

2. External cylindrical grinding

2.1 Grinding with diamond wheels

The main objective of the present study was to evaluate the technique of minimum quantity of lubrication (comparing to conventional cooling) in the external cylindrical grinding of advanced ceramics, using a diamond wheel, analyzing output variables such as roughness, acoustic emission, G-ratio, circularity errors and scanning electron microscopy (SEM) analysis.

2.1.1 Materials and methods

The experiments were performed in a SulMecânica 515 H RUAP CNC external cylindrical grinder, equipped with Computer Numerical Control (CNC).

Hollow cylinders of commercial alumina (96% of aluminum oxide and 4% of bond oxides as SiO_2, CaO and MgO) were ground. The apparent density of this material was 3.7g/cm^3.

It was used a resin bonded diamond grinding wheel, having the following dimensions: 350mm (external diameter) x 15mm (width) x 5mm (abrasive layer), 127mm (internal diameter), specification code D107N115C50 from Nikkon Cutting Tools Ltd..
The cutting fluid was a semi-synthetic ROCOL 4847 Ultracut 370 emulsion of 5% concentration in water, which had already in its composition: anti-corrosives, biocides, fungicides, and other additives. To control the MQL, was employed an Accu-lube device provided by ITW Chemical Products Ltd., which uses a pulsating system for oil supply and allows the air and lubricant flow rates to be adjusted independently.
Measurements of acoustic emissions were made by a Sensis DM12 sensor, positioned at the head of the mobile near the tailstock. The roundness was measured on a Taylor Hobson Tayrond 31c. The surface roughness was obtained through a Surtronic $^{3+}$ profilometer (with a *cut-off* length of 0.8mm). The microstructure analysis was performed by scanning electron microscopy (SEM).
The wheel wear was measured by printing its profile on a 1010 steel workpiece, and then, with a TESA comparator gauge the data from this variable could be assessed.
For the tests were established the following machining conditions: plunge speed (V_f) of 1 mm/min, wheel peripheral speed of 30m/s, depth of cut of 0.1mm, 5 seconds of spark-out, fluid flow rate in conventional cooling of 22l/min, fluid the flow rate in MQL of 100ml/h and air pressure of 8bar, outlet air velocity in MQL nozzle of 30m/s, and 13 workpieces per test.
The three feed rate were chosen: 0.75mm/min, 1mm/min and 1.25mm/min, corresponding to the respective equivalent thicknesses of cut h_{eq1} = 0.0707mm, h_{eq2} = 0.094mm and h_{eq3}= 0.118mm.

2.1.2 Acoustic emission

Figure 4 presents the results of acoustic emission (RMS), expressed in Volts (V), according to the number of ground pieces.
The values on the figure above indicate no significant differences in relation to acoustic emissions. It can be seen that the condition which showed lower values was the conventional cooling with h_{eq1} (smaller equivalent thickness of cut), while the one that showed higher values was the MQL technique with h_{eq1}.
One explanation for these phenomena is the small influence of the equivalent thickness of cut in MQL caused by other significant variables, such as the thermal dissipation of the cutting region. Since this method dissipates less heat, its removal occurs mainly by the thermal conduction of the grinding wheel, constant for all tests. As the equivalent thickness of cut is determined by the feed rate, the higher thickness of cut provides greater contact area, causing then more heat conduction.
It can be noted that this type of conclusion can be made just because that the workpiece has small thickness in relation to the thickness of the grinding wheel. For those with greater thickness, the thermal conduction of the wheel can be limited.

2.1.3 G-Ratio

This item presents the G-Ratio for each equivalent thickness of cut and lubri-cooling condition. This value was calculated by measuring the wheel wear and volume of worn material. The first could be measured due to the greater width (15mm) in relation to the workpiece (4mm).

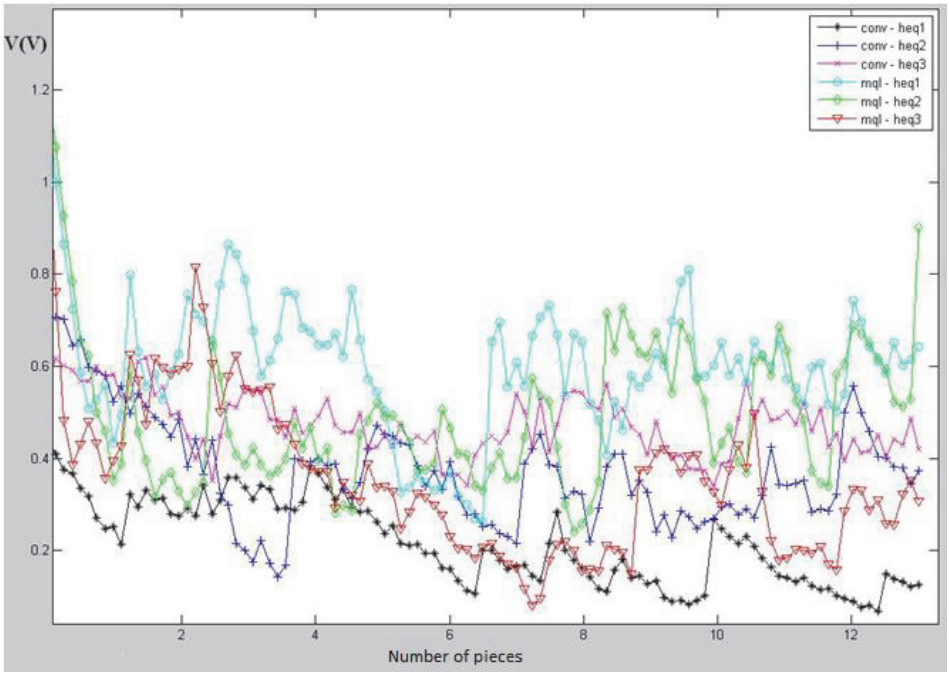

Fig. 4. Acoustic emission results.

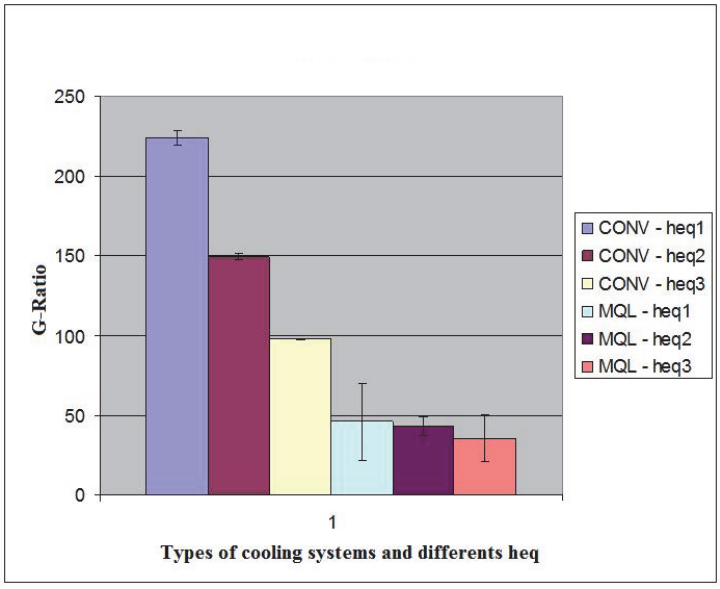

Fig. 5. G-Ratio results for each condition tested.

Through the analysis of the figure above, it can be noticed that the higher values for the G-Ratio were obtained for conventional cooling. One possible reason of these is the lower heat dissipation in the cutting region caused by the MQL, resulting in losing of bond resistance, thus wearing more the grinding wheel.
It can be also seen that, for the conventional cooling, the equivalent thickness of cut is a great factor of influence concerning wheel wear, therefore the G-Ratio. The higher its value, the more accented the wear, consequently, providing lower values for the G-Ratio.
For the MQL technique, the equivalent thickness of the cut could not influence effectively in the G-Ratio. This can be explained by other factors which probably prevailed in the wear, i.e., the lower heat dissipation on the cutting zone, making the influence of equivalent thickness of cut almost imperceptible.

2.1.4 Scanning electron microscopy (SEM)

Figure 6 represents the results for scanning electron microscopy (SEM) obtained conventional lubri-refrigeration (1000x zoom).

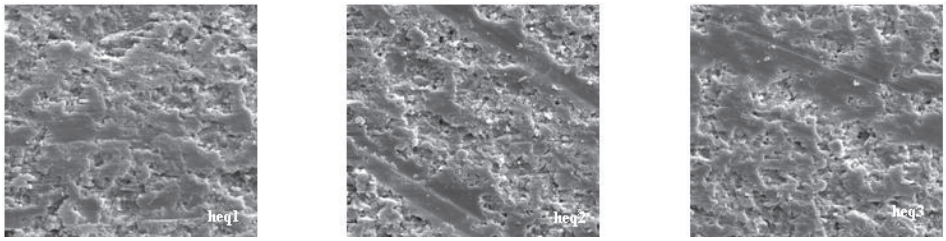

Fig. 6. SEM for conventional cooling with h_{eq1}, h_{eq2} and h_{eq3}.

In the conventional cooling occurred the fragile mode of material removal. The tendency to ductile mode removal increases as does the equivalent thickness of cut, providing an improvement the workpiece finishing.
Figure 7 represents the results for the MQL technique (1000x zoom).

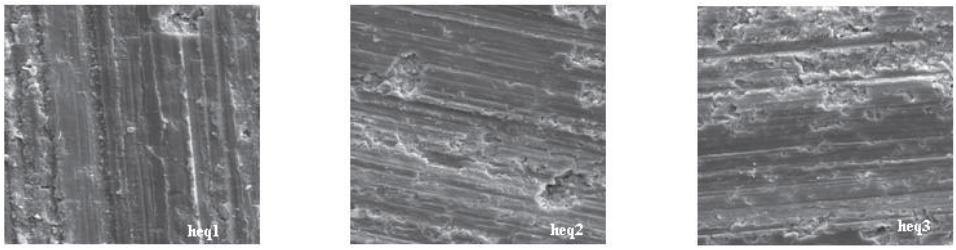

Fig. 7. SEM for cooling the MQL for h_{eq1}, h_{eq2} and h_{eq3}.

It can be noticed that the predominant mode of material removal using MQL was the ductile, which provides optimal conditions for surface finish with the strength of the material due to the reduction of micro-fractures, responsible for stress concentrators. By observing the figures, it can be seen that, the lower the equivalent thickness of cut, the more ductile is the process of material removal.

The better surface characterization with MQL may be explained by the greater power of the lubricating oil used, in comparison to the emulsion employed in conventional cooling.

2.1.5 Roundness

Figure 8 shows an evolution of the roundness for all conditions tested.

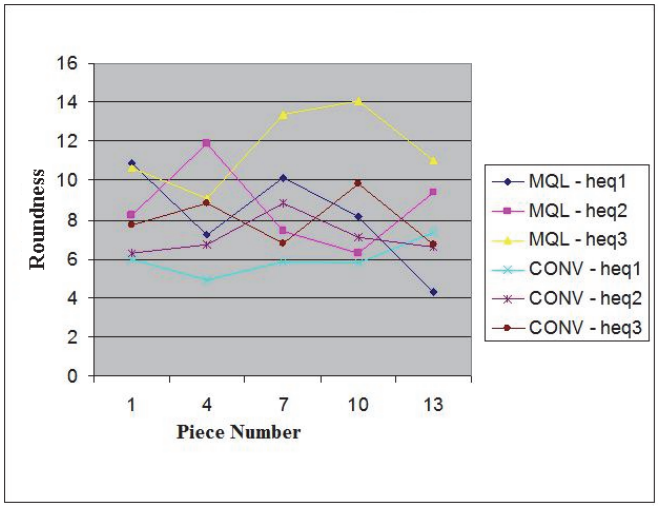

Fig. 8. Evolution of roundness errors.

It can be noted that only for the more severe condition of MQL lubrication, the roundness has increased dramatically.

Analyzing the results obtained as a whole, the values for less severe conditions using MQL did not differ significantly.

On the roundness, there were no significant differences between both methods, with h_{eq1} and h_{eq2}.

2.1.6 Surface roughness

The figure below shows the results for the average surface roughness (R_a), on the comparison between conventional lubri-cooling and MQL (in micrometers). The values shown are averages of five measurements at different positions, for each of the 3 tests, with their respective standard deviations.

In general, the values were lower for the conventional lubri-cooling method than with MQL, possibly due to the better chip removal from the cutting zone, by conventional cooling. When applying the MQL technique there was formed a paste of fluid and chips, even with compressed air at high speeds. This affected considerably the values of surface roughness.

The lower values for MQL are observed in the lowest values of h_{eq}, proving that the smaller thicknesses of cut allows smaller values of surface roughness, due to lower material removal rate and greater lubrication achieved.

The surface roughness is mainly influenced by the lubrication condition. The emulsion presents the characteristics of low lubrication but great cooling, thus affecting this variable.

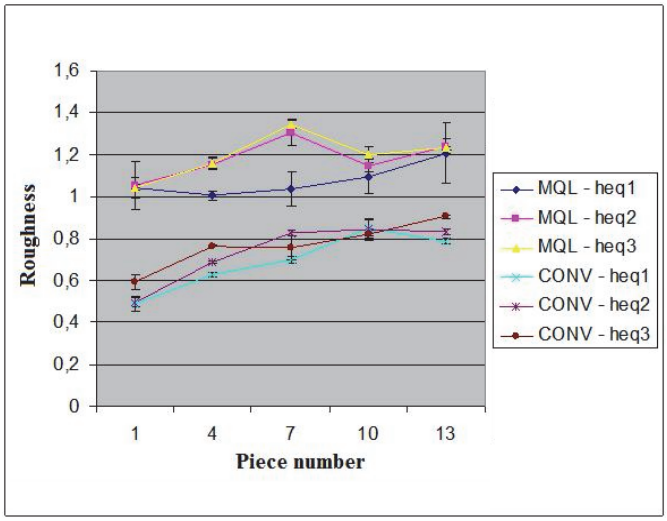

Fig. 9. Evolution of surface roughness during the tests.

2.2 Application of MQL with water (H_20)

Silva et al. (2007) showed that surface roughness values and diametral wheel wear are significantly lower when using MQL technique, as well as tangential cutting forces and specific energy, demonstrating thus the good capability of lubrication by MQL.

Yoshimura et al. (2005) state that minimum quantity lubrication with water, known as Oil-on-Water (OoW), presents high cooling capability, due to the water droplets covered by a layer of oil, which evaporate easily on the part and tool surfaces, and cool them due to its sensitivity and latency to heat.

The concept of water droplets covered by an oil layer can be seen in Figure 10.

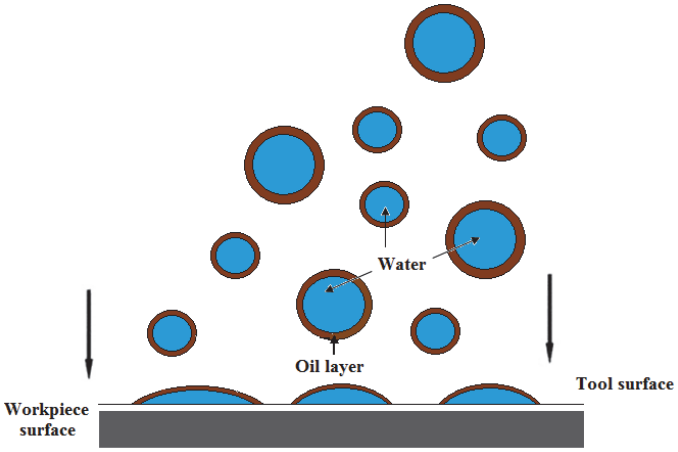

Fig. 10. Water droplets covered by an oil layer

Itoigawa et al. (2006) also presented that cooling capacity due to the water droplets is not important only to the dimensional precision, but also to avoid some deleterious effects between tool and workpiece surface, such as adhesion.

2.2.1 Materials and methods

Machining conditions were determined after some preliminary tests, which provided the best values to assess the viability of OoW grinding. These values are presented in Table 1.

Grinding mode	External Cylindrical Grinding
Abrasive Tool	D140 N100V
Grinding Machine	SulMecânica RUAP 515 H-CNC.
Cutting speed (V_c)	V_c = 30m/s
Depth of cut (a_e)	a_e = 0.1mm
Lubrication-cooling method	Conventional, MQL
Cutting fluid (Conventional)	Rocol 4847 Ultracut 370 with 5% concentration
Oil flow rate (MQL)	Q = 100ml/h
Cutting fluid (MQL)	Rocol Cleancut
Air pressure	P = 8 bar
Workpiece material	Comercial alumina (D_e= 54mm, D_i = 30mm, e = 4mm)
Dresser	*Fliese* multigranular dresser
Depth of dressing (a_d)	a_d = 0.04mm
Feed rates	f=0.25 mm/rev; 0.50 mm/rev; 0.75 mm/rev

Table 1. Machining conditions

Three different lubri-refrigeration modes were used: conventional lubri-refrigeration, MQL method, and MQL with water (OoW), with oil/water ratio of 1:1.

It was used a wheel cleaning system by compressed air jets, with two nozzles directed tangentially to the wheel surface, which assures better results for cylindrical grinding of advanced ceramics, as proved by the preliminary tests.

Before each test, the wheel was dressed, allowing for the same initial conditions of the tool. After dressing, the ceramic workpiece was normalized parallel to the grinding wheel. For each test, five hollow cylinders were used.

In order to use the whole wheel width, two tests were conducted before each dressing. After these two tests, the wheel wear was measured by printing its profile on steel cylinders, and then the tool was dressed.

Before each conventional lubri-refrigeration test, the cutting fluid concentration was evaluated by an Atago N-1 E manual refractometer, and then corrected if needed (by adding more water or cutting fluid into the reservoir).

The wheel diametral wear was obtained through the printing of its profile on a steel workpiece, and then it was measured by Talymap Silver software, which provided the mean values for this variable, considering each lubri-refrigeration condition.

Surface roughness values were obtained using a Taylor Hobson Surtronic $^{3+}$ rugosimeter, while the roundness values were obtained by a Taylor Hobson Talyrond 31C roundness meter.
Data acquisition of grinding power and acoustic emission data were obtained by Labview 7.1. The signals were then filtered and treated in Matlab, which provided average values for both variables.
Acoustic emission signals were gathered by a Sensis DM12 sensor, which was fixed on the grinding machine tailstock, aiming to detect the possible variations of this variable, and consequently making it possible to relate it with the other output variables.

2.2.2 Surface roughness

For the surface roughness values, it can be seen in Figure 11 that conventional lubri-refrigeration provided the lower values for all feed rates tested, due to the better capability to remove machined chips from the cutting zone (abundant fluid flow).
Traditional MQL method provided medium surface roughness values, about 65% higher than when using conventional lubri-refrigeration, due to the formation of a grout (oil+chips) which lodged into the wheel pores, and is very difficult to remove. Those microchips lodged in the wheel scratch the workpiece surface, increasing its surface roughness. Part of this grout was removed by the compressed air jet, which cleans the wheel, providing then better results on the workpiece finishing, compared to MQL without wheel cleaning.

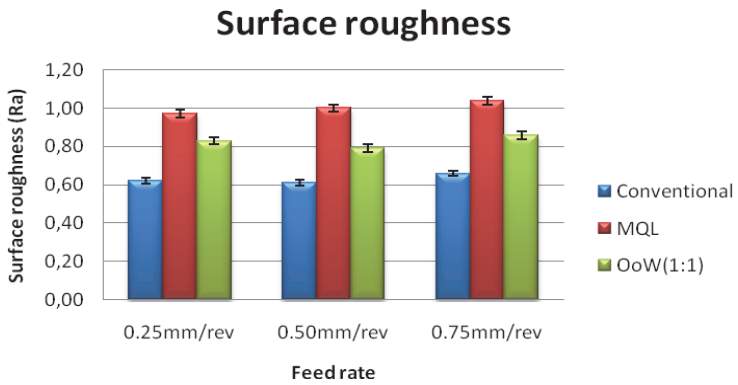

Fig. 11. Surface roughness results for each lubri-refrigeration condition

However, it can be seen that MQL with water provided lower values for surface roughness, than when using traditional MQL. OoW (1:1) tended to decrease this variable, being 35% higher compared to conventional lubri-refrigeration, and 20% lower compared to traditional MQL. A possible explanation for this better performance of air-oil-water mixture, in relation to air-oil (traditional MQL) is the fact that, following the same reasoning presented above, the water lower viscosity makes the grout less adherent to the wheel, and consequently easier to be removed from the wheel pores.

2.2.3 Roundness

For the roundness values presented in Figure 12, the conventional lubri-refrigeration also presented the best results for all feed rates tested, due to the better ability of cleaning the wheel provided by this method.

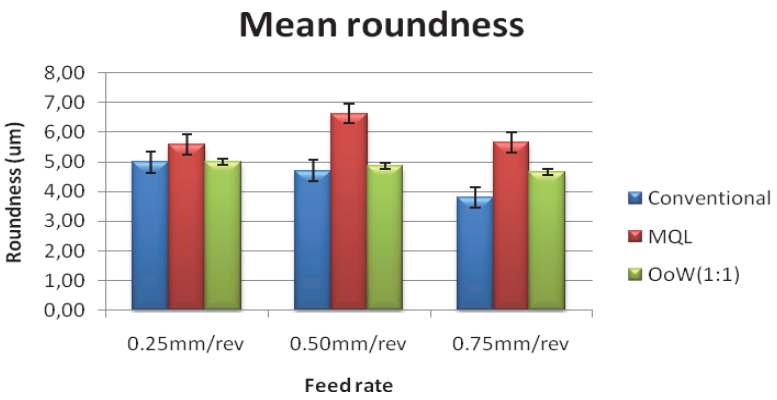

Fig. 12. Roundness results for each lubri-refrigeration condition

Again it can be seen that the presence of water in the air-oil combination increases the roundness values, since they increased when using OoW. That was caused by the reduction of lubrication capability of this mixture, since there are lower amounts of oil. On the other side, when using only oil in combination with air (traditional MQL), that it, when the lubrication capability is higher (for MQL systems), the roundness values were higher than when using OoW (1:1). This is possibly due to the fact that, despite the increase in the lubricating capability of traditional MQL, the combination of air-oil loses wheel cleaning capability, which also influences the results for roundness.

2.2.4 Acoustic emission

For the acoustic emission values, it can be observed that conventional lubri-refrigeration provided the higher results, while the others provided relatively lower values, about 75% of the conventional, as shown in Figure 13.

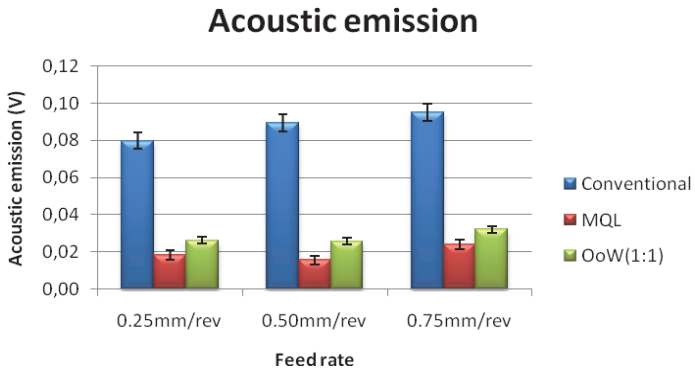

Fig. 13. Acoustic emission results for each lubri-refrigeration condition

It can be concluded that acoustic emission was mainly influenced by the lubrication capability of the lubri-refrigeration method, and less influenced by the wheel cleanliness. As the lubrication capability increased, and wheel cleaning capability decreased, acoustic

emission values were lower. Even when the wheel had machined chips loged into its pores (as when using traditional MQL), the presence of oil on the grout provided less friction between the grains (and lodged chips) and the workpiece.

2.2.5 Grinding power

Observing Figure 14, it can be noticed that the lower values of grinding power were obtained when using conventional lubri-refrigreration. This same decreasing tendency was observed for OoW, with oil/water ratio of 1:1. This occurs because in conventional lubri-refrigeration, the capability of cooling the wheel/workpiece interface is the better, among the conditions tested.

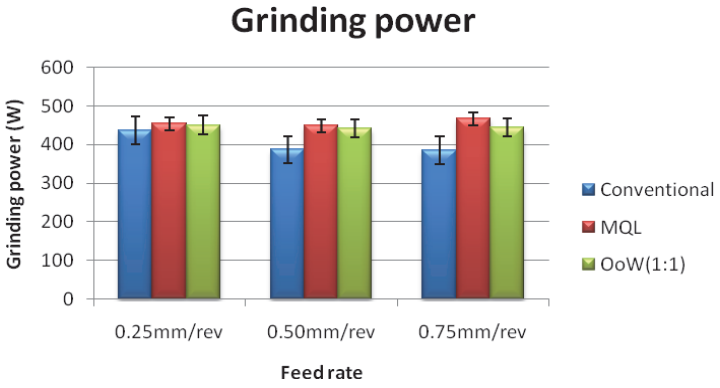

Fig. 14. Grinding power results for each lubri-refrigeration condition

When used traditional MQL, it can be seen that the required power tended to be slightly higher than when using OoW (1:1) method. This can be explained by the fact that, when using only oil the cooling is less efficient, probably causing thermal deformations of the machine/workpiece/wheel system, which requires more power. On the other hand, OoW (1:1) combines efficient cooling and lubrication in a way that grinding power necessary is lower.

2.2.6 Diametral wheel wear

According to the results presented in Figure 15, it can be observed that, for all feed rates tested, MQL was the lubri-refrigeration method which provided the higher wear values, about 28% higher than conventional lubri-refrigeration, for the feed rate of 0,25mm/rev, 25% higher for 0,50mm/rev and 14% higher for 0,75mm/rev.

As previously mentioned, traditional MQL was the lubri-refrigeration method which was less effective in cleaning the wheel, that is, it is the condition on which more chips remained lodged in the wheel pores. Then, the friction between these adhered chips and the workpiece contributed to wear the wheel more intensely. On the other side, the most efficient method for wheel cleaning, which was conventional lubri-refrigeration, did not provide lower diametral wheel wear values, as it could be supposed by the aforementioned reasons. It is possible that the factor which caused high wheel wear was the low capability of lubrication of this abundant flow, which consists of oil diluted in water.

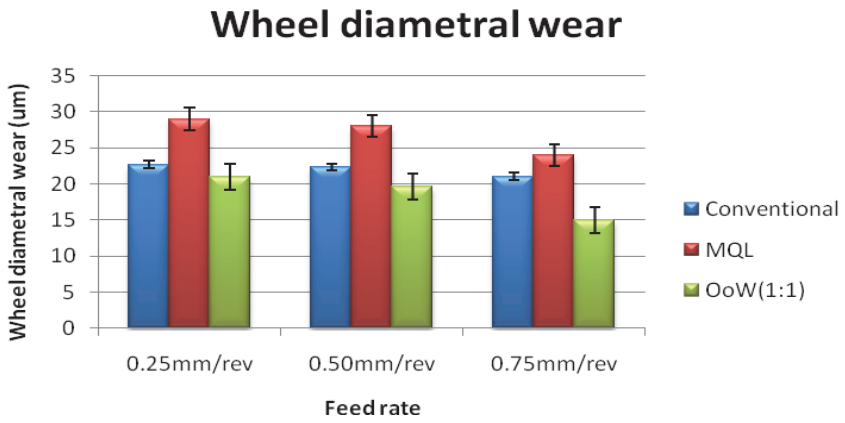

Fig. 15. Diametral wheel wear for each lubri-refrigeration condition

When used a lubri-refrigeration method which is intermediary in terms of wheel cleaning and lubrication capability (OoW), it was obtained a satisfactory combination of both variables, and the diametral wheel wear was not as high as the one obtained when using conventional lubri-refrigeration.

2.2.7 Conclusions

Based on the obtained results on this work, it can be concluded that, when grinding ceramics with diamond wheels, in similar conditions to the ones tested:

In terms of surface roughness, conventional lubri-refrigeration was the method which provided the best results, due to its better ability to clean the wheel, by removing the machined chips which lodge in the wheel pores. Traditional MQL presented the worst results, because, despite being very efficient in lubricating the wheel/workpiece interface, it was the worst condition for wheel cleaning.

In terms of roundness, the results were similar to surface roughness. Conventional lubri-refrigeration was the most satisfactory method, while traditional MQL was the less satisfactory.

Acoustic emission signals generated from the process was strongly influenced by lubrication capability of the lubri-refrigeration methods (it can be inferred that it is an indirect measurement of this capability). Thus, the higher acoustic emission values were obtained when using conventional lubri-refrigeration, while the lower was obtained for traditional MQL.

The lubri-refrigeration condition which provided the higher diametral wheel wear was the less efficient when considering wheel cleaning (traditional MQL). However, the condition most efficient in cleaning the wheel (abundant fluid flow) was not the one which provided lower wheel wear, since it has poor lubrication capability.

2.3 Wheel cleaning by a compressed air jet

According to Lee et al. (2002), an alternative to overcome the issue of having oil and impurities lodged on the Wheel pores, when using MQL technique, would be the application of compressed air jets, directed straightly onto the cutting zone, which would clean the wheel surface.

The depth of cut can be thus increased, since the diametral Wheel wear would be lower, and, beyond that, it is possible to obtain better surface quality, reducing surface roughness and fulfilling efficiently the geometrical and shape requirements of the component.

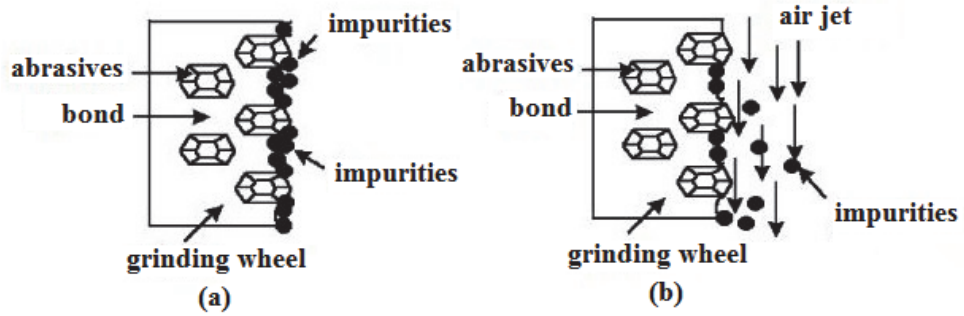

Fig. 16. Effect of compressed air jet. (a) grinding without wheel cleaning, (b) grinding with wheel cleaning (Lee et al., 2002).

2.3.1 Materials and methods

The tests were conducted on a SulMecânica RUAP 515 H-CNC surface grinder, equipped with computer numerical control (CNC). Workpieces were made from commercial alumina 96% of aluminium oxide, 4% of other oxides like SiO_2, CaO and MgO). The apparent density was 3.7 g/cm^3. The grinding wheel was a resin bonded diamond wheel (D140N100V) with dimensions of: 350mm (external diameter) x 15mm (width) x 5mm (layer) and internal diameter of 125mm.

The cutting fluid used for minimal quantity of lubricant was a Rocol Cleancut, and the MQL application device was an ITW Chemical Accu-Lube, which allow independent flow rate regulation of oil and air. The air flow rate used was monitored with a turbine type flow rate meter, calibrated to a pressure of 8 kgf/cm^2.

For the wheel cleaning compressed air jet, the air flow rate was $8.0.10^{-3}$ m^3/s and the pressure was $7.0.10^5$ Pa at the nozzle.

The cutting fluid for convenetional lubri-refrigeration was soluble semi-sinthetic oil (Rocol Ultracut 370), with 5% concentration on water.

The measurement of roundness was conducted by a Taylor Hobson Talyrond 31C roundness meter, which provided the average value for each test.

Surface roughness (R_a) was measured five times for each workpiece, obtaining an average value for each test, using a Taylor Hobson Surtronic^{3+} rugosimeter.

Diametral wheel wear was measured by printing the wheel profile on an AISI 1020 steel workpiece. Then the average value was calculated by the software Talymap Silver.

The microstructural analysis was made through the analysis of SEM micrographs, after adequate preparation of the workpieces.

The grinding power data were gathered in real-time with the data acquisition software NI LABView.

Each test was repeated twice, and five workpieces were used. The feed rate used was 0.50 mm/min.

The lubri-refrigeration conditions were: Conventional lubri-refrigeration (abundant flow); MQL without wheel cleaning; and MQL with wheel cleaning, with four different incident angles for the compressed air jet on the tool surface (tangent, 30°, 60° and 90°). The cleaning nozzle placement is shown in Figure 17.

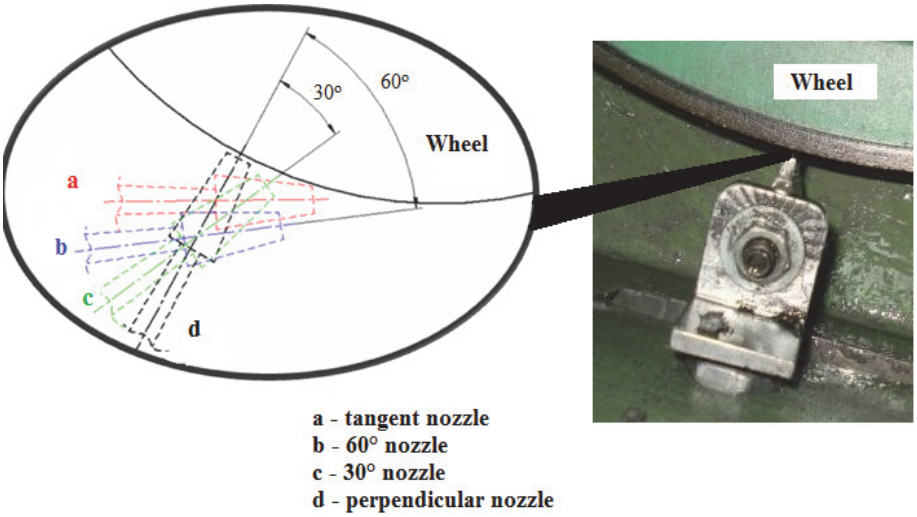

Fig. 17. Incidence angles for compressed air jet.

2.3.2 Surface roughness

Figure 18 presents the results obtained for the average surface roughness (R_a).

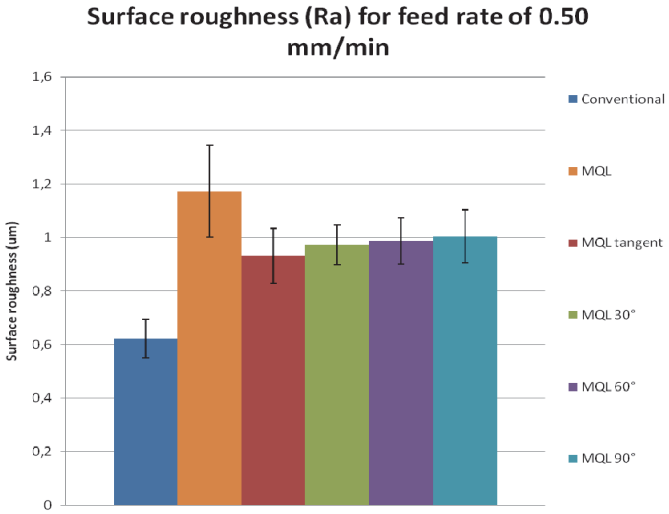

Fig. 18. Surface roughness results for each lubri-refrigeration condition

Analyzing the results obtained, it can be observed that the surface roughness value was lower for conventional lubri-refrigeration, in comparison to MQL technique, possibly caused by the better removal of machined chips from the cutting zone. When using MQL, a grout is formed (mixture of oil and chips), which is difficult to remove, causing an increase on the surface roughness.
In relation to MQL with wheel cleaning, it can be seen clearly an improvement of the results for this variable, when comparing to traditional MQL (without wheel cleaning), but they still remained worse than the results for conventional lubri-refrigeration. This is due to the worse capability of removing the grout formed, and the heat generated on the cutting zone, when using MQL. Considering the average values for surface roughness for conventional lubri-refrigeration, in comparison to the tangent angle for the cleaning air jet (best condition of wheel cleaning), it can be seen that the conventional lubri-refrigeration provided values almost 40% lower.
In relation to the efficiency of the cleaning system by compressed air, it is a function of the air jet incident angle, since the pressure and flow rate were kept constant.
Thus, it can be noticed that the wheel cleaning conditions provided better results than when using traditional MQL, for all incident angles tested. Besides that, the angle which provided the best results was the tangent angle.

2.3.3 Diametral wheel wear

Figure 19 shows the results obtained for diametral wheel wear, using as a reference the conventional lubri-refrigeration, since it is widely applied on the industries.

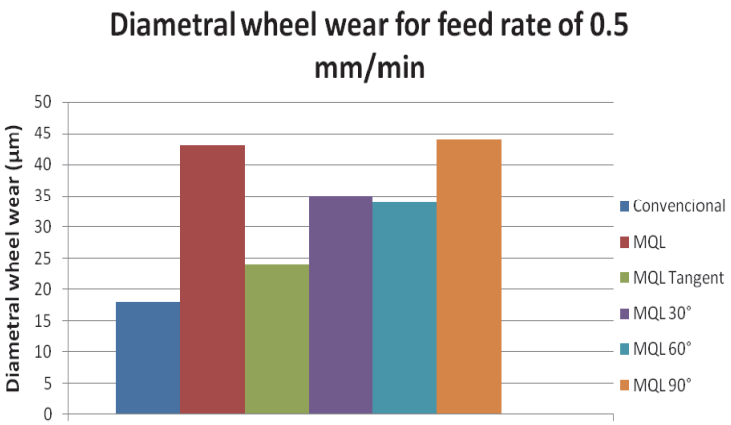

Fig. 19. Diametral wheel wear results for each lubri-refrigeration condition tested.

Analyzing the results obtained, it can be seen that conventional lubri-refrigeration obtained again the best results, and the wheel cleaning method provide clear improvements when comparing to traditional MQL, with exceptions to the normal angle in this case (which was very close to traditional MQL).
When considering diametral wheel wear, the tangent angle was the most efficient, as occurred for surface roughness results, being about 40% higher in comparison to

conventional lubri-refrigeration. Again, as the wheel cleaning was not so efficient in removing the material lodged, the results were harmed; however, this prejudice was lower when using the air jet with an incident angle tangent to the tool surface. Thus, it can be noted a coherence with the resuls obtained for surface roughness and diametral wheel wear.

2.3.4 Roundness

Figure 20 presents the results obtained for roundness errors, for a clear comparison among the lubri-refrigeration conditions tested.

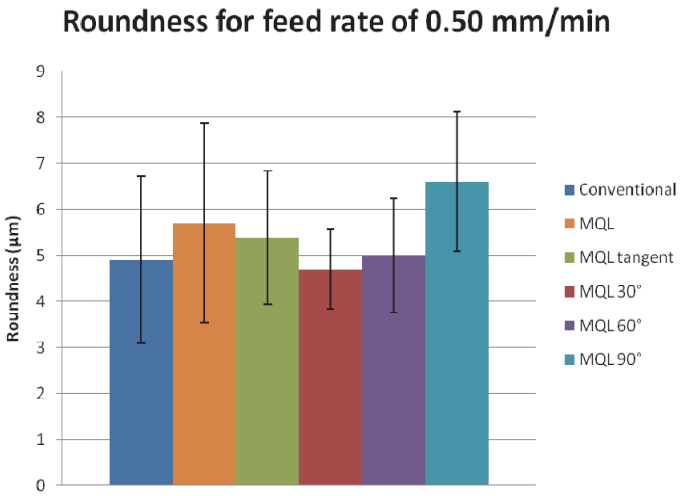

Fig. 20. Roundness results for each lubri-refrigeration conditions

It can be noticed that, generally, the average values were close, being the wheel cleaning jet with incidence angle of 30° the best condition. However, wheel cleaning for other angles presented worse results than when using conventional lubri-refrigeration. It can be also observed that, with exception to normal jet (90°), all angles improved the results in comparison with traditional MQL.

The incidence angle of 30° provided very satisfactory results, even better than when using conventional lubri-refrigeration. With that, the most efficient angle was not the tangentially directed, as in surface roughness and wheel wear results. However, this angle provided also better results than traditional MQL, becoming also viable. The difference between the average values of roundness results for conventional lubri-refrigeration and MQL with wheel cleaning (30°) was only about 2%.

The results for roundness did not behave as the expected, when considering surface roughness and Wheel wear, because this variable is more sensitive to the stiffness of the process, i.e., grinding machine, tool, workpiece, and others.

An example for these unexpected values is that the incidence angle of 30° provided better results than conventional lubri-refrigeration, which did not occur in surface roughness and wheel wear results. Another one is the fact that the tangent angle was not the most efficient condition of wheel cleaning, as in the previous output variables evaluated.

2.3.5 Grinding power

Figure 21 presents the results obtained for grinding power (gathered in real-time), for each lubri-refrigeration condition.

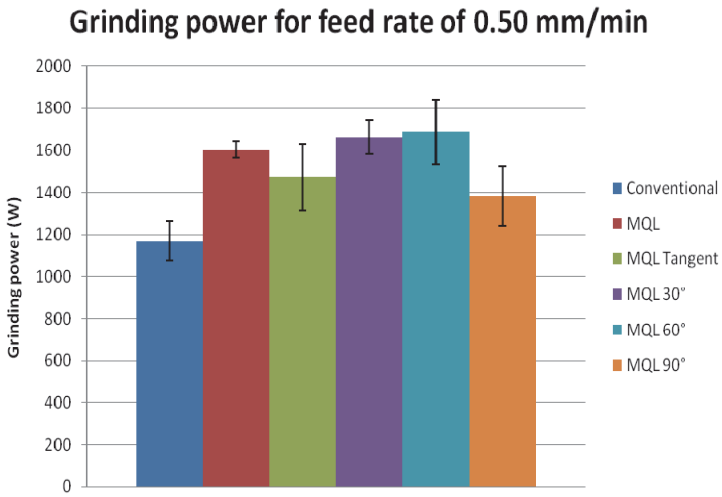

Fig. 21. Results of grinding power for different lubri-refrigeration condition.

It can be noted that the conventional lubri-refrigeration test provided the lower grinding Power values, which is coherent with the results of surface roughness and diametral wheel wear. That occurs probably due to the more efficient chip removal from the cutting zone, favoured by this lubri-refrigeration method.

Also, traditional MQL did not provide the worst result, because MQL with wheel cleaning jets using 30º and 60º provided higher grinding power values. When using the wheel cleaning jet with incidence angles of 30° and 60°, it can be observed that the results for surface roughness were better, in comparison to traditional MQL, because the compresse air jet creates higher reaction forces on the grinding wheel, which contributes to the removal of lodged chips, reducing then the surface roughness. At the same time, this reaction generates higher components of tangential force, against wheel rotation, increasing thus grinding power values. This explains the fact that this variable, for the wheel cleaning incidence angles of 30° and 60°, was higher than for traditional MQL.

This also explains why the grinding power values, for the wheel cleaning jet with incidence angle of 90° (normal to wheel surface), were lower than when using compressed air jet directed tangentially (which provided lower surface roughness, in comparison to the first). Tangential compressed air jet generates higher forces against the wheel rotaion, increasing then the grinding power.

2.3.6 Scanning electron microscopy (SEM)

Surface integrity is of undeniable importance, when concerning grinding operation. Damages caused to the material surface can affect it negatively, harming wear resistance, causing nucleation and propagation of cracks, and accelerating fatigue.

Scanning electron microscopy is a powerful technique of microstructural assessment and characterization, making possible to analyze the material surface as a consequence of each condition of grinding, specifically in the present situation.

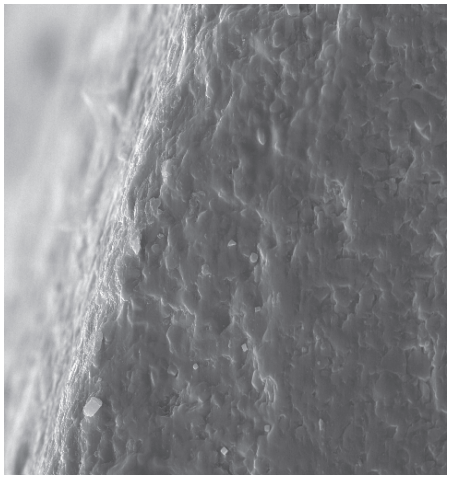

Fig. 22. Scanning electron micrograph for conventional lubri-refrigeration tests (1000x)

Analyzing Figure 22, it is possible to notice that, when using conventional lubri-refrigeration, the fragile material removal mechanism prevailed. It is also noteworthy the good finishing surface, despite the fragile removal, which can cause microcracks.

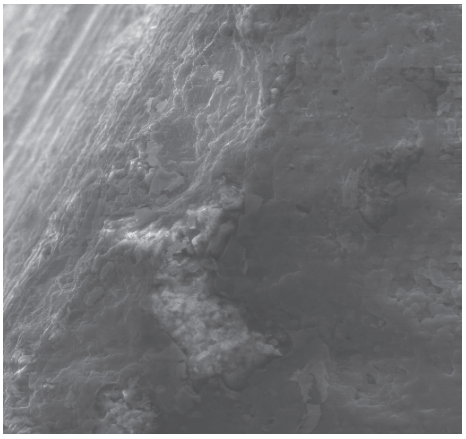

Fig. 23. Scanning electron micrograph for MQL lubri-refrigeration tests (1000x)

Analysing Figure 23, it can be seen that, when using MQL lubri-refrigeration, ductile material removal mode prevailed, which provided otpimal conditions of surface finishing, in relation to material strength, due to the reduced presence of microcracks, which are stress concentration agents.
The best surface characterization of the ground workpiece A melhor caracterização da superfície da peça retificada com a refrigeração utilizando a técnica do MQL em relação à peça retificada com a refrigeração convencional pode ser explicada pelo maior poder lubrificante do óleo utilizado na técnica do MQL em comparação ao fluido de corte emulsificado utilizado na refrigeração convencional.

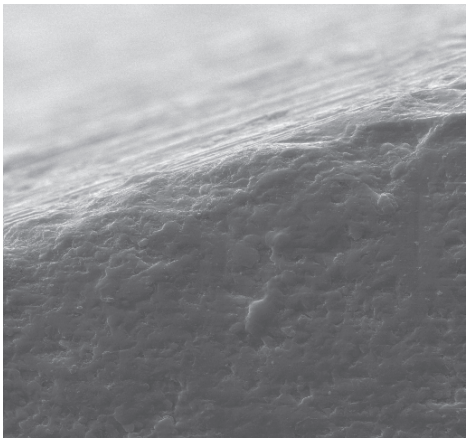

Fig. 24. Scanning electron micrograph for MQL technique with tangent wheel cleaning (1000x)

When observing Figure 24, it can be noticed that ductile mode of material removal also prevailed, due to the use of the same cutting fluid as when applying traditional MQL. Moreover, this finishing surface is even better than when using MQL without Wheel cleaning, because this method could effectively remove the grout lodged in the pores, providing consequently better surface finishing.

2.3.7 Conclusions

A general analysis of the presented results indicates that conventional lubri-refrigeration is the method which provided better results for surface roughness, roundness and wheel wear. However, MQL with wheel cleaning system is also viable, when comparing to traditional MQL, since it provided better results concerning surface quality and wheel wear, in comparison with the latter.
The tangent jet from the wheel cleaning system was the best incidence angle tested. It clearly improved MQL technique; however, it could not provide results as good as when using conventional lubri-refrigeration. Nevertheless, MQL with wheel cleaning system has its own advantages, when concerning environmental and health hazards of cutting fluids,

combining the vantages provided by MQL with better results, closer to the conventional lubri-refrigeration.
Grinding power presented inversely proportional results, when comparing to surface roughness, diametral wheel wear and roundness, for the MQL with wheel cleaning jet. This is due to the fact that, besides the influence of material removal, there is also the influence of fluid flow forces from the air jet (wheel cleaning system). The higher the cleaning efficiency, higher grinding power values can be observed.
Thus, it is possible to replace traditional lubri-refrigeration methods for new ones, as when using MQL with compressed air jets which, directed to the cutting surface, aim to clean the wheel, which improves its performance for the external cylindrical grinding.

3. Conclusions

As can be seen, minimum quantity lubrication – MQL can be widely applied in different machining processes, including grinding (in many different application modes). The increasing need of sustainable manufacture stimulated the researchers (and the research itself), for it was aimed to study alternative lubri-cooling methods, such as the wheel cleaning and MQL with water, when grinding advanced ceramics.
Nevertheless, if carefully applied in grinding, minimum quantity lubrication can provide satisfactory results concerning surface quality and microstructural integrity of the ceramics workpieces. Moreover, it results in environmentally friendly and technologically relevant gains.
An open door for future research in this branch is the optimization of nozzles, cutting fluid composition and control of the machining parameters, allied with some computational modeling and simulation concerning thermal distribution and fluid flow.
In addition, cost estimations should be done for each case, in order to enable more efficient applications of MQL in ceramic grinding. The costs related to this technology can be offset by lack of need for maintenance and disposal of cutting fluid, which today represents a considerable cost, due to the current standards aiming the environment preservation.

4. Acknowledgements

The authors are indebted to Sao Paulo State University, and to FAPESP and CNPq (Brazil) for its financial support of the researches.

5. References

Hafenbraedl, D. & Malkin, S. (2001). Technology environmentally correct for internal cylindrical grinding, *Machines and Metals Magazine*, pp. 40-55, ISSN 0025-2700

Heisel, U.; Lutz, D.; Wassmer, R. & Walter, U. (1998). The minimum quantity lubricant technique and its application in cutting processes, *Machines and Metals Magazine*, No.386, pp 22-38, ISSN 0025-2700

Itoigawa, F.; Childs, T. H. C.; Nakamura, T. & Belluco, W. (2006). Effects and mechanisms in minimal quantity lubrication machining of an aluminum alloy, *Wear,* Vol.260, No.3, pp. 339-344, ISSN 0043-1648

Klocke, F. & Eisenblätter, G. (1997). Dry Cutting, *CIRP Annals – Manufacturing Technology*, Vol.46, No.2, pp. 519-526, ISSN 0007-8506

Klocke, F.; Beck, T.; Eisenblätter, G.; Fritsch, R.; Lung, D. & Pöhls, M. (2000). Applications of minimal quantity lubrication (MQL) in cutting and grinding, *Proceedings of the 12th International Colloquium Tribology Industrial and Automotive Lubrication*, Technische Akademie Esslingen, Germany.

Lee, E. S. & Kim, N. H. (2001). A study on the machining characteristics in the external plunge grinding using the current signal of the spindle motor, *International Journal of Machine Tools and Manufacture*, Vol.41, No.7, pp. 937-951, ISSN 0890-6955

Lee, S. W.; Lee, Y.C.; Jeond, H. D. & Choi, H. Z. (2002) The effect of high pressure air jet on form accuracy in slot grinding, *Journal of Materials Processing Technology*, Vol.128, No.1-3, pp. 67–72, ISSN 0924-0136

Liao, Y. S.; Luo, S. Y. & Yang, T. H. (2000). A thermal model of the wet grinding process, *Journal of Materials Processing Technology*, Vol.101, No.1-3, pp. 137-145, ISSN 0924-0136

Malkin, S. (1989). *Grinding Technology: theory and application of machining with abrasives*, 1. Ed., Chichester, Ellis Horwood Ltd., ISBN 087-263-480-9

Malkin, S. & Hwang, T. W. (1996). Grinding Mechanisms for ceramics, *CIRP Annals – Manufacturing Technology,* Vol.45, No.2, pp.569-580, ISSN 0007-8506

Mamalis, A. G.; Kundrak, J.; Gyani, K. & Horvath, M. (2002) On the Precision Grinding of Advanced Ceramics, *International Jounal of Advanced Manufacturing Technology*, Vol.20, No.4, pp. 255–258, ISSN 1433-3015

Ramesh, K.; Yeo, S. H.; Gowri, S. & Zhoul, L. (2001) Experimental Evaluation of Super High Speed Grinding of Advanced Ceramics, *International Jounal of Advanced Manufacturing Technology*, Vol.17, No.2, pp. 87–92, ISSN 1433-3015

Silva, L. R.; Bianchi, E. C.; Catai, R. E.; Fusse, R. Y.; França, T. V. & Aguiar, P. R. (2005). Study on the behavior of the minimum quantity lubricant – MQL technique under different lubrication and cooling conditions when grinding ABNT 4340 steel, *Journal of the Brazilian Society of Mechanical Sciences and Engineering*, Vol. 27, pp. 192-199, ISSN 1678-5878

Silva, L. R.; Bianchi, E. C.; Fusse, R. Y.; Catai, R. E.;; França, T. V. & Aguiar, P. R. (2007). Analysis of surface integrity for minimum quantity lubricant – MQL in grinding, *International Journal of Machine Tools and Manufacture*, Vol.47, No.2, pp. 412-418, ISSN 0890-6955

Tawakoli, T. & Azarhoushang, B. (2008). Influence of ultrasonic vibrations on dry grinding of soft steel, *International Journal of Machine Tools and Manufacture*, Vol.48, No.14, pp. 1585-1591, ISSN 0890-6955

Tawakoli, T. (2003). Minimum coolant lubrication in grinding, *Industrial Diamond Review*, No.1, pp. 60-65, ISSN 0989-8294

Tawakoli, T.; Hadad, M. J.; Sadeghi, M. H.; Daneshi, A.; Stöckert, S. & Rasifard, A. (2009). An experimental investigation of the effects of workpiece and grinding parameters on minimum quantity lubrication – MQL grinding, *International*

Journal of Machine Tools and Manufacture, Vol.49, No.12-13, pp. 924-932, ISSN 0890-6955

Webster, J. (1995). Selection of coolant type and application technique in grinding, *Supergrind*, pp. 205-218

Yoshimura, H.; Itoigawa, F.; Nakamura, T. & Niwa, K. (2005). Development of Nozzle System for Oil-on-Water Droplet Metalworking Fluid and Its Application on Practical Production Line, *JSME International Journal Series C*, Vol.48, pp. 723-729, ISSN 1347-538X

15

Reducibility of Ceria-Based Materials Exposed to Fuels and under Fuel/Air Gradients

Domingo Pérez-Coll[1], Pedro Núñez[2] and Jorge R. Frade[3]
[1]*Instituto de Cerámica y Vidrio (CSIC),*
[2]*Universidad de La Laguna,*
[3]*Universidade de Aveiro,*
[3]*Portugal*
[1,2]*Spain*

1. Introduction

Ceria-based materials have been extensively studied in recent years for their potential use as solid electrolytes for alternative solid oxide fuel cells (SOFC) concepts, with emphasis on intermediate temperature SOFCs (Steele, 2000), single chamber SOFC (Yano et al., 2007), etc. However, the decrease in the oxygen partial pressure exerted by the presence of the fuel increases the non-stoichiometry accompanied by the reduction of Ce^{4+} to Ce^{3+}. In these cases, reducibility of ceria-based solid electrolytes is a critical limitation, mainly because this implies onset of electronic conductivity (Blumenthal & Hofmaier, 1974; Blumenthal & Sharma, 1975; Tuller & Nowick, 1977; Navarro et al., 1997) and corresponding risks of internal short circuiting and decrease in cell voltage. The reducibility of cerias is affected by trivalent additives and their contents (Wang et al. 1997; Wang et al. 1998; Kobayashi et al., 1999), altering the mixed transport properties under low values of oxygen pressure according to the defect chemistry models. However some discrepancies are found in literature regarding the level of oxygen losses as well as the electronic conductivity (Mogensen et al., 2000; Zachau-Christiansen et al., 1996). On the other hand, ceria and related materials are also promising catalysts, including use as SOFC anode components for hydrocarbon conversion (McIntosh & Gorte, 2004; Tsipis et al., 2004). Performance in these prospective applications is likely to be promoted by the redox behaviour of cerias. Thus, one has studied the onset of electronic conductivity of the most promising ceria-based materials $Ce_{1-x}Gd_xO_{2-0.5x-\Delta\delta}$ (CGO) and $Ce_{1-x}Sm_xO_{2-0.5x-\Delta\delta}$ (CSO), including its dependence on temperature and composition (Pérez-Coll et al., 2004; Abrantes et al., 2003). The impact of low temperature sintering with suitable additives on the onset of n-type contribution under reducing conditions has also been studied (Fagg et al., 2003). In this chapter the dependence on oxygen partial is revised in detail, and corresponding effects imposed by fuels such as hydrogen or methane are examined by taking into account thermodynamic correlations between oxygen partial pressure and fuel conditions. This is extended for fuel/electrolyte/air gradients, as expected for SOFC operation.

Ceria based materials also undergo significant chemical expansion upon reduction of Ce^{4+} to Ce^{3+}, causing non negligible strain under reducing conditions and important chemically induced stresses under fuel/air gradients. Thus, one re-examined strain/stress effects on combining the dependence of oxygen stoichiometry on working conditions with reported results of chemical expansion coefficient and relevant elastic properties of ceria-based materials. This included: (i) chemical strain in ceria-based anode components, and its dependence on temperature, fuel composition and electrode overpotential; (ii) strain/stress effects on ceria-based electrolytes fuel/air gradients, and other conditions imposed by SOFC operation.

2. Changes in oxygen stoichiometry under reducing conditions

2.1 Defect chemistry

The ionic conduction character in ceria-based compounds is generated by the introduction of aliovalent cations in the CeO_2 fluorite structure giving rise to the creation of oxygen vacancies due to a charge compensation mechanism (Yahiro et al., 1989; Mogensen et al., 2000). In particular rare earth additives are commonly employed to produce oxygen vacancies according to:

$$Ln_2O_3 \xrightarrow{CeO_2} 2Ln_{Ce}' + V_O^{\bullet\bullet} + 3O_O^x \tag{1}$$

This combines with oxygen stoichiometry changes under low values of oxygen partial pressure, due to partial reduction of ceria as follows:

$$O_O^x + 2Ce_{Ce}^x \Leftrightarrow \frac{1}{2}O_2(gas) + V_O^{\bullet\bullet} + 2Ce_{Ce}' \tag{2}$$

the last relation assumes that electrons resulting from oxygen exchange are localized as trivalent cerium ions Ce^{3+}, (Panhans & Blumenthal, 1993; Steele, 2000; Mogensen, 2000) producing small polarons (Tuller & Nowick, 1977; Panhans & Blumenthal, 1993; Navarro et al., 1997). If we assume that there is no interaction between defects, the mass action law of Eq. 2 is expressed as:

$$K_R = \frac{[V_O^{\bullet\bullet}][Ce_{Ce}']^2 pO_2^{1/2}}{[O_O^x][Ce_{Ce}^x]^2} \tag{3}$$

The electroneutrality condition for the most relevant defects is expressed as:

$$2[V_O^{\bullet\bullet}] = [Ce_{Ce}'] + [Gd_{Ce}'] \tag{4}$$

The concentration of the small polarons $[Ce_{Ce}']$ is directly related to the changes in oxygen stoichiometry $\Delta\delta$ according to:

$$[Ce_{Ce}'] = 2\,\Delta\delta \tag{5}$$

Recombination of Eqs. 4-5 allows one to express the concentration of remaining defects as functions of the stoichiometric changes and of the fraction of trivalent additive (x) as follows:

$$[V_O^{\bullet\bullet}] = \Delta\delta + x/2 \tag{6}$$

$$[O_O^{x}] = 2 - x/2 - \Delta\delta \tag{7}$$

$$[Ce_{Ce}^{x}] = 1 - x - 2\,\Delta\delta \tag{8}$$

and the mass action constant can be expressed as:

$$K_R = \frac{4(\Delta\delta)^2\,(\Delta\delta + x/2)\,pO_2^{1/2}}{(2 - x/2 - \Delta\delta)(1 - x - 2\Delta\delta)^2} \tag{9}$$

Equation 9 has been deduced without any assumption concerning the dependence of oxygen stoichiometry on the oxygen partial pressure, and allows one to obtain the mass action constant as function of oxygen loss. On the other hand the mass action constant relates to corresponding thermodynamic changes as:

$$\ln K_R = \frac{\Delta S_R}{R} - \frac{\Delta H_R}{RT} \tag{10}$$

which allows the determination of the entropy (ΔS_R) and the enthalpy change (ΔH_R) of reduction (Eq. 2). For low changes in oxygen loss, the oxygen nonstoichiometry is mainly determined by the trivalent-additive content ($\Delta\delta << x$), which corresponds to the ionic domain in ceria-based compounds. This produces nearly constant values for the concentration of oxygen vacancies, and validates a simpler approximation of Eq. 9, as follows:

$$\frac{K_R(2\text{-}x/2)(1\text{-}x)^2}{2x} = (\Delta\delta)^2 pO_2^{1/2} \tag{11}$$

Recombination of Eqs. 5 and 11 supplies an expression for the dependence of polaron concentration on the oxygen partial pressure according to:

$$[Ce_{Ce}'] = 2\Delta\delta \approx K_R'\, pO_2^{-1/4} \tag{12}$$

Note that Eq. 12 fails for relatively high oxygen losses and corresponding changes in oxygen stoichiometry. On the other hand, for low values of trivalent contents and/or relatively high oxygen loss ($\Delta\delta >> x$) the dependence of polaron concentration as function of the oxygen partial pressure may converge to:

$$[Ce_{Ce}'] \approx K_R''\, pO_2^{-1/6} \tag{13}$$

2.2 Determination of the oxygen loss by coulometric titration

Changes in oxygen stoichiometry are often determined by coulometric titration (Ferreira et al., 2000; Tikhonovic et al., 2002; Abrantes et al., 2003) using the cell design shown in Fig. 1. The whole electrochemical system is composed by YSZ-components. A highly-densified YSZ-tube is sealed between two YSZ-sintered pellets obtaining gas tight conditions. Powders of the compounds are introduced in a Pt-crucible which is inserted in the electrochemical cell. The YSZ-tube and one of the YSZ-pellets possess symmetrical Pt-

electrodes in the internal and the external surfaces. When the electrodes of the tube are submitted to a voltage difference, with the internal electrode under cathodic polarisation, by means of Pt-wires attached to an external d.c. source, there is a flow of oxygen ions through the YSZ-ionic conductor from the inner chamber to the external atmosphere. In this process the YSZ-tube acts as an electrochemical pump to extract oxygen, thus decrease the oxygen partial pressure inside the chamber. This imposes reduction conditions on the ceria-based material (Eq. 2), and the extent of oxygen losses can be evaluated by integrating the electrochemically pumped current. The voltage drop between both terminals of an auxiliary resistance connected in series to the electrochemical pump account for the current by means of the Ohm's law ($I=V_R/R$).

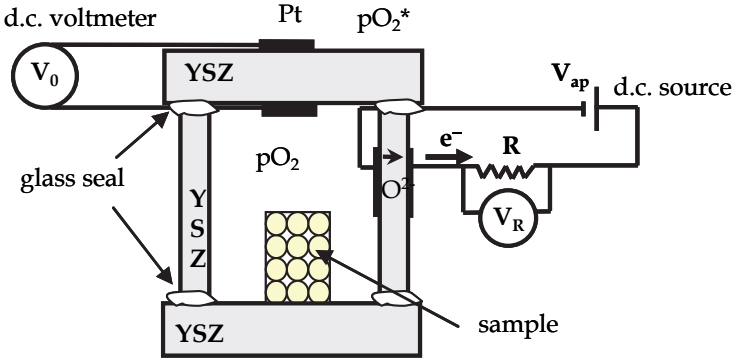

Fig. 1. Coulometric titration electrochemical cell used to determine changes in oxygen stoichiometry.

Pt-wires are also attached to the Pt-electrodes of the upper YSZ-pellet to connect to a d.c. voltmeter. In this situation the YSZ-pellet acts as a pO_2 probe and allows one to monitor the oxygen partial pressure inside the chamber by means of the voltage difference in both sides (V_0) according to the Nersnt equation:

$$V_0 = \frac{RT}{4F} \ln\left(\frac{pO_2^*}{pO_2}\right) \tag{14}$$

where F is the Faraday constant and pO_2* and pO_2 are the oxygen partial pressures of the outside atmosphere and of the inner chamber, respectively. The use of air as external atmosphere establishes pO_2*=0.21 atm. The experimental procedure consists in the application of several steps of potential to the pump, while recording transient changes until steady state conditions are restored. The overall molar amount of oxygen (O_2) extracted from the cell (chamber + stoichiometry change of the sample) between a generic step of applied potential is obtained by:

$$n_{O_2-overall} = \frac{1}{4F} \int_{t_1}^{t_2} (I(t) - I_\infty) \cdot dt \tag{15}$$

where t_1 and t_2 are the initial and the final times of the transient step, I(t) is the current through the electrochemical pump and I_∞ is the residual current when the steady-state

condition is reached; this allows one to account for possible leaks. The molar amount of oxygen (O_2) corresponding to the gas phase of the chamber after a generic step of voltage between t_1 and t_2 is determined by:

$$n_{O_2-chamber} = \frac{pO_2(t_1) - pO_2(t_2)}{RT} \cdot V_{chamber} \tag{16}$$

where $V_{chamber}$ corresponds to the volume of the chamber after the subtraction of the volume of the sample and the crucible (Fig. 1), $pO_2(t_1)$ and $pO_2(t_2)$ correspond to the oxygen partial pressures at the starting and final steady-state situations. The oxygen stoichiometry change of the sample after a generic step is determined by:

$$\Delta\delta = 2\frac{M_{CLnO}}{m_{CLnO}}\left(n_{O_2-overall} - n_{O_2-chamber}\right) \tag{17}$$

where M_{CLnO} and m_{CLnO} are the formula weight and the mass of the sample. In the experimental procedure the voltage supplied to the pump is increased in steps of 50 mV, to analyze the change in oxygen stoichiometry as a function of the oxygen partial pressure. Figure 2 shows an example of two steps of applied potential to the electrochemical pump and the corresponding values of current and voltage of the electrochemical cell as function of time. The values of stoichiometry loss between two steps of equilibrium are determined by the numerical integration of current in the corresponding transient regime. Figure 3 shows the dependence of the oxygen loss on the oxygen partial pressure for $Ce_{1-x}Gd_xO_{2-0.5x-\Delta\delta}$ (x=0, x=0.1, x=0.2, x=0.3) at 1000 ºC and 800 ºC. Results reveal that there are important stoichiometry changes at low values of oxygen partial pressure which are clearly suppressed at lower temperatures, due to the decrease of equilibrium constant (Eq. 11). The extent of oxygen stoichiometry changes in ceria-based materials may account for significant oxygen storage ability with impact on catalytic or electrocatalytic processes.

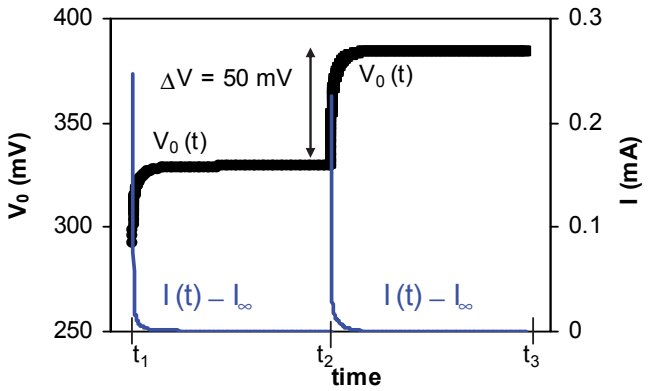

Fig. 2. Time dependence of current and voltage in the coulometric titration cell for two steps of applied potential from the d.c. source.

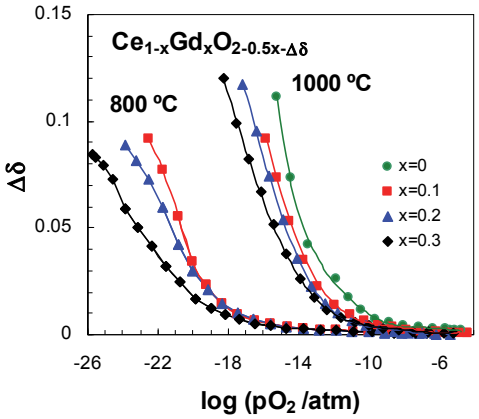

Fig. 3. Stoichiometry loss of $Ce_{1-x}Gd_xO_{2-0.5x-\Delta\delta}$ (x=0, 0.1, 0.2, 0.3) at 800 ºC and 1000 ºC as a function of the oxygen partial pressure.

Deviations from the nearly exponential behaviour are observed at very low values of oxygen partial pressure, mainly for lower temperature. An analogous behaviour was found by other authors (Riess et al., 1987; Panhans et al., 1993; Wang et al., 1998) and could be due to deviations from the simple defect chemistry model, or limitations of the experimental procedure. Though the steady state current I_∞ should account for residual permeability through the YSZ cell components, this may not be the case for deviations from material/gas equilibrium or differences between the measured emf and the true conditions inside the cell. Figure 3 also shows that the introduction of the trivalent dopant (Gd^{3+}) in the CeO_2 fluorite structure decreases the reducibility and the effect is more pronounced for higher contents of dopant. Samples with higher contents of Gd^{3+} possess higher concentrations of extrinsic oxygen vacancies (Eq. 1); this should decrease the reducibility of the compounds in order to preserve the equilibrium in Eq. 2. On the other hand, coulometric titration results could be conveniently treated (Abrantes et al., 2003) to obtain an estimation of the mass action constant according to Eq. 9, without any assumption concerning the dependence of the oxygen loss on the oxygen partial pressure; this is represented in Fig. 4 for $Ce_{1-x}Gd_xO_{2-0.5x-\Delta\delta}$ (x=0.1, x=0.2, x=0.3) at 800, 900 and 1000 ºC.

Fig. 4 shows that changes in stoichiometry do not produce considerable effects in the equilibrium constant. Deviations from the ideal model are mainly observed at lower temperature for sample with higher content of extrinsic vacancies (x=0.3), which could be related to defect interactions between oxygen vacancies and trivalent cations as Gd^{3+} or even Ce^{3+} (Schneider, 1997; Butler, 1983; Catlow, 1983; Minervini, 1999) probably because they are far from dilute conditions. Moreover, Fig. 4 shows similar values for samples with different contents of Gd^{3+} as observed in Fig. 5 for the effect of temperature on the mass action constant. Typical values of enthalpy of reduction in the range 410-430 KJ/mol are extracted by using Eq. 10, which are comparable to other results reported in literature (Wang et al., 1997; Wang et al. 1998; Kobayashi et al., 1999; Kudo & Obayashi, 1976; Schneider et al., 1997). The simple defect chemistry behaviour can be used to model the theoretical dependence of oxygen loss on oxygen partial pressure (Eq. 9), allowing one to obtain the values of K_R from experimental data (Fig. 4) and to use this to describe the dependence of

defect concentrations as ([Ce_{Ce}^{x}], [Ce_{Ce}'] and [$V_O^{\bullet\bullet}$]) on working conditions (Eqs. 5-8). This dependence is shown in Fig. 6.

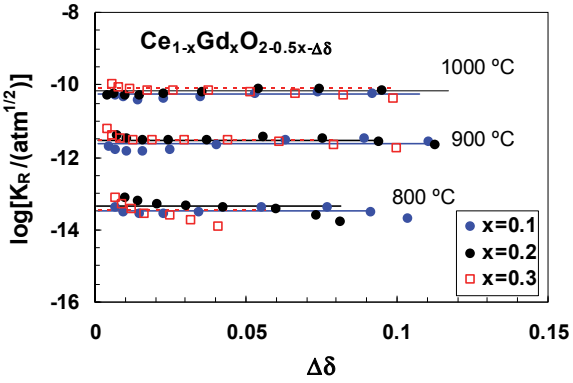

Fig. 4. Estimation of the mass action constant as a function of the oxygen loss for $Ce_{1-x}Gd_xO_{2-0.5x-\Delta\delta}$ (x=0.1, x=0.2, x=0.3).

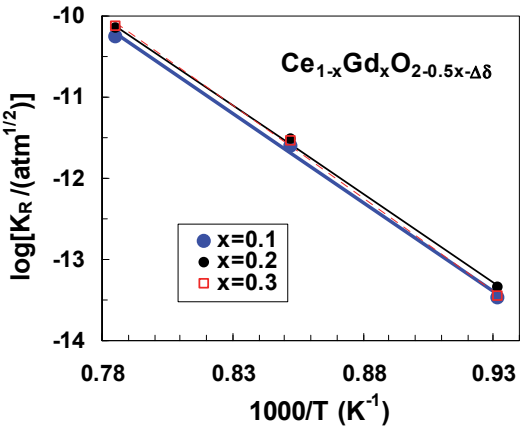

Fig. 5. Temperature dependence of the mass action constant for $Ce_{1-x}Gd_xO_{2-0.5x-\Delta\delta}$ (x=0.1, x=0.2, x=0.3).

The simple defect chemistry model seems to fit well experimental results for moderately reducing conditions, whereas deviations are observed for very reducing conditions, as previously mentioned. Though Eq. 9 was obtained without any *a priori* assumption concerning the dependence of defect concentration on the oxygen partial pressure, the

actual results still show transition for the dependence of log ([Ce_{Ce}']) on log (pO_2) with -1/4 slope, for oxidizing conditions (Eq. 12), to -1/6 for very reducing conditions (Eq. 13).

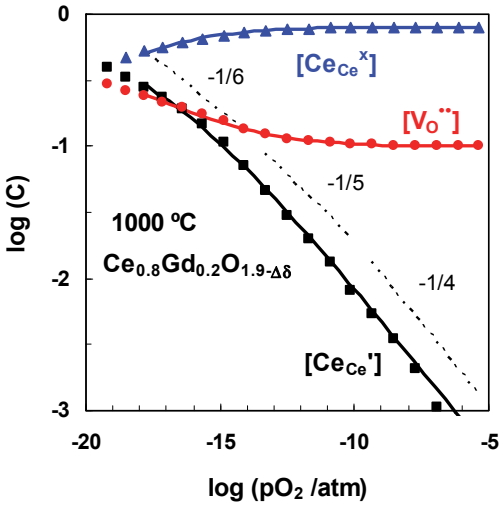

Fig. 6. Defect chemistry concentrations (molar fractions) as functions of oxygen partial pressure for $Ce_{0.8}Gd_{0.2}O_{1.9-\Delta\delta}$ at 1000 ºC. Single points correspond to the experimental values obtained from coulometric titration, whereas straight lines correspond to theoretical values using the simple defect chemistry model.

3. Electronic conductivity under reducing conditions

3.1 Theoretical analysis

The electronic transport in ceria-based materials is attributed to thermally activated-polaron hopping (Tuller & Nowick, 1977; Panhans & Blumenthal, 1993; Suzuki et al., 2002), and the electronic conductivity is expressed as:

$$\sigma_n = q_e \; n \; \mu_e \tag{18}$$

where q_e, n and μ_e are the charge, the concentration and the mobility of the electron. Since electrons are localized on trivalent cerium it is usually assumed that n= [Ce_{Ce}'], and mobility of electrons for the thermally activated polarons is expressed as follows:

$$\mu_e = \frac{\mu_{e,0}}{T} \exp\left(\frac{-\Delta H_m}{RT}\right) \tag{19}$$

where ΔH_m is the enthalpy of mobility of polarons. As noted by Navarro et al. (Navarro et al., 1997) the hopping conductivity should be proportional to [Ce_{Ce}'][Ce_{Ce}^x], which describes the probability of the small polaron to have a Ce^{4+} as neighbour, and thus to provide charge transport. However, the mole fraction [Ce_{Ce}^x] is usually included in the mobility term. Under the assumption that the oxygen nonstoichiometry is determined by the trivalent content ($\Delta\delta << x$; Eqs. 11-12), the expression for electronic conductivity reads:

$$\sigma_n = \frac{\sigma_{e,0}}{T} \exp\left(-\frac{(\Delta H_m + \Delta H_R / 2)}{RT}\right) pO_2^{-1/4} \quad (20)$$

As consequence, the activation energy for hopping conduction is comprised of the enthalpy of mobility and half enthalpy of reduction.

3.2 Measurement of electronic conductivity by Hebb-Wagner ion-blocking

The determination of the electronic conductivity as function of the oxygen partial pressure requires a special procedure to separate the electronic and ionic contributions. The Hebb-Wagner procedure is a suitable technique based on blocking the transport of oxygen ions through the membrane submitted to a gradient of oxygen partial pressure (Hebb, 1952; Wagner, 1957; Navarro et al. 1997; Lübke & Wiemhoefer, 1999). For this purpose, symmetrical Pt-electrodes are placed on both surfaces of a gas tight ceria sample, and an alumina impervious disk is then sealed on one of the electrodes, avoiding oxygen leakage to the internal chamber (Fig. 7). Two Pt wires are attached to the outer electrode and another two wires are attached to the inner. One pair of these wires are connected to the d.c. source to supply the voltage difference between the inner and the outer electrodes, thus providing the oxygen partial pressure gradient, and the other pair is connected to a voltmeter to read the voltage difference in the pellet, acting as sensor of pO_2.

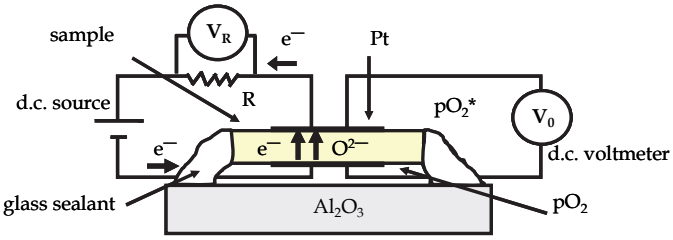

Fig. 7. Schematic view of the ion-blocking experimental setup.

When the internal electrode is cathodically polarized, oxygen ions flow through the membrane from the inner chamber to the outside atmosphere until steady-state conditions are reached. Since the blocking electrode prevents ion transport, the residual current reduces to the electronic contribution, after a transient regime (Fig. 8).

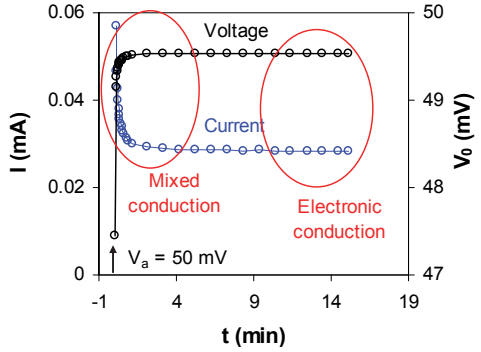

Fig. 8. Electrical current and voltage in the sample after applying a generic potential of 50 mV from the d.c. source.

The procedure includes application of cathodic voltages to the internal electrode from 50 to 1200 mV in steps of 50 mV, thus decreasing the oxygen partial pressure in the chamber from air to very reducing conditions. The voltage difference between the two electrodes is related to the oxygen partial pressure gradient by the Nernst equation (Eq. 14). An auxiliary resistance is connected in series to the sample and the d.c. source to account for the electrical current by means of the voltage drop at the former (V_R). Figure 9 shows the current-voltage curves of $Ce_{1-x}Gd_xO_{2-0.5x-\Delta\delta}$ (x=0, x=0.1, x=0.2, x=0.3) under the steady-state situation in ion-blocking conditions. The onset of electronic conduction is observed for moderate reducing conditions, and it is displaced towards more reducing conditions when the content of the trivalent-dopant increases, suggesting a decrease of the n-type electronic conductivity.

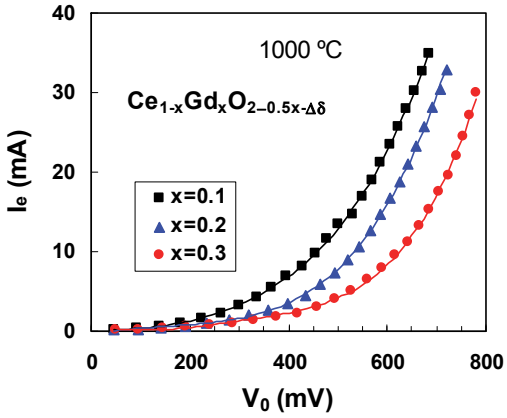

Fig. 9. Steady-state current-voltage for $Ce_{1-x}Gd_xO_{2-0.5x-\Delta\delta}$ (x=0.1, x=0.2, x=0.3) at 1000 ºC.

The electronic conductivity in the reduced side of the sample (σ_e) can be obtained by differentiation of the current against the voltage difference of the sample in steady-state conditions (Lübke & Wiemhoefer, 1999; Abrantes et al., 2003) according to:

$$\sigma_e = \frac{L}{A}\frac{dI_e}{dV_0} \tag{21}$$

where L and A are the thickness of the pellet and the area of the electrodes and I_e and V_0 are the current (electronic current) and the voltage of the pellet in steady-state conditions (ion-blocking). Note that the differentiation performed to the voltage gradient across the sample is related to changes in the oxygen partial pressure in the side of the chamber. At relatively high values of oxygen partial pressure (moderate reducing conditions) the dependence of the n-type electronic conductivity on the oxygen partial pressure could be assumed to follow a -1/4 single power law (Eq. 20). In similar conditions, the p-type electronic conductivity could be assumed to follow a +1/4 power law as function of the oxygen partial pressure (Panhans & Blumenthal, 1993), yielding the following dependence for total electronic conductivity:

$$\sigma_e = \sigma_n^* \left(\frac{pO_2}{pO_2^*} \right)^{-1/4} + \sigma_p^* \left(\frac{pO_2}{pO_2^*} \right)^{1/4} \quad (22)$$

where σ_n^* and σ_p^* are the n-type and p-type electronic conductivities at the reference oxygen partial pressure (pO_2^*). Recombination of Eqs. 14 and 22 yields the following relation between electronic current and applied voltage (Navarro et al. 1997):

$$I_e = \frac{ART}{FL} \left\{ \sigma_n^* \left[\exp\left(\frac{FV_0}{RT} \right) - 1 \right] + \sigma_p^* \left[1 - \exp\left(\frac{FV_0}{RT} \right) \right] \right\} \quad (23)$$

Experimental results were also fitted to Eq. 23 to show that this approximation is only acceptable for oxidising or moderate reducing conditions (Fig. 10). Representative electronic conductivity results are shown in Fig. 11 for the ceria-samaria system.

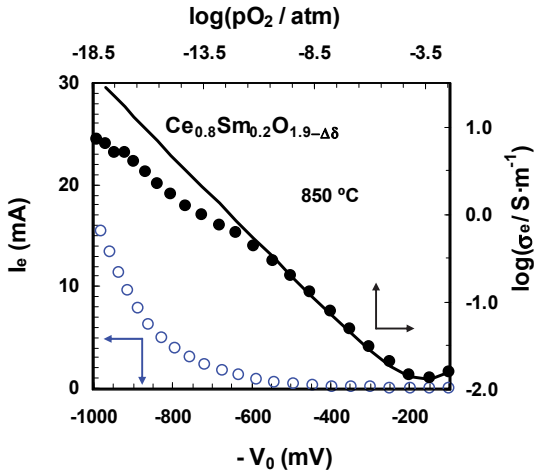

Fig. 10. Steady-state current-voltage curves for $Ce_{0.8}Sm_{0.2}O_{1.9-\Delta\delta}$ (open symbols) and corresponding electronic conductivity (closed symbols for secondary axes). The solid line represents $\pm 1/4$ power laws for the n- and p-type electronic conductivities (Eqs. 21 and 23).

Figure 11 shows that n-type electronic conductivity predominates under strongly reducing conditions, with a slight p-type electronic contribution for oxidising conditions. The decrease in contents of aliovalent additive increases the n-type electronic conductivity, mainly for moderately reducing conditions, due to the higher reducibility of the samples as argued in section 2.2. Moreover, the onset of p-type electronic conductivity is displaced towards higher pO_2 values, in good agree with the lower concentration of holes for samples with lower oxygen vacancy concentration under oxidising conditions, according to:

$$\frac{1}{2}O_2(gas) + V_O^{\bullet\bullet} \Leftrightarrow O_O^x + 2h^{\bullet} \quad (24)$$

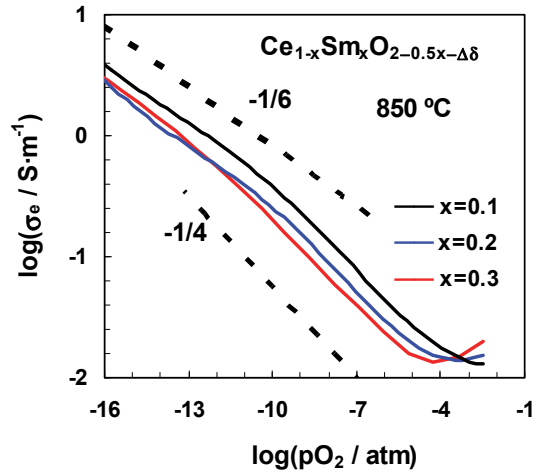

Fig. 11. Electronic conductivity versus oxygen partial pressure for $Ce_{1-x}Sm_xO_{2-0.5x-\Delta\delta}$ (x=0.1, x=0.2, x=0.3) extracted from differentiation of current-voltage curves given by Eq. 21.

Results of electronic conductivity under reducing conditions could be also analysed as function of temperature at fixed values of oxygen partial pressure (Eq. 20). Figure 12 shows results for ceria-samaria samples at $pO_2=10^{-10}$ atm.

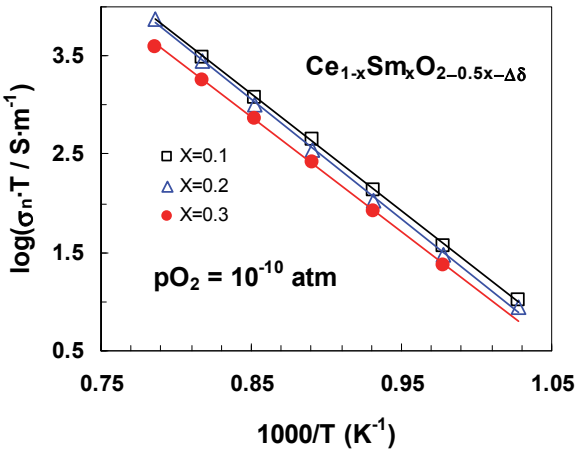

Fig. 12. Arrhenius plot of n-type electronic conductivity of ceria-samaria at $pO_2=10^{-10}$ atm.

The temperature dependence shown in Fig. 12 was used to estimate the activation energy of hopping of small polarons. Values in the range of 2.2-2.4 eV were obtained at $pO_2= 10^{-10}$ atm, which agree very well with our values of 2.3-2.4 eV previously reported for ceria-gadolinia (Pérez-Coll et al., 2007) and with those reported by other authors for cerias with different

lanthanides (Lübke & Wiemhofer, 1999; Steele, 2000; Xiong et al., 2004). According to Eq. 20 and using the results of enthalpy of reduction obtained in section 2.2 we have estimated values of activation energy for polaron mobility in the range 0.2-0.6 eV (Pérez-Coll et al., 2007).

The impact of reducibility of ceria-based solid electrolytes is determined mainly by the average transport number under high gradients of oxygen partial pressure, or corresponding dependence of average electronic conductivity on Nernst potential (Eq. 14) under steady-state conditions according to (Pérez-Coll et al., 2007):

$$\sigma_{e,av} = \frac{L}{A}\frac{I_e}{V_0} \tag{25}$$

Equation 25 directly relates the electronic conductivity with the voltage difference between both sides of the pellet. For this reason it describes the average electronic conductivity of the sample submitted to a difference of oxygen partial pressure (i.e. pO_2^*/ceria-sample/pO_2).

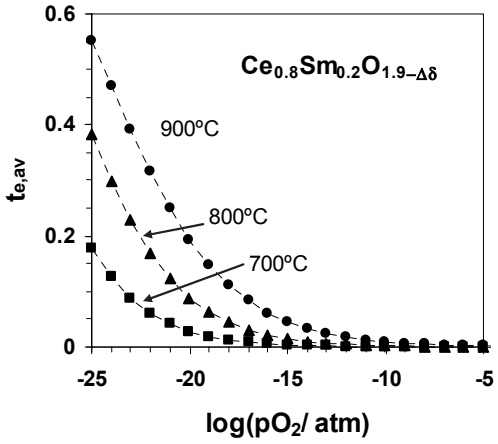

Fig. 13. Electronic transport number averaged across the mixed conducting membrane submitted to ion-blocking conditions as function of the oxygen partial pressure for $Ce_{0.8}Sm_{0.2}O_{1.9-\Delta\delta}$ at 700, 800 and 900 ºC

The electronic transport number could be averaged across the sample as follows:

$$t_{e,av} = \frac{\sigma_{e,av}}{\sigma_i + \sigma_{e,av}} \tag{26}$$

where σ_i corresponds to ionic conductivity averaged across the membrane, which is usually assumed to be constant. Figure 13 shows an example of the effect of oxygen partial pressure and temperature on the averaged electronic transport number of $Ce_{0.8}Sm_{0.2}O_{1.9-\Delta\delta}$ estimated from ion-blocking and impedance spectroscopy results. The electronic character is revealed by substantial increase in the electronic transport number for very reducing conditions. However, due to the higher activation energy values for electronic conduction in the order

of 2.2-2.4 eV compared to those of ionic conduction in the order of 0.5-0.7 eV (Pérez-Coll et al., 2006) the averaged electronic transference number is decreased when temperature is lowered.

4. Fuel operating conditions

Previous sections emphasized that reduction of tetravalent cerium and thus the electronic conductivity in ceria based materials is highly influenced by the oxygen partial pressure. Under realistic situation in a SOFC the electrochemical reactions at the fuel electrode generate reaction products in the anode and corresponding changes in gas composition vs oxygen chemical potential (Frade et al. 2004). Thus interaction of the atmosphere with the anode materials and also with the contacting electrolyte surface will modify their electrical and electrochemical properties. In fact, one could expect different levels of fuel conversion along the anode surface that would be reflected in changes in the mixed transport properties of ceria-based materials, affecting the local performance of the SOFC due to non-uniform distribution of current density and corresponding heat management issues.

4.1 Dependence on conversion of hydrogen

The use of hydrogen as fuel in a SOFC produces water at the anode (for an oxide-ion conductor electrolyte) due to the reaction with the oxygen ions transported through the electrolyte and electronic transport in the external circuit (Fig. 14). Working conditions imposed by fuel conversion can be assessed by assuming nearly equilibrium for the overall reaction:

$$2\,H_2 + O_2 \Leftrightarrow H_2O \tag{27}$$

and corresponding mass action constant:

$$K = \frac{(pH_2O)^2}{pO_2(pH_2)^2} \tag{28}$$

where pH_2O, pO_2 and pH_2 are partial pressures of water, oxygen and hydrogen, respectively. Moreover, the relation between the equilibrium constant and the Gibbs free energy (ΔG) is expressed as:

$$K = \exp\left(-\frac{\Delta G}{RT}\right) \tag{29}$$

Recombination of Eqs. 28-29 allows one to express the oxygen partial pressure as a function of steam to hydrogen ratio as follows:

$$pO_2 = \left(\frac{pH_2O}{pH_2}\right)^2 \exp\left(\frac{\Delta G}{RT}\right) \tag{30}$$

Equation 30 shows that local variations in steam to hydrogen ratio have considerable effects on the oxygen partial pressure.

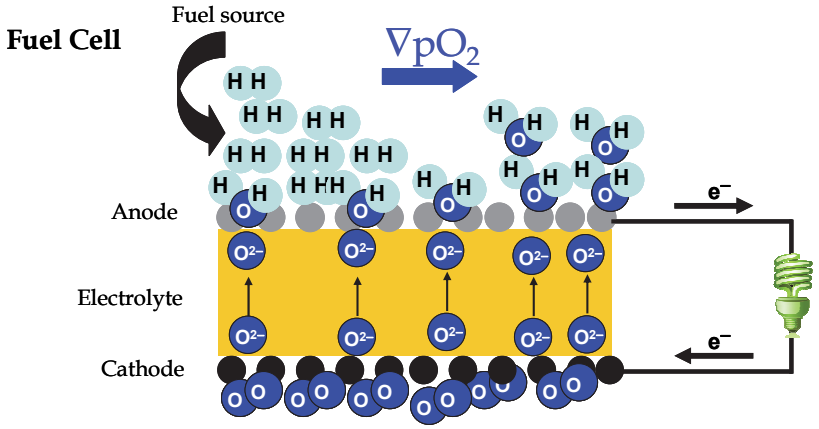

Fig. 14. Representation of a possible situation in a SOFC with different levels of conversion and different gas composition at the anode.

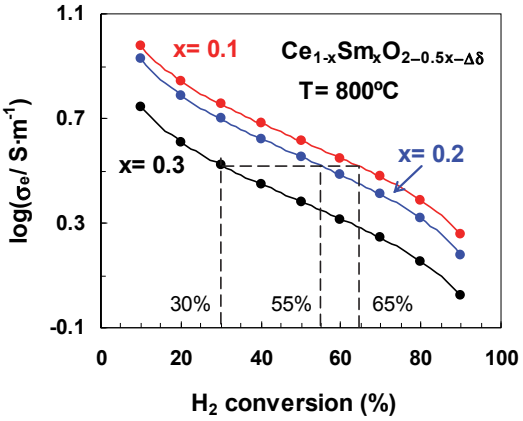

Fig. 15. Electronic conductivity in the reduced side of the samples as a function of the hydrogen conversion along the surface of the fuel side in the cell for a Sm-doped ceria system at 800 ºC.

Dependence of oxygen partial pressure on hydrogen conversion should, thus, be reflected in considerable changes in the electronic properties of ceria-based materials as illustrated in Fig. 15 for ceria-samaria electrolytes. The increase in the hydrogen conversion has the effect of lowering the electronic conductivity of the ceria-based materials as the atmosphere becomes less reducing. In extreme situations the electronic conductivity could be decreased by 5 to 6 times when the hydrogen conversion is increased from 10% to 90%. On the other hand, in spite of differences in electronic behaviour for samples doped with different contents of aliovalent cations, changes in hydrogen conversion may suppress the differences. The onset of electronic conductivity has also effects on the open cell voltage of

the mixed conducting membrane (OCV_{mc}), which can be estimated in a first approximation as:

$$OCV_{mc} \approx OCV_0 \left(1 - t_{e,av}\right) \tag{31}$$

where OCV_0 is the ideal open cell voltage for a pure ionic conductor (Eq. 14). Averaged electronic transport numbers of the mixed conducting membranes estimated from Eq. 26 could be recombinated with Eq. 30 to be represented as a function of the hydrogen:steam ratio (Fig. 16). It is observed that the increase in the H_2:H_2O ratio increases considerably the electronic transference number, due to more severe reducing conditions, mainly at higher temperature and for lower values of Sm-content. Values of averaged transport number were also used to estimate the open cell voltage as function of hydrogen:steam ratio according to Eq. 31 and some results obtained at 700 ºC are represented in Fig. 17.

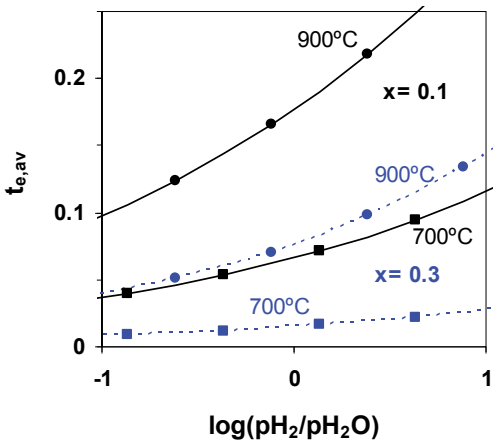

Fig. 16. Averaged electronic transport number at 700 and 900 ºC as a function of hydrogen:steam ratio in the mixture H_2+H_2O, for different Sm-contents in the system $Ce_{1-x}Sm_xO_{2-0.5x-\Delta\delta}$. [Continuous line: x= 0.1; dashed line: x=0.3)]

Figure 17 evidences that different mixtures of H_2+H_2O produce important changes in the open cell voltage of the system. In spite of the relatively low temperature of 700 ºC, we can see substantial differences between the ideal open cell voltage and the current open cell voltage of the mixed conducting membrane. These differences are more important for higher values of H_2:H_2O ratio and also for lower contents of trivalent dopant, according to the higher values of averaged electronic transport numbers (Fig. 16). Nevertheless, onset of mixed conductivity has recognized impact on electrocatalytic processes, which justifies its use in cermet anodes (Marina et al, 1999). Oxygen stoichiometry changes, and corresponding oxygen storage ability, may even contribute to minimize carbon deposition in those ceria-based anodes.

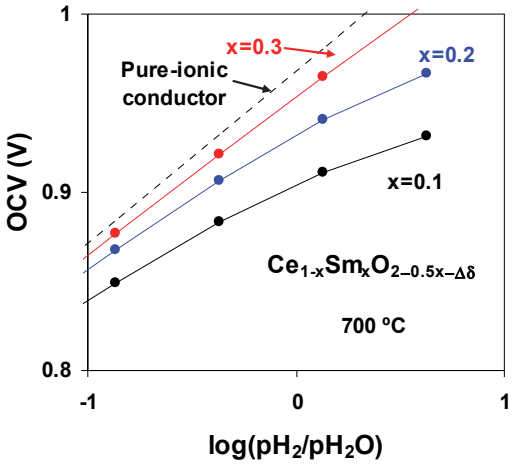

Fig. 17. Predictions of open cell voltage vs hydrogen:steam ratio for several contents of Sm in $Ce_{1-x}Sm_xO_{2-0.5x-\Delta\delta}$ at 700 °C, based on the experimental dependence of electronic transport properties.

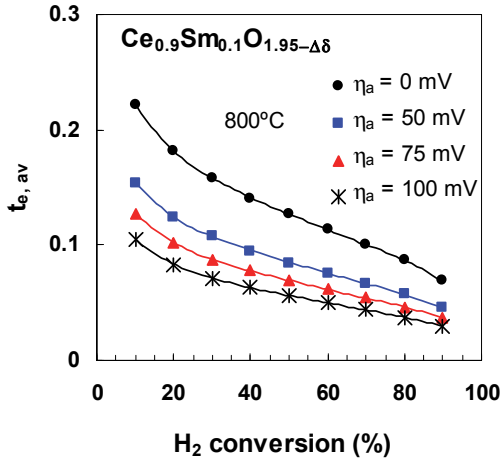

Fig. 18. Electronic transport number averaged across the membrane as function of hydrogen conversion for several values of anodic overpotential.

SOFC operation also yields overpotential contribution η_a at the anode, and corresponding changes in actual reducing conditions imposed on materials exposed to fuels, i.e. (D. Pérez-Coll et al., 2010):

$$\eta_a = \frac{RT}{4F} \ln\left(\frac{pO_2}{pO_{2\text{-}R}}\right) \tag{32}$$

where the real oxygen partial pressure imposed on materials ($pO_{2\text{-}R}$) differs from the equilibrium oxygen partial pressure in the atmosphere (Eq. 30). Figure 18 shows the values of averaged electronic transport number as function of hydrogen conversion for different values of anodic overpotentials. It is highlighted that the increase in anodic overpotential decreases the averaged electronic transport number mainly for lower values of hydrogen conversion (higher reducing conditions). In fact, the current values of electronic transport number in the range 0.22-0.07 obtained at 800 ºC for hydrogen conversions in the range 10-90%, drops considerably to 0.1-0.03 under anodic polarisation, in the same range of conversion. Thus, differences in real working conditions change considerably the mixed conducting character of ceria-based compounds.

4.2 Dependence on conversion of methane

The use of methane as fuel produces more complex reactions and correlations between oxygen chemical potential and gas composition. (Frade et al., 2004). In this sub-section one will analyse the use of methane as fuel and the impact of conversion on the mixed transport properties. The thermodynamics of methane conversion may be analysed by a combination of partial oxidation to syngas:

$$CH_4 + \frac{1}{2}O_2 \Leftrightarrow CO + 2H_2 \qquad K_1 = \frac{pCO \cdot pH_2^{\,2}}{pO_2^{\,1/2} \cdot pCH_4} \tag{33}$$

with subsequent oxidation of CO and H_2 to fully oxidised species as follows:

$$CO + \frac{1}{2}O_2 \Leftrightarrow CO_2 \qquad K_2 = \frac{pCO_2}{pO_2^{\,1/2} \cdot pCO} \tag{34}$$

$$H_2 + \frac{1}{2}O_2 \Leftrightarrow H_2O \qquad K_3 = \frac{pH_2O}{pO_2^{\,1/2} \cdot pH_2} \tag{35}$$

where K_1, K_2 and K_3 are the equilibrium constants of corresponding equilibrium reactions and p_i is the partial pressure of the corresponding species i. In real conditions, fuel conversion is preceded by steam reforming to minimize risks of methane cracking and corresponding blocking of gas channels and anode porosity. This also yields less reducing conditions and, thus, lower impact on OCV and electrochemical leaks. Actually, the equilibrium reaction under water vapor reforming could be expressed as:

$$CH_4 + H_2O \Leftrightarrow CO + 3H_2 \tag{36}$$

Equation 36 is a combination of Eqs. 33 and 35. Thus, reforming does not imply further changes in truly independent reactions required for thermodynamic analysis of methane conversion, and even contributes to validate the ideal assumption that methane cracking does not occur in fuel cell operation. The current procedure allows one to obtain partial pressures of different gas species as function of methane conversion (α) and vs oxygen partial pressure with fixed values of starting steam:methane ratio ($w_0 = H_2O:CH_4$) (Frade et

al., 2004). A revision of this procedure has also been performed to account for conditions when carbon depositions are likely to occur. This extension combines the previous reactions with the equilibrium constant for methane cracking:

$$CH_4 \Leftrightarrow C(s)+2H_2 \tag{37}$$

and additional conditions for conservation of every elemental species (C, H and O). A representative example is shown in Fig. 19, for initial H_2O:CH_4=0.5:1 ratio, at 750ºC. A vertical dashed line shows the lowest level of oxidation oxygen:methane ratio required to ensure thermodynamic inhibition of carbon deposition. Note that this transition is also revealed by discontinuities in dependence of gas fractions on O_2:CH_4 ratio. Higher steam:metane ratio is, thus, needed to minimise risks of carbon deposition.

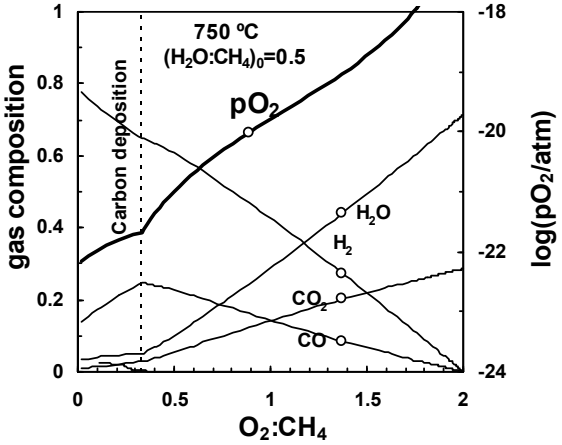

Fig. 19. Equilibrium gas composition (left vertical axis) and oxygen partial pressure (right vertical axis) at 750ºC as a function of oxygen:fuel ratio and with steam:methane ratio 0.5.

The dependence of the gas species on the oxygen partial pressure can be combined with the electronic properties of materials to obtain the electronic transport number as function of the fully oxidised species (CO_2 and H_2O). One example is shown in Fig. 20 for a $Ce_{0.8}Gd_{0.2}O_{1.9-\Delta\delta}$ sample at 750 ºC, with starting value H_2O:CH_4 = 1 and with several imposed values of anodic overpotentials. The increase in the content of fully oxidised species, and increasing anodic polarisation produces decrease of the electronic transport, thus lowering the impact of very reducing atmospheres. The analysis could be also performed paying attention to the effect produced by gradual oxidation on the cell voltage of the mixed conducting membrane. Figure 21 shows an example of the open cell voltage for $Ce_{1-x}Sm_xO_{2-0.5x-\Delta\delta}$ (x= 0.1, 0.2, 0.3) as a function of the contents of fully oxidised species. The increase of the concentration of these species reduces the open cell voltage, as expected for the decrease in oxygen chemical potential difference, with a moderate difference relative to the behaviour expected for a pure ionic conductor (Nernst potential). Yet, the contribution of this difference decreases gradually with increasing fuel oxidation, due to corresponding decrease in electronic conductivity. As a final consideration the values of open cell voltage

presented in this chapter may still deviate from the ideal behaviour for a solid electrolyte with residual electronic conductivity, due to the residual anodic polarisation caused by the internal current leakage (Frade et al., 2006 and 2008). As consequence the predictions for open cell voltage may still be somewhat overestimated, and the actual corrected solution should include these overpotential terms related to internal leakage:

$$OVC_{mc} = OCV_o(1-t_{e,av}) + \eta_{a,leak} + |\eta_{c,leak}| \quad (38)$$

where $\eta_{a,leak}$ and $\eta_{c,leak}$ are the anodic and cathodic overpotential contributions.

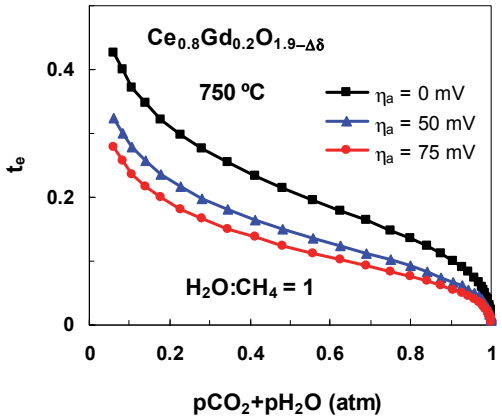

Fig. 20. Electronic transport number of $Ce_{0.8}Gd_{0.2}O_{1.9-\Delta\delta}$ at 750 ºC vs. fraction of fully oxidised species (CO_2 and H_2O) for η_h = 0, 50 and 75 mV, with initial H_2O:CH_4 = 1:1.

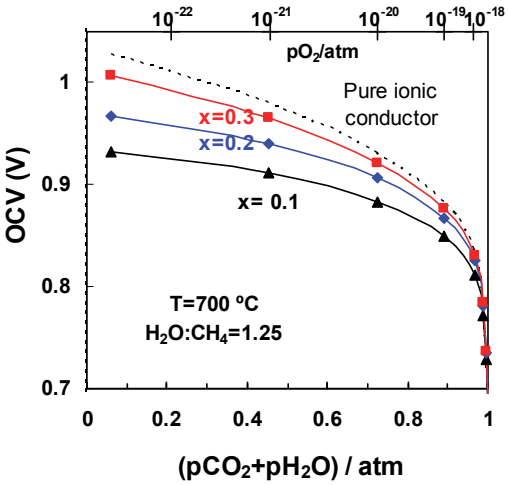

Fig. 21. Open cell voltage at 700 ºC as function of the content of pO_2+pH_2 for $Ce_{1-x}Sm_xO_{2-0.5x-\Delta\delta}$ system (x= 0.1, 0.2, 0.3) and for a starting steam:methane ratio 1.25.

5. Constraints imposed by chemical expansion

Reduction from Ce^{4+} to Ce^{3+} also causes lattice expansion, and risks of significant stresses under high gradients of chemical potential (Atkinson & Ramos, 2000). Chemical expansion is usually correlated to oxygen stoichiometry changes relative to air (reference conditions), and described by the chemical expansion coefficient $\varepsilon'_C = \Delta\varepsilon/\Delta\delta$. Representative results are shown in Fig. 22. One can see that cerias often show quite higher chemical expansion coefficient than typical perovskite mixed conductors such as LSCF (Lein et al, 2006). On combining the chemical expansion coefficient with the dependence of oxygen stoichiometry on oxygen:fuel ratio, and overpotential one obtained the results shown in Fig. 23. For very low fuel conversion and low anodic polarisation this yields a strain contribution in the order of 0.6%. Indeed, chemical strain may also contribute to the enhanced redox tolerance of Ni-CGO cermet anodes (Ouweltjes et al, 2009), as chemical contraction of CGO may provide compensation for expansion caused by partial oxidation of Ni to NiO.

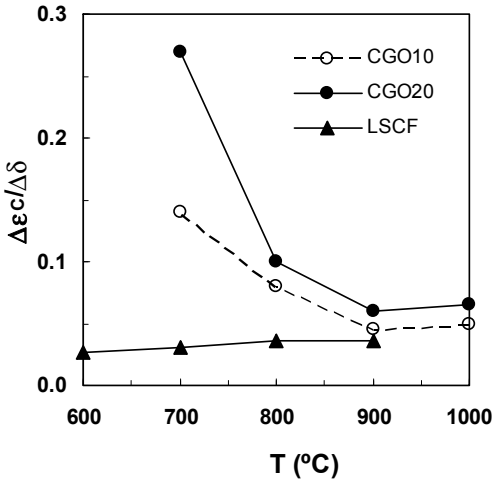

Fig. 22. Representative results of chemical expansion coefficient of $Ce_{0.9}Gd_{0.1}O_{2-\delta}$ (CGO10), $Ce_{0.8}Gd_{0.2}O_{2-\delta}$ (CGO20) (Atkinson & Ramos, 2000), and $La_{0.5}Sr_{0.5}Fe_{0.5}Co_{0.5}O_{3-\delta}$ (LSCF) (Lein et al, 2006).

In order to assess the impact of chemical expansion on thermochemical stresses one may combine chemical strain $\varepsilon_C(x)$ superimposed on a stress related contribution, in flat constrained conditions as follows:

$$\varepsilon_\gamma = \sigma(x)(1-\nu)/E + \varepsilon_C(x) \tag{39}$$

where $\sigma(x)$ denotes stress, E is Young modulus and ν is the Poisson ratio.

For flat constrained conditions, the resulting strain ε_γ remains uniform across the membrane, and thus:

$$\sigma(x) = \frac{E}{(1-\nu)}\left[\varepsilon_\gamma - \varepsilon_C(x)\right] \tag{40}$$

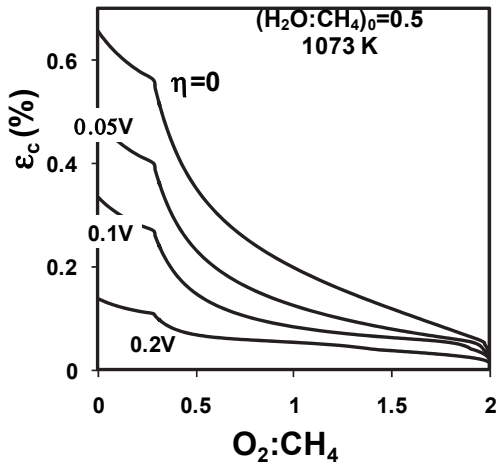

Fig. 23. Chemical expansion of CGO20 vs O_2:CH_4 ratio for $(H_2O:CH_4)_0$=0.5, at 800ºC, and for anodic polarisation η=0, 0.05, 0.1, 0.2 V.

This can be combined with the additional condition for externally unconstrained membranes:

$$\int_0^L \sigma \, dx \approx \frac{L}{\Delta \mu O_2} \int_{\mu O_2'}^{\mu O_2''} \sigma \, d\mu O_2 = 0 \tag{41}$$

where L is the thickness of membrane, and $d\mu O_2 = RTd\ln(pO_2)$ is the elemental change in chemical potential. For linear dependence of chemical potential across the membrane, and on combining Eqs. 40 and 41 one obtains:

$$\varepsilon_\gamma = \log\left(pO_2'' / pO_2'\right)^{-1} \int_{pO_2'}^{pO_2''} \varepsilon_C \, d\log(pO_2) \tag{42}$$

If x represents distance from air, and this is taken as reference, i.e. $\varepsilon_c(0)=0$, the stresses at surfaces in contact with air x=0 and contact with fuel (x=L) become:

$$\sigma(0) = \frac{E \, \varepsilon_\gamma}{(1\text{-}\nu)} \tag{43}$$

$$\sigma(L) = \frac{E\left(\varepsilon_\gamma - \varepsilon_C(L)\right)}{(1\text{-}\nu)} \tag{44}$$

Dependence on oxygen partial pressure is then easily transformed to the corresponding conversion of fuels, based on the previous thermodynamic analysis for hydrogen or methane-based fuels.

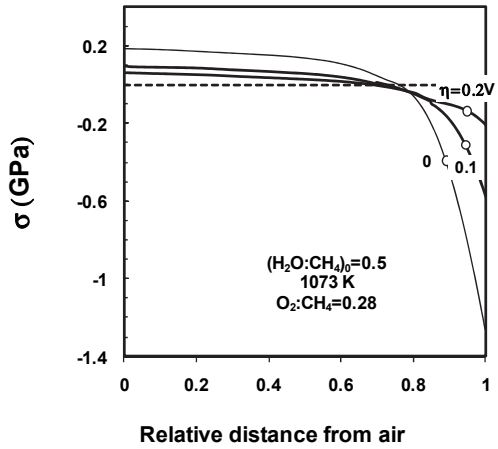

Fig. 24. Predictions of stresses in a CGO20 membrane vs. relative distance to air, under air/membrane/fuel conditions with $(H_2O:CH_4)_0$=0.5, at the lowest conditions to avoid carbon deposition $O_2:CH_4$≈0.28, and for different anodic overpotentials η=0, 0.1, and 0.2V.

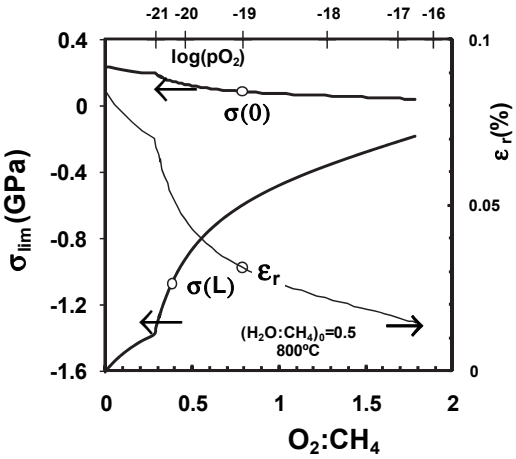

Fig. 25. Predicted dependence of overall chemical strain and stresses induced by chemical expansion at the air side σ(0) and at the fuel side σ(L) versus oxygen:fuel ratio, at 800ºC and for the initial steam methane ratio = 0.5.

On combining with corresponding dependence of oxygen sub-stoichiometry on pO_2, for typical values of chemical expansion coefficient, one estimated the stress profiles across a ceria based membrane for representative conditions, as shown in Fig. 24, using also the values of parameters E=187 GPa and ν=0.334 reported by (Atkinson & Selçuk, 2000). Note that slightly tensile stresses develop at the oxidising side and much higher compressive stresses at reducing side. This is, probably, the most favourable condition because ceramics show much higher resistance under compression. Still, relatively high chemical expansion in contact with the fuel may still raise risks of delaminating at ceria/electrode contacts. Figure 25 shows additional results for the dependence of stresses in contact with air $\sigma(0)$ and in contact with the fuel $\sigma(L)$, vs. oxygen:methane ratio in the feed, or upon the gradual oxidation. The discontinuities in overall strain and stresses in contact with air or contact with fuel represent the minimum oxidation required to avoid carbon deposition.

6. Conclusions

Partial reducibility of ceria-based materials exposed to fuels or other reducing agents causes onset of significant electronic conductivity, decrease in oxygen stoichiometry and chemical expansion. These changes are closely dependent on oxygen partial pressure and can also be related to gradual conversion of fuels until nearly complete conversion to fully oxidised gases (i.e. H_2O and/or CO_2); this can be described by thermodynamic analysis of fuel conversion, yielding a description for effects on electronic conductivity, changes in oxygen stoichiometry and chemical strain. Fuel rich atmospheres yields mixed conducting properties, with negative impact on electrolytic domain and open circuit voltage (OCV) for a ceria-based membrane under air/membrane/fuel gradients. For this configuration, one must consider the average value of electronic conductivity across the membrane to account for effects on OCV. Simultaneously, the gradient of chemical potential yields variable oxygen stoichiometry across the ceria-based membrane, and corresponding chemically induced stresses. Under flat constrained conditions, stresses may change gradually from moderate tensile stresses, in the air side, to compressive stresses in the fuel side. Thus, onset of electronic conductivity and chemical expansion may impart operation conditions for ceria-based solid electrolytes. Yet, reducibility may also confer unique electrocatalytic properties to ceria-based materials, and applicability in cermet anodes due to mixed conductivity, possibly combined with variable oxygen storage. In addition, one may anticipate enhanced redox tolerance for ceria-based cermet anodes, as chemical contraction of the ceria-based component upon reoxidation may counter expansion induced by partial oxidation of metallic Ni to NiO.

7. Acknowledgment

This work was sponsored by MCINN (Spain) (ENE2009-14750-C05-03) and co-financed by FEDER-EU (MAT2007-60127 and MAT2010-16007). Domingo Pérez-Coll is also grateful to MCINN and CSIC for a "Ramón y Cajal" contract.

8. References

Abrantes J.C.C., Pérez-Coll D., Núñez P., Frade J.R., *Electrochim. Acta*, 48 (2003) 2761

Atkinson A., Ramos T.M.G.M., *Solid State Ionics*, 129 (2000) 259
Atkinson A., Selçuk A., *Solid State Ionics*, 134 (2000) 59
Butler, V.; Catlow, C.R.A.; Fender, B.E.F.; Harding, J.H.; *Solid State Ionics,* 8 (1983) 109
Blumenthal, R.N.; Hofmaier, R.L. *J. Electrochem.Soc* 121 (1974) 126
Blumenthal, R.N.; Sharma, R.K.; *J. Solid State Chem*. 13 (1975) 360.
Catlow, C.R.A.; *Solid State Ionics* 8 (1983) 89
Fagg, D.P.; Abrantes, J.C.C.; Pérez-Coll, D.; Núñez, P.; Kharton,V.V.; Frade, J.R.; *Electrochim. Acta*, 48 (2003) 1023-1029
Ferreira, A.A.L.; Abrantes, J.C.C.; Jurado, J.R.; Frade, J.R.; *Solid State Ionics*, 135 (2000) 761
Frade, J. R.; Kharton, V.V.; Yaremchenko, A.; Naumovich, E.; *J. Power Sources,* 130 (2004) 77
Frade, J. R.; Kharton, V.V.; Yaremchenko, A.A.; Tsipis, E.V.; *J. Solid State Electrochem.,* 10 (2006) 96-103
Frade, J. R.; Kharton, V.V.; Shaula, A.L.; Maques, F.M.B.; *Sensor Letters.,* 6 (2008) 370-380
Hebb, M.H.; J. Chem. Phys. 20 (1952) 185
Kobayashi, T.; Wang, S.; Dokiya, M.; Tagawa, H.; Hashimoto, T.; *Solid State Ionics,* 126 (1999) 349
Lein H.L., Wiik K., Grande T., *Solid State Ionics*, 177 (2006) 1795
Lübke, S.; Wiemhoefer, H.-D.; *Solid State Ionics,* 117 (1999) 229
Marina O.A., Bagger C., Primdahl S., Mogensen M., *Solid State Ionics,* 123 (1999) 199
McIntosh S., Gorte R.J., *Chem. Rev*., 104 (2004) 4845
Minervini, L.; Zacate, M.O.; Grimes, R.W.; *Solid State Ionics,* 116 (1999) 339
Mogensen, M.; Sammes, N.M.; Tompsett, G.A.; *Solid State Ionics,* 129 (2000) 63
Navarro, L.; Marques, F.; Frade, J.R.; *J. Electrochem. Soc*, 144 (1) (1997) 267
Ouweltjes J.P., van Tuel M., Sillessen M., Rietveld G., *Fuel Cells,* 9 (2009) 873
Panhans, M. A.; Blumenthal, R. N.; *Solid State Ionics,* 60 (1993) 279
Pérez-Coll D., Núñez P., Marrero-López D., Abrantes J.C.C., Frade J.R., *J. Solid State Electrochem*., 8 (2004) 644
Pérez-Coll D., Núñez P., Frade J.R., *J. Electrochem. Soc.,* 153 (3) (2006) A478
Pérez-Coll D., Marrero-López D., Ruiz-Morales J.C., Núñez P., Abrantes J.C.C., Frade J.R., *J. Power Sources*, 173 (2007) 291
Pérez-Coll D., Aguadero A., Núñez P., Frade J.R., *Int. J. Hydrog. Energy*, 35 (2010) 1148
Riess, I. ; Janczikowski; Nölting, J.; *J. Appl. Phys*., 61 (1987) 4931
Schneider, D.; Godickemeier, M.; Gauckler, L.J.; *J. Electroceramics,* 1 (1997) 165
Steele, B.C.H.; *Solid State Ionics,* 129 (2000) 95-110
Suzuki,T.; Kosacki, I,; Anderson, H.U.; *J. Am. Ceram. Soc*., 85 (2002) 1492
Tikhonovich, V.N.; Naumovich, E.N.; Kharton, V.V.; Yaremchenko, A.A.; Kovalevsky, A.V.; Vecher, A.A.; *Electrochim. Acta*, 47 (2002) 3957
Tsipis E.V., Kharton V.V., Bashmakov I.A., Naumovich E.N., Frade J.R., *J. Solid State Electrochem*., 8 (2004) 674
Tuller, H.L.; Nowick, A.S.; *J. Phys. Chem. Solids*, 38 (1977) 859
Wagner, C.; Proceedings of the Seventh Meeting of the International Committee on
Electrochemical Thermodynamics and Kinetics, Lindau, Butterworths Scientific
Publication, London, (1957), p. 361
Wang, S. R.; Inaba, H.; Tagawa, H.; Hashimoto, T.; *J. Electrochem. Soc*.,144 (1997) 4076

Wang, S.R.; Inaba, H.; Tagawa, H.; Dokiya, M.; Hashimoto, T.; *Solid State Ionics,* 107 (1998) 73
Xiong, Y.; Yamaji, K.; Horita, T.; Sakai, N.; Yokokawa, H.; *J. Electrochem. Soc.*, 151 (2004) A407
Yano, M., Tomita A., Sano M., Hibino T., *Solid State Ionics*, 177 (2007) 3351
Zachau-Christiansen B.; Jacobsen, T.; Skaarup, S.; *Solid State Ionics*, 86-88 (1996) 725

16

Reinforcement of Austenitic Manganese Steel with (TiMo) Carbide Particles Previously Synthesized by SHS

Jose Ignacio Erausquin
Tecnalia Research and Innovation
Spain

1. Introduction

Production parameters and the properties or final characteristics of each particular material are interrelated, as well as the service performance of the manufactured product. Then, a possible scheme to continue in the process of optimization/design of materials is shown in Figure 1. The two basic steps for this would be the following: a) Cause-Effect Relationship: Analysis and study of the effects of the manufacturing process of the material (composition, refining, solidification, heat treatment, etc.) in the micro or nano-structure (phases, constituents, grain size, etc.), of this structure in the mechanical properties (toughness, hardness), and of these in the final performance of the product in service (fatigue, impact, creep failures, wear, deformation, corrosion, etc...); b) Objective-Means Relationship: In reverse order to the previous definition, to optimize the mechanical properties for the desired behavior in service identifying the micro-nano structural parameters that govern such characteristics (particles of second phase, martensite on laths, etc.), in order to establish the best production process to obtain the desired material in each case once designed and defined its optimal internal parameters.

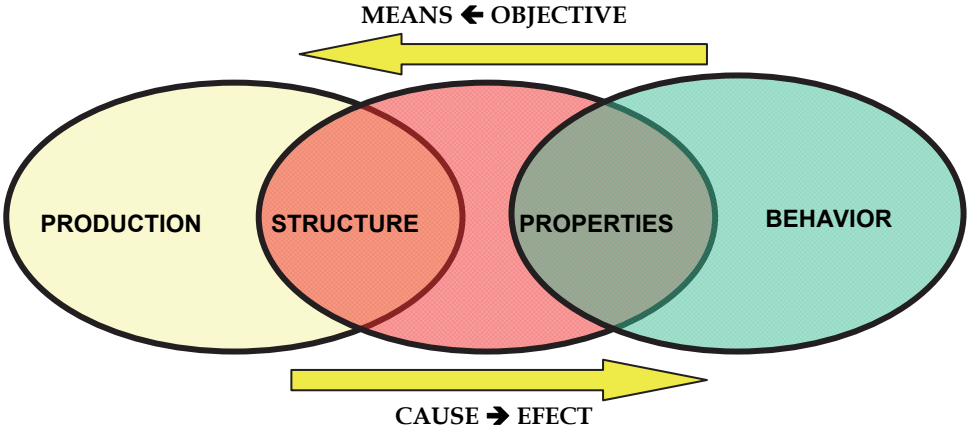

Fig. 1. Scheme for optimization/design of materials

In this context, the main priorities for improving the mechanical properties of materials, in general, can be simplified into two main groups: Those aiming to increase its mechanical strength, stiffness and toughness; Those that can lead to an increase in fracture toughness of the material. Latter consists in adding second phase particles embedded in the matrix, which generate energy absorbing processes during the growth of cracks in the matrix as well as acting as a barrier to it and the movement of dislocations, while the mechanical strength is increased, among other factors, with decreasing grain size of the microstructure. The elastic constants, on the other hand, increases with a higher ratio "length / diameter" of the second phase particles (Tinklepaugh & Crandall, 1960). The development of these materials leads to the so-called composed materials or "composites." With this term is called, in general, a material made by a constituent discrete (reinforcement) distributed and dispersed in a continuous phase (matrix) and whose characteristics are a function of both constituents, the geometry and structure of them and the properties of its boundaries or interfaces (Steen, 1992). Among the wide variety of these composite materials (classified, on the one hand, based on physical or chemical nature of the matrix and, secondly, in terms of continuous or discontinuous reinforcement), one of the major groups is the conformed by those whose higher fraction is a metal, owing to the superiority of some of its properties compared with those of ceramic matrix material (toughness and ductility) and organic matrix (high temperature resistance, hardness, etc.). In the former ones, the constituent of reinforcement is usually non-metallic, predominantly ceramic. About the geometry of the reinforcement, some of the metal matrix composites most commonly used are those known (Chesney, 1990) as: a) Metals reinforced with continuous fibers, parallel or not, and a diameter of less than 20 microns; b) Metals reinforced with short fibers, staple, and "whiskers"; c) Metals reinforced with particles, approximately equiaxed. All types are presented in Figure 2.

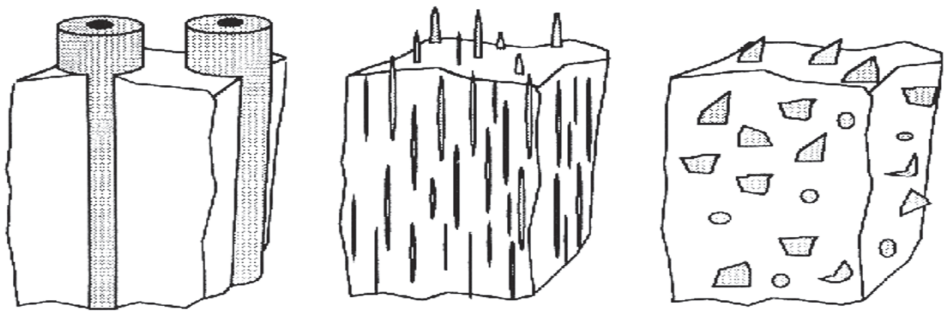

Fig. 2. Metallic matrix reinforcement types.

In this sense, in the last 30 years almost all efforts have focused on composites of low melting point alloys (Al, Ti, Mg, Cu), being the most developed ones the aluminum alloys containing particles of SiC or alumina and the titanium alloys with carbides and borides (Kelly& Macmillan, 1987; Terry & Chinyamakobvu, 1992). At the end of 80th start the first attempts in order to produce ferrous materials reinforced with constituents more hard, added after its previous synthesis. R.M. Hathaway et al., in your "Ferrous Composites: a Review" (Hathaway et al., 1997), revise the development achieved in this matter (until 1997) by powder metallurgy process as well as liquid metallurgy one. Subsequently, Tecnalia

Research and Innovation (Agote et al., 2005; Erausquin et al., 2009; Erausquin, 2009) have studied the possibility of developing such other iron matrix (steels), in order to combine in one material at the macroscopic level, the ductility, toughness, etc.., related to them, with the hardness (translated into greater wear resistance) and stiffness (translated into greater yield strength and creep) of the strengthening particles. However, apart from a few later publications in this line of steel with carbide and borides particles previously developed (Nutting, 1998; Bates et al., 1998; Galgali et al., 1999; Degnan & Shiway, 2002) and others relating to training "in-situ" the precipitation, from alloying elements, of TiC particles in ferrous materials (Das et al., 2005; Dogan et al., 2006), there is hardly any progress on the matter. One proper steel alloy to be intended to reinforce is the Hadfield type steel because the austenite of this manganese steel (1.0-1.4%C; 12–14%Mn), even though able to be hardened by impact, explosion, etc., is very ductile, tough and deformable, so that the industrial parts made with this material often suffer important geometric deformations during its work. To minimize this problem, it is necessary to insert harder particles in the matrix in order to increase the austenite stiffness preserving it sufficient toughness. Refractory metal carbides as Titanium, Tungsten or Zirconium carbides are the most common ceramic elements used for these applications (Steen, 1992), because the carbides of the transition metals in Groups IV - VI have extremely high melting points and are therefore referred to collectively as the "refractory carbides." In addition to their stability at high temperatures, these compounds are extremely hard, finding industrial use in cutting tools and wear-resistant parts. Their hardness is retained to very high temperatures, and they have low chemical reactivity (they are attacked only by concentrated acid or base in the presence of oxidizing agents at room temperature), and retain good corrosion resistance to high temperatures. The refractory carbides are strong, with Young's modulus values (a measure of elastic deformation resistance) rivalling those of SiC at room temperature. In addition, they have good thermal shock resistance and good thermal conductivity, permitting heat to be drawn away from the working surface of the tool. This gives them a benefit over other refractory materials, which do not conduct heat so well (Storms, 1967; Toth, 1971). Most of the transition metal monocarbides form in the *B1* (NaCl) structure, *fcc* metal with carbon occupying the octahedral interstitial sites. The shortest M-M distance is about 30% greater in the *B*1 carbide than in the pure metal for the Group IV and V carbides, but drops to less than 10% greater for the Group VI or VII carbides. At 100% site occupancy, the stoichiometry of the carbide is $MC_{1.0}$, though this situation is rarely realized. The concentration and ordering, if any, of the vacancies that result from a nonstoichiometric M-C ratio have a great effect on the thermodynamic, mechanical, electronic, and magnetic properties of the metal carbides; however, the details of these effects are a matter of some debate in the literature, due to the difficulties inherent in synthesizing pure compounds and in measuring the exact details of the crystal structure of a given sample (Storms, 1967). In this field, one of the most attractive reinforcing ceramic constituent is the titanium carbide, because of its high hardness, thermal stability and low density. But the low wetability and segregation tendency (Terry & Chinyamakobvu, 1992; Wood et al., 1995) of these carbide particles make them technically difficult to incorporate into manufactured or semi manufactured metallic alloys, cermets or coating materials.

Indeed, the development of a liquid metallurgy process enabling the reinforcement by means of the addition of the ceramic material to the molten metal in the melting furnace would become an important advance in this field. Nevertheless, these titanium carbide products are also prone to the coalescence and have poor wettability into molten bath, so

that, the resulting operation yield and the subsequent property improvement is very low. These disadvantages are solved if the ceramic particle is a complex carbide (TiMo)C, if it is bonded by metallic Fe, having a masteralloy of Fe(TiMo)C type, and making this masteralloy by self-propagated high temperature synthesis (SHS). After that, it addition to the liquid austenitic manganese steel, the pouring of the mix (steel+carbides), it solidification, for example in sand molds, and the subsequent heat treatment (solution annealing and rapid quenching) produces composite castings or parts composed by a matrix of austenite and discrete carbide particles of (TiMo)C inserted in it (Erausquin et al., 2009).
This chapter describes the necessary process for it and the characteristics of the obtained products.

2. Experimental

The process includes the following fundamental steps: 1) Previous preparation of the material of reinforcement, in this case a masteralloy of Fe(MoTi)C type. 2) Melting of the high carbon high manganese steel bath by means of conventional electric furnace and addition of the masteralloy to the molten steel bath. 3) Pouring, solidification and heat treatment of the "composite" product.

2.1 Masteralloy synthesis

The masteralloy is synthesized by self-propagating high temperature synthesis using raw materials containing Fe, Ti, Mo and C. This process allows obtain products with very low energetic consumption and high purity, favourable this parameter for the wettability. The SHS, or materials synthesis by combustion, is based in exothermic chemical reactions solid+solid or solid+gas and the heat generated in the reaction allows it self-propagation by means a wave or combustion front (Tamburini et al., 2000). The full process is indicated in the figure 3.

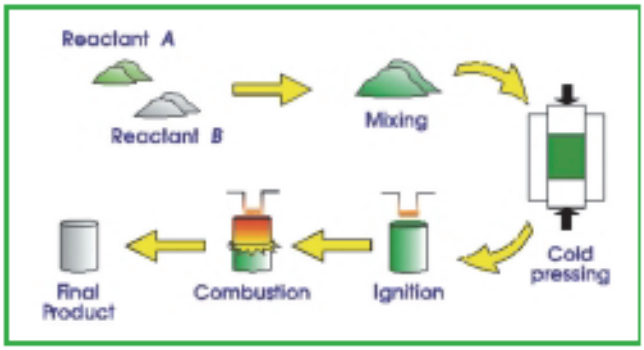

Fig. 3. Full process for SHS (Tamburini et al., 2000)

The figure 4 shows the selfpropagating synthesis of the NiAl intermetallic in air atmosphere.
The exothermic power of a reaction is deduced from the Ellingham diagrams, as the figure 5 for the carbides formation. At less AG, more exothermic is the reaction, as the case of the synthesis of TiC

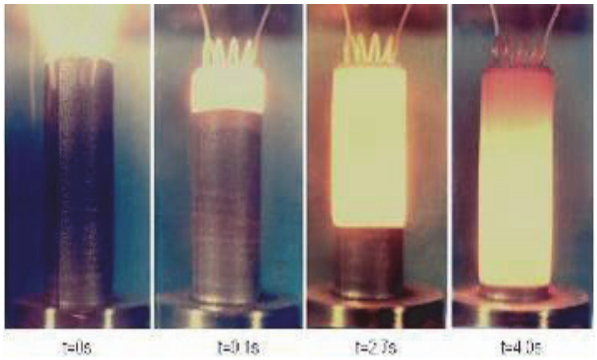

Fig. 4. NiAl SHS (Courtesy of ISMAN Institute of Moscow)

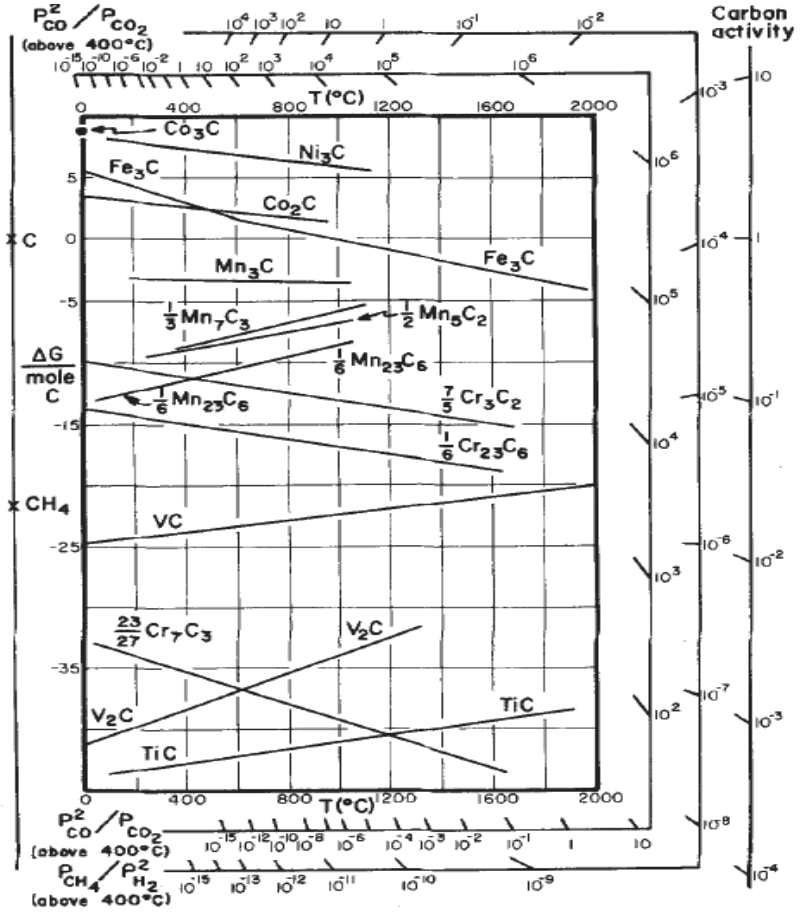

Fig. 5. Ellingham diagram of carbides formation (Shatynski, 1979)

Also, although AG values for the formation of the molybdenum carbides are positives at room temperature, at high temperature these values are very negatives (low AG) as we can see in the figure 6. This fact facilitates the insertion de molybdenum atoms within titanium carbide cell (Erausquin, 2009).

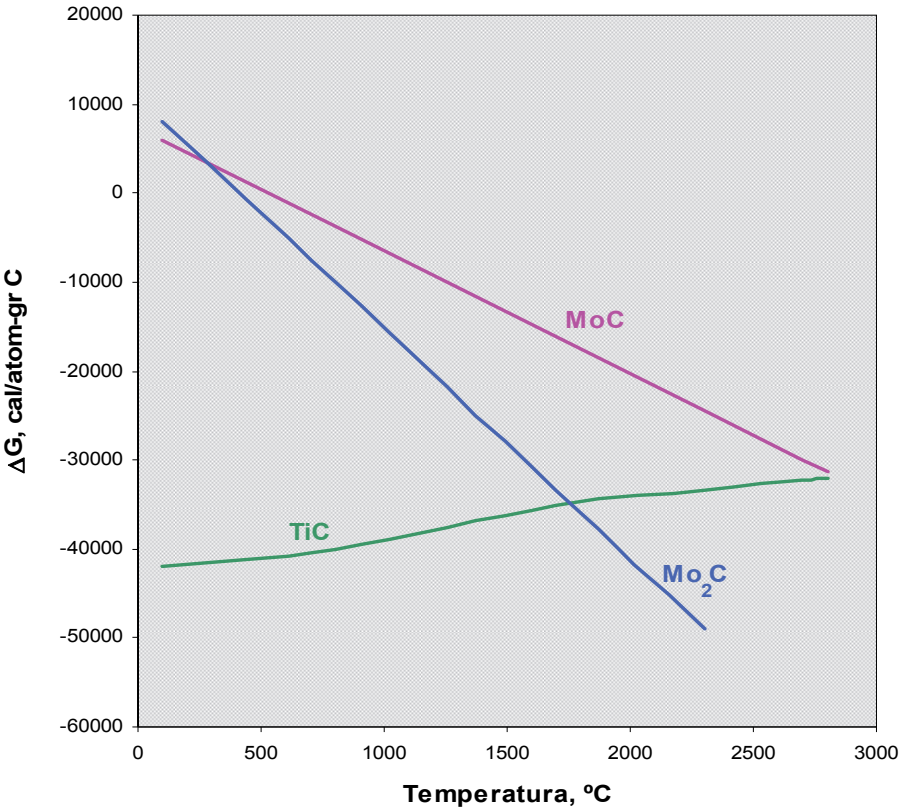

Fig. 6. Ellingham diagram of titanium and molybdenum carbides formation (Erausquin, 2009)

In the present work, the raw materials, its quantities and its characteristics are the next: 12% pure Carbon of 1-3 μ of grain size; 73% FeTi (67-70% Ti; 5% Al; remainder: Fe), crushed to 100 μ of grain size; and 15% FeMo (66% Mo; 1% Si; remainder: Fe), crushed to 100 μ of grain size. Mixed the three materials and pressed the mix to 4-6MPa., the synthesis is made in a steel reactor with argon atmosphere and a wolfram resistance in an edge. The heat of this resistance produces the start of the reaction and after that this one is propagated in wave front due the formation heat of the masteralloy, taking place the total mix synthesis (Erausquin et al., 2009). At macroscopic level, the resultant masteralloy is a brittle and porous material, with ceramic aspect (Erausquin et al., 2009).
The figures 7, 8 and 9 show the SHS equipment, the product formation, and the synthesis propagation, respectively.

Fig. 7. Powder mixer (left); Powder press (centre); SHS reactor (right)

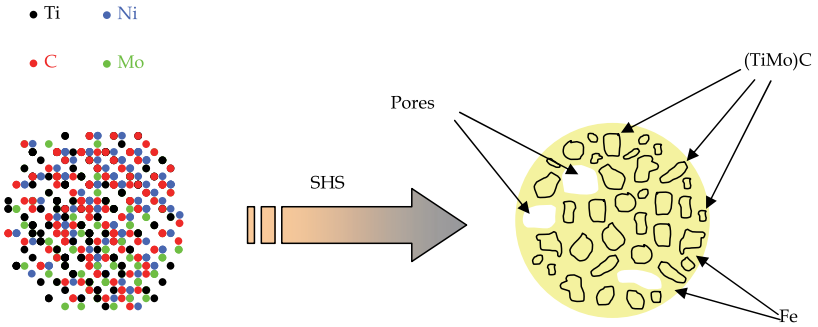

Fig. 8. Masteralloy formation (Erausquin, 2009)

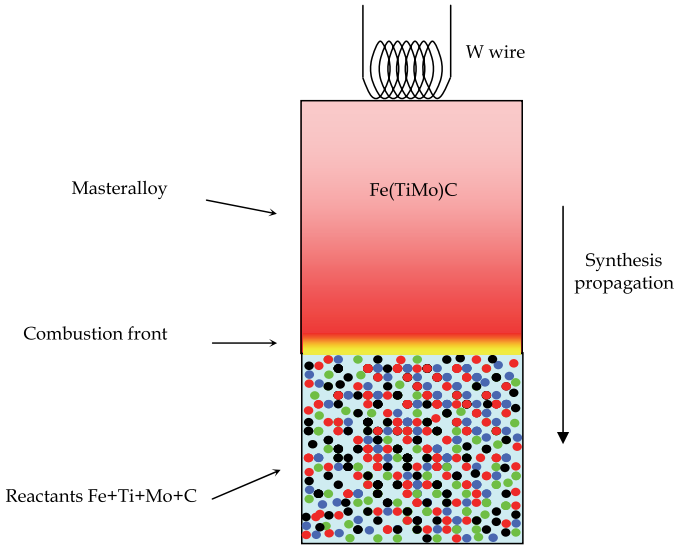

Fig. 9. Synthesis self-propagation

2.2 Melting of steel and masteralloy addition

The base austenitic steel is obtained by melting, in an induction furnace of 300 Kg. of capacity and 1000 Hz. of frequency, the next raw materials and quantities: 83% carbon steel scrap; 13% Fe-Mn high carbon and 4% Fe-Mn low carbon, in order to achieve the chemical composition, in % mass, of the table 1.

C	Si	Mn	P	S	Cr	Ni	Mo
1.00-1.20	0.30	12.0-14.0	0.035	0.010	-	-	-

Table 1. Chemical composition (% mass) of the base steel

The process include the next steps (Erausquin et al., 2009): Melting of the raw materials in the furnace and heating of the liquid alloy up to 1873ºK.; Addition of the reinforcing material, consisting in a 10% of weight, over the base steel, of masteralloy Fe(TiMo)C previously crushed to 2-20 mm. grain size; After that, heating the bath (steel+carbides) up to pouring temperature (about 1823ºK).

2.3 Pouring, solidification and heat treatment

The resulting liquid material, steel alloy + reinforcing carbides, can be poured to produce ingots o castings. In this case, we have obtained sample-blocks and industrial castings solidified in sand molds. After that, these ones have been heat treated (solution annealing at 1373ºK and rapid quenching in water), as the same manner that a conventional austenitic manganese steel product. The samples for metallographic and mechanical tests have been prepared from this heat treated material.

The reinforcement full process is schematized in the figure 10.

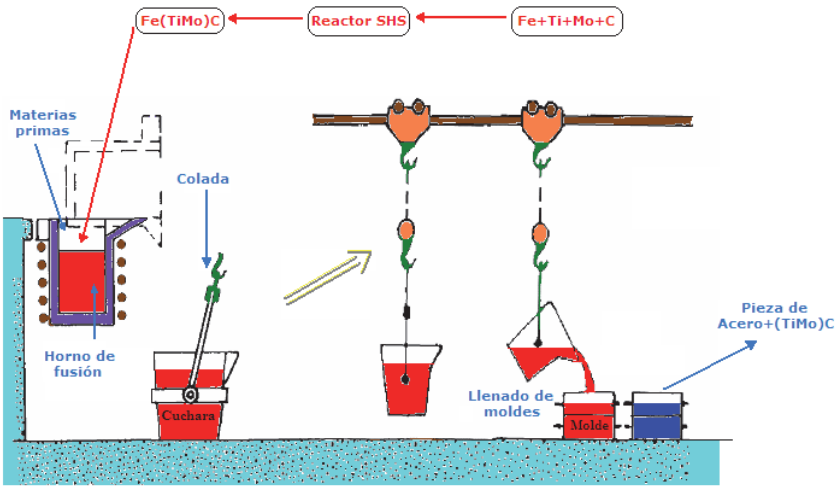

Fig. 10. Reinforcement process

The figures 11 and 12 show the alloy preparation and pouring, and the mould filling steps, respectively.
The figure 13 shows the mould filled with reinforced steel.

Fig. 11. Masteralloy addition and pouring of steel+carbides

Fig. 12. Mould filling with steel+carbides

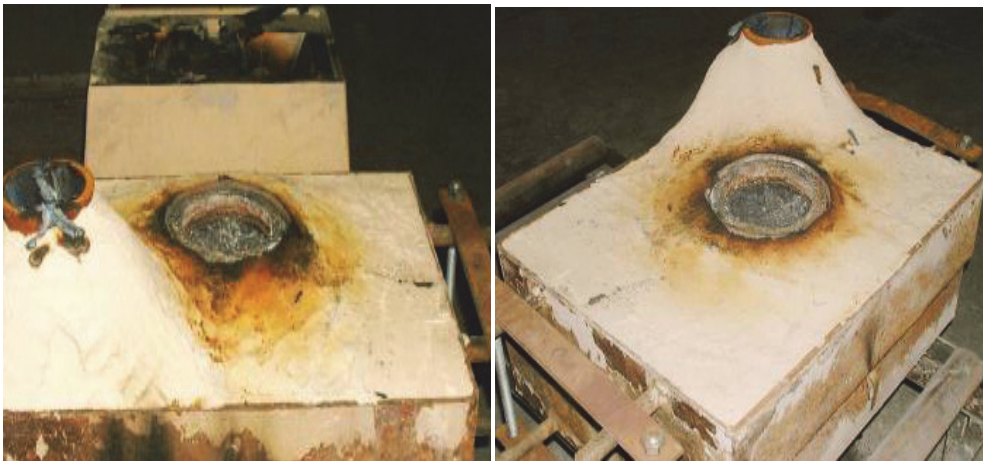

Fig. 13. Mould filled with steel+carbides

2.4 Characterization

The metallographic characterization has been made by means of optic and electronic microscopy (SEM with analytical equipment EDS), while the mechanical properties have been tested by means of a Vickers microhardness tester FM-100, tensile test machine Instron 8034, Charpy test machine Tinius Olsen model 74 and a pin on disk tribometre Biceri (05-168.02) for wear test. Also, we have used the difractometer Siemens D-500 in order to obtain the X ray diffraction diagram of samples of masteralloy finely crushed. The peaks of crystallographic planes of the resultant diffraction tests are contrasted and compared with those of the JCPDS (Joint Comittee Pattern for Diffraction Standards).

3. Results

3.1 Masteralloy

The visual aspect of the masteralloy produced by SHS is shown in figure 14.

Fig. 14. Blocks of masteralloy Fe(TiMo)C

In the figure 15 is presented the masteralloy crushed (left), and polished (right). In this one, we can see two constituents: the binder (white) and the polygonal-rounded particles (grey).

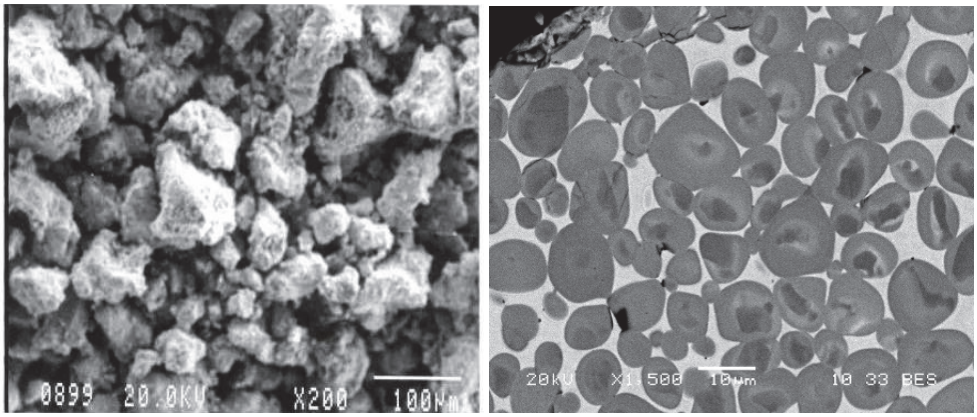

Fig. 15. Masteralloy crushed (left), and polished (right)

The figure 16 shows the spectra of the white constituent or binder (left), and of the grey particle (right). From them, we can deduce that the binder is iron, while the particles could be complex carbides of titanium and molybdenum. The semicuantitative chemical composition (obtained by EDS) of these particles is presented in the table 2.

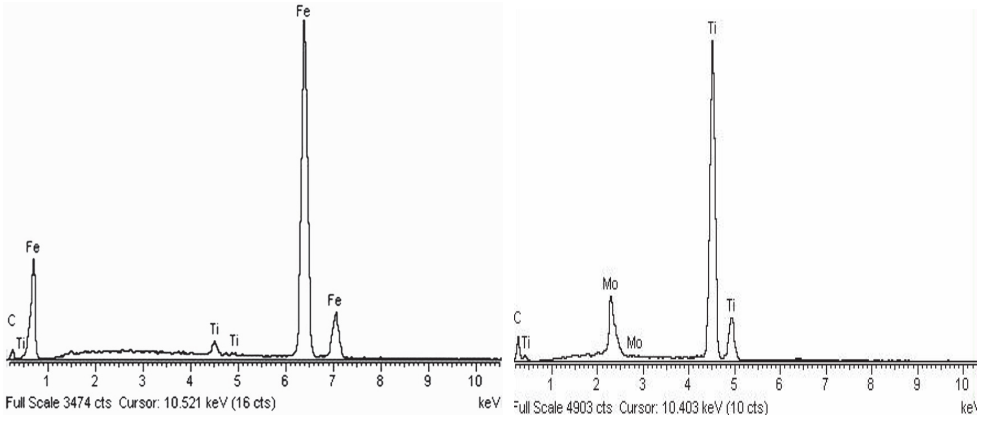

Fig. 16. Binder spectrum (left), particle spectrum (right)

Spectrum Label	C	Al	Ti	Fe	Mo	Total
Grey particle	18.43		68.07		13.50	100.00

Table 2. Semicuantitative composition (% mass) of the masteralloy grey particles

Besides these results, by means of the X ray diffraction tests we can demonstrate (Erausquin, 2009) the grey particles of the masteralloy are carbides of (TiMo)C type, because being unknown the θ angle of this complex carbide, the peak of diffraction results in the TiC angle, as is indicated in the figure 17.

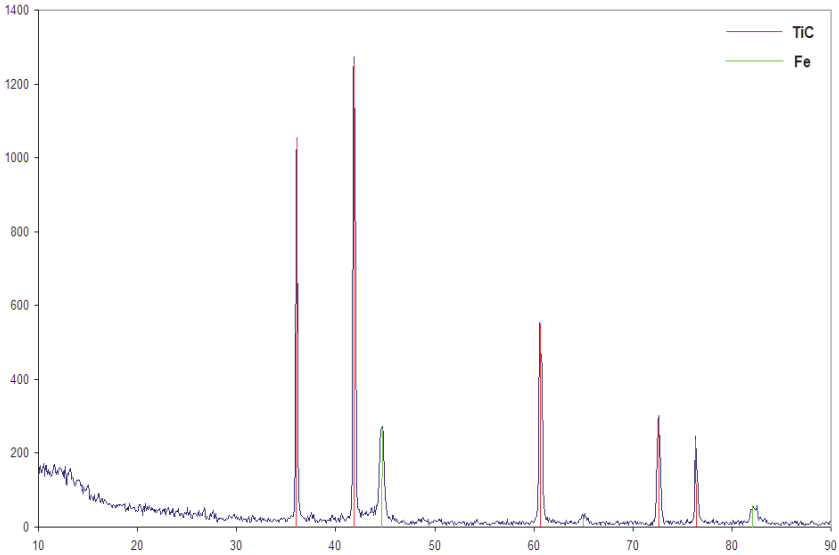

Fig. 17. X ray diffraction of the masteralloy

So that, if the reactants of a SHS reaction are C and Ti, the product is the monocarbide TiC, while if we add a small quantity of Mo to the mix, the result of the synthesis is the complex (TiMo)C, with the same crystallographic configuration as the former, but substituting a few atoms of Ti (green) by Mo ones (red), as indicated in the figures 18 and 19 (Erausquin, 2009).

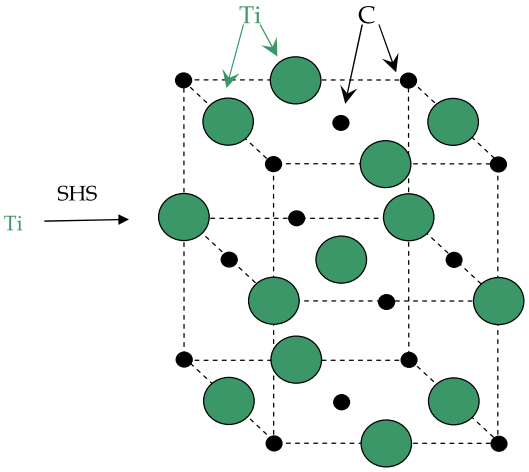

Fig. 18. TiC synthesis

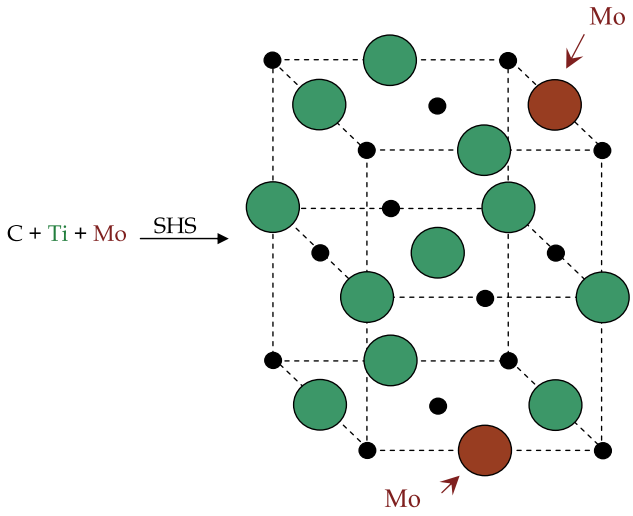

Fig. 19. (TiMoC synthesis

3.2 Reinforced steel

The mechanism of reinforcement of the steel by the carbides of the masteralloy is schematized in the figure 20.

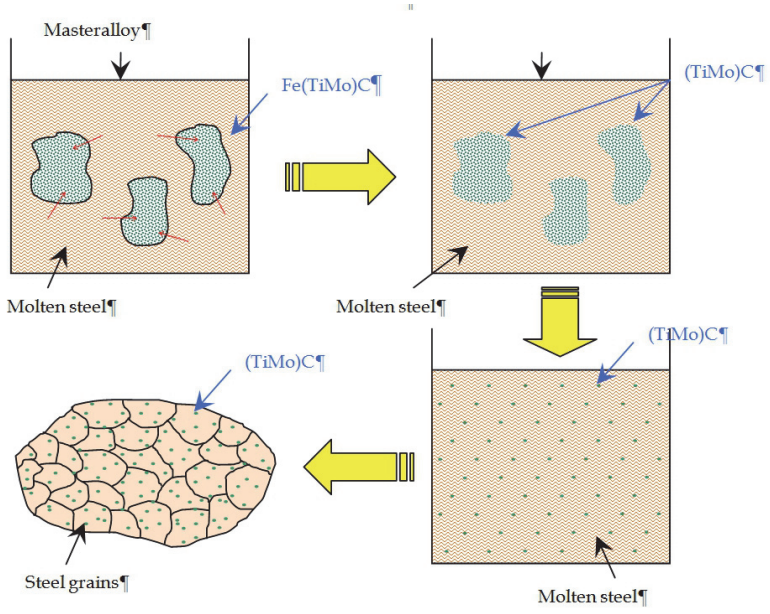

Fig. 20. Carbide reinforcement of the steel

In the figure 21 are shown the castings (hammers for crushing stone) of reinforced steel and in the figure 22, three hammers working in a rotary mill.

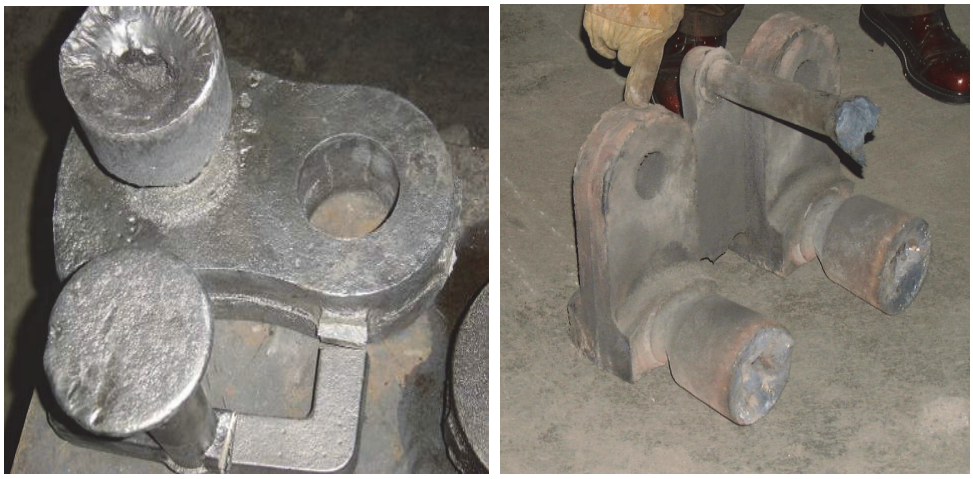

Fig. 21. Castings of reinforced steel

Fig. 22. Three experimental hammers in a rotary mill

3.2.1 Microstructure of the reinforced steel

The figure 23 shows the microstructure (unetched) of the reinforced austenitic steel (left), and the same but obtained with images analyser (right, x400)). In both, we can see discrete, microscopic and polygonal particles (dark grey at left, blue at right) into matrix (light at left, red at right).

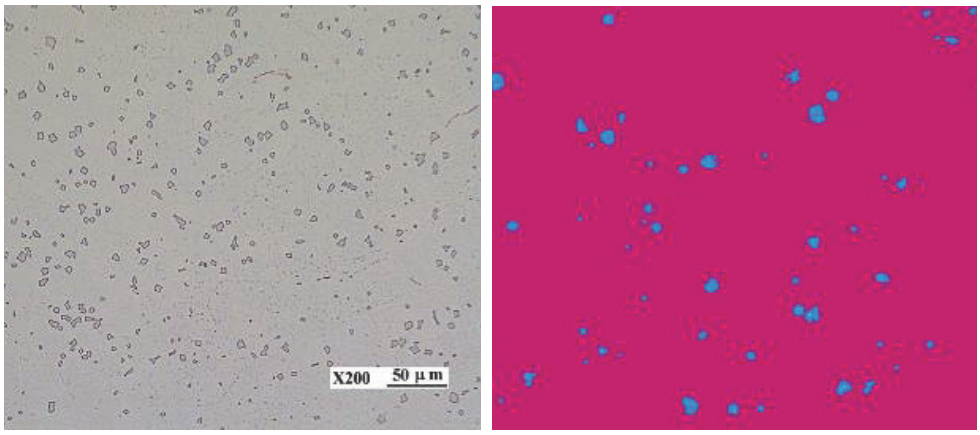

Fig. 23. Microstructure of the reinforced steel

The figure 24 shows the last microstructure, etched, at 40 and 400 magnifications respectively, where we can see the former particles inserted within austenite grains.
In the figure 25 we can see the spectra of the matrix of the reinforced steel (left) and of the particles inserted in it (right). Finally, in the tables 3 and 4 are shown the both semicuantitative composition (similars to base steel of the table 1 and to the grey particles of the masteralloy of the table 2, respectively).

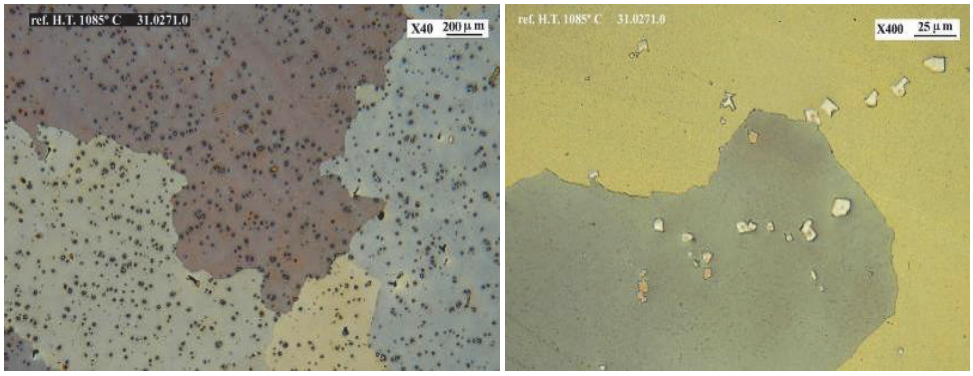

Fig. 24. Microstructure of the reinforced steel

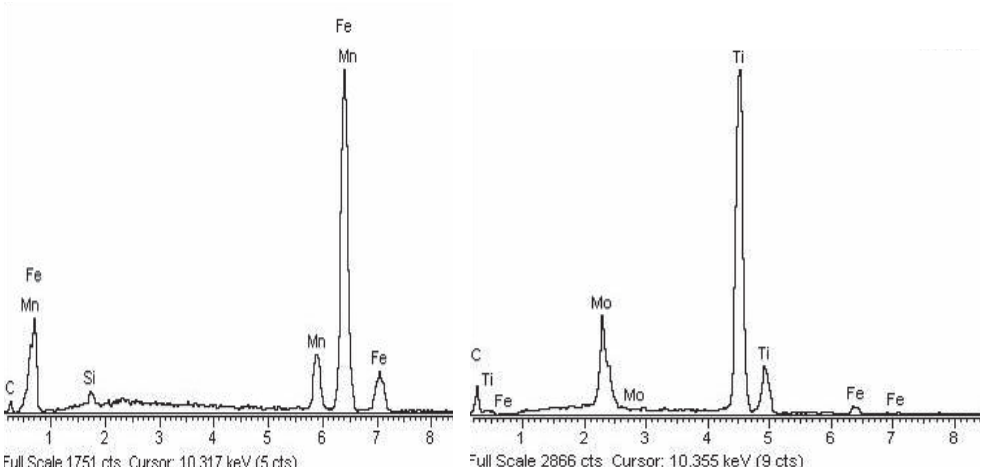

Fig. 25. Matrix spectrum (left) and particle spectrum (right) in the reinforced steel

Spectrum Label	C	Al	Si	Mn	Fe	Total
Steel matrix	1.15		1.14	12.75	84.96	100.00

Table 3. Semicuantitative composition (% mass) of the matrix of the reinforced steel

Spectrum Label	C	Al	Ti	Fe	Mo	Total
Grey particle	18.62		61.00	2.57	17.81	100.00

Table 4. Semicuantitative composition (% mass) of the particles of the reinforced steel

From them, we can deduce that these particles could be titanium and molybdenum complex carbides. Their chemical composition (semicuantitative, obtained by EDS) and that of the grey particles of the masteralloy (table 2) are similar, with a bit more Mo in the former in detriment of the Ti.

3.2.2 Mechanical properties

3.2.2.1 Hardness.

The microhardness values of the polygonal particles inserted in the austenitic grains of the reinforced steel are between 2400 and 3100 $HV_{0.025}$. This indicate the particles are carbides.

3.2.2.2 Tensile and Charpy tests.

In the table 5 we can see the values obtained in these tests (according to the norm EN-ISO 6506-1) for Hadfield conventional steel and the reinforced steel of this work. Of these values we can deduce the reinforced steel is less tough and ductile than the conventional one, although its toughness is certainly enough for a satisfactory behaviour under impact conditions. On the other hand, the yield strength of the reinforced steel is higher and, with

it, we expect the stiffness and the fatigue resistance, two characteristic-lacks of the Hadfield steel, will be increased.

	Tensile strength (MPa)	Yield strength(0.2%) (MPa)	Elongation (%)	Reduction of area (%)	Impact energy (J)
Conventional steel	636	371	35	41	162
Reinforced steel	575	482	16	22	128

Table 5. Mechanical properties of the reinforced steel

3.2.3 Wear resistance

It has been evaluated by means of the pin (of martensitic steel) on disk test on the conventional and reinforced steel samples, during 30 hours under a normal stress of 90 MPa (N/mm2) and 150 rpm. The results, in wear rate of the disks, are in the table 6. From them, we can deduce the wear resistance (under stress) of the reinforced austenitic steel is twice the conventional.

	Hadfield steel	Reinforced steel
Wear rate ($mm^3/N \cdot m$)	$6.8 \cdot 10^{-8}$	$3.5 \cdot 10^{-8}$

Table 6. Wear behaviour

4. Conclusions

From the figures 15, 16 and table 2, we can deduce the grey particles of the masteralloy synthesized by SHS are complex carbides of (TiMo)C type. The reaction synthesis is the sum of the next sequential (almost infinitesimal in time) partial reactions:

Formation of a 68%Ti-32%Fe intermetallic eutectic and it melting at 1086 º C aprox. due to heat generated by an electrical resistance; Diffusion of solid C in the Ti-Fe liquid and formation of TiC (very exothermic reaction with spontaneous generation of heat, rising the temperature, while Fe remains as binder phase);Replacement, in the TiC cell, of some Ti atoms by Mo ones, because the atomic radii values are similar (1,40-1,47 Å of the Ti, 1,39-1,45 Å of the Mo) and at high temperature the combination of C and Mo is very favourable. Then, TiC+Mo+Fe → Fe(TiMo)C.

From the microstructure (fig. 23 and 24), the spectra (fig. 25, table 4) and the microhardness values (point 3.2.2.1), we can deduce that the particles inserted within austenite grains of the reinforced steel are (TiMo)C carbides.

We can thus assure that these carbides are just the same grey particles present in the carbide of the masteralloy Fe(TiMo)C added to the steel. The small difference in composition is not representative because the EDS semicuantitative analysis is not exact. Likewise, the small change in shape (less rounded in the steel) is due to erosive action of the molten steel.

The mechanism of formation of the composite steel+carbides is the next: When the masteralloy Fe(TiMo)C contacts the liquid steel (iron base), the binder Fe of the former melts

and adds up to the metallic alloy, while the (TiMo)C particles, separated already from the binder and wetted by the liquid, remain embedded within it. Due to its high refractoriness and thermal stability, the carbide particles are not changed much even after the heat treatment of the solid material.

The polygonal titanium-molybdenum carbides, inserted metallurgically within the very ductile and tough austenite grains, decrease some mechanical characteristics (elongation, reduction of area, etc.). However, the impact energy values of the new material are sufficiently high for the expected service conditions of the typical components made in Hadfield steel (railway crossings, crushing jaws, hammers), so that, there is no risk of component fracture if this reinforced steel is used.

Besides, the beneficial effect of the carbides on the properties of the reinforced austenite such as deformability (expected to be lower, due to lower elongation), stiffness (expected to be higher, due the same reason as before), fatigue resistance (expected to be higher, due to higher yield strength), and wear resistance (clearly higher) are very interesting and promising in order to solve the characteristic shortcomings of the austenitic Hadfield steel.

In summary, the main conclusions of the present experimental work are:

a. The powder metallurgy process SHS allows the manufacture of a masteralloy Fe(TiMo)C, wettable by molten steel and composed by particles of complex carbide in an iron binder.
b. The addition of this masteralloy to a molten Hadfield steel bath and the subsequent solidification and heat treatment of the mix, allows the insertion of the complex carbide particles (TiMo)C of the masteralloy within the austenite grains of the steel.
c. This insertion produces a reinforcement of the austenitic matrix, with an appreciable increase in yield strength and wear resistance, but keeps the values of the other properties, such as elongation and impact energy, within adequate levels.

In this manner, we can contribute to improve the behaviour of a material (figure 1), optimizing its properties by means of a modification of it microstructure through the combination of two metallurgical techniques of fabrication, the powder metallurgy (SHS) and the liquid metallurgy, for casting production.

5. Acknowledgment

This work is the result of more of 10 years of research and experimentation of a team established with the arriving of the doctor Sergei Vadchenko, an authority in the SHS field, to Inasmet (now Tecnalia). Any years later, arrived the doctor Ara Sargysan (also an specialist in powder metallurgy) substituting to the former and the development of the works increased, achieving very promising results as demonstrate the present chapter. So that, the author gratefully acknowledge these researchers, the rest people of the team and, also, the companies have financially supported several projects in this field (Fundiciones del Estanda, Talleres ZB, JEZ Sistemas Ferroviarios).

6. References

Agote, I.; Gutierrez, M.; Orbegozo, M.; Asensio, M.; Rrausquin, J.I.; Erausquin, L.A. & Roncal, J. (2005). Desarrollo de Aceros Reforzados con Carburos Primarios Vía

Metalurgia Liquida *Revista de Metalurgia*, Madrid, (volumen extraordinario 2005), 53-57. ISSN 0034-8570.

Bates, P.; Walsh, M.A. & Price, S. (1998). Properties of 12% CrMoV high temperature turbine steel containing FeWTiC, *Proc. Advanced Heat Resistant Steels for Power Generation*, San Sebastián, Spain, April, 27-29, 1998.

Chesney, P. (1990). *Metals and Materials*, New York, 373.

Das, K.; Bandyopadhyay, T.K. & Chatterjee S. (2005). Synthesis and characterization of austenitic steel matrix composite reinforced with in-situ TiC particles. *Journal of Materials Science,* Volume 40, Number 18, (September 2005), 5007-5010.

Degnan, C.C. & Shiway P.H. (2002). Influence of reinforcement volume fraction on sliding wear behaviour of SHS derived ferrous based metal matrix composites. *Materials Science and Technology,* Vol.18, Number 10, (October 2002), 1156-1162.

Dogan, O.N.; Hawk, J.A.; Schrems, K.K. (2006). TiC-reinforced cast Cr steels. *Journal of materials engineering and performance*, vol. 15, nº 3, (May 2006), 320-327.

Erausquin, J. I.; Sargysan, A. &. Arana, J. L. (2009). Reinforcement of Austenitic Manganese Steel with (TiMo) Carbide Particles Previously Synthesized by SHS. *ISIJ International*, Vol. 49, No. 4 (April 2009), 582- 586.

Erausquin, J. I (2009). Aceros Reforzados con Partículas de Carburos Primarios (TiMo)C elaboradas por SHS. Obtención Mediante Metalurgia Líquida, Conformado por Moldeo y Caracterización. *Doctoral Thesis*, Escuela Ingenieros, Bilbao, (November 2009), 56.

Galgali R.K.; Ray H.S. & Chakrabarti A.K. (1999). Preparation of TiC reinforced steel composites and their characterization. *Materials Science and Technology*, Volume 15, Number 4, (April 1999), 437-442.

Hathaway, R.M.; Rohatgi, P.K.; Sobczak, N. Sobczak, J. (1997). Ferrous composites: A review, *Proc. Int. Conf. High Temperature Capillarity,* Cracow, Poland, June 29-July 2, 1997.

Kelly, A. & Macmillan, N.H. (1987). Strong Solids, Clarendon Pr, Oxford, 332.

Nutting, J. (1998). The structural stability of low alloy steels for power generation applications. *Proc. Advanced Heat Resistant Steels for Power Generation*, San Sebastián, Spain, April 1998.

Shatynski, S. R. (1979). The Thermochemistry of Transition Metal Carbides", *Oxidation of Metals*, Vol. 13, No. 2, (Mars 1979), 106.

Steen, W.M. (1992). Future Developments of Metals and Ceramics, Institute of Materials, London, (1992), 261.

Storms, E.K. (1967). The refractory carbides. *Academic Press*, NewYork, 1967.

Tamburini, U.A.; Maglia, F.; Spinolo, G. Munir, Z.A. (2000). *Chimica & Industria*, (December 2000), 1.

Terry, B.S. & Chinyamakobvu, O.S. (1992). Dispersion and reaction of TiC in liquid iron alloys. *Materials Science and Technology*, Vol. 8, (1992), 399-405.

Tinklepaugh, J.R. & Crandall, W.B. (1960). Cermets. *Reinhfold Publishing Corporation*, New York, (1960), 146.

Toth, L.E. (1971). Transition metal carbides and nitrides. *Academic Press*, NewYork, 1971.

Wood, J.V.; Dinsdale, K.; Davies, P. & Kellie, J.L.F. (1995). Production and properties of steel-TiC composites for wear applications. *Materials Science and Technology*, Vol. 11, (1995), 1315-1320.

17

Surface Equilibrium Angle for Anisotropic Grain Growth and Densification Model in Ceramic Materials

Sergio Cava[1], Sergio M. Tebcherani[2], Sidnei A. Pianaro[2], Elson Longo[3] and José A. Varela[3]

[1]*Universidade Federal de Pelotas*
[2]*Universidade Estadual de Ponta Grossa*
[3]*Universidade Estadual Paulista*
Brazil

1. Introduction

Sintering is the main operation in powder technology. This explains the attention of scientists and practical engineers towards sintering.

Currently there are two main cardinally different approaches to describing sintering: classical physical sintering theory and phenomenological. The first rests on physical constants at the level of individual particles, and the second is based on continuum equations for solid (viscous medium) mechanics, and it requires for its implementation presence of empirical coefficients and it is used for describing macroscopic problems of powder technologyGalakhov (2009).

Experimentally, the most common way to investigate the relative energy of the grain boundary consist in establishing a relationship of the surface free energy of the material with its grains geometryJin et al. (2000); Kinderlehrer et al. (2002); Xin & Wong (2003). This relationship was firstly quantified by HerringHerring (1951) who found out that the surface free energy is stationary when the balance process is reached. In this way, it is possible to determine the whole interface energy by observing the geometry of a certain number of interfaces among crystals of well-known orientation.

Thus, the flow of atoms j_a of a system is related to the intrinsic diffusion coefficient D and the gradient of chemical potential difference between the atom and the vacancy, in accordance with the Herring equation Herring (1950).

$$j_a = -\frac{D}{\Omega_a k_B T} \nabla \left(\mu_a - \mu_v \right) \tag{1}$$

where $\frac{D}{k_B T}$ represent the relative term of material mobility through the grain boundary or diffusion by the lattice, k_B is the Boltzman constant, T is an absolute temperature, Ω_a is the atomic volume, μ_a and μ_v are the chemical potentials of atom and vacancies, $\nabla(\mu_a - \mu_v)$ is the gradient between the chemical potentials difference that leads to the mass transport.

In a general way, Hansen et al. (1992) has obtained a relationship denominated as a flow general equation:

$$j_{as} = \frac{D}{k_B T}\left(\frac{\alpha\gamma C_k}{C_\lambda G^2}\right) \tag{2}$$

where: α is a proportionality constant that relates the gradient with λ and is just dependent of the three-dimensional geometric relationship between sources and material drains along the limit of the grain boundary, being λ the linear average distance of defined diffusion for the intersection between a pore and the center of the neck among two grains, γ is the surface energy, G is the average grain diameter, C_k and C_λ are geometric proportionality constants where K defines the medium curvature of pore.

In surface techniques, the excess of the grain boundary free energy per surface free energy (γ_{gb}/γ_S)Dhalenne et al. (1983); Kingery (1994); Moment & Gordon (1964); Readey & Jech (1968); Shackelford & Scott (1968); Wolf (1983) is a function of the dihedral angle of experimental surface measured by the intersection Ψ_S giving the equation:

$$\frac{\gamma_{gb}}{\gamma_S} = 2\cos\frac{\Psi_s}{2} \tag{3}$$

The determination of materials structures in polycrystals ceramics with high surface area are being facilited microscopy techniquesMunoz et al. (2004); Saylor et al. (2000); Saylor & Rohrer (1999). The liquid phase formed during sintering process is found by means of determination of dihedral angleBelousov (2003; 2004).

Under appropriate experimental conditions, surface dihedral angles, relative grain boundary energies, and surface diffusivities determined from Atomic Force Microscopic (AFM) measurements are consistent with data acquired by more laborious techniquesSaylor & Rohrer (1999).

The densification equations for pressure less solid state sintering can be easily extended to describe the densification behavior during hot-pressing or hot-isostatic-pressingBeeman & Kohlstedt (1993); Shi (1999).

In this paper the use of the AFM technique to determine the dihedral surface angle for compacts sintered in solid-phase with anisotropic grain growth of 0.5 Mol% MnO_2-doped tin dioxide obtained by the chemical method of the polymeric precursor is described.

2. Experimental procedure

The polymeric precursor solution was prepared by the Pechini method, which has been used to synthesize polycationic powders Cassia-Santos et al. (2005); Cava, Sequinel, Berger & Tebcherani (2009); Cava, Sequinel, Tebcherani, Michel, Lazaro & Pianaro (2009); Cava et al. (2006; 2007); de Lucena et al. (2005); Gonzalez et al. (2004); Pontes et al. (2004); Simoes et al. (2004); Simoes, Ramirez, Perruci, Riccardi, Longo & Varela (2005); Simoes, Ramirez, Riccardi, Ries, Longo & Varela (2005); Simoes, Ries, Moura, Riccardi, Longo & Varela (2005). The process is based on the metallic citrate polymerization using ethylene glycol. A hydrocarboxylic acid, such as citric acid, is used to chelate cations in an aqueous solution. The addition of a glycol such as ethylene glycol leads to the formation of an organic ester. Polymerization, promoted by heating the mixture, results in a homogeneous resin in which metal ions are uniformly distributed throughout the organic matrix.

In the experiments, tin chloride dehydrated $SnCl_2.2H_2O$ (Merck) was first dissolved in distilled water. Subsequently ammonium hydroxide - NH_4OH (Synth) was added in order to form tin hydroxide - $Sn(OH)_2$ Besso (n.d.), according to equation 4.

$$SnCl_2 + NH_4OH \rightarrow Sn(OH)_2 + NH_4Cl \tag{4}$$

The presence of chloride in the solution was analyzed after decantation by means of the addition of silver nitrate in the filtrate liquid. Due to the silver chloride formed as a white solid insoluble in water Baccan et al. (1990) it is possible to predict the absence of Cl^- within tolerance limit for the following equation.

$$Ag^+_{(aq)} + Cl^- \rightarrow AgCl_{(s)} \tag{5}$$

With the controlled addition of citric acid anhydrous - $C_6H_8O_7$, dissolved at 50°C for 1h, the formation of tin citrate took place. The citric acid/metal molar ratio was fixed at 3:1.
Manganese acetate (Carlo Erba) was added at 0.5 mol% to obtain the doped compositions 0.5 Mol% MnO_2-doped tin dioxide. The polymerization occurred upon the addition of ethylene glycol - $C_2H_6O_2$. The mass ratio of the citric acid/ethylene glycol was set at 60:40.
This mixture was then stirred at 80°C for 1h until the solution became completely transparent. This solution was further heated at 130°C to promote polymerization and remove excess solvents.
The powder obtained was heat-treated in an oxygen atmosphere at 400°C for 4 hours, in order to oxidate the remaining organic matter. The powder obtained in this way is referred to as the "precursor". In the furnace, the precursor was heat-treated at the 600°C during 15 hours, in an Al_2O_3 boat, and then cooled to room temperature.
This obtained powder was compacted by uniaxial pressing (SCHWING SIWA-15T) using pressure of 15 MPa followed by isostatic pressing (CARLZEISS-JENA) using pressure of 210 MPa forming cylindrical disks of approximately 6.0 mm of diameter and 6.0 mm of height, where the green density reached 60% of the theoretical density. The sintering process was performed in a dilatometer (NETZSCH 402E) using a constant heating rate of 2.5°C/min under atmosphere of synthetic air, reaching the final temperature of 1350°C and soak time ranging from 30-120 minutes.
The disks of sintered 0.5 Mol% MnO_2-doped tin dioxide were observed by Transmission Electronic Microscopy (TEM) employing a Philips CM200 equipment.
A standard procedure for TEM sample preparation starting from bulk samples which included cutting, grinding and dimpling was used.
Atomic force microscopy (AFM) was used to obtain an accurate analysis of the sample surface and the quantification of very important parameters such as roughness and average grain size. A Digital Instruments Multimode Nanoscope IIIa (Santa Barbara, CA) was used. AFM imaging was carried out in the contact mode, using a triangular-shaped 200-μm long cantilever with a spring constant of 0.06 N/m.

3. Results

The curves of linear shrinkage and shrinkage rate are depicted in the Fig. 1. By means of this analysis it was possible to verify that the 0,5 Mol% manganese doping in tin dioxide is a sufficient amount to obtain sintered samples with densification closer to theoretical densitiy (25%). The derivative of the curve represents a sintering in solid phase without chemical substance transformation.

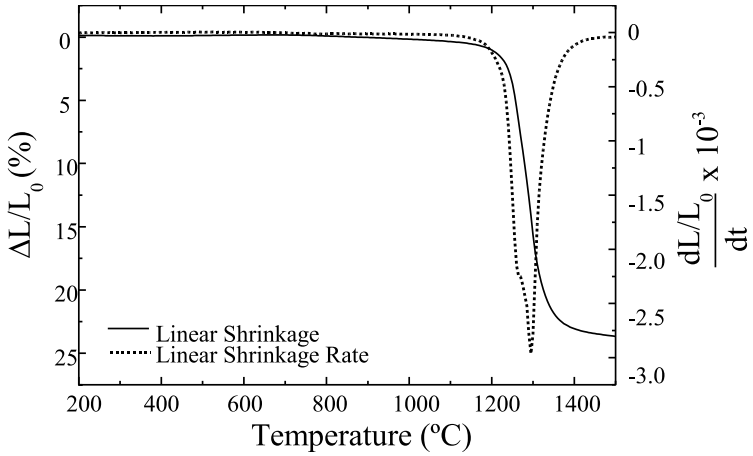

Fig. 1. Linear shrinkage and shrinkage rate of the sintered 0.5 Mol% MnO_2-doped tin dioxide samples.

The sintered tin dioxide tend to form an equilibrium angle of 120° in the bulk interior due to the vectorial action of the resultants in agreement with the micrograph of transmission electronic microscopy of the Fig. 2

Fig. 2. Micrograph of transmission electronic microscopy of sintered sample of 0.5 Mol% MnO_2-doped tin dioxide.

By means of atomic force microscopy (AFM) an accurate analysis of the interaction among the grains, surface roughness and porosity was obtained, according to Fig 3.

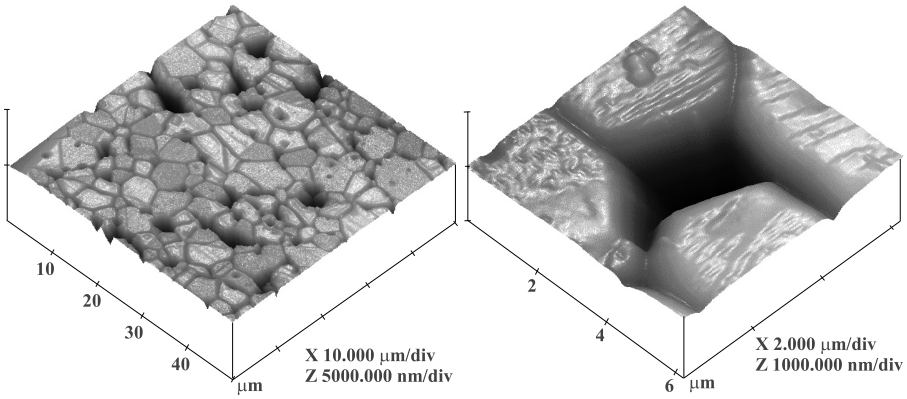

(a) (b)

Fig. 3. AFM micrographs of the sintered 0.5 Mol% MnO_2-doped tin dioxide samples. Soak time of (a) 30 minutes, (b) 50 minutes, indicating the pore detail.

Data of dihedral angles was obtained by means of AFM using procedures of section analysis, according to Fig. 4. An imaginary line is inserted under the micrograph by means of a cursor (indicated by an arrow in the Fig. 4a). The porosity and dihedral angles are determined when the cursor moves along the line. The dihedral angle was determined by extracting and adding, two adjacent angles were subtracted from 180°.

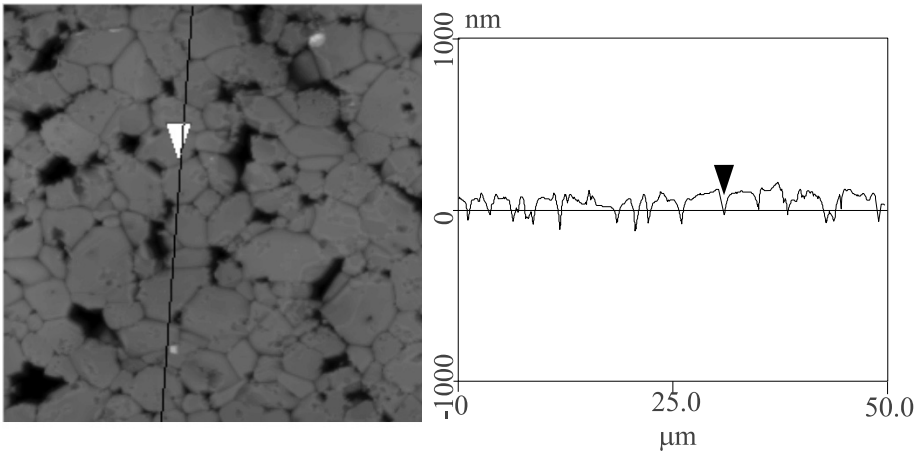

(a) (b)

Fig. 4. Determination of dihedral angle and porosity by AFM. a) Micrograph with imaginary line and lecture cursor represented by an arrow. b) Representation of the cross-section attained by the cursor.

In this way, the obtained dihedral angles are of statistic significance. An average of 300 angles per sample was considered in order to obtain a more precision value (±2.1°). Thus, the dihedral angles are changed when the soak time is raised, in accordance with Fig. 5.

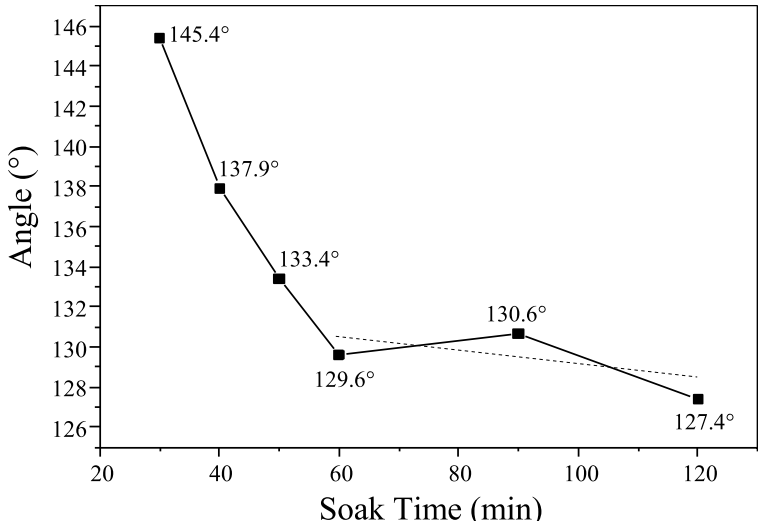

Fig. 5. Angular evolution according to the time required to reach the equilibrium angle. SnO_2.0.5Mol%MnO_2. AFM Dihedral angle Thermal treatment. Er=± 1.38. FFT linear = 129.22°

With the soak time ranging from 30 up to 120 minutes, the angle is decreased from 145° to 129°. However, the angle remain practically constant around 129.22° (±1.38°) for thermal treatment with soak times higher than 60 minutes. In this way, the dihedral equilibrium angle was determined.

This process is due to the migration of the manganese to the surface of tin dioxide caused by the higher temperature of thermal treatment. The exudation causes disequilibrium in the vectorial composition among the interfaces energy. Consequently, the chemical potential of SnO_2 grain boundaries is reduced as a attempt to return at the equilibrium.

The equilibrium of the grain growth in the surface is attained through thermal treatment with soak time higher than 60 minutes. This process is named as equilibrium dihedral angle.

Tab. 1 shows the number of times (fraction) that the dihedrals angles was extracted from AFM micrographs in function of the values of those angles and, for each thermal treatment. The angles were counted at each 10° starting from 90° up to 160°. In this way, the frequency in each angular interval was determined.

Fig. 6 was plotted from results of Tab. 1 by means of Gaussian fitting. In this plot, the angular fraction appearances (in percentage) is a function of the angular intervals obtained by AFM micrographs.

A displacement of the plots was made in order to verify the effect of manganese migration into the SnO_2 surface. Thus, the maximum point of each plot was moved to a same point related to the angles axis to evaluate the width at half maximum of each plot. Such width is reduced when the time of thermal attack is increased, in accordance with the Table 2). Consequently, the manganese exudation is more effective and the SnO_2 dihedral surface angles became more uniforms along the whole analyzed surface for samples heat treated with soak times higher than 60 minutes.

Thus, by means of Fig. 6 it is possible to observe that the manganese is moved to surface in a homogeneous way related to the time of thermal attack. Furthermore, the

	Soak time (min)					
Angle (°)	30	40	50	60	90	120
90°	3 %	3 %	2 %	2 %	0 %	2 %
100°	3 %	3 %	3 %	3 %	1 %	3 %
110°	3 %	3 %	8 %	8 %	8 %	8 %
120°	6 %	5 %	19 %	19 %	22 %	23 %
130°	24 %	16 %	29 %	29 %	31 %	33 %
140°	38 %	33 %	25 %	24 %	25 %	21 %
150°	19 %	27 %	11 %	11 %	10 %	6 %
160°	4 %	10 %	3 %	4 %	3 %	4 %

Table 1. Angular fraction corresponding for the soak times.

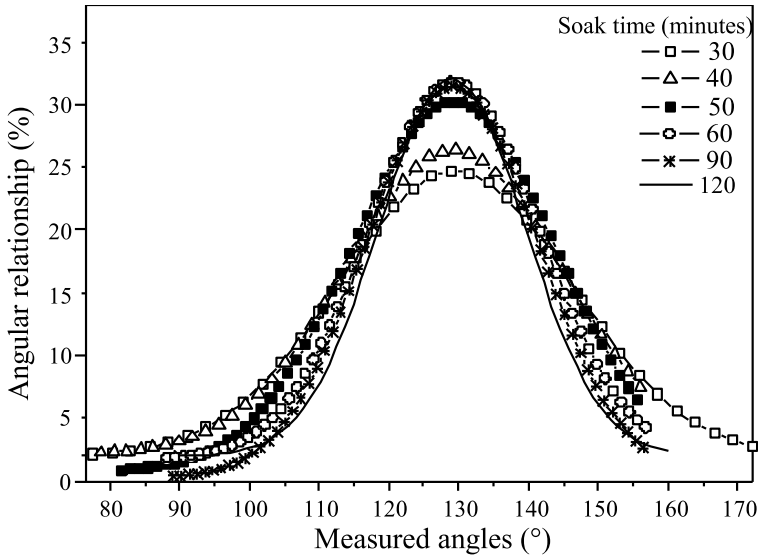

Fig. 6. Gaussian curve of the angular proportion according to the dihedral angles values.

Soak time (min)	Width at half maximum
30	33°
40	27.3°
50	28.3°
60	24.9°
90	24°
120	24.3°

Table 2. Angular difference of width at half maximum related to the soak time.

appearing frequency of the SnO_2 dihedral angles in the surface is also related to the time and temperature.

4. Conclusion

The tin dioxide doped with a densifier agent, such as MnO_2, has a high energy gradient in the external surface when sintered. The observed grain growth is an indicative that the surface is affected by the thermal treatment. SEM micrographs showed the manganese exudation effect on the surface when the sample was heated at optimized conditions. This manganese migration at the surface led to a new grain growth in the extenal surface of the sample due to the gradient in the potential energy surface. The temperature influenced by the dynamic geometry of the oxide surface was characterized by AFM analysis. Also, this is true for anisotropic grain growth, such as in this case of SnO_2. This grain growth originated in the oxide surface is only stopped when a new angular equilibrium is stablished. In this way, a relationship between time of thermal attack and formation of a new surface equilibrium can be obtained. This process is named as equilibrium dihedral angle.

5. Acknowledgments

The authors gratefully acknowledge the financial support of the Brazilian financing agencies PIBIC/CNPq and Paraná Tecnologia.

6. References

Baccan, N., Aleixo, L., Stein, E. & Godinho, O. (1990). 3rd edition edn, Unicamp, Campinas.

Beeman, M. L. & Kohlstedt, D. L. (1993). Deformation of fine-grained aggregates of olivine plus melt at high-temperatures and pressures, *J. Geophys. Res.-Solid Earth* 98(B4): 6443–6452.

Belousov, V. V. (2003). Wetting of grain boundaries in cuprate ceramics, *Inorg. Mater.* 39(1): 82–89.

Belousov, V. V. (2004). Wetting of grain boundaries in ceramic materials, *Colloid J.* 66(2): 121–127.

Besso, M. (n.d.). US Patent No 3123120. 19-10-65.

Cassia-Santos, M. R., Souza, A. G., Soledade, L. E. B., Varela, J. A. & Longo, E. (2005). Thermal and structural investigation of $(Sn_{1-x}Ti_x)O_2$ obtained by the polymeric precursor method, *J. Therm. Anal. Calorim.* 79(2): 415–420.

Cava, S., Sequinel, T., Berger, D. & Tebcherani, S. M. (2009). Synthesis and characterization of microspheres composed of SnO_2 nanoparticles processed via a chemical route, *Powder Technol.* .

Cava, S., Sequinel, T., Tebcherani, S. M., Michel, M. D., Lazaro, S. R. & Pianaro, S. A. (2009). Microstructure of ceramic particles infiltrated into float glass surfaces by high gas pressure impregnation, *J. Alloys Compd.* doi:10.1016/j.jallcom.2009.05.061: .

Cava, S., Tebcherani, S. M., Pianaro, S. A., Paskocimas, C. A., Longo, E. & Varela, J. (2006). Structural and spectroscopic analysis of γ-Al_2O_3 to α-Al_2O_3-$CoAl_2O_4$ phase transition, *Materials Chemistry and Physics* 97: 102–108.

Cava, S., Tebcherani, S. M., Souza, I. A., Pianaro, S. A., Paskocimas, C. A., Longo, E. & Varela, J. A. (2007). Structural characterization of phase transition of Al_2O_3 nanopowders obtained by polymeric precursor method, *Mater. Chem. Phys.* 103(2-3): 394–399.

de Lucena, P. R., Pessoa-Netob, O. D., dos Santos, I. M. G., Souza, A. G., Longo, E. & Varela, J. A. (2005). Synthesis by the polymeric precursor method and characterization of undoped and Sn, Cr and V-doped $ZrTiO_4$, *J. Alloy. Compd.* 397(1-2): 255–259.

Dhalenne, G., Dechamps, M. & Revcolevschi, A. (1983). *Advances in Ceramics*, Americam Ceramic Society, Columbus, OH, chapter Character of grain boundaries, pp. 139–150.

Galakhov, A. V. (2009). Numerical method for simulating sintering, *Refractories and Industrial Ceramics* 50(3): 191–197.

Gonzalez, A. H. M., Simoes, A. Z., Zaghete, M. A., Longo, E. & Varela, J. A. (2004). Effect of thermal treatment temperature on the crystallinity and morphology of $LiTaO_3$ thin films prepared from polymeric precursor method, *J. Electroceram.* 13(1-3): 353–359.

Hansen, J. D., Rusin, R. P., Teng, M. H. & Johnson, D. L. (1992). Combined-stage sintering model, *J. Am. Ceram. Soc.* 75(5): 1129–1135.

Herring, C. (1950). Effect of change of scale on sintering phenomena, *J. Appl. Phys.* 21(4): 301–303.

Herring, C. (1951). *The physics of powder metallurgy*, McGraw-Hill.

Jin, M. X., Shimada, E. & Ikuma, Y. (2000). Atomic force microscopy study of surface diffusion in polycrystalline CeO_2 via grain boundary grooving, *J. Ceram. Soc. Jpn.* 108(5): 456–461.

Kinderlehrer, D., Ta'asan, S., Livshits, I. & Mason, D. E. (2002). The surface energy of mgo: Multiscale reconstruction from thermal groove geometry, *Interface Sci.* 10(2-3): 233–242.

Kingery, W. D. (1994). *J. Am. Ceram. Soc.* 77(2): 349–355.

Moment, R. L. & Gordon, R. B. (1964). Energy of grain boundaries in halite, *J. Am. Ceram. Soc.* 47(11): 570–573.

Munoz, N. E., Gilliss, S. R. & Carter, C. B. (2004). Remnant grooves on alumina surfaces, *Surf. Sci.* 573(3): 391–402.

Pontes, F. M., Leite, E. R., Nunes, M. S. J., Pontes, D. S. L., Longo, E., Magnani, R., Pizani, P. S. & Varela, J. A. (2004). Preparation of $Pb(Zr,Ti)O^{-3}$ thin films by soft chemical route, *J. European Ceram. Soc.* 24(10-11): 2969–2976.

Readey, D. W. & Jech, R. E. (1968). Energies and grooving kinetics of [001] tilt boundaries in nickel oxide, *J. Am. Ceram. Soc.* 51(4): 201–&.

Saylor, D. M., Mason, D. E. & Rohrer, G. S. (2000). Experimental method for determining surface energy anisotropy and its application to magnesia, *J. Am. Ceram. Soc.* 83(5): 1226–1232.

Saylor, D. M. & Rohrer, G. S. (1999). Measuring the influence of grain-boundary misorientation on thermal groove geometry in ceramic polycrystals, *J. Am. Ceram. Soc.* 82(6): 1529–1536.

Shackelford, J. F. & Scott, W. D. (1968). Relative energies of [1100] tilt boundaries in aluminum oxide, *J. Am. Ceram. Soc.* 51(12): 688–&.

Shi, J. L. (1999). Solid state sintering of ceramics: pore microstructure models, densification equations and applications, *J. Mater. Sci.* 34(15): 3801–3812.

Simoes, A. Z., Gonzalez, A. H. M., Riccardi, C. S., Souza, E. C., Moura, F., Zaghete, M. A., Longo, E. & Varela, J. A. (2004). Ferroelectric and dielectric properties of lanthanum-modified bismuth titanate thin films obtained by the polymeric precursor method, *J. Electroceram.* 13(1-3): 65–70.

Simoes, A. Z., Ramirez, M. A., Perruci, N. A., Riccardi, C. S., Longo, E. & Varela, J. A. (2005). Retention characteristics in $Bi_{3.25}La_{0.75}Ti_3O_{12}$ thin films prepared the polymeric precursor method, *Appl. Phys. Lett.* 86(11): 112909.

Simoes, A. Z., Ramirez, M. A., Riccardi, C. S., Ries, A., Longo, E. & Varela, J. A. (2005). Influence of temperature on the dielectric and ferroelectric operties of bismuth titanate thin films obtained by the polymeric precursor method, *Mater. Chem. Phys.* 92(2-3): 373–378.

Simoes, A. Z., Ries, A., Moura, F., Riccardi, C. S., Longo, E. & Varela, J. A. (2005). Influence of the solution ph on the morphological, structural and electrical properties of $Bi_{3.25}La_{0.75}Ti_3O_{12}$ thin films obtained by the polymeric precursor method, *Mater. Lett.* 59(22): 2759–2764.

Wolf, D. (1983). *Advances in Ceramics*, Americam Ceramic Society, Columbus, OH, chapter Character of grain boundaries, pp. 36–43.

Xin, T. H. & Wong, H. (2003). Grain-boundary grooving by surface diffusion with strong surface energy anisotropy, *Acta Mater.* 51(8): 2305–2317.

18

Microstructural Evolution in α-Al_2O_3 Compacts During Laser Irradiation

Marina Vlasova, Mykola Kakazey and
Pedro Antonio Márquez -Aguilar
CIICAp-Universidad Autonoma del Estado de Morelos,
Cuernavaca, Morelos
Mexico

1. Introduction

Laser opening (Ali et al.,1960; Maiman, 1960 ; Townes, 1960) and development of many various types of lasers (Goodison, 2008; Injeyan & Goodno, 2011; Träger, 2007; Weber, 2001) stimulated their wide practical application (Rastogi & Asundi, 2011; Ready, 2001; Ready, 1971; Webb & Jones, 2003; Weber, 1994). The basic properties distinguishing laser radiation from radiation of usual light sources are intensity, an orientation, monochromaticity and coherence (Ready, 1971). The important role has both maximum peak pulse power, and possibility to allocate energy in the set point of space. More important characteristic, than the absolute value of peak power, is a power on an unit of surface of target. The directivity, monochromaticity and coherence of laser beam allow to focus laser light into a spot of very small size. Depending on intensity and duration of action of laser radiation, the following stages of interaction of radiation with a treated material distinguish: supply of laser radiation to a material, an absorption of a light flux and transfer of its energy to a solid body, heating of a material without visible destruction, a melting of material, evaporation and elimination (ablation) of products of destruction, electronic and ionic emission from the surface, plasma formation, cooling of a material after the ending of laser influence (Shishkovskii, 2009). Selective laser sintering (SLS) of powders is one of new technologies of obtaining of superficial coverings from nano-structured materials (Deckard, 1988). This direction results to develop a concept model of prototypes ("Rapid Prototyping"). This is method of formation of 3d-model level-by-level sintering of powder materials (Gebhardt & Hancer, 2003). At first, main direction of works of SLS had practice character: an obtaining of a material with specified properties, and with specified forms, etc. At the same time, the high-speed heating inherent to laser influence in processes of SLS and the technologies integrated with it, opens possibilities for investigation of features of diffusion, kinetic, structurally-phase, rheological, and mechanical processes, in conditions far from equilibrium and poorly studied. In the present work we will bring some results of investigation of the reactionary and structural changes proceeding in pressings from mixtures of α-Al_2O_3 and α-Cr_2O_3 powders at their superficial laser treatment. An important moment here is that the processed system (pressings) also is under nonequilibrium condition.

Alumina (α-Al_2O_3) has many industrial applications, including refractory bricks, electric insulators, and protective coatings (Dorre & Hubner, 1984; Gebhardt & Hancer, 2003). So alumina ceramics is used in nuclear power plants as a heat and an electric insulator in the active zone, for IR windows or as armor for low threat applications where thinner tiles can be used (Pampuch & Haberko, 1997; Shevchenko & Barinov, 1993; Tretyakov, 1987; Wefers & Misra, 1987). Its properties can be changed significantly by the introduction of different impurity centers. Among corundum-based ceramics, ruby, which is a solid solution of chromium ions in the solid structure of covalent Al_2O_3, is the most extensively used material. Ruby single crystals are used as working elements of lasers. The compounds α-Al_2O_3 and α-Cr_2O_3 are isomorphous and their mutual solid solutions α-$Cr_xAl_{2-x}O_3$ form a single phase with a corundum structure within the composition range $0 \le x \le 2$. The method of horizontal directed crystallization (HDC) is widely used in the synthesis of large corundum (sapphire) and ruby monocrystals (Bagdasarov, 2004; Bagdasarov & Goryainov, 2001; Bagdasarov & Goryainov, 2007; Lukanina et al., 2006; Hurle,1994; Lyubo, 1975). The HDS method consists in the following (Bagdasarov, 2004): a mixture in the form of a powder, crystal breakage, or ceramic tablets is loaded into a boat-shaped container. By moving this container through the heating zone, the mixture is melted, and then the melt is crystallized in the cold zone. To obtain a strictly oriented monocrystals, a seeding agent is placed in the top of boat, after which both the moment of crystallization and the shape of the crystallization front in the process of monocrystal growth is monitored. The thermophysical processes play a decisive role in the crystallization of high-quality monocrystals because they are responsible for the generation of substantial internal mechanical stresses, porosity, and high dislocation density (Bagdasarov & Goryainov, 2001; Bagdasarov & Goryainov, 2007; Denisov et al., 2007; ; Dobrovinskaya et al., 2009; Lukanina et al., 2006; Malukov et al., 2008).

In recent years, along with traditional powder metallurgy methods for the synthesis of corundum ceramics, SLS has been used (Liu et al., 2007; Shishkovskii, 2009; Shishkovsky et al., 2007; Subramanian & Marcus, 1995; Subramanian et al., 1993; Xu et al., 2005), what makes it possible to combine complete and partial melting in a single cycle. The next stage of development of this technology is layer-by-layer SLS.

Results of investigations of the laser melted specimens (Ferkel et al., 1997; Majumdar et al., 2004; Triantafyllidis et al., 2002; Triantafyllidis et al., 2004; Wang et al., 2004; Zum-Gahr et al., 1995) show that laser scanning influences significantly the surface morphology, microstructure, and phase components of laser-treated zones. Thus, the laser treatment of the surfaces of ceramic samples, accompanied by its melting and resolidification, can be successfully used to modify their surface properties. In this the processes proceeding during laser treatment of powder mixtures of different compositions deserve particular attention. So, the temperature conditions, fast melting - fast crystallization, produced during the process is an interesting direction of preparing new ceramic materials (on the basis of mixes of powders with various temperature properties) in which a controlled inhomogeneous distribution of the impurities, the phases, etc. can be realized. In layer by layer SLS of corundum, additives which play the role of binders of grains of the basic material in the stage of powder pressing and sintering are introduced in Al_2O_3 powder to provide the required density and strength of the consolidated material (Bai & Li Y. 2009; Ferkel et al., 1997; Shishkovskii, 2005; Shishkovsky et al., 2007; Subramanian & Marcus, 1995; Subramanian et al., 1993). Among these methods are SLS of both α-Al_2O_3 (Da Shen et al., 2007; Zhao et al., 2003) and α-Al_2O_3-α-Cr_2O_3 (Nubling & Harrington, 1997; Quispe Cancapa et al., 2002; Yen, 1999).

A large number of studies by different methods were performed on dilute both low-chromium and high-chromium α-Al_2O_3 solid solutions (Carman & Kroenke 1968; de Biasi & Rodrigues 1985; Galoisy & Calas 1993; Manenkov & Prokhorov, 1955; O'Reilly & Maciver, 1962; Statz et al., 1961; Stone & Vickerman 1971;). Gradual increases in the *a* and *c* parameters of the hexagonal unit cell of the corundum structure with increasing chromium concentration were noted (de Biasi & Rodrigues 1985). The fine structure of the electron paramagnetic resonance (EPR) spectrum of the ion Cr^{3+} in corundum crystal was investigated (Manenkov & Prokhorov 1955). Four types of EPR spectra were observed in α-$Cr_xAl_{2-x}O_3$ polycrystalline specimens (Carman & Kroenke, 1968; Stone & Vickerman 1971).
This work is concerned with an experimental investigation of the surface solutionizing, crystallization, microstructure, and properties induced by a laser beam in pressings of α-Al_2O_3 + *n*α-Cr_2O_3 powders with using EPR spectroscopy, X-ray diffraction and electron microscopy methods. In the methodical plan the work is constructed in the following way. In the beginning of the work we will consider evolutionary processes in compacted α-Al_2O_3 + α-Cr_2O_3 mixtures at one-pass laser treatment. Farther we will examine the layer by layer laser sintering of Al_2O_3-xCr_2O_3 powder mixture. After that the laser surface solutionizing and crystallization in Al_2O_3-xCr_2O_3 pellets will be analyzed. And then will be discussed the laser synthesis of crystalline ruby rods from Al_2O_3- xCr_2O_3 ceramic rods.

2. Experimental procedure

2.1 Initial reactives

Commercially available α-Al_2O_3 and α-Cr_2O_3 (Reasol, Reactivo Analitico) with a particle size of 40 nm and 1.8 nm, respectively, were used as starting materials. Powder mixtures of α-Al_2O_3 + *n*α-Cr_2O_3 with *n* = 0.1 wt %, 0.5 wt %, 1.0 wt %, 3.0 wt %, 5.0 wt % and 10.0 wt % were homogenized mixing in ball mill with a low rotation rate (around 50 rpm) during 30 min.

2.2 Preparation of samples for laser processing

On the base of these powder mixtures a series of cylindrical specimens (pellets and cores) with a diameter 3 – 30 mm and a thick (length) of 3 to 15 mm were made by axial pressure, *P* (to 5 MPa) or isostatical pressure (to 5 GPa). Also was using the extrusion technology for obtaining of cylindrical specimens with a diameter 3 mm and a length of 10 to 15 mm with their subsequent sintering at 1200 ^oC.

2.3 Laser processing

The laser processing of the samples was carried out with using a 10.6 μm CO_2 laser (CW-CO_2 Spectra Physics 820, the output power was 130 W) and LTN-103 continuous-action Nd^{3+}:YAG laser (λ = 1064 nm, maximum output power is ~ 200 W, Russia). Different conditions of irradiation: the diameter of the laser spot (d), the scanning velocity (v), the irradiation power (P) were used.
In case of trying out an experiment on horizontal directed crystallization (HDC) of ruby the LTN-103 laser, d = 0.2 mm and d = 0.8 mm, v ~ 0.0094 mm/s 0.019, and 0.075 mm/s, P ~ 70 W were used. The laser irradiation was performed along long axes of the compacts prepared by using extrusion technology and following thermal treatment at 1200 ^oC for 1 h. The compacts have a diameter 3 mm and a length of 10 to 15 mm. Specimens were placed in channels formed on surfaces of compacts made from the same mixture by one-pass treatment with a laser beam. After irradiation, the specimens had the shape of rods with a length of 5 to10 mm and a diameter of 1.5 to 2 mm.

In more details conditions of laser treatment of specimens are given in the beginning of paragraphs 3.1, 3.2, 3.3 i 3.4.

2.4 Experimental methods

The initial samples and the laser-treated (LT) sample surface were characterized using powder XRD (Siemens D-500) in CuK_α radiation.

The method of Electron Paramagnetic Resonance (EPR; SE/X 2547-Radiopan; x-ray range; at room temperature) spectroscopy was used to study the different paramagnetic centers (PC) in LT-samples. EPR-recording was carried out through the whole volume of specimens. EPR-measurements were also performed depending on the angle between the external magnetic field and an LT-surface of a specimen. Also, single crystal of Cr doped α- Al_2O_3 was used in this studies.

Infra Red (IR) spectra were obtained with a Specord M80 spectrometer (Karl Zeiss, Germany).

An electron microscopy study was performed with a Superprobe-733 scanning electron microscope (JEOL, Japan) and a SEM/FIB NOVA 200 system (Bruker, Gemany).

3. Experimental results and discussion

3.1 One-pass laser treatment of powder pellets of Al_2O_3- xCr_2O_3

Using the laser facility, one-pass treatment of the surface of a pellets prepared at 5 MPa were performed at P = 60, 70, 160 and 190 W. The scanning velocity (v) of laser beam was 0.075, 0.15, 0.25, and 0.3 mm/s. The size of laser beam was d = 0.2 – 0.6 mm. In this case, concave channels formed on the surface (Fig. 1a). On the surface, one can see arcs. Theirs formation is a result of melting → cooling of corundum during transverse of the laser beam. On the lateral walls of the channel, strips formed as a result of dissociation of Al_2O_3 (Fig. 1 b) are seen. The depth of the channel, the thickness of the melting-recrystallized layer (h_1), and zone of sintering (h_2) depends on irradiation parameters, namely, the irradiation power and the traverse speed of the laser beam (Fig. 2) (Vlasova et al., in pres. accept.). In Fig. 3, the growth of corundum crystallites from the bottom part of the track to its surface is shown. The color of the superficial layer changes from pink to deep-brown depending on the α-Cr_2O_3 amount in the initial specimen. Also the color changes from superficial to a zone of sintering and further up to initial colour of compacted mixture.

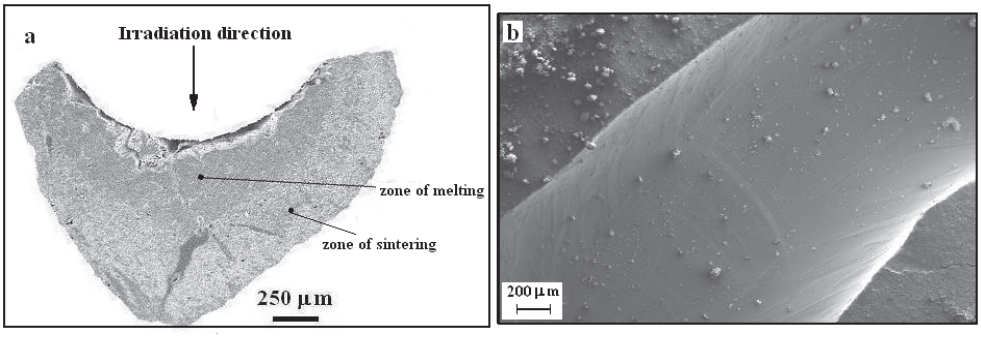

Fig. 1. Micrographs of channels formed in one-pass laser treatment of a compact at P = 160 W and v = 1.25 mm/s. (a) cross section; (b) the top view.

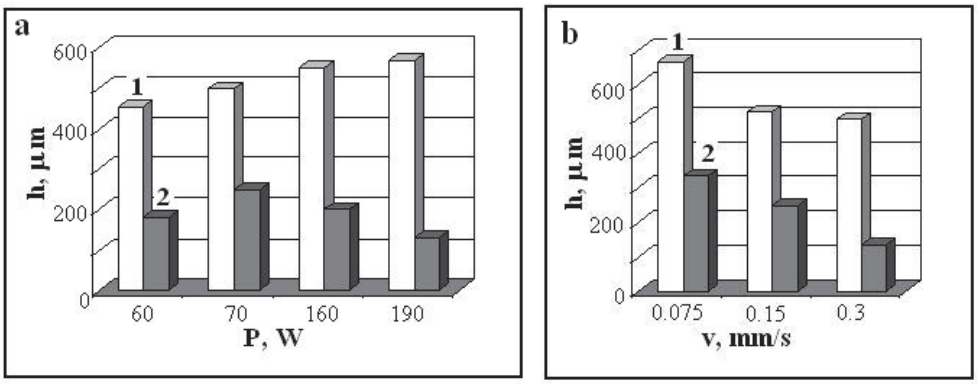

Fig. 2. Changes in the maximal thicknesses of the recrystallized layer (1) and sintered layer (2) depending on the power (a) and the traverse speed (b) of the laser beam in one-pass laser treatment. For (a) at v = 0.15 mm/s. For (b) P = 70 W.

IR absorption spectra of corundum for different layers of the material located under the track illustrate the gradual weakening of the band at ν_2 ~ 500 cm^{-1} as the distance to the track decreases (Fig. 4, spectra 2–6). The weak intensity of band ν_2 is characteristic for a ruby. A spectrum obtained from the track is assigned to the IR spectrum of α-Al_2O_3 (Vlasova et al., 1972) (see Fig. 4, spectra 1, 2 and 6). For the superficial layer of track, the intensity of the spectrum appears to be much weaker than for the subsurface layers. The weakening (see Fig. 4 curve 1) is connected with the gradual defects accumulation and increasing electroconductivity in the surface layer of the track.

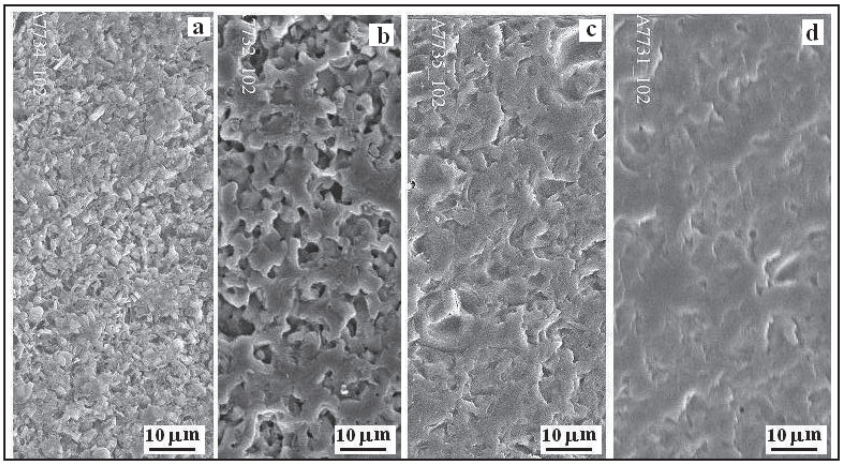

Fig. 3. Micrographs of channels formed in one-pass treatment at P = 70 W and v = 0.075 mm/s: (a)–(d) correspond to the direction of photographing from the bottom of the channel to its surface.

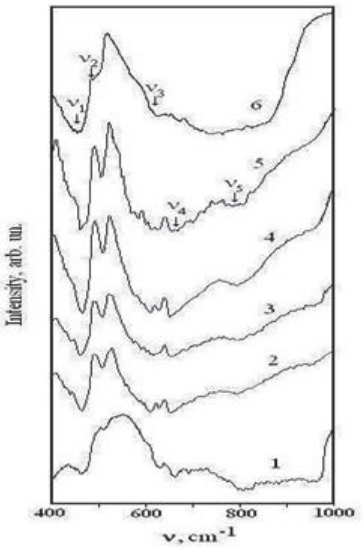

Fig. 4. IR absorption spectra of the superficial layer of a track (1) and in layers under the superficial layer by 0.5 μm (2), 1.0 μm (3) and 1.5 μm (4). Comparison of spectra of corundum (5) and ruby (6). The sample:KBr ratio is 1:150 for spectrum (1) and 1:300 for spectra (2-6).

3.2 Layer by layer laser treatment of pellets of Al_2O_3- xCr_2O_3 (Vlasova et al., 2010)

An experiments on the layer-by-layer selective laser sintering (SLS) were carried out on pellets obtained by axial pressing at P = 5 MPa. Used capacities of the LTN-103 laser were P ~ 90, 120, 160, and 190 W, v ~ 0.13 mm/s 0.13, 0.26, 0.4, 0.64, and 1.25 mm/s, d = 0.2 mm. The system of vertical movement of a sample without changes in the size of the laser spot enabled us to perform additional operations on the surface of compacts. At the beginning the unitary treatment of surface of compact by laser beam was carried out. At multiple-run treatment an originally formed concave track was filled up by the powder mixture. A powder was consolidated and planed. After this procedure a filled channel was subjected to irradiation. The procedure of filling of the channel by a powder mixture and its irradiations again was repeated. The number of such backfills of channel and procedure of irradiation was from 2 to 12. Gradually above the specimen surface a convex track appeared. The height of backfill inside each series of experiments was constant. A series of experiments was realized in which the height of backfills was different: h_1 = 125 μm, h_2 = 250 μm, h_3 = 350 μm, and h_4 = 500 μm.

As the layers build up, the thickness of the new-formed product (α-Al_2O_3) gradually increases (Fig. 5). This means that, in the chosen mode of treatment, not the whole volume of the backfill is melted and recrystallized. Most pores and cracks are present between the layers. The size and the number of pores increase as the traverse speed of the laser beam rises. These data show that to obtain a low-porosity track material, it is necessary to reduce substantially the traverse speed of the laser beam. As a result, a new-formed liquid phase can fill cavities, pores, and cracks of the underlying layer. Note that, as a result of the

dissociation and ablation of Al_2O_3 (Vlasova et al., 2010) the largest number of cavities and channels form in the surface layers of tracks. As in a case of the one-layer tracks, with decrease in v at a rather low power (P ~ 60–70 W), the thicknesses of the layers h_1 and h_2 increase. At a low traverse speed of the laser beam, a multilayered building-up of corundum (layer h_1) is accompanied by a decrease in the thickness of the sintered layer (h_2). It is likely that cause of this effect is the high thermal conductivity of corundum.
X-Ray measurements and EPR investigation of spectrum of Cr^{3+} in polycrystalline Al_2O_3 haven't revealed appreciable differences in different layers.

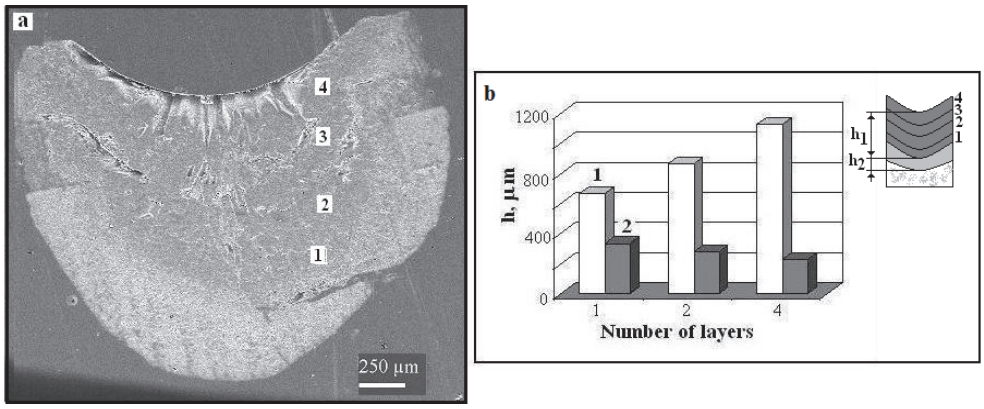

Fig. 5. Micrographs of channels formed in four-run treatment (a) and changes in the maximal thicknesses of the recrystallized layer (1) and sintered layer (2) depending on the number of backfills at (b). P = 70 W, v = 0.075 mm/s. 1–4 correspond to the numbers of layers.

3.3 Laser surface treatment of powder pellets of Al_2O_3- xCr_2O_3 (Kakazey et al., 2009)

For irradiation of pellets obtained by hydrostatic pressure at 5 GPa, the CO_2-laser with P = 130 W, d = 0.3 mm, v = 0.7 mm/s were used. Three laser scannings of the same trace were performed in a spiral motion with a step of 0.25 mm beginning from the center of a pellet.
During one-pass laser treatment of dense pellets, concave tracks also forms on their surfaces. However, in this case, the depth of tracks is much smaller than that in the case irradiation of loose powder specimens. The thickness (h_1) of the formed ruby layer is ~0.3 mm even under high-power irradiation (160–190 W). The thickness of the sintering zone is comparable or slightly larger than the thickness of the recrystallization zone. On a chip of a track (Fig. 6), we can see that a sintering zone transforms into a recrystallization zone and that corundum crystallites increase in size as the distance to the surface of the track decreases. On the surface of the track, cracks, boundaries of crystallites, and striation, which appears due to the ablation of the track material, are present. So, the growth of crystallites occurs from the lower layers of pellets to the surface. Crystallites are initially directed perpendicularly to the surface of the track. However, as the distance to the surface decreases, crystallites begin to deviate from vertical to horizontal direction. They take the bent shape and an identical orientation, i.e., texturing that is set by the traverse of the laser beam occurs.
For the given case it was possible to carry out the x-ray analysis of the irradiated tracks without destroying specimen. The XRD pattern of the initial sample is shown in Fig. 7 (1).

The positions and normalized intensities of their X-ray peaks are very close to those of X-ray peaks for an ideal powder specimen consisting of the α-Al_2O_3 and α-Cr_2O_3 (JCPDS-International Centre for Diffraction Data, 1999) (see Table 1). The XRD patterns of superficial layer of different LP-samples (with different contents α-Cr_2O_3) are shown in Fig. 7 (2-6). The normalized intensities of the LT samples (see Fig. 7 and Table 1) show the presence of the following preferred orientations of α-Al_2O_3 crystallites: [1010] in an α-Al_2O_3 + 0.1% α-Cr_2O_3 sample; [116] in an α-Al_2O_3 + 0.5% α-Cr_2O_3 sample; [116] and [113] in an α-Al_2O_3 + 1.0% α-Cr_2O_3 sample; [116] in an α-Al_2O_3 + 5.0% α-Cr_2O_3 sample; [116] and [012] in an α-Al_2O_3 + 10.0% α-Cr_2O_3 sample. The normalized intensities of α-Cr_2O_3 in LT α-Al_2O_3 + 10.0% α-Cr_2O_3 sample show (Fig. 7) that the [110]-preferred orientation of α-Cr_2O_3 crystallites take place.

2-Theta	(h k l)	d(nm)	I_{theor}	I_{exp} Init. 10.0%	I_{exp} LT 0.1%	I_{exp} LT 0.5%	I_{exp} LT 1.0%	I_{exp} LT 5.0%	I_{exp} LT 10.0%
25.568	(0 1 2)	0.3479	683	370	20			130	999
35.140	(1 0 4)	0.2552	999	840	< 10		250		65
37.763	(1 1 0)	0.2379	460	370	< 10		220		250
43.339	(1 1 3)	0.2085	961	999	40		550		220
46.183	(2 0 2)	0.1964	2.0	3.0	60			130	
52.533	(0 2 4)	0.1740	467	470	10			270	
57.482	(1 1 6)	0.1601	906	940	100	999	999	999	900
66.493	(2 1 4)	0.1404	343	340	85		50		
68.181	(3 0 0)	0.1374	521	550			340		
76.854	(1010)	0.1239	145	180	999				

Table 1. Diffraction data for α-Al_2O_3.

In the initial α-Al_2O_3 + *n*α-Cr_2O_3 samples, only a weak broad EPR signal, which was due to defect states of the α-Cr_2O_3 phase, was registered at $g \sim 1.9$. In Fig. 8, the room-temperature EPR spectra of laser-treated α-Al_2O_3 + *n*α-Cr_2O_3 samples are shown. Some singularities (I—IV at $g_I \approx 1.22$, $g_{II} \approx 1.47$, $g_{III} \approx 3.38$, and $g_{IV} \approx 22$) of different intensities and shape were found in the EPR spectra.

The EPR spectra of Cr^{3+} ions in the Al_2O_3 lattice may be described by the axial spin Hamiltonian

$$H = g\beta BS + D\left[S_z^2 - \frac{1}{2}S(S+1)\right] \tag{1}$$

with parameters g = 1.984 and D = 5.746 GHz (Manenkov & Prokhorov, 1955). In polycrystalline samples the EPR spectrum represents a set of singularities (narrow signals) which position is defined by expression

$$\left|\nabla_0 B_r(\theta,\phi)\right| = \left[\left(dB_r/d\theta\right)^2\Delta\theta^2 + 1/\sin^2\theta\left(dB_r/d\phi\right)^2\Delta\phi^2\right)\right]^{1/2} = 0, \tag{2}$$

where $B_r(\theta,\phi)$ is angular dependence of fine structure EPR-lines in crystal, θ and ϕ are specify the spherical coordinates giving the relative orientation between direction of magnetic field B and the crystal axes (Kliava, 1988). The EPR spectrum of Cr^{3+} (singularities I—III) in Al_2O_3 polycrystalline samples is well known (Carman & Kroenke, 1968; de Biasi & Rodrigues, 1985; O'Reilly & Maciver, 1962; Stone & Vickerman, 1971). In order to identify signal IV, we compared the EPR spectrum for polycrystalline samples with an angular dependence of EPR curves of Cr^{3+} in ruby crystals (Fig. 8). In Fig. 9, we show that singularities I, II, III, and IV correspond to the EPR transitions (Cr^{3+}:Al_2O_3) -3/2 ↔ -1/2 (θ = 90°), -1/2 ↔ +1/2 (θ =35°), +1/2 ↔ +3/2 (θ =90°) and a forbidden transition (FT) (θ = 0 – 30°), respectively.

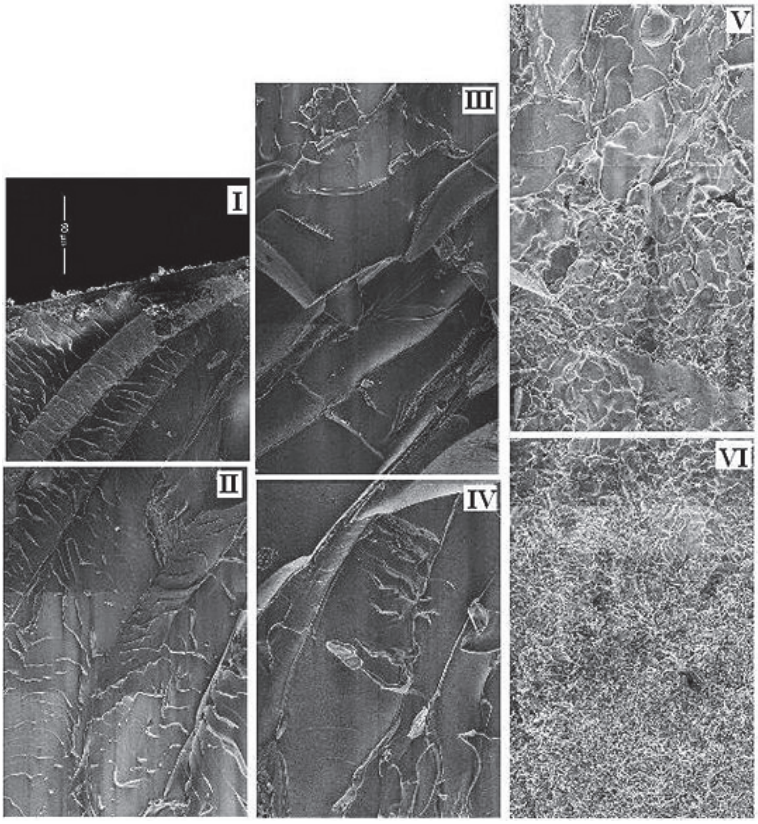

Fig. 6. Micrographs of the longitudinal section of channel. I → VI corresponds from the surface of channel to the bottom.

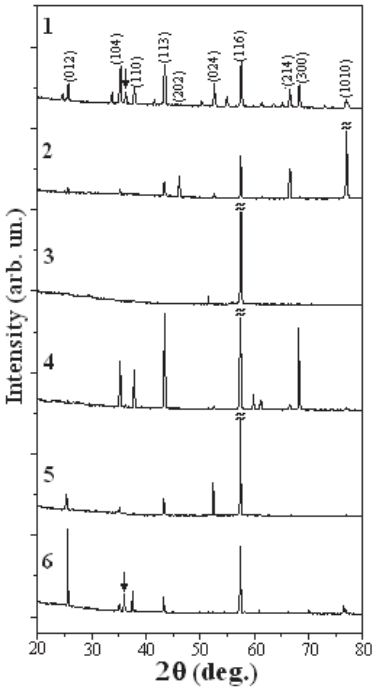

Fig. 7. X-ray diffraction patterns of α-Al_2O_3 + *n* α-Cr_2O_3 samples before and after LT: 1 , *n* = 10 wt. %, initial; 2, *n* = 0.1%, LT; 3, *n* = 0.5%, 4, *n* = 1.0%, LT; 5, *n* = 5.0%, LT; 6, *n* = 10.0%, LT. The arrow in 1 and 6 diffraction patterns indicates the (110) peak of α-Cr_2O_3.

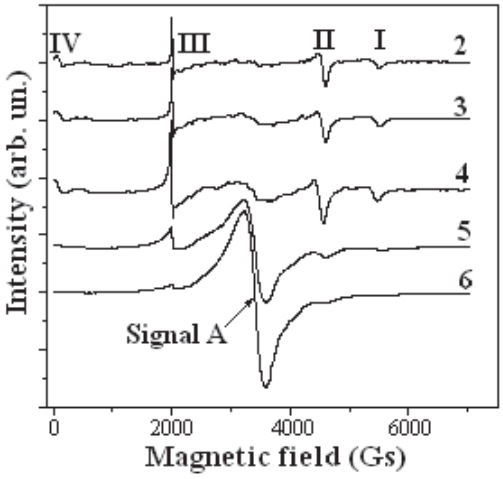

Fig. 8. EPR spectra in α-Al_2O_3 + *n*α-Cr_2O_3 laser treated samples. I - IV are designations of singularities (see text). 2, samples with *n* = 0.1% after LT; 3, *n* = 0.5%, 4, *n* = 1.0%, LT; 5, *n* = 5.0%, LT; 6, *n* = 10.0%, LT.

In Fig. 10, dependences of the amplitudes of singularities II and III on the angle φ between the external magnetic field and a perpendicular to the LT surface of a sample are presented. A decrease in the amplitude of the EPR singularity II and an increase in the amplitude of the EPR singularity III are observed as the angle φ increases from 0 to 90°. An increase in the amplitude of the EPR singularity II and a decrease in the amplitude of the EPR singularity III are observed as the angle φ increases from 90 to 180° (Fig. 10).

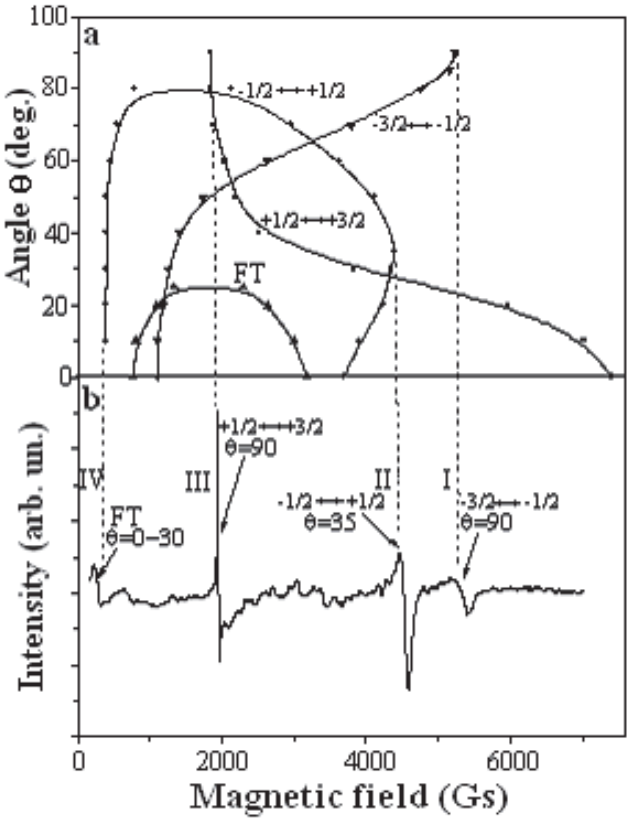

Fig. 9. The observed angular dependence of the EPR spectrum of Cr^{3+} ions in α-Al_2O_3 single crystal (a) and EPR spectrum in an α-Al_2O_3+0.1%α-Cr_2O_3 LT sample (b). I—IV are designations of singularities.

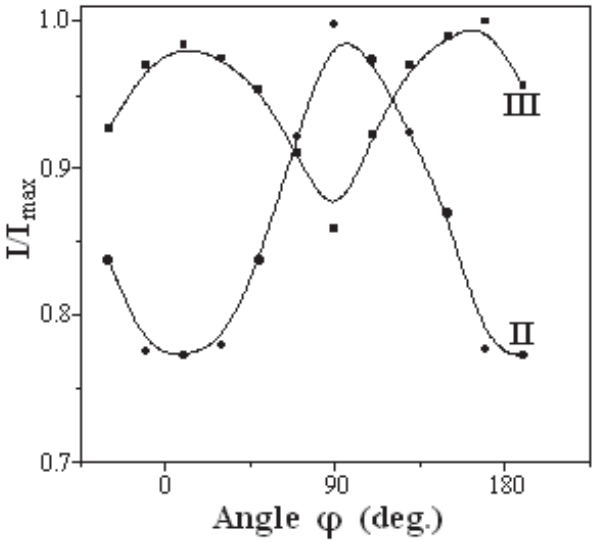

Fig. 10. Variations the I/I_{max} ratio for EPR-singularities II and III in an LT α-Al_2O_3 + 0.1% α-Cr_2O_3 specimen as functions of the angle φ between the external magnetic field and the perpendicular to the LT-sample surface.

At n > 1 wt %, in the α-Al_2O_3 + nα-Cr_2O_3 samples, decreases the amplitudes of singularities I—IV, the appearance and an increase of a new signal A at $g \approx 1.98$ are observed (Fig. 8). The decreases of the amplitudes of the singularities I—IV is accompanied by increases peak-to-peak line width and by the smearing of line. The width of signal A decreases with increasing n (ΔB_A is ~ 520 Gs for n = 1.0 wt %, ~ 380 Gs for n = 5.0 wt %, and ~ 320 Gs for n = 10.0 wt %). The A signal intensity is nearly proportional to the α-Cr_2O_3 on the amount in the initial samples.

The initial samples consist of mechanical mixtures of α-Al_2O_3 and α-Cr_2O_3 particles. The melting point of Al_2O_3 is 2046 °C and the melting point of Cr_2O_3 is 2334 °C. During high-temperature laser treatment, the fully melting of the α-Al_2O_3 particles and partially melting of the α-Cr_2O_3 particles occurs in the processed surface layer of sample (Fig. 6). The formed Al_2O_3 melt covers α-Cr_2O_3 particles. In this case, α-Cr_2O_3 particles dissolve gradually in the α-Al_2O_3 melt. However, as a result of the relatively short treatment, complete dissolution of α-Cr_2O_3 particles does not occur in the Al_2O_3 melt (Fig. 7). At cooling, the directed crystallization of the formed ceramic material takes place. In the wide class of ceramics, the orientation of crystallites is not usually distributed randomly, as in the case of an ideal powder sample. The observed differences in the preferred orientations of α-Al_2O_3 crystallites in crystallized layers of different samples indicate some unsystematic character of the preferred direction of crystallization. Though the [116] orientation, one of some preferred orientations of crystallization, take place in LT α-Al_2O_3 samples with 0.5%, 1.0%, 5.0% and 10.0% α-Cr_2O_3. In such surface layer the undissolved α-Cr_2O_3 particles also show the preferred orientation. Preferred orientations in surface crystallized layers and particles Cr_2O_3 in stiffening Al_2O_3 melt may be connected with the anisotropic shape of initial particles α-Al_2O_3 and α-Cr_2O_3.

During LT, the whole sample is subjected to the temperature influence. Parameters of the influence in different regions of the samples are determined by their geometry, thermal conductivity, etc. Dissolution of Cr_2O_3 particles in α-Al_2O_3 leads to appearance of the EPR spectra of Cr^{3+} centers in α-Al_2O_3. Let us consider the formation of EPR spectra at a spatial homogeneous concentration distribution of paramagnetic centers (PC) in samples.

3.3.1 EPR Spectra at a homogeneous distribution of impurities in samples

In general, at low impurities concentration (c < 0.05%), the shape and width of an individual EPR signal are determined by relaxation parameters. In this case, I is proportional to the amount of PC in the specimen, i.e., to c. At higher concentration, dipole–dipole broadening, which is proportional to the impurity content, manifests itself (Berger et al., 1995; Kittel & Abrahams, 1953). By generalizing results of (Berger et al., 1995; Kittel & Abrahams, 1953) for $S = 3/2$, we obtain

$$\Delta B_{dd} \approx 8\beta g\left(\frac{c}{d^3}\right) \tag{3}$$

where d is the shortest distance between paramagnetic ions, c is concentration in mole percents. Note that ΔB_{dd} is about 1000 Gs at chromium concentration in the sample of 15 mol %. In complex EPR spectra different lines may have different widths ΔB_{ind}, and their changes with increasing ΔB_{dd} require individual consideration. In groups of closely located lines (GL) their overlapping occurs with increasing linewidth and a single signal (SS) forms. Note that the signal assigned to the β_1 phase in (Carman & Kroenke, 1968; Stone & Vickerman 1971) is most likely connected with the superposition of wider (than I—IV) curves in the central part of the spectrum (see spectra 3 and 4 in Fig. 8 and curves for -1/2↔+1/2 and FT transitions in Fig. 9).
At c > 15 mol %, we should expect the exchange-interaction-related phenomena, which lead to the exchange narrowing of dipolar broadening (Barnes, 1974). Thus, signal A (Fig. 8) is a typical EPR signal in highly concentrated α-Al_2O_3 + nα-Cr_2O_3 samples (β_N phase (Carman & Kroenke 1968; Stone & Vickerman 1971)). It is due to the development of dipole and exchange (a mixture of ferromagnetic and antiferromagnetic) Cr^{3+} — O — Cr^{3+} interactions (Stone & Vickerman 1971). And in α-Cr_2O_3, a final antiferromagnetic mechanism of exchange interaction sets up.
From the performed analysis it follows that at a homogeneous distribution of the impurity, as its content increases, the gradual transition from the spectrum of individual atoms to EPR spectra of highly concentrated states occurs. The use of formula (2) and data of experimental works (Carman & Kroenke, 1968; Knappwost & Gunsser, 1959; Poole & Itzel, 1964; Stone & Vickerman 1971; Wenzel & Kim, 1965) makes it possible to construct a rough dependences of changes in the linewidths of EPR signals in $Cr_xAl_{2-x}O_3$ samples at $0 \le x \le 2$ (Fig. 11, the solid curve for $T \sim 400$ K. For α-Cr_2O_3 the Neel temperature is 307 K (McGuire et al., 1956). The case the concentration range from 0 to ~ 3.5 wt % of Cr_2O_3 (zone A) is favorable for precise recording the EPR spectra from individual PC. The case the concentration of PC range from 3.5 wt % to 55.0 wt % (zone B) is unfavorable for precise recording EPR spectra due to large widths of signals. The case the concentration of PC range from 55.0 wt % to 100.0 wt % (zone C) is favorable for recording EPR spectra from exchange-related complexes.

3.3.2 EPR Spectra at an inhomogeneous distribution of impurities in specimens

The discrepancies between measured and calculated values for the linewidths or the simultaneous existence of two or more EPR spectra, which are characteristic for different

concentration states of impurities, indicate an inhomogeneous distribution of impurities in the samples. Thus, the recording of two distinctly different EPR spectra, namely, from individual Cr^{3+} ions (signals I - IV) and the signal from highly concentrated states of $Al_{2-x}Cr_xO_3$ (signal *A*) (Fig. 8) shows the high degree of inhomogeneity of distribution of the chromium in our samples. Note that, in most works on the EPR investigation of the α-Al_2O_3 + $n\alpha$-Cr_2O_3 samples with even a small value of *n*, a similar situation can be observed (Carman & Kroenke, 1968; O'Reilly & Maciver, 1962). This indicates that the preparation of α-$Al_{2-x}Cr_xO_3$ samples with a homogeneous distribution of chromium impurities by solid-state synthesis is an intricate problem.

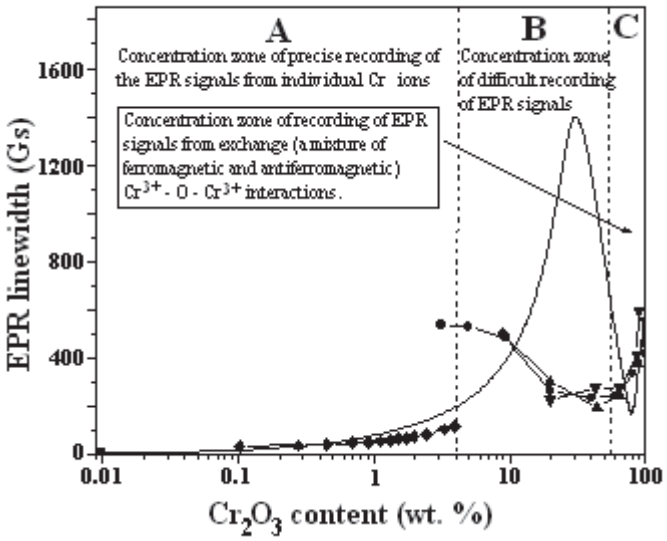

Fig. 11. The dependence of the EPR linewidth on the amount of α-Cr_2O_3 in α-$Cr_xAl_{2-x}O_3$ samples for T = 400 K (100wt % of α-Cr_2O_3 corresponds chromium concentration in the sample of 40 mol %). The solid curves is a dependence of the linewidth for a homogeneous distribution of a chromium impurity in the samples; (●) — experimental data of (Stone & Vickerman 1971); (◆) data of (de Biasi & Rodrigues 1985); (▼) data of (Wertz & Bolton 1972); (▲) data of (Kittel & Abrahams, 1953); (■) data of (Berger et al., 1995). A is the concentration zone of precise recording of the EPR signals from individual Cr^{3+} ions; B is the concentration zone of difficult recording of EPR signals; C is the concentration zone of recording of EPR signals from exchange (a mixture of ferromagnetic and antiferromagnetic) Cr^{3+} - O - Cr^{3+} interactions.

3.3.3 Diffusion processes in α-Al_2O_3 + $n\alpha$-Cr_2O_3 during laser treatment

The process of dissolution of the α-Cr_2O_3 particles in the Al_2O_3 melt is diffusion of surface chromium atoms in the volume of the melt. As result, the chromium diffusion profile (i.e., a smooth curve of the concentration *c* vs. distance, *r*) around undissolved α-Cr_2O_3 particles are formed

$$C_x = C_0 erfc \frac{r}{2\sqrt{Dt}} \quad (4)$$

where D is the diffusion coefficient, t is the heat treatment time (Akulova, 1986). From this expression it follows that the impurities are inhomogeneously distributed in the sample. Thus, each registered EPR spectrum of such a sample is a superposition of signals from Cr^{3+} ions located in different concentration states of the sample (from 0 to 100 wt % of Cr_2O_3). From this standpoint, the manifestation of one or another features of the spectra (e.g., the presence or the absence of singularities I—IV and a signal A) reflects a certain statistics of the Cr^{3+} concentration distribution in the sample. To determine the statistics, not only individual singularities, but the whole spectrum must be processed. Note that in the formation of narrow singularities, the zones of the sample with a low local content of the impurity play the main role. The zones with $c \leq 1.0$ mol % play particular role in this respect. In the case when diffusion profiles of the nearest α-Cr_2O_3 particles are not overlapped, the shape of the spectra is independent of their amount (n) in the samples, and the spectrum intensity is proportional to n.

A change in the shape of the EPR spectrum with increasing n (Fig. 8) indicates the overlapping of the chromium diffusion zones of the nearest α-Cr_2O_3 particles. In Fig. 12, a scheme of overlapping of the diffusion profiles about the nearest α-Cr_2O_3 particles depending on their on the amount (i.e., on the change in the distance l between them) in the samples is shown. From Fig. 12, it is seen that the decrease in l is accompanied by a decreasing in the volume of the low-concentration zones A in the samples. The volume of the high-concentration zones C located near α-Cr_2O_3 particles is nearly proportional to the amount of these particles in the specimen.

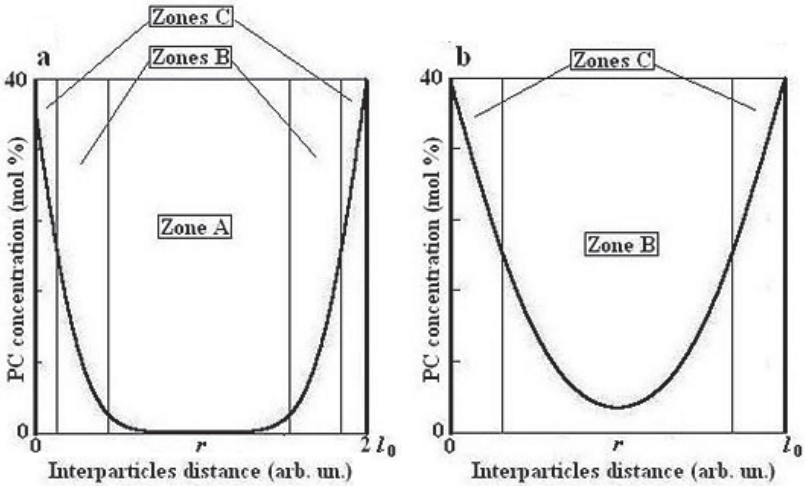

Fig. 12. Scheme of overlapping of concentration diffusion profiles between the nearest α-Cr_2O_3 particles depending on the distance between them: a — the interparticle distance is $2l_0$ (in arb. un.); b — the interparticle distance is l_0 (in arb. un.). A is the concentration zone of precise recording of the EPR signals from individual Cr^{3+} ions; B is the concentration zone of difficult recording of the EPR signals; C is the concentration zone of recording of the EPR signals from exchange (a mixture of ferromagnetic and antiferromagnetic) Cr^{3+} - O - Cr^{3+} interactions.

These analyses explain the nature of changes in the observed EPR spectra. At small values of n (insignificant overlapping of diffusion zones), the low-concentration regions (c ~ 0.5 mol %) occupy the maximal volume of the specimen. Though the total content of the impurity in these zones is insignificant, due to small widths of curves, we observe clear intensive singularities, on the background of which a weak and wide signal from high-concentration regions is poorly distinguishable. As n increase, the diffusion zones of the nearest particles begin to overlap. It favors a decrease in the volume of low-concentration zone. The amplitudes of singularities I - IV decrease, and the amplitude of the signal A continues to increase proportionally to n.

Angular dependences of the amplitudes of singularities II and III (Fig. 10) confirm the textured character of the samples after the laser beam surface treatment (Kakazey et al., 2002). However, relatively small changes in the amplitudes of these signals (for φ = 0 and 90°, they range from ~ 15 % to ~ 20 %) indicate that the Cr^{3+} ions located both in the strongly textured surface layer and in the part of the sample which is not textured take part in the formation of these singularities. This part includes regions of the sample adjacent to the surface layer. The temperature of these regions was lower than the melting point of Al_2O_3, but it was sufficient to cause the local sintering and different types of diffusion processes.

Obtained results show that the melting of the surface layers of pressed α-Al_2O_3 + nα-Cr_2O_3 samples take place during the performed laser treatment. In such a layer the Al_2O_3 melt covers the α-Cr_2O_3 particles. The α-Cr_2O_3 particles dissolve gradually in Al_2O_3 with the formation of a number of α-$Cr_xAl_{2-x}O_3$ mutual solid solutions throughout the composition range from x = 0 to x = 2. Complete dissolution of α-Cr_2O_3 in Al_2O_3 does not occur. During cooling of the sample the crystallization of the α-Al_2O_3 layer take place. The crystallized layer show preferred orientation, which is different in different samples. In the surface layer the undissolved α-Cr_2O_3 particles also acquire preferred orientation, the direction of which does not coincide with the direction of the preferred crystallization of α-Al_2O_3. Dissolution of Cr_2O_3 particles in α-Al_2O_3 leads to appearance of the EPR spectra of Cr^{3+} centers in α-Al_2O_3. Analysis of changes of width singularities and the shape of the EPR spectra with an increasing of content of paramagnetic centers shows that the distribution of chromium impurities in α-Al_2O_3 is determined by the diffusion laws. This distribution is inhomogeneous and depends on the amount of α-Cr_2O_3 particles in the samples.

The observed EPR spectra reflect the statistics of the inhomogeneous concentration distribution of the Cr impurity in the samples. To determine the statistics of the concentration distribution of the impurity in the sample on the basis of EPR data, a computer analysis of the whole spectrum, rather than an analysis of individual singularities, must be performed.

3.4 Laser synthesis of crystalline $Al_2O_3:Cr^{3+}$ rods (Vlasova, Kakazey, et al., 2010)

It is necessary to expect that the decreasing of laser beam surface scanning velocity lead to the increasing of the heat energy absorbed by molten layer and the increasing of it width and depth at cross section (Rastogi & Asundi, 2011; Ready, 2001; Shishkovskii, 2009; Weber, 1994). Thus conditions of crystallization of a melt improves. In turn, it supposes the possibility of use of a superficial laser fusion for obtaining crystalline samples from polycrystalline objects (from pressings, ceramics and others).

Cylindrical ceramic specimens were irradiated with an LTN-103 continuous-action Nd^{3+}:YAG facility (Russia) using a wave length λ = 1064 μm. The diameter of the laser spot

was 0.2 mm. The power (P) of irradiation was 70 W. The laser beam was traversed over the surface of the specimens at a traverse rate of a coordinate table (v) of 0.0094, 0.019, and 0.075 mm/s. The irradiation of specimens was performed along their long axes. Specimens were placed in channels formed on surfaces of compacts made from the same mixture by one-pass treatment with a laser beam. After irradiation, the specimens had the shape of rods with a length of 5 to10 mm and a diameter of 1.5 to 2 mm. In Fig. 13, an irradiated specimen removed from a track is shown.

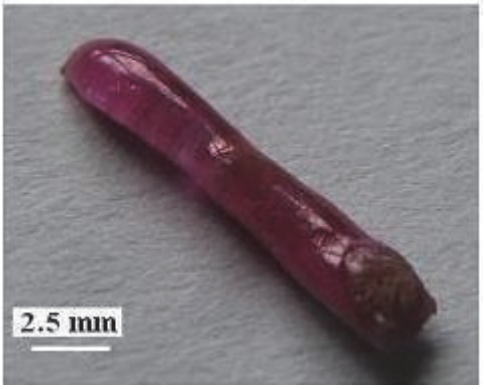

Fig. 13. View of a specimen after laser irradiation at P = 70 W and v = 0.0094 mm/s.

After one-pass laser treatment, on the cross-section of a rod, several zones are distinguished. On the irradiated surface of the specimen, large pores and cracks form. On the opposite side of the specimen, much smaller pores are present. The central part of the rod (in the radial direction from the irradiated surface) is most homogeneous (Fig. 14). In the lower part of the specimen, the formation of necks between particles takes place (see Figs. 15 a, a'), which is characteristic of the process of sintering of powders. In Fig. 15 a, this sintering zone is marked by S. The core (central part) of the specimen consists of polycrystals of different size (Fig. 15 b). More homogeneous zones are dark (see Fig. 15 b, b'). They can be considered monocrystalline regions. In Fig. 15 b', one of such regions is marked by M. On the surface of the specimen, including a part of the lateral surface, fracture along grain boundaries (Fig. 15 c) and reprecipitation of vapor-gas products inside pores (Fig. 15 c') are observed. The rough assessment of the thickness of the melting-recrystallization zone of corundum (h_1) and the thickness of the sintering zone (h_2) shows that h_1 increases substantially as the traverse rate of the laser beam decreases (Fig. 16).

The fracture (cleavage) of the specimens occurs along grain boundaries of ruby (in the sintering zone) and along boundaries of microcrystallites (in the recrystallization zone) (Fig. 17). Crystallites have a lamellar (tabular) shape. The size of crystallites in the lower part of the specimen ranges from ~10 to ~30 μm. In the central part of the specimen, the size of crystallites ranges from ~25 to ~40 μm. In the surface layer, their size increases to about 35–53 μm.

In the initial nonirradiated Al_2O_3–Cr_2O_3 specimens, only a weak broad EPR signal, which was due to defective states of the α-Cr_2O_3 phase, was registered at g ~ 1.9. After laser treatment, EPR signals of both typical isotropic polycrystalline singularities (I—IV at $H_I \approx$ 5337 Gs, $H_{II} \approx$ 4505 Gs, $H_{III} \approx$ 1909 Gs, and $H_{IV} \approx$ 340 Gs) of different intensities and sets of EPR signals with a strong angular dependence were registered (Fig. 18 b).

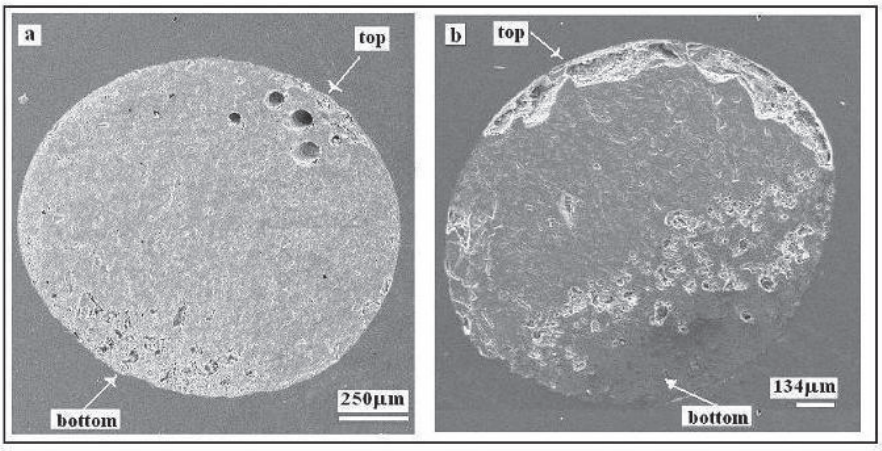

Fig. 14. Micrographs of cross-sections of specimens after laser treatment. P = 70 W. (a) v = 0.0094 mm/s; (b) v = 0.075 mm/s.

Analysis of the EPR spectrum of Cr^{3+} (singularities I—III) in Al_2O_3 polycrystalline samples we have made in part 3.3 (see also (Carman & Kroenke, 1968; de Biasi & Rodrigues 1985; O'Reilly & Maciver, 1962; Stone & Vickerman, 1971). Figures 9 and 18 a shows that singularity I corresponds to the transition -3/2 ↔ -1/2 of ions Cr^{3+} in Al_2O_3 (θ = 90°, where θ is the angle between crystal axes c and the direction of the magnetic field). Singularity II corresponds to the transition -1/2 ↔ +1/2 (θ =35°). Singularity III corresponds to the +1/2 ↔ +3/2 transition (θ = 90°). Singularity IV is a forbidden transition (FT) (θ = 0 – 30°).

The observation of the strong angular dependence of the set of EPR signals (Figs. 18 b, 3) implies that, under laser treatment, the formation of several Cr^{3+}:Al_2O_3 monocrystals in samples take place. The width of these lines ranges from ~40 to ~50 Gs. The angular dependences of the EPR signals agree well with the positions of singularities I –IV (see Fig. 18b, 19), which indicates that anisotropic EPR signals correspond to Al_2O_3:Cr^{3+} crystals oriented differently in the specimen.

In general, the angular dependence of the EPR spectrum of the crystal is dependent on the crystal orientation. In Fig. 18a, such a dependence for the case where the crystal axis c is perpendicular to axis of rotation (ψ = 90° and angle θ are between 0 and 180°) is shown. In the case where ψ ≠ 90°, during crystal rotation in the magnetic field, the angle θ is larger than 90° – ψ and smaller than 90° + ψ. The character of the angular dependence of the EPR spectrum of Cr^{3+} in Al_2O_3 for ψ = 75°, ψ = 60° and ψ = 45° are shown in Fig. 20.

From the performed analysis it follows that, independently of the orientation of crystalline formations in the specimen, the angular dependences of all EPR lines of the fine structure pass through the central part of the spectrum ($H_{III} < H < H_{II}$). Note that, in this part of the spectrum, the superposition of the EPR lines of different formations (crystals) complicates their rigorous identification. In the region $H_{IV} < H < H_{III}$, the transitions-3/2 ↔-1/2, +1/2 ↔ +3/2 (θ =90°) and a forbidden transition (FT) show an angular dependence. In the region $H > H_I$, only the transitions +1/2 ↔ +3/2 show an angular dependence. Thus, the lines of the last transitions can serve as a probe of the number of monocrystalline formations and their approximate orientation in the sample.

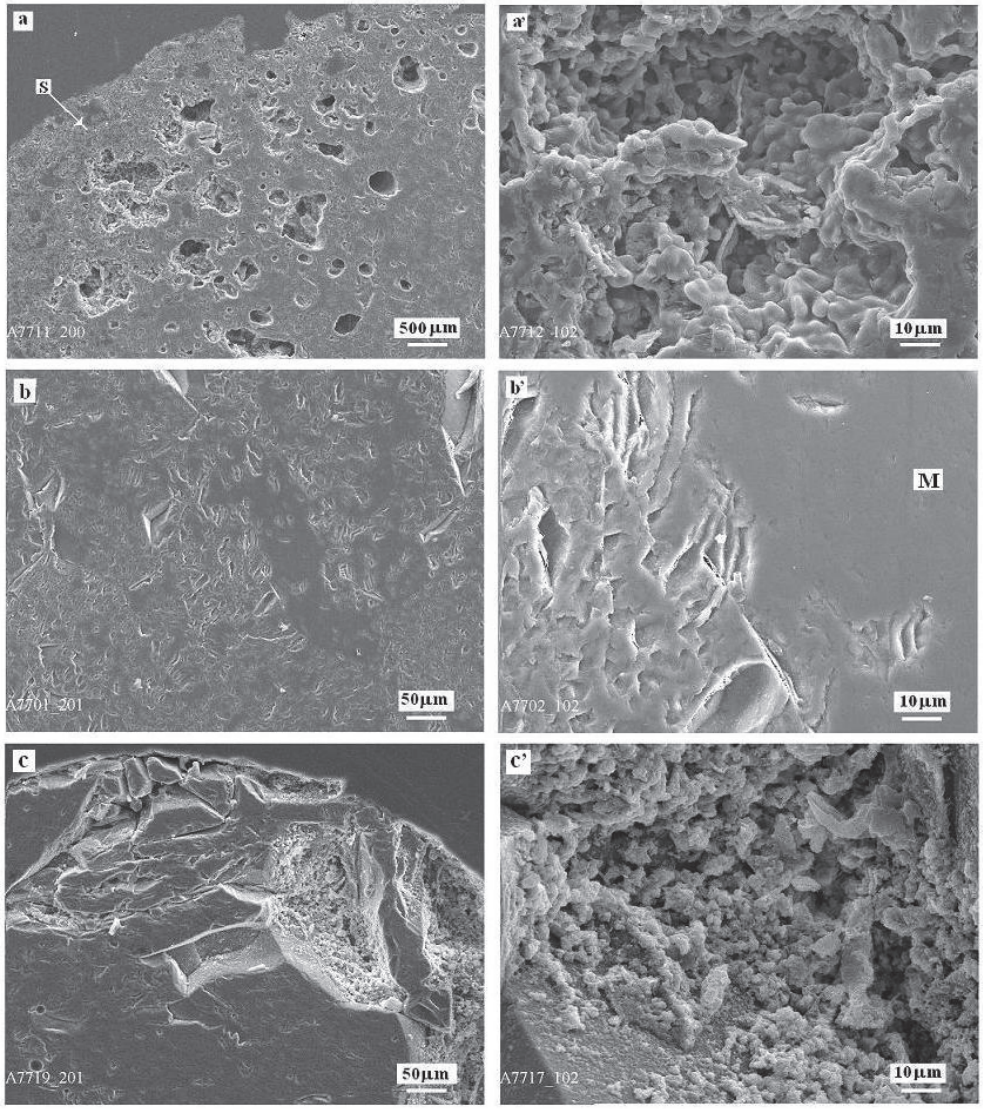

Fig. 15. Micrographs of cross-sections of specimens after laser treatment at P = 70 W and v = 0.075 mm/s. (a, a′) the lower surface of the rod ; (b, b′) the middle part of rod; (c, c′) the upper surface of the rod. S designates the sintering zone and M designates the monocrystalline zone.

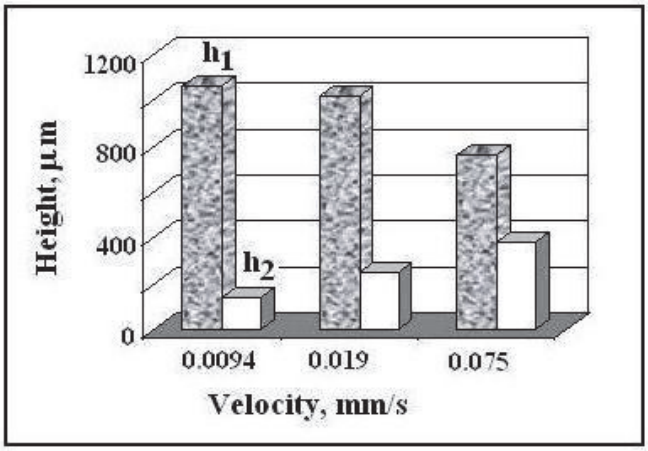

Fig. 16. Changes in the maximal values of the thickness of recrystallized layer (h_1) and the thickness of the sintered layer (h_2) depending on the traverse speed of the laser beam. P = 70 W.

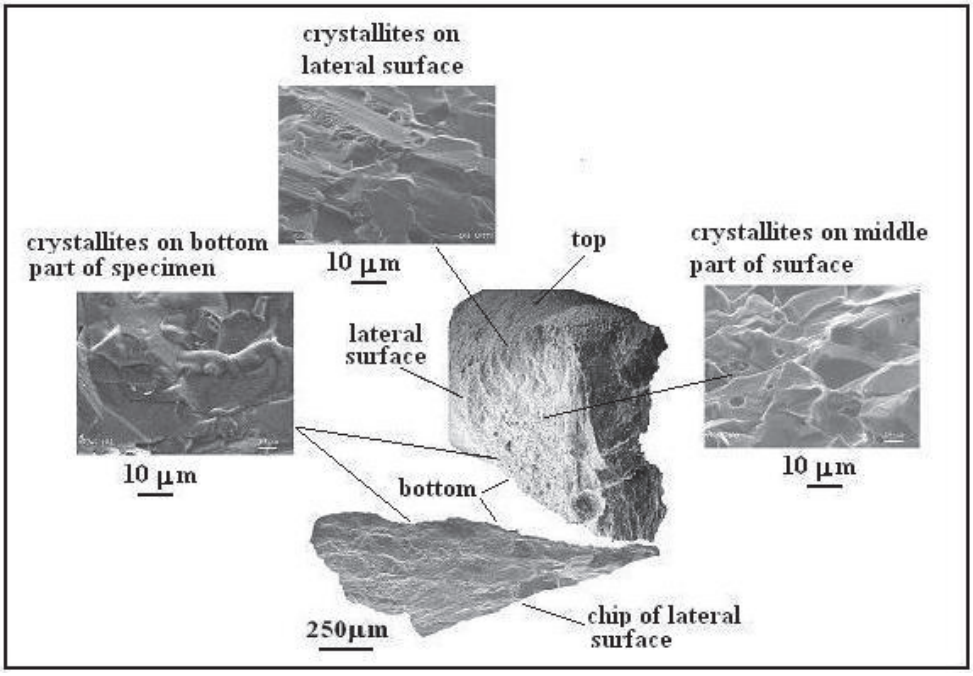

Fig. 17. Micrographs of a chip of a specimen after laser treatment at P = 70 W and v = 0.075 mm/s.

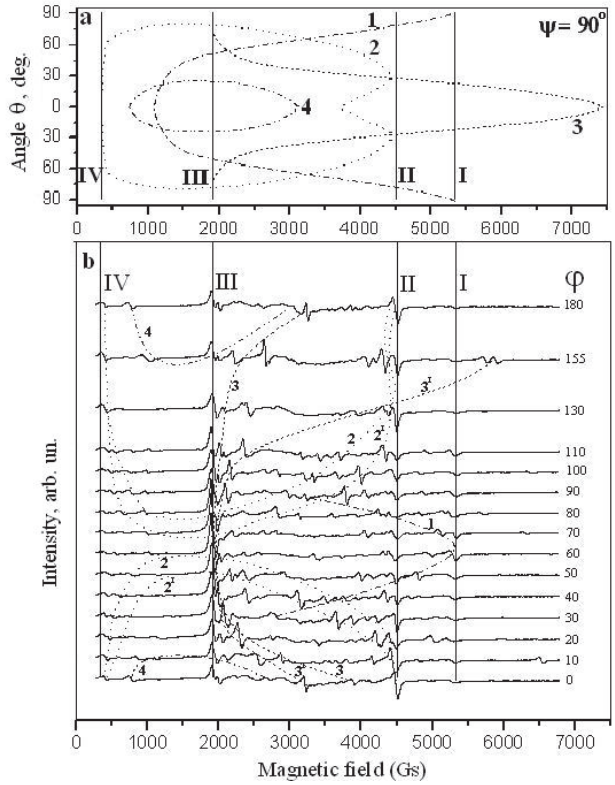

Fig. 18. Angular dependences of the EPR spectrum of Cr^{3+}:Al_2O_3 in: a) monocrystal, ψ = 90°; b) laser-synthesized rod. The axis of rod was inclined at an angle of 90° to the axis of rotation. 1, 1' corresponds to the -3/2 ↔ -1/2 transition; 2, 2' corresponds to the -1/2 ↔ +1/2 transition; 3, 3' corresponds to the +1/2 ↔ +3/2 transition; 4, 4' correspond to the forbidden transition; I, II, II, and IV are singularities of transitions 1, 2, 3, and 4, respectively, in the polycrystalline part of the specimen. Signals 1, 2, 3 and 4 and 1 ', 2 ', 3 ' and 4 ' correspond to large crystallites of different orientations in the rod.

The performed analysis of the angular dependences (Figs. 18b, 19) shows that about 7 monocrystalline formations of nearly equal sizes (~0.3 mm) are present in the investigated specimen. These monocrystals have an arbitrary orientation. None of the axes of crystals coincides with the direction of the axis of synthesis of the rod. At the same time, the intensities of singularities I – IV show anisotropy, which is typical of textured polycrystalline specimens. Unfortunately, by virtue of the fact that these signals are overlapped with the signals from monocrystalline formations, precise measurements of angular amplitude changes are complicated. According to our rough assessments, the plane of texturing of the polycrystalline part of the specimen is inclined by an angle of ~20 to ~30° to the axis of the investigated rod.

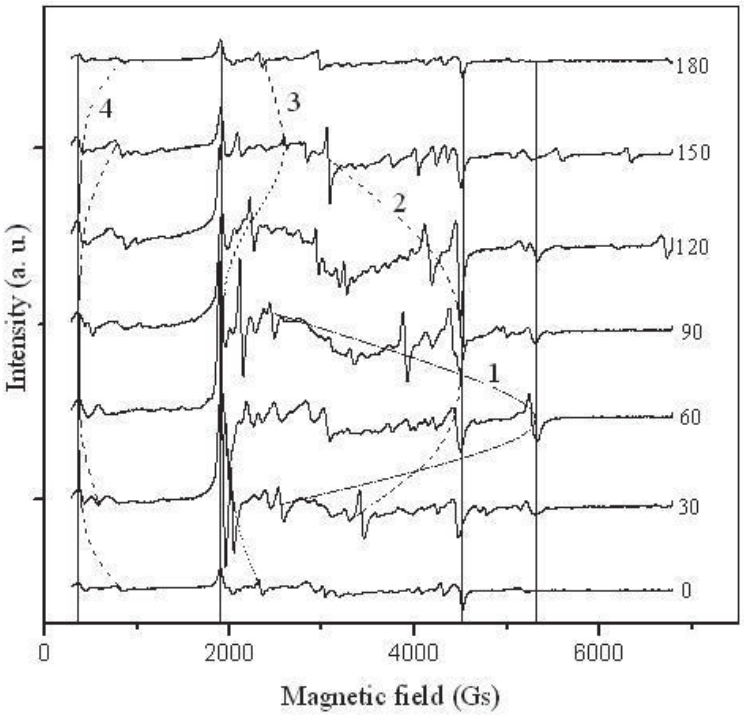

Fig. 19. Angular dependence of the EPR spectrum of Cr^{3+} in a laser-synthesized rod. The axis of rod coincides with axis of rotation. Others symbols are as in Fig. 18.

Thus, the results obtained by the EPR method show that, during the laser treatment of α-Al_2O_3–Cr_2O_3 rods, a number of processes are realized. These are: the formation of the solid solution Al_2O_3:Cr_2O_3 (the synthesis of ruby), the formation of textured polycrystalline regions in the specimen (the plane of texturing is inclined by an angle of about 20–30° to the axis of the rod), and the formation of ruby monocrystals in the rod. The direction of the axes *c* of these crystals is arbitrary.

The performed investigations showed that, in the chosen irradiation mode of the 97 wt. % Al_2O_3 + 3 wt. % Cr_2O_3 mixture, polycrystalline ruby with monocrystalline inclusions of different size was synthesized. This means that, in the narrow irradiation zone, synthesis of ruby, which includes the penetration of Cr^{3+} ions into the corundum lattice, is realized. In this context, we can speak about selective laser synthesis of ruby.

The polycrystalline part consists of differently directed crystallites, which are predominantly concentrated in the sintering zone and partially in the melting zone. Monocrystals form in the melting zone of corundum. Since the growth conditions of monocrystals depend on thermophysical processes (on the ramification of the heat flow in the vertical and horizontal direction) (Bagdasarov, 2004; Bagdasarov & Goryainov, 2001; Bagdasarov & Goryainov, 2007; Lukanina et al., 2006), in the melting-recrystallization zone, the size of crystallites increases as the distance from the irradiated surface decreases.

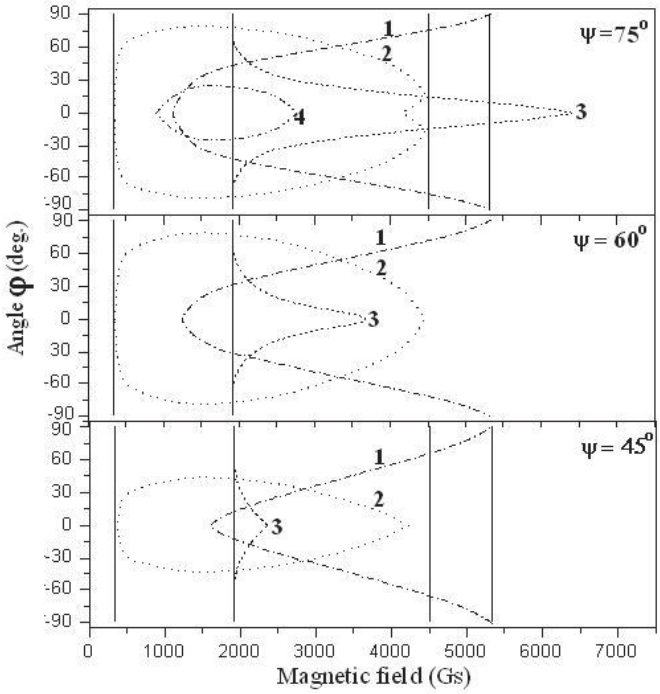

Fig. 20. Angular dependences of EPR spectrum of Cr^{3+} in a crystalline Al_2O_3 specimen for different values of ψ.

As in the case of HDC of ruby monocrystals, for horizontally directed laser synthesis of ruby, there exists a strong dependence of the sizes of the melting-recrystallization zone and sintering zone on the traverse rate of the beam at the chosen power of beam. This is due to the distribution of temperature from the surface to the bulk of the specimen (a temperature gradient). From Fig. 16 it follows that the traverse rate of the beam must be much less than 0.0094 mm/s. Judging from traditional HDS of corundum monocrystals (Bagdasarov & Goryainov, 2001; Lukanina et al., 2006), v must approach the value of about 0.0027 to 0.0022 mm/s.

The presence of a large number of pores of various size in the lower part of the rod (see Figs. 14, 15a, a ') is caused by a number of factors, namely, the incompleteness of the sintering process and shrinkage (Vedula et al., 2001) and the absence of the sufficient amount of a corundum melt. With increase in the amount of the melt, the porosity substantially decreases (see Figs. 14, 15b, b'). However a part of intergranular voids are encapsulated. Under complete melting of the material, these microvoids cause the blistering of the melt and remain in the volume of the material during its crystallization (Dobrovinskaya et al., 2009; Malukov et al., 2008). The formation of large pores and damages in the upper part of the rod (on an irradiation surface) is predominantly caused by the development of high-temperature processes of dissociation of Al_2O_3 (Ristic et al., 2009; Pankratz, 1982). The reprecipitation of vaporous products in pores (see Fig. 15 c, c ") is a confirmation of the given assumption. Nucleation of cracks in the volume and on the lateral surfaces of the rod

(see Figs. 15c, 17) is a direct consequence of the development of thermal stresses and the plastic deformation, which arise as the front of crystallization moves (Denisov et al., 2007; Ivanovic et al., 2003; Lebedev et al., 2008; Samsonov, 1973).
Note that the commonly used sintering temperature of corundum powders ranges from 1700 to 1750°C (Ivanovic et al., 2003). The melting point and sublimation point of Al_2O_3 are 2046 and 2980°C, respectively (Pankratz, 1982 ; Samsonov, 1973). Consequently, on the irradiated surface, a temperature of about 3000°C develops, and the average temperatures in the melting-recrystallization zone and in the sintering zone are about 2000 and 1700°C. In each zone, temperature decreases with distance from the irradiated surface.

4. Conclusion

Depending on intensity of an irradiation and velocity of removing of a laser beam on a surface of pressings from powder mixtures Al_2O_3:Cr_2O_3 a number of physical and chemical processes is passing (Weber, 1994 proceeds; Ready, 2001; Rastogi and Asundi, 2011; Shishkovskii, 2009)., defined by non-uniform character of distribution of temperature on volume of the sample. In a superficial layer the temperature reaches the maximum value ~ 3000 °C. This initiates not only evaporation of material but also its dissociation. As a result, in a superficial zone of specimens a layer of Al_2O_3 with high deficiency is formed. This layer has a raised electrocoductivity. In a fusion zone dissolution Cr_2O_3 in Al_2O_3, formation of solid solution Cr^{3+} : Al_2O_3 takes place. The new result is that during process of cooling-crystallization in this layer a textured packing from crystalline particles is forming. This is typical for all processed surfaces. The direction of texturing has casual character. Most likely, texturing is set by crystallization conditions in an irradiation starting point. Supervision in some samples of several directions of texturing is connected with heterogeneity of packing of particles in pressings. The sintering zone is set by temperature range: T_{melt} ÷ ~2/3 T_{melt}. Owing to it it isn't homogeneous neither on structure, nor on properties. In this zone formation of non-uniform solid solution Cr^{3+}: Al_2O_3 is observed. In layers close to a fusion zone more dense packing of particles of a powder, than in the layers adjoining to non-sintered part of pressings is marked.
Decreasing of velocity of scanning of a laser beam on a surface of polycrystalline specimen leads to an increase of sizes of zone of a heating-melting. This allows to spend out a laser fusion in region 10 times more the size of a spot of an irradiation. After treatment in such regime of Al_2O_3-Cr_2O_3 specimens the formation of several large crystallites of a ruby was observed. These results show possibility of laser synthesis of crystals of a ruby with the considerable big sizes.

5. Acknowledgment

The authors wish to thank CONACYT for financial support (Project 48361).

6. References

Akulova, L. T.; Vlasova, M. V.; & Kakazey, M. G. (1986). Interaction of melt glass with chromium diboride, *Glass Phys. Chem*., Vol.12, No. 5, pp. 574-578
Ali, J.; Bennett W. & Herriot, D. (1960) (US Patent 3,149,290)

Bagdasarov, H. S. (2004). *The High Temperature crystallization from melt*, Moscow, Pub. Phismatlit, 160, (in Russia)

Bagdasarov, H. S. & Goryainov, L. A. (2007). *Heat and mass transfer at a growing of monocrystals by directed crystallisation*, Moscow, Pub. Phismatlit, 224, (in Russia)

Bagdasarov, H. S. & Goryainov, L. A. (2001). Thermal processes of a growing of monocrystals of sapphire by the horizontal directed crystallisation, *Perspective materials*, No.6, pp. 45-50, (in Russia)

Bai, P. & Li, Y. (2009). Study on high temperature sintering processes of selective laser sintered Al_2O_3/ZrO_2/TiC ceramics, *Science of Sintering*, Vol. 41, No.1, pp. 35-41

Barnes, S. E. (1974). Fine-structure splitting of a localized moment in a metal: A diagrammatic analysis, *Phys. Rev. B*, Vol..9, pp. 4789 - 4807

Berger, R.; Kliava, J.; Yahiaoui, E.; Bissey, J.-C.; Zinsou, P.K. & Beziade, P. (1995). Diluted & non-diluted ferric ions in borate glasses studied by electron paramagnetic resonance, *J. Non-Cr. Sol.*, 180 [2] 151-163

Carman, C. J. & Kroenke, W. J. (1968). Electron spin resonance of α-chromia-alumina solid solutions, *J. Phys. Chem.*, Vol.12, pp. 2562-2566

Da Shen, L.; Huang, Y.H.; Tian, Z. J. & Hua, G. R. (2007). Direct Fabrication of Bulk Nanostructured Ceramic from Nano-Al_2O_3 Powders by Selective Laser Sintering, *Key Engineering Materials*, v. 329 (Advances in Abrasive Technology IX), pp. 613-618

De Biasi, R.S. & Rodrigues, D.C.S. (1985). Measurement of small concentrations of Cr & Fe in α-Al_2O_3 using electron spin resonance, *J. Am. Ceram. Soc.*, Vol.68, No.7, pp. 409-412

Deckard, C. R. (1988). *Selective laser sintering*, University of Texas at Austin

Denisov, A. V.; Ktumov, V. M. & Punin, Yu. O. (2007). Investigation of optical anomalies & residual stress in base facetting tapes of sapphire crystals grown up by a method of Stepanov, *Phys. Solid State*, Vol. 49, Iss. 3, pp. 454-459

Dobrovinskaya, E. R.; Lytvinov, L. A. & Pischik, V. (2009). *Sapphire. Material, Manufacturing, Application*, New York, Springer, 481

Dorre, E. & Hubner, H. (1984). *Alumina Processing, Properties, & Applications*, Springer-Verlag, New York

Ferkel, H.; Naser, J. & Riehemann, W. (1997). Laser-induced solid solution of the binary nanoparticle system Al_2O_3-ZrO_2, *Nanostructured Materials*, Vol. 8, No. 4, pp. 457-464

Gahler, A.; Heinrich, J. & Gunst, G. (2009). Direct laser sintering of Al_2O_3-SiO_2 dental ceramic components by layer-wise slurry deposition, *J. American Ceramic Society*,Vol. 89, No.10, pp. 3076-3082

Galoisy, L. & Calas, G. (1993). Inhomogeneous distribution of Cr impurities in α –Al_2O_3 during refractory aging," J. Mater. Res., Vol.8, No. 5, pp.1153 -1157

Gebhardt, A. & Hancer, C. (2003). *Rapid prototyping*, Verlag, Munich

Goodison, P., (2008). RYA *Laser Handbook*, Royal Yachting Association

Hurle, D.T. J. (1994). *Handbook of crystal Growth., v. 2a, Basic Techniques*, North-Holl&, Amsterdam

Injeyan, H. & Goodno, G. (2011). *High Power Laser Handbook*, McGraw-Hill Higher Education

Ivanovic, M. R.; Nenezic, M. & Jokanovic, V. (2003). High Temperature Sintering Kinetics of α-Al_2O_3 Powder, Sci. Sintering, Vol. 35, pp. 99-102

JCPDS-International Centre for Diffraction Data (1999).

Kakazey, M.; Vlasova, M.; Gonzalez-Rodriguez, J.G. & Salazar-Hernández, B. (2002). Fine structure of EPR spectra of Fe^{3+} in α-Al_2O_3 crystal, powders, & textured ceramics, *Mat. Sci. Eng. B*, Vol.90, No. 1-2, pp. 114-119

Kakazey, M.; Vlasova, M.; Márquez Aguilar, P. A.; Bykov, A.; Stetsenko, V. & Ragulya, A. (2009). Laser Surface Solutionizing & Crystallization of Al_2O_3-Cr_2O_3, *International Journal of Applied Ceramic Technology*, Vol. 6, No 2, pp. 335-343

Kittel, C. & Abrahams, E. (1953). Dipolar Broadening of Magnetic Resonance Lines in Magnetically Diluted Crystals, *Phys. Rev.*, Vol.90, No. 2, pp.238-239

Kliava, J. (1988). EPR Spectroscopy of Disordered Solids, Zinatne, Riga

Knappwost, A. & Gunsser, W. (1959). Magnetic resonance absorption in mixed crystal a-Al_2O_3-Cr_2O_3 by aid of a modified reflection method, *Z. Phys. Chem. N.F.*, Vol. 21, pp.305-325

Lebedev, G. A.; Malukov, S. P.; Stefanovich, V. A. & Cherednichenko, D. I. (2008). Thermophysical processes during sapphire crystal growth by the horizontal Bridgman method, Crystallography Reports, Vol. 53, No. 2, pp. 331-335

Liu, Z. H.; Nolte, J. J.; Packard, J. I.; Hilmas, G.; Dogan, F. & Leu, M. C. (2007). *Selective Laser Sintering of High-density Alumina Ceramic* Parts, Proceedings of the 35th International MATADOR Conference, Springer, London, pp. 351-354

Lukanina, M. A.; Hodosevitch, K. V. ; Kalaev, V. V.; Semenov, V. B.; Sytin, V. N. & Raevsky, V. L. (2006). 3D numerical simulation of heat transfer during horizontal direct crystallization of corundum single crystals, *J. Crystal Growth*, v.287, Iss. 2, pp. 330-334

Lyubo, B. Ya. (1975). *The crystallisation theory in large volumes*, Moscow, Nauka (in Russia)

Maiman, T. H. (1960). Stimulated optical radiation in ruby. *Nature,* Vol. 187, No.4736, pp. 493–494

Majumdar, J. D.; Chandra, B. R.; Mordike, B. L.; Galun, R. & Manna, I. (2004). Laser surface engineering of a magnesium alloy with Al+Al_2O_3, *Surf. Coat. Technol.*, Vol.179, No. 2-3, pp. 297-305

Malukov, S. P.; Stefanovich, V. A. & Cherednichenko D. I. (2008). Study of model of self-coordinated growth of single crystals of sapphire by horizontal directed crystallization, *Semiconductors*, Vol. 42, No.13, pp.1508-1511

Manenkov, A. A. & Prokhorov, A. M. (1955). The fine structure of the paramagnetic resonance of the ion Cr^{3+} in chromium corundum, *Soviet Phys.-JETP*, Vol.1, pp.611-616

McGuire, T. R.; Scott, E. S. & Grannis, F. H. (1956). Antiferromagnetism in a Cr_2O_3 Crystal, *Phys. Rev.*, Vol.102, No. 4, pp. 1000-1003

Nubling, R. K. & Harrington, J. (1997). Optical properties of single-crystal sapphire Fibers, *Applied Optics*, Vol.36, No. 24, pp.5934-5940

O'Reilly, D. E. & Maciver, D. S. (1962). Electron paramagnetic resonance absorption of chromia-alumina catalysts, *J. Phys. Chem.*, Vol. 6, pp. 276 – 281

Pampuch, R. & Haberko, K. F. (1997). *Role of Ceramics in a Self-Sustaining Environment,*: "Techna".

Pankratz, L.B. (1982). Thermodynamic properties of elements & oxides, U.S. Bur. of Mines., No. 672. p. 509

Poole, C. P. & Itzel, J. F. (1964). Electron Spin Resonance Study of the Antiferromagnetism of Chromia Alumina, *J. Chem. Phys.*, Vol. 41, No. 2, 287-295

Quispe Cancapa, J. J.; De Arellano Lopez, A. & Saoir, R., A. (2002). Propiedades Mecanicas de Fibras de Al_2O_3 Dopadas con Cr_2O_3 Fabricadas por Fusion Laser, VIII Congreso Nacional de Propiedades Mecanicas de Solidos, G&ia, pp.691-697

Rastogi, P. & Asundi, A. (2011). Optics and Lasers in Engineering,

Ready, J.F. (1971). *Effects of high-power laser radiation*, Academic Press, New York-London

Ready, J. F (2001). *LIA Handbook of Laser Materials Processing*, Published by the *Laser* Institute of America

Ristic, M.; Vlasova, M.; Ragulya, A.; Stetsenko, V.; Kakazey, M.; Márquez Aguilar, P.A.; Timofeeva, I. ; Tomila, T. & Juarez Arellano, E. A. (2009). The layer by layer selective laser sintesis of ruby, *Report on "International Conference Sintering*, Kiev, Ukraine, 7-11 september, 2009

Samsonov, G. V. (1973). *The Oxide handbook*. New York, IFI/Plenum, 524 Maiman, T. H. (1960). Stimulated optical radiation in ruby. *Nature,* Vol. 187, No.4736, pp. 493–494

Shevchenko, V. Ya. & Barinov, S. M. (1993). *Engineering Ceramics* [in Russian], "Nauka", Mosco

Shishkovskii, I. B. (2005). Selective Laser Sintering and Synthesis of Functional Structures [in Russian], Author's Abstract of the Doctor's Degree Thesis (Physico-Mathemathical Sciences), Chernogolovka

Shishkovskii, I. V. (2009). *Laser Synthesis of Functional Mesostructures and Bulk Articles* [in Russian], "Fizmatlit", Moscow

Shishkovsky, I.; Yadroitsev, I.; Bertrand, Ph. & Smurov, I. (2007). Alumina–zirconium ceramics synthesis by selective laser sintering/melting, *Applied Surface Science*, Vol. 254, No.4, pp. 966-976

Statz, H. ; Rimai, L. ; Weber, M. J. ; de Mars, G. A. & Koster, G. F. (1961). Chromium Ion Pair Interactions in the Paramagnetic Resonance Spectrum of Ruby*, J. Appl. Phys*., Vol. 32, pp. 218S-220S

Stone, F. S. & Vickerman, J. C. (1971). Magnetic properties of chromium ions in oxide matrices. 1. Solid solution, *Trans. Faraday Soc*., Vol. 67, pp. 316 – 328

Subramanian, P. K. & Marcus, H. L. (1995). *Selective Laser Sintering of Alumina Using Aluminum Binder*, Materials and Manufacturing Processes, Vol. 10, Iss. 4, pp. 689 – 706

Subramanian, P. K. ; Zong, G. ; Vail, N. ; Barlow, J. W. & Marcus, H. L. (1993). Selective Laser Sintering of Al_2O_3, *Solid Freeform Fabrication Proceedings,* pp.350-359

Townes, C. H. (1960). *The first laser*. University of Chicago. Retrieved 2008-05-15

Träger, F. (2007). *Handbook of Lasers and Optics*, (Ed.), Springer, XXVI, 1332

Tretyakov, Yu. D. (1987). Ceramics – Material of Future [in Russian], "Znanie", Moscow

Triantafyllidis, D.; Li, L. & Stott, F. H. (2002). Surface treatment of alumina-based ceramics using combined laser sources, *Appl. Surf. Sci.,* Vol.186, No. 1-4, pp.140-144

Triantafyllidis, D.; Li, L. & Stott, F. H. (2004). Laser cladding of high performance ceramic sheets on a low quality ceramic substrate, *Thin Solid Films*, Vol. 453-454, No. 1, pp.80-83

Vedula, V. R.; Glass, S. J.; Saylor, D. M.; Rohrer, G. S.; Carter, W. C.; Langer, S. A. & Fuller, Jr. E. R. (2001). Residual-stress Predictions in Polycrystalline Alumina, *J. Am.Ceram.Soc*., Vol. 84, No.12, pp. 2947-2954

Vlasova, M.; Kakazey, M.; Márquez Aguilar, P. A.; Guardian Tapia, R.; Juarez Arellano, E.; Stetsenko, V.; Ragulya, A.; Bykov, A. & Timofeeva, I. Peculiarites of Ruby

Synthesized from Al_2O_3-Cr_2O_3 Powder Mixture by Selective laser Sintering, *J. Laser Micro/Nano Engineering*, (in press. accept.).

Vlasova, A. G.; Florinskaya, V. A.; Venediktov, A. A.; Dutova, K. P.; Morozov, V. N. & Smirnova, E. V. (1972). *Infrared Spectra of Inorganic Glasses & Crystals*, Edited by A. G. Vlasova, V. A. Florinskaya [in Russian], "Izdatelstvo Khimiya", Leningrad

Vlasova, M.; Ragulya, A.; Stetsenko, V.; Kakazey, M.; Márquez Aguilar, P. A.; Timofeeva, I.; Tomila, T. & Juarez Arellano, E. A. (2010). The Layer by Layer Selective Laser Synthesis of Ruby, *Science of Sintering*, Vol.42, No 1, pp. 3 – 13

Vlasova, M.; Kakazey, M.; Márquez Aguilar, P. A.; Stetsenko, V.& Ragulya, A. (2010). Laser horizontally directed synthesis of ruby, *Superficies y Vacio,* Vol. 23(S), pp.15-20

Wang, H.; Wang, W. Y.; Xie, C. S.; Song, W. L. & Zeng, D. W. (2004). Microstructural characteristics of Al_2O_3-based refractory containing ZrO_2 induced by CO_2 laser melting, *Appl. Surf. Sci.*, Vol. 221, No.1-4, pp. 293-301

Weber, M. J , (2001). *Handbook of Lasers*, CRC Press

Webb, C.E. & Jones, J.D.C. (2003). *Handbook of Laser Technology and Applications* (Three-Volume Set) (Vols 1-3), Taylor & Francis

Weber, M. J (1994). *CRC Handbook of Laser Science and Technology* Supplement 2: Optical Materials (Laser and Optical Science and Technology)

Wefers, K. & Misra, C., (1987). *Oxides & Hydroxides of Aluminum*, Aluminum Company of America

Wenzel, R. F. & Kim, Y.W. (1965). Linewidth of the Electron Paramagnetic Resonance of $(Al_2O_3)_{1-x}(Cr_2O_3)_x$, *Phys. Rev.*, Vol.140, No. 5A, pp. A1592-A1598

Wertz, J.E. & Bolton, J.R. (1972). Electron Spin Resonance. *Elementary theory & Practical application,* McGraw-Hill Book Company, New York,

Xu, Z. ; Zhang, J. ; Zheng, H. ; Cai, C. & Huang, Y. (2005). *Morphology & mechanical properties of PS/Al_2O_3 Nanocomposites Based on Selective Laser Sintering*, J. Mater. Sci. Technol., Vol. 21, No. 6, pp. 866-870

Yen, W. M., (1999). Synthesis, Characterization & Applications of Shaped Single Crystals, *Solid State Phys.*, Vol.41, No.5, pp.770-773

Zum, G. K. -H.; Bogdanow, Ch. & Schneider, J. (1995). Friction & wear reduction of Al_2O_3 ceramics by laser-induced surface alloying, *Wear*, Vol. 181-183, No. 1, pp. 118-128

Zhao, J.-F.; Huang, Y-H.; Hua, G-R.; Zhang, J-H.; Wang, L.; Zhang, Y-K.; Zhou, J-Z. & Zhou, M. (2003). Free fabrication of nano-Al_2O_3 bulk materials by SLS, *Cailiao Kexue yu Gongcheng (Materials Science & Engineering)* (China). Vol. 21, May-June 2003, pp. 339-341

Part 3

Special Topics in Advanced Ceramic Materials

19

Ceramic Materials for Solid Oxide Fuel Cells

Taroco, H. A., Santos, J. A. F., Domingues, R. Z. and Matencio, T.
Department of Chemistry/Universidade Federal de Minas Gerais
Brasil

1. Introduction

Solid oxide fuel cells (SOFC) are environmentally friendly energy conversion systems to produce electrical energy with minimal environmental impact. They have several additional advantages over conventional power generation systems such as high power density, high energy-conversion efficiency, low emissions of CO_2, CO, NO_X, SO_2, fuel flexibility, modularity, ability to utilize high temperature exhaust for cogeneration or hybrid applications (with an efficiency up to approximately 70 % in this case). (Fergus et al. 2009; Singhal & Kendall, 2001; Taroco et al., 2009).

The single cell is composed of two electrodes (anode and cathode), an electrolyte, interconnects and sealing materials. The electrodes are porous, they exhibit an electronic conductivity and preferably also an ionic conductivity at the SOFC operating temperature. The electrolyte must be dense with good ion conducting characteristics (Badwal, 2001).

The conventional SOFC's operate at high temperature (800-1000 ^{o}C). Currently, there is an increasing interest in the development of SOFC's operating at intermediate temperatures (IT_SOFC: 600 – 800 °C) (Badwal, 2001; Charpentier et al., 2000; Wincewicz & Cooper, 2005). The main difficulty with SOFC´s operating at intermediate temperatures is the significant decline in performance mainly due to lower ion conduction of the electrolyte, and to a strong cathode polarisation. Solutions to improve the cell performance include the use of alternative electrolyte and electrode materials, besides a decrease in the electrolyte thickness (Charpentier et al., 2000; Singhal & Kendall, 2001; Sun et al., 2007, 2009).

On the anode (fuel electrode) side the gaseous fuel is oxidized according to equation (in the case of a hydrogen fuel): $2H_{2(g)} + 2O^{2-} \rightarrow 2H_2O + 4e^-$. The electrons flow through the external electrical circuit. On the cathode (air electrode) side, oxygen reacts with incoming electrons and ions O^{2-} are formed: $O_{2(g)} + 4e^- \rightarrow 2O^{2-}$. The oxygen ions migrate through the electrolyte and combine with hydrogen on the anode side as schematized by the first equation (Fig. 1).Most of the electrochemical reactions occur at three-phase boundaries (TPB), which are defined as the sites where the ionic, electronic conductor and the gas phase are in contact i.e. where the electrode, the electrolyte and the gas phase are in contact. TPB characteristics have a large influence on the electrochemical performance of cell.

The ideal voltage (E°) of a single cell under open circuit (OCV) conditions is close to 1.01 V at 800 ^{o}C as calculated from the Nernst equation with pure hydrogen at the anode and air at the cathode (Acres, G. , 2001). Under operation, the useful voltage output (V), is given by:

$$V = E^{\circ} - IR - \eta c - \eta a \quad (1)$$

where I is the current passing through the cell, R the cell resistance, ηc the cathode polarization losses and ηa the anode polarization losses, as detailed in Fig. 2 (Sun et al., 2007).

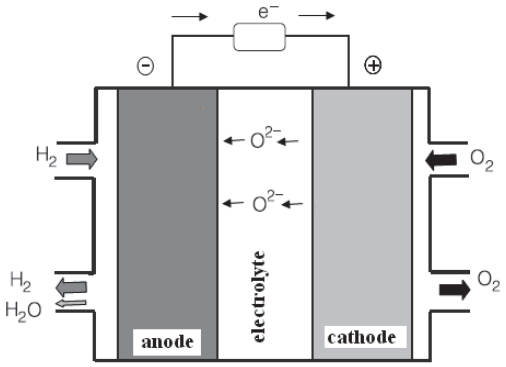

Fig. 1. Schematic of a solid oxide fuel cell (SOFC).

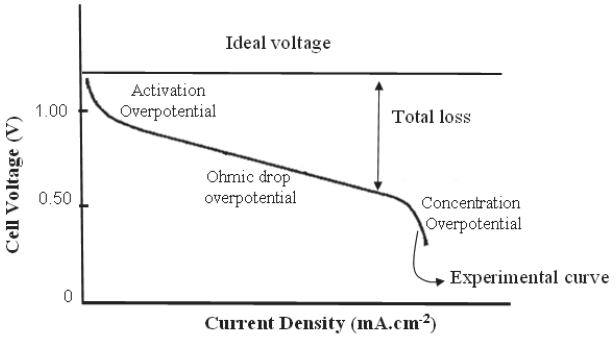

Fig. 2. Typical fuel cell voltage-current characteristic at 800 °C with pure hydrogen as fuel. (Adapted from Sun et al., 2007).

To technically characterize the overall voltage drops at each electrode, a parameter called the Area Specific Resistance (ASR) has been defined (Fabbri et al., 2008). Its use implies an approximately linear behaviour of the cell under the operating conditions.
The maximum efficiency ($\varepsilon_{max} = 1 - T\,\Delta S/\Delta H$, where T is the temperature in Kelvin, ΔS the entropy variation in Joule.K^{-1} and ΔH the enthalpy variation in Joule) can not be achieved because of the electrode polarization losses and the material ohmic resistances. The challenge is to improve the efficiency through an optimization of the cell components and their microstructures. Nowadays an efficiency of approximately 40 % can be reached.
This chapter gives emphasis on the characteristics of the main ceramic materials used as cathode, anode and electrolyte. It includes manufacturing features and techniques and electrical and microstructural characterizations of these materials.

2. SOFC components

This section deals with the SOFC components: anode, cathode and electrolyte materials and their characteristics. The interconnects and sealings will not be dealt with.

2.1 Cathode

The cathode is the SOFC electrode where electrochemical reduction of oxygen occurs. For this, the cathode must have: (1) adequate porosity (approximately 30-40%) to allow oxygen diffusion; (2) chemical compatibility with the other contacting components (usually the electrolyte and interconnect) under operating conditions; (3) a thermal expansion coefficient (TEC) matching those of the another components; (4) chemical and microstructure stability under an oxidizing atmosphere during fabrication and operation; (5) low cost and relatively simple fabrication procedure; (6) high catalytic activity for the oxygen reduction reaction; (7) large TPB; (8) adhesion to electrolyte surface and (9) high electronic and ionic conductivity (Fergus, et al., 2009; Singhal .& Kendall, 2003; Sun et al., 2010).

In the Intermediate temperature Solid oxide fuel cells (IT-SOFCs), the low operating temperatures reduces the oxidative degradation, and make possible the use of metallic interconnects. On the other hand, the electrode kinetics becomes slower which results in large interfacial polarization resistances especially at the cathode. The cathode polarization losses must be minimized by an appropriate cathode material selection and an interface microstructure optimization. The choice of the cathode material is largely dependent on that of the electrolyte. Care must be taken to match the TEC's and avoid undesirable interface chemical reactions.

The cathode reaction is:

$$\frac{1}{2}O_2(gas)+2e^-(cathode)\rightarrow O^{2-}(electrolyte) \tag{2}$$

It is widely believed that the electrochemical reactions can only occur at the TPBs which are the sites where the oxygen ion conductor, electronic conductor, and the gas phase are in contact. The TPB is represented in Fig. 3:

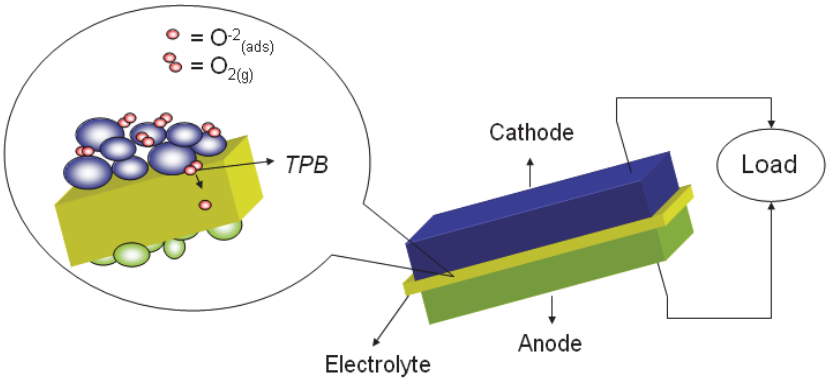

Fig. 3. Triple-phase boundaries (TPB).

For electron-conducting perovskite-type materials the cathode reaction may occur in many steps and along different pathways depending on the electrode material . With the pure electronic conductor materials the surface pathway is the most accepted mechanism. The bulk pathway is predominant in mixed ionic electronic conductor and the electrolyte surface pathway prevails with a composite material, e.g. LSM/YSZ) (Fleig, 2003 as cited in Sun et al., 2010) as shown in Fig. 4.

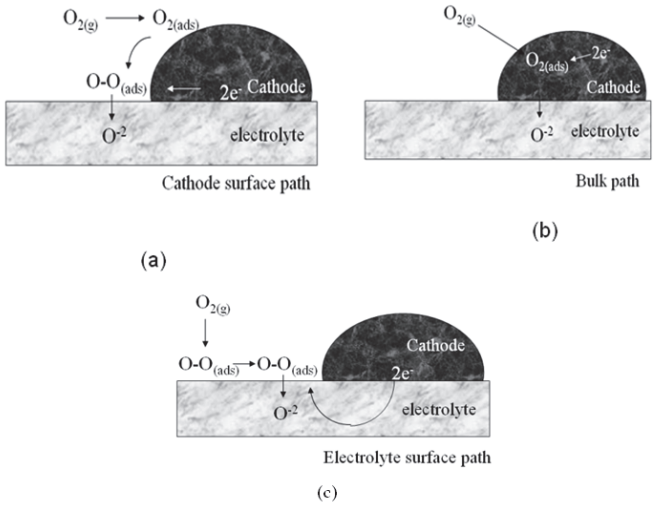

Fig. 4. TPB: Three reaction pathways of the oxygen reduction and some possible rate-determining steps: (a) cathode surface pathway, (b) bulk pathway and (c) electrolyte surface pathway (adapted by Sun et al., 2010).

Perovskite-type oxides with general formula ABO_3 are mostly used as cathode materials. The Fig. 5 shows their structure in which A and B are cations with an overall charge of +6.

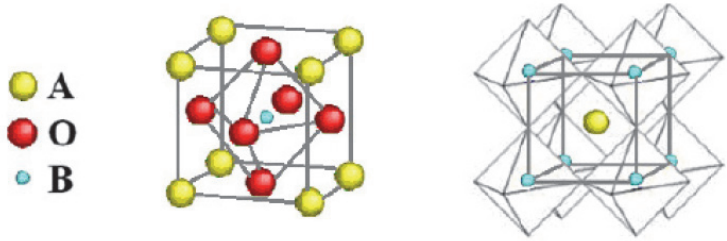

Fig. 5. Schematic representation of lattice structure of perovskite, ABO_3, adapted from Guarany, 2008.

The A cations (such as, La, Sr, Ca, Pb, etc.) have lower valences. They are larger in size and are coordinated to twelve oxygen anions. The B cations (such as, Ti, Cr, Ni, Fe, Co, Zr, etc.) occupy a much smaller space and are coordinated to six oxygen anions (Singhal & Kendall, 2003; Sun et al., 2010).

Lanthanum manganites ($LaMnO_3$: LSM) are still the most common material for high temperature SOFCs because of their compatibility with ZrO_2/Y_2O_3 (YSZ: yttria stabilized zirconia) electrolytes (Belardi et.al; 2009; Brant, et al.; 2001, 2006; Sun et al., 2010). They can be doped on the A site by cations such as Sr^{2+} (at 10–20 mol %) or Ca^{2+} (at 10–30 mol %) (Singhal & Kendall, 2003; Sun et al., 2010; Wincewicz & Cooper, 2005). This material can be formulated as $La_{1-x}A_xMnO_{3\pm\delta}$ (where A is divalent cation, "+" denotes an oxygen excess and "-"an oxygen deficiency).

In the Sr-doped lanthanum manganite ($La_{1-x}Sr_xMnO_{3-\delta}$ with x< 0.5) a manganese ion oxidation has been observed (Sun, et al., 2010):

$$2SrO + \frac{1}{2}O_{2\,(g)} \xrightarrow{LaMnO_3} 2Sr'_{La} + Mn_{Mn}^{\cdot} + 3O_O^x \tag{3}$$

According this reaction, the Sr doping increases the electron-hole concentration and improves the electrical conductivity of the electrode material. Its crystalline structure is influenced by temperature and oxygen partial pressure (Fergus et al., 2009; Singhal & Kendall, 2003).It is rhombohedral at room temperature while the undoped lanthanum manganites is orthorhombic (Fergus et al., 2009; Singhal & Kendall, 2003).

LSM reacts with YSZ at temperatures above 1300 °C and unwanted electronic insulating phases like $La_2Zr_2O_7$ and $SrZrO_3$ are formed (Brant et al., 2006; Ralph et al., 2001 as cited in Wincewicz & Cooper, 2005). The amounts of these electronically insulating phases depend on the La/Sr ratio in the LSM (Sun et al., 2010). For temperatures below 1200 °C and Sr content of 30 mol % ,YSZ is compatible with LSM and unwanted phases are not formed (Jiang et al., 1999 as cited in Wincewicz & Cooper, 2005).

The dopant concentration influences the TEC and electronic conductivity, according Table 1. For example, the TEC of undoped $LaMnO_3$ is 11.2 x 10^{-6} K^{-1} in the temperature range 35-1000 °C (Fergus et al., 2009; Singhal & Kendall, 2003) while that of doped manganite (e.g. $La_{1-x}Sr_xMnO_3$, x: 0.05 – 0.30) is 12.8 x 10^{-6} K^{-1}. The substitution of La by lower valence cations decreases the TEC. The increasing amount of dopants on the A site increases the TEC and the electronic conductivity.

Below 800 °C, the $LaSrMnO_3$ materials exhibit fairly poor catalytic activities for the oxygen reduction and their electronic conductivity is significantly reduced, so new SOFC cathode materials have to be developed for intermediate temperature operation.

Mn substitution by Co or Fe on B sites (LSCF: $La_{1-x}Sr_xFe_{1-y}Co_yO_{3-\delta}$) gives promising cathode materials for IT-SOFC (Sun et al., 2010). They have high electronic and ionic conductivities and excellent catalytic activity for oxygen reduction at intermediate temperatures. Moreover, these materials have a TEC similar to that of the intermediate temperature electrolytes based on Ceria.

In general, the Sr concentration on the A-site enhances the ionic conductivities while the increase of the electronic conductivities is obtained by Fe and Co doping on the B-site (Sun et al., 2010).

Table 1 shows LSCF perovskites used as cathodes. It can be seen that the A-site deficiency has only a small effect on the TEC while an increasing of Sr content results in a higher TEC due to higher oxygen vacancy concentrations. In the LSCF system, the electrical conductivity of $La_{1-x}Sr_xCo_{0.2}Fe_{0.8}O_{3-\delta}$ increases from 87 to 333 Scm^{-1} with an increase of Sr^{2+} (x = 0.2–0.4) at 800 °C, but the TEC also increases from 14.8×10^{-6} to 15.3 ×10^{-6} K^{-1}.

The ionic conductivity of $LaMnO_3$ is lower than that of the YSZ electrolyte and it increases with the Mn substitution by Co.

Composition	TEC (x10^{-6} K^{-1})	References	σ_e (Scm^{-1})
$La_{0,5}Sr_{0,5}MnO_{3-\delta}$	300 (947)^c	(Badwal & Forger, 1997 as cited in Florio et al., 2004)o	-
$La_{0.6}Sr_{0.4}MnO_{3-\delta}$	13 (800)	(Kenjo & Nishiya, 1992)	130
$La_{0.7}Sr_{0.3}MnO_{3-\delta}$	12.8 (25 – 1100)	(Badwal & Forger, 1997 as cited in Florio et al., 2004)o	265 (947)
$La_{0.7}Sr_{0.3}MnO_{3-\delta}$	11.7 (800)	(Yamamoto et al., 1987)	240
$La_{0.8}Sr_{0.2}MnO_{3-\delta}$	11.8 (900)	(Jiang, 2002)	300
$La_{0,85}Sr_{0,15}MnO_{3-\delta}$	-	(Badwal & Forger, 1997 as cited in Florio et al., 2004)	175 (947)
$La_{0.4}Sr_{0.6}Co_{0.2}Fe_{0.8}O_{3-\delta}$	16.8 (600)	(Tai, et al,1995)	-
$La_{0.6}Sr_{0.4}Co_{0.8}Mn_{0.2}O_{3-\delta}$	18.1 (500)	(Chen et al., 2003)	1,400
$La_{0.6}Sr_{0.4}Co_{0.8}Fe_{0.2}O_{3-\delta}$	21.4 (800)	(Petric et al., 2000; Teraoka, 1991)	269
$La_{0.6}Sr_{0.4}Co_{0.2}Fe_{0.8}O_{3-\delta}$	15.3 (600)	(Tai et al., 1995)	330
$La_{0.8}Sr_{0.2}Co_{0.2}Fe_{0.8}O_{3-\delta}$	14.8 (800)	(Ullmann et al., 2000)	87
$La_{0.8}Sr_{0.2}Co_{0.8}Fe_{0.2}O_{3-\delta}$	19.3 (800)	(Ullmann et al., 2000; Petric et al., 2000)	1,000
$La_{0.8}Sr_{0.2}Fe_{0.4}Co_{0.6}O_{3-\delta}$	435 (1000)	(Tai et al., 1995)	20 (100 – 900)
$La_{0.8}Sr_{0.2}Fe_{0.6}Co_{0.4}O_{3-\delta}$	305 (1000)]	(Tai et al., 1995	17.6 (100 – 900)
$La_{0.8}Sr_{0.2}Fe_{0.8}Co_{0.2}O_{3-\delta}$	150 (1000)	(Tai et al., 1995	15.4 (100 – 800)
$La_{0.8}Sr_{0.2}Mn_{0.4}Co_{0.6}O_{3-\delta}$	255 (1000)	(Florio et al.,2004)	17.2 (200 – 800)
$La_{0.8}Sr_{0.2}Mn_{0.6}Co_{0.4}O_{3-\delta}$	125 (1000)	(Badwal & Forger, 1997 as cited in Florio et al., 2004)o	16.1 (200 – 800)
$La_{0.8}Sr_{0.2}Mn_{0.8}Co_{0.2}O_{3-\delta}$	130 (1000)	(Badwal & Forger, 1997 as cited in Florio et al., 2004)o	13.9 (200 – 800)

*In parenthesis are temperatures in ^oC.

Table 1. Electronic conductivity and TEC of several solid oxide fuel cell cathodes (adapted from Florio et al., 2004 and Sun et al., 2010)

Dutta et al., 2009 synthesized different perovskites with different dopants ($La_{0.8}Sr_{0.2}FeO_{3-\delta}$; $La_{0.8}Sr_{0.2}Co_{0.8}Fe_{0.2}O_{3-\delta}$ and $La_{0.5}Sr_{0.5}Co_{0.8}Fe_{0.2}O_{3-\delta}$) by a combustion synthesis technique. According to their results $La_{0.5}Sr_{0.5}$ $Co_{0.8}Fe_{0.2}O_{3-\delta}$ shows the highest electrical conductivity and superior electrochemical performance. Highest current density of approximately 1.72 $A.cm^{-2}$ and power density of 1.2 $W.cm^{-2}$ at 0.7 V, at a operating temperature of 800 °C, is obtained with this cathode composition and YSZ electrolyte (~10 μm) with GDC interlayer (~15 μm). The value of total area specific resistance (ASR) of this cathode is approximately 0.211 $A.cm^2$.
LSCF-based cathodes have a lower ASR than LSM perovskites but they are incompatible with YSZ electrolytes due to undesirable interface reactions. Therefore, Ceria based electrolytes such as gadolinia doped ceria (GDC) are used with LSCF cathodes (Uhlenbruck et al., 2009). Furthermore, the TEC values of the GDC electrolytes (12.8×10^{-6} K^{-1}) better match that of the LSCF's (equal or greater than 17×10^{-6} K^{-1}.).
Many other perovskites are used as cathodes in SOFC such as: $Pr_{0.5}Sr_{0.5}FeO_{3-\delta}$; $Sr_{0.9}Ce_{0.1}Fe_{0.8}Ni_{0.2}O_{3-\delta}$; $Sr_{0.8}Ce_{0.1}Fe_{0.7}Co_{0.3}O_{3-\delta}$; $LaNi_{0.6}Fe_{0.4}O_{3-\delta}$ (LNF); $Pr_{0.8}Sr_{0.2}Co_{0.2}Fe_{0.8}O_{3-\delta}$; $Pr_{0.7}Sr_{0.3}Co_{0.2}Mn_{0.8}O_{3-\delta}$; $Pr_{0.8}Sr_{0.2}FeO_{3-\delta}$; $Pr_{0.6}Sr_{0.4}Co_{0.8}Fe_{0.2}O_{3-\delta}$; $Pr_{0.4}Sr_{0.6}Co_{0.8}Fe_{0.2}O_{3-\delta}$; $Pr_{0.7}Sr_{0.3}Co_{0.9}Cu_{0.1}O_{3-\delta}$; $Ba_{0.5}Sr_{0.5}Co_{0.8}Fe_{0.2}O_{3-\delta}$; $Sm_{0.5}Sr_{0.5}CoO_{3-\delta}$; $LaNi_{0.6}Fe_{0.4}O_{3-\delta}$ (Sun et al., 2010). Their features will not be addressed in this work.

2.2 Electrolyte

The electrolyte is the component of the cell responsible for conducting ions between the electrodes, for the separation of the reacting gases and for the internal electronic conduction blocking, forcing the electrons to flow through the external circuit (Singhal & Kendall, 2001). Without significant ion conduction, no current would pass through the cell and only a potential difference would be detected. There are three types of electrolytes that differ by the ion transport mechanism: anionic, protonic and mixed ionic. However, most of the high temperature fuel cells operate via oxygen ion (O^{2-}) conduction from the air electrode to the fuel electrode. This conduction occurs because of the presence of oxygen ions vacancies, so the crystallites forming the electrolyte must have unoccupied anionic sites. The energy required for the oxide ion migration from one site to the neighboring unoccupied equivalent site must be small (Faro et al., 2009).
For satisfactory performance, the electrolyte must meet some requirements that limit the choice of the material. These include (EG&G Technical services, 2000; Fergus et al., 2009; Singhal & Kendall, 2001): (1) an oxide-ion conductivity greater than10^{-2} $S.cm^{-1}$ at the operating temperature; (2) negligible electronic conduction, which means an electronic transport number close to zero; (3) high density to promote gas impermeability; (4) thermodynamic stability over a wide range of temperature and oxygen partial pressure; (5) TEC compatible with that of the electrodes and other cell materials from ambient temperature to cell operating temperature; (6) suitable mechanical properties, with fracture resistance greater than 400 MPa at room temperature; (7) negligible chemical interaction with electrode materials under operation and fabrication conditions to avoid formation of blocking interface phases; (8) ability to be elaborated as thin layers (less than 30 μm); (9) low cost of starting materials and fabrication.
Zirconia based ceramic materials have been the most investigated and developed electrolytes for high temperature use. At room temperature, pure zirconia is monoclinic. At 1170 °C, it undergoes a phase transition to a tetragonal structure with a large volume

change. Above 2370 °C, pure zirconia is transformed into the cubic fluorite structure. The cubic phase still remains up to the melting point at 2680 °C as showed below (Faro et al., 2009; Fergus et al., 2009). The fluorite lattice is an interpenetration of a cubic oxygen lattice in the middle of the face-centered cubic zirconium lattice (Fig. 6).

Monoclinic $\xrightarrow{1170\ °C}$ tetragonal $\xrightarrow{2370\ °C}$ cubic $\xrightarrow{2680\ °C}$ molten phase

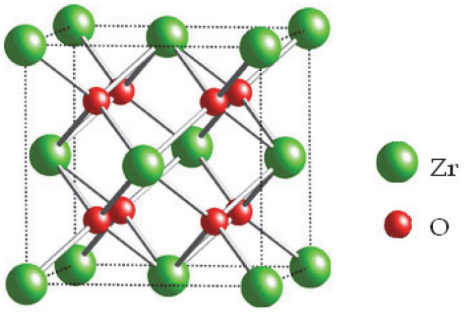

Fig. 6. Unit cell of zirconia fluorite (Adapted from Crystal Maker ® Demonstration version)

Doping zirconia with aliovalent ions is a common practice to stabilize the cubic fluorite structure from room temperature up to its melting point. The doping process increases the oxygen vacancy concentration, and consequently improves the ionic conductivity. According to the Kröger-Vink notation (Mitchell, 2004) for a typical trivalent dopant, M, the oxygen vacancies formation can be represented as:

$$Mn_2O_3 \overset{ZrO_2}{\rightarrow} 2M'_{Zr} + 3O^*_o + V^{\cdot\cdot}_o \tag{4}$$

So oxygen vacancies doubly ionized are produced at concentrations proportional to the dopant content.

The main dopants of zirconia are CaO, MgO, Y_2O_3, Sc_2O_3, Sm_2O_3 and Yb_2O_3 (Table 2). They exhibit high solubility in the zirconia fluorite structure . Among these, the most frequently used is Y_2O_3 followed by Sc_2O_3.

The conductivity of doped zirconia depends on the dopant concentration. Several studies show that the conductivity of zirconia increases with adding Y_2O_3 until 8 mol % and then decreases for higher yttria additions. $(Y_2O_3)_{0.08}(ZrO_2)_{0.92}$ is widely employed as an electrolyte material in high temperature SOFCs because of its sufficient ionic conductivity and stability in both oxidizing and reducing environments. Beyond that, its components are abundant, inexpensive and it is easy to produce (Tarancón, 2009). Yttria doped zirconia (YSZ) is also stable in contact with a lot of electrode materials below 1100°C. Unfortunately, La and Sr containing cathodes, react with YSZ at higher temperature producing insulating phases such as $La_2Zr_2O_7$ and $SrZrO_3$ at the cathode-electrolyte interface. It blocks the ion migration (EG&G Technical services, 2000; Brant, 2006).

Scandia doped zirconia (ScSZ) has drawn attention for its utilization as electrolyte because of its high ionic conductivity (Table 2). However, at high temperature, ScSZ suffers thermal aging, reducing its conductivity. Its high ionic conductivity might enable the use of ScSZ at

intermediate temperatures, in which there is no significant degradation. The main limiting factors in this case are the purity and availability of scandium oxide (Kharton et al., 2004).

Dopant	Content (% mol)	σ_i at 1000 °C (S.cm^{-1})	Activation energy (kJ.mol^{-1})*
Y_2O_3	8	10.0	96
Sm_2O_3	10	5.8	92
Yb_2O_3	10	11.0	82
Sc_2O_3	10	25.0	62

*96.488 kJ.mol^{-1} = 1 eV

Table 2. Values of ionic conductivity and activation energy of zirconia stabilized with different cations (adapted from Florio et al., 2004)*

The characteristics of the electrolyte, mainly its ionic conductivity and thickness, determine the operating temperature range of the SOFC. YSZ electrolyte cells operate satisfactorily only at temperatures above 850 °C.. Doped CeO_2 and doped $LaGaO_3$ have shown promise for the replacement of YSZ in intermediate temperature SOFCs (600-800 °C) (IT-SOFC) due to their higher conductivity. Other new materials for use in IT-SOFC are salt-oxide composite materials and NANOCOFC materials (nanocomposites for advanced fuel cell technology) (Nesaraj, 2010; Raza et al., 2010).

When compared to stabilized zirconia, doped ceria presents ionic conductivities approximately one order of magnitude greater, for similar temperature conditions. This is due to the larger ionic radius of Ce^{4+} (0.87 Å) as compared to Zr^{4+} (0.72 Å) producing a more open structure through which oxide ions can easily conduct (Faro et al., 2009).

Unlike zirconia, ceria naturally presents a fluorite structure since room temperature up to its melting point at 2400 °C. So, in its case the only function of the doping is an increase of the ionic conductivity through the formation of vacancies. The main doping cations used for ceria are Gd^{3+}, Sm^{3+} and Y^{3+}. Among them, Gd^{3+} is the most commonly used. The ions Gd^{3+} and Ce^{4+} have the lowest ionic radius mismatch, so in the case of Gd doping the lattice presents the smallest internal stress and consequently the lowest activation energy for the O^{2-} conduction (Fergus et al., 2009). The $Ce_{0.9}Gd_{0.1}O_{1.95}$ composition is promising for IT-SOFC applications because of its high ionic conductivity at 500 °C (Table 3).

Composition	Dopant	σ_i 500 °C (S.cm^{-1})	σ_i 600 °C (S.cm^{-1})	σ_i 700 °C (S.cm^{-1})
$Ce_{0.9}Gd_{0.1}O_{1.95}$	Gd^{3+}	0.0095	0.0253	0.0544
$Ce_{0.9}Sm_{0.1}O_{1.95}$	Sm^{3+}	0.0033	0.0090	0.0200
$Ce_{0.887}Y_{0.113}O_{1.9435}$	Y^{3+}	0.0087	0.0344	0.1015
$Ce_{0.8}Gd_{0.2}O_{1.9}$	Gd^{3+}	0.0053	0.0180	0.0470

Table 3. Ionic conductivities of the means dopants of ceria at different temperatures (Adapted from Steele, 2000)

Beside its high ionic conductivity, gadolinium doped ceria (GDC) also is compatible with the use of LSCF cathodes, since the chemical reaction between these materials is negligible. Their TEC values are also fairly similar (Dutta et al., 2009). However, Ce^{4+} reduces to Ce^{3+} under the reducing anode atmosphere at elevated temperatures. This induces an electronic conductivity (and phase changes) which decreases the open circuit voltage and increases the fuel consumption, consequently reducing the cell performance (Nesaraj, 2010; Steele, 2000). To avoid the Ce^{4+} reduction, it is common to insert an YSZ thin film between the ceria electrolyte and the anode (Dutta et al., 2009; Tietz et al., 2006). At temperatures lower than 500 °C the electronic conductivity is smaller and it has been suggested that this could be an optimal operating temperature range for the fuel cells based on ceria (Kharton et al, 2004).

2.2.1 Doped lanthanum gallate

Oxygen conductors with perovskite cubic structure based on lanthanum gallate $LaGaO_3$ have also been investigated as SOFC electrolytes. In these ceramics, La can be partially replaced by Sr, Ca, Ba, Sm and Nd, while Ga may also be partially replaced by Mg, In, Al or Zn, as in $La_{1-x}Sr_xGa_{1-y}Mg_yO_{3-\delta}$ (LSGM). Compositions containing Sr and Mg substitutions respectively for La (between 10 and 20%) and Ga (between 10 and 20%) showed high ionic conductivities in both oxidizing and reducing atmosphere. Their TEC are comparable to the other usual cell components. The higher ionic conductivity was found for the $La_{0.8}Sr_{0.2}Ga_{0.83}Mg_{0.17}O_{3-\delta}$ composition. It reaches about 0.17 $S.cm^{-1}$ at 800 °C (Badwal, 2001). However, these ceramics are unstable under reducing atmospheres and Ga losses are observed, resulting in the formation of new phases (Kharton et al., 2004; Wincewicz & Cooper, 2004). These facts decrease the use of doped lanthanum gallate as SOFC electrolyte.

Composition	σ_i at 800 °C ($S.cm^{-1}$)	TEC ($x10^{-6}$ K^{-1})
$(Y_2O_3)_{0.08}(ZrO_2)_{0.92}$	10.5	0.03
$(Sc_2O_3)_{0.08}(ZrO_2)_{0.92}$	10.7	0.13
$Ce_{0.8}Gd_{0.2}O_{1.9}$	12.5	0.053
$Ce_{0.8}Sm_{0.2}O_{1.9}$	12.2	0.095
$La_{0.9}Sr_{0.1}Ga_{0.8}Mg_{0.2}O_{2.85}$	10.7	0.1

Table 4. Ionic conductivity and TEC of electrolyte materials in air at 800 °C (Adapted from Sun et al., 2010)*

2.3 Anode

The anode provides reaction sites for the electrochemical oxidation of the fuel gas. An adequate anode has: (1) high electrical conductivity; (2) a TEC that matches those of the adjoining components; (3) the capacity of avoid coke deposition; (4) fine particle size; (5) chemical compatibility with another cell components (electrolyte and interconector) under a reducing atmosphere at the operating temperature; (6) large TPB; (7) high electrochemical or catalytic activity for the oxidation of the selected fuel gas; (8) high porosity (20 - 40 %) adequate for the fuel supply and the reaction product removal; (9) good electronic and ionic conductive phases (Florio et al., 2004; Singhal .& Kendall, 2003).

Ni/YSZ cermet (YSZ: yttria stabilized zirconia) is the most common anode material in the SOFC which implement hydrogen as a fuel. The raisons for this choice are its low cost, its chemical stability and its TEC closed to that of the YSZ electrolyte. The high catalytical activity of Ni for the H-H bond breaking and its relatively low cost justify the use of Ni. Other catalytic components including Cu, Co and phosphorous composites are being investigated, but they need further improvements before they can be effectively used (Florio et al., 2007; Martins et al., 2009; Sun et al., 2007).

The Ni particles coalescence is the main cause of the anode degradation. The YSZ grains constitute a framework which acts as an inhibitor for the coarsening of the Ni powders during cell operation. The TEC of nickel (16.9×10^{-6} K^{-1}) is much larger than that of YSZ (11.0×10^{-6} K^{-1}); the use of YSZ as a composite component also makes the TEC of the composite closer to those of other SOFC components. Furthermore, it improves the ionic conductivity of the material (Badwal, et al., 2001; Florio et al., 2004).

The Ni to YSZ volume ratio usually varies from 35:65 to 55:45. This ratio influences in the conductivity of the material. It may vary by several orders of magnitude (~0.1 S/cm to the range of ~10^3 S/cm) because of the electrical conductivity of Ni which is more than 5 orders of magnitude greater than that of YSZ under the fuel cell operating conditions. The choice of an adequate composite composition is determining.

The cermet conductivity occurs through two mechanisms: ionic (through the YSZ phase) and electronic (through the metallic nickel phase). For Ni concentrations below 30 % in volume, the conductivity is predominantly ionic. Above 30 % in volume, it is predominantly electronic (typical of metals). The electrical conductivity of the Ni/YSZ cermet attains its maximum at Ni percolation estimated to be at approximately 30 % in volume (Amado et al., 2007; Badwal, et al., 2001; Florio et al., 2004). The internal resistance (the resistance to the transport of electrons within the anode), contact resistance (caused by poor adherence between anode and electrolyte), concentration polarization resistance (related to the transport of the gaseous species through the electrodes) and activation polarization resistance (associated to the charge transfer processes) influence strongly the ASR of the anode. The anode performance is also largely depending on its thickness, its microstructure (grain size distribution, grain morphology, connectivity of Ni particles, porosity,) and number of TPBs (Sun et al., 2007).

Through these parameters, the anode performance is also influenced by the sintering temperature and the initial Ni and YSZ particle sizes. A fitting contact between Ni and YSZ particles decreases both the anode bulk and interfacial resistances. A high sintering temperatures (~1350–1400 °C) provides better anode performance and electrolyte interfacial contact and limits Ni coarsening (Bao et al., 2005; Singhal & Kendall, 2003).

Anode films are employed as cell support with different thicknesses depending on the SOFC cell design. In the planar designs, the thickness is about 1–3 mm.

For SOFC intended to use ethanol, methanol and gasoline or natural gas as fuels, the Ni/YSZ composite is not a good choice, because of its low tolerance to sulfur and carbon deposition. This problem can be avoided by reducing the operating temperature or by the development of alternative anode materials.

Cu-anodes based on Cu/Ni alloys have been used but Cu is not as good an electrocatalyst as Ni and with the YSZ electrolyte the power density is lower than with the Ni anodes. To increase the activity and stability of the Cu-based anodes, Cu can be alloyed with a second metal, for this purpose, nickel seems to be a good choice (Sun et al., 2007). Various metallic

alloys as components of the cermets such as (Cu, Co, Fe) Ni–YSZ; (Ni,Co)–YSZ; (Ni,Fe)–YSZ; (Ni,Cu)–YSZ and (Cu,Co)-YSZ have been used for the direct oxidation of CH_4 (Benyoucef et al., 2008; Ringuede et al., 2001).

Alternative materials which exhibit mixed ionic and electronic conductivity have been investigated as potential SOFC anodes capable of reforming hydrocarbons. Ceramics based on CeO_2 are good examples of mixed conduction materials under a reducing atmosphere, (due to the partial reduction of Ce^{4+} into Ce^{3+}.) These ceramics have an excellent catalytic activity for the hydrocarbon reforming reactions and they are resistant to carbon deposition. This allows for a direct supply of dry hydrocarbon fuels to the anode (Ramirez-Cabrera et al., 2000 as cited in Sun et al, 2007). The efficient catalytic activity of CeO_2 based materials has been emphasized by Sun et al., 2006 as cited in Sun et al., 2007. The addition of Ni, Co or a noble metal such as Pt, Rh, Pd or Ru which easily breaks the C-H bonds (Fergus et al., 2009; Sun et al., 2007) in the hydrocarbons is a further improvement. For example, Ru-Ni-GDC anodes used in a Ceria-based SOFC showed good results, with various hydrocarbons according to Hibino et al., 2003 (see Table 6 for the materials performance).

New materials with the cubic perovskite structure have also been suggested as alternative anode materials. The perovskite structure with general formula ABO_3 where A are cations such as, La, Sr, Ca and Pb, etc and B cations such as Ti, Cr, Ni, Fe, Co and Zr exhibit a very broad range of physical properties.

A $La_{0.6}Sr_{0.4}Fe_{0.8}Co_{0.2}O_{3-\delta}$ - $Ce_{0.8}Gd_{0.2}O_{1.9}$ (LSFCO–GDC) composite anode materials and $La_{0.75}Sr_{0.25}Cr_{0.5}Mn_{0.5}O_{3-\delta}$ (LSCM) were investigated and are efficient anode electro-catalysts (Huang et al., 2009; Morales et al., 2006; Sin et al., 2005; Sun et al, 2007). These materials showed good performance and stability in methane-fed SOFC in absence of Ni or noble metal catalysts. These anodes can be used withYSZ or GDC electrolytes. They are resistant to carbon deposition. Some examples of cell performance and operating conditions are given in Table 6.

Another perovskite, A-site deficient, is the La-doped $SrTiO_3$ (LST). It has been evaluated as a potential anode component for IT-SOFCs due to its thermal and chemical compatibilities with the electrolyte material to its sulfur tolerance. Some researchers have reported a sulfur poisoning by H_2S in the range of 26 to 1000 ppm, others have reported no poisoning effect in 1000 ppm H_2S and an enhancement effect in 5000 ppm. (Savaniu & Irvine, 2010; Yoo & Choi, 2010).

La-doped $SrTiO_3$ ($La_{0.2}Sr_{0.8}TiO_3$) is a candidate as an anode material to solve the problem of Ni-based anode in $LaGaO_3$-based SOFC according to Yoo & Choi (Yoo & Choi, 2010). Some details of their tests are showed in Table 6. The addition of GDC into LST reduces the anode polarization, leading to an increased performance.

The cell performance with Ni based anodes decreases quickly by sulfur poisoning which generally becomes more severe as the temperature decreases or as the pH_2S/pH_2 increases (Fergus, et al., 2009; Sun et al., 2007). Matsuzaki et al., 2007 showed that SOFCs which utilize Ni–YSZ cermet anodes are susceptible to poisoning by sulfur contents as low as 2 ppm H_2S at 1273 K. In their work it was observed that the performance loss is reversible at H_2S concentrations less than 15 ppm.

3. Manufacturing ceramic films

SOFC thin films are prepared by slurry or suspension depositions. The suspensions are constituted of ceramic powders, dispersants, binders, solvents and plasticizers. Only stabilised precursor suspensions must be used to avoid the formation of any agglomerates

which would affect negatively the final quality of the films. The flocculation and sedimentation are frequent situations observed during the preparation of slurries. The formation of flocculates occurs due to the van der Waals attractive forces between the particles. When the oxide particles are placed in a liquid medium an electrical double layer is formed around them with one layer composed of ions tightly adsorbed on the surface of the particles (Stern layer). The other layer is composed of ions less firmly adsorbed (diffuse layer), as showed in Fig. 7. This results in a potential profile between the particle surface and the bulk of the dispersing liquid. The last part of the potential difference is called the zeta potential and it is measured at the slipping plane (boundary of the diffuse layer). The zeta-potential is a measurement of the amount of charge present on the particle surface relative to the bulk of the dispersing media (Ramanathan et al., 2005).

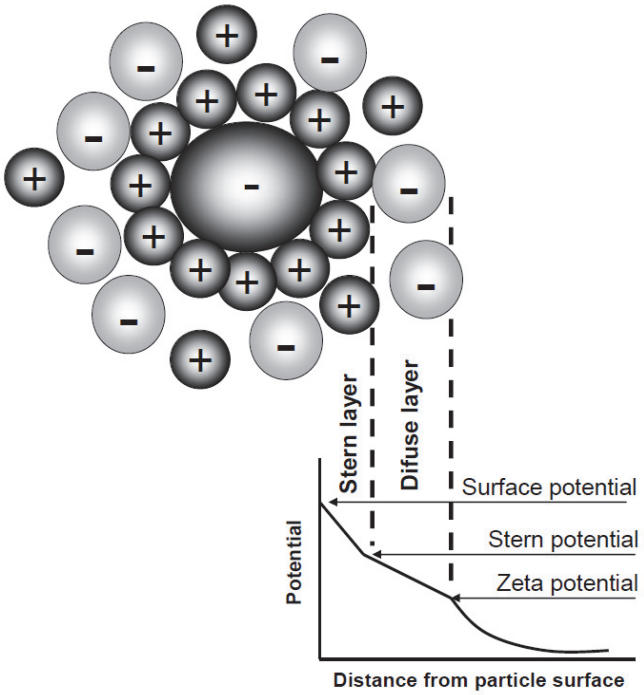

Fig. 7. Schematic representation of zeta potential.

The zeta potential depends on the suspension pH and measures indirectly the magnitude of repulsive forces necessary to prevent the formation of flocculates. The higher the zeta potential, the more predominant is the electrostatic repulsion between the electric double layers, resulting in a lower agglomeration and a lower viscosity value. The zero value of the zeta potential, the isoelectric point, indicates the pH at which the particles tend to form flocculates. It is important that the suspensions are prepared in pH giving the maximum zeta potential (in module) (Fonseca et al., 2009; Maiti & Rajende, 2002; Ramanathan et al., 2005).

Parameters such as the slurry composition and preparation and the grain size of the powders affect the particle surface charge and on the Zeta potential (Fonseca et al., 2009; Maiti & Rajende,2002).

The stabilisation mechanisms of the suspension are caused by both, steric hindrance and steric stabilisation. Organic components such as dispersants, binders and plasticisers which are added to the suspension contribute to the stabilisation, making the repulsive forces between the electric double layers larger than the attractive forces. The dispersant keeps the ceramic particles in a stable suspension in the slurry (Maiti & Rajende, 2002). It permits the particles to settle into a densely packed green tape when the solvent evaporates. So an effective dispersant can increase the quality of the green films. Maiti & Rajende, 2002 showed, that terpineol is an effective dispersant in the preparation of green ceramic tape of yttria stabilized zirconia. It has higher density both in green and fired stages, higher flexibility of green tapes that the conventional dispersants such as menhaden fish oil (MFO) and phosphate ester (PE). Accordingly, rheological measurements made by Maiti and Rajender, 2002 showed that the lowest viscosity of a 50 g powder suspension was obtained with 0.39 mL of phosphate ester, 2 mL of fish oil and 1.5 mL of terpineol.

Tseng & Chen, 2003 studied the effect of polymeric dispersants on the rheological behavior of nickel suspensions in a terpineol solvent. The rheological behavior was investigated according to the dispersant type, dispersant concentration (0.5 - 10% of the powder weight) and solids loading (3 - 10 vol.%) over a shear-rate range of 1 -1,000 s^{-1}. The suspensions exhibited pseudoplastic behavior, revealing that the mixtures were flocculated in structure. The suspension viscosity showed a minimum when the dispersant concentration exceeds 2 wt.% of the solids. For this dispersant concentration the viscosity was about 60 % of the sample without dispersant.

Mukherje et al., 2001 studied the role of the dispersant (MFO and PE) and the YSZ powder dimensions on the slurry rheology and the effect on green as well as sintered densities of tape cast YSZ. Their results showed that the MFO was more effective than PE and the best dispersion was obtained with finer particle.

Fonseca et al., 2009 fabricated NiO/YSZ anode functional layer with 40 wt.% of NiO. The slurries were prepared by two concentrations of polymethylmethacrylate (PMMA): 1 and 2 wt.%. The slurries presented pseudoplastic and thixotropic behaviors. The suspension with 2 wt.% PMMA was more homogeneous, and maintained chemical stability over a longer period of time. It was adequate for the SOFC anode functional layer preparation.

Suspensions with flocculates are known to have shear-thinning behaviour (pseudoplastic behaviour), usually with a higher viscosity that decreases with the rate of shear. The flocculates present in slurries trap water inside their structure, thereby making it unavailable for flow and thus increasing the slurry viscosity. Upon shearing, the flocculates break and the water become available for flow, thereby decreasing the slurry´s viscosity (Fonseca et al., 2009; Nascimento et al., 2009; Ramanathan et al., 2005). It is important to determine how zeta potential and rheology measurements are correlated with the stability of slurries.

The choice of the deposition method (Table 5) essentially depends on the type of selected cell configuration, desired characteristics of the films, cost, potential for automation and reproducibility.

Deposition Technique	Brief Description	Common application	Features
Screen printing (Tiez et al., 2002; Fergus et al., 2009; Lu et al., 2010; Singhal & Kendall, 2001)	The suspension to be deposited is placed on a screen and its passage is forced by pressure.	Cathode, anode and electrolyte	Scale-up is easily feasible. Insufficient densification and cracking of some ceria based electrolytes.
Tape casting (Tiez et al., 2002; Fergus et al., 2009; EG&G Technical services, 2000; Singhal & Kendall, 2001)	The ceramic film is deposited on a temporary support, which consists of a mobile sheet. The desired thickness is obtained by a doctor blade device.	Anode and electrolyte	Scale-up is easily feasible, production of multilayer cells, able to product electrolyte with various thicknesses. Inappropriate for large cell areas.
Atmospheric Plasma spray (APS) (Fergus et al., 2009, Singhal & Kendall, 2001)	The method uses a plasma jet (~10,000 K) to melt particles which are sprayed on a substrate with fast solidification.	Cathode, anode, electrolyte and interconnector	Fast deposition, achievement of films with different compositions and microstructure, possibility of depositing SOFC layers on metallic substrates without subsequent sintering, scale-up is easily feasible.
Spray pyrolyse (Fergus et al., 2009, Singhal & Kendall, 2001; Perednis & Gauckler, 2004)	The film is deposited by spraying a suspension containing powder precursor and/or the already produced powder onto a hot substrate followed by sintering.	Electrolyte	Thin and gas-tight electrolytes, possibility of producing multiple gradient layers by changing the solution.
Colloidal spray deposition (CSD) (Fergus et al., 2009)	A colloidal sol is released through a pump to a liquid dispersing apparatus, like an ultrasonic nozzle onto a heated substrate.	Cathode and electrolyte	Low cathode ASR (area specific resistance), increasing in power density.
Chemical vapor deposition (CVD) (Fergus et al., 2009; Santillán et al., 2009)	Deposition is done by gas phase reaction between metal halide precursors and a heated substrate.	Cathode and electrolyte	Electrolyte thin film Low deposition, high temperatures required, high equipment costs, corrosive products.

Deposition Technique	Brief Description	Common application	Features
Electrochemical vapor deposition (EVD) (Fergus et al., 2009; Singhal & Kendall, 2001)	In a chamber at one side of the substrate, is placed metal chloride vapors and at the other side it is placed water vapor or oxygen. First, there is the pore closure of the substrate by the reaction between the metal chloride and water vapor. After that, the formation of an electrochemical potential gradient causes the film growth.	Electrolyte in tubular cells and interconnect	Dense film deposition on porous substrate; it can be used on tubular substrate, obtaining of homogeneous films with good mechanical properties; do not require high temperature for sintering. Increase SOFC´s cost, high temperature required for fast deposition.
Spin coating (Fergus et al., 2009, EG&G Technical services, 2000; Singhal & Kendall, 2001)	A sol gel precursor is spun on a dense or porous substrate to produce a film which thickness is controlled by the stir rate.	Electrolyte	Thin and dense electrolyte
Dip coating or Slurry coating (Matsuda et al., 2007; EG&G Technical services, 2000; Fergus et al., 2009; Santillán et al., 2009; Singhal & Kendall, 2001)	The substrate is submerged in an aqueous or alcoholic suspension. After that, the film is dried at room temperature, preheated and following sintered. This process is repeated several times.	Cathode, anode and electrolyte	Low cost. Time consuming.
Tape calendaring (Fergus et al., 2009; EG&G Technical services, 2000; Singhal & Kendall, 2001)	Similar to tape casting, but the film thickness is controlled by the spacing between rollers. The deposited suspension is a thermoplastic material.	Electrolyte and anode	Able to product electrolyte with various thicknesses, production of multilayer cells.
Sputtering (Fergus et al., 2009; Singhal & Kendall, 2001)	A target material is bombed with noble gas ions, commonly argon ions. Then, atoms or ions of the target are released and deposited on the substrate.	Cathode, anode and electrolyte	Obtaining of thin films of electrolyte; control of composition and morphology; relatively low temperature of deposition. Cracking of ceria films; high cost; some techniques, like radio-frequency (RF) sputtering and direct current (DC) sputtering can be slow.

Deposition Technique	Brief Description	Common application	Features
Electrophoretic deposition (EPD) (Matsuda et al., 2007; EG&G Technical services, 2000; Santillán et al., 2009; Fergus et al., 2009; Singhal & Kendall, 2001)	An electric field is applied forcing charged particles suspended in a liquid to move toward an electrode with opposite charge.	Cathode and electrolyte	Simple operation; short time consuming; uniform films, easy deposition on substrates with complex forms; film thickness control, scale-up is easily feasible; it is a cheaper option for electrolyte deposition onto tubular cathode.
Pulsed-laser deposition (PLD) or laser ablation) (Fergus et al., 2009)	A material is removed from a surface by laser at vacuum and then deposited on a substrate at temperature about 700 °C.	Cathode and electrolyte	Production of miniaturized SOFC, potential for automation, obtaining of nano-structures.
Sol Gel (Fergus et al., 2009)	The salts of the cations of interest are dissolved forming a sol system. The colloid is then dried to obtain a powder that is deposited by conventional methods or it is partially dried to yield viscous slurry that is deposited by a wet method.	Electrolyte	Do not require high temperature for sintering.
Painting (Fergus et al., 2009)	The suspension is deposited by a paint bush on the substrate.	Electrodes and electrolyte	Simple method. Difficult to scale up, not reproducible.

Table 5. Some deposition techniques and their features*

4. SOFC performance

After optimizing the type of material of each component and the appropriate parameters for a stable suspension, the performance is evaluated by potential versus current density measurements. According Table 6 is possible to observe that the power density values can change according some parameters such as type anode, electrolyte and cathode, the fuel gas, the temperature and type of the cell configuration (electrolyte or electrode supported). The comparison between the power density values can be made only when tests are done under the same conditions. The operation of the cell at low temperatures is related to the significant decline in SOFCs performance. Solutions to improve the cell performance include the use of alternative components materials which has good performance in IT-SOFC, as discussed in previous sections, together with electrode supported cell which the power density is higher than electrolyte supported SOFC.

Ref	Anode	Cathode	Electrolyte	Fuel gas	Maximum power density ($mW.cm^{-2}$)	Temperature (^oC)
Ding & Liu, 2008	NiO–YSZ (0.5 mm)	$La_{0.7}Sr_{0.3}MnO_3$/YSZ	ZrO_2/Y_2O_3 14.9 µm	H_2 (3 wt.% H_2O)	990	800
Murata et al. 2005	NiO–YSZ (support cell)	$La_{0.6}Sr_{0.4}Co_{0.2}Fe_{0.8}O_{3-a}$	ZrO_2/Y_2O_3 (0.2 mm)	H_2 (3 wt.%H_2O)	500	700
Matsuda et al., 2007	NiO–YSZ (support cell)	$La_{0.6}Sr_{0.4}Co_{0.2}Fe_{0.8}O_{3-\delta}$ (30 µm).	ZrO_2/Y_2O_3 (4 µm) + SDC (1 µm)	H_2 (3 wt.%H_2O)	600	700
Fan & Liu, 2009	NiO–YSZ 0.8 mm	$La_{0.54}Sr_{0.44}Co_{0.2}Fe_{0.8}O_{3-\delta}$ 6 µm	ZrO_2/Y_2O_3 8 µm	H_2	855	700
Chen et, al., 2010	NiO–YSZ (support cell)	$La_{0.6}Sr_{0.4}Co_{0.2}Fe_{0.8}O_{3-\delta}$/ Y_2O_3 /YSZ_2	YSZ dense + YSZ porous (9 µm)	H_2	473	750
Liu & Barnett, 2002	NiO–YSZ (0.5 mm)	$La_{0.6}Sr_{0.4}Co_{0.2}Fe_{0.8}O_{3-\delta}$ / $Ce_{0.9}Gd_{0.1}O_{1.95}$	ZrO_2/Y_2O_3 25 µm	H_2 (3 wt.% H_2O)	930	800
Tietz et al., 2006	NiO–YSZ 1.5 mm	$La_{0.58}Sr_{0.4}Co_{0.2}Fe_{0.8}O_{3-\delta}$ 45 µm	ZrO_2/Y_2O_3 $Ce_{0.8}Gd_{0.2}O_{2-\delta}$ interlayer	H_2 (3 wt.%H_2O)	1230	800
Savaniu & Irvine, 2010	$La_{0.2}Sr_{0.7}TiO_3$	$La_{0.6}Sr_{0.4}CoO_3$	ZrO_2/Y_2O_3 50–75 µm	H_2 (3 wt.%H_2O)	500	750
Yoo & Choi, 2010	$La_{0.2}Sr_{0.8}TiO_3$ (~15 µm)	$La_{0.6}Sc_{0.4}Co_{0.2}Fe_{0.8}O_3$ (~15 µm)	$La_{0.9}Sr_{0.1}Ga_{0.8}Mg_{0.2}O_3$ (~ 600 µm – support cell)	H_2 (3 wt.%H_2O)	300	800
Liu et al., 2007	NiO/GDC: NiO–$Ce_{0.9}Gd_{0.1}O_{1.95}$	$La_{0.6}Sr_{0.4}Co_{0.2}Fe_{0.8}O_{3-\delta}$/$Ce_{0.9}Gd_{0.1}O_{1.95}$ (2mm - support cell)	$Ce_{0.9}Gd_{0.1}O_{1.95}$ (thickness: < 20 µm)	H_2 (3 wt.%H_2O)	35 (550 °C) and 60 (600 °C)	550 and 600
Hibino et al., 2003	NiO/$Ce_{0.9}Gd_{0.1}O_{1.95}$/ RuO_2 (1.0 mm)	$Sm_{0.5}Sr_{0.5}CoO_3$	$Ce_{0.9}Gd_{0.1}O_{1.95}$ (25-40 µm)	Methane/ Ethane/propane	750 (methane), 716 (ethane), 648 (propane)	600
Sin et al., 2005	$La_{0.6}Sr_{0.4}Fe_{0.8}Co_{0.2}O_3$/$Ce_{0.8}Gd_{0.2}O_{1.9}$	$La_{0.6}Sr_{0.4}Fe_{0.8}Co_{0.2}O_3$ (5 µm)	$Ce_{0.8}Gd_{0.2}O_{1.9}$ (300 µm – support cell)	Methane	170	800
Morales et al., 2006	$La_{0.75}Sr_{0.25}Cr_{0.5}Mn_{0.5}O_{3-\delta}$	$La_{0.75}Sr_{0.25}Cr_{0.5}Mn_{0.5}O_{3-\delta}$	ZrO_2/Y_2O_3 (1.6 mm)	Hydrogen/methane	300 (CH_4) and 500 (H_2)	950

Table 6. Materials and electrical performance of SOFC according some authors*

The configuration NiO-YSZ /YSZ / LSM-YSZ reported by Ding & Liu, 2008 was intensively studied using hydrogen fuel. Later, there was a trend of substitution of LSM by LSCF because of its higher ionic and electronic conductivity. This material was studied by Murata et al. 2005, Matsuda et al. 2007 and Fan & Liu, 2009 (Table 6). To further increase the ionic conductivity of LSCF, some researchers investigated the production of a composite of LSCF and an electrolyte material, as the work of Chen et al. 2010 and Liu & Barnett, 2002. However, the reaction between LSCF and YSZ led many researchers to study the use of a protective layer of GDC between the LSCF and YSZ layers. In order to reduce the operating temperature of the cell, new materials for anode (as LST, studied by Savanna & Irvine, 2010) and electrolyte (as LSGM studied by Yoo & Choi, 2010 and CGD studied by Liu et al., 2007) were also tested. The latest research in terms of fuel cells seek to obtain high power densities through the use of fuels other than hydrogen, as studied by Hibino et al., 2003, Sin et al., 2005 and Morales et al., 2006.

5. Conclusion

SOFC technology offers a real alternative for relatively clean distributed power generation. Nowadays there is an intense search for materials and configurations of IT-SOFC cells with power densities as high as possible. For this intent new materials which have a long term stability with very low degradation are been tested such as perovskite-type oxides and fluorites. They are replacing conventional materials, especially in the SOFC operating with hydrocarbon. Besides the composition, the microstructure also needs further optimization. For this purpose, the preparation of stable suspensions and the choice of suitable deposition methods are crucial in order to improve electrochemical characteristics and the cost-effective fabrication of the cells. However for SOFCs commercialization, cost reduction is still a key issue.

6. Acknowledgment

The authors wish to thank CAPES (Coordenação de Aperfeiçoamento de Pessoal de Nível Superior); CNPq (Conselho Nacional de Desenvolvimento Científico e Tecnológico) CEMIG (Companhia Energética de Minas Gerais) and FAPEMIG (Fundação de Amparo a Pesquisa do Estado de Minas Gerais) for their financial support.

7. References

Acres, G. (2001). Recent advances in fuel cell technology and its applications. *Journal of Power Sources*, Vol. 100, No. (November 2001), pp. (60–66), ISSN 0378-7753

Amado, R. S.; Malta, L. F. B; Garrido, F. M. S.; Medeiros, M. E. Solid oxide fuel cells: materials, components and configurations. *Química Nova* , Vol. 30, No. 1, pp. (189-197) ISSN 0100-4042

Badwal, S.P.S. (2001). Stability of solid oxide fuel cell components. *Solid State Ionics*, Vol.143, No. 1-4 (June 2001), pp.(39-46), ISSN 0167-2738

Bao,W.; Qibing, C.; Guangyao, M. (2005). Effect of NiO/YSZ compositions on the cosintering process of anode-supported fuel cell. *Journal of Membrance Science*,Vol. 259, No.1-2, (August 2005), pp. (103-109), ISSN 0376-7388

Belardi, R.M.; Brant, M. C. ;Matencio, T.; Domingues (2009). Electrical study of cathodic activation and relaxation of $La_{0,80}Sr_{0,20}MnO_3$. *Ionics,* Vol. 15, No.2,(July, 2009), pp.(227-232), ISSN 0947-7047

Benyoucef, A.; Klein, D.; Coddet, C.; Benyoucef, B. (2008). Development and characterisation of (Ni, Cu, Co)-YSZ and Cu-Co-YSZ cermets anode materials for SOFC application. *Surface and Coating Technology*. Vol. 202, No.10, (February 2008),pp. (2202-2207), ISSN 0257-8972

Brant, M. C. ;Matencio, T.; Dessemond, L. ; Domingues (2001), Fernandes, R. Z; Domingues, R.Z. (2001). Electrical and microstructural aging of porous Lanthanum Strontium Manganite/Yttria-doped cubic Zirconia Electrodes. *Chemistry of Materials*, USA American Chemical Society, Vol. 13, No. 11, (October 2001) pp. (3954-3961), 2001. ISSN (electronic): 1520-5002

Brant, M. C. ;Matencio, T.; Dessemond, L. ; Domingues (2006), Electrical degradation of porous and dense LSM/YSZ interface. *Solid State Ionics,* Vol. 177, No. 9-10, (March, 2006), pp. (915-921). ISSN 0167-2738

Chen, W.; Wen,T.;Nie, H.; Zheng, R. (2003) Study of $Ln_{0.6}Sr_{0.4}Co_{0.8}Mn_{0.2}O_{3-\delta}$ (Ln=La, Gd, Sm or Nd) as the cathode materials for intermediate temperature SOFC. *Materials Reserch Bulletin,* Vol. 38, No. 8, (July 2003), pp. (1319-1328), ISSN 0025-5408

Chen, J.; Liang, F.; Yan, D.; Pu, J.; Chi, B.; Jiang, S. P.; Jian, L.(2010) . Performance of large-scale anode-supported solid oxide fuel cells with impregnated $La_{0.6}Sr_{0.4}Co_{0.2}Fe_{0.8}O_3-\delta + Y_2O_3$ stabilized ZrO_2 composite cathodes. Journal of Power Sources, Vol. 195, No. 16, (August 2010), pp. (5201-5205), ISSN 0378-7753

Charpentier, P.; Fragnaud, P.; Schleich, D. M.; Gehain, E. (2000). Preparation of thin film SOFCs working at reduced temperature. *Solid State Ionics*, Vol. 135, No. 1-4 (November 2000), pp.(373-380), ISSN 0167-2738

Ding, J.; Liu, J. (2008). An anode-supported solid oxide fuel cell with spray-coated yttria-stabilized zirconia (YSZ) electrolyte film. *Solid State Ionics*, Vol. 179, No. 21-26, (September 2008), pp. (1246–1249), ISSN 0167-2738

Dutta, A.; Mukhopadhyay, J.; Basu, R.N. (2009). Combustion synthesis and characterization of LSCF-based materials as cathode of intermediate temperature solid oxide fuel cells. *Journal of the European Ceramic Society*. Vol. 29, No. 10, (July 2009), pp. (2003-2011), ISSN 0955-2219

EG&G Technical services. (Ed(s).). (2000). *Fuel Cell Handbook* (5th), Parsons, Inc., ISBN 1603220178, Morgantown, West Virginia, EUA

Fabbri, E.; Pergolesi, D.; D´Epifanio, A.; Bartolomeo, E. D.; Balestrino, G.; Licoccia, S.; Traversa, E. 2008. Design and fabrication of a chemically-stable proton conductor bilayer electrolyte for intermediate temperature solid oxide fuel cells (IT-SOFCs). *Energy & Enviromental Science*, Vol. 1, No. 3, (September 2008), pp. (355-359), ISSN 17545692

Fan, B.; Liu, X. (2009). A-deficit LSCF for intermediate temperature solid oxide fuel cells. *Solid State Ionics*, Vol. 180, No. 14-16, (June 2009), pp. (973–977), ISSN 0167-2738

Faro, M. L.; Rosa, D. L.; Antonucci, V.; Arico, A. S. (2009). Intermediate temperature solid oxide fuel cell electrolytes. *Journal of the Indian Institute of Science*, Vol. 89, No.4, (October–December 2009), pp. (363-381), ISSN 09704140

Fergus, J.; Hui, Rob.; Li, X.; Wilkinson, D.P.; Zhang, J. Jeffrey (Ed(s)) (2009) .*Solid oxide fuel cells : materials properties and performance*, CRC Press, ISBN 978-1-4200-8883-0, London, NY.

Florio, D. Z. de; Fonseca, F. C.; Muccillo, E. N. S.; Muccillo, R. (2004). Ceramic materials for fuel cells. *Cerâmica*. Vol. 50, No. 316, (October -December 2004), pp. (275-290), INSS 0366-6913

Fonseca, C. G.; Basaglia, R.M.F; Brant, M. C.; Matencio, T.; Domingues, R. D. (2009). Study of the rheological behavior of an anode slurry and the microstructural properties of an anode functional film obtained by spray coating. *Powder Technology*, Vol. 192, No.3, (June 2009), pp. (352-358), ISSN 0032-5910

Guarany, C. A. (December 2008). Estruturas ferroelétricas, In: *Ferroelétricos.com*, 21.03.2011, Available from <http://ferroeletricos.com/perovskita.html>

Hibino, T.; Hashimoto, A.; Yano, M.; Suzuki, M.; Sano, M (2003). Ru-catalyzed anode materials for direct hydrocarbon SOFCs. *Electrochimica Acta*, Vol.48, No.17, (July 2003), pp. 2531-2537, ISSN 0013-4686

Huang, T. J; Chou, C. L.; Chen, W. J.; Huang, M. C.(2009) Coal syngas reactivity over Ni-added LSCF–GDC anode of solid oxide fuel cells. *Electrochemistry Communications*, Vol. 11, No. 2**, (**February 2009), pp. (294-297), ISSN 1388-2481

Hui, S.; Petric, A. Evaluation of yttrium-doped $SrTiO_3$ as an anode for solid oxide fuel cells. *Journal of the European Ceramic Society*. Vol. 22, No. 9-10, **(** September 2002), pp. (1673-1681) , ISSN 0955-2219

Jiang, S. P. (2002). A comparison of O2 reduction reactions on porous (La,Sr)MnO3 and (La,Sr)(Co,Fe)O3 electrodes. *Solid State Ionics*, Vol.146, No. 1-2.,(January 2002), pp. (1-22), ISSN 0167-2738

Kenjo, T.; Nishiya, M. (2002) $LaMnO_3$ air cathodes containing ZrO_2 electrolyte for high temperature solid oxide fuel cells. *Solid State Ionics*, Vol. 57, No. 3-4, (October 1992), pp. (295-302), ISSN 0167-2738

Kharton, V. V.; Marques, F. M. B.; Atkinson, A. (2004). Transport properties of solid oxide electrolyte ceramics: a brief review. *Solid State Ionics*, Vol. 174, No. 1-4, (October 2004), pp. (135-149), ISSN 0167-2738

Koide, H., Someya, Y., Yoshida, T.; Maruyama, T., (2000). Properties of Ni/YSZ cermet as anode for SOFC. S*olid State Ionics* , Vol.132,No.3-5, (July, 2000) pp.(253-260), ISSN 0167-2738

Liu, J.; Barnett, S. A. (2002). Thin Yttrium Stabilized zircônia electrolyte solid oxide fuel cells by centrifuge casting. *Journal of the American Ceramic Society*, Vol. 85, No. 12, (December 2002), pp. (3096–3098), ISSN 15512916

Liu, Y.; Hashimoto, s.; Nishino, H.; Takei, K.; Mori, M. (2007) Fabrication and characterization of a co-fired $La_{0.6}Sr_{0.4}Co_{0.2}Fe_{0.8}O_{3-\delta}$ cathode-supported $Ce_{0.9}Gd_{0.1}O_{1.95}$ thin-film for IT-SOFCs. *Journal of Power Sources*. Vol. 164, No. 1,(January 2007), pp. 56-64, ISSN 0378-7753

Lu, Z.; Zhou, X.-d.; Fisher, D.; Templeton, J.; Stevenson, J.; Wu, N.; Ignatiev, A. (2010). Enhanced performance of an anode-supported YSZ thin electrolyte fuel cell with a laser-deposited Sm0.2Ce0.8O1.9 interlayer. *Electrochemistry Communications*, Vol. 12, No. 2, (February 2010), pp. (179-182), ISSN: 1388-2481

Maiti, A. K.; Rajende, B. (2002). Terpineol as a dispersant for tape casting yttria stabilized zirconia powder. *Materials Science and engineering A*, Vol. 333, No. 1-2, (August 2002), pp. (35-40), ISSN 0921-5093

Martins, R. F.; Brant, M. C.; Domingues, R. Z.; Paniago, R. M.; Sapag, K.; Matencio, T. (2009). Synthesis and characterization of NiO-YSZ for SOFCs, Materials *Research Bulletin*, Vol. 44, No. 2, (February 2009), pp. 451-456, ISSN 0025-5408

Matsuda, M.; Hosomia, T.; Murata, K.; Fukui, T.; Miyake, M. (2007). Fabrication of bilayered YSZ/SDC electrolyte film by electrophoretic deposition for reduced-temperature operating anode-supported SOFC. *Journal of Power Sources*, Vol. 165, No. 1, (February 2007), pp. (102-107), ISSN 0378-7753

Matsuzaki, Y; Yasuda, I.(2007). The poisoning effect of sulfur-containing impurity gas on a SOFC anode: Part I. Dependence on temperature, time, and impurity concentration. *Journal of Power Sources*, Vol. 171, No. 2, (September 2007), pp. (247-260), ISSN 0378-7753

McIntosh, s.; Vohs, J.M.; Gorte, R.J.(2002). An examination of lanthanide additives on the performance of Cu–YSZ cermet anodes. *Electrochemica Acta*, Vol. 47, No. 22-23, (August 2002), pp. (3815-3821), ISSN 0013-4686

Mukherjee, A.; Maiti, B.; Das Sharma, A.; Basu, R. N.; Maiti, H. S. (2001). Correlation between slurry rheology, green density and sintered density of tape cast yttria stabilised zirconia. *Ceramics International*, Vol. 27, No. 7, (August 2001), pp. (731-739), ISSN 0272-8842

Murata, K.; Fukui, T.; Abe, H.; Naito, M.; Nogi, K. (2005). Morphology control of La(Sr)Fe(Co)O_{3-a} cathodes for IT-SOFCs. *Journal of Power Sources*. Vol. 145, no. 2, (August 2005), pp. 257-261, ISSN 0378-7753

Mitchell, B. S. (2004). An Introduction to Materials Engineering. and Science for Chemical and Materials Engineers, Jonh Wiler & Sons, Inc., Hoboken, ISBN 0-471-43623-2, New Jersey, EUA

Nascimento, A. C; Basaglia, R. M. F.; Cunha, F. T. A; Fonseca, C. G; Brant, M. C; Matencio, T.; Domingues, R. Z. (2009) Correlation between yttria stabilized zirconia particle size and morphological properties of NiO–YSZ films prepared by spray coating process. *Ceramics International*, Vol. 35, No. 8, (December 2009),pp. (3421-3425), ISSN 0272-8842

Nesaraj, S. A. (2010). Recent developments in solid oxide fuel cell technology – a review. *Journal of Scientific* and Industrial Research, Vol. 69, No. 3, (March 2010), pp. (169-176), ISSN:0022-4456

Perednis, D.; Gauckler. L. J. (2004). Solid oxide fuel cells with electrolytes prepared via spray pyrolysis. *Solid State Ionics*, Vol. 166, No. 3-4, (January 2004), pp. (229–239), ISSN 0167-2738

Petric, A.; Huang, P.; Tiet, F. (2000) Evaluation of La–Sr–Co–Fe–O perovskites for solid oxide fuel cells and gas separation membranes. *Solid State Ionics*, Vol. 135, No. 1-4, (November 2000), pp. (719-725), ISSN 0167-2738

Ramanathan, S.; Krishna Kumar, K. P.; DE, P. K.; Banerjee, S. (2005). Role of dispersion conditions on grindability of yttria stabilized zirconia (YSZ) powders, *Bull. Mater. Sci*., Vol. 28, No. 2, (April 2005), pp. (109–114), *ISSN*: 0250-4707

Raza, R.; Wang, X.; Ma, Y.; Liu, X.; Zhu, B. (2010). Improved ceria–carbonate composite electrolytes. *International Journal of Hydrogen Energy*, Vol. 35, No.7, (April 2010), pp. (2684-2688), ISSN 0360-3199

Ringuede, A.; Labrincha, J.A.; Frade, J.r. (2001). A combustion synthesis method to obtain alternative cermet materials for SOFC anodes. *Solid State Ionics.* Vol. 141-142,(May 2001), pp. (549-557), ISSN 0167-2738

Ruiz-Morales, J.C., Canales-Vázquez, J.; Peña-Martínez, J.; López, D. M. ; Núñez, P. (2006). On the simultaneous use of $La_{0.75}Sr_{0.25}Cr_{0.5}Mn_{0.5}O_{3-\delta}$ as both anode and cathode material with improved microstructure in solid oxide fuel cells, *Electrochemical Acta*, Vol. 52, No.1 (October 2006), pp. (278-284), ISSN 0013-4686.

Sanson, A.; Pinasco, P.; Ronconi, E. Influence of pore formers on slurry composition and microstructure of tape cast supporting anodes for SOFCs (2008). *Journal of the European Ceramic Society*, Vol. 28, No. 6, (February 2008), pp. (1221-1226), ISSN 0955-2219

Santillán, M. J.; Caneiro, A.; Quaranta, N.; Boccaccini, A. R. (2009). Electrophoretic deposition of $La_{0.6}Sr_{0.4}Co_{0.8}Fe_{0.2}O_{3-\delta}$ cathodes on $Ce_{0.9}Gd_{0.1}O_{1.95}$ substrates for intermediate temperature solid oxide fuel cell (IT-SOFC). *Journal of the European Ceramic Society*, Vol. 29, No. 6, (April 2009), pp. (1125–1132), ISSN 0955-2219

Savaniu, C.D.; Irvine, J.T.S. La-doped $SrTiO_3$ as anode material for IT-SOFC (2010). *Solid state Ionics*, Article in Press, ISSN 0167-2738

Sin, A; Kopnin, E.; Dubitsky, Y.; Zaopo, A.; Aricò, A. S.; Gullo, L. R.; La Rosa, D.; Antonucci, V. (2005) Stabilisation of composite LSFCO–GDC based anodes for methane oxidation in solid oxide fuel cells. *Journal of Power Sources*, Vol. 145, No. 1, **(**July 2005), pp. (68-73), ISSN 0378-7753

Singhal, S.C.& Kendall, K. (2003). *High temperature solid oxide fuel cells: fundamentals, design, and applications*: Elsevier Science Ltd, ISBN 1-85617-387-9, Oxford, UK.

Steele, B. C. H. (2000). Appraisal of $Ce_{1-y}Gd_yO_{2-y/2}$ electrolytes for IT-SOFC operation at 500 ^{o}C. *Solid State Ionics*, Vol. 129, No. 1-4, (April 2000), pp. (95-110), ISSN 0167-2738

Sun,C.; Stimming, U.; Sun,C.; Stimming, U. (2007). Recent anode advances in solid oxide fuel cells. *Journal of Power Sources*, Vol. 171, No.(2), (September 2007), pp. (247–260), ISSN 0378-7753

Sun, C.; Hui, R.; Roller, J. (2010) Cathode materials for solid oxide fuel cells: a review. *J Solid State Electrochem*, Vol. 14,No (7), (July 2010), pp.(1125–1144), ISSN: 1432-8488 (print version)

Tai,L.-W.; M. M. Nasrallah, M.M.; Anderson, H.U.; Sparlin, D.M.;. Sehlin, S. R (1995)**.** Structure and electrical properties of $La_{1-x}Sr_xCo_{1-y}Fe_yO_3$. Part 1. The system $La_{0.8}Sr_{0.2}Co_{1-y}Fe_yO_3$.*Solid State Ionics*, Vo.l.76, No.3-4, (March 2000), pp (259-271), ISSN 0167-2738

Tarancón, A. (2009). Strategies for lowering solid oxide fuel cells operating temperature. *Energies*, Vol. 2, No. 4, (November 2009), pp. (1130-1150), ISSN 1996-1073

Tarôco, H.A.; Andrade, S. T. P; Brant, M. C.; Domingues, R. Z.; Matencio, T. (2009). Assembly and electrical characterization of solid oxide fuel cell stacks. *Quím. Nova*, Vol.32, No.5, pp. (1297-1305) ISSN 0100-4042

Teraoka, Y.; Nobunaga, T.; Okamoto, K.; Miura, N.;Yamazoe, N.;(1991). Influence of constituent metal cations in substituted $LaCoO_3$ on mixed conductivity and oxygen

permeability. *Solid State Ionics*, Vol. 48, No. 3-4, (November 1991), pp. (207-212), ISSN 0167-2738

Tietz, F.; Buchkremer H.-P.; Stöver D. (2002). Components manufacturing for solid oxide fuel cells. *Solid State Ionics,* Vol. 152-153, (December 2002), pp. (373-381), ISSN 0167-2738

Tietz, F.; Haanappel, V. A. C.; Maim A.; Mertens, J.; Stöver, D. (2006). Performance of LSCF cathodes in cell tests. *Journal of Power Sources*, Vol. 156, No. 1-19, (May 2006), pp. (20-22), ISSN 0378-7753

Tseng, W. J.; Chen,; C. N. (2003). Effect of polymeric dispersant on rheological behavior of nickel-terpineol suspensions. *Materials Science and Engineering A*, Vol. 347, No. 1-2, (April 2003), pp. (145-153), ISSN 0921-5093

Ullmann, H.; Trofimenko, N.;Tietz, F.; Stöver, D.; Ahmad-Khanlou, A. (2000). Correlation between thermal expansion and oxide ion transport in mixed conducting perovskite-type oxides for SOFC cathodes. *Solid State Ionics*, Vol., No.1-2, **(**December 2000), pp. (79-90), ISSN 0167-2738

Uhlenbruck, S.; Moskalewicz, T.; Jordan, N.; Penkalla, H.-J.; Buchkremer, H. P. (2009). Element interdiffusion at electrolyte–cathode interfaces in ceramic high-temperature fuel cells. *Solid State Ionics*, Vol. 180, No. 4-5, (April 2009), pp. (418-423), ISSN 0167-2738

Wincewicz, K.C.; Cooper; J. S. (2005). Taxonomies of SOFC material and manufacturing alternatives. *Journal of Power Sources,* Vol. 140, No.2, (February 2005) pp. 280–296, ISSN 0378-7753

Yamamoto, O.; Takeda, Y.; Kanno, R.; Noda,N. (1987). Perovskite-type oxides as oxygen electrodes for high temperature oxide fuel cells, *Solid State Ionics*. Vol. 22, No. 2-3 (January 1987), pp. (241-246), ISSN 0167-2738

Yoo, K.B.; Choi, G.M. LST–GDC composite anode on LaGaO3-based solid oxide fuel cell (2010). *Solid State Ionics,* Article in Press, ISSN 0167-2738

Zhu, w. Z.; Deevi, S. C.(2003). A review on the status of anode materials for solid oxide fuel cells. *Materials Science and Engineering A*, Vol. 362, No. 1-2, (December 2003), pp. (228-239), ISSN 0921-5093

20

Laser Applications of Transparent Polycrystalline Ceramic

Qihong Lou, Jun Zhou, Yuanfeng Qi and Hong Cai
Shanghai Institute of Optics and fine mechanics
P.R.China

1. Introduction

High power lasers are widely used in a variety of applications, including materials processing, remote sensing, free-space communications, laser particle acceleration, gravitational wave interferometers, and even inertial confinement fusion (ICF) [1]. The optical gain media of the system is the key factor for efficient laser oscillation. Since Maiman discovered the first ruby laser in 1960, numerous materials have been developed and improved to achieve high efficiency and high power for all-solid-state lasers. There are three primary groups of solid state host materials: single crystals, glasses and ceramics. Among them Nd:YAG single crystal may be the most widely used laser media. But Nd:YAG single crystal grown by conventional Czochralski method has its own insurmountable disadvantages such as expensive, time-consuming, small size and low concentration [2], which has limited its applications in high power lasers. And for Nd-doped glass material, though it is very easy to get large size and high concentration, but its thermal conductivity and gain are quite low and the laser efficiencies were not satisfying. Polycrystalline ceramics is an aggregate of crystalline grains, each randomly oriented with respect to neighboring grains. Since the 1960s, it has been speculated that a dense polycrystal of an isotropic, pure material would be optically indistinguishable from a single crystal of the same material. The only problem has been finding a fabrication method. Now materials scientists in Japan have come up with a way to mass-produce polycrystalline ceramics materials that maintain high conversion efficiency and good optical characteristics as well as single crystals. Further more, the ceramics laser materials manufacturing method has five distinct advantages over single-crystal growth:

- Ease of manufacture: It takes 4-6 weeks to grow crystals using the Czochralski method, but thes method makes rods in just a few days.
- Less expensive: Single crystals have to be grown in an expensive iridium crucible. Ceramics rod growth requires no crucible and is also faster. The cost of a single crystal increases dramatically with its size, unlike ceramics.
- Fabrication of large size and high concentration laser medium: Size of rods Single-crystal growth limits crystal size, which in turn limits the potential output power. The maximum crystal size is about 23 cm long and the Nd^{3+} doping concentration is no more than 2 at.%. But polycrystalline ceramic YAG can be made as large as 1 m×1 m×0.02 m and up to 4 at.% doping with no gradient.

- Multi-layer and multi-functionality Ceramics structure: Ceramics fabrication could enable the incorporation of Q-switching and Raman shifting within the source, which is impossible with a single crystal.
- Mass-production: Suitability Ceramics materials can be fabricated in a production-line fashion, reducing the time and cost required for single-crystal YAG rod manufacturing.

2. The development of transparent ceramics (history)

Since 1960's, a number of researchers had speculated that a theoretically dense polycrystal of an isotropic, pure material would be optically indistinguishable from a single crystal of the same material. In 1966, Hot-pressed CaF2 doped dysprosium appears to be the first reported polycrystalline material which established laser oscillation [4]. Then several decades passed, no remarkable development had been acquired. The problem with making laser materials from ceramics material is that ceramics are polycrystalline and some of their characteristics, such as grain boundaries, pores, composition gradients and lattice imperfections, increase the scattering of light in the host. This adds to the opacity of the material, making it unsuitable for laser action. The key is to find a manufacturing method in which the crystals that make up the rod are very similar in size and small enough to have little effect on incident light with a wavelength of around 1 μm. Only in the last decade have ceramics laser materials received much attention, after manufacturing breakthrough coming with highly transparent nanocrystalline YAG doped with Ln^{3+} activators, in particular Nd3+ ions. In 1995, the first Nd:YAG ceramics laser was developed by Akio Ikesue and colleagues at Japan's Krosaki Corporation. Ikesue used a hot-press method to make the ceramics laser materials. [5] Later in 1999, another research team led by Ken-ichi Ueda improved Nd:YAG ceramics successfully by combining liquid-phase chemical reaction with vacuum sintering technique to produce the similarly-sized nanoparticles for ceramics formation. The nanoparticles are homogenous, so any pressure need not use. [6-7]. High quality, high transparent Nd:YAG ceramics with much low scattering losses have been fabricated. Optical absorption, fluorescence and emission spectra, physical and laser properties of Nd: YAG ceramics have been measured and compared with those of Nd: YAG single crystals, and almost identical superiority features have been obtained in qualitative analysis [8-10]. It shows that Nd:YAG ceramics are indeed potential superexcellent gain media for high efficient and high power lasers. Using these Nd:YAG ceramics samples, high slope efficiency of 68 % was achieved under end-pumping disk laser [11]. And for high power laser oscillation, output power from 499mW→31W→72W→88W→128W→1460W were reported one by one [12-15]. Now Nd:YAG ceramics slabs for solid-state heat capacity laser were reported hit 67kW high power. In order to suppress parasitic oscillation, Sm:YAG ceramics was fabricated as for an absorber, and its optical properties were investigated. Higher power ceramics laser is still-evolving. The biggest advantage is the scaling to the meter-size plate. As a result, the ceramics laser is the most promising active medium for the laser fusion drivers.

Making ceramics YAG crystals is not restricted to neodymium-doped material or YAG crystals. Er^{3+}, Yb^{3+}, Nd^{3+}, Eu^{3+}, Dy^{3+} and Cr^{4+} as well as Sesquioxide host crystals can be made also. Nd:Y_2O_3 and Yb:Y_2O_3 ceramics laser materials as having an extra advantage over single crystals. It is very hard to grow a single Y_2O_3 crystal because its melting temperature is 2430 °C. The sintering temperature for Y_2O_3 is some 700 °C lower than its melting point,

meaning that large Y_2O_3 ceramics could be manufactured using a vacuum sintering method. One of the advantages of Y_2O_3 is its thermal conductivity, which is twice that of YAG for ceramics materials. This could make it more appropriate for using in the femto-second lasers for industry. Ceramics Y2O3 laser generated Sub-200 fs Fourier-limited pulses in the SESAM mode locking.

Another possibility is that ceramics laser rods could incorporate multiple-laser functionality. All ceramics passively Q-switched Yb:YAG/Cr4+:YAG microchip laser with shortest pulse width of 380 ps has been achieved.

The still developing Nd:YAG ceramics are very good alternative to Nd:YAG single crystals for high energy pulse laser applications in the near future.

3. Comparison of laser characteristics between transparent ceramics and single crystal

3.1 Spectroscopic analysis

Optical absorption and emission measurements were carried out as follows. The normalized intensity of room temperature absorption spectrum of 1at.% Nd:YAG ceramics and 1.1at.% Nd:YAG single crystal is shown in Figure. 1(a). From this figure, we see that the main absorption peak of 2% ceramics is centered at 808.56 nm which is slightly red shifted compared to that of single crystal ~808.48 nm! Because of a slight change in the crystal field in the high neodymium concentration samples. Figure. 1(b) shows the room temperature fluorescence spectra for 1at.% Nd:YAG ceramics and 1.1at.% Nd:YAG single crystal, respectively. For comparison, the fluorescence spectrum for single crystal and ceramics are normalized and put together. A slight redshift was also observed in emission spectrum because of high neodymium concentration. The emission peak of Nd:YAG ceramics is centered at 1064.2 nm which is 0.1 nm redshifted away from that of Nd:YAG single crystal. Except the slight redshift, the two spectra are almost identical to each other.

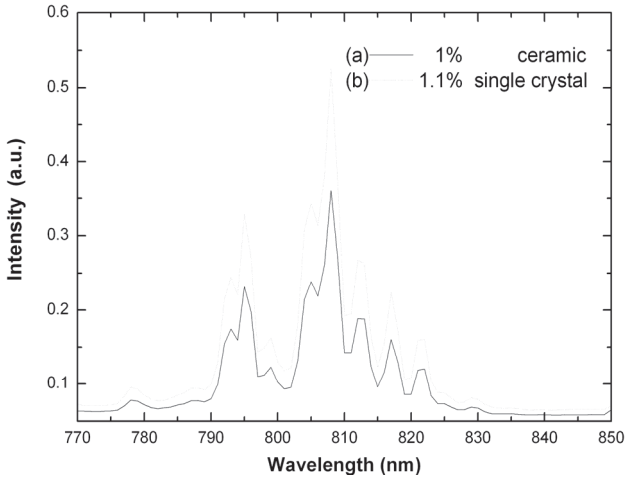

Fig. 1. (a). Comparison of room-temperature absorption spectrum from 770 nm to 850 nm between Nd:YAG ceramic and single crystal.

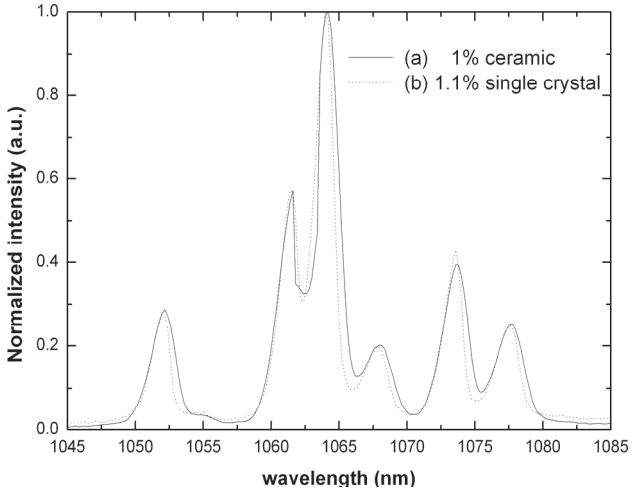

Fig. 1. (b). Comparison of room-temperature fluorescence spectrum from 1045 to 1085nm between Nd:YAG ceramic and single crysPulse trains from Q-switched ceramic

3.2 Fluorescence lifetime

As reported by Konoshima Chemical, Co., Ltd. and Ueda's research group, [16] the fluorescence lifetime for single crystal and ceramics have been obtained through curve fitting on the fluorescence decay curve. The fluorescence lifetime of Nd:YAG ceramics and single crystal versus neodymium concentration. The fluorescence lifetime for 0.6% Nd:YAG single crystal and 0.9% Nd:YAG single crystal are 256.3 μs and 248.6 μs, respectively(Figure. 2), which agrees well with the earlier reports [17]. Fluorescence lifetimes of 257.6 μs, 237.6 μs, 184.2 μs and 95.6 μs have been measured, respectively, for 0.6%, 1%, 2% and 4% Nd:YAG ceramics. These data also agree well with the results in [17]. The fluorescence

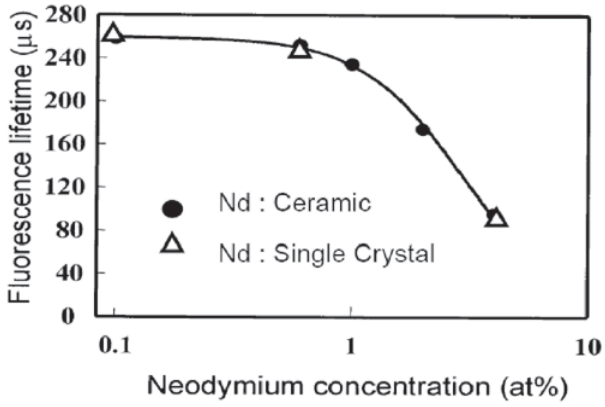

Fig. 2. Fluorescence lifetime of Nd:YAG ceramics and single crystal versus neodymium concentration. Solid line is the fitted curve for ceramics fluorescence lifetime.

lifetime decreases dramatically when neodymium concentration exceeds 1%. The fluorescence lifetimes for 0.6% doped single crystal and ceramics are almost identical (only 1.3 μs difference). The fluorescence lifetime difference between 0.9% Nd:YAG single crystal and 1% Nd:YAG ceramics is 11 μs. It can be predicted that for the same concentration of Nd:YAG single crystal and ceramics, for example, 0.9% concentration, the lifetime difference should be less than 11 μs. From the fitted curve for ceramics fluorescence lifetime, the lifetime for 0.9% Nd:YAG ceramics is 244.2 μs, which is only 4.4 μs different from that of 0.9% Nd:YAG single crystal. It indicated that the neodymium ions inside the grain have the same conditions as those of single crystal, and the fluorescence lifetime difference is caused only by the neodymium ions in the vicinity of grain boundaries.

The wavefront distortion picture of a single crystal YAG slab and ceramics YAG slab near the facet part measured by a Zygo interferometer is show in Figure. 3. From this figure, one can see that near the facet part, the wavefront was seriously distorted for the single crystal YAG. But for a ceramics Nd： YAG slab, because there is no facet problem, the wavefront distortion picture (right) shows a homogeneous pattern, which is much better than that of a single crystal. A crystalline YAG has poor optical homogeneity because of its facet structure during growing process. The optical homogeneity of ceramics YAG is good as well as glass.

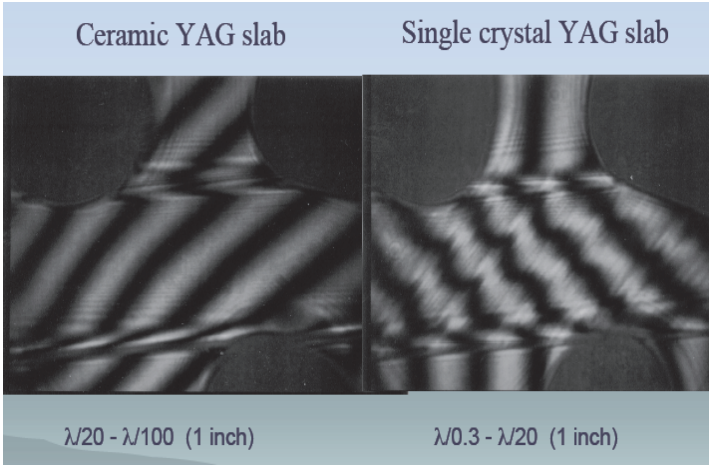

Fig. 3. The wavefront distortion picture of a single crystal YAG and ceramics YAG slab

4. High efficiency Nd: YAG ceramics laser

4.1 Quasi-CW Nd:YAG ceramics laser

By using a quite uniformly side-around arranged compact pumping system, A high efficiency high power quasi-CW laser with a Nd:YAG ceramics rod has been demonstrated. With 450 W quasi-CW stacked laser diode bars pumping at 1064 nm, 236 W optimum output laser at 1064 nm was obtained. The optical-to-optical conversion efficiency was 52.5% and corresponding slope efficiency was 62%.

A schematic diagram of the laser setup is shown in Figure. 4. The Nd:YAG ceramics rod used in the experiment was 75 mm in length and 5 mm in diameter with neodymium

doping level of 1 at.%. Both the end facets of the rod were flat and antireflection coated at 1064 nm in order to reduce the intra-cavity losses, and the lateral surface was frosted. The rear mirror of the laser cavity was high-reflection mirror at 1064 nm and a series of output coupling mirrors were prepared with reflectivity from 30% to 84% at 1064 nm. Thus we could find the optimized output in experiment. The cavity length was about 195 mm. The pump source was operated at 808 nm. Liquid cooling was employed to remove heat from the ceramics rod and diode heat sink. The operation temperature was kept at about 16 ℃.

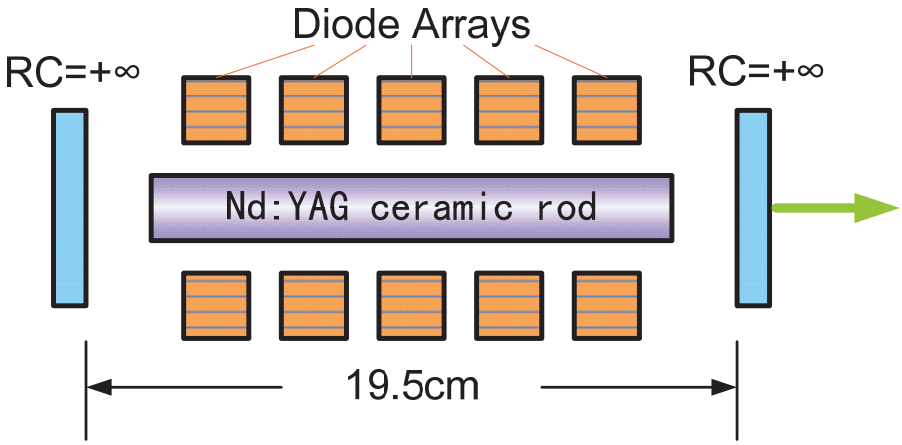

Fig. 4. Schematic diagram of experimental setup for side-pumped Nd:YAG ceramics rod laser.

In order to optimize the uniformity and radial profile of the pump distribution within the gain medium and decrease the coupling losses, we designed a compact side-around arranged direct radial-pumping head, of which cross-section configuration was illustrated in Figure. 5. The optical pump head consisted of nine LD stacked arrays mounted around the rod from 9 directions with proportional angle. The ceramics rod was mounted inside a flow-tube. The side-face of the ceramics rod and the emitting surface of the laser diodes were close proximity, and no coupling optics was employed between them. The coupling efficiency was by far the most desirable. Each LD stacked array consisted of five quasi-CW types LD bars, which were placed along the length of the laser rod and pumped perpendicularly to the direction of propagation of the laser radiation. Each bar generated 60 W peak powers. The arrays operating at 20% duty cycle were pulsed at a repetition rate of 1 kHz with a pulse width of 200 μs. The design of 9 LD arrays arranged around the ceramics rod symmetrical allowed optimizing the uniformity and radial profile of the pump distribution within the gain medium with good spatial overlap between pump radiation and low-order modes in the resonator, which in turn leads to a high-brightness laser output. Figure. 6 showed the 2D contour plot of pump intensity distribution simulated by computer with ray tracing method.

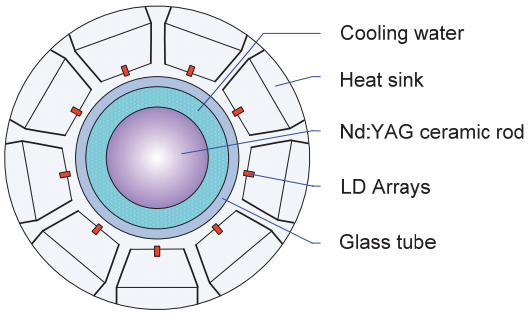

Fig. 5. Cross-section of large diode arrays compact side-pumped Nd:YAG ceramics laser head.

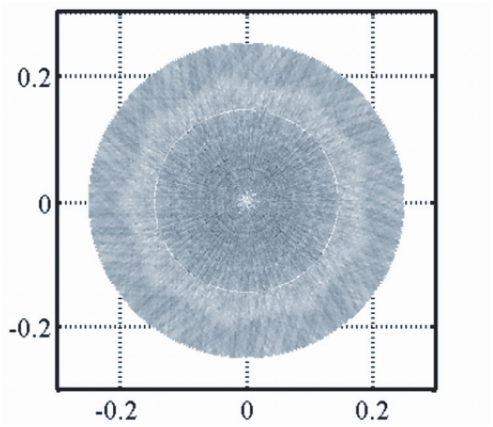

Fig. 6. 2D Contour plot of pump intensity distribution simulated by computer with ray tracing method.

By changing the rear mirror with different reflectivity of 30%, 50%, 62.5%, 78%, and 83.4%, we get a relationship laser output power as a function of the average pumping power, which was shown in Figure. 7. The output power increased almost linearly with the pumping power, and the optimum output appeared with the coupling mirror of the reflectivity near 78%. When the pump current rose to 60 A, the total average pump power was about 450 W, and the maximum average power of 236 W multi-mode laser output was obtained by using optimum output coupling mirror. The optical-to-optical conversion efficiency was as high as 52.5% and corresponding slope efficiency was 62%. No obvious evidence of saturation was observed from the output curve, which means higher output power is possible if higher pump power is available. It also indicated that the laser cavity is stable enough.

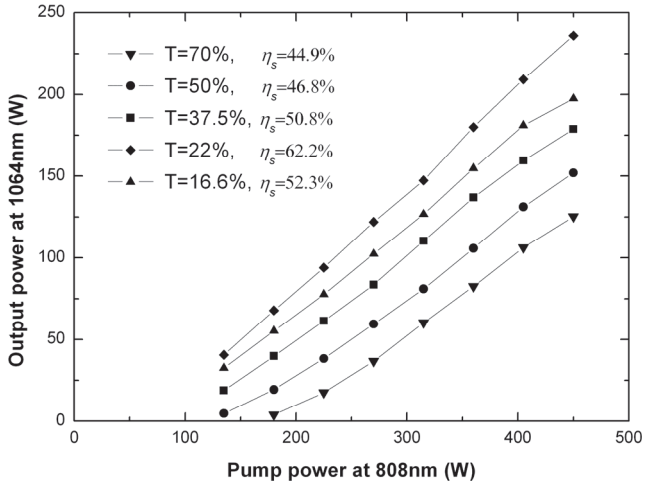

Fig. 7. Output power versus pump power for Nd:YAG ceramics laser with different coupling mirrors.

Referring to the former experimental record of a Nd:YAG single crystal with the same concentration and size using in this system with an output coupling mirror of T=70%, we made a comparison between ceramics and crystal, which was shown in Figure. 8. The optical to optical efficiencies were 29% and 27% for the ceramics laser and for the single crystal laser, respectively. The corresponding slope efficiency was 46% for ceramics laser, and 44% for single crystal laser. It showed that these two kinds of laser materials share extraordinary the same laser output properties in quasi-CW operating.

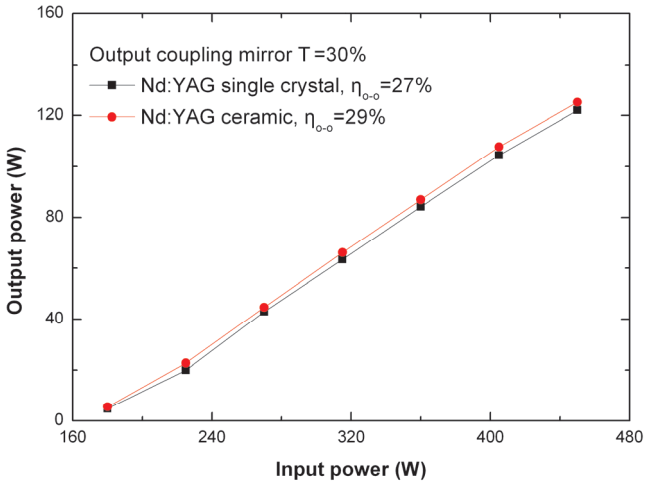

Fig. 8. Comparing output power of Nd:YAG ceramics and Nd:YAG single crystal at the same condition.

Figure. 9 showed the two and three-dimensional beam profiles of the Nd:YAG ceramics laser from CCD. Some interference stripes could be seen because the cavity length was fixed and the pass length differences between the transmitted beams were multiple numbers of the laser wavelength. It can be eliminated just by adjusting the cavity length slightly. The divergence angle of laser beam was measured about 12 mrad. For high power rod Nd:YAG lasers, thermal lensing and thermal stress-induced birefringence play very important roles. They would result a distortion of the laser beam and cause a significant decrease in beam quality and optical efficiencies. The detailed study will be explored later.

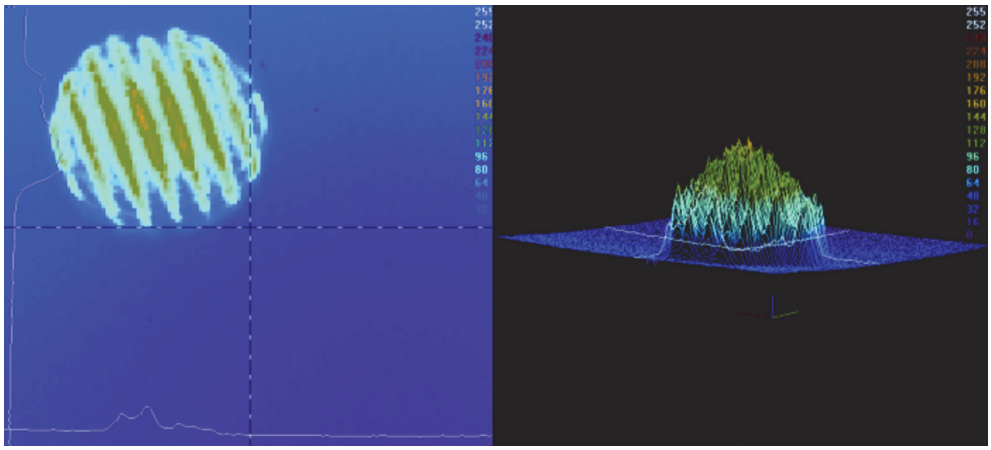

Fig. 9. Two and three-dimensional beam profiles o of a 236W Nd:YAG ceramics laser from CCD.

In conclusion, a high efficiency high power quasi-CW Nd:YAG ceramics rod laser operating at 1064 nm was demonstrated by using compact quasi-CW LD stacked arrays side-pumping system. High average output power of 236 W was achieved under 450 W pumping, corresponding to an optical-to-optical efficiency of 52.5% and slope-efficiency of 62%.

4.2 Q-switched Nd:YAG ceramics laser

Based on previous work, we improved the system and thus demonstrated a high energy electro-optical Q-switched Nd:YAG ceramics laser. With 420 W quasi-CW LDA pumping at 808 nm and Q-switched repetition rate at 100 Hz, 50 mJ pulsed laser at 1064 nm was obtained with pulse width of 10 ns, an average output power of 5 W and peak power of 5 MW. Its corresponding slope-efficiency was 29.8%.

The experimental setup of LDA side-pumped electro-optical Q-switched Nd:YAG laser was shown schematically in figure. 10. The radiation light emitted from the ceramics rod was first linearly polarized by a polarizer and then introduced a phase difference of a quarter of a wavelength through the quarter-wave plate. A KD*P nonlinear crystal was employed as a Pockels cell Q-switch with longitudinal field. The total length of the cavity was about 260 mm.

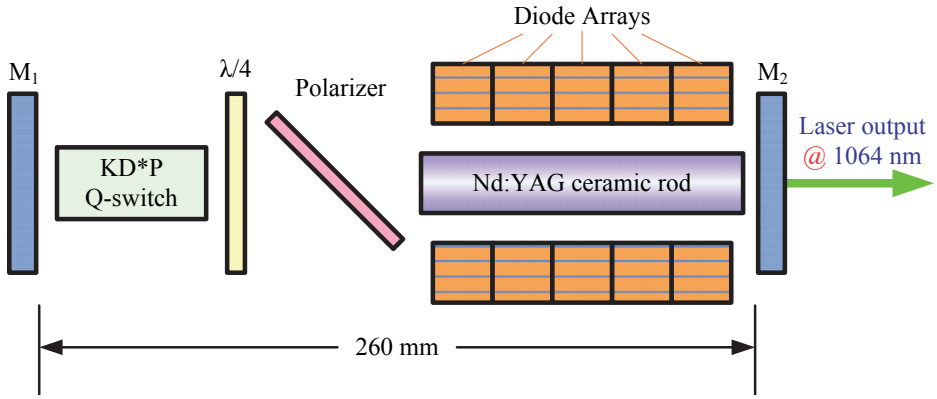

Fig. 10. Schematic diagram of experimental setup for side-pumped E-O switched Nd:YAG ceramics rod laser.

We employed two Nd:YAG samples with the same concentration and size in our experiment. One was ceramics, and the other was single crystal. Figure. 11. showed the comparative laser output power of the two samples with different conditions. At first, the two Nd:YAG lasers were easy to operate at quasi-CW mode without the polarizer, quarter-wave plate and KD*P Q-switch. Their average output power and pulse energy increased almost linearly with the increasing of the pumping energy. The corresponding slope efficiency was 46% for ceramics laser, and 44% for single crystal laser. And the optical to optical efficiencies were 29% and 27% for the ceramics laser and for the single crystal laser, respectively. When those modulating devices were inserted into the laser cavity, the actively

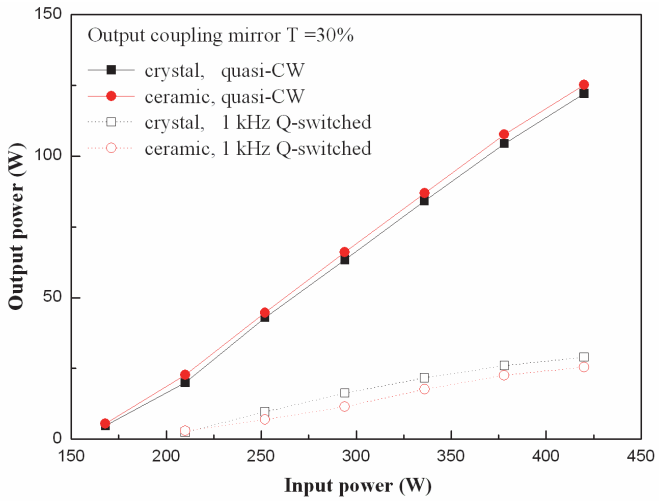

Fig. 11. Comparing output power of Nd:YAG ceramics and single crystal at the same condition.

Q-switched operation has been observed. Both of the single crystal and ceramics Nd:YAG lasers are affected by the thermal depolarization losses, so caused a little roll over of the E-O Q-switched output power curves and a significant decrease of the optical efficiencies when compared with quasi-CW operations.

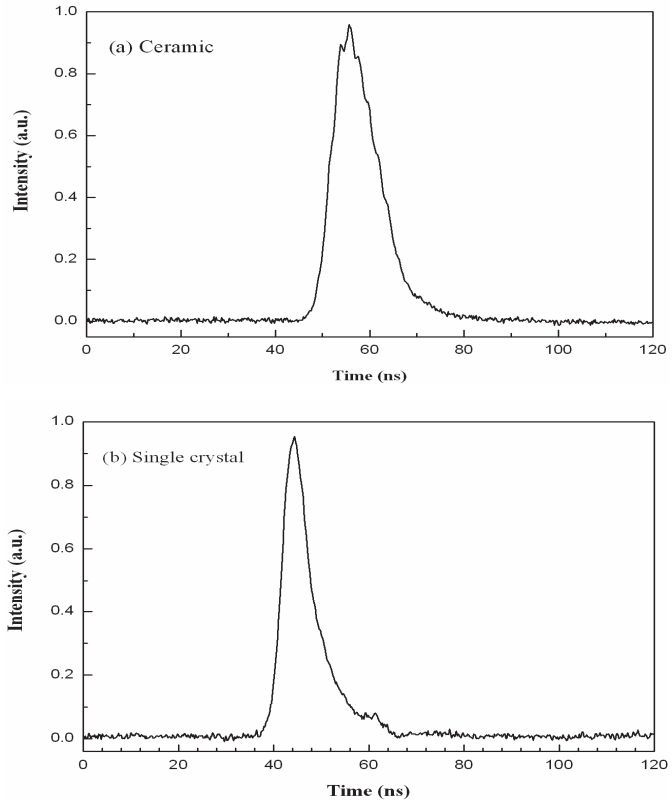

Fig. 12. Single pulse waveform of Electro-Optical Q-switched Nd:YAG lasers under modulating repetition rate of 1 kHz. (a) ceramics; (b) single crystal.

Under the max average pumping power of 420 W and 1 kHz modulating rate, the slope efficiency of ceramics sample was 15.2 % and its pulse width is 12 ns and those of single crystal sample were 17.5 % and 9.6 ns. Figure. 12. showed the single pulse shape from electro-optical Q-switched Nd:YAG crystal and ceramics lasers. The above data showed that these two kinds of laser material shared very similar laser output characteristics. The ceramics has a little better performance in quasi-CW operating while the single crystal was better in pulse operation. We speculated that the polycrystalline structure inside the ceramics body, which changes the path length of photons in the rod and adds the scattering losses of the cavity, extended the waveform distortion of the Q-switched laser pulse, and resulted in lower efficiency and broaden pulse width. As well as Nd:YAG single crystal, Nd:YAG ceramics are affected by the thermal effects when high energy pulse operation. The

detail research on the thermal-optical effects of Nd:YAG ceramics laser is to be explored in another paper.

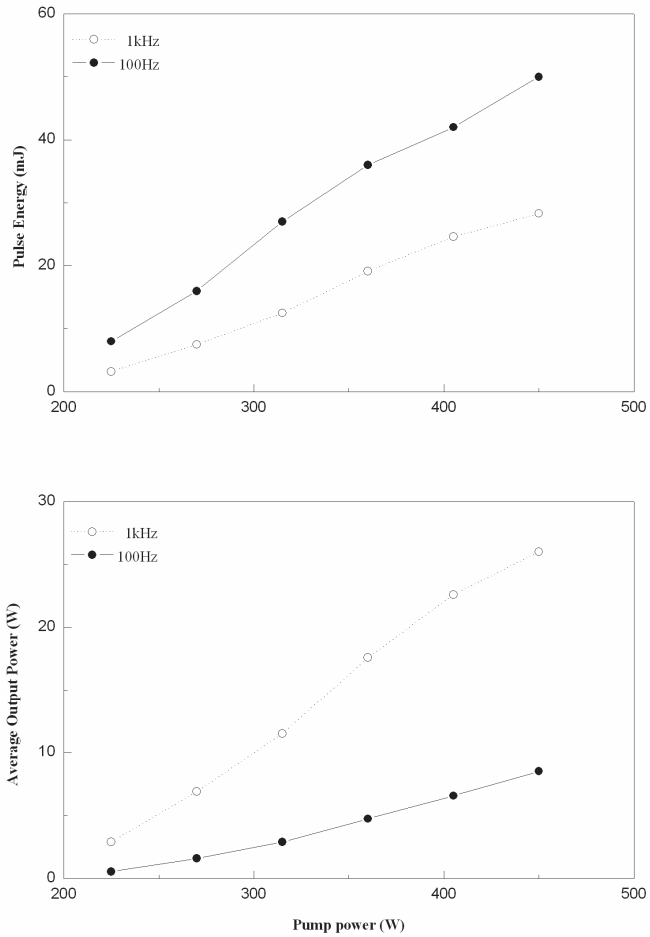

Fig. 13. Paverage power, pulse energy vs. Ppump and repetition rate of Nd:YAG ceramics laser.

Next we changing the pumping condition and modulating rate to 100 Hz operation, and compared the pulse performances of Nd:YAG ceramics laser under different repetition rates. The average output power and pulse energy as functions of the pumping energy with different repetition rates have been measured and plotted in Figure. 13. With 420 W max average pumping power, an average output power of 28.3 W was achieved under the repetition rate of 1 kHz. The pulse energy was 28.3 mJ and its peak power was 2.36 MW with pulse width of 12 ns. Its slope-efficiency was 15.2%. While under the modulating repetition rate of 100 Hz, the average output power of 5 W with pulse width of 10 ns was observed. The pulse energy was 50 mJ and its peak power was 5 MW. And the

corresponding slope-efficiency was 29.8%. Electro-optical Q-switched ceramics laser with higher modulating repetition rates generated higher average output power but broader pulse width and lower pulse energy and peak power. No saturation phenomenon was observed and higher output energy could be in expectation. Because the thermal build up of higher repetition rate pulse laser is more serious than that of lower repetition rate pulse laser, so the thermal depolarization losses of 1k Hz pulse laser were higher than those of 100 Hz pulse laser, which resulted lower efficiency than the latter.

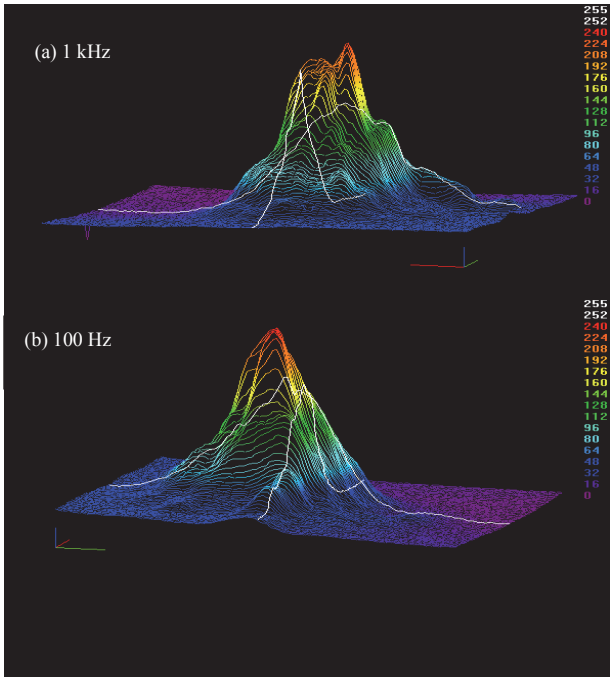

Fig. 14. Beam profile of Nd:YAG ceramics laser under different modulating rates from CCD.

Figure. 14. showed the three-dimensional beam profiles of the pulse Nd:YAG ceramics laser with different modulating rates and under the max pumping power of 420 W from CCD. They were approximate Gaussian beam intensity distribution, but a little distortion indicated some thermal stress-induced birefringence was existed.

In conclusion, a high energy electro-optical Q-switched Nd:YAG ceramics laser has been demonstrated by employing a quite uniformly compact side-pumping system. The laser parameters between ceramics and single crystal Nd:YAG lasers have been compared and the pulse characteristics of ceramics laser with different repetition rates have been discussed in detail. With 100 Hz modulating rate, output energy of 50 mJ has been attained with pulse width of 10 ns and average output power of 5 W. And its corresponding peak power was 5 MW. While with 1 kHz modulating rate, output energy of 28.3 mJ has been achieved with pulse width of 12 ns and an average output power of 28.3 W. Table.1. Summarized the measured laser parameters with the effective pumping energy of 420 mJ at 1064 nm. It approved in experimental that Nd:YAG ceramics has comparable good performance with

Nd:YAG single crystal in mJ-level energy laser output. By optimizing the design of the laser cavity, adopting higher pumping power and choosing proper repetition rate, the Nd:YAG ceramics Electro-optical Q-switched laser will obtain better performance with higher pulse energy and narrower line width as well as better beam quality.

1at.% Ceramics	Average output Power	Pulse energy	Pulse width	Peak power	Slope efficiency
Quasi-CW	236 W	236 mJ	160μs	1.6 kW	62 %
Pulse （1 kHz）	28.3 W	28.3 mJ	12 ns	2.36 MW	15.2 %
Pulse （100 Hz）	5 W	50 mJ	10 ns	5 MW	29.8 %

Table 1. Experimental laser parameters of Nd:YAG lasers at 1064 nm with effective pumping energy of 390W.

5. Q-switched pulsed ceramics laser

5.1 CW and Q-Switched performance of a Yb:YAG/YAG composite thin disk ceramics laser

Since the emergence of semiconductor laser diodes (LD) that emit at 900 ~ 1100 nm, high power LD array are used as stabilized pumping source. The Yb doped laser material with the pumping wavelength requirement at this wavelength range attracts a lot of attention. [17] Figure. 15. shows the energy level of Yb^{3+} ion in the crystal Yb:YAG.[18] Yb^{3+} ion has very simple energy diagram with $^2F_{7/2}$ as lower level and $^2F_{5/2}$ as excited state manifolds separated by about 10,000 cm^{-1} . The laser wavelength of ~ 1030 nm with transition of $^2F_{5/2}$ - $^2F_{7/2}$ has a terminal level of 612 cm^{-1} above the ground states. While the thermal energy at room temperature is 200 cm^{-1}, the terminal state is thermally populated making the Yb:YAG a quasi-three level system. At room temperature, the thermal population of the lower laser level is about 5.5%.

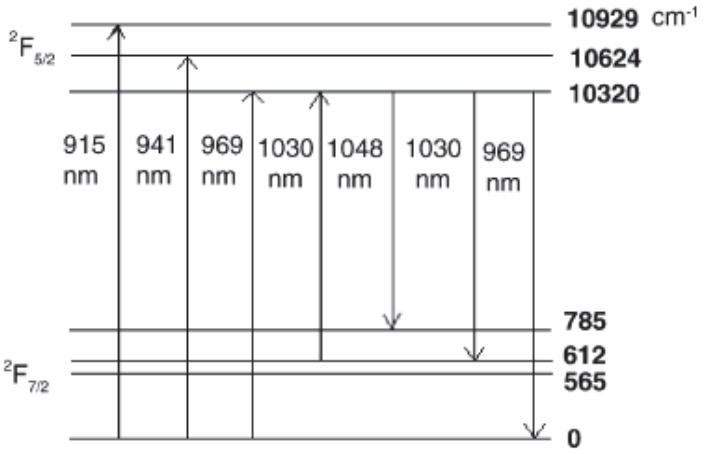

Fig. 15. Energy level of Yb [2]

Table 2 summarized physical, chemical and laser properties of Yb:YAG single crystal. [19-21] Comparing to the Nd:YAG laser material, Yb doped laser material have the merits of (1) wide pumping range, (2) high quantum efficiency of over 90%, (3) longer upper-state lifetime of ~1ms, (4) no excited state absorption, (5) no up-conversion, and (6) minimal concentration quenching. With the fast development of the Nd:YAG transparent ceramics, the Yb doped laser ceramics also shows its potential as one of the ideal candidates for high-power laser application.

Crystal Structure	Cubic
Lattice Parameters (nm)	1.201
Melting Point (K)	2243
Moh Hardness	8.5
Density (g/cm^3)	4.56±0.04
Specific Heat (0-20) (J/g.cm^3)	0.59
Modulus of Elasticity (GPa)	310
Young's Modulus (Kg/mm^2)	3.17*104
Poisson Ratio (est.)	0.3
Tensile Strength (GPa)	0.13 ~ 0.26
Thermal Expansion Coefficient(/K) (0~250℃)	
[100]Direction	8.2*10^{-6}
[110]Direction	7.7*10^{-6}
[111]Direction	7.8*10^{-6}
Thermal Conductivity (W/m/K)	14 @ 20℃, 10.5 @ 100℃
Thermal Optical Coefficient (dn/dT, /K)	7.3*10^{-6}
Thermal Shock Resistance(W/m)	790
Laser Transition	$^2F_{5/2} \rightarrow {}^2F_{7/2}$
Laser Wavelength	1030nm，1048nm
Photon Energy (J)	1.93*10^{-19} @ 1030nm
Emission Linewidth (nm)	9
Emission Cross Section (cm^2)	2.0*10^{-20}
Fluorescence Lifetime (ms)	1.2
Diode Pump Band (nm)	940 or 970
Pump Absorption Band Width (nm)	8
Index of Refraction	1.82
Thermal Optical Coefficient (/K)	9*10^{-6}
Loss Coefficient (cm^{-1})	0.003

Table 2. Physical and chemical property of Yb:YAG

Comparing to rod shape medium in which heat is along the radius of the rod, so there is strong thermal gradient induced lensing and birefringence, in the thin disk shaped gain medium heat is extracted through the large faces with thermal gradients which is established across the smallest dimension and aligned with the beam propagation direction. [22] But thermo-mechanical distortion is still the bottleneck of high-power thin disk laser. Researchers brought up the idea of using composite media. During the pumping process, the undoped part of the medium helps to defuse the heat generated by the doped part,

because the thermal conductivity of undoped part is usually higher than that of doped part. In the case of Yb:YAG/YAG medium, the undoped YAG acts as a passive heat sink and rebuilds the temperature field, especially along the thickness direction, and it seems that there is an imaginary cooling effect on the front face of the gain medium. [23] So by using a composite gain medium, which consists of both Yb:YAG and undoped YAG, the bending of the medium can be eliminated to some degree. Additionally, the composite medium eliminates the radiation trapping to a larger degree because the undoped YAG mitigates the effects of total internal reflection at the undoped-YAG-air interface. [24]

Figure. 16. shows the pictures of the composite Yb:YAG/YAG thin disk ceramics made by BAIKOWSKI, Japan. The thin disk is ~10 mm in diameter with very thin absorbing part of the disk (~0.6 mm) bonded together with a thicker undoped piece of YAG ceramics (~2.5 mm). The doping concentration is 9.8 at.% in the doped part. The composite ceramics disk is AR coated for the wavelength of ~930-970 nm and laser radiation 1030 nm at the front side and HR coated for both wavelengths at the back side. Figure.17. shows the double-pass absorptivity of the disk ceramics. There are mainly three absorption peaks in the range of 900 nm ~ 1100 nm: 937nm，968nm and 1027nm, with absorption efficiency of ~ 75%, 58% and 38.7%, absorption bandwidth of ~ 37nm, 10nm and 14nm respectively.

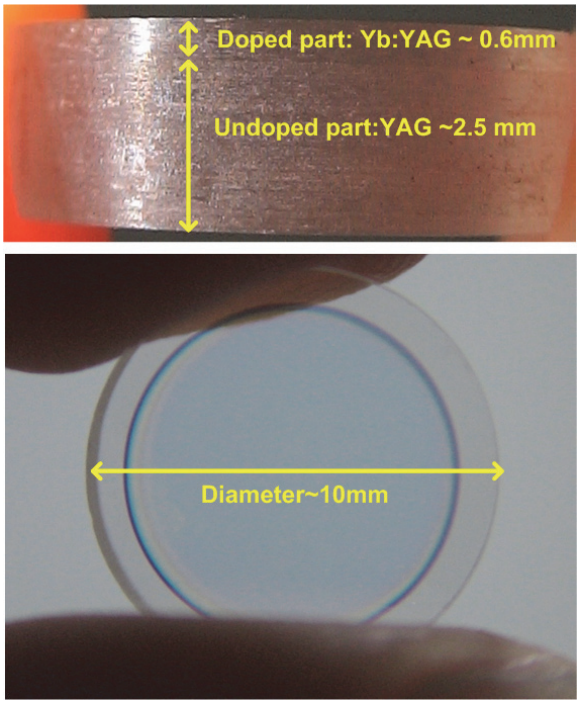

Fig. 16. Pictures of Yb:YAG/YAG composite transparent ceramics disk

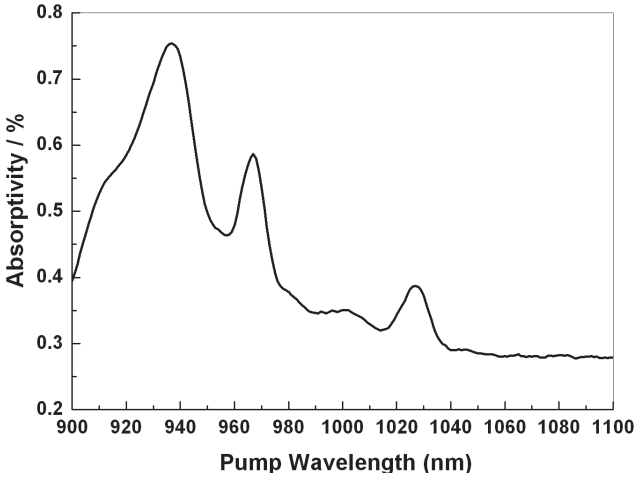

Fig. 17. Double-pass absorptivity of the composite ceramics

In order to lengthen the effective absorbing length in the thin-disk medium and make a good overlap between pump and resonator mode, a face-pumped CAMIL structure is chosen. With this structure, diode pump radiation is injected into the back face of the disk and then reflected by the face several times. The schematic diagram of the experimental setup is shown in 18. The laser medium is a composite Yb:YAG/YAG thin disk ceramics as described above. It is fixed with a layer of indium onto a heat sink, which is cooled with water from the back side. A collimated LD array with central wavelength at 970 nm working at 15 ^{o}C is used as pump source. By a focal length of ~ 9.4 cm lens, the pumping light is focused on the back side of the ceramics and the unabsorbed pumped radiation is reflected for another turn of absorption, i.e., the effective absorbing length is twice the length of the doped ceramics. A dichroic beam splitter (45^{o}) which is coated with AR film at 970nm and HR film at 1030nm is inserted between the focusing lens and the composite ceramics for redirecting the laser to the output couplers.

In the CW mode, output couplers with the same radius of curvature of 100 mm, and transmissions of 1%, 2%, 5% and 10% are used respectively. The whole cavity length is ~80 mm. In the Q-switched mode, output coupler with transmission of 10% is used. The output laser power is measured by a power meter (OPHIR, NOVA II) and the spectrum is recorded by a spectroscopy (YOKOGAWA, AQ6370), while the pulse width is recorded by an oscillograph (Lecroy, WR62XR).

In the CW mode, the laser output power increases as the pump power increases with different output couplers, as shown in figure. 19. Up to 1.05W CW power is achieved with optical to optical efficiency of 5.25% with 2% output coupler. Central laser wavelength is at 1031 nm, as shown in Fig.20. We also get Q-switched output of the laser using an acousto-optic (A-O) Q-switch. We insert the A-O Q-switch device (Gooch & Housego, M080-2G) into the cavity with 10% transmission output coupler. Stable operation is achieved with the repetition rate of 1 kHz, 5 kHz, 10 kHz, 20 kHz and 30 kHz, along with the average output power of 0.44 W, 0.446 W, 0.452 W, 0.461 W and 0.47 W respectively. Figure. 21. shows the width of the pulse enlarges with the increasing repetition rate. Figure 22 shows the pulse waveform at 1 kHz: a minimal pulse width of 166 ns and corresponding peak power of 2.6

kW. Figure. 22. inset also shows the pulse serial, which appears to be a bit unstable but acceptable.

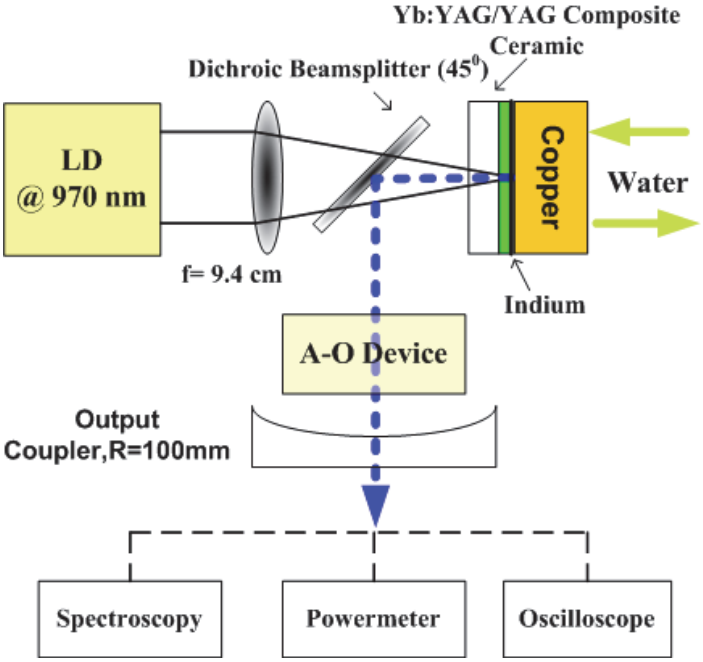

Fig. 18. Schematic diagram of the experimental setup

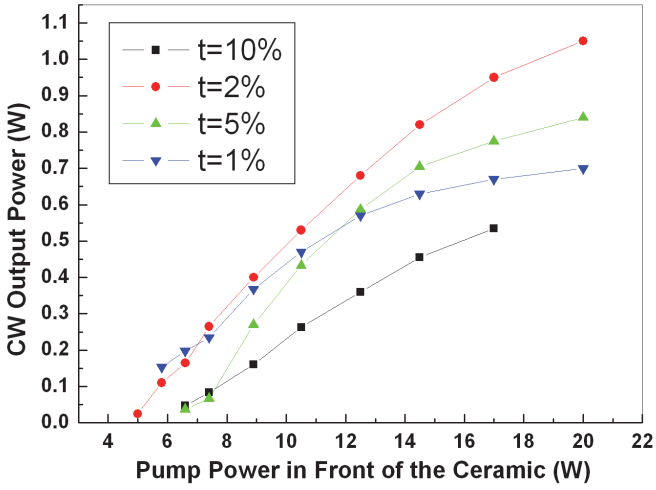

Fig. 19. CW laser output power vs. Pump power with different output transmission

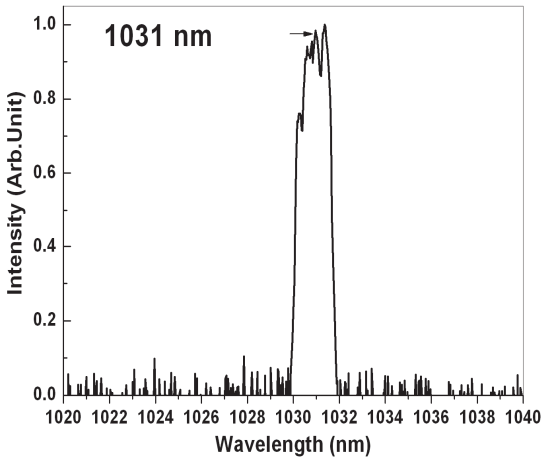

Fig. 20. Laser output spectrum

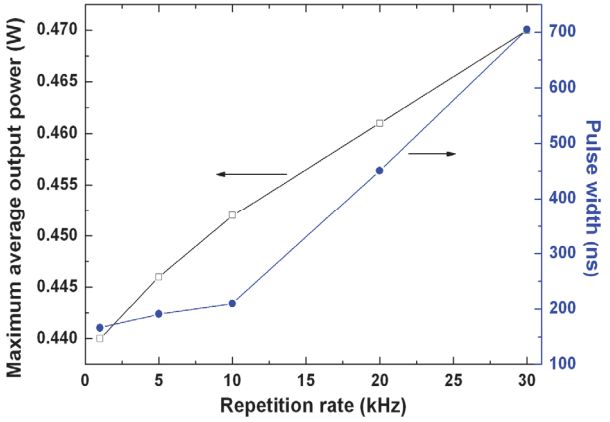

Fig. 21. Average output power and Pulse width vs. Repetition rate

Both for CW and AO Q-switched mode, the optical to optical efficiency is low according to the data figure 19 and figure 21. But when we considered the actual absorbed pump power, the case would be different. There is only 53.5% of the pump power can be absorbed at the pump wavelength 970 nm, as shown in Fig.17. Moreover, further measurement reveals that the pumping wavelength drifted dramatically along with the increasing pump power. Figure 23 shows the measured relationship of pump wavelength and pump power while maintaining the temperature of the cooling water at 15°C. The pumping central wavelength drifts from 970 nm to 979 nm with the decreased pumping absorptivity from 53.5% to 38%, respectively. Figure. 19. also suggests that in higher pump power region, the laser power tended to be "saturated", which is possibly caused by the decreasing absorption efficiency of the medium. Form this experiment, we found that it's difficult to control the pump

wavelength only by cooling in this pump source. Figure 17 indicates that the lengthened absorbing length inside the laser medium brought about 28% background absorption of the pump power, which might be caused by the quality of the media. It would raise the laser threshold. Figure 17 also shows that there is another absorption peak at around 1031 nm where is exactly the output laser wavelength located, indicating the reabsorption effect at 1031 nm. Thus, the increasing pumping power would lead to a stronger reabsorption results in a quick saturation at this wavelength. Moreover, the unabsorbed pump energy would contribute to the difficulty of the population inversion, thermal lensing, which would further reduce the efficiency and the laser output power.

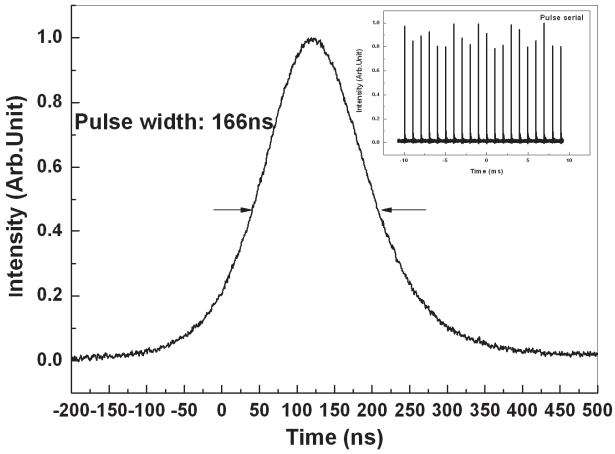

Fig. 22. Pulse profile of minimum pulse width at 1 kHz. Inset shows the pulse serial.

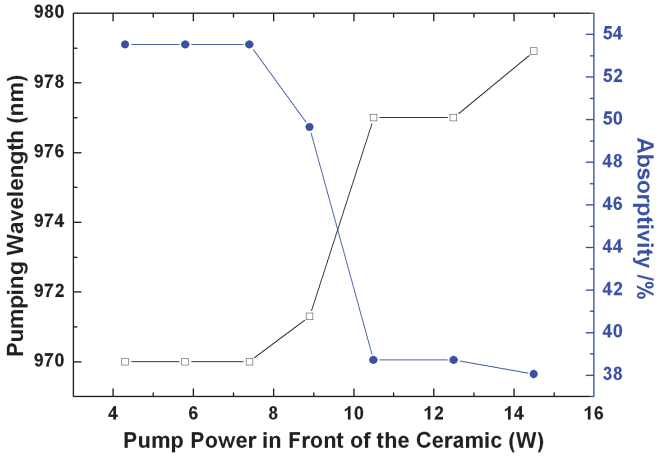

Fig. 23. Pump wavelength drifted with pump power and their corresponding absorptivity

5.2 Experimental setup for 933 nm pumping experiment

We also study the CW and AO Q-switched laser performance of this Yb:YAG/YAG composite ceramics disk under the pumping wavelength of ~933 nm in order to further explore the high-power potential of this material by increasing the media absorption of pumping power.

Figure 24 shows the schematic diagram of the experimental setup using 933 nm pump source. The experimental setup is similar to that of ~970 nm pump source. The pump source is a fiber coupled LD array with central wavelength at 933 nm working at 20℃.

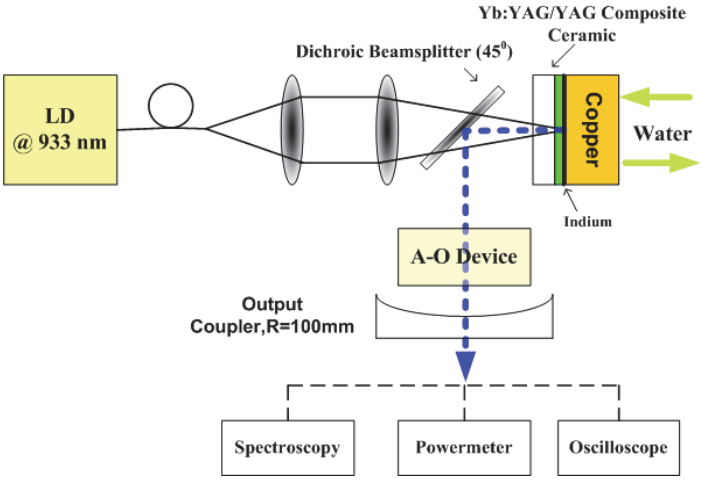

Fig. 24. Schematic diagram of the experimental setup

In the CW mode, output couplers with the same radius of curvature of 100 mm, and transmissions of 1%, 2%, 5% and 10% are used respectively. The whole cavity length is ~80 mm. In the Q-switched mode, output coupler with transmission of 10% is used. The output laser power is measured by a power meter (OPHIR, NOVA II) and the spectrum is recorded by a spectroscopy (YOKOGAWA, AQ6370), while the pulse width is recorded by an oscillograph (Lecroy, WR62XR).

In the CW mode, the laser output power increases as the pump power increase with different output couplers, as shown in Figure. 25. When the transmission of the output coupler is 2%, up to 2.575 W CW power is achieved with optical-optical efficiency of 17.6% and slope efficiency of 31.2%. Central laser wavelength is at 1030.2 nm, as shown in Fig.26. Because of the limited output power of the pump source, the maximum output laser power is not high enough. But from figure 25, the output laser shows no saturated intention, which means higher laser output can be achieved in the future.

We also get Q-switched output of the laser using an acousto-optic (A-O) Q-switch. We insert the A-O Q-switch device (Gooch & Housego, M080-2G) into the cavity with 10% transmission output coupler. Stable operation is achieved with the repetition rate of 1.1 kHz, 5 kHz, 10 kHz, 20 kHz, 30 kHz, and 40 kHz along with the average output power of 1.29 W, 2.119 W, 2.221 W, 2.237 W, 2.246 W and 2.249W respectively. Figure 27 shows the width of the pulse enlarges and the maximum peak power of the pulse decreases with the increasing

repetition rate. Fig. . shows the pulse waveform at 1.1 kHz: a minimal pulse width of 29 ns and corresponding peak power of 40.4 kW, single pulse energy of 1.17mJ.

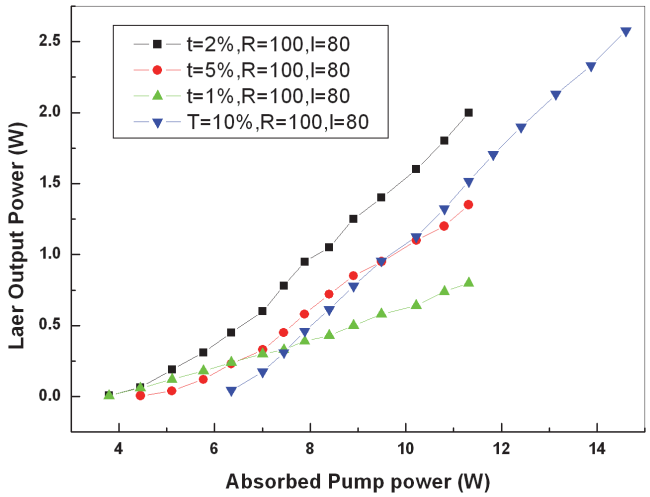

Fig. 25. CW laser output power vs. Pump power with different output transmission

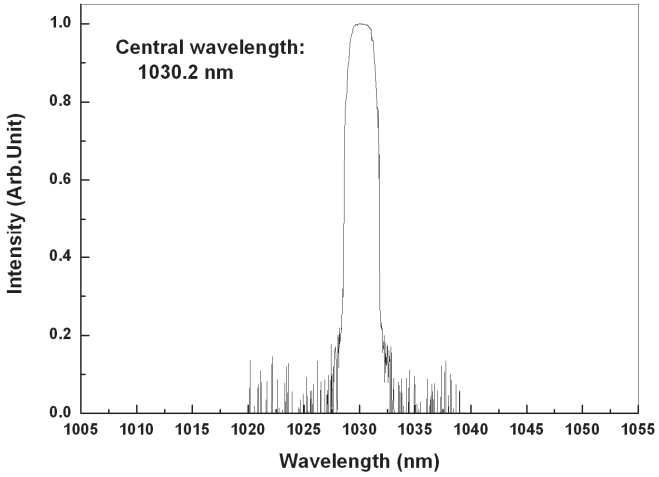

Fig. 26. Laser spectrum

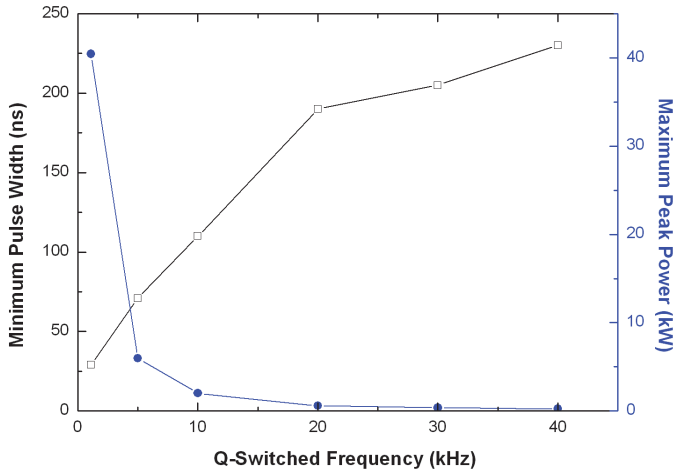

Fig. 27. Maximum peak power and Pulse width vs. Repetition rate

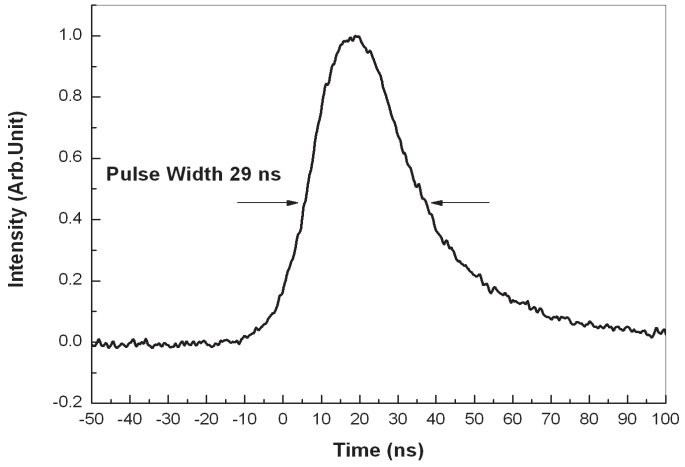

Fig. 28. Pulse profile of minimum pulse width at 1.1 kHz.

We demonstrated a CW and Q-switched laser with composite Yb:YAG/YAG ceramics pumped by 970 nm and 933 nm LD. For the 970 nm pumping experiment, a maximum laser power of 1.05W with central wavelength at 1031 nm is obtained. A minimal pulse-width of 166ns and the maximal peak power of 2.6KW at 1 kHz are achieved, corresponding to an average output power of 0.44W. The repetition ranged from 1 kHz to 30 kHz. For the 933 nm pumping experiment, a maximum laser power of 2.575 W with central wavelength at 1030.2 nm is obtained. A minimal pulse-width of 29ns and the maximal peak power of 40.4 KW at 1.1 kHz are achieved. The repetition ranged from 1.1 kHz to 40 kHz. Table 3 summarizes the detailed results.

Pump source	**970 nm**	**933 nm**
Ceramics absorptivity of pump power	53.5%@970 nm	73%@933 nm
Diameter of footprint of focusing pump laser	500 μm	600 μm
Central wavelength of laser output	1031 nm	1030.2 nm
FWHM of output laser	2 nm	5 nm
CW maximum output power	1.05 W	2.575 W
CW optical-optical efficiency	5.25%	17.6%
CW slope efficiency	7%	31.2%
Q-switched repetition rate	1 kHz－30 kHz	1.1 kHz－40 kHz
Maximum average power under Q-switched mode	0.47 W	2.249 W
Shortest pulse-width	166 ns	29 ns
Maximum peak power	2.6 kW	40.4 kW

Table 3. Experimental results of 970nm and 933nm pumping experiment

6. Nd:$Y_3Sc_{1.5}Al_{3.5}O_1$ ceramics as the disk laser media, dual – wavelength competition output

The Nd:YAG ceramics has proven its advanced merits [25,26] and can be manufactured commercially. But scientists also exploree forward to develop new kind of ceramics in order to overcome the disadvantage exists in Nd:YAG single crystal. Recently, a new kind of laser material based on Nd:YAG-Nd:YSAG has been prepared, in which Sc^{3+} replaces Al^{3+} in YAG. Because Sc^{3+} has a larger size than Al^{3+}, the entrance of Sc^{3+} leads to lattice expansion. In this way, more Nd^{3+} can be accommodated in the lattice, in other words, higher doping level is expected comparing to Nd:YAG. By far, highly and homogeneous doped Nd:YSAG has been fabricated successfully. Due to the associated increase of the absorption coefficient, it's possible for us to use thinner laser media, which promises a higher cooling efficiency because of the higher surface area per unit volume. Thus we can reduce optical distortion and thermal stress, which are important for improving the laser beam quality. Moreover, the enhanced emission intensity, prolonged fluorescence lifetime [27, 28] and lower threshold comparing to the quasi-four-level Yb^{3+} doped material together highlight this novel material. It's a suitable media for short-pulse microchip laser. 10ps ultra short-pulse laser has been generated from a passive mode-locked Nd:YSAG ceramics laser [29]. Therefore, transparent ceramics Nd:YSAG will find its way to the application of thin-disk laser and high-power miniature laser.

But Nd:YSAG ceramics is an interesting material besides its merits discussed above. In our experiment, we demonstrated a dual-wavelength competitive laser output in Nd:$Y_3Sc_{1.5}Al_{3.5}O_{12}$ ceramics disk. In former published papers, many scientists have reported dual-wavelength in many laser materials, such as J. Lu et al. [30]. Yoichi Sato et al. also reported the appearance of dual-wavelength in Nd:YSAG [29]. We further compare the laser spectra in Nd:YAG and Nd:YSAG and then figures out possible reasons for this interesting

phenomenon from the view of the material structure. The competitiveve behavior of these two wavelengths prognosticates a possible simpler way to generate Terahertz radiation.

Splitting laser level of Nd3+ in YSAG and Fluorescence spectra of Nd:YSAG ceramics

Since introducing Sc3+ into the Nd:YAG, which means that the surrounding of the optical center Nd3+ is modified, the energy level structure would be altered. By using a model Hamiltonian that assumes D2 site symmetry for the Nd3+ ions in the garnet lattice, John B. Gruber et al. figured out the energy level of Nd:YSAG [31]. The splitting laser levels of Nd3+ in YSAG-$^4F_{3/2}$ and $^4I_{11/2}$ -are shown in Figure. 29.

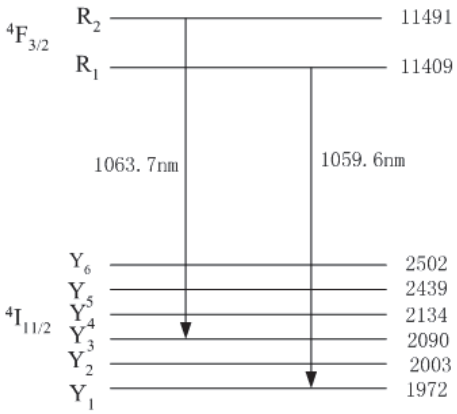

Fig. 29. The splitting laser level of Nd^{3+} in YSAG, $^4F_{3/2}$ and $^4I_{11/2}$

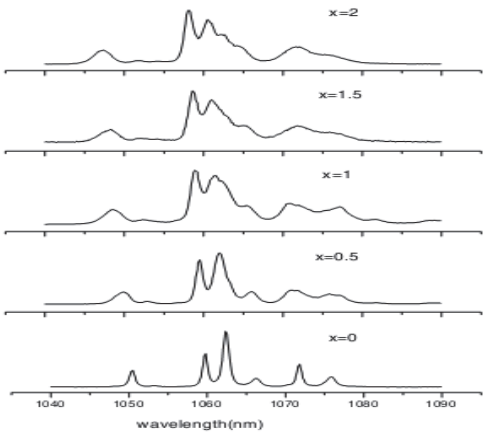

Fig. 30. Fluorescence spectra is influenced by x in Nd:$Y_3Sc_xAl_{5-x}O_{12}$

The Nd:YSAG ceramics disks used in our experiment are made by Shanghai Institute of Ceramics, Chinese Academy of Science. By changing the x in Nd:Y3ScxAl5-xO12, we obtain the fluorescence spectra, as shown in figure 30. The two strongest peaks locate from

1060.5nm to 1062.5nm depending on the concentration of Sc, corresponding to the transition of R1-Y1 and R2-Y3 in in figure 29.Along with the increasing amount of Sc3+, the bandwidth of fluorescence broadens. Moreover, the branching ratio and position of emission peaks also change. We attributed this inhomogeneous line broadening to the expansion of lattice and complex surroundings of Nd3+ ions in the disordered YSAG lattice.

The schematic diagram of experiment setup is shown in Figure. 31. The size of Nd:$Y_3Sc_{1.5}Al_{3.5}O_{12}$ ceramics disk is Ø12mm*1mm with Nd^{3+} 4 at. % doped and both the surfaces of the sample are coated with antireflection-film at 1064nm. The laser experiments are carried out at room temperature without active cooling system. A fiber-coupled LD working at the central wavelength of 808nm is used as pump source. The fiber core diameter is 200 μm with the numerical aperture of 0.22. By 2 lenses coupling system, the pump beam is focused on the ceramics' surface to produce a pump light footprint of about 60μm in diameter. We apply a plan-plan cavity with an overall length of ~7 mm. The front mirror is antireflection coated at 808nm and highly reflecting at 1064nm. The rear mirror is the plane-parallel one as output coupler. A dichroic beam splitter (45^0) is used to reflect the laser and filter out the pump light. The laser output characteristics are analyzed for their spectral content and power with an optical spectrum analyzer (YOKOGAWA AQ6370) and a power meter (Spectra-Physics 407A), respectively.

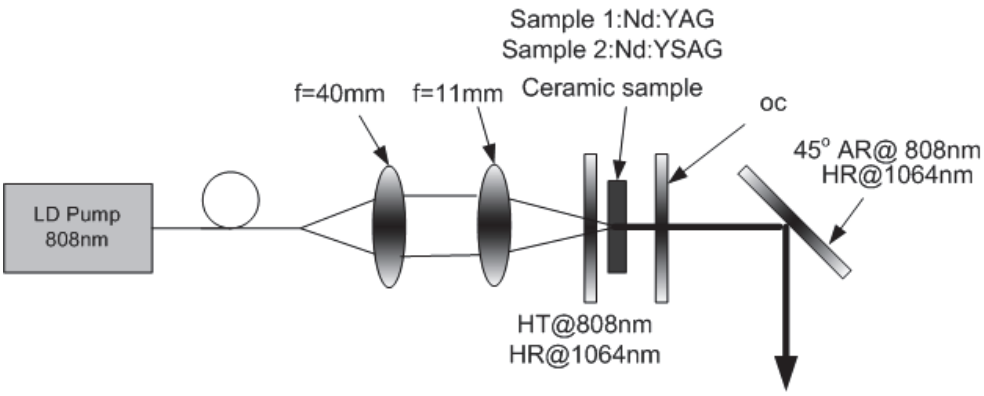

Fig. 31. Schematic diagram of the experimental setup

In the experiment, the ceramics absorbs about 64% of the pump power set on its surface. The output couplers with different transmission 3%, 3.9%, 6% and 10% at 1064nm are used for laser output experiments respectively. The results are shown in Figure. 32. The laser threshold increases from 0.345W to 1.03W with the increasing of transmission of the output coupler. The maximum output power of 0.356W is achieved at absorbed pumping power of 1.96W with the output coupler of T_{oc}=10%. Correspondingly, the optical-optical efficiency is 18.2% and the slope efficiency is 23.2%. The emission spectra of the laser output is shown in Figure. 33., in which the absorbed pump power is 1.52 W with the output coupler transmission of 10 %. We observes two wavelengths oscillate simultaneously.

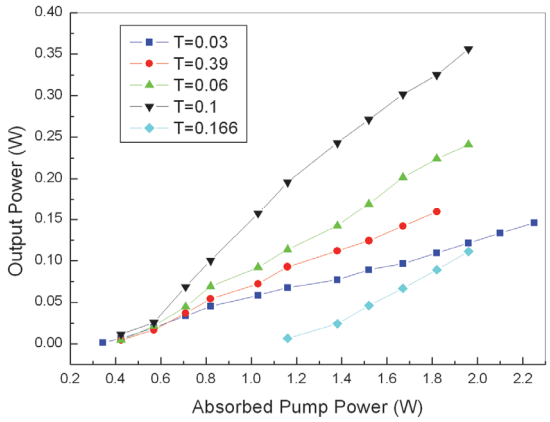

Fig. 32. Output power of the laser emission vs. absorbed pump power for different output couplers

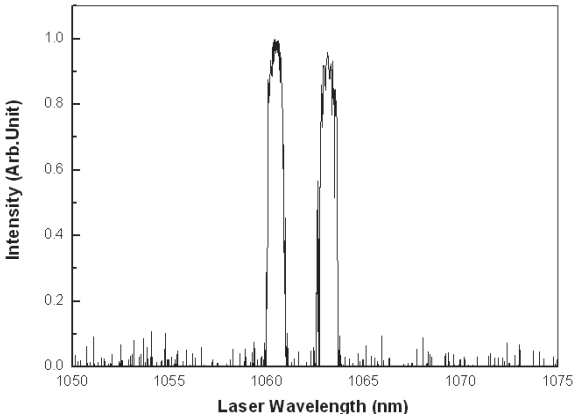

Fig. 33. Emission spectra of the laser: two wavelengths oscillates simultaneously

In order to make a comparison and get more conclusive results, we apply the same experimental environment to another 2 at. % doped Nd:YAG ceramics disk. The output transmission is T_{oc}=3%. During the experiment, two-wavelengths' oscillation is also observed in Nd:YAG ceramics disk. But the behavior of the two wavelengths in Nd:YAG is totally different with that in Nd:YSAG when the pump power is increasing. In Figure. 34(a), at the absorbed pump power of 0.347W which is just above the threshold, only 1064nm can oscillate in Nd:YAG. When the pumping intensity enhanced, another wavelength at 1061nm appears. Further increasing the pumping power, the intensity of 1061nm and 1064nm increase synchronously. In Figure. 34 (b), the first laser wavelength operated at 1059.9nm in Nd:YSAG. Increasing the pump power, signal laser at the wavelength of 1063.8nm and 1059.9nm radiate form Nd:YSAG simultaneously. Boosting the pumping power, a competitive laser output is shown, in which the intensity of laser at 1059.9nm decreases and that of laser at 1063.8nm increases.

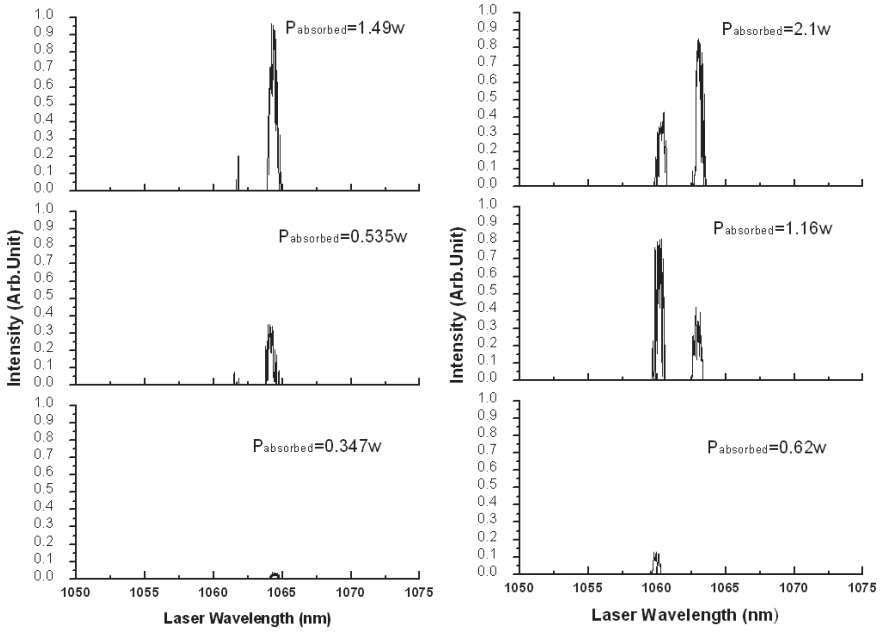

(a) Nd:YAG (b) Nd:YSAG

Fig. 34. Different behavior of (a) Nd:YAG and (b) Nd:YSAG along with increasing pump power.

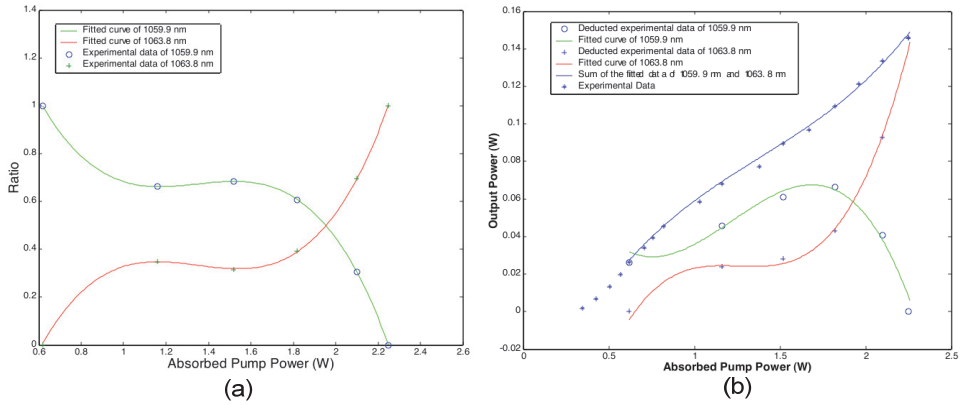

Fig. 35. Experimental and deducted data of the two wavelengths

By assuming that the total laser output only contains the power of 1059.9nm and 1063.8nm, which ignores noise, we can safely calculate the ratio of each wavelength contributed to the laser output power from the recorded 6 groups of spectrum data for different absorbed pump power. The results are shown in Figure. 35.(a), the ring (o) for 1059.9nm and the plus (+) for 1063.8nm. The green solid line is polynomial fitting curve for 1059.9nm，and the red line is for 1063.8nm. Correspondingly, the output power of each wavelength can be deducted from the

recorded experimental data for T_{oc}=3%, as shown in Figure. 35. (b). We also work out the fitted functions of the power of 1059.9nm and 1063.8nm. Laser 1059.9nm experienced a whole climbing-hill process, in which its power ascended when absorbed pump power is under 1.7W and then descended. On the other hand, laser 1063.8nm exhibited an always-climbing process. The blue line, corresponding to the sum up fitted function, is consistent with the experimental data obtained by power meter marked by start (*) in (b).

6.1 Explanation for dual-wavelength output behavior in Nd:YSAG

While considering the different laser behavior of the two ceramics samples, we attribute these to the different structure of the ceramics. By inviting Sc^{3+} to the Nd:YAG to make Nd:YSAG, we actually change the structure of the crystal lattice within the ceramics. When the Sc^{3+} ions (with ion radii larger than Al^{3+} ions but smaller than Y^{3+} and Nd^{3+} ions) enter the lattice, part of the Al^{3+} will be replaced. But the replacement is random. The difference of ion radii, chemical and physical properties between Sc^{3+} and Al^{3+} ions would lead to an almost unpredictable replacing situation. It is highly possible that around the optical center-Nd^{3+}, one site is covered with Al^{3+} and the other site covered with both Al^{3+} and Sc^{3+}, as illustrated in Figure.36 . Besides, at different part within the ceramics, Nd^{3+} are affected by different but similar crystal field, originated from the disorder nature of this new material. Thus the introduction of Sc^{3+} creates different local environments for the Nd^{3+} ions which results in multiple sites having different symmetries. The effect of this substitutional disorder is also illustrated: the more Sc^{3+} enters YAG, the more asymmetric the lattice is, and the more evident the inhomogeneous broadening is presented. Moreover, the transition possibility between different stark levels is also changed. We assume it as multi-sites. The grain boundary within the ceramics material would produce even more complex multi-sites of optical centers, such as Nd^{3+} ions right at the grain boundary or within a single-crystal grain, for instance.

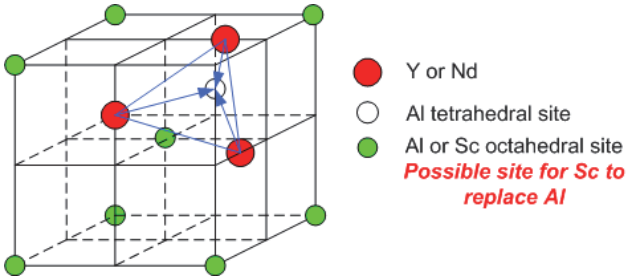

Fig. 36. Positions of Y3+, Al3+ in YAG lattice: when Sc3+ enters the lattice, the replacement of Al3+ in octahedral site is random

In order to give a reasonable explanation of this competitive phenomenon, mutual interactions between ions (instead of isolated ion) are considered and an energy transfer model is applied, as illustrated in Figure.37. When the concentration of active ions is increased, such as in high doped materials, long before the appearance of new lines due to pairs or modifications in radiative transition probabilities, a migration of energy between centers is found. In fact, the energy transfer probability is proportional to the activator concentration [32]:

$$W_t = UN_A,$$

where U is a constant that depends on the type of interaction; N_A is the activator concentration.

Let us consider the simple case of two ions with excited states of different energies, see Figure.37. (a). Then for small energy mismatch (about 100cm^{-1}), energy transfer assisted by one or two phonons can take place [33]. As far as Nd:$Y_3Sc_{1.5}Al_{3.5}O_{12}$ ceramics is concerned, the fluorescent intensity around 1059nm is stronger than that of around 1062.5nm. Without any control of the output laser, laser at 1059.9nm will certainly oscillate first. Meanwhile, when energy transfers from one particular site to another which has slightly different surroundings, the lattice will absorb energy as non-radiative transitions. Thus the "losing of frequency" (lowered energy) leads to the switching to longer wavelength. From the fluorescence spectra, the second highest peak is at around 1062.5nm. Since the energy mismatch between R_1 (upper laser state for 1059.9nm) and R_2 (upper laser state for 1063.8nm) is small (~ 82cm^{-1}), along with the high doping concentration (4 at. % doped), it is possible that energy transfers from centers (lattice A) which radiate mainly at 1059. 9nm, to the other centers (lattice B) mainly radiating at 1063.8nm. In fact, we can assume the 1059.9nm center as sensitizer and the 1063.8nm center as activator see Figure.37. (a). With the increasing of pumping intensity, more and more transfer would take place. As a result, the 1063.8nm reaches its threshold later and forms the second laser. For there is no outside assistance to influence the transfer, it is natural that higher energy from part of active ions is transferred to other different part of ions and emitted photon with lower energy there. The thermal load of the ceramics will enhance such process. That is the reason for the competitiveve output between 1059.9nm and 1063.8nm.

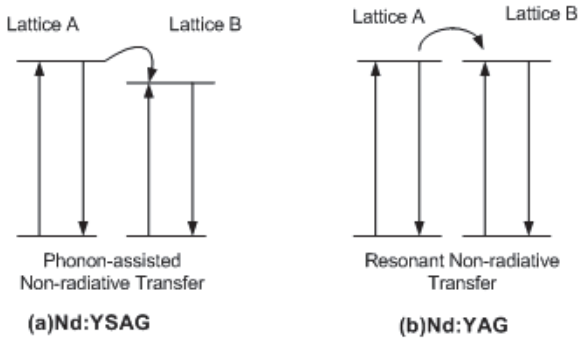

Fig. 37. Different energy transfer styles between Nd:YAG and Nd:YSAG

If now we consider another situation: two ions with their nearly equal energy of the excited state, which is the case of Nd:YAG. Bbecause the Nd^{3+} ions occupy identical sites in the ordered lattice and the doping concentration is much lower (2 at. % doped), the excitation will jump from one ion (lattice A) to the nearby ion (lattice B) and resulted in almost no energy loss, see Figure. 37. (b). Therefore, with the development of pumping intensity, both the two laser output power increased correspondingly. Again, this proves that the dual-wavelength output behavior is the result of Nd:YSAG's own special and complex structure.
Terahertz wave attracts many scientists because of its ability to penetrate common materials without harming human tissue like typical X-rays. Several methods are developed to generate it. A very effective way to achieve that is by Difference Frequency Mixing (DFM) of near-IR lasers, usually using 2 seed sources. One of these outstanding jobs is done by Daniel Greeden et al. [9]. Since they used two seed diodes whose wavelengths are 1064.2nm and 1059nm respectively, there is highly possible that this kind of Nd:YSAG ceramics disk can be used to replace the two seed sources in the future. From Figure. 33., when absorbed

pump power is 1.96W, the output of 1059.9nm and 1063.8nm are the same. From this point, utilizing this kind of ceramics laser as seed source to output two near-IR lasers amplified by double-clad fiber laser and then applying DFM methods to generate Terahertz radiation is our future blueprint of a compact Terahertz source.

In our experiment on Nd:YSAG thin disk ceramics, we get CW laser output and demonstrated the dual-wavelength competitive output phenomenon. By comparing the different laser performance between Nd:YAG and Nd:YSAG and applying an energy transfer model, we discuss and give reasonable explanation for the dual-wavelength competetive output in Nd:YSAG as the disordered replacing of Al^{3+} ions by Sc^{3+} ions. This disordered replacing leads to a different energy transfer system in Nd:YSAG. Through the analysis of the behavior of the two wavelengths, we proposed a possible solution to make compact Terahertz source by using one laser source in the future.

7. References

[1] Q. Liu, M. Gong, F. Lu, W. Gong, and C. Li, "520-W continuous-wave diode corner-pumped composite Yb:YAG slab laser," Opt. Lett. 30, 726-728 (2005).

[2] R.R. Monchamp, "The distribution coefficient of neodymium and lutetium in Czochralski grown Y3Al5O12," J. Cryst. Growth. 11, 310-312 (1971).

[3] "Ceramics YAGs set to challenge single crystals," Opto & Laser Europe, (2001) http://optics.org/articles/ole/6/12/5

[4] E. Carnall, S. E. Hatch, and W. F. Parsons, "Optical Studies on Hot-Pressed. Polycrystalline CaF2 with Clean Grain Boundaries," Mater. Sci. Res. 3, 165-173 (1966).

[5] A. Ikesue, T. Kinoshita, K. Kamata, and K. Yoshida, "Fabrication and Optical Properties of High-Performance Poolycrystalline Nd:YAG Ceramics for Solid-State Lasers," J. Am. Ceram. Soc. 78, 1033-1040 (1995).

[6] T. Yanagiya, H. Yagi, and A. Ichikawa, "Production of yttrium-aluminum-garnet fine powder," Japanese patent (24 September 1996).

[7] T. Yanagiya, H. Yagi, and H. Yamazaki, "Production of fine power of yttrium aluminum garnet," Japanese patent: (24 September 1996).

[8] Baikowski. Ceramic YAG technical datasheet [EB/OL]. http://www.baikowsku.com/components/pdf/ceramic_yag/YAG_DATA_SHEET.pdf, 2003. 9.

[9] J. B. Gruber, D. K. Sardar and R. M.Yow, "Energy-level structure and spectral analysis of Nd3+ (4f3) in polycrystalline ceramic garnet Y3Al5O12," J. Appl. Phys. 96, 3050-3056 (2004).

[10] G. A. Kumar, J. Lu, A. A. Kaminskii, K. Ueda, H. Yagi, T. Yanagitani, and N. V. Unnikrishnan, "Spectroscopic and Stimulated Emission Characteristics of Nd3+ in Transparent YAG Ceramics," IEEE J. Quantum Electron. 40, 747-758 (2004)

[11] J. Lu, M. Prabhu, J. Song, C. Li, J. Xu, K. Ueda, A. A. Kaminshii, H. Yagi, and T. Yanagitani, "Optical properties and highly efficient laser oscillation of Nd:YAG ceramics," Appl. Phys. B 71, 469-473 (2000).

[12] J. Lu, J. Song, M. Prabhu, J. Xu, K. Ueda, and H. Yagi, "High-power Nd:$Y_3Al_5O_{12}$ Ceramic Laser," Jpn. J. Appl. Phys. 39, 1048-1050 (2000).

[13] J. Lu, T. Murai, K.Takaichi, T. Uematsu, K. Misawa, M. Prabhu, and J. Xu, "72 W Nd:$Y_3Al_5O_{12}$ ceramic laser," Appl. Phys. Lett. 78, 3586-3588 (2001).

[14] J. Lu, M. Prabhu, K. Ueda, H. Yagi, T. Yanagitani, A. Kudryashov, and A. A. Kaminshii, "Potential of Ceramic YAG Lasers," Laser. Phys. 11, 1053-1057 (2001).

[15] J. Lu, K. Ueda, H. Yagi, T. Yanagitani, Y. Akiyama, and A. A. Kaminshii, "Neodymium doped yttrium aluminum garnet (Y3Al5O12) nanocrystalline ceramics——a new generation of solid state laser and optical materials," J. Alloy. Compd. 341, 220-225 (2002).
[16] J. Lu1,*, M. Prabhu1, J. Song1, C. Li1, J. Xu1, K. Ueda1, A.A. Kaminskii2, H. Yagi3, T. Yanagitani3, Optical properties and highly efficient laser oscillation of Nd:YAG ceramics, Appl. Phys. B 71, 469–473 (2000) / Digital Object Identifier (DOI) 10.1007/s003400000394
[17] W. Koechner, Solid State Laser Engineering, 40－41(2002)。
[18] Xiaodan Wang , Xiaodong Xu, Xionghui Zeng, Zhiwei Zhao,Benxue Jiang , Xiaoming He, Jun Xu；Effects of Yb concentration on the spectroscopic properties of Yb: Y3Al5O12
[19] Xiaodong Xu, Zhiwei Zhao, PingXin Song, Jun Xu, Peizhen Deng；Growth of high-quality single crystal of 50 at.% Yb:YAG and its spectral properties；Journal of Alloys and Compounds 364, 311–314(2004)
[20] Takunori Taira, William M.Tulloch, and Robert L.Byer, Modeling of quasi-three-level lasers and operation of CW Yb:YAG lasers, Applied Optics,36(1997)
[21] S.Belogurov, G.Bressi,et al,Properties of Yb-doped scintillators:YAG,YAP,LuAG, Nuclear Instruments and Methods in Physics Research A 516,58-67(2004)
[22] Tsunekane, Masaki; Taira, Takunori, Optics Letters, 31(13),2003-2005 (2006)
[23] Haiwu Yu, Gilbert Bourdet, Applied Optics,44, 7161(2005)
[24] D.S.Sumida, T.Y.Fan,Optics Letters, 19(17),1343(1994)
[25] J. Lu, H. Yagi, K. Takaichi, T. Uematsu, J.F. Bisson, Y. Feng, A.Shirakawa, K. Ueda, T. Yanagitani, and A.A. Kaminskii, "110W ceramic Nd3+:Y3Al5O12 laser," Appl. Phys.B. 79 (2004)25-28.
[26] http://www.llnl.gov/nif/psa/sshcl.html
[27] Tao Feng, Jianlin Shi, Jiyang Chen, and Danyu Jiang, "Fluorescence emission enhancement of transparent Nd:YSAG ceramics by Sc2O3 doping," J. Opt. Soc. Am. B. 22(2005)2134-2137.
[28] Tao Feng, "Synthesis and greatly enhanced fluorencence emission of transparent Nd-doped Y3ScxAl5-xO12 ceramic," J. Mater. Res. 20(2005)2322-2327.
[29] Yoichi Sato, Jiro Saikawa , Takunori Taira , and Akio Ikesue.,"Characteristics of Nd3+-doped Y3ScAl4O12 ceramic laser," Optical Material .29(2007)1277-1282.
[30] J.Lu, K.Takaichi, T.Uematsu, A.Shirakawa, M.Musha, and K.Ueda, "Promising ceramic laser material: Highly transparent Nd3+:Lu2O3 ceramic," Appl. Phys. Lett.. 81(2002)4324-4326.
[31] John B.Gruber, Marian E. Hills, Toomas H.Allik, C.K.Jayasankar, John R. Quagliano, and F.S.Richardson "Compararive analysis of Nd3+(4f3) energy levels in four garnet hosts," Physical Review B. 41 (1990)7999-8012.
[32] Daniel Creeden, John C, McCarthy, Peter A.Ketteridge, Peter G.Schunemann, Timothy Southward, James J.Komiak, and Evan O.Chicklis, "Compact,high average power,fiber-pumped terahertz source for active real-time imaging of concealed objects," Optics Express.15(2007)6478-6483.
[33] F.Auzel and R.Hull, Spectroscopic Properties of Rare Earths in Optical Materials, Chap. 5 , Tsinghua University Press and Springer-Verlag Berlin Heidelberg, 2005.

21

Co-Ionic Conduction in Protonic Ceramics of the Solid Solution, $BaCe_{(x)}Zr_{(y-x)}Y_{(1-y)}O_{3-\delta}$ Part I: Fabrication and Microstructure

W. Grover Coors
CoorsTek, Inc.
USA

1. Intoduction

Protonic ceramics have unique transport properties that make them suitable for applications in intermediate temperature fuel cells and steam electrolyzers, hydrogen separation membranes, and various membrane reactors for chemical synthesis. Since the discovery of ceramic proton conductors more than twenty years ago, and the ensuing enthusiasm, practical issues relating to ceramic fabrication have hampered advancement of the technology. The best ceramic proton conductors were thought to be acceptor-doped barium cerates, but these turned out not to be chemically stable in the typical use environments. The other leading candidates, acceptor-doped barium zirconates, proved too difficult to sinter. Most other protonic ceramics investigated either exhibited much lower conductivity or poor chemical stability. Two breakthroughs have recently taken place making it feasible, for the first time, to manufacture these ceramic proton conductors commercially and inexpensively with the prerequisite properties. First, the recognition that barium cerate and barium zirconate form a complete solid solution ($BaCe_xZr_{y-x}Y_{1-y}O_{3-\square}$, for all values of $1 > y > 0.8$ and x between 0 and y), has made it possible to tailor the mechanical, chemical and transport properties for various applications. Second, the discovery of solid state reactive sintering has made it possible to prepare dense, phase-pure ceramics at reasonable temperatures. This chapter describes fabrication and characterization of BCZY proton conductors using 1-2 wt% NiO as a sintering additive for solid state reactive sintering.

2. Background

Certain ABO_3 perovskite ceramic oxides containing acceptor dopants have high concentrations of extrinsic oxygen ion vacancies that give rise to unique ionic transport properties. Many ceramic proton conductors in this group have been identified, most notably where A = Ba or Sr and B = Ce or Zr. Certain aliovalent cations, where Y^{+3} is prototypical, may substitute for B sites otherwise occupied by Ce^{+4} or Zr^{+4}, in mole fractions as high as 20-30% before the structure becomes unstable. The resulting charge imbalance in the crystal lattice is compensated for by the creation of oxygen ion vacancies on the anion sublattice. These oxygen ion vacancies each carry a net double-positive charge, so that two dopant ions are required for each oxygen ion vacancy created, in order to maintain

electroneutrality. Yttrium-doped barium cerate, $BaCe_{(1-x)}Y_xO_{3-d}$ (BCY), has long been recognized as one of the best ceramic proton conductors. Iwahara carried out the first systematic evaluation of the ionic conduction properties of barium cerate in 1988 (Iwahara, et al., 1988). It is straightforward to fabricate this ceramic material by traditional solid-state reaction, and for this reason, it has been one of the most extensively studied of all the ceramic proton conductors. Nonetheless, concerns have persisted about the chemical stability in moist carbon dioxide, which corrodes the ceramic to form barium carbonate and hydroxide. Since many applications for ceramic proton conductors involve operation in hot, moist CO and CO_2 atmosphere, interest in BCY as a practical material has waned.

Yttrium-doped barium zirconate, $BaZr_{(1-x)}Y_xO_{3-d}$ (BZY) has also been recognized as a good ceramic proton conductor for many years, but without the same concerns about chemical stability in moist CO_2 as with BCY. Kreuer reported transport properties of BZY for the first time using single crystals and sintered ceramics (Kreuer, 1999). Schober and Bohn were also able to prepare dense ceramic specimens (Schober & Bohn, 2000), although as was the case with Kreuer, a sintering temperature above 1700 ^oC for 30 hours was required. Difficulty in producing dense polycrystalline specimens has hindered the development of this material. The traditional processing routes of synthesizing fine powders by solid-state reaction or spray pyrolysis produce powders that are difficult to sinter below 1700 ^oC, even when hot-pressed. The reason that the material is so difficult to sinter is not yet fully understood, but firing at such high temperatures tends to volatilize barium, leaving the material A-site deficient, and the resulting ceramic exhibits poor proton conductivity. Magrez and Schober successfully synthesized dense BZY at 1500 ^oC by a polyacrilamide gel method (Magrez & Schober, 2004), but the method has apparently never been fully optimized. Münch published a comparative analysis of BCY and BZY by quantum molecular dynamics simulation (Münch, et al., 2000), which suggested that BZY should be, in principle, a very good proton conductor. However, high impedance to proton transport across grain boundaries in polycrystalline specimens is thought to be the main reason that measured ionic conductivity is much lower than predicted. More recently, many interesting methods have been proposed for synthesizing polycrystalline BZY. Perhaps one of the most ingenious involves converting a thin layer of 8 mol% yttria-stabilized zirconia (8YSZ) into BZY by reacting with $BaCO_3$ in situ (Schober, 2005). Nonetheless, to our knowledge, the high grain boundary impedance problem has never been solved using traditional synthesis, dampening commercial interest in pure BZY as a proton conductor. A comprehensive review of the progress on these materials prior to 2003 has been provided by Kreuer (Kreuer, 2003).

A critical breakthrough in producing BZY was first reported by Babilo and Haile, who found that dense BZY ceramics could be prepared at a sintering temperature of only 1300 ^oC for four hours when transition metal oxides, ZnO, CuO or NiO, were added up to 4 mol% (Babilo & Haile, 2005). Without the addition, BZY remained substantially porous. Independently, Tao and Irvine demonstrated the same discovery of ZnO as an effective sintering additive for preparing BZY (Tao & Irvine, 2006, 2007). The effect has subsequently been reported by several investigators (Tong, et al., 2010a, 2010b; Wang, et al., 2009; Xu, et al., 2010). Enhanced sinterability of BZY with 1 wt% NiO has been demonstrated in our lab (Coors, 2008). The exact mechanism responsible for the dramatic improvement in sinterability remains controversial, but the result has been widely confirmed. Transition

metal oxides have also been used as sintering aids with BCY to lower the sintering temperature and to investigate the effect of these additions on conductivity. Shimura used Mn, Co and Fe - finding cobalt to be the most effective (Shimura, et al., 2005). Costa reported that 4 mol% NiO lowered the sintering temperature of BCY by 200 ^{o}C (Costa, et al., 2009). Tong used 2 mol% NiO to fabricate BCY20 (Tong, et al. 2010c), and we also confirmed this effect with NiO in our lab (Coors, et al., 2009). In all cases, no significant difference in conductivity of BCY has been observed, with or without these sintering aids, so it has generally been concluded that small additions of 2^{+} transition metal oxides has negligible impact on the transport properties and structure, other than to enhance sintering and increase average grain size. In the case of BZY20, Tong and O'Hayre reported high conductivities in moist argon (Tong, et al., 2010a, 2010b). A clear path forward to producing these protonic ceramic materials now seems possible.

In the meantime, a parallel path in the development of ceramic proton conductors was being pursued. The idea of solid solutions of BCY and BZY was initially proposed by Wienströer & Wiemhöfer stating that, "A solid proton conductor that combines the higher chemical stability of the zirconates and the high conductivity of the cerates could solve these problems" (Wienströer & Wiemhöfer, 1997). Since barium cerate and barium zirconate are nearly isomorphic, it was expected that they would be end members of a binary solid solution where B-sites are randomly occupied by either Zr^{+4} or Ce^{+4}. This idea was demonstrated for $BaCe_{0.9-x}Zr_xNd_{0.1}O_{2.95}$ for $0.1 \leq x \leq 0.6$ by Ryu (Ryu & Haile, 1999) and subsequently for $BaCe_{0.9-x}Zr_xGd_{0.1}O_{2.95}$ for $0<x<0.4$. Katahira (Katahira, et al. 2000), Zhong (Zhong, 2007), Ricote (Ricote, et al., 2009a, 2009b) and Guo (Guo, et al. 2009) extended the investigation to yttria dopant in $BaCe_{0.9-x}Zr_xY_{0.1}O_{2.95}$ for $0 \leq x \leq 0.9$. These papers all confirmed that a stable solid solution existed, and that chemical stability could be improved without significantly diminishing the protonic conductivity. However, it still proved difficult in practice to obtain uniform mixing of the BCY and BZY phases, and high sintering temperatures were still required to prepare dense polycrystalline specimens.

The solution to this problem was, naturally, to extend the use of transition metal oxide sintering additives, originally used only with the end members, BCY and BZY, to the whole range of solid solutions. This approach was first reported by Tao (Tao & Irvine, 2007) and more recently by Wang (Wang, et al., 2009). Azimova reported BCZY using CoO as a sintering aid (Azimova & McIntosh, 2009). Most recently Ricote reported very satisfactory results for $BaCe_{0.2}Zr_{0.7}Y_{0.1}O_{2.95}$ prepared by solid state reactive sintering using 1-2 wt% NiO (Ricote, et al., 2011). The development of protonic ceramics based on BCY-BZY solid solutions with transition metal oxide sintering aids has provided new latitude in the design of functional proton conductors and has now become a significant factor in the development of practical protonic ceramics.

2.1 Nomenclature

A note on nomenclature is in order. The number of compositional variants of these materials is enormous. In order to avoid writing out the entire formula each time, abbreviations are typically used, but almost every investigator has a unique system, and there has been no consistency in the literature. Also, $BaCe_xZr_{0.9-x}Y_{0.1}O_{2.95}$ often appears as $BaCe_{0.9-x}Zr_xY_{0.1}O_{2.95}$ – the only difference being which B-site cation the variable applies to. Ricote and colleagues at Risø in Denmark recently proposed a simple notation that solves these problems, and will be used throughout the following text (Ricote, et al., 2009). The basic formula is BCZM*nm*,

for barium, cerium, zirconium and M-dopant (Y, Gd, Nd, etc.). The cerium and zirconium mole fractions are n and m times ten. The nominal B-site occupancy is $x_M+x_n+x_m$ =1. The critical ratio n/m can be correlated to chemical stability. The dopant mole fraction x_M is implied as $(1-x_m-x_n)$. For example, $BaCe_{0.5}Zr_{0.4}Y_{0.1}O_{3-d}$ becomes BCZY54, and BCZY44 refers to $BaCe_{0.4}Zr_{0.4}Y_{0.2}O_{2.95}$. The end members of the solid solution, which were previously often designated as BCY20 and BZY20, now become BCZY80 and BCZY08, respectively, in the new nomenclature. A complication with this notation arises when sintering aids or secondary dopants are used. The Risø notation cannot easily accommodate multiple B-site dopants. Nonetheless, without some type of simplifying notation, the formulas become needlessly complex and difficult to compare. In what follows, only the major dopant will be included in the formula with the sintering additive given as a prefix, for example, 2NiBCZY26 is just $BaCe_{0.2}Zr_{0.6}Y_{0.2}O_{2.95}$ plus 2 wt% NiO.

For hydrogen/air protonic ceramic fuel cells PCFCs and steam electrolysis cells PCECs (Irvine, et al. 2007), where humid air is used, chemical stability against CO_2 below about 1% may be sufficient. But the most interesting applications for protonic ceramics that are now being considered will require stability against much higher concentrations. For example, the anode gas of a PCFC operating on methane or other hydrocarbon fuels at high fuel utilization will approach 100% CO_2. Various electrolytic cells for producing syngas, including membrane reactors, may also be expected to have high CO and CO_2 concentrations in contact with the ceramic at moderate temperatures ranging from 500 to 800 ºC. The end member, barium cerate (BCZY90), is unstable in CO_2, but several investigations have been carried out to determine the maximum value of the ratio of Ce/Zr (n/m) for which the ceramic is chemically stable. Tao reported ZnO-BCZY53 to be stable in pure CO_2 in this range of temperatures (Tao & Irvine, 2006). Ryu reported that the more ceria-rich, ZnO-BCZY72 is also stable in CO_2 for the ratio of $n/m \leq 7/2$ (Ryu & Haile, 1999). However, Zhong observed a small amount of $BaCO_3$ formation at BCZY72, but not in BCZY54 (Zhong, 2007). Ricote similarly found BCZY63 to be unstable, while BCZY27 was completely stable in pure CO_2 (Ricote, et al., 2009).

3. Reactive sintering

It is a good idea from the outset to carefully lay down definitions for the term, *reactive sintering*, and the other related terms that have to do with how polycrystalline ceramic materials are actually fabricated from powders. The idea of reactive sintering is nothing new. Kingery described it in his definitive textbook on ceramics, "During the firing process…in many ceramics there may be solid-state reactions forming new phases, polymorphic transformations, [and] decompositions of crystalline compounds to form new phases …" (Kingery 1960, p.448). Reactive sintering is an important industrial process, but it is often overlooked during the research and development phase because of the convenience of procuring high purity pre-calcined ceramic powders.

Solid-state reaction: Solid state-reaction is a general term that pertains (in the context of making ceramics) to producing new solid product phases from other reactant phases below the melting point of either products or reactants. At a given temperature, the phase with the lowest Gibbs free energy will prevail, but because ion mobility in solids is often very low, even near the melting point, equilibrium may not be achieved in reasonable time scales. Solid-state reactions require intermixing of ions from reactant phases by solid state diffusion, therefore, solid-state reactions are enhanced by making the diffusion lengths as

short as possible. This is commonly accomplished by starting with very fine, well-mixed reactant crystallites that can be obtained by attrition milling, sol-gel methods or pyrolysis of salts precipitated from solution. Almost all specialty ceramic powders are prepared by one of these techniques. One common method for making fine, single phase BCZY powder is by solid-state reaction using carbonates and oxides.

$$BaCO_3 + xCeO_2 + (0.8-x)ZrO_2 + 0.1Y_2O_3 \xrightarrow{\geq 1300\,^{\circ}C} BaCe_xZr_{0.8-x}Y_{0.2}O_{3-\delta} + CO_2(g) \quad (1)$$

Traditional sintering: The traditional approach to fabricating ceramic perovskites is to begin by preparing phase pure powders of the correct stoichiometry by solid-state reaction (such as Eq.1), milling the resulting powder, called *calcine*, and then compacting the powder into green bodies for subsequent ceramic sintering at high temperatures.

Solid-State Reactive Sintering: For solid-state reactive sintering, SSRS, the discrete steps of solid-state reaction and traditional powder sintering are combined into a single processing step. The precursor powders are mixed with binders and compacted into a green body. This is only possible when the kinetics of solid state reaction are fast enough so that reaction-product crystallites form prior to, or simultaneously with, sintering. This fabrication method has been described by Babilo and Haile, where certain transition metal oxides, such as NiO, ZnO, and CuO, were included in the formulation (Babilo & Haile, 2005), and Tao with ZnO (Tao & Irvine, 2006). The transition metal oxides promote the formation of the equilibrium phase while simultaneously enhancing densification by sintering.

Sintering additives: The metal oxide is more than just a "sintering aid". A traditional sintering aid promotes transport at the surface along grain boundaries, assisting densification, without substantially interacting with the bulk phases. In reactive sintering, the metal oxide ions are believed to play a crucial role in ion exchange and diffusion within the grains as well as at grain boundaries. Often a eutectic liquid phase forms between the transition metal oxide and the alkali metal, dissolving the other oxides, from which the desired perovskite phase is produced. In this sense, transition metal oxides are used as reactive sintering *additives*. The solubility limit of NiO in the host BCZY is about 1 wt%. Any additional NiO shows up as a distinct second phase. There is some controversy surrounding where the dissolved nickel ions end up after sintering – whether they go into interstitial sites or substitute for B- or even A-sites, or remain at grain boundaries as an amorphous second phase. These questions may have considerable bearing on the electronic properties, but as a practical matter, it is nearly impossible to draw any concrete conclusions about nickel in the structure at such low concentrations.

In a recent development, Yamazaki reported that dense BZY ceramics could be prepared at moderate sintering temperature by SSRS without any sintering additives at all (Yamazaki, et al., 2009). That is, the solid-state reaction and sintering steps were carried out simultaneously, but apparently without the need for sintering additives (beyond the trace impurities in the starting materials). This raises new questions about what role played by transition metal oxides in the sintering process, possibly opening up a whole new direction in practical protonic ceramic fabrication. In our lab, we have found that when a slurry of precursor oxides and carbonates is applied to the surface of a NiO-BCZY composite substrate, a thin film membrane of dense BCZY electrolyte forms during co-sintering, even when no NiO is added to the slurry. During sintering, some NiO diffuses from the substrate into the membrane up to the solubility limit of about 1 mol%, but whether or not this NiO is actually necessary for densification of the membrane is not known at this time. A polished

section of a supported membrane produced this way is shown in Figure 1. The light areas are BCZY26 phase and the grey areas are NiO grains. (The dark region on the left is potting compound.) A dip coated and co-fired BCZY26 electrolyte membrane, about 15 μm thick, and typical of the membranes required for various practical devices, is shown. It is apparent from the image that both phases are independently contiguous except through the membrane region, which shows no evidence of penetration by NiO. It is also apparent in the image that the sintered specimen is almost fully dense. The residual spherical pores visible within the NiO grains are typical of liquid phases formed during sintering. No porosity is visible in the BCZY26 phase or at BCZY26/NiO grain boundaries.

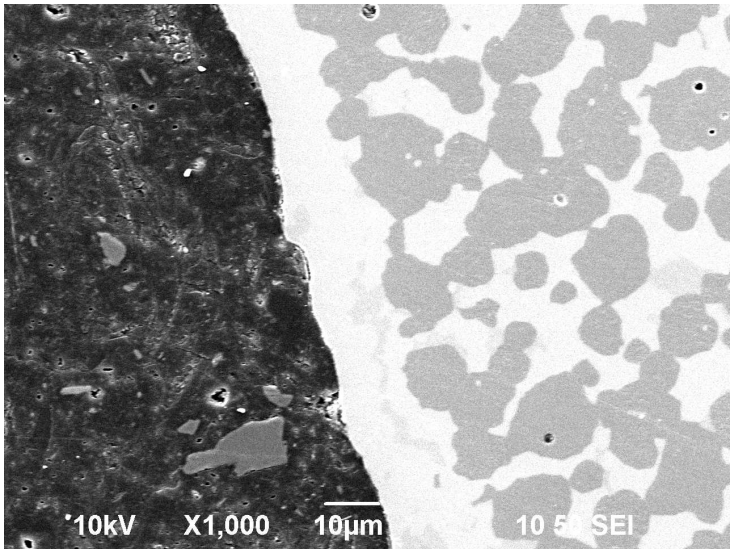

Fig. 1. Polished cross section of as-fired (unreduced) 68NiBCZY26 with 15 μm dip-coated membrane. Light regions are BCZY26 and dark regions are NiO (SEI-1000x).

4. Ceramic fabrication method

Precursor powders, $BaCO_3$, CeO_2, ZrO_2 and Y_2O_3 were dried and weighed to obtain the desired nominal stoichiometery for the $BaCe_xZr_{0.8-x}Y_{0.2}O_{2.9}$. An additional 1 wt% NiO was included as a sintering additive, but was not included in the stoichiometry, as we have found that NiO resides at grain boundaries, and nickel ions do not remain in the ABO_3 perovskite structure after sintering. Specimens of 1NiBCZY, with 20 mol% Y and Ce-Zr; 80, 44, 26, and 08, and 10 mol% Y with Ce-Zr; 45, 36, 27, 18, 09 were prepared for XRD analysis by conventional powder processing in a 19mm diameter uniaxial compaction die. Extruded 1NiBCZY26 and 1NiBCZY27 tubes were also fabricated by solid state reactive sintering from precursor oxides and carbonates. Barium carbonate (Alfa Aesar, tech grade, 99.6%, Item# 43478, $BaCO_3$), zirconium oxide (Neo Performance Materials (AMR Ltd), ≥99.5%, Item# 2802004, ZrO_2), cerium oxide (Neo Performance Materials (AMR Ltd), ≥99.5%, Item# 4-02-13-01, CeO_2), yttrium oxide (HJD Intl. 99.99+%, ultra fine, Y_2O_3) and nickel oxide (Inco, Grade F NiO) were used for the synthesis of the ceramic tubes, prepared according to the

powder formulation given in Table 1 for BCZY26, as an example. The precursor powders were blended with water soluble acrylic and cellulosic ether plasticizers. The tubes were extruded on a 40-ton Loomis extruder. The spindle diameter was 7.14 mm and die diameter was 9.91mm. The extruded tubes were dried for a week in controlled humidity on plaster V-groove setters. The dried tubes were hang-fired on zirconia pins extending through one end. The length of the green tubes was 46 cm. The tubes were sintered at 1500 ^oC for 4 hours in air at a heating rate is 50 ^oC/hr up to 450 ^oC and 100 ^oC/hr up to 1500 ^oC. All specimens were greater than 98% dense as determined by Archimedes method.

Material	Form.wt.	Mole/FU	Wt./FU	Wt.fract.
$BaCO_3$	197.35	1.0	197.35	0.595
CeO_2	172.12	0.2	34.42	0.104
ZrO_2	123.22	0.6	73.93	0.223
Y_2O_3	225.81	0.1	22.58	0.068
NiO(1w%)	74.71	-	-	0.010
		total	328.28	1.000

Table 1. Powder formulation for 1NiBCZY26 (based on $BaCe_{0.2}Zr_{0.6}Y_{0.2}O_{3-d}$, form.wt. = 284.263 g/mol)

The stoichiometry of the sintered BCZY26 tubes was confirmed by X-ray Fluorescence using fused samples and standards in lithium tetraborate glass on a PANalytical MagiX Model 2440, sequential 3.0 kW XRF. The results are given in Table 2, which shows weight percent based on oxides and calculated mol%. A significant fraction of strontia was found to coexist with baria. Also, some alumina and a trace of iron oxide were detected. The site fractions were calculated assuming pure ABO_3 perovskite with Ba and Sr only on A-sites and Ce, Zr and Y on B-sites, giving the nominal stoichiometry: $Ba(Sr)_{1.002}Ce_{0.202}Zr_{0.586}Y_{0.198}O_{2.90}$. B-site occupancy sums to 1.004, giving an error less than 1%. Thus, a small amount of B-site Ni ions (Ni^{+2} or Ni^{+3}) cannot be ruled out, but the net effect is negligible.

Material	Wt%	Form.wt.	Mol/100g	Mol.fract
BaO	51.70	153.326	0.3372	0.959
SrO	1.59	103.619	0.0153	0.043
CeO_2	12.20	123.223	0.0709	0.202
ZrO_2	25.40	172.115	0.2061	0.586
Y_2O_3	7.88	225.81	0.0349	0.198
			total	1.988
NiO	1.05	74.693	0.0141	
Al_2O_3	0.22	101.961	0.0022	
Fe_2O_3	<0.01			

Table 2. XRF analysis of 1NiBCZY26 based on formula wt. = 284.263 g/mol

XRD was performed using an X'Pert XRD diffractometer from 10 to 90 degrees with 0.02 degree increments. SEM analysis was performed on a JOEL JSM-6390 and field emission FESEM was performed on a JEOL JSM-7000F with an energy dispersive spectroscopy detector (EDS) from EDAX. Imaging was conducted using a 2 kV electron beam and EDS was obtained using a 5 kW electron beam. Bright field TEM was performed on FIB-prepared

specimens. Magnetic characterization measurements on a reduced specimen was performed on a Quantum Design PPMS equipped with the VSM and oven options. The relative amounts of metallic nickel and residual nickel ions were measured at 2K against a pure nickel wire scaled to the same 1 wt% NiBCZY26 specimen.

5. Phase and microstructure

5.1 XRD

The XRD patterns for dense ceramic specimens of BCZY prepared by reactive sintering with 1 wt% NiO addition are shown in Figure 2. The four specimens span the entire composition range from pure BZY (BCZY08) to BCY (BCZY80). The major perovskite peaks are shown indexed to the cubic system of $BaZrO_3$ (74-1299). $BaCeO_3$ (83-0532) is orthorhombic, so the index is pseudocubic in this case (45° rotation with respect to the cubic lattice parameter $\bar{a} = \left(a/\sqrt{2} + b/\sqrt{2} + c/2 \right) / 3$). The dominant feature of the XRD patterns is the uniform decrease in lattice parameter in going from BCZY80 to BCZY08.

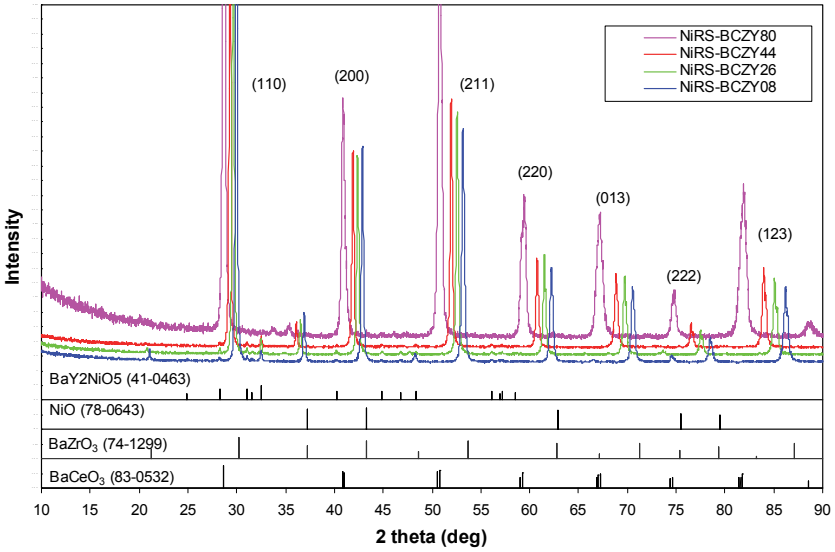

Fig. 2. XRD patterns for 1wt% NiO-reactive sintered BCZY80, BCZY44, BCZY26 and BCZY08 dense ceramics. The major perovskite peaks are shown indexed to the cubic system.

It may be observed that in each set, the major peak in BCZY80 shifts to the corresponding peak in BCZY08 as the Ce/Zr ratio decreases. It may also be seen that the BCZY08 peaks are shifted to the left from the undoped $BaZrO_3$, which is characteristic of the decrease in lattice parameter when Y^{3+} ions substitutes for the larger Zr^{+4} ions on B-sites. The peaks that did not shift were identified as a second phase, BaY_2NiO_5 (41-0463), believed to reside primarily within pores, and possibly also at grain boundaries (Tong, et al. 2010). The pattern for NiO (78-0643) is also included. All of the NiO peaks coincide with $BaZrO_3$ peaks, however, an expanded high index portion of the patterns between 76° and 80° is shown in Figure 3, which indicates the location of the (222) peaks for both NiO and $BaZrO_3$. It may be seen that

there is no evidence for the existence of NiO as a second phase, which would be clearly seen even at the 1 wt% concentration. The highest intensity peaks for the compounds $NiBaO_2$ and $NiBaO_3$ are at 26.26° and 26.06° respectively, and neither is visible in any of the patterns. The conclusion is that most of the original NiO has been incorporated into BaY_2NiO_5. However, the existence of this phase requires excess zirconia and ceria, but no peaks of either of these phases were detected.

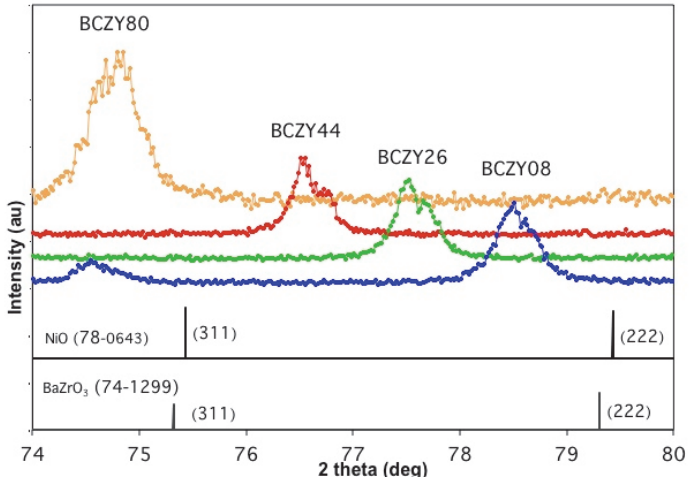

Fig. 3. XRD patterns for 1wt% NiO-reactive sintered BCZY with 20 mol% Y from Fig 1 between 74° and 80°. The (222) peaks are shown for NiO and $BaZrO_3$. The corresponding (222) peaks for the BCZY series are shifted to smaller angles (decreasing lattice parameter).

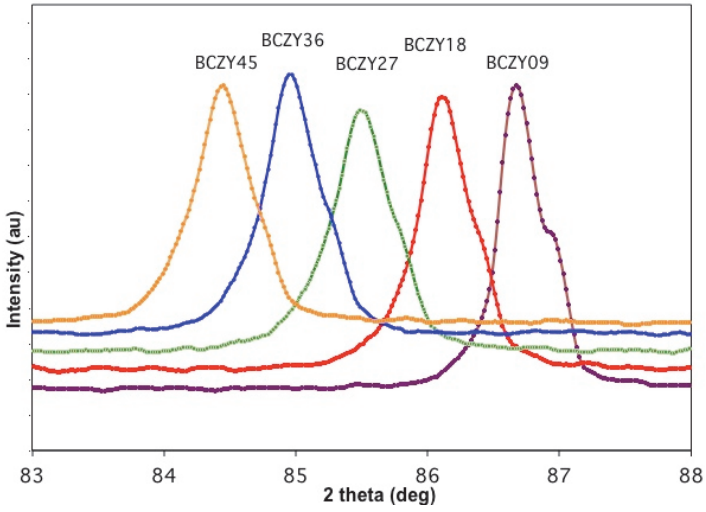

Fig. 4. Set of (123) XRD peaks for 1wt% NiO-BCZY with 10 mol% Y showing uniform spacing. (Shoulders are due to Cu K-β radiation.)

It is also seen in Figure 3 that the peaks are evenly spaced across the whole range of the solid solution for the 20 Mol% Y series. This effect is even more striking in Figure 4 for the 10 mol%Y BCZY series where the highest-index (123) peaks are shown. The shoulders slightly to the right of the central peaks are due to Cu K-β radiation.
The pseudocubic lattice parameters are given in Table 3 along with the other bulk properties derived from the lattice constant. The end members of the solid solution, $BaZrO_3$ and $BaCeO_3$ are listed first, followed by the set of 20 mol% and then 10 mol% Y BCZY specimens.

Ceramic Material	**Pseudocubic Lattice Param. (A)**	**Theoretical Density (g/cm³)**	**Formula Wt. (g/mol)**	**Mol.Vol. (cm³/mol**
$BaZrO_3$ (74-1299)	4.1816	6.279	276.55	44.041
$BaCeO_3$ (83-0532)	4.4073	6.316	325.45	51.528
BCZ(20 mol%Y)				
1NiBCZY08	4.2110	6.103	274.49	44.974
1NiBCZY26	4.2547	6.128	284.27	46.391
1NiBCZY44	4.3051	6.118	294.05	48.059
1NiBCZY80	4.3959	6.245	319.52	51.164
BCZ(10 mol%Y)				
1NiBCZY09	4.1970	6.188	275.52	44.528
1NiBCZY18	4.2212	6.190	280.41	45.304
1NiBCZY27	4.2461	6.188	285.30	46.108
1NiBCZY36	4.2674	6.200	290.19	46.806
1NiBCZY45	4.2881	6.214	295.08	47.490

Table 3. Pseudocubic lattice parameters for 1wt% NiO-reactive sintered BCZY. The major perovskite peaks are indexed to the cubic system. Theoretical density, formula molecular weight and molar volume are based on the lattice parameters derived from fitting XRD data.

The XRD peaks in Figures 3 and 4 clearly show that a complete BCZY solid solution has been achieved by reactive sintering. No mixed phases are present, and all the data is well indexed to the cubic system. The lattice parameters from Table 3 have been plotted in Figure 5 versus the ratio of B-sites occupied by cerium to the occupation by either cerium or zirconium. It may be observed that a linear relationship exists from which the unit cell volume may be estimated,

$$\overline{a} = 0.194 \frac{[Ce]}{[Ce]+[Zr]} + 4.204 \tag{2}$$

where $\overline{a}$ is in Å, and the pseudocubic unit cell volume, $V_c = \overline{a}^3$. The lattice parameters for undoped $BaCeO_3$ (83-0532) and $BaZrO_3$ (74-1299) are 4.4073Å and 4.1816Å, respectively. The corresponding extrapolations using our linear fit are 4.398Å and 4.204Å. The regression underestimates the lattice constant for $BaCeO_3$ while over estimating it for $BaZrO_3$, but the discrepancy is less than 1%, suggesting that the change in lattice parameter resulting from substitution of 10-20 mol% yttrium on B-sites is relatively small compared with the

difference resulting from zirconium and cerium, alone. Also plotted are several published values from the literature. The striking feature is that all barium cerate-zirconate solid solutions exhibit almost the same linear behavior, independent of dopant type, dopant concentration or sintering additive used. The slopes are about the same in all cases, and only BCZNd (Ryu & Haile, 1999) exhibits a slightly smaller overall lattice constant than all the specimens doped with gadolinium or yttrium.

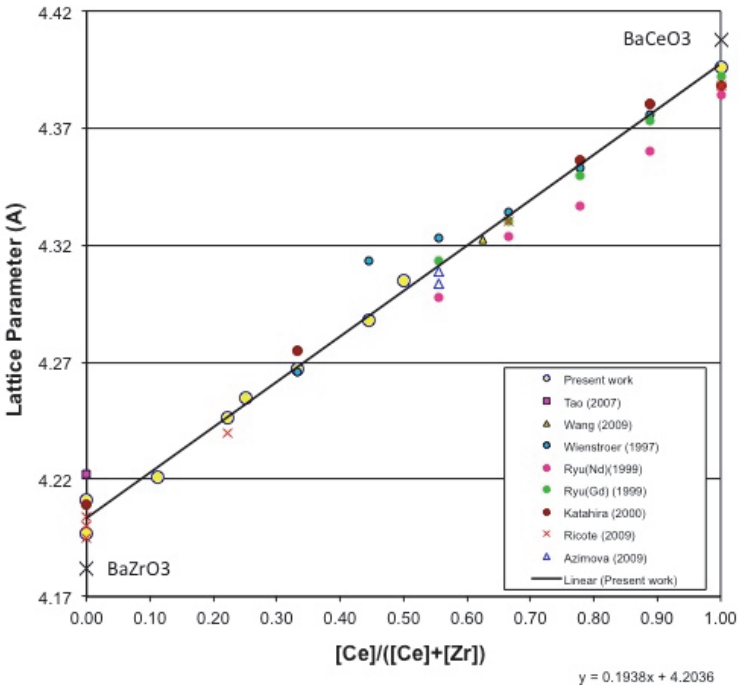

Fig. 5. Pseudocubic lattice parameters vs. the ratio of occupied B-sites $Ce^{+4}/(Ce^{+4}+Zr^{+4})$. The slopes are invariant to dopant, dopant concentration or MOx sintering additive.

5.2 As-fired NiRS-BCZY26 microstructure

For the further study, the compositions *n/m* = 1/3 (BCZY26) and 2/7 (BCZY27) were selected. These specimens were prepared from extruded tubes 6mm OD x 4.5mm ID. A SEM image of an as-fired NiRS-BCZY26 polished and thermally etched at 1425 ^{o}C for 35 minutes is shown if Figure 6. The ceramic is well-sintered with average grain size of 2 to 5 microns. Figure 7 shows a micrograph of an attempt to reactive sinter BCZY without NiO addition. The precursor powders have barely reacted at all and practically no sintering has taken place. This underscores the dramatic effect brought about by a small addition of NiO.

A specimen prepared by focused ion beam (FIB) etching and removal from a bulk ceramic is shown in bright field TEM in Figure 8. It is clear by the 120^{o} dihedral angles at triple points and absence of pores that sintering is complete. The investigation concluded that most of the grain boundaries were clean, but evidence of some amorphous grain boundaries was observed. A high resolution TEM is shown in Figure 9 showing a clean grain boundary

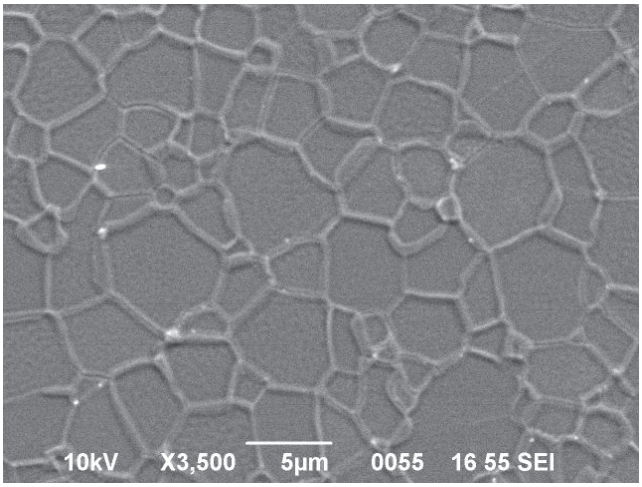

Fig. 6. As-fired polished and thermally etched (1425 ºC, 35 min.) surface of 1wt% NiO-reactive sintered BCZY26 (3500x).

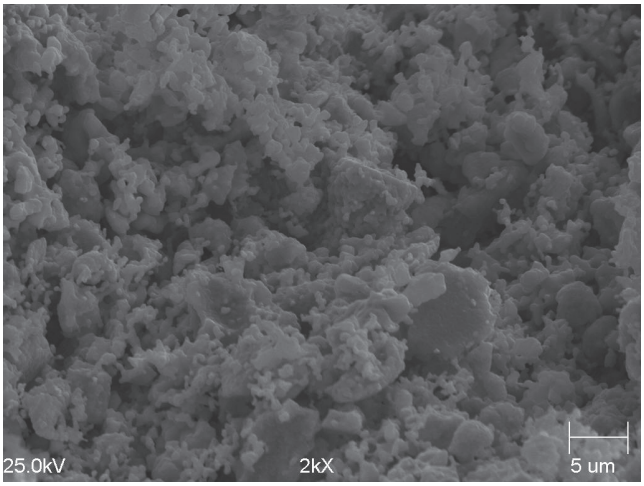

Fig. 7. Micrograph of attempt to reactive sintered BCZY26 without NiO addition (2000x).

intersecting with two amorphous ones at a triple point. This is obviously a significant finding, since high grain boundary impedance has long been suspected as the reason why the proton conductivity of doped barium zirconate is lower than expected. If a continuous network of amorphous grain boundaries were to form during sintering, these could well be blocking to proton transport on a macroscopic scale. The nature and extent of these amorphous grain boundaries is currently receiving a great deal of attention.

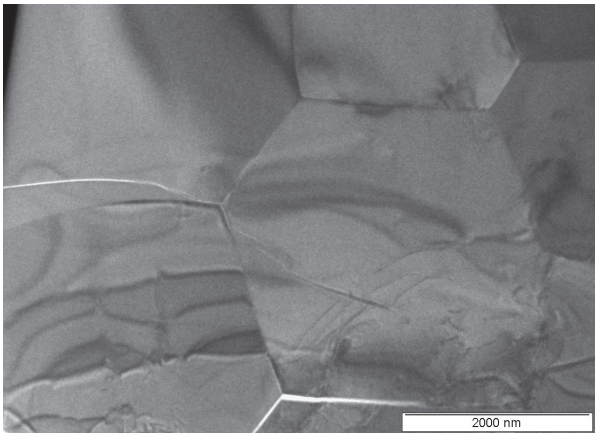

Fig. 8. Bright field TEM of reactive sintered BCZY26. The fracture at lower grain boundaries is the result of mechanical sectioning of specimen.

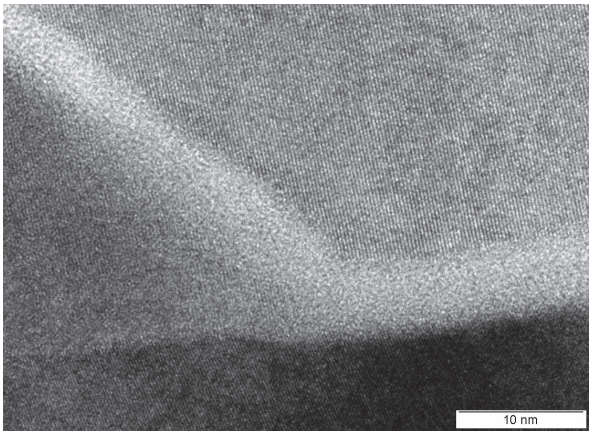

Fig. 9. HR TEM of reactive sintered BCZY26. The image shows that some of the grain boundaries are amorphous .

5.3 Solid state reactive sintering

Pure barium zirconate $BaZrO_3$ and barium cerate $BaCeO_3$ powders are relatively easy to fabricate by solid state reaction, but the incorporation of the large, aliovalent yttrium ions into the lattice is necessary in order to create the oxygen vacancies required for ion transport. In earlier experiments at CoorsTek in Golden, attempts to synthesize phase-pure BZY10 (10 mol% yttria-doped barium zirconate ($BaZr_{0.9}Y_{0.1}O_{3-d}$)) by solid-state reaction of ZrO_2, Y_2O_3 and $BaCO_3$ powders were not successful at temperatures as low as 1550 ^oC. Only recently was it discovered that very phase-pure BZY10 (BCZY09) calcine powder could be produced with the addition of a small amount of NiO. This was suggested by the analogy to the experience gained in fabricating NiO reactive sintered yttria stabilized zirconia

(NiYRSZ) (Swartzlander & Coors, 2009). However, when binders were added and the pre-calcined powder was compacted and sintered at 1550 ^{o}C, the resulting ceramic specimens were porous, with a fired density of only 60-70%. Subsequent experiments demonstrated that dense BZY10 could be fabricated by eliminating the traditional calcining step altogether. By mixing and compacting just the precursor powders of zirconia, yttria, barium carbonate, and a small amount of NiO, dense, phase-pure BZY10 could be fabricated with relative ease at only 1550 ^{o}C. This has become the process we refer to as NiO reactive sintered BCZY. A variant process was attempted to make BZY10 from pre-calcined 10 mol% yttria-stabilized zirconia (Tosoh 10YS), barium carbonate plus some NiO, but this led to sintering difficulties and considerable residual YSZ phase in the resulting ceramic. Apparently it is necessary to simultaneously create the cubic barium zirconate phase, incorporate the yttria dopant, and obtain the well-sintered grain boundaries during sintering in order to fabricate this ceramic. Ironically, this simple process uses very inexpensive raw materials, costing no more than about $5-10 per kilogram, and readily accessible air-fire sintering temperatures, making the commercialization of this important material very straightforward.

Clearly, reactive sintering involves several complicated steps. We hypothesize the following: Upon decomposition of $BaCO_3$, the reaction of BaO and NiO, beginning about 1100 ^{o}C, produces a liquid phase that enhances the transport along grain boundaries of all the cations involved in the solid state reactions. As temperature increases, $BaCe_xZr_{(1-x)}O_3$ begins to form, making the BaO-NiO melt increasingly nickel oxide rich and raising the melting temperature. Initially, $BaCe_xZr_{(1-x)}O_3$ has only a small concentration of intrinsic oxygen vacancies. Incorporation of some percentage of aliovalent dopants on B-sites lowers the Gibbs free energy, but without oxygen vacancies, diffusion by relatively large acceptor dopant ions like yttrium is difficult. In the case of BCZY, the yttrium ions must substitute on B-sites in the perovskite lattice by first diffusing into the zirconia or ceria grains. Since small cations, such as Ni^{2+} (0.69Å), are much more facile than Y^{3+} (0.92Å), the defect reaction initially takes place with the smaller, Ni^{2+} dopant ions, which can easily diffuse into the grain by substituting on B-sites. However, diffusion of Ni^{2+} into the grain requires extra charge compensation by creating oxygen vacancies on the anion sublattice (although more complex defect reactions involving electron holes are certainly possible). As the concentration of oxygen vacancies increases, diffusion of the larger Y^{3+} ion is facilitated by the vacancy transport mechanism. The nickel ions are too small to stabilize the perovskite structure by occupying the space of a B-site Ce^{4+} (0.94Å) or Zr^{4+} (0.79Å) and the requirement for charge compensation too great. The perovskite structure is more stable with the closer matched yttrium than nickel on B-sites, so nickel ions will ultimately be displaced by yttrium above a certain threshold concentration. This ion exchange mechanism occurs simultaneously throughout the entire body matrix promoting phase equilibria within grains and at grain boundaries during sintering. Ultimately, as the equilibrium BCZY phase forms, the nickel ions are exsolved and precipitated once again at grain boundaries as NiO or BaY_2NiO_5. The reason that reactive sintering does not work with pre-calcined YSZ powder is because it is already a stable phase that has no tendency to convert from the flourite phase to the perovskite phase at the low reactive sintering temperature, and nickel ions have no role to play in the required solid state ion exchange reactions. Similarly, precalcined BCZY powder does not densify even when NiO is added, which demonstrates that reactive sintering involves much more than just conventional liquid phase sintering. The kinetics of

reactive sintering involves the coordination of liquid phase sintering for grain boundary formation and ion exchange for bulk BCZY phase formation.

5.4 Microstructure after reduction

Conductivity testing of BCZY requires extended operation in moist and dry hydrogen at elevated temperatures. Post-reduction microstructure analysis was conducted to determine if the residual NiO causes any deleterious effects. Figure 10 shows a FESEM fracture surface of BCZY26 after multiple temperature cycles between 200 and 1000 °C in moist and dry 5% H_2/bal Argon. It may be observed in the image that nearly all of the fracture has occurred at grain boundaries, unlike the as-fired ceramic that exhibited mostly transgranular fracture. This suggests a weakening of the structure at grain boundaries due to a combination of reducing atmosphere and strain from temperature excursions. Also visible in the micrograph is a network of microcracks. The ceramic specimens typically failed catastrophically upon decreasing temperature in moist hydrogen or argon at some point below about 400 °C. In dry atmosphere, no fracture was observed. We believe the fracture is due to the strain induced by water of hydration at elevated temperatures that remains "frozen-in" at low temperatures from stoichiometric expansion. We have demonstrated with BCY and BZY that lattice hydration causes a measureable length dilation that has actually been used in TCE measurements to determine the extent of hydration (Coors & Swartzlander, 2005). Apparently, in the case of reactive sintered BCZY, the stress exceeds the strength of the material. This obviously is a matter of concern that will require careful management of operating parameters. Recently, preliminary investigations have indicated that much stronger and durable ceramic results when $BaSO_4$ is substituted for $BaCO_3$. In this case the sintering temperature is higher (~1600 °C) because of the higher decomposition temperature of the sulfate, but distinctly improved grain boundaries are obtained. Also, reduction of the yttrium dopant concentration from 20 to 10 mol% seems to improve the mechanical properties without

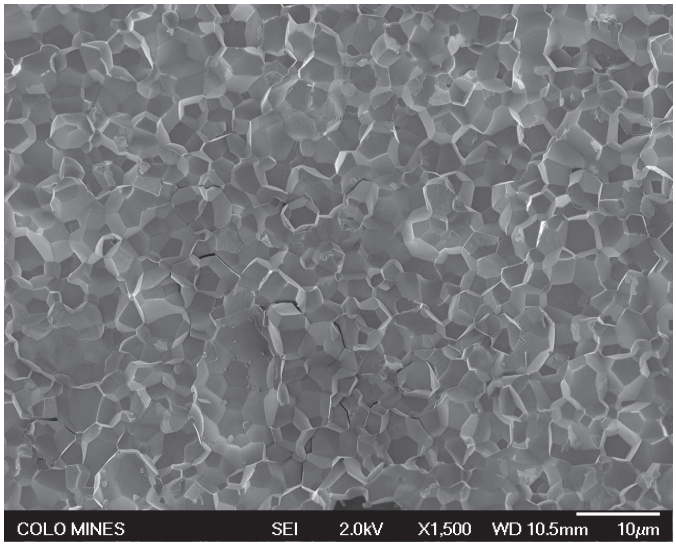

Fig. 10. FESEM Micrograph reduced BCZY26 fracture surface (1500x).

much sacrifice in conductivity, even though the oxygen vacancy concentration is one half as much. The formulation that seems to provide the best compromise of chemical stability, mechanical strength and proton conductivity is 1NiBCZY27.

Figure 11 is an enlarged view of a residual pore in 1NiBCZY26 after reduction. In this case, the surfaces of the grains are as-fired. The fracture is clearly visible along some grain boundaries. The most interesting feature of the micrograph is the presence of nanoprecipitates occurring predominantly along grain boundaries. Figure 12 is an EDS scan of one of these compared to the bulk grain. The precipitates were found to be mostly nickel.

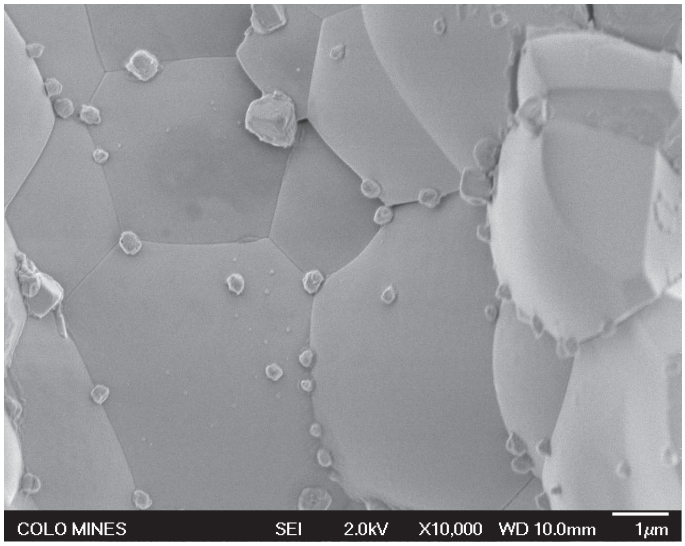

Fig. 11. FESEM Micrograph reduced BCZY26 surface of internal void with metallic Ni precipitates (10000x).

The specimen was subsequently analyzed for magnetic properties to determine the nature of the nickel precipitates using a Quantum Design PPMS. Figure 13 (top) shows the magnetic moment versus temperature. The sharp drop at 620K, the Currie temperature for bulk nickel, is the signature for metallic nickel. In Figure 13 (bottom), the magnetic moment versus field strength, H, is shown. The black curve is for a piece of nickel wire calibrated to the same nickel mass as in the 1NiBCZY26 specimen. The red curve is for the fully reduced BCZY26 specimen. It may be seen that the magnetic saturation is characteristic of ferromagnetic bulk metallic nickel. Also, the shallow slope of the magnetization curve at low field is characteristic of small, isolated nickel particles, which is consistent with the small precipitates in Figure 11. Even at 1000 Gauss, the magnetization has reached less than half its saturation value, in sharp contrast to the curve for the bulk nickel wire, which was almost fully saturated at this same field. It was possible to determine quantitatively from the saturated magnetization at 5000 Gauss that the wt% of metallic nickel in the specimen was 0.854%. A subsequent measurement using a QD-SQUID gave a value of 0.882%. The actual value for the 1NiBCZY26 specimen determined by X-ray Fluorescence was 0.825%. Within experimental error, virtually 100% of the original NiO has been reduced to bulk Ni metal. It

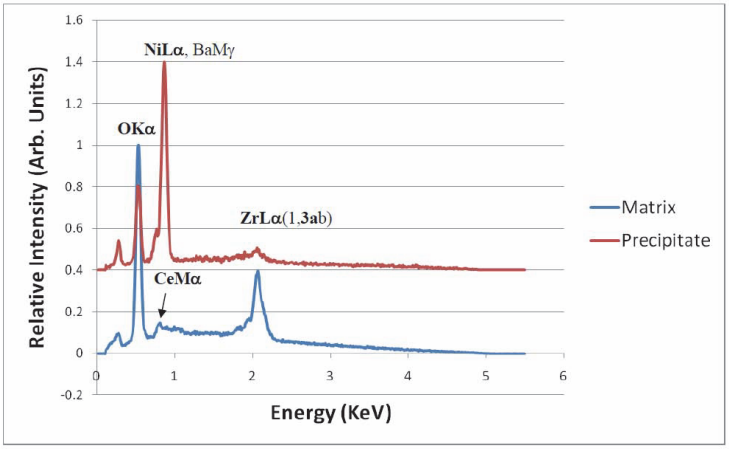

Fig. 12. EDS acquired using an electron beam with 5 KeV of energy. Ce and Ba have weak M band excitations (strong L bands for both occur at ~4 KeV). Nickel present predominantly in the nanoprecipitate.

is possible to draw two important conclusions from this finding: 1) very little, if any, nickel was lost during sintering and subsequent elevated temperature operation, and 2) a negligible fraction of the original nickel remains in the ceramic as ions. Although it is not possible to rule out that some Ni nanoprecipitates may exist within grains, as was found to be the case with Ni-reactive sintered yttria-stabilized zirconia (Coors, et al. 2009). The SEM image in Figure 11 suggest that most occur at grain boundaries. In any event, the possibility of nickel residing intersticially or substitutionally on regular lattice sites as ions may be considered remote.

XRD patterns were obtained on 1NiBCZY26 after reduction. The as-fired and post reduction patterns are shown in Fig. 14. There was no change in lattice parameter, and the strongest metallic nickel line (111) at 44.5° is just barely visible. The lower figure expands the region from 28° to 33° in which the four strongest peaks of the phase, BaY_2NiO_5 (00-041-0463) occur. These peaks are clearly visible in the as-fired ceramic, but have completely disappeared in the reduced specimen. The phase was identified as a grain boundary phase left over from SSRS (Tong, et al. 2010). With some of the barium tied up in this grain boundary phase, it is expected that the as-fired perovskite is slightly A-site deficient, but upon reduction, metallic nickel nanoprecipitates form, and the barium and yttrium are apparently dissolved back into the perovskite lattice. For most commercial applications envisioned with these protonic ceramics, reducing atmosphere is anticipated. This will certainly be the case for hydrogen separation and membrane reactors. In the case of PCFCs, the ceramic will be exposed to reducing atmosphere on one side and oxidizing on the other. For steam permeable membranes, SPMs, intermediate oxygen partial pressures may be encountered which are not low enough to reduce the barium-yttrium nickelate phase. It has yet to be determined if the reduction of this grain boundary phase is reversible or to what extent proton transport across grain boundaries may be influenced by this phenomenon.

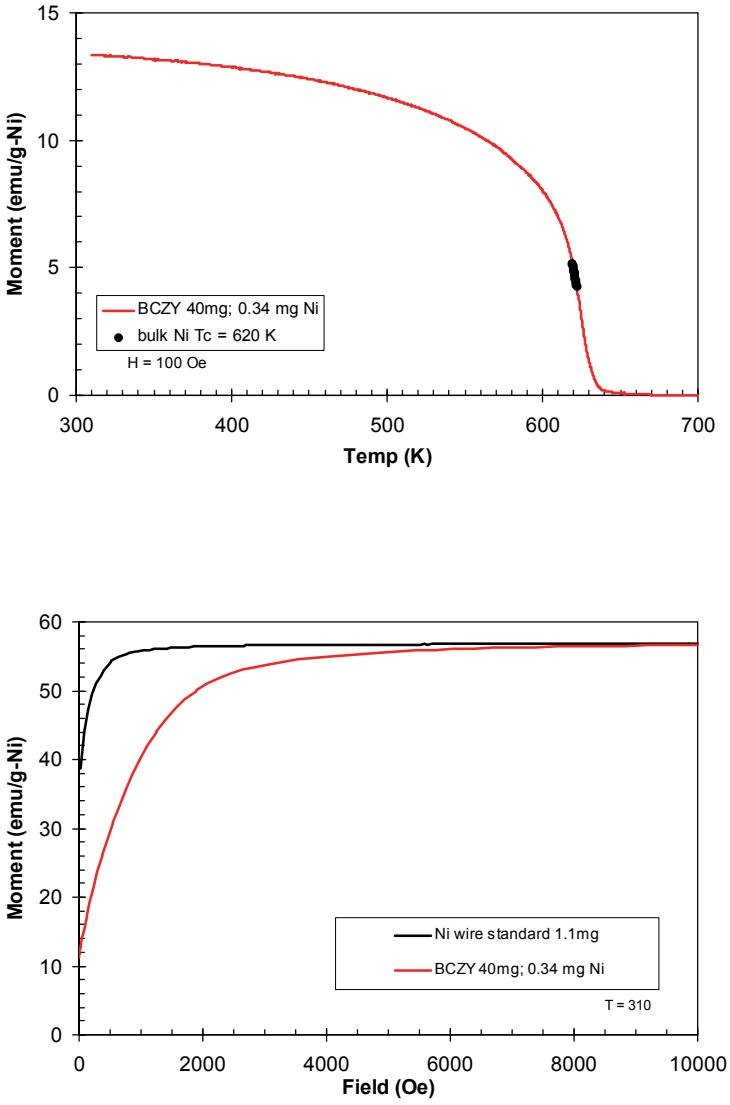

Fig. 13. Reduced NiRS-BCZY26 (top) magnetic moment vs. temperature at fixed field 100 Oe and (bottom) vs. field at fixed temperature (310 K) by QD-PPMS.

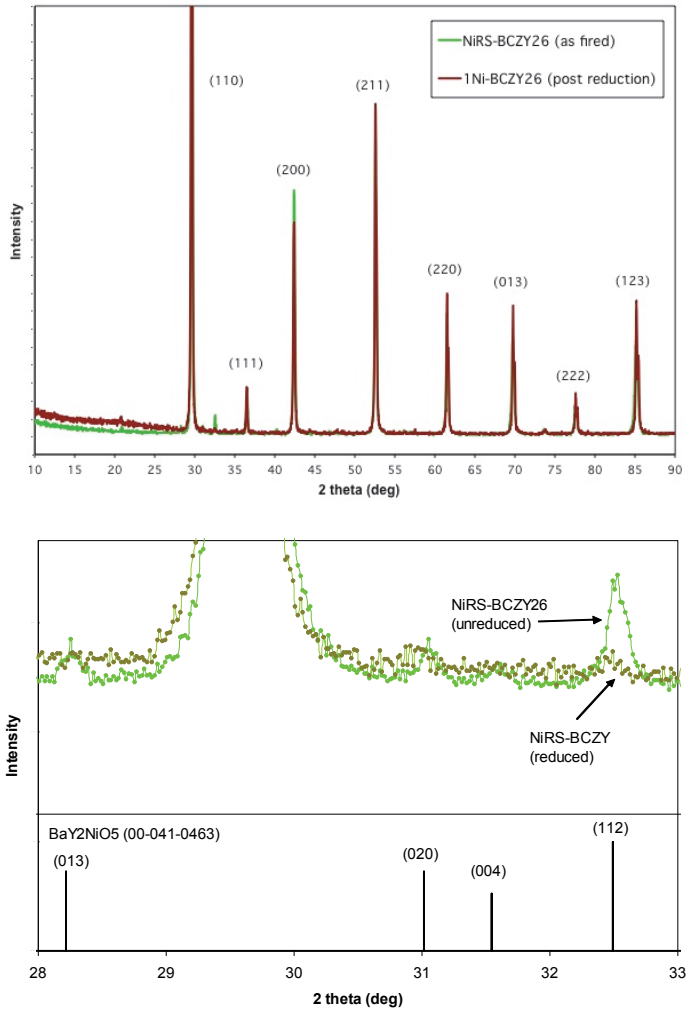

Fig. 14. NiRS-BCZY26 XRD as-fired (light green) and after reduction (dark green) Top figure 10-90° 2 θ and lower pattern 28-33° with four strongest peaks of BaY_2NiO_5 (00-041-0463) pattern.

6. Conclusions

Several compositions of the solid solution $BaCe_xZr_{0.8-x}Y_{0.2}O_{3-d}$ ($0 \le x \le 0.8$) were prepared by solid state reactive sintering SSRS using 1 wt% NiO as a sintering additive. Dense, phase-pure ceramics were obtained with NiO while practically no solid-state reaction or sintering took place without NiO. It was found that a complete solid solution existed over the entire composition range, and it was observed that a linear relationship existed between the pseudocubic lattice constant and the ratio of ceria to ceria plus zirconia on B-sites:

a(Å)=0.194*[Ce]/([Ce]+[Zr])+4.204). A relatively weaker dependency of lattice constant on dopant ion was observed. XRD of as-fired ceramics exhibited BaY_2NiO_5 as the only identifiable second phase in the, otherwise, phase-pure perovskites. Thought to be a grain boundary phase, BaY_2NiO_3 was found to be reduced completely to metallic nickel precipitates that decorated grain boundaries after extended processing in moist and dry hydrogen at high temperatures. The mechanical strength of as-fired ceramic was excellent, while the strength of reduced material was considerably lower – a condition that warrants caution. Stoichiometric expansion due to frozen in hydration causes ceramic failure at low temperatures. However, substitution of $BaSO_4$ for $BaCO_3$ in the starting powders and reduction of yttria dopant concentration seem to hold promise as a solution to this problem. Further evaluation the grain boundary integrity is necessary as these materials are being considered for practical applications. It may be necessary to add other components to compensate for loss of strength at grain boundaries. NiO solid state reactive sintering was demonstrated to be a remarkably easy and inexpensive way to fabricate this potentially important class of protonic perovskites.

7. Acknowledgments

Special thanks Sophie Menzer and Anthony Manerbino at CoorsTek, Inc. for fabricating and evaluating specimens. Thanks to Josh White for providing FESEMs and to Prof. Brian Gorman at the Colorado School of Mines for FIB specimen preparation and HRTEM, and to Jim O'Brien at Quantum Design, San Diego, CA for providing quantitative magnetometry analysis on reduced specimens.

8. References

Azimova, M. & McIntosh, S. (2009). Transport properties and stability of cobalt doped proton conducting oxides. *Solid State Ionics,* Vol.180[2-3], pp.160-167

Babilo, P. & Haile, S.M. (2005). Enhanced sintering of yttrium-doped barium zirconate by addition of ZnO. *J. Am. Ceram. Soc*., Vol.88, No.9, pp.2362-2368

Coors W.G. & Swartzlander, R. (2005). Partial conductivity measurements in $BaCe_{0.9}Y_{0.1}O_{3-d}$ by impedance spectroscopy. *Proceedings of the 26th Risø International Symposium on Materials Science: Solid State Electrochemistry*, Linderoth, et al., Eds., September 4-8, pp.185-196

Coors, W.G.; Zhao, F.; Heck, B. (April 2008). Reaction sintered BCY10 ceramic – Fabrication and microstructure," Internal CoorsTek Report (available from author upon request)

Coors, W.G. (Sept 2008). Reaction sintered BZY10 ceramic - Fabrication and microstructure, Internal CoorsTek Report, (available from author upon request)

Coors, W.G.; O'Brien, J.; & White, J. (2009). Conductivity degradation of NiO-containing 8YSZ and 10YSZ electrolyte during reduction. *Solid State Ionics,* Vol.180, pp.246-251

Costa, R.; Grünbaum, N.; Berger, M.-H.; Dessemond, L.; Thorel, A. (2009). On the use of NiO as sintering additive for $BaCe_{0.9}Y_{0.1}O_{3-a}$. *Solid State Ionics,* Vol.180, pp.891-895

Galasso, F.S. (1969) *Structure, Properties and Preparation of Perovskite-type Compounds*, Pergamon Press, Ltd.,

Guo, Y.; Lin, Y.; Ran, R.; Shao, Z. (2009). Zirconium doping effect on the performance of proton-conducting $BaZr_yCe_{(0.8-y)}Y_{0.2}O_{3-\square}$ ($0.0 \leq y \leq 0.8$) for fuel cell applications. *J. Power Sources*, Vol.193, pp.400-407

Irvine, J; Tao, S.; Savaniu, C.; & Kruth, A. (2007). Steam Electrolysis, US Patent Application 2007/0278092, Dec. 6, 2007

Iwahara, H.; Uchida, H.; Ono, K.; & Ogaki, K. (February 1988). Proton conduction in sintered oxides based on $BaCeO_3$. *J. Electrochem. Soc.: Solid State Science and Technology*, pp.529-533

Katahira, K.; Kohchi, Y.; Shimura, T.; & Iwahara, H. (2000). Protonic conduction in Zr-substituted $BaCeO_3$. *Solid State Ionics*, Vol.138, pp.91-98

Kingery, W.D.; Bowen, H.K.; & Uhlmann, D.R. (1960) *Introduction to Ceramics*, (2nd Ed.), John Wiley & Sons, ISBN 0-471-47860-1, p.448

Kreuer, K.-D. (1999). Aspects of the formation and mobility of protonic charge carriers and the stability of perovskite-type oxides. *Solid State Ionics*, Vol.125, pp.285-302

Kreuer, K.-D. (2003). Proton-conducting oxides. *Annu. Rev. Mater. Rev.,* Vol.33, pp.333-359

Magrez, A. & Schober, T. (2004). Preparation, sintering, and water incorporation of proton conducting $Ba_{0.99}Zr_{0.8}Y_{0.2}O_{3-\square}$, *Solid State Ionics*, Vol.175, pp.585-588

Munch, W.; Kreuer, K.-D.; Seifert, G.; & Maier, J. (2000). Proton diffusion in perovskites: Comparison between $BaCeO_3$, $BaZrO_3$, $SrTiO_3$, and $CaTiO_3$ using quantum molecular dynamics. *Solid State Ionics*, Vol.136-137, pp.183-189

Ryu, K. & Haile, S. (1999). Chemical stability and proton conductivity of doped $BaCeO_3$ – $BaZrO_3$ solid solutions. *Solid State Ionics*, Vol.125, pp.355-367

Ricote, S.; Bonanos, N.; Marco de Lucas, M.C.; Caboche, G. (2009). Structural and conductivity Study of the proton conductor $BaCe_{(0.9-x)}Zr_xY_{0.1}O_{3-\square}$ at intermediate temperatures. *J. Power Sources,* Vol.193, pp.189-193

Ricote, S.; Bonanos, N.; Caboche, G. (2009). Water vapour solubility and conductivity study of the proton conductor $BaCe_{(0.9-x)}Zr_xY_{0.1}O_{3-\square}$,. *Solid State Ionics,* Vol.180, pp.990-997

Ricote, S.; Bonanos, N.; Wang, H.J.; Haugsrud, R. (2011). Conductivity, transport number measurements and hydration thermodynamics of $BaCe_{0.2}Zr_{0.7}Y_{(0.1-x)}Ni_xO_{(3-d)}$. *Solid State Ionics,* Vol.185, pp.11-17

Schober, T. & Bohn, H. (2000). Water vapor solubility and electrochemical characterization of the high temperature proton conductor $BaZr_{0.9}Y_{0.1}O_{2.95}$. *Solid State Ionics*, Vol.127, pp.351-360

Schober, T. (2005). Transformation of an oxygen ion conductor to a proton conductor by solid state reaction. *Solid State Ionics*, Vol.176, pp.2275-2277

Shimura, T.; Tanaka, H.; Matsumoto, H.; & Yogo, T. (2005). Influence of the transition-metal doping on conductivity of a $BaCeO_3$-based proton conductor. *Solid State Ionics* Vol.176, pp.2945-2950

Swartzlander, R. & Coors, W.G. (2009). Preparation of yttria-stabilized zirconia reaction sintered products. US Patent 7,527,761, May 5, 2009

Tao, S. & Irvine, J. (2006). A stable, easily sintered proton-conducting oxide electrolyte for moderate-temperature fuel cells and electrolyzers. *Advanced Materials,* Vol.18, pp.1581-1584

Tao, S. & Irvine, J. (2007). Conductivity studies of dense yttrium-doped $BaZrO_3$ sintered at 1325 °C. *J. Solid State Chem.,* Vol.180, pp.3493-3503

Tong, J.; Clark, D.; Bernau, L.; Subramaniyan, A. & O'Hayre, R. (2010). Proton-conducting yttrum-doped barium cerate ceramics synthesized by a cost-effective solid-state reactive sintering method. *Solid State Ionics*, Vol.181, pp.1486-1498

Tong, J.; Clark, D.; Hoban, M.; & O'Hayre, R. (2010). Cost-effective solid-state reactive sintering method for high conductivity proton conducting yttrium-doped barium zirconium ceramics. *Solid State Ionics*, Vol.181, pp.496-503

Tong, J.; Clark, D.; Bernau, L.; Sanders, M.; & O'Hayre, R. (2010). Solid-state reactive sintering mechanism for large-grained yttrium-doped barium zirconate proton conductiving ceramics. *J. Mater. Chem.*, Vol.20, pp.6333-6341

Wang, H.; Peng, R.; Wu, X.; Hu, J.; & Xia, C. (2009). Sintering behavior and conductivity of yttrium-doped $BaCeO_3$-$BaZrO_3$ solid solutions using ZnO additives. *J. Am. Ceram. Soc.*, Vol.92, No.11, pp.2623-2629

Wienströer, S. & Wiemhöfer, H.-D. (1997). Investigation of the influence of zirconium substitution on the properties of neodymium-doped barium cerates. *Solid State Ionics*, Vol.101-103, pp.1113-1117

Xu, X.; Tao, S.; & Irvine, J. (2010). Proton conductivity of potassium doped barium zirconates. *J. Solid State Chem.*, Vol.183, pp.93-98

Yamazaki, Y.; Hernandez-Sanchez, R.; Haile, S. (2009). High total proton conductivity in large-grained yttrium-doped barium zirconate. *Chem. Mater.*, Vol.21, pp.2755-2762

Zhong, Z. (2007). Stability and conductivity of the $BaCe_{0.9-x}Zr_xY_{0.1}O_{2.95}$ systems. *Solid State Ionics*, Vol.178, pp.213-230

22

Co-Ionic Conduction in Protonic Ceramics of the Solid Solution, $BaCe_{(x)}Zr_{(y-x)}Y_{(1-y)}O_{3-\delta}$ Part II: Co-Ionic Conduction

W. Grover Coors
CoorsTek, Inc
USA

1. Intoduction

BCZY protonic ceramics described in the previous chapter constitute a class of model co-ionic conductors, meaning their transport properties are determined almost exclusively by two ionic species, protons and oxygen ion vacancies. The co-ionic conduction regime is a range of moist atmospheres spanning about 15 orders of magnitude of oxygen pressure, from $10^{-20} < pO_2 < 10^{-5}$ atm., where the total conductivity is independent of oxygen pressure. Evaluation of transport properties in these materials requires new techniques not typically required for traditional ion conductors, or even mixed ionic/electronic conductors. In this chapter, a model for co-ionic conduction, called the CIC model, is proposed that provides both a qualitative and a quantitative understanding of these commercially important ceramic materials. In the last section, the model will be used to deconstruct total conductivity measurements on BCZY27 to obtain partial conductivities as a function of temperature.

Arrhenius analysis is a powerful scientific technique for studying transport properties in ceramic ion conductors. The self-diffusivity of a particular ionic species can be described by,

$$D_i = D^* \exp\left(-\frac{E_a}{k_B T}\right) \tag{1}$$

where D^* is a temperature-independent constant and E_a is the activation energy for migration of the ionic species in the lattice. When log D_i is plotted against reciprorocal temperature, a straight line is obtained where D^* may be found as the y-axis intercept at "infinite" temperature, and E_a may be determined from the slope of the line. Unfortunately, it is often quite difficult to obtain self-diffusivities directly from experiments. Indirect methods are used – most commonly, conductivity measurements, which are easy to make as a function of temperature and surrounding atmosphere. Self-diffusivity and conductivity are related by the well-known Nernst-Einstein relationship,

$$\sigma_i = \left(\frac{z_i^2 F^2 c_i}{RT}\right) D_i \tag{2}$$

It is observed immediately that the proportionality between conductivity and diffusivity involves the concentration of the ionic species. In most cases with ceramic ion conductors, the species concentrations are fixed by a known concentration of extrinsic dopants, which is practically constant over a wide range of operating temperatures, making Arrhenius analysis from conductivity data straightforward and convenient. However, when concentrations of ionic species change appreciably with temperature, traditional Arrhenius analysis is no longer valid. Only in special cases, where the dependence of species concentrations on temperature and pressure is known, can the relationship between conductivity and self-diffusivity be determined. In protonic ceramics, both oxygen ion vacancies and protons are simultaneously present in the lattice, and their respective concentrations depend on the degree of hydration of the host ceramic. Correspondingly, the degree of hydration has a strong dependence on temperature and the surrounding gas atmosphere and can vary spatially throughout the material. However, the respective concentrations of protons and oxygen ion vacancies are not independent. Instead, they are found to change relative to one another in a predictable way. This fixed relationship can be exploited for interpreting conductivity data obtained on protonic ceramic co-ionic conductors and correlating it to species self-diffusivities. Finally, even though many important applications for protonic ceramics are in high pO_2 atmospheres, once the self-diffusivities of protons and oxygen ion vacancies have been determined in the co-ionic regime, the contribution from electronic defects can be inferred by subtraction from the total conductivity at low or high pO_2.

2. Isobaric hydration

The BCZY perovskite ceramics described in Part I contain some compliment of oxygen ion vacancies and electron holes after sintering in air. Y^{3+} ions that substitute on the regular Ce^{+4} and Zr^{+4} B-sites carry an effective negative charge designated by $[Y'_{Ce,Zr}]$ in Kröger-Vink notation. Electroneutrality in the lattice requires charge compensation that results in extrinsic oxygen ion vacancies of double positive effective charge, $[V_O^{\bullet\bullet}]_{extrinsic}$ – one vacancy created for every two substituted dopant ions. A subsequent hydration step is necessary to insert protons into the lattice by means of an exchange reaction with water vapor at the surface of the ceramic. This occurs by the Wagner reaction (Wagner, 1968),

$$H_2O(g) + V_O^{\bullet\bullet} + O_O^{\times} \leftrightarrow 2OH_O^{\bullet} \tag{3}$$

The process of hydration requires the annihilation of an oxygen ion vacancy at the surface (while dehydration requires the creation of an oxygen vacancy). In the process, quasi-free protons are introduced into (or removed from) the oxygen ion sublattice, designated by $[OH_O^{\bullet}]$. Electroneutrality requires that the sum of oxygen vacancies and protons be conservered.

$$2\left[V_O^{\bullet\bullet}\right] + \left[OH_O^{\bullet}\right] = \left[Y'_{Ce,Zr}\right] \tag{4}$$

All of the yttrium ions in this case are assumed to reside only on cerium or zirconium B-sites, and it is equally probable that either Ce^{+4} or Zr^{+4} will otherwise occupy the sites in the solid solution. Although the total concentration of oxygen vacancies and protons is fixed,

their relative concentrations may vary, so that an ensemble of two independent mobile ionic species may be present in the ceramic. As straightforward as it may seem, this phenomenon of coexistence of two mobile ionic species in oxide ceramics leads to unusual behavior.

The defect chemistry of protonic ceramics is further complicated by the presence of electronic defects. For example, n-type conductivity may be introduced in very dry atmosphere at low oxygen pressure and high temperatures – a condition not typically encountered where proton conductors are likely to be used. Electron holes, on the other hand, are generated at moderate oxygen pressure by the reaction,

$$\tfrac{1}{2}O_2(g) + V_O^{\bullet\bullet} \rightarrow O_O^{\times} + 2h^{\bullet} \tag{5}$$

These holes may subsequently be annihilated by water vapor by the reaction,

$$H_2O(g) + 2h^{\bullet} + 2O_O^{\times} \rightarrow \tfrac{1}{2}O_2(g) + 2OH_O^{\bullet} \tag{6}$$

The summation of Eq. 5 and Eq. 6 gives Eq. 3, and it is possible (and perhaps, likely) that Wagner hydration actually occurs by this two-step process. Not all ceramic oxides with oxygen vacancies undergo Wagner hydration. In fact, the phenomenon seems to be restricted to a relatively small group of ceramics, possibly pointing to the important role played by holes in the overall hydration process. Recently, Yoo and colleagues (Yoo, et al. 2009) have proposed that holes play a fundamental role in the transient behaviour of hydration in protonic ceramics upon sudden changes in pH_2O. However, since holes are created and subsequently annihilated, their concentration at equilibrium is low in moist atmosphere at intermediate oxygen pressure ($pO_2 < 10^{-5}$ atm). For this reason, by assuming equilibrium under fixed water vapor pressure, the contribution of electronic defects to total conductivity may generally be neglected at equilibrium. On the other hand, holes are expected to contribute to ambipolar diffusion at higher pO_2. A comprehensive theory for multi-species transport in ceramic proton conductors was originally proposed by Tan (Tan et al., 2000) and more recently expanded by Sanders (Sanders & O'Hayre, 2009).

The CIC model only applies in the ionic regime of the Kröger-Vink diagram where defect concentrations are independent of oxygen pressure. Wagner hydration occurs by Eq. 3, where hydration and dehydration at equilibrium depend on temperature and water vapor partial pressure as well as the concentration of oxygen ion vacancies at the surface according to the mass action law,

$$K_{eq} = \frac{\left[OH_O^{\bullet}\right]^2}{p_{H_2O}\left[O_O^{\times}\right]\left[V_O^{\bullet\bullet}\right]} \tag{7}$$

The usual thermodynamic meaning applies,

$$-RT\ln K_{eq} = \Delta G = \Delta H - T\Delta S \tag{8}$$

Brackets refer to mole fractions. Molar concentrations are obtained by dividing by the molar volume. In the crystalline lattice, oxygen ion sites are conserved so the molar volume V_m is equivalent to N_a times the unit cell volume V_c of the cubic ABO_3 perovskite. The fraction of extrinsic oxygen vacancies "stuffed" by water molecules is defined as the extent of

hydration, Chi (χ), where $0 < \chi < 1$. Two protons are generated for each oxygen vacancy "stuffed", and there are two dopant ions required for every oxygen ion vacancy.

$$\chi = \frac{[H_2O]}{\left[V_{O,extrinsic}^{\bullet\bullet}\right]} = \frac{\left[OH_O^{\bullet}\right]}{\left[Y'_{Ce,Zr}\right]} \quad ; 0 \le \chi \le 1 \tag{9}$$

At equilibrium, the extent of hydration, χ, is a strong function of temperature and water vapor pressure. Its value may be calculated using the formula derived by Kreuer, obtained by inserting the O-site conservation and electroneutrality condition into Eq. 7 (Kreuer, 1999).

$$\chi = \frac{3K - \sqrt{K(9K - 6KS + KS^2 + 24S - 4S^2)}}{(K-4)S} \tag{10}$$

$K \equiv K_{eq} p_{H_2O}$. The partial pressure of water vapor p_{H_2O} is at the gas/solid interface and K_{eq} is the equilibrium constant for Eq. 3. (If hydration occurs by the two step process of Eq. 5 and Eq. 6, then $K_{eq} = K_{eq,5}\ K_{eq,6}$). The constant S is the fraction of dopant ions per formula unit, equal to $\left[Y'_{Ce,Zr}\right]$ in the absence of electronic defects or A-site substitution. For BCZY doped with 10 mol% yttria, $S = 0.1$. When χ is plotted as a function of temperature, a sigmoidal curve is produced. At high temperatures the ceramic becomes dehydrated ($\chi \rightarrow 0$), and at low temperatures, the hydration is "frozen in" at the hydration limit ($\chi \rightarrow 1$). This is an idealization since, as a practical matter, the limits of total hydration and dehydration are not thermodynamically achievable. Some residual vacancies and some residual hydration will always be present. The value of χ as a function of temperature may be determined experimentally by either isobaric thermogravimetry or dilatometry. Alternatively, it may be determined by curve fitting of total conductivity data. This latter technique has been explored with some success on rare earth calcium-doped niobates by Haugsrud (Haugsrud & Norby, 2006).

3. Partial conductivities

Extent of hydration is related to defect concentrations in units of mol/cm^3 by,

$$c_{OH_O^{\bullet}} = \frac{S}{V_m}\chi \quad ; \quad c_{V_O^{\bullet\bullet}} = \frac{S}{V_m}\frac{(1-\chi)}{2} \tag{11}$$

Substituting the concentrations from Eq. 11 into the Nernst-Einstein relationship (remembering that z^2 is 1 for protons and 4 for oxygen ion vacancies) leads to the partial conductivities,

$$\sigma_{OH_O^{\bullet}} = \left(\frac{1}{T}\right)\beta\,\chi\,D_{OH}^{\circ}\exp\left(-\frac{E_{a,OH}}{k_B T}\right) \tag{12}$$

$$\sigma_{V_O^{\bullet\bullet}} = \left(\frac{1}{T}\right)\beta\,2(1-\chi)\,D_V^{\circ}\exp\left(-\frac{E_{a,Vo}}{k_B T}\right) \tag{13}$$

D_{OH}° and D_{V}° [cm²/s] are temperature independent, pre-exponential self-diffusion coefficients, and $E_{a,OH}$ and $E_{a,Vo}$ are the corresponding activation energies for migration. β is a constant for a given ceramic material evaluated as,

$$\beta = \frac{F^2 S}{R V_m} = \frac{e^2 S}{k_B V_c} \left[\frac{\mathrm{K\,s}}{\Omega\,\mathrm{cm}^3} \right] \tag{14}$$

where F is Faraday's constant, R is the universal gas constant, e is the elementary charge, k_B is Boltzmann's constant, V_m is the molar volume, and V_c is the cubic ABO_3 unit cell volume in cm³. It is observed that the dimensionality of β is consistent so that when multiplied by D/T, in units of cm²/K.s, the proper units of conductivity, $(\Omega\ \mathrm{cm})^{-1}$, are obtained.
The co-ionic conduction model treats the total conductivity as the sum of only the two ionic species.

$$\sigma_{tot} = \sigma_{OH_O^{\bullet}} + \sigma_{V_O^{\bullet\bullet}} \tag{15}$$

By combining partial conductivities (Eq. 12 and 13), an important linear relationship between σ_{tot} and χ is found,

$$\sigma_{tot} T = \beta \chi \left(D_{OH_O^{\bullet}} - 2 D_{V_O^{\bullet\bullet}} \right) + 2 \beta D_{V_O^{\bullet\bullet}} \tag{16}$$

In the limit of complete hydration, the total conductivity is equal to the proton conductivity, and in the limit of complete dehydration, the total conductivity is equal to the oxygen ion vacancy conductivity. At intermediate extent of hydration, the total conductivity reflects the ionic species ensemble. χ is constant at steady state once equilibrium with the surrounding atmosphere is reached. Under transient conditions, such as when temperature and water vapor pressure change or a water vapour pressure gradient is imposed, χ is a local variable that depends on position and time within the ceramic. Using Eq. 16, it is possible to determine the partial conductivities from total conductivity measurements if extent of hydration is known as a function of temperature. The determination of partial conductivities of protons and oxygen ion vacancies and proton transference number is important for electrochemical applications such as protonic ceramic fuel cells, steam electrolyzers, and hydrogen separation membranes; but it is also important for steam permeable membranes (Coors, 2007) since one important consequence of having two, independent, mobile ionic species is the possibility of ambipolar water diffusion.
It is necessary to stress an important point about applying the Nernst-Einstein equation to an ensemble of mobile ionic species by the preceding derivation. Equations 12 and 13 imply that protons and oxygen ion vacancies may diffuse independently. In the conductivity experiment this condition is met by using electrodes that are reversible to both species, which requires electrochemical redox reactions at the surface for both hydrogen and oxygen independently. However, the Wagner reaction (Eq. 3) is not an electrochemical redox reaction. That is, no electrons flow into an external circuit, and electrodes are, therefore, not required for hydration and dehydration. The Wagner reaction only describes the chemical interaction of the ceramic with water vapor and the relative defect concentrations that ensue. In the absence of electrodes, Eq. 16 still applies, as diffusion is constrained by electroneutrality resulting in chemical diffusion of water, but the partial conductivities are no longer defined by electrode potentials.

The protonic transference number is defined as,

$$t_{proton} \equiv \frac{\sigma_{OH_O^\bullet}}{\sigma_{OH_O^\bullet} + \sigma_{V_O^{\bullet\bullet}}} = \frac{1}{1 + \frac{2(1-\chi)}{\chi}\left(\frac{D_V}{D_{OH}}\right)} \tag{17}$$

Protonic transference number, it is observed, is not a constant, but a function of concentration - that is, the extent of hydration. Extent of hydration (Eq. 10) and proton transference number (Eq. 17) both have the same sigmoidal functional form. In fact, it may be seen for the special case where the self-diffusivity of oxygen ion vacancies is exactly half that of proton diffusivity, $D_V / D_{OH} = \frac{1}{2}$, that t_{proton} is identical to χ.

The co-ionic conduction model is highly idealized, containing several fundamental underlying assumptions:

1. Conduction due to electrons and holes is neglected. This assumption is valid under moist atmosphere as long as the temperature and oxygen pressure are not too high or too low.
2. Mobile $OH_O^\bullet$ and $V_O^{\bullet\bullet}$ defects each have a single, temperature-independent pre-exponential diffusion constant and activation energy, which is also independent of atmosphere. Strictly speaking, this assumption is valid only at equilibrium in the dilute limit, where the concentration of defects is low enough so that they do not interact with one another. Also, the crystal lattice is known to expand when protonic ceramics hydrate, causing a change in migration enthalpy. This effect has been neglected in the present model.
3. The total concentration of $OH_O^\bullet$ plus $V_O^{\bullet\bullet}$ is fixed by the extrinsic dopant concentration. Furthermore, all dopant ions are assumed to reside exclusively on B-sites in the ABO_3 perovskite.
4. Extent of hydration χ, is a temperature- and water vapor pressure-dependent variable that is determined by an equilibrium constant for hydration with a constant value of enthalpy and entropy. $\left[OH_O^\bullet\right] \propto \chi$ and $\left[V_O^{\bullet\bullet}\right] \propto (1-\chi)$

With these four assumptions, it is possible to develop a useful analytical model that yields further insight into co-ionic conduction. Despite its apparent simplicity, the model is deceptively complex due to the exponential terms, which make routine algebraic evaluation impossible. Fortunately, the execution of the model can be carried out with ease in a spreadsheet like Microsoft Excel.

4. Hydration and dehydration

Co-ionic conduction is obviously only possible when protons and oxygen vacancies co-exist in the lattice. At equilibrium, the Wagner reaction is assumed to be thermodynamically reversible, so that at constant water vapor pressure, the ratio of protons to oxygen vacancies depends only on temperature. If no hydration were to occur, only oxygen vacancies would be present and the material would behave just like an ordinary oxygen ion conductor. If dehydration did not occur - that is, if hydrogen, rather than water vapor, could enter the lattice directly by a different mechanism - proton conduction would prevail at all

temperatures. Defect reactions of this type are only possible in very dry hydrogen in ceramic proton conductors or, as pointed out by Tan (Tan, et al. 2000) mixed proton-hole conduction is possible when a pO_2 concentration gradient is present.

The details of how the ratio of protons to oxygen vacancies changes with temperature are captured in Kreuer's formula for isobaric degree of hydration. From Eq. 10 it may be shown that hydration achieves a saturation value at low temperatures, where the protonic defect concentration is frozen in, i.e. $\chi \rightarrow 1$ as $T \rightarrow 0$. Eq. 10 also requires that $\chi \rightarrow 0$ as $T \rightarrow \infty$. Complete dehydration in these materials typically occurs below 1200 ^{o}C, but there is no fundamental requirement for total dehydration to take place below the melting point. This equation generates a sigmoidal plot versus temperature with a characteristic inflection at the mid-point. The temperature at the inflection point, T_c, is a strong function of hydration enthalpy. Figure 1 shows plots of Eq. 10 at pH_2O = 0.025 atm for three different hydration enthalpies (ΔH = -80, -100, and -120 kJ/mol) at constant entropy (ΔS = -120 J/mol.K). It may be seen that a change in ΔH of only 40 kJ/mol causes a 400 ^{o}C translation of T_c. The slope of the curve in the transition region is determined by the hydration entropy. Figure 2 shows this effect for ΔS = -80, -120, and -160 J/mol.K, where the enthalpy has been adjusted so that each curve has the same inflection point. It is observed that the hydration/dehydration transition becomes more abrupt as the reaction entropy becomes more negative, but the effect is not nearly as pronounced as for different enthalpies.

Total conductivity vs. temperature measurements of ceramic proton conductors are routinely made and reported in the literature, but often with little underlying recognition of the consequences of co-ionic conduction. This has resulted in confusion in interpretation of Arrhenius plots. Only recently has it become more widely recognized that there is a requirement for deconvolving partial conductivities from the total conductivity data. This can be a formidable challenge. Looking at Eqs. 12 and 13 it may be observed that these coupled equations contain one common unknown variable, χ, and two decoupled unknown parameters for each species - the pre-exponentials and migration activation energies. At low temperature, in moist atmosphere, it is generally valid to assume that the total conductivity is due to protonic conduction alone (Eq. 12). Thus, the bulk protonic activation energy, $E_{a,OH}$, may be immediately determined from the slope of the Arrhenius conductivity plot at low temperature. The pre-exponential D_{OH}, however, cannot be determined from the extrapolation of the low temperature plot to the y-axis, as is usually done with single-ion conduction data, without knowing the terminal hydration limit, χ as $T \rightarrow 0$. Variations in this value will shift the low temperature portion of the curve up and down, moving the intercept. At high temperatures in dry atmosphere, it is often safe to assume that conduction is due to oxygen vacancies alone (Eq. 13). In this case, the activation energy, $E_{a,Vo}$, may be determined by the slope. The pre-exponential, D_{Vo}, may be determined by the y-intercept of the extrapolation of the high temperature portion of the curve since, in this case, it may also be generally assumed that the ceramic is essentially dehydrated so that $\chi \approx 0$. However, caution must be exercised if either the hydration enthalpy is strongly negative or the entropy is not too negative, as evident from Figure 1. Once the self-diffusivities of protons and oxygen ion vacancies are determined at the high and low temperature extremes, the portion of the conductivity plot at intermediate temperatures, where χ is variable, must provide a smooth transition that obeys Eq. 16 at all temperatures. This reflects the fact that the species partial conductivities are not constant. The total conductivity is the sum of the two partial conductivities at a given temperature. The important features are apparent at intermediate temperatures, where proton conductivity reaches a maximum before dropping at higher temperatures due to dehydration, and oxygen vacancy conduction begins to

dominate. The oxygen ion vacancy partial conductivity curve is characterized by a "dog leg" caused by an increase in oxygen vacancy concentration due to dehydration. The sum of the two curves produces the characteristic "crook" often observed in conductivity plots of these materials. Many examples of co-ionic conduction are seen in the literature exhibiting this hydration/dehydration "crook". A good example is shown in Fig. 16 of Kreuer's 2003 review on Proton-Conducting Oxides (Kreuer, 2003), where this behavior is clearly visible in the total conductivity portion of each of the plots. The co-ionic conductivity model provides a good qualitative understanding of this phenomenon.

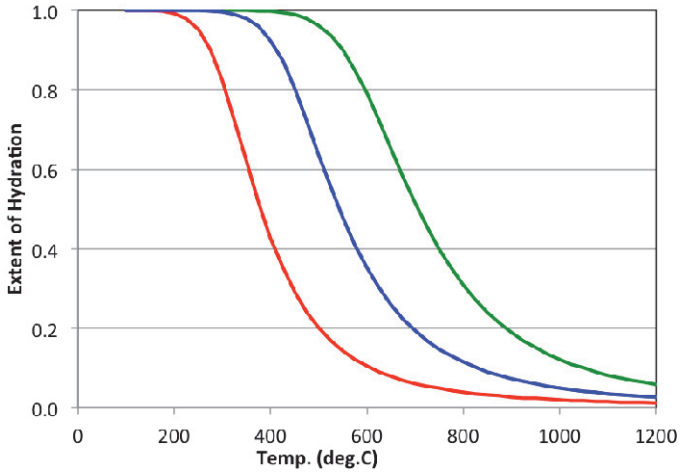

Fig. 1. Extent of hydration vs. temperature by Eq. 10 (isobaric p_{H2O} = 0.025 atm).ΔH = -80 (red), -100 (blue), -120 (green) kJ/mol, with constant ΔS = -120 J/mol.K.

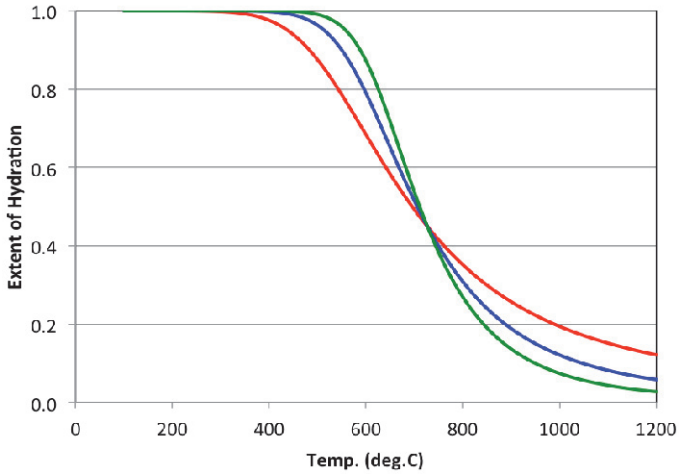

Fig. 2. Extent of hydration vs. temperature by Eq. 10 (isobaric p_{H2O} = 0.025 atm). ΔS [J/mol.K], ΔH [kJ/mol] = -80, -80 (red), -120, -120 (blue), -160, -160 (green).

5. Ambipolar diffusion

Ambipolar diffusion occurs in the co-ionic ensemble with chemical diffusivity derived by Kreuer (Kreuer, 1999).

$$\tilde{D}_{H_2O} = \frac{(2-\chi) D_{OH_O^\bullet} D_{V_O^{\bullet\bullet}}}{\chi D_{OH_O^\bullet} + 2(1-\chi) D_{V_O^{\bullet\bullet}}} \tag{18}$$

$D_{OH_O^\bullet} = D^*_{OH} \exp\left(-E_{a,OH}/k_B T\right)$ and $D_{V_O^{\bullet\bullet}} = D^*_V \exp\left(-E_{a,V}/k_B T\right)$ where D^*_{OH} and D^*_V are the temperature independent, pre-exponential self-diffusion coefficients [cm²/s], and $E_{a,OH}$ and $E_{a,Vo}$ are the corresponding activation energies for migration of protons and oxygen ion vacancies, respectively. It is interesting to consider the derivative of the chemical diffusivity with respect to extent of hydration,

$$\frac{d\tilde{D}_{H_2O}}{d\chi} = \frac{-2 D_{OH_O^\bullet} D_{V_O^{\bullet\bullet}} \left(D_{OH_O^\bullet} - D_{V_O^{\bullet\bullet}}\right)}{\left[\chi D_{OH_O^\bullet} - 2 D_{V_O^{\bullet\bullet}} (1-\chi)\right]^2} \tag{19}$$

Surprisingly, this derivative has no roots. So, unlike proton conductivity, there is no value of χ between 0 and 1 that produces a maximum in chemical diffusivity. This unusual behavior results from the exact cancellation of all terms containing χ in the numerator, and shows that ambipolar diffusion must increase monotonically with temperature.
It is seen in Eq. 11 that χ and concentration are proportional, making it possible to cast Fick's 2nd Law in the more convenient dimensionless variable, χ which has implicit dependency on time and space variables, $\chi = \chi(r,t)$.

$$\frac{\partial \chi}{\partial t} = \nabla\left(\tilde{D}_{H_2O}(\chi) \nabla \chi\right) \tag{20}$$

Eq. 20 must be solved numerically because the spatial derivatives of Eq. 18 result in nonlinear coefficients. At steady state, the concentration gradient is stationary, and Eq. 20 may be integrated to give the spatial dependence of $\tilde{D}_{H_2O}$ across the membrane. In the absence of an externally applied electrical potential, the effective steam permeation flux (in units of mol/cm2.s) may be found.

$$J_{H_2O} = -\tilde{D}_{H_2O}(c) \nabla c = -\frac{S}{2 V_m \Delta x} \int_{\chi_1}^{\chi_2} \frac{(2-\chi) D_{OH_O^\bullet} D_{V_O^{\bullet\bullet}}}{\chi D_{OH_O^\bullet} + 2(1-\chi) D_{V_O^{\bullet\bullet}}} d\chi \tag{21}$$

In one dimension, Δx is the electrolyte membrane thickness and $dc(H_2O) = (S/2V_m) d\chi$. χ_1 and χ_2 are the extent of hydration at the respective gas/solid interfaces of the membrane ($\chi_2 \geq \chi_1$). The concentration of dopant ions is proportional to the proton concentration, but two protons make one effective "water" in the lattice – thus, the additional factor of 2 in the denominator. Eq. 21 may be solved analytically (the complete solution may be found in (Coors, 2004)), but a much more intuitive form may be obtained if partial conductivities are substituted for partial diffusivities. This is only strictly valid for the case of uniform

temperature and where the steam gradient is small. This simplification permits the partial conductivities to be moved out of the integral and mathematically separates conductivity from extent of hydration. The result is given in Eq. 22 and 23.

$$J_{H_2O} = -\frac{RT}{4F^2\Delta x}\left(\frac{\sigma_{OH}\sigma_{Vo}}{\sigma_{OH}+\sigma_{Vo}}\right)\int_{\chi_1}^{\chi_2}\frac{(2-\chi)}{\chi(1-\chi)}d\chi \tag{22}$$

$$J_{H_2O} = -\frac{RT}{4F^2\Delta x}\left(\frac{\sigma_{OH}\sigma_{Vo}}{\sigma_{OH}+\sigma_{Vo}}\right)\ln\left[\frac{\chi_2^2(1-\chi_1)}{\chi_1^2(1-\chi_2)}\right]; \quad (0<\chi<1) \tag{23}$$

As can be seen by this simplification, the steam flux only depends on the extent of hydration at the interfaces. The term containing the partial conductivities in Eq. 23 is characteristic of ambipolar diffusion. It is equivalent to $\sigma_{Vo}\, t_{proton}$. It may be observed that the magnitude of the flux is determined by the partial conductivity with the smaller value – generally the oxygen ion vacancy conductivity. The following logarithmic term, however, is peculiar to the behavior of steam permeable membranes. This term is an enhancement factor that is dominated by the square of the ratio of the extent of hydration at the interfaces. This serves to greatly enhance the steam flux beyond what would normally be expected. For example, with χ on the moist side equal 0.5 and χ on the dry side equal to 0.002, a steam flux enhancement of more than ten times is predicted. This is an important consideration when the dry side contains hydrocarbon species, because any steam that permeates will be quickly consumed. Although the steam permeation flux is generally small – on the order of 10 nmol/cm^2.s for typical values of the partial conductivities at 700 ^{o}C – the enhancement factor has the potential to boost the steam flux significantly.

6. Electrical characterization

6.1 Introduction

A co-ionic conduction model for protons and oxygen ion vacancies in protonic ceramic perovskites was presented in the previous section. Even in its most simplified form, six fitting parameters are still required: two self-diffusivity pre-exponentials, two migration activation energies, and hydration enthalpy and entropy. In this section a fitting procedure, based on isobaric, steady-state conductivity analysis over a wide temperature range is used for determining these parameters with experimental data for the proton conductor, BCZY27.

6.2 Conductivity experiments

The experiments for measuring conductivity and diffusivity are generally not the same. The distinction is subtle, and often leads to errors in interpreting experimental data. Conductivity measurements require electrodes and the measurement of the electrochemical potential gradient. On the other hand, hydration and dehydration occur by ambipolar diffusion, which does not require electrodes. The conductivity experiment generally presupposes a uniform, steady-state concentration of mobile defect species. Electrodes, reversible to hydrogen and electrons, provide an alternative way for protons to enter the lattice, perturbing the defect equilibrium in unanticipated ways. Generally specimens used

for conductivity measurements have large area, planar electrodes separated by a relatively thin specimen. Under well-equilibrated test conditions, in a balanced cell arrangement, with uniform atmosphere at each electrode, proton or mixed proton/hole conductivity may be measured once the extent of hydration reaches a steady-state value. For unbalanced cells with different water vapor or hydrogen pressure at each electrode, the measurement is no longer valid since a constant flux of steam is induced. Specifically, the Nernst potential cannot be used to determine the protonic transference number in this case as proposed by Norby (Norby, 1988; Sutija, et al., 1995).

For conductivity measurements of the co-ionic ensemble in ceramic proton conductors, electrodes must be placed so as not to perturb the defect concentrations. This has been accomplished in the present experiments by using a long, rod with circumferential electrodes placed at each end. This rod has a large surface area for optimal surface exchange with gaseous species, and a relatively small electrode area. Most importantly, diffusion occurs in the radial direction, and conductivity is measured in the axial direction – the direction of the electric field lines required for the conductivity measurement. This means that the conductance instrument measures the arithmetic mean conductance of the rod (Maier, 2004, p.229),

$$R^{-1} = \frac{2\pi}{L}\int_{r=0}^{r=R_b} \sigma(r)\, r\, dr \tag{24}$$

where R is the measured specimen resistance. Eq. 24 is valid as long as the conductivity depends only on the radial, and not the axial (z-axis), position along the length of the rod between the electrodes. Previously it was shown,

$$\sigma_{tot} T = \beta\chi\left(D_{OH_O^\bullet} - 2D_{V_O^{\bullet\bullet}}\right) + 2\beta D_{V_O^{\bullet\bullet}} \tag{16}$$

Inserting Eq. 16 into Eq. 24 provides the necessary bridge between the conductivity and diffusion experiments.

$$R^{-1} = \frac{2\pi\beta}{TL}\int_{r=0}^{r=R_b} \left[\left(D_{OH_O^\bullet} - 2D_{V_O^{\bullet\bullet}}\right)\chi(r) + 2\beta D_{V_O^{\bullet\bullet}}\right] r\, dr \tag{25}$$

Of course, $\chi(r, t)$ is not generally known except at steady-state. It must be determined by solving the diffusion equation (Eq. 20) subject to boundary and initial conditions,

$$\begin{aligned} &\chi(R_b, t > 0) = \chi^\circ \\ &\chi(r, t = 0) = \chi_i \\ &\chi(r, t \to \infty) = \chi^\circ \end{aligned} \tag{26}$$

The measurement of conductivity can only sense the mean conductivity of all the mobile species in the cross-section of the specimen between the electrodes. The concentration of defects may or may not be uniform depending on whether or not the specimen has reached thermodynamic equilibrium with the surrounding atmosphere. The important feature of the experiments described herein is that the partial conductivities of individual species may be extracted from the diffusion experiment because diffusion and migration are orthogonal –

diffusion is perpendicular to free surfaces (radial) and migration is perpendicular to the electrodes (axial). Direct current measurements cannot be employed here because the defects would become polarized in the axial direction. Low frequency a.c. is necessary so that, even though the charged defects oscillate back and forth in the axial direction, their average concentration does not change as long as the mean free path is short compared to the length of the specimen.

Isobaric conductivity measurements are made under constant p_{H_2O} and p_{H_2} atmosphere by changing temperature slowly enough to maintain defect equilibrium over the entire range of temperatures. Also, $\chi(T, p_{H_2O})$ must be known, which means that either $\Delta G^\circ(T, p_{H_2O})$ for hydration must be known in advance, or ΔG° must be determined empirically by fitting isobaric conductivity vs. temperature data. In this method, $D_{OH_O^\bullet}$ is determined by Arrhenius analysis of conductivity in the hydration limit ($\chi \rightarrow 1$) at low temperature and $D_{V_O^{\bullet\bullet}}$ in the dehydration limit ($\chi \rightarrow 0$) at high temperature, and fitting the conductivity measurements at intermediate temperatures to the CIC model.

6.3 Specimen preparation

The fabrication and microstructure of the protonic ceramic, BCZY, was presented in Part I. For the conductivity measurements, an extruded rod of 2NiBCZY27, 3.36 mm diameter was used. The rod was cut to a length of 4 cm. A platinum wire was wrapped around each end and twisted into a pigtail. A band of platinum paste (ESL 5524) was painted on each end and covering the wires. The platinum paste and leads were sintered at 975 °C for 15 minutes in air. The distance between electrodes was 3.45 cm, giving a resistance cross-section (A/t) of 0.0257 cm.

6.4 Test apparatus

All conductivity measurements were carried out in a sealed, 5 cm diameter alumina ceramic process tube in a horizontal tube furnace (Thermolyne 21100). Four platinum wires extended to the specimen through gas-tight feedthroughs for connection to the measuring instruments outside the furnace. Two Pt lead wires were attached to each pigtail on the specimen for 4-point measurements, and a type-K thermocouple was mounted about 1 cm from the specimen. Process gas was introduced at a flow rate of 100 ml/min about 1 cm upstream of the specimen, and an in-situ zirconia oxygen sensor tube (CoorsTek Pt-ZDY4), referenced to ambient air with a second intergral type-K thermocouple, was positioned about 5 cm downstream of the specimen to give very rapid and sensitive response to changes in local p_{O_2}. Gas flowed out of the far end of the process tube through a bubbler. Outlet flow calibration was obtained using a flow-rate bubble meter.

Moist and dry 4% H_2-bal Ar gases were prepared by splitting the flow from the gas cylinder from a common manifold through two precision needle valves. One stream passed through a chromatography drying column (CRS Big Trap) and the second stream passed through a water bubbler at room temperature. The moist and dry streams were then connected to the two inlet ports of a 2-position, 4-way ball valve. Whenever the valve position was switched, the selected output flowed into the furnace and the non-selected output exhausted into room. This way, each gas steam continued flowing at steady-state regardless of valve position, without any build up of back pressure that would otherwise occur if one of the streams was stopped while the other was flowing. With the 4-way valve configuration no pressure transients were introduced when the process gas was switched between the moist and dry condition.

6.5 Resistance measurement

The resistance of the specimen was measured using an Agilent 4338B Precision Miliohmmeter. This instrument provides 4-probe resistance measurements at a fixed frequency of 1000 Hz, which is a good frequency for this type of experiment because the frequency is high enough to eliminate noise and polarizations due to electrodes, contact potentials and thermoelectric effects while still capturing the true bulk resistance of the specimen. The 4338B generates a single pair (real and imaginary) of impedance data at each measurement. As long as the reactance value is much less than the real resistance, the measurements can be considered to be representative of the true bulk specimen resistance. Of course, the fixed frequency measurement does not afford the detailed analysis of impedance spectroscopy, such as grain vs. grain boundary conductance. A Hewlett Packard 4195A Network analyzer operating between 10 Hz and 5 MHz was also used periodically to confirm that the measurement at 1000 Hz was representative of the bulk conductance. Since the total electrode area was small, electrode impedance effects were negligible. At high temperatures, features of impedance spectra were difficult to resolve, and no significant difference between the "bulk" resistance and the resistance at 1000 Hz was observed. Above 400 ^{o}C, where most of the measurements were made, no grain boundary arcs were visible in the spectra and only a single bulk arc was present above 1000 Hz. At intermediate temperatures, where impedance spectroscopy is often useful, the arcs resulting from mixed protons and oxygen ion vacancies overlap, making attempts to resolve impedance arcs separately virtually meaningless in the range of temperatures where the partial conductivities are about the same order of magnitude. Again, fixed frequency measurements proved to be a good compromise and considerably more convenient from the standpoint of the enormous amount of data generated during temperature scans lasting several days in some cases. Because of the large ratio of cross-sectional area to length in the rod specimens, resistance values ranged from about 5000 Ω at the highest temperatures to about 150 kΩ at the lowest temperatures. With such large resistance values, there was no concern about the instrument input impedance as often plagues the measurements of thin specimens that can typically be in the milliohm range.

Resistance measurements, thermocouple readings, and O_2 sensor voltages were continuously logged using a data acquisition computer running in the LabView environment. The complete test apparatus is shown in Figure 3.

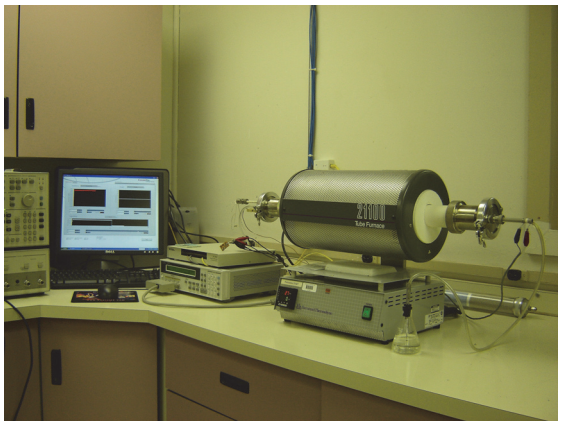

Fig. 3. Conductivity test apparatus

6.6 pH_2O determination

The extent of hydration, as determined by Eq. 10, depends strongly on the water vapour pressure at the surface of the specimen. A common mistake that is made in experiments for evaluating ceramic proton conductors is to assume that the p_{H_2O} inside the processes vessel is the same as the saturated pressure at the bubbler used to moisten the process gas. Since both hydrogen and water vapour are exchanged with the ceramic specimen, it is not correct to assume that p_{H_2O} is invariant, and it needs to be measured along with temperature and conductivity. This can be done with an external dew point monitor, but also with an in-situ oxygen sensor, which is mounted in close proximity to the test specimen. The oxygen pressure is determined from the Nernst voltage by,

$$P_{O_2} = P_{O_2,ref} \exp\left(-\frac{4FV_N}{RT}\right) \tag{27}$$

where F is Faraday's constant, R is the universal gas constant and T is absolute temperature. The reference oxygen pressure in this case is ambient air, 0.2095 atm, adjusted for Salt Lake City, Utah, (0.858atm/atm), or 0.180 atm. The ratio of water vapour pressure to hydrogen pressure is determined by the oxygen sensor,

$$\frac{P_{H_2O}}{P_{H_2}} = K_w\sqrt{P_{O_2}} \tag{28}$$

where K_w is the temperature-dependent equilibrium constant for water formation evaluated by the empirical relationship (JANAF),

$$\begin{aligned}\Delta G_f^o = -RT\ln K_w = (&-57.031 + 2.799x10^{-3}T\ln T \\ &- 0.576x10^{-6}T^2 + 1.650T^{-1} - 7.798x10^{-3}T)x4.1868\ kJ/mol\end{aligned} \tag{29}$$

In this experiment, the process gas used was 4.2% H_2-bal Ar. The moist gas was prepared by bubbling in water at 21 °C, providing a saturated water pressure of 0.025/0.858 = 0.029 atm. Since the mole fraction of argon is invariant, the known pressures of Ar, H_2O, and H_2 in the process gas permit the calculation of the sum of p_{H_2O} and p_{H_2} as,

$$p_{H_2O} + p_{H_2} = (0.025 + 0.042\times 0.858\times(1-0.025)) = 0.060\,atm \tag{30}$$

Eq. 28 and 30 may be solved simultaneously to give,

$$p_{H_2O} = \frac{0.060\,K_w\sqrt{p_{O_2}}}{1 + K_w\sqrt{p_{O_2}}} \tag{31}$$

which relates the local water vapour pressure to the measured oxygen pressure. For dry gas, the prefactor in the numerator is just 0.042 x 0.858 = 0.036. The calculated p_{H_2O} for moist and dry 4.2% H_2-bal Ar as a function of temperature are plotted in Figure 4. Also plotted are the calibration curves for the moist and dry gas without any specimen in the process vessel. It is seen that the water vapour pressure is considerably higher when the specimen is included.

In the case of the calibration runs, the water vapour pressure is the same as expected from the prepared inlet gas, but with the specimen in place, the p_{H_2O} is about 50% greater for the moist case and almost 10 times greater for the dry case.

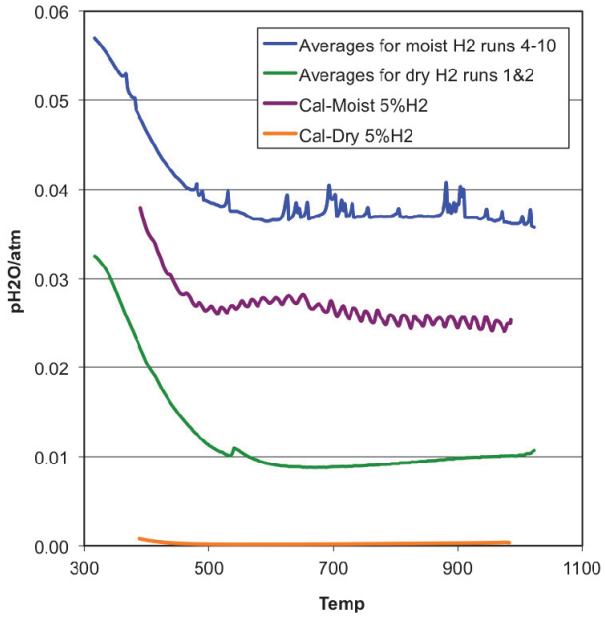

Fig. 4. Water vapor pressure for moist and dry 4.2% H_2-bal Ar process gas with specimen, and calibration without specimen, as calculated from the Nernst voltage of the in-situ oxygen sensor.

6.7 Isobaric conductivity measurements

Isobaric conductivity measurement requires that steady-state equilibrium of the specimen be maintained with the surrounding atmosphere so that the concentration profile of the mobile ionic species in the specimen is completely uniform. Even with the relatively thin cross-section of our rod specimens, this presented a challenge. Rapid equilibration above about 800 ^oC is easily achieved, but below this temperature, where most of the hydration and dehydration actually takes place, equilibration times become progressively longer because the self-diffusivities of protons and oxygen ion vacancies decrease exponentially. If the rate of change of temperature is too great, the measured conductivity does not reflect the true equilibrium defect concentration profile. This is typically observed as hysteresis in the data between increasing and decreasing temperature measurements. For these experiments impedance data for analysis was obtained under isobaric conditions upon decreasing temperature from 1030 ^oC to 250 ^oC at 0.5 ^oC per minute followed by rapid heating at 5 ^oC to the starting temperature. The experiment was repeated ten times in moist hydrogen to ensure repeatability and the absence of hysteresis effects. This extreme cyclic testing confirms the mechanical and chemical integrity of 2NiBCZY27 prepared from barium sulphate instead of barium carbonate (see Part I for details) since practically no change in conductivity was observed. Figure 5 shows an Arrhenius conductivity plot of the specimen measured in both moist and dry 4.2%H_2/bal Ar.

The curve for moist hydrogen represents the average for the final seven separate runs, and the curve for dry hydrogen is for the average of two runs.

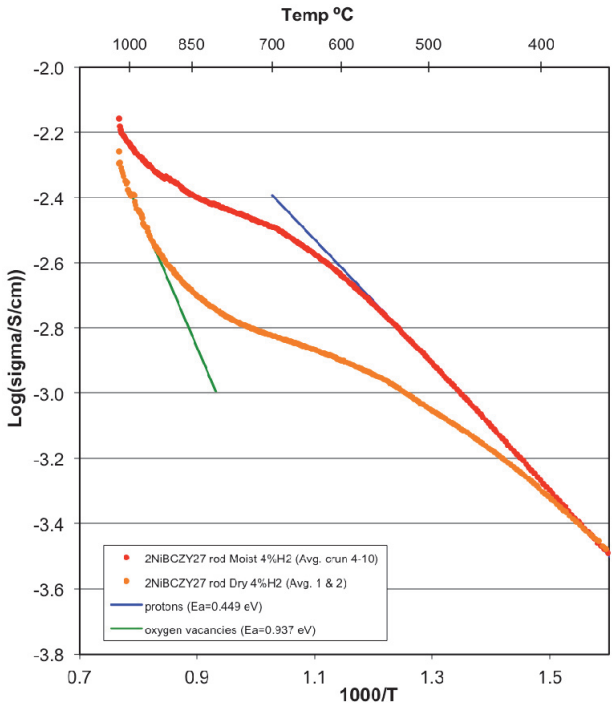

Fig. 5. Arrhenius plot of log(base 10) conductivity vs. reciprocal temperature. Upper curve is for moist and lower curve is for dry 4.2% H_2.

The curves exhibit the characteristic hydration/dehydration "crook". Below 500 °C in moist hydrogen, the specimen was assumed to be hydrated at the hydration limit of χ = 1. Conductivity in this region has been attributed exclusively to protons, and the slope and intercept are indicated by a linear extension. At the highest temperature obtained in moist hydrogen, the specimen still retained substantial hydration, however, in dry hydrogen, the specimen was assumed fully dehydrated (χ = 0) with conduction attributed exclusively to oxygen ion vacancies. The linear extension in this region is also shown. At the two extremes it is possible to determine the species self diffusivities using conventional Arrhenius analysis where the slope times 1000 k_B gives E_a and the y-axis intercept give the log term on the right containing the diffusion pre-exponential.

$$\ln(\sigma_{OH}T) = -\frac{E_{a,OH}}{kT} + \ln(\beta D^*_{OH}) \tag{32}$$

$$\ln(\sigma_{Vo}T) = -\frac{E_{a,Vo}}{kT} + \ln(2\beta D^*_{Vo}) \tag{33}$$

For BCZY27, the constant β evaluates to 2.403x10^6 [K.s/Ω.cm^3]. Species self-diffusivities are presented in Table 1.

species	D^* (cm/s)	E_a (eV)
Protons	3.45×10^{-4}	0.449
Oxygen ion vacancies	5.65×10^{-3}	0.937

Table 1. Measured transport parameters for protons and oxygen ion vacancies in NiBCZY27

Figure 5 highlights a common misinterpretation of Arrhenius plots in the literature. The foundation of Arrhenius analysis is based on exponentially activated diffusivity. Since, from the Nernst-Einstein equation, conductivity is proportional to the product of diffusivity and concentration, diffusivity can only be correlated with conductivity data when the species concentration is constant. The slope of an Arrhenius conductivity curve cannot be interpreted as the activation energy when the species concentrations are changing. This may be clearly seen from Eq. 16, where $\ln(\sigma T)$ only has a meaningful slope when χ is either 0 or 1. The assumption of fixed defect concentrations in single-species ionic conductors is (usually) valid, but this is not the case with co-ionic conductors during hydration and dehydration, where concentrations of defects depend on temperature. Arrhenius analysis is only strictly valid in co-ionic conductors in the limits of total hydration and dehydration.

6.8 Data fitting to CIC model

With the species self-diffusivities determined in the previous section, it was possible to fit the total conductivity data over the intervening temperature range as a function of χ. This was done using the conductivity and in-situ water vapour measurements in moist hydrogen. A least-squares fit for Eq. 16 was obtained for hydration enthalpy and entropy as the two fitting parameters, which were -120.6 kJ/mol and -110.6 J/mol.K, respectively. This enthalpy value is slightly less negative than the value of -125 ± 2 kJ/mol obtained by TG-DSC recently reported by Ricote (Ricote, et al. 2011), and in line with the empirical curve proposed by Norby based on electronegativity of A and B-sites (Norby, 2009). The fitted entropy is close to the value of -120 J/mol K predicted by Norby based on the entropy of vaporization of water. This is by no means an assertion that the present fitted values are correct. It mostly draws attention to the difficulty in making this measurement with confidence. The scatter in reported values for enthalpy and entropy of hydration that has appeared in the literature over the years is a matter for concern. Fitting of conductivity data to give reasonable values, as reported by us, is encouraging, but may be just a happy accident. Norby's group at the University of Oslo has been making progress with this measurement lately, but the matter is far from resolved.

The hydration enthalpy and entropy values obtained by fitting the moist hydrogen conductivity data were used in an attempt to fit the dry hydrogen conductivity data, as shown in Figure 6. It is observed that, although the curve has the right qualitative features, the CIC model does not fit the dry hydrogen data very well. The upper green curve is for the CIC model prediction using the measured water vapour pressure, as presented in Figure 4. The CIC model considerably over-estimates the conductivity throughout the hydration-dehydration region. The lower blue curve is the CIC prediction using fixed p_{H_2O} = 0.0015 atm – in line with the dry hydrogen entering the process vessel. The fit is slightly better, but does not answer the obvious question why the conductivity does not reflect the measured p_{H_2O} near the specimen. Apparently defect reactions take place at low extent of hydration that compete with Wagner hydration, causing the CIC model to break down.

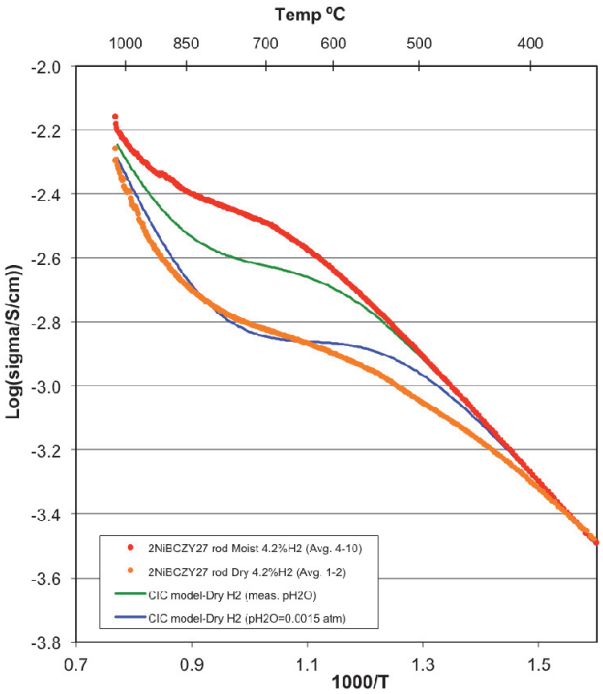

Fig. 6. Moist hydrogen data fit (red curve) with ΔH = -120.6 kJ/mol and ΔS = -110.6 J/mol.K. Failure of CIC model in dry hydrogen (orange). Green curve represents predicted values at the measured *p*H2O , and the blue curve, the predicted values for dry hydrogen (pH_2O = 0.0015 atm)

The complete conductivity plot, based on all the fitted parameters, is shown in Fig. 7. The decomposition of total conductivity into partial conductivities of protons and oxygen ion vacancies is accomplished using the Co-Ionic Conductivity model. The proton transference number refers to the right-hand axis. The figure captures the important transport features of the co-ionic ensemble. Proton conductivity reaches a maximum at 775 °C. This maximum in proton conductivity is characteristic of dehydration at higher temperatures. The peak proton conductivity for BCZY27 is 3.3 mS/cm. This relatively low conductivity value is consistent with values reported in the literature in the absence of hole conduction. Oxygen ion vacancy conductivity is greater than proton conductivity above 1000 °C, but at the peak in proton conductivity, is already about one order of magnitude lower. Oxygen ion vacancy conductivity bows downward as the concentration of vacancies decreases with decreasing temperature, and below about 500 °C the "dog leg" appears (not shown on the chart) where the residual vacancy concentration become frozen in at some small value. From the partial conductivities, the protonic transference number, t_p, was determined. At the peak in proton conductivity, t_p is only about 0.9, meaning that considerable ambipolar steam permeation is expected to occur at 740 °C. At 600 °C protonic conductivity is only slightly reduced, but t_p is 0.98. Any process that requires high selectivity for proton transport must, therefore, operate below 600 °C

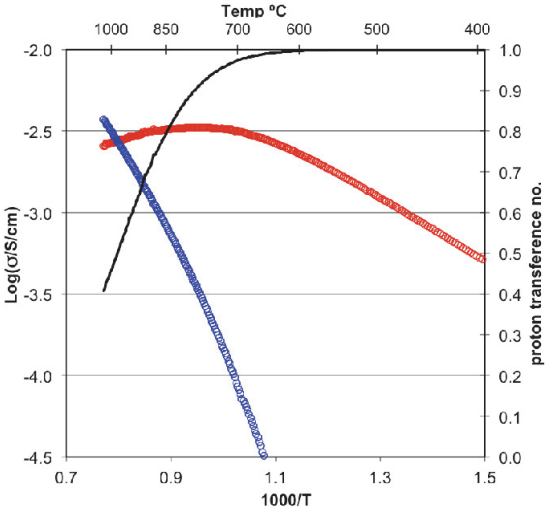

Fig. 7. Isobaric BCZY27 conductivity in moist 4.2%H_2/bal Ar based on CIC model. Partial conductivities are for protons (red) and oxygen vacancies (blue). Protonic transference (black) refers to right-hand axis.

7. Conclusions

Wagner hydration and Kreuer's transport models unambiguously predict that ambipolar, co-ionic conduction takes place in protonic ceramics. This has been well demonstrated by isobaric dehydration weight loss and isotope transport experiments. The co-ionic conduction model presented above is a logical extension of this transport theory that provides insight into the qualitative features of the total conductivity in Arrhenius plots that have appeared in the literature over the years – specifically, the hydration "crook" that is characteristic of these materials at intermediate temperatures. This is where proton conductivity decreases with increasing temperature due to dehydration while oxygen ion vacancy conductivity increases, both in a way that is not very intuitive without the aid of the idea of partial conductivities of the two ionic species that includes a term for the degree of hydration. An attempt has been made to justify the model quantitatively by applying it to empirical conductivity data. The CIC model with all of its underlying assumptions explains the conductivity behaviour quite well in moist hydrogen, but breaks down in dry hydrogen for reasons yet to be determined. Knowing the partial conductivities of protons and oxygen ion vacancies is a prerequisite for predicting species fluxes, which has important implications for the practical uses of these materials in steam permeable membranes, fuel cells, electrolyzers, membrane reactors, and the like. A major challenge going forward is to understand what controls hydration enthalpy and entropy and to learn how to tailor these values in practical materials for specific applications, and to gain a better understanding of the role of electronic defects.

8. Acknowledgments

Special thanks to Dr. Ryan O'Hayre at the Colorado School of Mines for help in preparing the material in Part II. Also, special thanks to Dr. Sandrine Ricote at DTU/Riso in Denmark for valuable input.

9. References

Coors, W.G. (2004). Steam reforming and water–gas shift by steam permeation in protonic ceramic fuel cells. J. Electrochem. Soc., Vol.151, No.7, pp.A994-A997

Coors, W.G. and Swartzlander, R. (2005). Partial conductivity measurements in $BaCe_{0.9}Y_{0.1}O_{3-d}$ by impedance spectroscopy. Proceedings of the 26th Riso International Symposium on Materials Science: Solid State Electrochemistry, Denmark, Ed. Linderoth, et.al. pp.185-196

Coors, W.G. (2007). Protonic ceramic steam-permeable membranes. *Solid State Ionics,* Vol.178, pp.481-485

Haugsrug, R. and Norby, T. (2006). Proton conduction in rare-earth ortho-niobates and ortho-tantalates. *Nature Materials, Letters.* Vol.5, pp.193-196

Kreuer, K.-D. (1999). Aspects of the formation and mobility of protonic charge carriers and the stability of perovskite-type oxides. *Solid State Ionics*, Vol.125, pp.285-302

Kreuer, K.-D. (2003). Proton-conducting oxides. *Annu. Rev. Mater. Rev.,* Vol.33, pp.333-359

Maier, J. (2004) *Physical Chemistry of Ionic Materials – Ions and Electrons in Solids*, John Wiley & Sons, Ltd. ISBN 0-470-87076-1, England

Norby, T. (1988). EMF method determination of conductivity contributions from protons and other foreign ions in oxides. *Solid State Ionics* Vol.28-30, pp.1586-1591

Norby, T. (2009). Ch. 11: Proton Conductivity in Perovskite Oxides, In: *Fuel Cells and Hydrogen Energy/ Perovskite Oxide for Solid Oxide Fuel Cells*, T. Ishihara, Ed., Springer Science+Business Media, LLC, US, pp.217-241

Ricote, S.; Bonanos, N.; Wang, H.J.; Haugsrud, R. (2011). Conductivity, transport number measurements and hydration thermodynamics of $BaCe_{0.2}Zr_{0.7}Y_{(0.1-x)}Ni_xO_{(3-d)}$. *Solid State Ionics,* Vol.185, pp.11-17

Sanders, M. and O'Hayre, R. (2008). Co-ionic materials for steam permeation: progress report. Colorado School of Mines, 10/22/2008

Sanders, M.; Elangovan, S.; Coors, W.G.; & O'Hayre, R. (2009). Results of steam flux measurements in BZY20," 17th International Conference on Solid State Ionics, Toronto, Canada, poster abstract, p.249

Sanders, M. (2009). Examining multi-species transport in BZY20 using water isotope permeation. Masters Thesis, Colorado School of Mines

Sanders, M. and O'Hayre, R., (2010). Development of a multi-species transport space theory and its application to permeation behavior in proton-conducting doped perovskites. *J. Mater. Chem.*, Vol.20, pp.6271-6281

Schober, T and Coors, W.G. (2005). Entry and exit of water vapor in bulk ceramic proton conductors. *Solid State Ionics*, Vol.176, pp.357-362

Sutija, D.; Norby, T.; and Bjornbom, P. (1995). Transport number determination by the concentration-cell/open-circuit voltage method for oxides with mixed electronic, ionic and protonic conductivity. *Solid State Ionics*, Vol.77, p167-174

Tan, X.; Liu, S.; Li, K.; & Hughes, R. (2000). Theoretical analysis of ion permeation through mixed conducting membranes and its application to dehydrogenation reactions. *Solid State Ionics*, Vol.138, pp.149-159

Wagner, C., (1968). *Ber. Bungsenges. Phys. Chem.,* Vol.70, p.781

Yoo, H-I; Yeon, J.; & Kim, J. (2009). Mass relaxation vs. electrical conductivity relaxation of a proton conducting oxide upon hydration and dehydration. *Solid State Ionics*, Vol.180, pp. 1443-1447